The Reactive Stabilisation of Al-Zn-X Foams via the Formation of a Transient Liquid Phase Using the Powder Metallurgy Approach

Maxime Lafrance

Department of Mining and Materials Engineering
McGill University, Montréal, Québec

April 2012

A Thesis submitted to McGill University in partial fulfillment of the requirements of the degree of Doctor of Philosophy

This page is intentionally left blank

Abstract

During the past few decades, aluminum foam research has focused on the improvement of properties. These properties include pore structure and process reproducibility. High energy absorption capacity, lightweight and high stiffness to weight ratio are some of the properties that make these foams desirable for a number of diverse applications. The use of a transient liquid phase and melting point depressant was studied in order to improve aluminum foam manufactured through the powder metallurgy process and to create reactive Stabilisation. The transient liquid phase reacts with aluminum and helps encapsulate higher levels of hydrogen, simultaneously reducing the difference between the melting point of the alloy and the gas release temperature of the blowing agent (TiH_2). A large difference is known to adversely affect foam properties.

The study of pure aluminum foam formation was undertaken to understand the basic foaming mechanisms related to crack formations under in-situ conditions. Elemental zinc powder at various concentrations (Al-10wt%Zn, Al-33wt%Zn and Al-50wt%Zn) was added to produce a transient liquid phase. Subsequently, an Al-12wt%Si pre-alloyed powder was added to the Al-Zn mixture in order to further reduce the melting point of the alloy and to increase the amount of transient liquid phase available (Al-3.59wtSi-9.6%Zn and Al-2.4wt%Si-9.7wt%Zn). The mechanical properties of each system at optimal foaming conditions were assessed and compared.

It was determined that pure aluminum foam crack formation could be suppressed at higher heating rates, improving the structure through the nucleation of uniform pores. The Al-10wt%Zn foams generated superior pore properties, post maximum expansion stability and mechanical properties at lower temperatures, compared to pure aluminum. The Al-Si-Zn foams revealed remarkable stability and pore

structure at very low temperatures (640 to 660˚C). Overall, the Al-10wt%Zn and Al-3.59wt%Si-9.6wt%Zn foams offer superior properties compared to pure aluminum.

Résumé

Depuis ses débuts, beaucoup de progrès a été réalisé concernant les mousses d'aluminium en termes d'améliorations de propriétées au niveau du procédé de production. Ces propriétées inclus les améliorations de la stabilité, reproductibilité et l'homogénéité. Les mousses métalliques ont plusieurs avantages leurs permettant d'être versatiles par rapport à de nombreuses applications. Ils incluent leurs capacités élevées d'absorption d'énergie, leurs faibles densités et leurs rigidités. Dans le cas de la production par métallurgie des poudres, certains de ces problèmes sont encore réels. Les résultats montrent qu'en utilisant un mélange précis de poudre élémentaire et allié, une phase liquide transitoire est créée de sorte à produire une stabilisation réactive des mousses. En utilisant des alliages contenant du silicium et du zinc, la température de moussage peut être grandement réduite. Ceci permet donc de réduire l'écart de température entre le point de fusion de l'alliage et la température de décomposition de l'hydrure de titane (TiH_2).

L'étude du procédé des métallurgies des poudres a eu lieu en utilisant de l'aluminium pur en but de comprendre la formation des fissures (in-situ) dans les précurseurs durant les stages initiaux de moussage. Des concentrations variées de poudre élémentaire de zinc ont été étudiées (A l-10wt%Zn, Al-33wt%Zn, Al-50wt%Zn) en but de produire cette phase liquide transitoire qui a pu être observée in-situ. Par la suite, des poudres pré-alliées Al-12wt%Si ont été ajoutés pour réduire davantage le point de fusion et augmenter le niveau de phase transitoire liquide (Al-3.59wt%Si-9.6%Zn, Al-2.4wt%Si-9.7wt%Zn). Les propriétés mécaniques de chaque système ont aussi été évaluées en but de comparaison.

Il a été déterminé que la fissuration observée dans les mousses d'aluminium pur peut être supprimé à l'aide d'une phase transitoire dû à une nucléation des pores uniformes, améliorent les propriétées globale de la mousse. De plus une stabilité

remarquable de la mousse suite à l'expansion peut être atteinte, tout en démontrant une homogénéité des pores et une stabilité de la mousse supérieure à l'aluminium pur.

Acknowledgements

I would like to express my sincere gratitude to Professor Robin A.L. Drew for giving me the opportunity to work with him and his research group. I would also like to thank my co-supervisor Professor Kristian Waters for helping me.

I would like to acknowledge Rio Tinto Alcan for awarding me with this generous graduate fellowship. I also want to thank the Materials Engineering Department and McGill University for the numerous bursaries I received over the course of my studies. I would like to acknowledge General Motors, FQRNT and NSERC for financial support for the project.

I would like to sincerely thank Barbara Hanley for all that she has done for me over the last few years. She is the one who is always in a good mood and always there to listen and help with anything, definitively improving the graduate student experience.

Finally, I would like to thank all my friends, family and co-workers for helping make the stressful graduate experience better. I do not think I could have made it without you although I cannot name you all. A special thanks goes out to Paula, Lydia, Phuong, Shamik, Luiz, Vince, Mom and Dad for listening to my numerous rants over the past few years and always helping out, again I could not have made it without all of you. Thanks to Farzad, Paula and Lydia who helped me start my project on the right foot, always helping out and being good friends. I would also like to thank Pierre Vermette and Robert Paquette for their valuable help and expertise.

This page is intentionally left blank

Table of Contents

This page is intentionally left blank

Table of Figures

This page is intentionally left blank

List of Tables

1 Introduction

Metallic foams have been around for at least 40 years but a recent resurgence in interest has fuelled research into the porous media fabrication, and are manufactured in various shapes and forms. Several properties of these types of materials exist making them favorable in a vast array of industries. These include high stiffness to weight ratio for structural components, and most of all their ability to absorb large quantities of energy when subjected to impact (blast mitigation) [2, 3]. Aluminum being a lightweight metal by nature, has proven to be a good candidate for use as metallic foam. Although mass production has become feasible, process improvement is still required. In recent years significant research has been dedicated to the production of aluminum foam in order to improve its quality, notably the pore homogeneity and the reproducibility of the process itself. As new potential applications emerge with respect to aluminum foams such as their use for blast mitigation panels, research is still required in order to obtain the desired properties. Several foam manufacturing techniques are used today such as the melt gas injection and powder metallurgy process being the focus of this research. The powder metallurgy manufacturing route offers the possibility of creating foam having a near net-shape without the need for the addition of abrasive stabilizing particles as in other commercialized techniques [4, 5].

The most commonly used blowing agent for aluminum-based foam production today is TiH_2, which is known to decompose at temperatures lower than the melting point of pure aluminum [6, 7]. Reported onset hydrogen release temperatures for TiH_2 start as low as 380 °C and going up to over 500 °C depending on powder characteristics, characterization technique, and treatment [1, 6-8]. The existing disparity between hydrogen dissociation of TiH_2 and the melting point of pure aluminum, results in poor foaming efficiency. Therefore, if the two temperatures can be correlated, a foam having superior properties (pore

homogeneity and reproducibility) can be obtained [8]. It has been shown that the release of hydrogen within an aluminum based foam compact having not yet reached the fusion temperature can lead to crack formations which cause significant hydrogen loss and poor expansion [9-11]. In order to resolve this dilemma, the aluminum melting temperature can be reduced by alloying or by modifying the gas release temperature of the blowing agent, augmented by post manufacturing treatments.

The goal of this research was to develop a tailored aluminum alloy foaming system to improve efficiency through the powder metallurgical manufacturing route. An alloy capable of simultaneously reducing the melting point of aluminum while generating a transient liquid phase would help encapsulate hydrogen at the early foaming stages and suppress fissure formations which are responsible for the reduced efficiency. In addition, an alloy with favorable physical properties such as viscosity and surface tension would help enhance foam stability.

The first objective was to analyze pure aluminum foam formation through *in-situ* confocal microscopy supported by differential scanning calorimetry and foam expansion curves correlated with sample temperature measurements. From this, the crack forming mechanism could be understood serving as a benchmark system for improvements. The second and main objective of this thesis focused on the development of a transient liquid phase(s) to create a uniform nucleation of the pores. A low melting transient liquid phase based on elemental zinc melting at temperatures near the hydrogen dissociation temperature of TiH_2 produced uniform nucleation of the pores suppressing fissure formations. Lastly, favorable alloy physical properties were shown to enhance post maximum expansion stability yielding improved pore characteristics.

The thesis is divided into several sections starting with Chapter 2 which presents a compilation of various references which has been written in order to provide the

most up to date information in the world of foaming. In Chapter 3, specific research objectives along with a detailed experimental plan are outlined. The experimental procedures employed in this research are covered thoroughly in Chapter 4, including characterization techniques and mechanical properties.

The results and discussions are divided into five chapters, pure aluminum foams, solid state diffusion in compacts, Al-Zn foams, Al-Si-Zn foams and mechanical properties. Chapter 5 is concerned with the foaming of pure aluminum as the base composition for improvement and benchmarking. Foaming stages, including crack forming temperatures and expansion are studied through various characterization techniques. Diffusion of powders (zinc and Al-Si) during the compaction process are studied in Chapter 6. The diffusion of elemental as well as pre-alloyed powders is analyzed to assess any potentially negative impacts on foaming. Al-Zn foams are developed in Chapter 7 in the context of forming a transient liquid phase to increase foaming efficiency and to suppress the formation of the crack network otherwise formed in pure aluminum. The mechanisms surrounding the improved foam are discussed and supported by confocal microscopy along with foaming curves and micrographs. The addition of an Al-Si pre-alloyed powder to the Al-Zn based system is covered in Chapter 8. The use of Al-Si pre-alloyed powder is used as a melting point depressant and is discussed thoroughly in the context of both pure aluminum and Al-Zn foams.

The mechanical properties based on uni-axial compression tests are briefly discussed in Chapter 9. A comparison between the different alloys developed in Chapter 5, Chapter 7 and Chapter 8 is drawn highlighting the benefits of using some of the developed alloy. Finally, conclusions summarizing the findings are presented in Chapter 10. The contributions to original knowledge are outlined in Chapter 11 and lastly, the future work with respect to the developed alloy systems is covered in Chapter 12.

This page is intentionally left blank

2 Literature Review

2.1 Foams and Cellular Solids

Porous low density cellular liquids and solids are present in everyday life; they are created both naturally and synthetically. Many different types of porous media exist, each having distinct properties and applications in an almost endless array of fields. Cellular solids or often referred to as foams, can be defined as a series of cells packed together in an interconnected network. The parent material of these foams will ultimately dictate their properties along with the nature of the cellular structure [12]. Man-made foams are widely used today in the form of soaps, ice cream, packaging, shaving cream, cleaning agents, beverages and in the mineral processing industry. Naturally occurring foams are also created in various forms and are most often anisotropic with elongated cells such as: wood, sponge, bee honeycomb, coral and cancellous bones [13, 14].

Examples of common applications of foams will be presented below. In the culinary field for example, foams are used to make deserts such as meringue, where egg white being rich in protein in conjunction with sugar or other additives is beaten or whipped into a foamy desert. An important industrial application of foams is for mineral recovery in flotation cells where air bubbles are used to concentrate valuable minerals for extraction. Another remarkable application of foam is for fire-fighting where it is used to suppress one or more of the three conditions for a fire: fuel, oxygen and heat. A blanket of foam over the fire isolates oxygen sources, cools the fuel and traps fuel vapours at the foam interface. Today, polymer foams are being widely exploited and are found in products such as disposable coffee cups, packaging material, to components in automotive car bumpers. The majority of man made solid foams are created from the liquid phase and quickly solidified into the desired structure [14].

The focus of this thesis is on the development of a certain type of less known cellular solid: metallic foam. Metallic foams are a relatively new type of material, and they are manufactured in various shapes and forms. Although metallic foams have been around since the 1960's and 1970's, only recently have new developments in manufacturing routes made them viable in terms of cost effectiveness which in turn has regenerated interest in the field and stimulated research [15].

In recent years, research on closed cell aluminum foams has taken off in order to improve its properties. This rise in interest has mostly been fuelled by the aluminum's elemental properties such as its low density, low melting point and the relative ease of foaming in comparison to other metals such as iron (or steel). Aluminum also has a relatively low melting point which coincides with the gas release temperature of some cost effective blowing agents [14]. This thesis is concerned with the production and improvement of closed cell aluminum metal foams manufactured via the powder metallurgy (PM) route.

Several properties of metallic foams exist, making them favorable in a vast array of industries. These properties include high stiffness to weight ratio for structural applications, low thermal and electrical conductivity and most of all their ability to absorb a large quantity of energy when subjected to high impact in comparison with the parent material. Metallic foam energy absorption becomes especially interesting for military blast mitigating applications for armor and vehicle crash boxes. The implications related to energy absorption will be discussed in the mechanical properties Section 2.6. Several polymer foams are elastic by nature and can recover their original shape after loading. In contrast, metallic foam is ductile with only a small level of recoverable energy and deforms mostly plastically. The main downside in producing metallic foams, unlike polymer foams which are highly commercialized today, is the lack of good porosity control, reproducibility and homogeneity of the pores as a result of the

manufacturing process control. Some of the factors responsible for these difficulties are related with the fact that these foams are created at high temperatures, are opaque and are highly reactive, making it a challenge to control these process parameters. For those reasons metallic foam are currently the subject of significant research [14, 16].

Two main types of cellular solids exist, the open and closed cell type. The open cell type can be seen in the Figure 2-1a below as a network of filaments whereby a fluid can freely pass through much like a sponge. This type of foam is commonly used as filters in a variety of applications [14]. On the other hand, the closed cell type which will be the focus of this study consists of entrapped gaseous bubbles surrounded by a solid/liquid matrix as shown in Figure 2-1b.

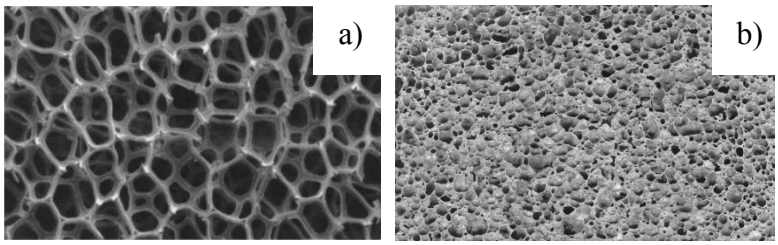

Figure 2-1: a) Open cell foam, b) Closed cell foam [14]

Closed cell foams can further be distinguished as wet or dry foams. The dry foams have thin cell walls and Plateau borders where the pores are polyhedral in shape, such as bubbles generated by household dish soap. When the foam has a higher liquid concentration ratio it is considered wet foam. The physical difference from dry foam is that it has thicker cell walls and Plateau borders making the bubbles more spherical in shape [12].

When looking at porosity levels of metallic foams, the most common way to assess this property is by comparing its density to the parent material. This is termed the relative density which is simply the ratio of the foam density to that of the base material [13]. This can be characterized as:

$$\textbf{Relative density} = \frac{\rho^*}{\rho^s} \qquad \textbf{Equation 2-1}$$

Where ρ^S (g cm^{-3}) is the parent material density and ρ^* (g cm^{-3}) is the cellular solid density. Foams can also be characterized in terms of percent porosity levels which is shown below:

$$\textbf{Porosity}\ \% = \frac{\rho - \rho_{foam}}{\rho} \cdot 100 \qquad \textbf{Equation 2-2}$$

In the present case the foam density is evaluated via the level of foam expansion in relation to the base material. The reason for this is that as the metallic foam composition is changed, and it is therefore easier to compare levels of expansions in reference to the base alloy and to look at the efficiency of the blowing agent (powder metallurgy method) [13].

As discussed above, relative density is an important factor in cellular material properties. Although it is important, the most crucial factor is the cell structure morphology itself such as cell size, and distribution. For example a homogeneous cell structure will behave quite differently under loading conditions than one in which the cells are elongated or flattened. It can then be concluded that the nature of the cell structure is as important as the cell size itself when it comes to properties. Several studies over the last century have been conducted in an effort to describe and understand the most efficient foam cell geometry in terms of minimizing surface area per volume [13].

2.2 Metallic Foam and its Manufacturing Routes

Metal foam manufacturing processes vary quite significantly. Various methods have been developed over the years and/or are in the process of being developed. Metal foam production can be divided into four main classes: Vapor phase

deposition, electro deposition, liquid state processing (from liquid metals) and solid state processing (metallic powders). These can be further divided into subclasses as seen in Figure 2-2 [14, 16]. The focus of this research will evolve around the improvement of the powder metallurgy technique.

Metal foam competes against a broad spectrum of other materials such as expensive honeycomb structures and even wood. Therefore it is always a requirement to assess production costs and scale of production based on a specific application [2, 14, 17]. Although there exists several ways to produce metal foams, significant work is being done on improving quality in general [16].

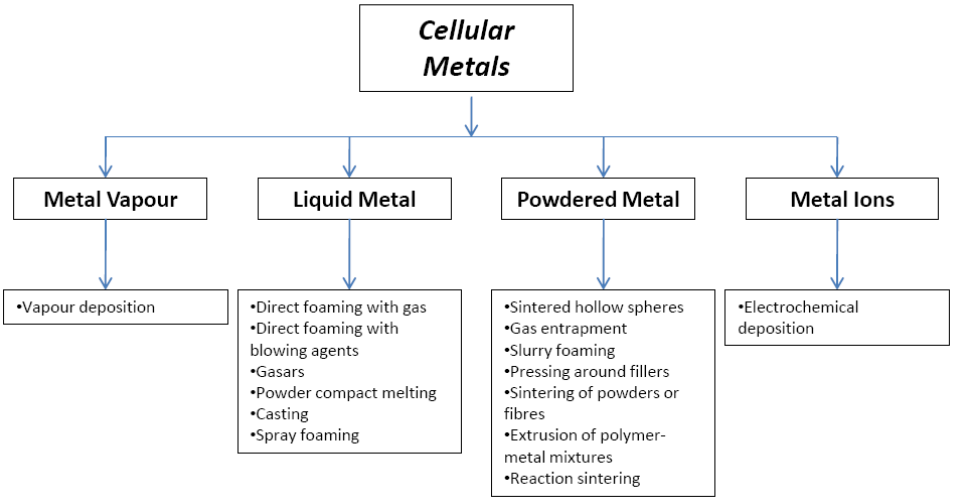

Figure 2-2: Classes of metallic foam production and methods [14]

2.2.1 Powder Metallurgy Foaming

The powder metallurgy process is an interesting method which is currently gaining momentum in the foam production industry and is also the focus of significant research in the field as a substitute or an alternative to the melt gas injection process. Although it can be produced quite easily in theory, stability and homogeneity problems have been plaguing this process. The benefit of this process is its versatility where several metals can easily be foamed such as zinc,

aluminum, tin and lead. Furthermore, the produced foam can take the shape of the mold making it easy to produce intricate parts without the need for extensive machining operations [14, 16, 18].

The process involves mixing metal powders along with a specific blowing agent, dependent upon the alloy used [14]. Once powders are mixed together, a hot or cold compaction process is performed in order to have a near theoretical density precursor , to ensure minimal open porosity within the compact [2, 14]. The hot or cold compaction process can take place via different routes such as through uni-axial pressing, rolling or extrusion [6]. Once the dense compact precursor is produced, it is heated to semi-solid or fully liquid temperatures where the gas from the blowing agent is released within the melted/melting compact creating the foam. Figure 2-3 shows the steps involved in manufacturing aluminum PM foams.

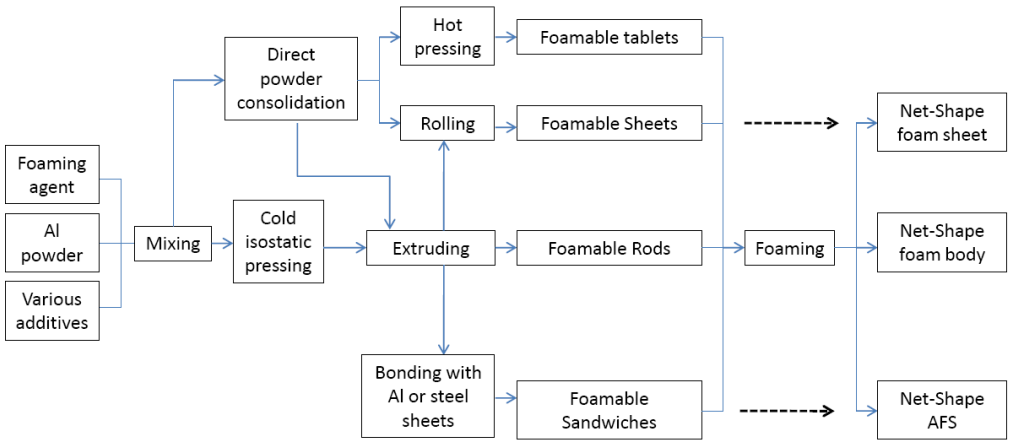

Figure 2-3: Powder metallurgy foaming process [16]

With this method, it is also possible to produce sandwich type panels as well. For example, foaming of a precursor between two sheets of the same or different metals can produce a composite sandwich panel. This can increase the strength of the foam and can be used for diverse composite structural applications such as for blast mitigation applications and sounds absorption. Such types of panels are

produced by Alulight in Austria [14, 19]. Other possibilities include filling tube interiors and parts with foam starting with precursors. A chart showing the advantages and disadvantages of the PM foaming process is given in Figure 2-4 [16].

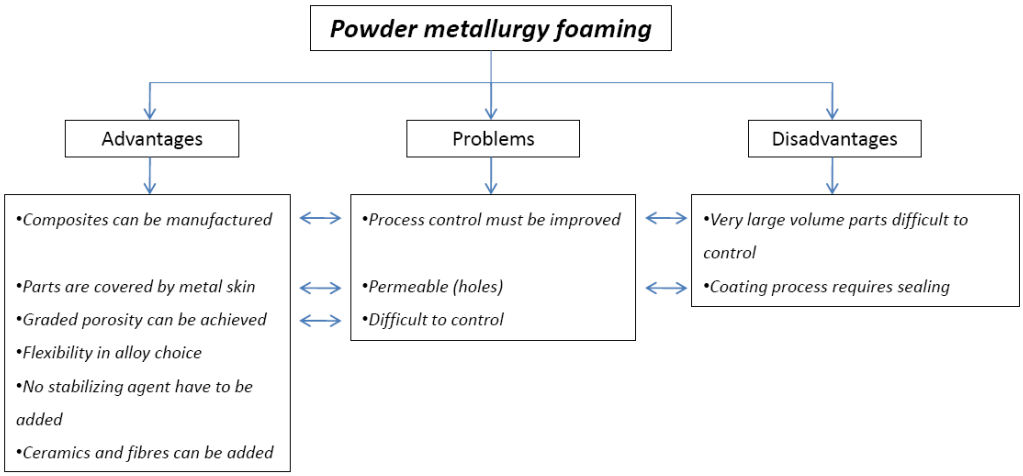

Figure 2-4: Advantages and disadvantages of the powder metallurgy foaming process [16]

The most commonly used blowing agent for creating zinc and aluminum foam is titanium hydride (TiH_2) which is known to decompose at temperatures ranging from 380 ˚C up to about 600˚C. This release temperature range happens to be below the melting point of pure aluminum. Since it is the most commonly available blowing agent, it is used in this project. The reason why TiH_2 is used for aluminum is because it is the blowing agent which releases its gas nearest to the melting point of aluminum [6-8]. Although the gas release temperature range of TiH_2 is quite broad, it can be subjected to diverse heat treatments to improve its gas release temperature pushing it closer to the aluminum melting point. Several defects can occur in the final foam structure as a result of this temperature mismatch if good control of the production parameters are not insured. These defects include drainage, poor cell distribution and non-uniform pores. For example if the compacted powders used to form a complex part are not compacted properly at some locations, the foam may have localized defects at the

low compaction zones resulting in cracking and poor cell homogeneity of the final structure.

2.2.1.1 Powder Compaction

Hot pressing, extrusion or powder rolling is an important parameter in order to achieve good compact density using the PM route. This step evidently influences the final outcome of the foam. The role of hot compaction is to reduce the amount of residual porosity present inside the compact. Hot compaction can also be used as a sintering stage before foaming. Generally, powders are cold pressed prior to being hot compacted, this step is somewhat redundant but helps make compacted powders into slugs, which can be handled easily and further processed [14, 16, 20]. A near theoretical density is desirable which results in low residual porosity which in turn has been associated with the production of good foams. It has been shown by Kennedy [4] and Asavavisithchai [21] that a compaction level of at least 94 % of theoretical density is favorable for foaming. This level ensures that interconnected porosities are eliminated from the compact, resulting in the encapsulation of more hydrogen [4, 21]. If the compaction level is not sufficient, cracks may form and hydrogen can escape prematurely [6, 22]. Another thought to keep in mind is the fact that aluminum alloys are compacted below their sintering temperature where powder bonding may not necessarily occur; therefore porosity and poor consolidation may promote crack formation along powder boundaries.

2.2.1.2 Blowing Agents

As previously stated, blowing agents play the most crucial role in foam production, because they are responsible for the gas that creates the pores. When choosing a blowing agent, the melting point of the metal or alloy has to be matched with the gas release temperature of the blowing agent. If these two temperatures correspond, crack formations in the compact are less likely to form prior to the alloy melting temperature which can result in poor foaming and reduced efficiency [23]. The blowing agents typically used in metal foam

production varies, from titanium hydride, zirconium hydride, magnesium hydride and calcium carbonate, with titanium hydride being the most popular for aluminum foams [6, 14, 24, 25]. These can either be mixed with powders to create a compact or can be injected directly into the liquid metal [6, 9, 26, 27]. Blowing agents are normally added in small quantities in the range of less than 1 wt%, which proves to be sufficient in producing adequate foam expansion [4, 26, 28]. The focus here will be on TiH_2, being the most common blowing agent for aluminum.

It can be seen from Figure 2-5, that as received TiH_2 powder shows two distinct peaks when differential scanning calorimetry (DSC) analysis is performed under an argon atmosphere. An explanation for why TiH_2 has two dissociation peaks has been presented, the first peak is associated with the lattice distortion or movement from a tetrahedral lattice to an octahedral lattice, accompanied by some hydrogen release [29, 30]. It has also been shown that heat treatment and increased heating rate affects the dehydrogenation where the gas release temperature is pushed up [6, 7].

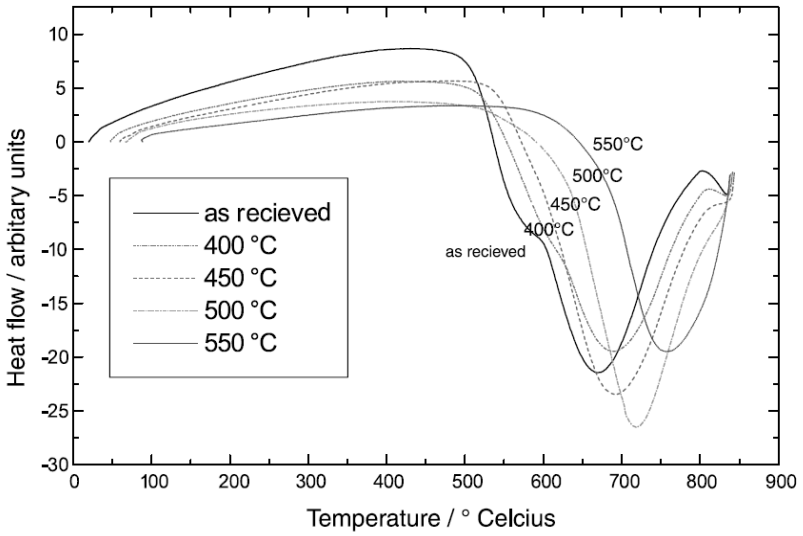

Figure 2-5: DSC curves of as received and heat treated (15 min) TiH_2 loose powders at a heating rate of 90 °C m^{-1} under argon to simulate foaming conditions [7]

It is also known that TiH_2 hydrogen release can be tailored to suit a specific alloy melting point by an oxidizing heat treatment. The thin oxide layer covering the blowing agents is a good barrier delaying the hydrogen release but can get sheared during compaction as it is very brittle. Heat treated blowing agents are mostly used where the blowing agent is introduced directly into the melt, because the powders do not experience shearing. What is meant by tailoring is that the blowing agent is heat treated in air at a specific temperature for a set period of time in order to modify its gas release temperature (through oxide layer formation). It can be seen from DSC curves in literature that peaks shift to higher temperatures after powders have been oxidized [6, 8]. By treating the blowing agent and modifying its hydrogen release temperature through surface oxidation, more uniform foams can be obtained, thus favoring reproducibility and improving key properties.

Figure 2-6 demonstrates different heat treatments performed on both loose powders and compacts. It can be seen that the release temperature range varies quite significantly between loose powders and compact precursors [8]. Untreated and treated TiH_2 is known to release its hydrogen at temperatures ranging from around 380 ˚C up to 650 ˚C [6, 8, 31]. The TiH_2 onset gas release can occur at low temperatures, but the bulk release is somewhere in the midrange. Kennedy [7] found that the heat treatment of TiH_2 had little effect on the total expansion of the foam where the gas release temperature was increased. These heat treatments although pushing up the gas release temperatures are not stipulated to help much in the foaming of pure aluminum compacts as the gas release temperature is still too low compared to the melting point of the aluminum. On the other hand, it was suggested by the author that it might be beneficial to use Al-Si alloys with the PM route and TiH_2 due to the low melting eutectic point of 577 ˚C [7].

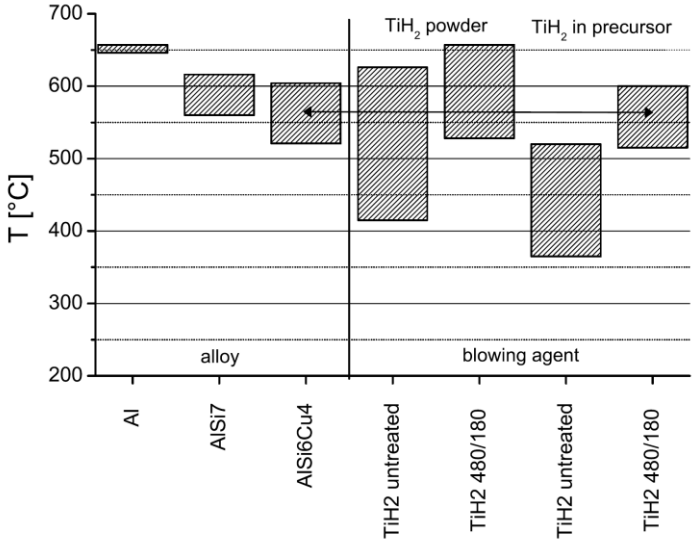

Figure 2-6: Tailored TiH_2 gas release range compared to alloy foaming range [8]

Lehmhus and Rausch [26] conducted a study on the heat treatment of TiH_2, and point out that the brittle oxide layer on the powders may fracture or shear during powder compaction which in turn affect release the temperature of the hydrogen. This in turn makes the heat treatment for the PM route less effective than the processes where the blowing agent is introduced directly into the melt [26]. Von Zeppelin [6] has also suggested that that blowing agents can be affected during compaction and their respective hydrogen release temperatures can deviate from those of loose powders analyzed using DSC. It has also been speculated in order to halt premature gas release from the blowing agent that an atmospheric pressure could also be applied during the heat up time of the precursor material before bulk foam expansion [32]. Other research conducted at McGill University involves coating the TiH_2 powders with metals such as Ni in order to form a metallic diffusion barrier of the TiH_2 powder surfaces [33]. An approximate calculation by Baumgärtner *et al*. [9] shows that only about 25 % of the blowing agent is effective in filling the foam pores. This is a result of several factors such as gas escaping through cracks formations or the blowing agent not fully releasing its hydrogen [9]. The importance of the blowing agent and the crack formation in

relation to the scope of the project will be addressed in Chapter 5, Chapter 7 and Chapter 8 of the Results and Discussion.

2.3 Foam Stability

One of the most important characteristics of foams, is their capacity to resist degradation over a given period of time. Foams by nature are thermodynamically unstable, meaning they will always degrade over time. Mechanisms of foam degradation can be described as the following: coalescence occurs when the film between two cells ruptures creating a larger bubble, bubble coarsening by gas diffusion between the cells and finally drainage whereby the liquid phase makes its way down the foam cell walls to accumulate as a liquid phase at the bottom as a result of gravity [16, 34]. Although a number of speculations have been brought forward for the explanation behind foam stability, a proper model has yet to be developed in order to describe the complex interactions between various forces, with most models developed being semi empirical [35]. Many forces act simultaneously on the foams, including gravity, gas pressure, surface tension and capillary forces [34, 36]. A balance between the interacting forces acting on the foam have great influence on its stability, gravity being the main force for drainage, capillary and surface tension forces being responsible for suction into the Plateau borders leaving thin cell walls, where a low surface tension is desirable [13]. Therefore a balance between the interacting forces is an essential requirement.

In order to balance the forces against foam degradation, a disjoining pressure in the cell wall between the bubbles is required. To achieve this stability (to create a disjoining pressure), the interacting forces can be balanced in several ways; via the addition of molecules or particulates to the liquid, by solidification of the foam into a stable structure or through a combination of several of these mechanisms such as in the case of metallic foams [35, 37, 38]. Once stabilized, the life span of a foam can extend from being almost instantaneously transient to

quite meta-stable in either the liquid or semi-liquid state [14, 35]. When it comes to pure liquids and especially liquid metals, it is impossible to produce stable foams without the use of stabilizing agents [39, 40]. Since pure metals would not foam because of high surface energy and the lack of surfactant, the cell walls have to be stabilized by adding solid constituents (particulates) to the melt and by adjusting viscosity along with surface tension [41].

A representation of a foam system can be seen in Figure 2-7. The Plateau border can be seen as the intersection point of bubbles (cells). The required disjoining pressure against cell rupture is depicted along with the liquid drainage. This disjoining pressure is generated through the addition of particulates or molecules to the foam.

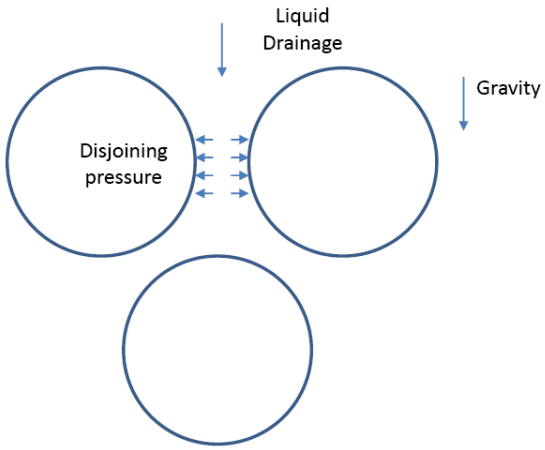

Figure 2-7: Foam system highlighting Plateau borders, drainage and disjoining pressure

The surface tension of a system can be defined as the specific interfacial free energy per unit area of the surface in terms of J-m^{-2} or N-m^{-1} (force per unit length). Due to this surface tension, the system will always tend to go to equilibrium where free energy is minimized through a lowered internal surface area [42, 43]. The surface tension will cause a tendency for cell wall thinning as a result of a capillary suction effect characterized as a pressure difference between

the cell wall and the Plateau border as described below by the Laplace equation [12, 32, 44]:

$$\Delta P = 2\frac{\gamma}{r} \qquad \textbf{Equation 2-3}$$

Where γ is the surface tension (N m^{-1}) and r (m) is the local radius of curvature of the surface. This Laplace pressure has implications in the nucleation of gas bubbles in supersaturated liquids, which will not be discussed here [12, 34].

The methods of measuring surface tension are discussed by Iida and Guthrie [43] in relation to liquid metals and the difficulties in obtaining representative values. It is important to note that the surface tension is not only a function of temperature and alloy composition but also a function of oxide content. Surface tension of metals is greatly affected by oxides [45] and the use of different equipment can result in varying surface tension values depending on residual oxygen partial pressure. This oxygen can significantly reduce the surface of the metal [46]. Surface tension is generally higher with higher melting point elements [12].

In liquid metals, the most frequently used methods for determining the surface tension are via the sessile drop and the maximum bubble pressure methods [43]. The sessile drop method consists of impinging a drop of liquid on a prescribed substrate giving the wetting behavior or the spread of the liquid in relation to the system (solid/liquid/gas). This is especially important with regards to selecting particle additives to stabilize both aqueous and metallic foams. The characterization of the wetting behavior of a liquid on a solid substrate can be described as the work of adhesion [47]. This being an equilibrium between the liquid, solid and vapor which can be described as a force balance or mechanical equilibrium in relation to the wetting angle of a drop onto a substrate between the

surface tension of the three phases. This phenomenon can be described via the Young equation described as [47, 48]

$$\gamma_{sv} = \gamma_{sl} + \gamma_{lv} \cdot \cos\alpha \qquad \textbf{Equation 2-4}$$

Where, γ is the surface tension in N m^{-1} for the different interfaces, γ_{sv} being between the gas and the solid, γ_{sl} between the solid and the liquid, γ_{lv} and α being the drop contact angle. The equation can then be rewritten as a function of the contact angle which is a common way of assessing wettability of a system. The equation can then be re-written as:

$$cos\theta = (\delta_{SV} - \delta_{SL})/\delta_{LV} \qquad \textbf{Equation 2-5}$$

In order to improve wetting, the δ_{SV} can be increased while δ_{Sl} and δ_{LV} can be reduced. δ_{SV} can be maximized by having a clean surface. δ_{SL} can be decreased by the addition of alloying elements but the practical considerations have to be kept in mind. The term δ_{LV} can be modified by the atmosphere itself and its pressure. To promote spreading in practice, the atmosphere pressure is reduced in high-vacuum brazing [47, 48]. In addition, an increase in viscosity reduces the fluid mobility towards degradation hindering the flow movement which can extend the foam life, while the lower surface tension would reduce the forces against cell rupture [10, 12, 15, 41, 49-52]. Therefore, it can be understood that a reduction in surface tension and simultaneous increase in viscosity would indeed help increase the stability life of the foam [10, 15, 41, 49-52]. The addition of particles to stabilize foams will be addressed the Section 2.3.2 with respect to the wetting angle necessary for Stabilisation.

2.3.1 Aqueous Foams and Surfactants

In aqueous systems, surfactants being surface active constituents are of significant importance as they help stabilize the foam into a meta-stable phase. What the

surfactant molecule does is lower the surface tension at the liquid-gas interface or increase surface viscosity and elasticity which promotes the dispersion of the gas phase and the creation of small bubbles [39, 44]. When a bubble is created within the aqueous system, it rises. As it rises, it collects these surfactant molecules around its gas/water interface. These surfactants align themselves in a particular fashion where the charged "hydrophilic" head adheres to the liquid phase while the "hydrophobic" tail is oriented toward the gas phase. This in return causes repulsion forces between the cell walls (also referred to as a disjoining pressure), creating stability and resistance against liquid drainage and bubble coalescence. When surfactants are present in significant numbers they form a cluster referred to as a micelle which accumulates around cell walls. A certain threshold exists where a critical concentration of surfactants is needed in order to stabilize the structure seen in Figure 2-8. As the film gets thinner a large electrostatic repulsive force (disjoining pressure) within the cell wall is generated and can stabilize the film by reducing the drainage driving force [35].

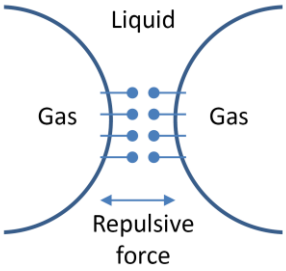

Figure 2-8: Aqueous surfactants present at the interface between two cells [35]

There are several types of surfactants used and available today for a wide range of applications. For example for transient foams (short life) short chain alcohols, aniline, phenol, pine oil and short chain undissociated fatty acids can be used. In the case where more stable foams are required, detergents, proteins and long-

chain fatty acids can be used as surfactants. In mineral processing for example an aqueous solution containing surfactants is used to create finely dispersed bubbles which rise and accumulate hydrophobic mineral particles at the gas/liquid interface to be collected at the top of a flotation cell [12, 35]. Although surfactants are known to work for water based foams, with regards to high temperatures and metals these hydrocarbon based surfactants would decompose or burn.

2.3.2 Particle Stabilized Foams

An alternative way to stabilize foams is by use of particles instead of surfactants given they have the right size and wetting characteristics. Metallic foams, since surfactants consist of hydrocarbon molecules cannot be used. Typically in the melt gas injection process and less frequently in the PM process, ceramic particles are added to enhance foam stability [53]. It has been shown that partially wetted particles can stabilize a foam gas/liquid interface [54-57]. Several early studies on metallic foam stability focused primarily on the viscosity and surface tension effects alone rather than on the role of particles themselves. Although they were successful at determining that the increase in viscosity and reduction in surface tension was beneficial for foam stability, mechanisms pertaining to particle stability itself were not discussed explicitly [49-52, 58]. This being an indication those early studies did not consider the effects particles on the liquid/gas interface and their role on the cell wall disjoining pressure [10, 15, 41].

It is generally agreed that particles, whether they are oxides present on powders or additional particles, are a requirement for any type of metal foam stability [15]. Particles used to stabilize metallic foam today include SiC, Al_2O_3 and TiB_2 [36, 56, 59]. Metal foam stability through particle addition is not yet fully understood but several proposals have been put forward [15, 36, 55]. It has also been established that a certain wettability of the particle is required to achieve foam stability. These particles are known to accumulate along the gas/liquid interface of the foam creating some type of disjoining pressure similarly to surfactants. If this

wettability requirement is not met, foam stability will be reduced. Several authors have experimentally and theoretically derived optimal particle wetting angles for foam stability. Values of optimal particle wetting angles are shown in Table 2-1

Table 2-1: Optimal particle wetting angles

Author	*Year*	*Angle range*	*Study*
Johansson and Pugh [60]	1992	40-80˚ (65˚ optimal)	Experimental
Sun and Gai [61]	2002	70-85˚	Experimental
Kaptay [56]	2003	50-90˚	Theoretical
Kaptay [57]	2006	75-86˚	Theoretical - Single or closed pack layer

The optimal wetting angle ensures that particles remain at the cell wall interface and do not protrude excessively through the gas or liquid phases. A network of partially wetted particles at the interface would therefore effectively act as barriers for liquid drainage and provide the necessary disjoining pressure to resist degradation [55]. On the other hand poor wetting characteristics of a particle would tend to enhance rupture of the film as it would be pushed out of the gas/liquid interface [35]. It can be concluded that a certain level of wetting in the range of 70-86˚ is necessary for the particles to stabilize foams. This wettability range is applicable not only to all liquid foam but to metallic foams. Furthermore, not only the wetting angle of the particles is important but also the size, concentration and shape of the particles themselves which can affect the stability of foams [35]. It is important to note that an excess of stabilizing particles can also decrease the foam quality as the melt becomes too viscous, therefore an optimum concentration is required [36].

One of the earliest aluminum foam studies which addressed wettability of particles was performed by Ip *et al.* [55] based on the melt gas injection method. They compared the results obtained through an aqueous system using SiO_2 particles as a stabilizing agent to aluminum foam stabilized with SiC. They showed that it was possible to enhance foam stability using SiC particles due to a favorable wetting angle of 75°. Accumulation of SiC particles was in fact

observed along the cell walls (gas/liquid interface) of the foam creating stability. Similar results where SiC accumulated at the cell walls were obtained through the PM method by Esmaeelzadeh *et al.* [62] by varying size and volume fraction of SiC along with temperature. Kennedy and Asavavisithchai [59, 63] have also investigated the addition of several ceramic particles in PM compacts to study their effect. They found that by adding as little as 3 vol% of particles, the expansion can be significantly improved and came to the conclusion that an intermediate wettability could be favorable in stabilizing foam [59, 63]. Another study by Asavavisithchai and Kennedy [64] involving the addition of Al_2O_3 in compacts has been carried out with Mg modification. The addition of Mg improved the wetting characteristics of the alumina with respect to the melt, increasing the stability of the foam [64].

2.3.3 Foam Stability in the PM Process by Particle Oxide

Atomized powders naturally contain an outer oxide film. These oxide films are very thin and in the nanometer range and decompose at temperature significantly higher than the melting point of the metal or alloy [65]. As the powder is compacted, the brittle oxide layers are fractured and produce an interconnected network of oxides [53]. These thin oxide shells on the metal powder surfaces have shown to be helpful in stabilizing the foams, whereby the addition of particles is not necessary given the powder oxide content level is acceptable. It is speculated that the oxides help keep the foam together forming some type of solid oxide skeleton network preventing drainage and pore coalescence [14, 15, 36]. Figure 2-9a shows a proposed representation of a cell wall whereby a skeleton network is formed, supported by a micrograph where Al-rich grains can be seen to retain their shape [14, 36]. Figure 2-9b shows an empirically determined optimal powder oxygen/oxide content range on the atomized powders for foam stability [36].

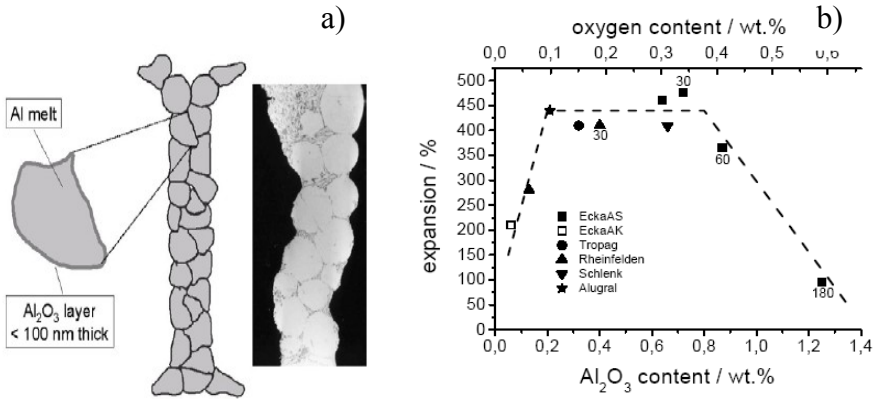

Figure 2-9: a) Powder compact cell wall, AlSi7+0.6%TiH_2 foamed at 600°C for 780s, b) oxygen content vs. expansion for put aluminum foams [36]

Microgravity foaming tests with lead, have revealed that powder oxide contents have a dominant effect on stability and that they create a separating force (disjoining pressure) stabilizing the foam. This disjoining pressure is analogous to the one formed through particle and surfactant additions as discussed in the previous Sections. Foams with low oxide content created large bubbles (bubble coalescence) under microgravity, while under gravity the foam was flattened and collapsed. In contrast, the foams having a higher oxide content proved to have very similar stable structures with higher cell counts under both gravity and microgravity [66-68]. This then shows that the oxides themselves play a leading role with respect to stability of the foam. Further work was conducted on varying levels of oxide on the atomized powders in relation to the stability of the foam. It was determined that optimal range of oxide content exists and is critical for foam stability. For instance, a foam with a low oxide content will experience significant drainage and coalescence, whereas too great an oxide content will hinder growth [53]. Figure 2-10 illustrates pure aluminum PM foams produced with different oxide contents. One can observe that the oxide content has significant effect on drainage and pore structure, where foams with low oxide levels have significant drainage whereas the others do not. As the foam is compacted, the brittle oxide

layers are fractured and they produce an interconnected network of oxide particles which is known to stabilize the foam [53].

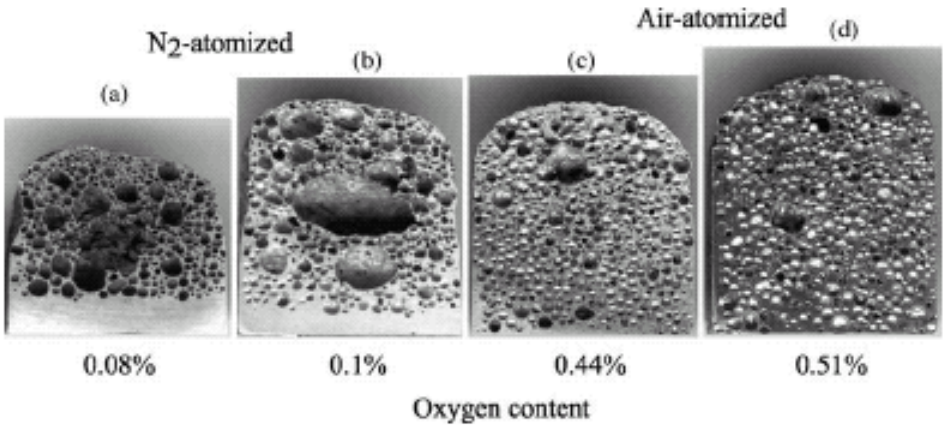

Figure 2-10: Pure aluminum foams created with varying oxide contents showing stability dependence [53]

Optimal aluminum powder oxide contents which have been determined experimentally by numerous authors have been tabulated in Table 2-2. Various authors have determined this range to be between 0.3-0.6 wt% oxygen for aluminum powders [21, 22, 69]. Asavavisithchai and Kennedy [22] have also studied the effects the hot compaction of powders on precursor oxidation in comparison to loose powder oxidation through furnace heat treatments. They highlight that oxidation of the aluminum powder during hot compaction is less significant (and not apparent at temperatures of 400 °C or below), than through loose powder heat treatment [22]. It is to be noted that the cold compaction process already densifies the structure which is tightly constrained in a die making the compact less prone to oxidation.

Table 2-2: Optimal atomized powder oxide content for foam stability

Optimal Oxygen Content	Measured	Compaction	Ref
0.1 -0.4 wt%	Powders	-	Banhart [36]
0.3-0.4 wt%	Powders	Cold	Asavavisithchai & Kennedy [21]
0.3-0.4 wt%	Powders and Compacts	Hot and cold	Asavavisithchai & Kennedy [22]
0.3-0.6 wt%	Powders	Cold	Asavavisithchai & Kennedy [69]

Korner *et al.* [53] looked in detail into the influence of the oxide content on PM produced foams. They observed that atomized aluminum powders contain a branched oxide structure within the powders themselves as a result of convection in the atomization process. As the foam was created, it was observed that the fracture oxides from powders as well as those from the atomization process were distributed within the structure and appeared to form interconnected networks of oxide clusters without apparent segregation. It was proposed that these oxides create barriers against cell rupture and drainage adding an additional interfacial force that balances the suction effects of the Plateau borders. This network was then able to mechanically transfer forces within the cell walls (disjoining pressure). A model describing the mechanism was also developed [36, 53]. Asavavisithchai and Kennedy [69] also observed the same type of interconnected network. Dudka *et al.* [70] came to the same conclusions while foaming under varying atmospheres. They showed that foaming in air reduced maximum expansion as an oxide outer shell is produced on the exterior surface of the foam. Furthermore, it was noticed that the oxides in the compact did not appear to collect at the gas/liquid interface but rather remained in the cell walls and Plateau borders where areas containing lower level of oxide were thinner. They determined that complex hierarchical oxide clusters in the nanometer range build to form the oxide networks [70]. Garcia-Moreno *et al.* [71] studied the rupture of an individual film with the use of synchrotron x-ray micro-radioscopy. They studied the film under high resolution which showed a very fluid rupture. It was shown that when a film ruptures it becomes very fluid once the oxide networks are destabilized and no longer holds the melt together (balancing the forces) [71]. Recently, more advanced numerical modeling on particle interaction and their effect on disjoining pressure has been proposed by Korner *et al.*, illustrating how foams are stabilized by the formed disjoining pressure in the cell walls [72].

Foam drainage modeling has also been carried out by Gergely and Clyne [32], measuring model parameters based on experimental data (cell size, cell face

thickness, foam porosity and specimen height). They determined that a small initial cell size coupled with high initial foaming porosity would inhibit drainage with effective melt viscosity. Furthermore, their analysis showed that with drainage a vertical capillary pressure gradient developed. This in turn counter balanced gravity driven flow (drainage). It was suggested that in order to have foams which have a small density gradients, focus should be made on rapid foaming, in order to minimize the low porosity period. They also suggest that external pressure can suppress premature expansion and cracking during the heating stage [32]. Studies conducted by Korner *et al.*under high pressure atmosphere showed that indeed high pressure was an effective way of suppressing crack formation, although somewhat impractical as the system has to be sealed, resulting in high costs [73]. If cracks form rather than micro-pores then hydrogen can be lost. A study by Helfen *et al.* [11] on the early foaming stages and crack formation was carried out using x-ray tomography. They determined that the cracks tend to form in the perpendicular direction to the compaction axis. The fact that the compacts are not consolidated (sintered) promotes crack formation. As the cracks are formed, the ex-situ analysis showed that these crack propagate through the solid phase until the liquidus temperature is reached. It has also been shown that higher heating rates promoted an enhanced foam structure, where it is stipulated that these large cracks have less time to grow under high heating rates [11, 20]. In a separate study by Baumgärtner *et al.* [9] where the heating rates were varied, it was concluded that a heating rate in the range of 100 °C min^{-1} is favorable for foaming. Too low a heating rate will result in poor expansion for which they attribute to either; hydrogen loss through initial cracking or oxidation of the structure during expansion [9]. These experimental studies appear to support the speculation brought forward by the model predictions of Gergely and Clyne [32]. The foam expansion mechanism has been studied by Banhart *et al.* [10] with the use of synchrotron radioscopy on PM foams. It was shown that particles (possibly oxides) do in fact collect along the cell walls and appear to act as mechanical barriers against cell rupture and drainage but how they stabilize the

foam is still debated. Furthermore, the formation of highly oblate crack like pores was observed during the initial foaming period.

2.4 Zinc foams and the use of alloys

The available literature on zinc foams based on the powder metallurgy process, dates back as early as the 1970's. The production of zinc foam has been mainly compared to aluminum. These studies focused primarily on pure or lightly alloyed zinc compositions [14, 74-78]. The principle reason behind the production of zinc foam is due to its low melting point (420 °C) as an alternative to aluminum (660 °C). The main advantage stems from the fact that its melting point corresponds well with the bulk hydrogen release temperature of TiH_2 [6, 7]. On the other hand, this advantage is offset by its high density (7.13 g cm^{-1}) which is almost three times that of aluminum (2.71 g cm^{-1}) rendering it unfavorable in some lightweight applications. Due to the concurrence of zinc's melting point to the gas release temperature of the blowing agent, it has been shown that the pore nucleation is typically round and homogeneous as opposed to aluminum where a complex network of cracks is formed [76, 79, 80]. Mechanical properties of zinc and zinc based foams have also been characterized by several authors [78, 81-84].

Research on zinc foams using ZrH_2 as a blowing agent was performed on the early stages of foaming by Banhart *et al.* [79] using Ultra Small-Angle Neutron Scattering (USANS) to look at pore morphology. Their goal was to observe pore formation mechanisms at early stages along with pore growth behavior and blowing agent distribution. They stipulate the existence of two types of pores, Type I pores formed at the blowing agent particles and the type II at grain boundaries triple point. They hypothesize that the Type II are formed through grain boundary diffusion. It was shown that the Zinc cells were almost always spherical when nucleated as opposed to aluminum which mostly formed a complex network of cracks [77, 79]. Similar results by Baumgärtner *et al.* [9] highlight the uniform and round formation of pores in zinc-based foams in

contrast to aluminum. Kovcik and Simancik [75, 85] studied the feasibility of using zinc (or lightly alloyed zinc) foam to fill hollow steel profiles as a substitute for aluminum. Their goal was to reduce the foaming temperature and to overcome the slow foaming of aluminum and its alloys and to prevent potential corrosion associated with aluminum/steel. It was determined that for an equal porosity, the foam strengths were similar but for an equal density, the zinc foams were significantly weaker. These authors looked at pure zinc foams using different temperatures while varying the blowing agent concentration. They determined that zinc foams required more TiH_2 (1 wt%) and superheat to achieve acceptable density as opposed to an Al-12Si (0.4 wt%) alloy [75]. They also attribute the high zinc expansion levels and increased levels of drainage to a viscosity reduction as a result of superheat. The use of higher levels of blowing agent for zinc foam was also highlighted by Sadaatfar *et al.* [80].

Yin *et al.* [86] studied the Al-7wt%Si PM foams through the semi-solid region. Elemental aluminum and silicon powders were used to produce their foams. The results indicated that the solid grains helped increase the effective viscosity of the melt but it was noted that to generate spherical cells, temperatures above the liquidus were required. At lower temperatures crack-like pores formed in contrast to larger expansion levels in the liquid state [86]. The Al-Si system was also assessed by Krirszt *et al.* [87] while varying the Si concentrations (2 wt%Si and 12 wt%Si), powder sizes and composition (pre-alloyed vs. elemental and blowing agent (TiH_2). It was concluded that a better foam structure could be obtained by the use of elemental aluminum and silicon powders rather than pre-alloyed ones with the Al-12wt%Si eutectic mixture. They attribute this increase in foam structural stability to the slower kinetics involved in the reaction between the elemental aluminum and silicon before reaching equilibrium without further explanation. They also determined that finer TiH_2 powders were favorable for the creation of smaller pores [87].

Variations in foaming atmospheres was studies by Simancik *et al.* [88] by varying the gas and pressure (air and argon). They determined that higher porosity could be attained under an argon atmosphere and that effects of oxidation could be countered by increases in the heating rate which reduces the oxidation time. They also note that the alloys less prone to oxidation were less dependent of heating rate (Al-Si alloys as opposed to magnesium containing alloys) [88].

A proposed concept by Banhart [36], is the use of a solid phase in the melt to form precipitates (or primary grains). He postulates that aluminum-based foams could be stabilized through the semi-solid region of an alloy relying on primary grains as stabilizing particles which could simultaneously increase viscosity [36]. Korner *et al.* [89], used a similar concept with magnesium, relying on the primary magnesium alloy α-phase to stabilize the foam during solidification without the use of additives. The successful production method relied on an increased viscosity of the melt in order to reduce the foam degradation process. It is believed that these particles (grains) work as barriers against the thinning of the cell walls. Several studies have shown that the addition of zinc, magnesium and silicon to aluminum can reduce the liquid surface tension and can help increase the stability of aluminum foams [58, 90, 91].

Karsu *et al.* [92] added 5 wt% Ti-6wt%Al-4wt%V to aluminum compacts to study intermetallic phase formation to increase stability. $TiAl_3$ intermetallics were formed due to the addition of these powders; as a result increased stability was obtained. They observed that foaming with larger Ti-6wt%Al-4wt%V powders rather than fine ones was beneficial. They explain this phenomenon as an increase in apparent viscosity, resulting in increasing stability. The reduced foamability with the use of smaller powders was attributed to the higher cumulative surface area of the powders resulting in the excessive formation of $TiAl_3$ resulting in viscosity that is too high. A thick outer reactive layer was observed surrounded this added particles. Brittle $Al_{13}Fe_4$ intermetallic formation in aluminum foam was

studied by Raj and Daniel [93, 94] as a result of the dissolution of a stainless steel stirrer in the melt. Intermetallics with higher aspect ratios improved stability by reducing drainage and cell wall collapse but increased the brittleness of the foam .

Significant work by Kobashi and Kanetake has been done regarding the self blowing process of aluminum-nickel foams by means of a combustion reaction. Their process relies on the formation of intermetallic compounds where blowing agents are not nessesarilly required. They believe that the gas is formed at the surface of the aluminum powders (usually covered with hydrous oxide $Al_2O_3 \cdot 3HO_2$) which outgases at high temperatures and that dissolved hydrogen is released which is present in the aluminum. Their study showed that with the higher aluminum content a more porous material is generated. Furthermore, they looked at reaction modifying compounds such as: B_4C (reaction enhancing) and TiC (heat-absorbing) agents [95]. The process is described in more detail in their most recent publications, where they discuss the self propagation of the reaction and the addition of a blowing agent [96-98].

2.5 Joining and sintering processes

Several joining and sintering processes rely on the use of transient liquid phases and will be reviewed in the context of aluminum alloys. It is well known that alloy compatibility, wetting, viscosity and surface tension play key roles in the success of each of the processes as well as with metallic foams.

2.5.1 Brazing

The brazing process relies on the melting of an interfacial filler material having a lower melting point than the base material to be joined. The brazing process is quite versatile whereby it can be used to join metals of different compositions, metal matrix composites and metals to ceramic systems [48]. Analogous to the brazing process is soldering, but it is typically performed at temperatures below 450 °C. Although this criterion is quite simple, generally speaking, solders can be

differentiated from brazes by their formation of intermetallics at the bond interface rather than through solid solutions (brazing) but exceptions exist [47, 48]. These particular techniques differ from the well known conventional fusion welding processes where both the substrate and the interface materials are melted together. A comparison of the different processes is shown in Table 2-3 [47]. The brazing process can be undertaken through different means such as in a vacuum furnace or with a torch depending on the joint material and type. Specific atmospheric conditions are sometimes necessary or beneficial in the formation of the join where low oxidation potentials are required in order to enhance wetting (spreading) characteristics. Once heated, the interface (the braze) melts and spreads onto the parent material to forms a metallurgical alloy bond between the filler and the substrate without full dissolution [47, 99].

Table 2-3: Comparison between different joining techniques[47].

Comparison of Soldering, brazing and welding

Parameter	Soldering	Brazing	Welding
Joint formed	Mechanical	Metallurgical	Metallurgical
Filler metal melt temperature (°C)	<450 °C	>450 °C	>=150 °C base material
Base metal	Does not melt	Does not melt	Melts
Fluxed used to protect and the assist in wetting of base-metal surfaces	Required	Optional	Optional
Typical heat sources	Soldering iron, Ultrasonics, resistance oven	Furnace, chemical reaction, induction, torch, infrared	Plasma, electron beam, tungsten and submerged arc, resistance, laser
Tendency to warp or burn	Atypical	Atypical	Potential distortion and warpage of base metal likely
Residual stresses			Likely around weld area

In the brazing process, as well as for other welding processes, surface cleanliness is essential. The reason surface cleanliness is required is to ensure proper wetting (or spreading) of the molten material onto the substrate. The wetting behavior of the system can be significantly affected by oxide layers and other surface contaminants as metals generally do not wet oxides which normally inhibit the spreading [48, 100, 101]. The metals must also be compatible even if the surface is free of oxides [47, 99]. Good wetting in this process is often reflected by the formation of nice fillet joints resulting in a tight seal as opposed to beading [48]. In some instances fluxes are used to remove surface oxides and impurities to improve the wetting behavior of the system but at the same time can leave undesirable residues which can affect the joint properties. Fluxes are chemical reagents that work to remove thin oxide layers and impurities, giving the molten metal a clean and fresh surface to spread upon. For aluminum alloys these fluxes can include chloride and fluoride solutions [47]. A simple example of wetting is the soldering of household copper pipes using a lead-tin solder without flux. Without the flux, the surface of the copper is not clean and is oxidized and therefore the solder is unable to wet the surface properly to seal the joint and just beads off. Good wetting of the braze onto the parent material is a fundamental requirement for any system in order to ensure the formation of a proper joint [47, 99]. In whole, the requirements needed for a good brazing material is one that wets the base metal without melting it. It has been shown that brazes tend to spread more over grain boundaries which are disordered regions which have surface energies up to 30 % larger than the free surface [100].

Brazes used for aluminum and aluminum alloys are often based on the Al-12Si eutectic for several reasons. These include, the composition's high fluidity, its ability to act as a melting point depressant, and the fact it does not significantly influence the corrosion potential of the joint [47, 102]. Ternary eutectics are also used based on the Al-Si system with additions of zinc, magnesium, silver and copper [47, 102-104]. Although these brazes can be effective in some instances,

they usually need to be coupled with fluxes due to the tenacious oxides which are responsible for reduced wetting [47, 102]. It has been reported that the use of zinc to brazing aluminum at low concentrations can cause undesirable conditions. Since zinc is extremely volatile above 500 °C at concentration as low as 10 %, the work piece and the furnace will be coated with zinc as a result of high partial pressure. Furthermore, porosity can be attributed to zinc's high partial pressure [105]. Therefore, the use of zinc as a braze material for aluminum has been quite limited but has been reported in numerous patents for its use in heat exchangers. On the other hand magnesium is also volatile but to a lesser extent than zinc. The use of magnesium or alloys containing magnesium, has been associated with improved wetting where it physically displaces oxide layers as it volatizes as well as its ability to gather oxygen from the surroundings [106-109]. Zinc can also be used to increase corrosion resistance in a system and in some instance not affecting the joint [102]. Although aluminum can be brazed, most of the brazes are close to the melting temperatures of commercial alloys, especially those with low melting points making it difficult to braze. The fluxes (if used) in aluminum can result in corrosive residues which are difficult to remove. Other drawbacks of brazing aluminum can be associated with the loss of alloys due to the high brazing temperatures [47]. In aluminum foam, the formation of porosity due to zinc is not as issue and may even enhance foaming. Moreover, the high fluidity and favorable spread characteristic of Al-Si compositions is likely beneficial in reactive type foaming systems.

2.5.2 TLP Bonding

An analogous technique to the above is termed Transient Liquid Phase (TLP) bonding which originates from the high vacuum brazing approach, where two similar or dissimilar metals are bonded together through a reactive layer which dissolves completely into the parent material. This process relies on a very thin low melting point layer which is typically inserted between two mating parts to be joined. This layer can be in the form of a thin foil or a coating with can be

electroplated, sputtered or applied through any other surface deposition technique. This thin layer normally consists of a melting point depressant usually no larger than 50 μm in thickness to ensure a time feasible process [100, 101, 110].The components are generally held at a constant temperature below that of the parent material under high vacuum in order to control oxide formation where the interface is able to react with the matrix. Therefore, once the interface layer is liquid, referred to as a transient liquid phase, it dissolves in the solid phase resulting in a bonded interface. This process can be referred to as isothermal solidification since the components are held at a constant temperature as the phase dissolves through the substrate.

This method can serve as an alternative to other joining processes such as diffusion bonding, conventional brazing or even fusion welding [100, 101]. Normally transient liquid phases are used to bond two parts or sections of the same material, the goal is to have a very similar microstructure and mechanical strength as the parent material [100]. Although the process is feasible, it can be difficult to obtain desirable properties depending on starting material and the complexity of the microstructural evolution. In practice, it has been shown that a diffusivity threshold of 10 cm^2 s^{-1} is required for the process to be feasible time wise [101].

A typical example of TLP bonding can be summarized as follows. A material of composition A is to be bonded to another component of composition A through an interlayer of material B. Material B consists of a phase that forms a eutectic with A. The components are heated above the eutectic point of A-B but below the melting point of A. As a result, a transient liquid phase is generated at the interface which dissolves through diffusion into both components of composition A. The entire process is achieved through three distinct processes: (i) the substrate dissolution, (2) isothermal solidification, (3) solid state homogenization. In substrate dissolution, the substrate A is dissolved by the melt created through

phase B until the equilibrium of liquid is reached to that of the solidus. During the isothermal solidification process which occurs after the dissolution, phase B begins to dissolve through the substrate by solid state diffusion until no liquid is left as depicted in Figure 2-11. As mentioned above, it is important to note that the diffusion of B through A is highly dependent on the diffusion coefficient and thickness of the interface layer and substrate, and can vary from minutes to hours. A very thick layer of B may require significant time to achieve the desired solid state diffusion. Following the isothermal solidification of the phase, a homogenization process can be used, which requires the temperature to be kept constant in order to avoid phenomena such as phase precipitation which could be undesirable. Although this example is ideal, not all TLP processes are as simple, issues such as solid state diffusion during heating can cause issues along with oxides [100, 101].

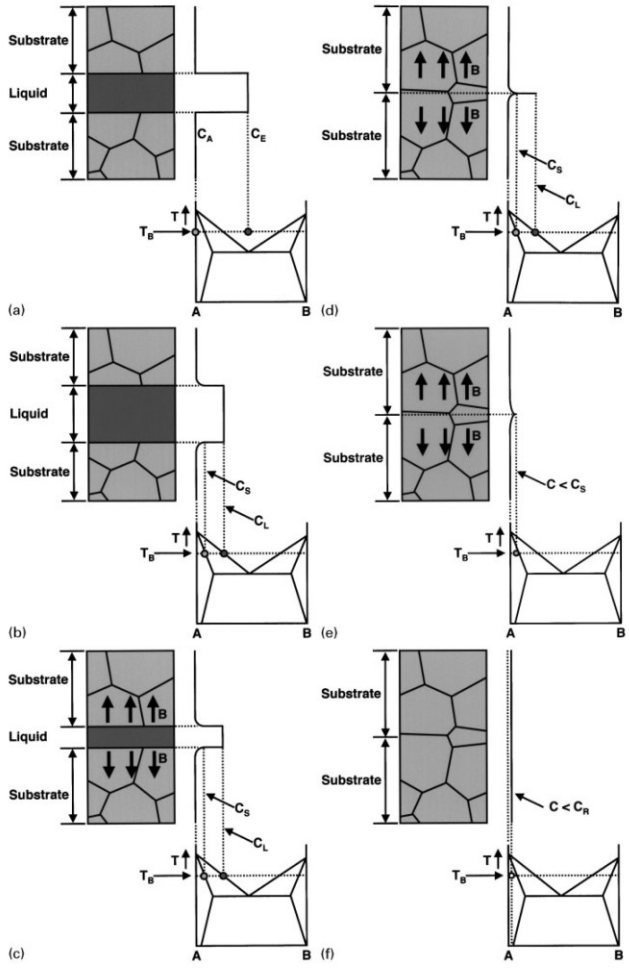

Figure 2-11: Transient liquid phase bonding interface reactions, joining approach [114]

In order for TLP bonds to be successful as is the case with brazing, good wettability and surface conditions are required [100]. Wettability in real systems depends on several parameters such as surface roughness and oxidation [101]. The oxides on the surface of the reaction layer can affect the reaction by containing the phase and restraining the interlayer from spreading as discussed in the case of brazing. Furthermore, the oxide layer can affect the interfacial reactions and energies. In order to promote wetting of the system, a reducing atmosphere (i.e.: hydrogen) and change in pressure can be used as is the case for vacuum based joining processes. Bond metal compatibility is of great importance in this system. It has been shown that spreading and good wetting was associated

with mutual solid solubility of the solid in the liquid. Spreading of the liquid can be achieved by two mechanisms, one by the reduction of the substrate oxide, through a wetting promoting chemical reaction or through the undermining of substrate oxide [100].

The transient liquid phase bonding process has been used in aluminum, mostly for metal matrix composites joining. The use of elements such as copper, nickel and zinc have been investigated for bonding aluminum [101, 111-113]. The oxide layer formation in aluminum makes the TLP process difficult as observed in the case of brazing. If an element is capable of reducing or modifying the aluminum oxide, then it would be beneficial to the bond formation. It has been reported that the use of magnesium in the transient layer has been beneficial whereby reducing and/or modify the aluminum oxide enhancing the wetting behavior of the phase [114]. Zinc in particular has been used as an interlayer for Al-Li alloys in order to overcome the oxide layer. The main downside with zinc as previously highlighted is its high partial pressure which can be a nuisance if used in higher concentration due to porosity formation, although it has a large solid solution region which is helpful in reactive bonding [101, 115].

2.5.3 Liquid State Sintering

Since the powder metallurgy route is utilized to produce foams, sintering will be discussed in relation to the formation of liquid phases. Two main types of sintering techniques exist and are commonly used; the first is referred to as solid state sintering and the other liquid state sintering. The typical solid state sintering process consists of bringing cold pressed powders (referred to as a green or a precursor) to elevated temperatures, generally 60-90 % of the alloy/metal melting point where powders can bond together through solid state diffusion. The higher temperatures increase the diffusion coefficients of the material enabling the bond formation [116]. Solid state diffusion of the materials being a thermally activated process, can take place through point defects, vacancies and interstitials in

crystalline solids as a result of a concentration gradient. Normally, diffusion along surfaces and grain boundaries is faster than in a single crystal as a result of higher numbers of defects [117]. Hydrogen atmosphere are sometimes used in powder metallurgy to reduce the oxides or through the use of additives.

In liquid state sintering, a mix of powders is again cold pressed and brought to a high temperature, but this time above the melting point of one of the system components. As a result, when the liquid is formed, the diffusion and consolidation can be accelerated and the porosity minimized [116]. In this case the liquid that forms is able to dissolve and wet the grains from the solid particles resulting in a capillary that pulls the grains together consolidating the structure. This process is often used for materials such as tool steels to bond carbides which are normally hard to form through conventional processes such as casting. An example of this is tungsten carbide and cobalt (WC-Co), where a eutectic is formed bonding the components together. It is worth noting that, coated particles can be used in the process and serve as a good starting point for liquid state sintering. The liquid itself can form from the formation of a eutectic or simply through the melting of a second phase. Depending on the solubility of the material, the liquid can be transient or present throughout the sintering stages. Capillary attraction of particles through liquid wetting produces fast densification [118]. Alloy compatibility is also very important as is the case for the joining processes.

Although this process appears simple in nature, if parameter are not well controlled, undesired conditions may arise such as distortion and porosity [119]. Several processing factors can influence the sintering itself including: furnace heating rate, powder size, green density, temperature, hold duration and cooling time. For instance, if too much liquid is generated in the structure, deformation and slumping of the shape can occur. Also, vapor phases can result in increased porosity which is undesirable [118]. High solid state solubility before the liquid is

formed can also hinder liquid formation [119]. For a system to be used for liquid phase sintering it must possess certain desirable characteristics. Ideally, the element to be added to the sintering matrix has to be one which melts below the temperature of the base and is able to form eutectic phase [116, 118] Furthermore, the solid solubility of the base in the additive should be greater than that of the additive in the base. In other word it is not beneficial for the additive (liquid phase) to dissolve easily into the solid [120]. Moreover, appropriate wetting is necessary for the liquid to react and stay in the matrix. A non wetting metal could be pushed out of the matrix or result in swelling of the structure [118]. In addition, a sintering atmosphere (such as hydrogen) is often necessary to ensure proper consolidation and to reduce oxidation. As with the joining techniques, the wetting behavior of the material can be greatly affected by the surface impurities which are common when using commercial powders. Wetting in this case is enhanced by the solubility of a solid into a liquid or by the formation of intermediate compounds and interdiffusion [119].

Certain characteristics are required for liquid state sintering have been outlined by German [118]: (i) the liquid forming constituent should have a lower melting point than the base alloy (or form a low melting point phase such as a eutectic). (ii) the liquid volume can be maximized by ensuring a low solubility of the liquid forming phase into the base solid (iii) the base solid phase should be soluble in the liquid phase in order to maximize the liquid. Completely miscible liquids ensure that mass transport is not constrained. In addition, the base solid should have a high diffusivity in the liquid to ensure high rates of mass transport to increase sintering.

Liquid state sintering of aluminum can be conducted with the help of several additives, including tin, copper, zinc and magnesium or a combination of the above [119, 121]. The principle systems used for liquid state sintering of aluminum will be discussed below. The Al-Cu system is the most widely used and

studied in PM alloys. It presents two ideal features where it has a maximum solid solubility in aluminum of 5.65 % at 548 °C and that there is only a single liquid phase. In some instances, magnesium and zinc are added to increase the strength of the alloy [122]. Although this system is widely used there are several drawback associated with it. For example copper has a high melting point and since there is solid solubility of copper in aluminum, the liquid is only partially transient if the parameters are not well controlled. If the copper content is initially low, at the end it can be completely absorbed by the aluminum. Moreover, the diffusivity of copper in aluminum is almost 5000 times faster than aluminum in copper. Therefore, the sintering of Al-Cu is very dependent on process variables, most notably the heating rate and the particle size [121, 122]

Another system used for liquid state sintering is tin. The tin shows properties which can be ideal for liquid phase sintering due to its low melting point, the lack of intermetallics and its low solubility in aluminum. The solid solubility of tin in aluminum is very low (<0.15 %) whereby aluminum is soluble in liquid tin. One drawback is when tin is solely sintered with aluminum it gets pushed out of the system (beads out) due immiscibility. Mircostructures of Al-Sn system only show that tin wets aluminum when magnesium is present. Without the use of magnesium the liquid is exuded from the melt [121]. The addition of magnesium is a very effective sintering aid where densities of 99 % can be achieved. On the other hand, although tin is good for sintering, the mechanical properties are low as it does not provide significant strengthening. It is suggested that specific alloys which are tailored for sintering would respond better than those replication based on commercial wrought alloys.

In contrast to copper, zinc has a lower melting point and has no intermediate intermetallics phases. Although it melts at a low temperature, its solid solubility in aluminum is not ideal (maximum of 83.1 % while the solid solubility of aluminum in zinc is 1.2 %). Therefore, it is possible that zinc dissolves entirely in

the aluminum before the liquid phase can form making it highly transient and very process sensitive [120]. Through process variations, it has been shown that, fast heating rates and coarse powder sizes are favorable in sintering aluminum with zinc. Research by Lumley and Schaffer [121] on an Al-10wt%Zn mixture was performed while varying the zinc particle size in the sample along with the heating rate (1 °C min^{-1} and 40 °C min^{-1}). Fine zinc particles (<45 μm) in a matrix of aluminum (average 60 μm) showed limited reaction and significant dissolution of the alloy. On the other hand, when large zinc powders were used (125-150 μm), more liquid phase (doubled) could be observed. At low heating rates of 1 °C min^{-1} liquid phase sintering was negligible with both large and small zinc particles while under a high heating rate of 40 C min^{-1}, the particle size effects could be well observed. It is then understood that the high solubility of zinc in the system can have a negative influence if the parameters are not well controlled. Therefore, a large quantity of zinc can be absorbed by the aluminum before it reaches equilibrium. It is to be noted that some earlier studies have mixed conclusions with regard to the dissolution of zinc [120]. The size of the aluminum particles also affects the swelling of the compacts along with porosity during the sintering. Larger aluminum particles and higher zinc contents will tend to result in higher levels of final porosity [120]. The same authors also studied pore formations in the Al-Zn-Mg-Cu system highlighting the effect of zinc high partial pressure. They show the formation of vapor pores near the zinc particles indicating evaporation. They also note that the pores are only present when the formation of liquid takes place. In another study, they stipulate that the pores are continuously produced since they are not accumulated at the top of the sintered part surface. A random distribution of the pores was observed through the matrix [123]. In foaming and particularly in the process utilized in this thesis, the initial heating rates are significantly higher than 40 °C min^{-1} and therefore, the dissolution of the liquid phase is highly unlikely. A table has been compiled comparing advantages and disadvantages of each alloy and is presented in the Research Objectives (Chapter 3).

2.6 Mechanical Properties

Metallic foam mechanical properties are those that make them viable for use in industrial applications. Although metal foams are currently not very commercialized, significant work is done on trying to improve and characterize these properties. Companies such as Cymat in Toronto, Canada are looking at a multitude of applications in the automotive and defense industries [124]. This section briefly discusses foam properties with focus on crushing and impact.

2.6.1 Mechanical Strength

Metallic foams and their mechanical properties have been studied in recent years. Gibson and Ashby published a book characterizing various existing foams and their relevant properties [13]. A design guide by Ashby *et al.* highlights the uses and properties of existent metal foams [2] and a comprehensive literature review by Banhart details production methods and uses of metal foams [14].

Typical stress strain curves for closed cell metallic foam are depicted in Figure 2-12. It characteristically has a long plateau region where the stress is constant for a given range of strain until densification due to the collapsing cells. When determining energy absorption capabilities it is important to be able to determine the densification strain (when the curve moves up steeply). Once the densification strain is calculated, the area under the stress strain curve can be determined giving the energy absorption potential [2].

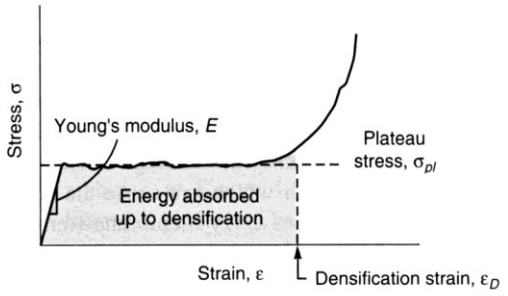

Figure 2-12: Typical foam stress-strain curve showing energy absorption up to densification [2]

In terms of compression strength and the stress-strain curves, the aluminum foam requires a minimum number of cells in order for its properties to fall into the bulk regime when crushed. The bulk regime of properties can be defined as the minimal amount of cells required in the foam to have constant properties where cell effects are not apparent. Values of minimum cell number requirements are shown in Table 2-4. One of the first studies on the cell size to sample ratio for cellular solids, indicated a minimum of 15-20 requirement for bulk properties. The material used in that study was reticulated vitreous carbon which is quite different from a metal foam by nature but cellular solids share similar properties under compression [125]. An early study on aluminum foam compression by Sugimara *et al.* [126] used the basis of 10 cells per side for their compression tests based on unpublished research. Several independent studies, have confirmed this ratio to be in the range of 6-10 cells [2, 16]. A more recent study on the deformation of aluminum foams found that the bulk stress plateau could be reached at a value of only 4 cells, although the foam height to width parameter was not studied [127]. Onck *et al.* [128] developed a model attempting to predict the cell size to specimen ratio. This model was in turn used by Chino *et al.* [129] with the use of experimental data, validating the model developed by Onck *et al.* [128]. This yielded a cell size to specimen ratio required is of at least 4 cells in all directions. Jeon and Ashida [130] have looked at the different defects inherent in aluminum foams such as partially coupled, missing and collapsed cells. They found that foam properties can be significantly affected, such as Young's modulus

or strength if the cell size to specimen size ratio is small. They also studied cell size effects to specimen ratio on defect free specimens and compared them to previous studies and found similar results whereby a minimum of 4-6 cells were required if defects are not present [130].

Table 2-4: Minimum cell requirement for bulk properties in compression.

Minimum Cell Requirement	***Year***	***Study***
15 to 20	1990	[125]
10	1997	[126]
6 to 10	2000	[2]
6 to 10	2002	[16]
4	2000	[127]
4	2001	[128]
4	2003	[129]
4 to 6	2005	[130]

In one study, a digital image correlation procedure was used to analyze the deformation of aluminum foam under crushing [127]. This indicated that a series of local deformation bands were formed as the foam was crushed. The foam crushed through the formation of bands from the strongest to the weakest. McCullough *et al.* [131] also observed that crushing bands were generated when metallic foam was crushed. Another study by Andrews *et al.* [132] also confirmed this formation of local deformation bands in the foam under compression, showing inhomogeneous deformation and strain [132]. It can be concluded that a minimum of 4 to 6 cells is required in order to fall into the bulk properties regime and that closed cell metallic aluminum foams collapse by the formation of deformation bands when crushed.

Banhart and Baumeister [81] performed a series of uniaxial stress tests on various foams produced via the PM method. In their study, they investigated the effect of the outer skin formation, composite foams (foam inside a metal tube) and the foam crushing orientation. They determined that the compression strength of the foam is influenced by the crushing orientation, this due to the alignment of cells

in certain directions during production due to buoyancy forces and drainage. The foam has shown to be stronger in the cell growth direction as the cells tend to be oriented vertically. In addition, they produced foams inside aluminum tubes and showed that the mechanical strength of the composite was greater than the sum of the two [81]. Other key properties such as the modulus of elasticity are affected by the force orientation. It can be seen that the foam is stronger when the force is parallel to the foaming direction [2, 81]. Various foam compressive stresses relative to density are plotted in Figure 2-13 based on different manufacturers [2]. Figure 2-13 has been slightly modified from its original version to highlight the properties of foams which are of interest in this project. Figure 2-12b emphasizes the effect of expansion (density) on the foam stress strain curve. It highlights that lighter foam will have low strength but a long plateau and that high density foam will have higher strength but a short plateau. Therefore, for given application, light or heavy foam may be desirable.

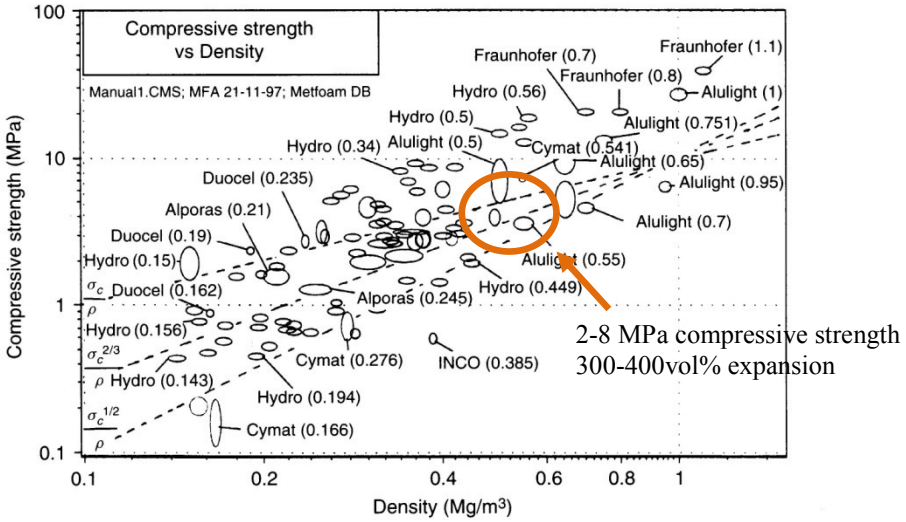

Figure 2-13: Compressive strength vs. density of various foams [2]

2.6.2 Impact and Crushing Properties

The deformation behavior of metallic foams is favorable for impact absorption, being particularly attractive for the automotive and defense industry as previously

discussed. Under impact, the foam crushes on itself to dissipate large quantities of energy. Configurations such as sandwich panels and aluminum foam filled tubes provide high stiffness to weight ratios and good impact characteristics [2, 14]. Figure 2-12a shows a typical foam stress-strain curve, where a large Plateau region can be observed [2, 77]. As shown in the Figure 2-12a, the area under the curve of the stress strain graph is the useful energy or the energy per unit volume in MJ m^{-3} (J cm^{-3}) as shown in the equation below [16]:

$$\boldsymbol{E_V = \int_{\varepsilon 1}^{\varepsilon 2} \sigma\,(\varepsilon) d\varepsilon} \qquad \textbf{Equation 2-6}$$

Where σ is the stress in MPa and ε is the strain over the range of the plateau stress.

Another important aspect when it comes to the crushing of aluminum foam is the strain rate (crushing rate). In conventional material, flow curves are obtained via the true stress strain (crosshead speed changes) as the physical dimensions of the sample change. Furthermore, the strain-rate sensitivity for most metals at room temperature is quite low. This becomes especially important for metals at higher temperature where thermally activated processes can take place such as dynamic recrystallization, precipitation and the generation of heat during the deformation process [38, 133]. Under the influence of crushing the foam crumbles on itself and does not expand in the lateral sense like a conventional material. Therefore sample friction and buckling no longer becomes an issue.

Deshpande and Fleck [134] performed a comprehensive study on the effects of quasi-static compression vs. impact with strain rate variations between 10^{-3} s^{-1} and 5000 s^{-1}. Tests were performed on both open and closed cell foams. They used a Split Hopkinson Pressure Bar (SHPB) to do the high strain rate tests. They show that the resulting stress-strain curves are independent of strain rate within the

typical scatter. Furthermore they have also investigated and analyzed the effect of shockwave propagation and determined that it only becomes significant at impact velocities greater than 50 m s^{-1}. In the case of closed cell aluminum foam they also observed the formation of deformation bands (as discussed earlier) as opposed to open cell foams where homogeneous compression occurred without deformation band. In addition, they looked at the effects of compressed gas pressure during high speed compaction in the closed cell foams and found it to be negligible (for tested velocities), where elevations of plateau stress were within the data scatter. In conclusion to their study, the strength and crushing behaviors of aluminum foams were independent of strain rate [134]. Another study by Tan *et al.* [135] reveals similar results where the dynamic plateau stresses of Hydro Aluminum foam is insensitive to impact velocities up to about 100 m s^{-1} (small cell size) and 50 m s^{-1} (large cell size). In contrast to the results presented above, Paul and Ramamurty [136] and Mukai *et al.* [137] conducted tests on ALPORAS type foams and concluded that they were strain rate sensitive. Hamada *et al.* [138] also studied dynamic compression of foam with different compositions with the spilt Hopkinson bar test method and determined that strain rate dependence was related to the specific alloy. A pure aluminum composition and an Al-Zn-Mg alloy were tested and it was found the strain rate dependence was greater in the case of pure aluminum. In order to look at the gas compression effect, they made small holes in the pure aluminum foams and found that the strain rate dependence was in fact lowered [138]. Dependence on manufacturing and composition has also been observed by other authors [139, 140]. In summary, depending on the foam manufacturing technique different strain rate dependencies have been shown. Factors such as internal pore cracks and alloying elements become important factors. In this thesis quasi-static strain rates will be used to assess the foam strength due to available equipment and the scope of the project.

3 Research objectives

3.1 Objectives

In recent years, significant research has focused on reducing the mismatch between the blowing agent gas release temperature and aluminum matrix melting temperature. Numerous authors have tried modifying the blowing agent through heat treatments or coatings [1, 6, 15, 26, 33, 141] while others have used lower melting commercially available alloys instead of pure aluminum [9, 15, 87, 141-143]. In this study the addition of an alloying element is used to produce a transient liquid phase and narrow the mismatch temperature in the powder metallurgy manufacturing method. The main objectives of this work are summarized below:

1. Assess pure aluminum foams in the context of crack formation. This will be used as a base point study from which improvements can be made.

2. Select an alloying element that alters the foaming properties of the aluminum matrix in the following manner:
    a. Reduces the matrix melting point in order to better match the gas release temperature of the blowing agent.
    b. Creates a transient liquid phase(s) that inhibits the formation of cracks and reduces hydrogen loss at the early stages of foaming. This will also promote the uniform nucleation of round pores.
    c. Widens the formation of the semi-solid region.
    d. Foams at the low possible temperature while keeping the alloy density as low as possible.

e. Produces foams that are resistant to degradation (drainage, coalescence and collapse) over a wide time frame and temperature range.

The concept behind the proposed objectives is based on a combined approach stemming from joining and sintering techniques discussed in the literature review Chapter 2. Select alloys with characteristics potentially favorable in the production of aluminum foams have been summarized in Table 3-1.

Table 3-1: Select alloy properties

Alloy	*Melting Temp. (°C) [144]*	*Advantages*	*Disadvantages*
Zinc	420	Low melting point close to TiH_2 hydrogen release High partial pressure [146, 147] No intermetallic formations[144] Cost effective Large semi-solid region with Al. Reduction in surface tension [58, 91] Lower heat of fusion [147]	Potential diffusion before foaming [121, 145] High solid solubility in aluminum[144] High density[144]
Al-12Si	577	High fluidity [47] Good mechanical strength [148] Cost effective Commonly used Eutectic with low levels of Si Lighter than aluminum [144] Reduction in surface tension [58, 91] No intermetallic formations [144]	Melting point higher than TiH_2 hydrogen release High fluidity can increase drainage and coalescence [87]
Tin	232	Low melting point[144] High liquid solubility with aluminum [121, 144] No intermetallic formations [144]	Very low melting point for hot pressing stage [144] Potentially poor mechanical strength Immiscible with aluminum (can be exuded from the structure unless modified with Mg) [121] High density [144] No semi-solid region [144]
Al-33Cu	546	Low melting point eutectic [144] Higher fluidity Large semi-solid region [122, 144]	Can form an intermetallic compound [144] Higher density Melting point possibly higher than TiH_2 hydrogen release [144] High solubility of Cu in Al Very dependent on process variables [121, 122]
Mg	650	Low melting powder when alloyed with aluminum [144] Improves wetting characteristics between alumina and aluminum [106-109] High partial pressure [147] Large semi-solid region with aluminum [144] Increase in strength [122]	High oxidation potential and partial pressure [148]

Based on the summarized advantages and disadvantages, elemental zinc and Al-Si pre-alloyed powders were chosen as base points for attempting to improve foamability.

3.2 Zinc

The first alloying element proposed was zinc. The main reason behind the use of zinc is that it forms a transient liquid phase which has the potential of inhibiting the formation of cracks and facilitating the nucleation of uniform pores below the onset dehydrogenation of TiH_2. This approach, which centralizes on the formation of this transient liquid phase differs from previous studies that focus explicitly on reducing the melting point of the aluminum matrix using mainly pre-alloyed powders [9, 15, 87, 141-143]. Zinc was also selected in this study for a number of other reasons: because it does not oxidize readily, reduces surface tension [58, 91], has a high partial pressure [146], does not reduce viscosity significantly [149], is cheap (not costly) and has a large semi-solid region when alloyed with aluminum [144]. The Al-Zn phase diagram is shown in Figure 3-1, where the large semi-solid region extends from pure aluminum to an Al-94wt%Zn eutectic forming at a temperature of 381°C [144].

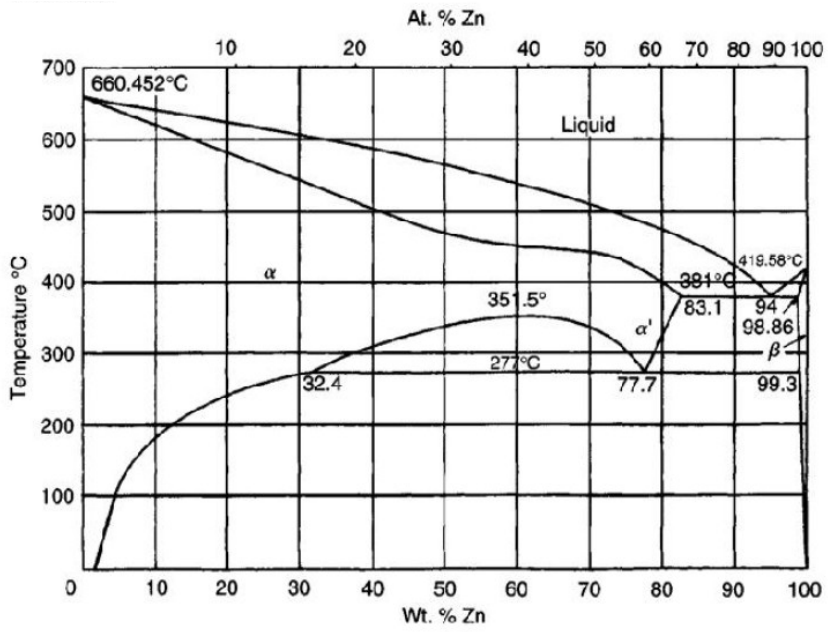

Figure 3-1: Al-Zn phase diagram [150]

The powder metallurgy technique that is used will focus on combining elemental aluminum and zinc powders together in a compact with selected ratios, whereby upon heating the zinc melts first creating a transient liquid phase just prior to the blowing agent gas release temperature enabling the formation of uniform bubbles which grow over time. This zinc phase would then dissolve in the aluminum to form a viscous semi-solid or liquid stabilizing the foam. The primary α-aluminum could have to the potential of stabilizing the foam in the same manner as magnesium foam discussed previously in the literature review section, where primary α-grains were formed [89]. This way, zinc will also serve as an effective melting temperature depressant in addition to providing additional liquid. Furthermore, unlike sintering and joining processes, high vapor pressure can be advantageous for numerous reasons. Zinc high partial pressure will generate vapor which can supply additional pressure within the pores once TiH_2 has released the bulk of its hydrogen. Increased foam internal surface area can also promote zinc evaporation and increase the melting temperature (and viscosity) as the zinc is lost. Figure 3-2 shows the proposed foam improvement mechanism in comparison to pure aluminum as has been observed in this thesis.

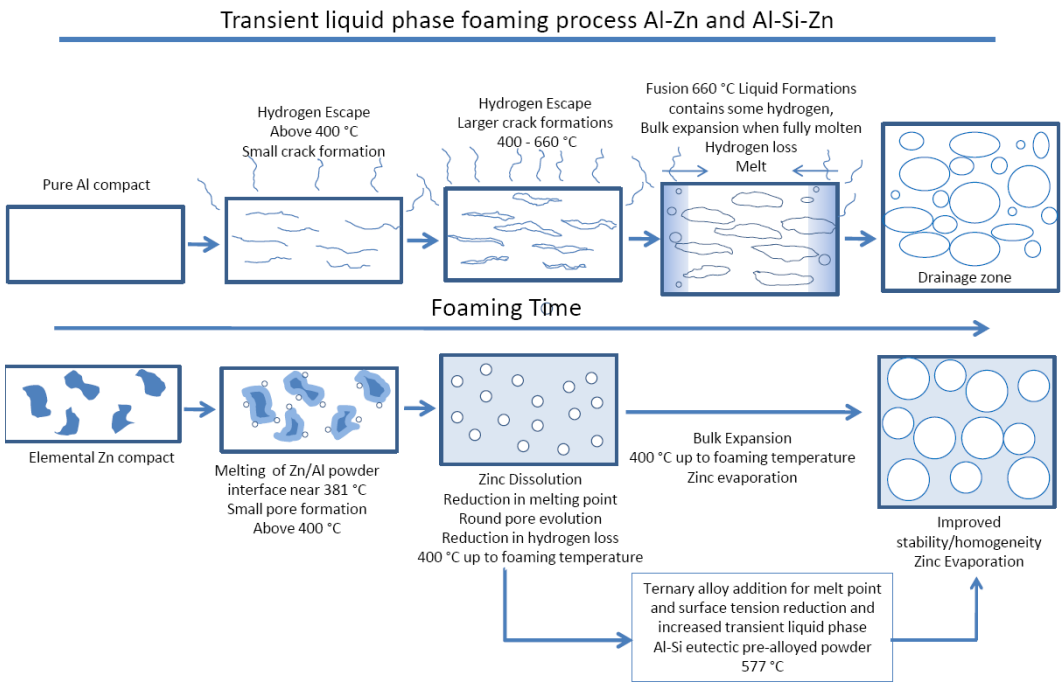

Figure 3-2: Proposed transient liquid phase foaming mechanism

3.3 Al-Si

The Al-Si system was chosen because it is well known in processes such as brazing and sintering that the use of mixtures having eutectic compositions or that form eutectics have favorable spread characteristic, and contribute to some level of surface tension reduction [47, 90, 91, 151]. The pre-alloyed Al-12wt%Si eutectic powder is chosen to lower foaming temperature and enhance stability by providing an additional transient liquid phase during the foaming process. Furthermore, silicon has a density of 2.33 g cm^{-3} which is close to aluminum and therefore, in terms of volume percent, it is more effective in supplying additional liquid without adding significant weight. Although the eutectic phase melts at 577 °C, slightly higher than the TiH_2 dehydrogenation onset temperature, it is likely to have good spread characteristics ensuring adequate liquid during the foaming

process. It is believed that, in combination with zinc (forming a lower temperature eutectic), foams with desirable properties can be produced. A ternary phase diagram generated through FactSage for Al-Si-Zn compositions is shown in Figure 3-3. From this, it can be seen that there is no intermetallics formation as well as a lowered semi-solid region onset of 551 °C proving favorable for foaming. The Al-Si-Zn foaming system is covered in detail in Chapter 8.

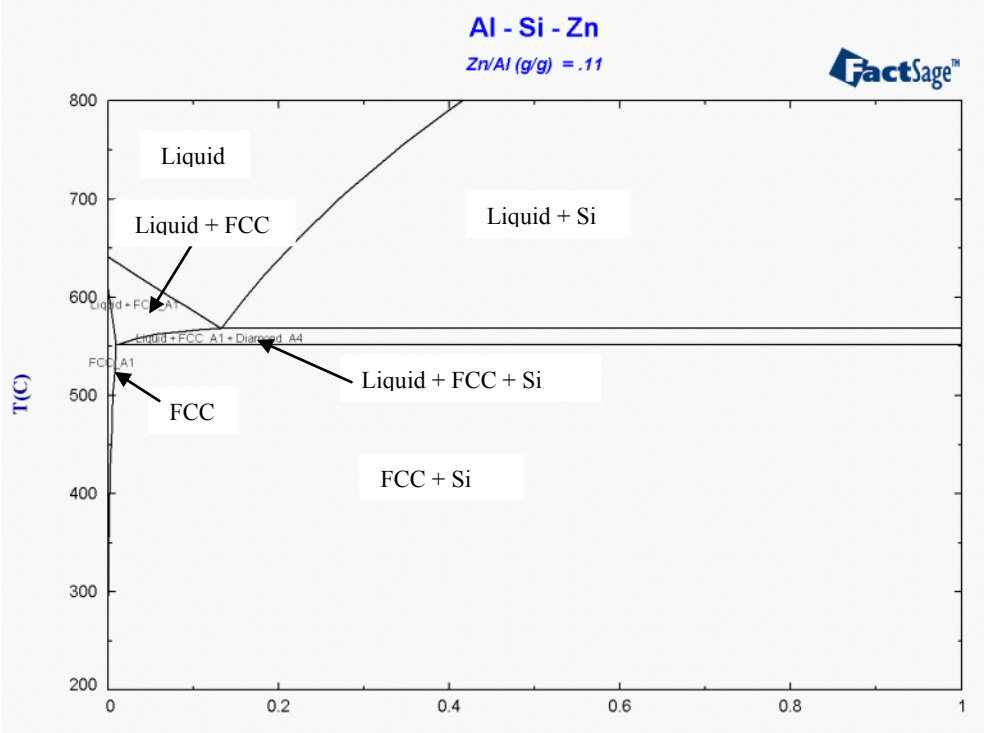

Figure 3-3: Al-Si-Zn phase diagram

3.4 Test Schedule

Work on pure aluminum has been performed as a benchmark for the research. The purpose of this was to validate the methodological methods as well as to have a basis for comparison for other analysis. The formation of cracks was studied in the aluminum compacts using *in-situ* confocal microscopy and expansion using an expandometer furnace. The information gathered from the pure aluminum systems was critical in determining appropriate alloying conditions and temperatures to avoid crack formations.

Tests were performed on low to high concentrations Al-Zn foams (10 %, 33 %, 50 %). Low concentrations of zinc are favorable for keeping the ultra-lightweight properties of the foam, however higher zinc concentrations were thought to provide additional stability against the formation of cracks. The use of pre-alloyed Al-12wt%Si eutectic powder (20 wt% and 30 wt% in total) was also tested to assess for their potential as a transient liquid during the foaming process as well. The variation in foaming temperature will be studied for the pure al, Al-Zn and Al-Si-Zn alloys to determine optimal foaming temperatures. A schematic of the experimental plan is shown in Figure 3-4.

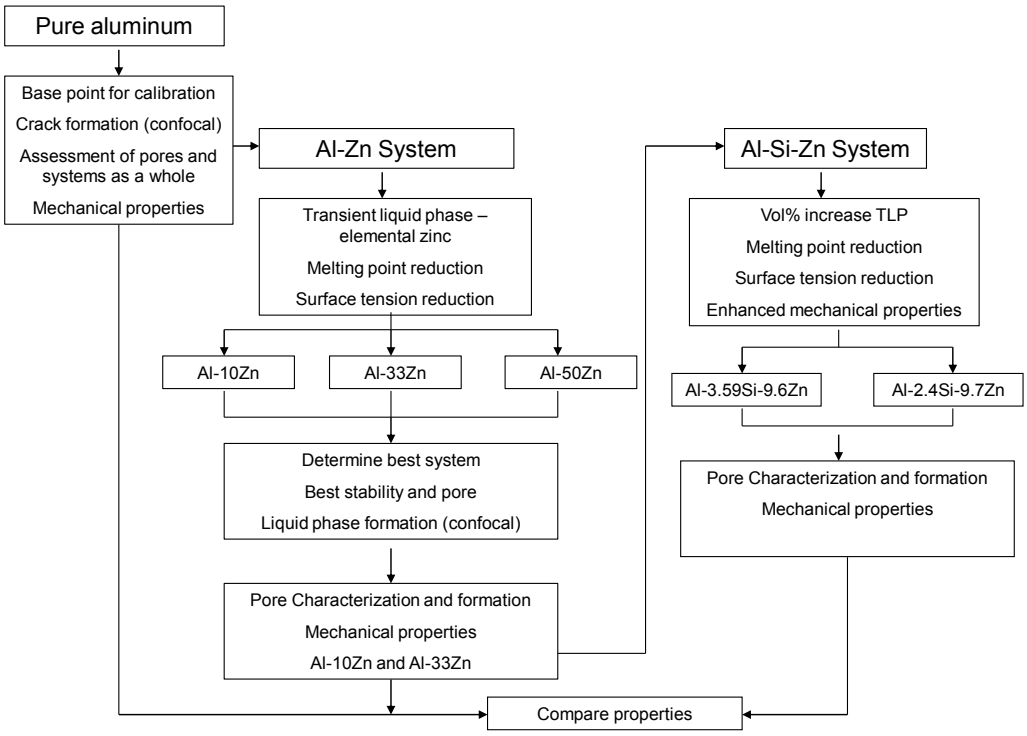

Figure 3-4: Experimental plan flow chart

This page is intentionally left blank

4 Experimental Procedures

4.1 Materials

The atomized aluminum base powder used for the foam fabrication was manufactured by Alfa Aesar, having a -325 mesh size and a 99.95 % purity level. The atomized zinc powders used in the compact production were purchased from Alfa Aesar, with a -100 mesh powder size having a purity of 99.9 %. Aluminum-silicon eutectic atomized powders were supplied by Valimet with a powder mesh size of -325 (85 % min) and +325 (15 % max), grade S-10. TiH_2 blowing agent powder was also purchased from Alfa Aesar, with a powder mesh size of -325 and a measured oxygen content of 0.41 wt%. Powder information is summarized below in Table 4-1.

Table 4-1: Powders used for foam production, mesh size, purity and oxygen content

Element/Alloy	Supplier	Size (mesh)	Purity (%)	Oxygen Content (wt%)
		Base powders		
Aluminum (batch 1)	Alfa Aesar	-325	99.5	0.3783
Aluminum	Alfa Aesar	-325	99.5	0.366
Zinc	Alfa Aesar	-100	99.9	0.079
TiH_2	Alfa Aesar	-325	N/A	0.41
Al-12wt%Si	Valimet	-325 (85% min), +325 (15% max)	N/A	0.152

Particle size analysis was performed using a Horiba LA950 on each of the individual powders used for foaming and the data has been summarized below in Table 4-2. The actual particle size distribution can be seen in Appendix A for each of the powders.

Table 4-2: Powder size analysis

Powder	Sample	Mean (µm)	Median (µm)	Std Dev (µm)	D90	D50	D10
Pure Al	Measured	16.08	16.15	4.34	21.74	16.15	10.23
Al-12 Si	Measured	26.86	29.77	12.07	41.76	29.77	10.33
	Valimet[152]				50	23	7.5
Zinc	Measured	66.48	61.54	36.46	106.12	61.53	26.63
TiH2	Measured	13.94	14.56	5.74	21.11	14.5	5.30

4.2 Powder Mixing and Pressing

In order to produce the required compact mixtures, powders along with the blowing agent were mixed in a tumble mill for 30 minutes. The powders were combined with alumina spheres to ensure proper mixing. Once the powders were mixed they were separated from the alumina balls. This is the standard procedure used for mixing powders to produce compacts at McGill University [1, 33, 153].

Prior to compaction, heat treated steel dies were lubricated with a thin layer of lithium stearate combined with denatured ethanol. The required amount of powder was then inserted into the 20 mm diameter or 30 mm diameter uni-axial die and cold pressed to 343 MPa (20 mm diameter) or 152.7 MPa (30 mm diameter). This step ensures preliminary compaction of the powders into solid precursors which can be easily handled thereafter in the die. Pressing parameters are described in Table 4-3.

Table 4-3: Powder pressing parameters

Powder Pressing Parameters				
Die diameter (mm)	***Sample thickness (mm)***	***Cold pressing pressure (MPa)***	***Hot pressing pressure (MPa)***	***Hot pressing time***
20	7 or 10	343	566	15 min. heating, 15 min. pressing
30	15	152	377	45 min. pressing

Once cold compacted, the 20 mm diameter die is inserted into a hot press which is subjected to weak vacuum without applying uni-axial pressure for 15 minutes (warm up time). Once the die is warm, it was uni-axially pressed for an additional 15 minutes at a pressure of 566 MPa (20 ton or 18.1 tonne press) and temperature of 350 ˚C. Time and temperature of pressing was optimized with pure aluminum to obtain 99 % density and applied to the Al-Zn and Al-Si-Zn systems. The addition of zinc promoted good compaction during pressing due to its lower melting point which makes it more malleable at these temperatures ensuring a high compaction density. As will be shown in Chapter 6, solid state diffusion of both zinc and silicon in aluminum was not considered an influential factor during the hot pressing stage.

In the case of the 30 mm diameter samples, the hot pressing parameters had to be adjusted due to the change in pressure as a result of the increase in die surface pressing area. An upgraded hydraulic system was installed in the hot press to achieve higher uni-axial force. The hydraulic pressing system was upgraded to a 30 ton (imperial), resulting in a lower pressure of 377 MPa due to the larger pressing area of the sample. Therefore, the pressing parameters had to be optimized and adjusted accordingly to obtain high compact density. In order to assess whether the pressing parameters were optimized, compact density levels were measured and expansion curves were compared to ensure a similar behavior. The optimization parameters are shown in Table 4-4. The pressing parameters were optimized with the pure aluminum system first as they proved to be more difficult to compact. The same pressing parameters were then applied to the Al-Zn and Al-Si-Zn systems where adequate compact density was attained. It was determined that direct uni-axial pressing for 45 minutes was the most effective and fastest method of reaching the required compact density above 97 % theoretical, without having adverse compaction effects. Pressing was conducted at 350 ˚C and under weak vacuum. The large 30 mm diameter samples provided a

larger number of cells which was favorable for compression and pore macrostructural evaluation.

Table 4-4: 30 mm compact pressing condition optimisation

30 mm die press parameter optimization			
Pressing Conditions	***Temperature***	***System***	***Results***
30 min warm up of die, 15 min pressing	350 °C	Pure Aluminum	Lower compact density < 90 % theoretical density, compaction rings during foaming due to low compaction at punch/die interface
1 hr direct pressing and simultaneous die warm up	350 °C	Pure Aluminum	Full consolidation >97 % theoretical density, comparable expansion levels to 20 mm samples, no compaction rings (due to low compaction at punch/die interface)
45 min direct pressing and simultaneous die warm up	350 °C	Pure Aluminum	Full consolidation >97 % theoretical density, comparable expansion levels to 20 mm samples, no compaction rings (due to low compaction at punch/die interface), system adopted

4.3 Foaming

4.3.1 Expandometer

The Expandometer was used to measure in-situ foam expansion. A 316 stainless steel crucible was first coated with boron nitride in order to ease the removal of the foamed sample and to prevent the sample from reacting with the crucible. Once a dense precursor has been prepared, the Expandometer furnace was set to a specific foaming temperature until the furnace and/or crucible reached the steady state temperature. The compact was then introduced into the pre-warmed or cold crucible. The furnace temperature measurement was verified using a separate K-Type reference thermocouple inserted below the hot crucible to measure heating rate. Once the compact has been introduced in the hot crucible a counterbalanced expansion motion measuring plunger rod is then inserted over the sample, translating the expansion motion of the foam. A laser measurement device connected to a data logging system linked to a computer interface then records the expansion away from the hot zone. The Expandometer system gives a complete expansion curve along with the heating rate profile in a single experiment without

the need for multiple interrupted experiments as opposed to a box furnace. Furthermore, the expansion/density of the foam is recorded automatically without requiring the use of Archimedes principle which is extremely time consuming. Once an expansion curve is obtained, it is easy thereafter to assess the optimal foaming time and expansion of the foam, making it easy to quickly assess a specific alloy. At least three curves were generated for each sample plus the required interrupted experiments for the compression tests and structure evolution.

The furnace interior is shown in Figure 4-1 along with a typical expansion curve in Figure 4-2. It can be readily observed that the expansion and heating rate can be obtained by a single experiment. Specifics related to the Expandometer are discussed in further details in Appendix A along with design related aspects. Error bars for the expansion curves shown in the thesis are based on the average minimum and maximum values between three foaming curves. Individual foaming curves are shown in the appropriate appendix.

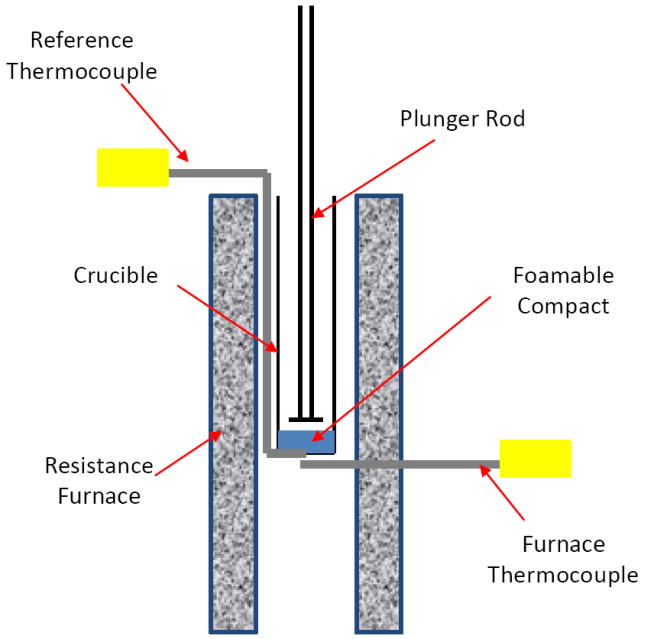

Figure 4-1: Interior of the Expandometer furnace

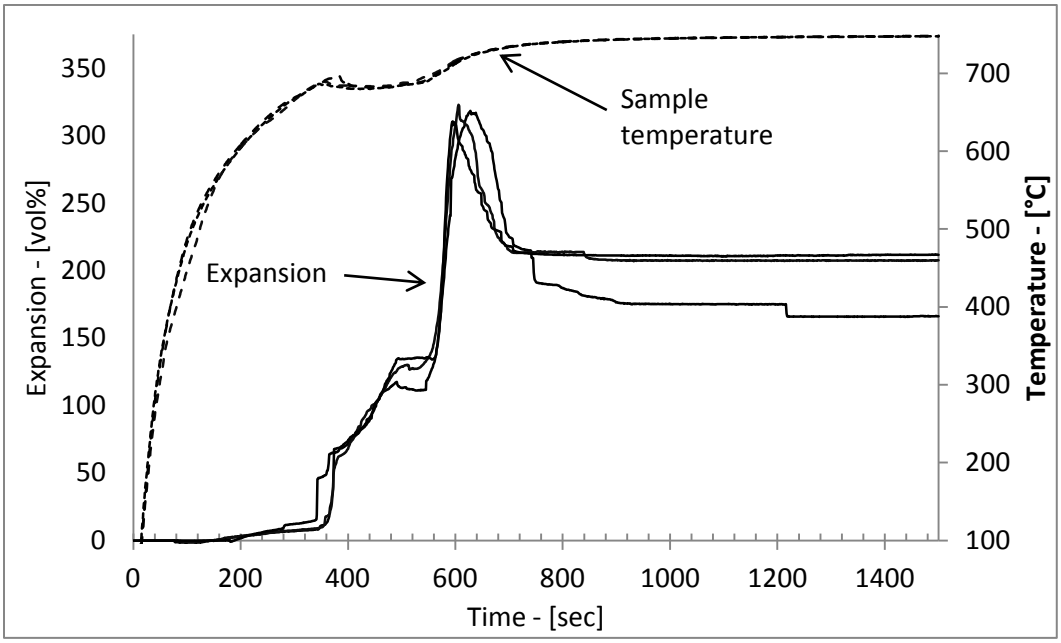

Figure 4-2: Expansion curve from the Expandometer where optimal conditions can be easily assessed

4.4 Characterization Techniques

4.4.1 Differential Scanning Calorimetry (DSC)

Thermal analysis was conducted using a Setaram Evolution 24 thermo-gravimetric analyzer. DSC curves were obtained for the different alloys in an argon atmosphere at a heating rate of 10 ˚C min^{-1} up to analysis temperature. Samples of 20 mg were measured and placed inside an alumina crucible for analysis. Subsequently the curves were analyzed in order to assess phase formation in terms of endo and exothermic reactions.

4.4.2 Inductively coupled plasma mass spectroscopy (ICP-MS)

ICP-MS analysis was performed on both the interior and exterior of Al-Zn foams and compacts to assess the zinc loss to the atmosphere. A Spectro Ciros was used to determine the composition of the alloys.

4.4.3 Oxygen Powder Content

The oxygen content of the powders used for foaming was determined using a LECO TC400 series nitrogen/oxygen determinator. The operation of this equipment relies on the vaporization of the sample and its oxides by bringing the sample up to temperatures exceeding 3000 ˚C. The oxide molecules are broken into their respective elements and vaporized. The vaporized oxides (in the form of oxygen) then react with the graphite crucible to produce carbon monoxide or dioxide. This gas is then detected using an infrared sensor [154].

4.5 Metallography and Microscopy

4.5.1 Sample Polishing

Compacts and foamed specimens were sectioned using a cut-off saw equipped with a lubricated diamond coated blade. Once sectioned, the samples were first ground down using SiC grinding paper in the following sequence: 400, 600, 800 and 1200 grit, changing the sample orientation by 90˚ at each step. The final polish on the sample was performed using 5 µm, 1 µm and 0.05 µm alumina powders suspended in water to obtain a mirror finish.

4.5.2 Optical Microscopy

Optical microscopy was conducted using a Nikon Epishot 200 equipped with the Clemex software. Various micrographs of polished samples were taken and recorded by the microscope camera using the Clemex Vision software. The Clemex software was also used to calculate pore size data based on 2-D images of the foams.

4.5.3 Foam Pore Structure Characterization

The foam samples were cut and subsequently spray painted with flat black paint, dried and sanded down to enhance cell interior to surface (cell wall) contrast.

4.5.4 Scanning Electron Microscopy

A JEOL JSM 840A scanning electron microscope was used to collect secondary electron images along with backscattered images of the polished foam samples and pore surfaces. In addition an attached Energy Dispersive Spectrometer (EDS) system was used to obtain qualitative compositional maps of samples along with x-ray spectrums. The EDS Genesis software was used to perform the analysis after images were collected.

A Hitachi S-3000N VP (Variable Pressure) scanning electron microscope was also used under high vacuum mode to observed secondary and backscattered electron images. The attached OXFORD EDS system was used to conduct qualitative sample elemental composition and x-ray spectra using the Inca microanalysis software.

4.5.5 Confocal Microscopy

A 1Lm21 Lasertec scanning laser confocal microscope was used to observe in-situ microstructure evolution of the metallic foams and interfacial melt reactions. This microscope is equipped with a scanning He-Ne laser having a 0.25 μm resolution and a hot stage with a programmable heating cycle. Samples of approximately 200 mg were polished and inserted into a small alumina crucible prior to analysis to prevent any oxidation. Once the sample was introduced in the chamber, it was vacuum purged and backfilled with argon four times to ensure the lowest possible residual oxygen content. The tests were then conducted under an argon atmosphere to the desired pressure (atmospheric in this case) at a heating rate of 60 $^{\circ}$C min^{-1}. The data was subsequently recorded in video format by a computer where images could be extracted.

4.6 Mechanical Testing

Cylindrical metallic foam specimens were prepared by machining using a lathe to dimensions of 30 mm diameter and height of 40 mm. The machined sample dimensions were chosen based on the foam which expanded the least in order to have test samples having all the same dimensions. Slight variations in density were apparent between samples therefore; three samples of each condition were prepared. The foam compression testing conditions were taken as the apparent optimal conditions based on foam structural appearance and expansion curves.

The tests were performed with an MTS Instron 100kN cell as shown in Figure 4-3. A standard constant strain rate of 10^{-3} s^{-1} based on initial dimensions was used for all tests up to an engineering strain of 0.7.

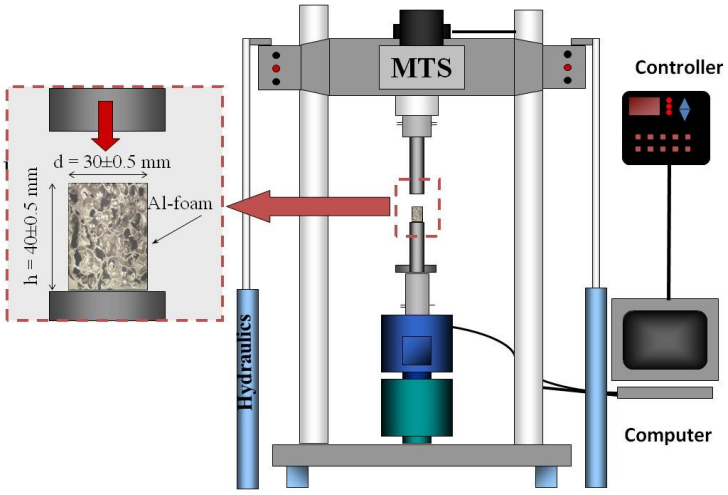

Figure 4-3: Compression test machine setup [1]

The stress-strain curves were obtained by the post processing of the data measured. The engineering stress σ and strain ε were calculated by the following:

$$\sigma = \frac{P_{inst}}{A} \qquad \textbf{Equation 4-1}$$

$$\boldsymbol{\varepsilon = \frac{-(L_o + \Delta L)}{L_o}} \qquad \textbf{Equation 4-2}$$

Where P_{inst} is the load, A is the constant cross-sectional area which does not change as the foam is being crushed. It is to be noted that little barreling or lateral movement of the foam was apparent during testing. L_o is the initial length of the foam sample and ΔL is the measured displacement.

Two common methods exist to determine the plateau stress. The reason more than one method can be used is because the stress-strain curves are not always smooth but can be very jagged and often have an initial high stress peak value before the flat plateau region. The curves for the brittle foam (cell fracture) will typically be very jagged in contrast to ductile foams (cells deform plastically) where the curves are very smooth [13]. The first method consists of taking the initial peak stress value apparent on the stress-strain curve as seen in Figure 4-4. The second method used consists of extrapolating the plateau stress tangent line so that it intersects the elastic portion of the stress strain curve. Generally the tangent method will yield lower values of plateau stress than the peak method [16]. A representation of the methods described above is shown in Figure 4-4.

The onset densification strain marks the end of the constant stress plateau region [135, 155, 156]. A commonly used method of determining densification strain is based on the intersection of tangent lines. A tangent line is drawn on the plateau stress and another where the curve becomes steep (densification) and once drawn the intersect of the two lines determines the densification strain as seen in Figure 4-4. [136, 157].

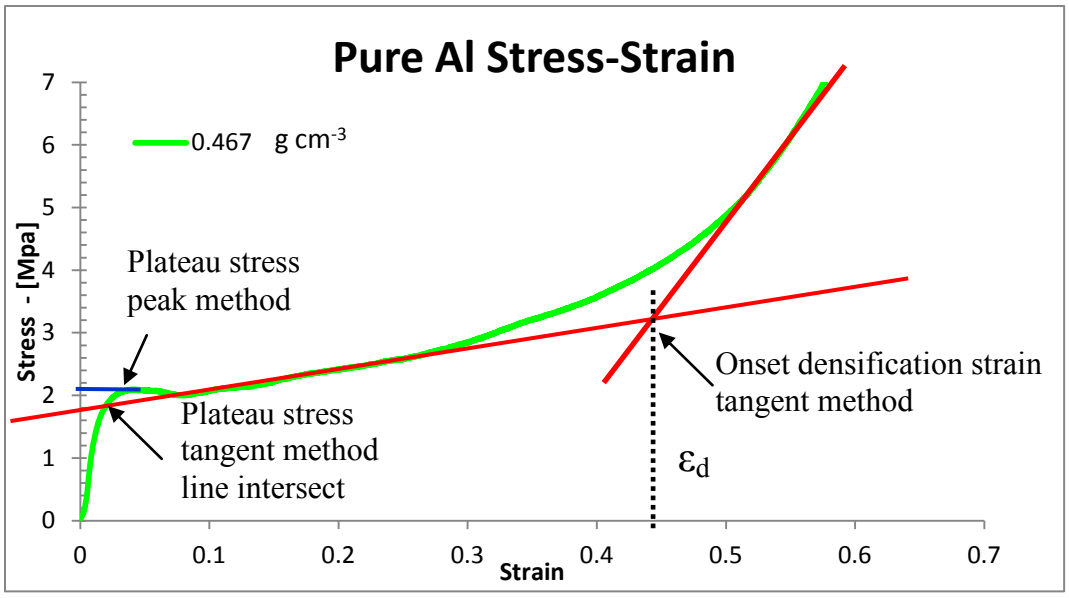

Figure 4-4: Pure aluminum stress-strain curve highlighting the tangent method and peak stress method for plateau stress and the densification strain

An alternative and less subjective method to assess the onset densification strain that has been used for foam is based on the energy absorption efficiency. The energy absorption efficiency is described below as:

$$\%E = \frac{\int_0^l F \cdot dl}{F_{max} L} \cdot 100 \qquad \textbf{Equation 4-3}$$

Where F is the instantaneous force integrated over the compressed foam distance l (area under the curve). F_{max} is the maximum force applied on the foam at a given location during crushing and L is the initial sample length [158]. It is obvious from the equation that for a foam with a flat plateau region such as in Figure 4-4, the numerator along with the denominator will increase proportionally over the flat plateau range. If the foam is perfectly uniform with a very flat plateau stress over a large strain, the energy absorption efficiency can be very high. The onset

densification strain maximum ε_d can in turn be defined as the peak of the curve where:

$$\boldsymbol{\varepsilon_d = \frac{d(\%E)}{d\varepsilon} = 0} \qquad \textbf{Equation 4-4}$$

The densification strain determination can be observed in Figure 4-5 which was plotted based on the raw data used for plotting Figure 4-4 [158]. In the present analysis, where stress-strain curves were not smooth, a third order polynomial fit on the data was applied to the efficiency curve to determine the maxima (densification strain).

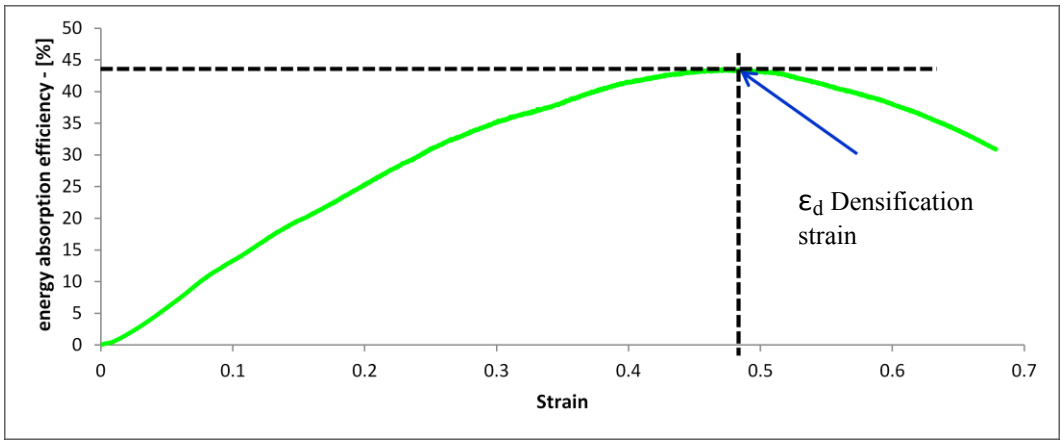

Figure 4-5: Energy absorption efficiency curve, densification strain determination based on efficiency method

Once the onset densification strain was obtained, the energy absorption potential of the foam could be calculated by Equation 2-6 described in Section 2.6 of the literature review.

4.7 Thermodynamic Calculations (FactSage)

The Thermodynamic modeling software package FactSage 6.0 was used as a means to predict possible phases present in the foam under equilibrium state. This software is the result of a joint effort between Thermfact/CRCT (Montreal,

Canada) and GTT Technologies (Aachen, Germany) over the last 20 years. The FactSage software consists of a series of databases used to calculate the conditions for multiphase (or multi-component) systems under equilibrium conditions [159].

For example, it can calculate the phases present in a specific alloy at a certain temperature along with phase diagrams. The reason it has been used is to give an idea of which phases may be present during the formation of the foam which is especially important when looking at the ternary phase diagram and phase formations pertaining to the Al-Si-Zn foams.

This page is intentionally left blank

5 Pure Aluminum Foam

Pure aluminum was assessed in the current thesis to observe the early stages of hydrogen release in the compact in order to determine appropriate process modifications and alloying additives to optimize foam formation. In this Chapter, *in-situ* hot-stage confocal microscopy analysis was used to precisely determine the early crack formation temperature using a controlled heating rate and subsequently compared to expansion curves, sample temperature measurements and foam structures. These measurements are not only crucial to evaluate the onset of hydrogen release but to propose potential alloying elements that will increase the foaming efficiency in relation to the onset of gas release and bulk melting events.

5.1 Hydrogen release temperatures

The most commonly used blowing agent for aluminum-based foam production today is TiH_2, which is known to decompose at temperatures lower than the melting point of pure aluminum [6, 7]. Over the years, numerous studies have identified the TiH_2 gas release temperatures through loose powder analysis and with respect to crack formation in Al-Si based alloys. Inter-study variability is however apparent, with reported onset release temperatures starting as low as 380 °C and going up to over 500 °C, as summarized in Figure 5-1 [1, 6-8]. Moreover, it has been shown that the compaction process itself and the blowing agent powder size affects the release of hydrogen in comparison to loose powders [1, 8]. As the temperature of TiH_2 decomposition directly affects foamability and crack formation prior to bulk melting of the foaming matrix, it is imperative to determine the temperature and extent to which hydrogen gas is lost and what measures can be undertaken to address this issue with respect to the utilized powders.

Table 5-1: Previous work related to early stages of foaming

Alloy	TiH_2 Content wt%	TiH_2 gas release onset temperature °C	Year	Author
Al-7wt%Si	0.5	380-400 °C	2002	Helfen *et al.* [11]
Al-7wt%Si	0.6	above 500 °C	2002	Kennedy [142]
Al-7wt%Si	0.6	Not specified	2001	Banhart *et al.* [10]
Al-7wt%Si	0.5	450 °C	2000	Yin *et al.* [86]
Al-7wt%Si & 6061	0.5	above 380 °C	1999	Duarte & Banhart [20]

TiH_2 powder gas release temperatures were measured under differential scanning calorimetry (DSC), at a heating rate of 10 °C min^{-1}. The onset of dehydrogenation was recorded at 475 °C with desorption temperature peaks at 502°C and 569 °C respectively as shown through Figure 5-1. Since the initial heating rates during the foaming process, as measured through sample temperature are significantly higher than 10 °C min^{-1} (227 °C min^{-1} linear approximation up to 550 °C with a 750 °C furnace set point), bulk hydrogen desorption temperatures can be shifted to higher values due to a temperature lag reaction onset [1, 160]. This phenomenon has been observed by Proa-Flores [1] for TiH_2 by varying the heating rates of the powders from 1°C min^{-1} to 15°C min^{-1} [1]. Moreover, the compaction process can have an influence on the outgassing temperatures along with the constraint of the blowing gas in the matrix [8]. Therefore, it is expected that actual hydrogen release can occur at higher temperatures than recorded through DSC, but thermal analysis equipment limitations and the small percentage of TiH_2 (in the foam compact) make it difficult to obtain quantitative results representative of the actual foaming process. The TiH_2 characteristics including powder size distribution and oxygen content have been tabulated in Table 4-1 in the experimental procedures. Consequently, *in-situ* confocal microscopy is used to identify cracking during the early stages of foaming for the pure aluminum system.

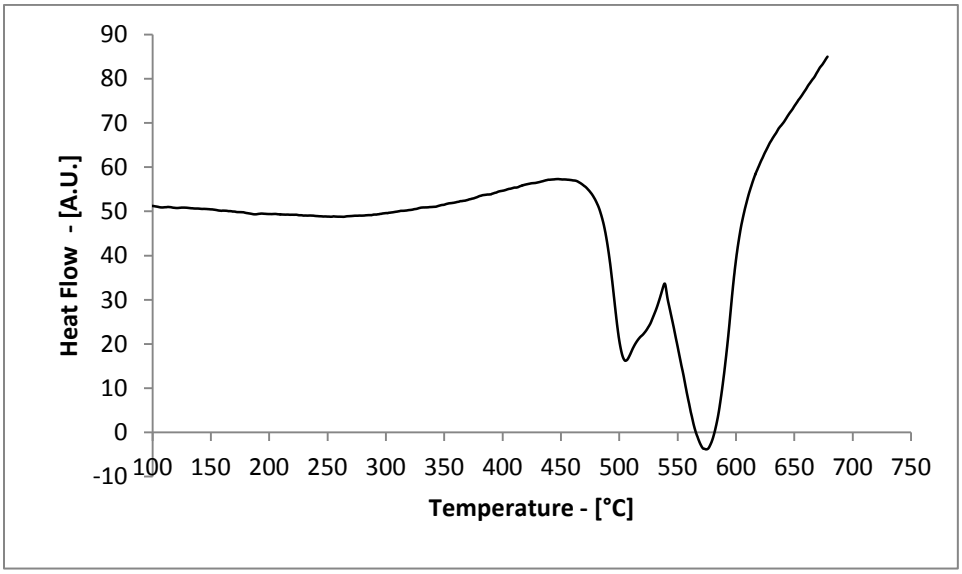

Figure 5-1: DSC measurement for TiH_2 loose powders

5.2 Crack Formation and Propagation

Polished pure aluminum compacts containing 0.8 wt% TiH_2 were cut and introduced into the confocal microscope so that the direction perpendicular to pressing could be observed. A heating rate of 60 °C min^{-1} was used up to a temperature of 750 °C, to simulate the actual foaming process as closely as possible. A video of the evolving microstructure was recorded where a series of images were subsequently extracted and shown in Figure 5-2. Due to the extraction of images from video, and frequent focus adjustments, the resolution is relatively poor. Quenched foam specimens of the evolving structure will presented in a later section as well as in Chapter 7 and Chapter 8 in support of this analysis.


Time 143.83
Temp 500.6
a)
100 µm

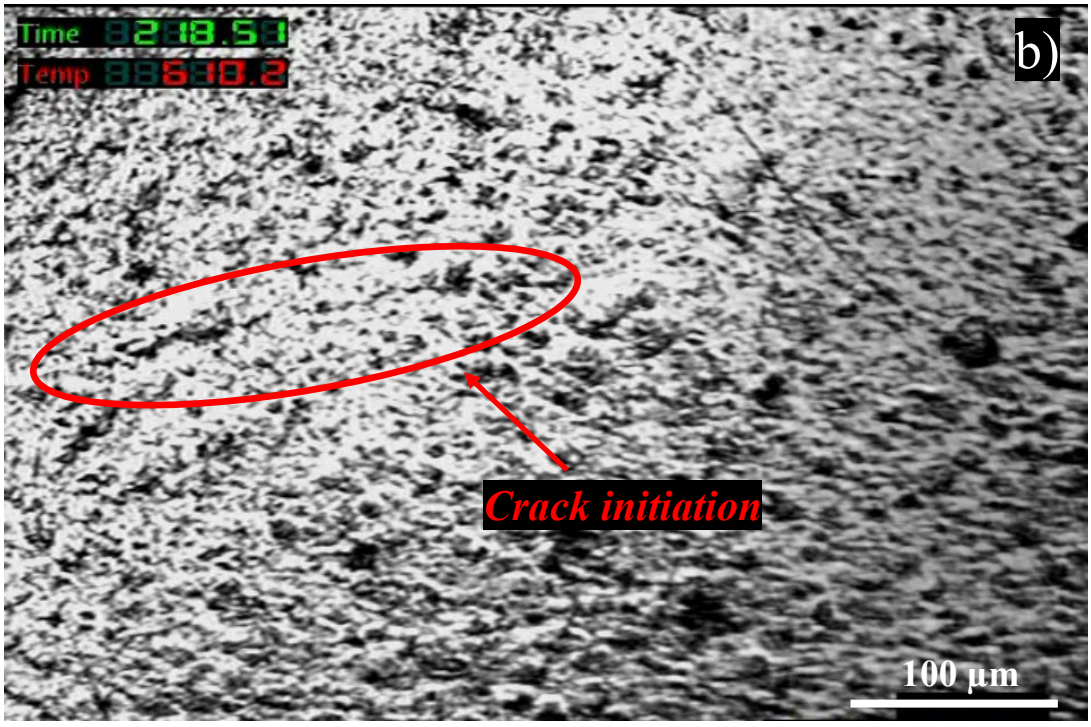
Time 218.51
Temp 610.2
b)
Crack initiation
100 µm

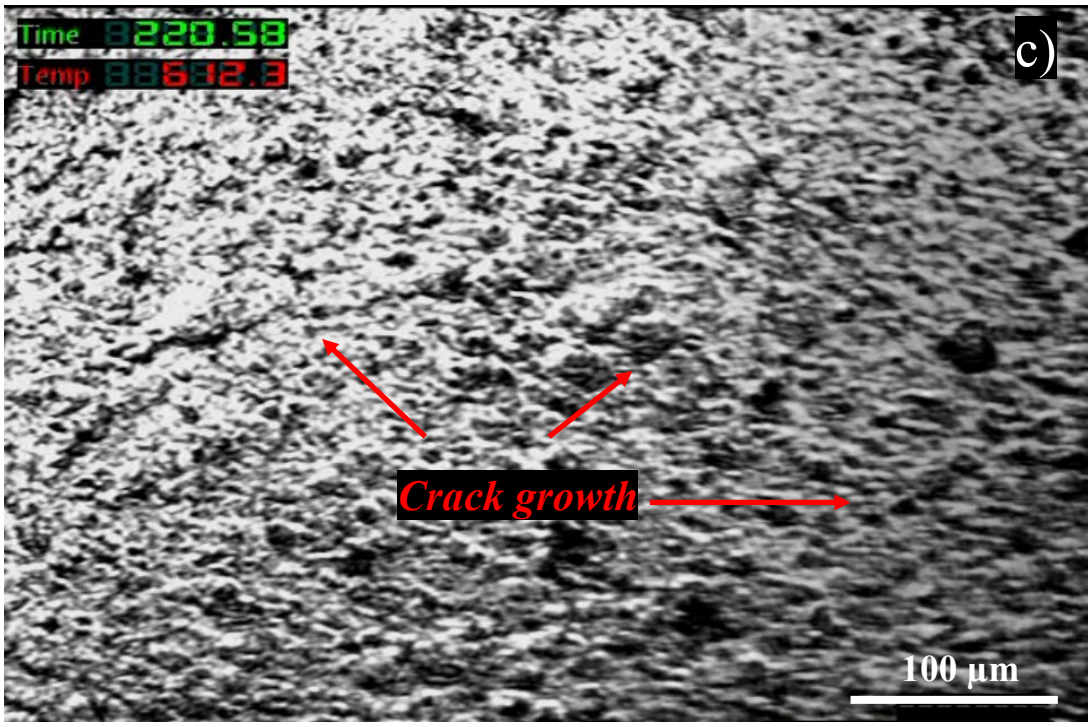
Time 220.58
Temp 642.3
c)
Crack growth
100 µm

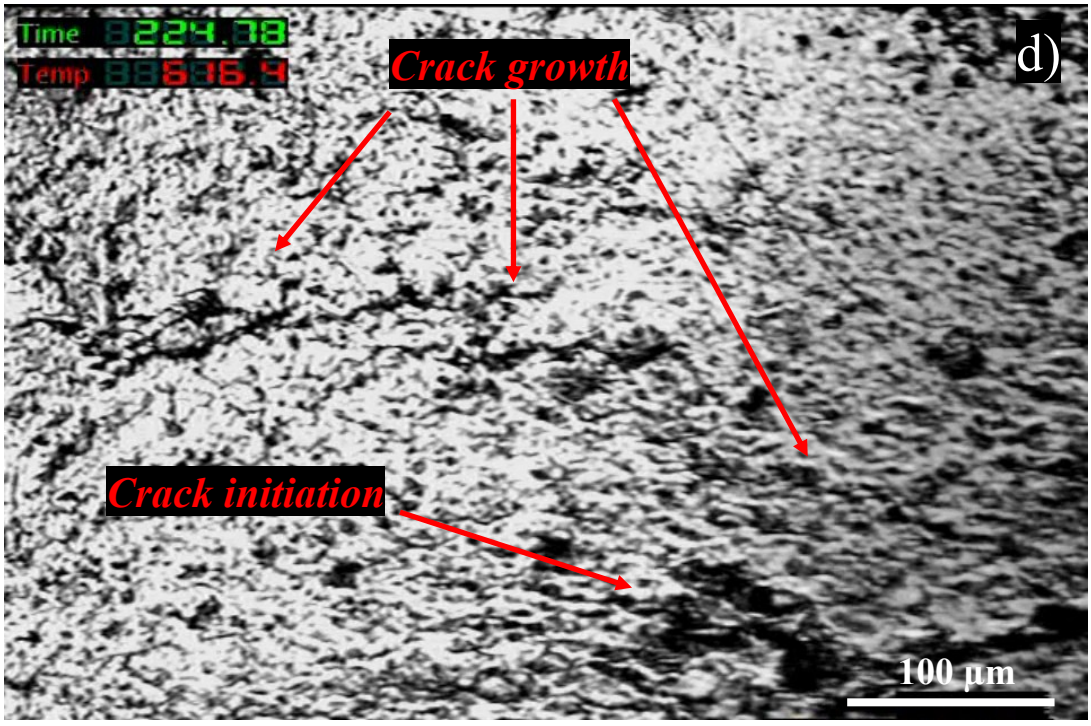
Time 224.78
Temp 646.4
Crack growth
d)
Crack initiation
100 µm

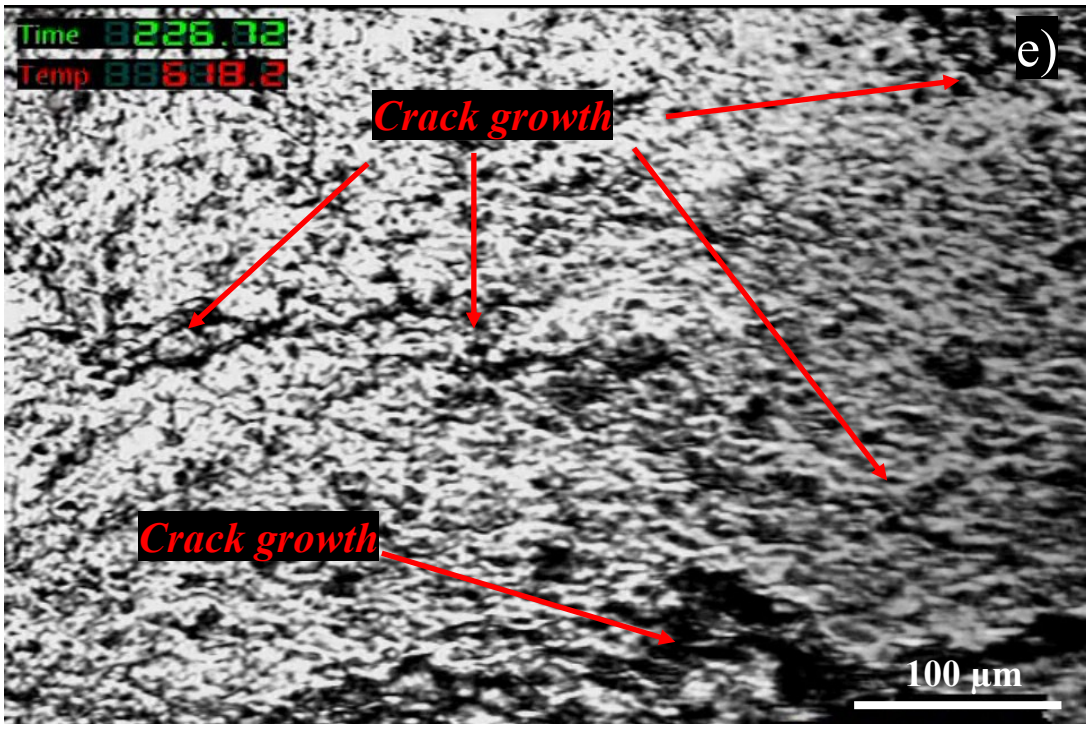
Time 8226.72
Temp 8848.2
e)
Crack growth
Crack growth
100 µm

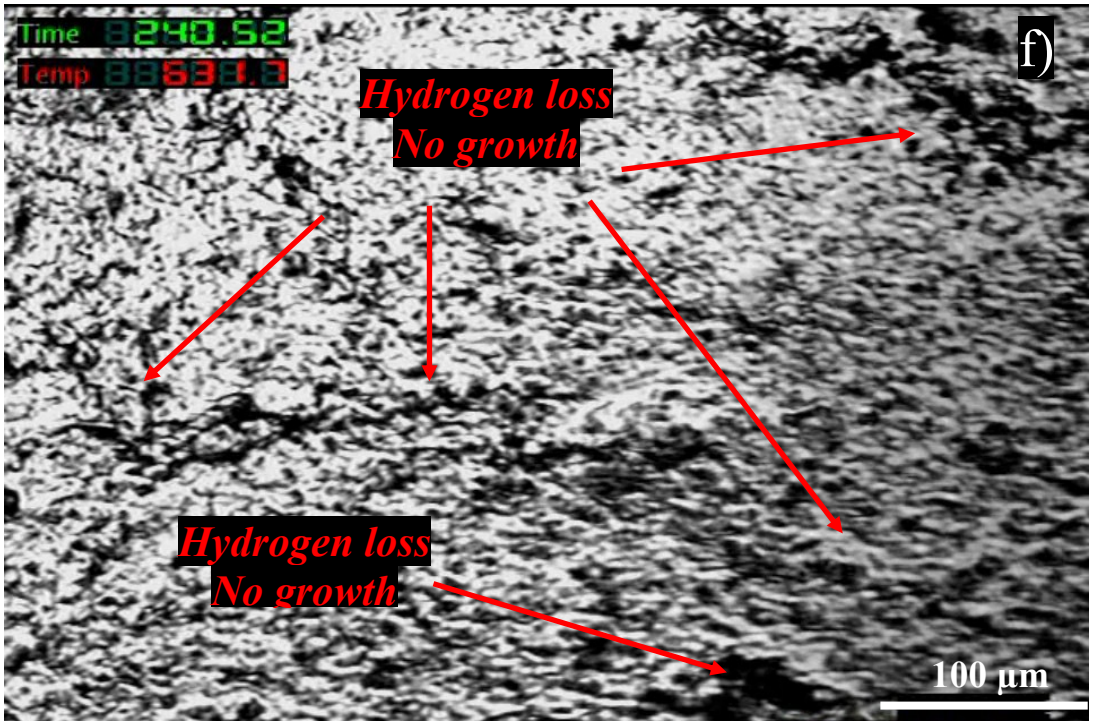
Time 8240.52
Temp 8831.7
f)
Hydrogen loss
No growth
Hydrogen loss
No growth
100 µm

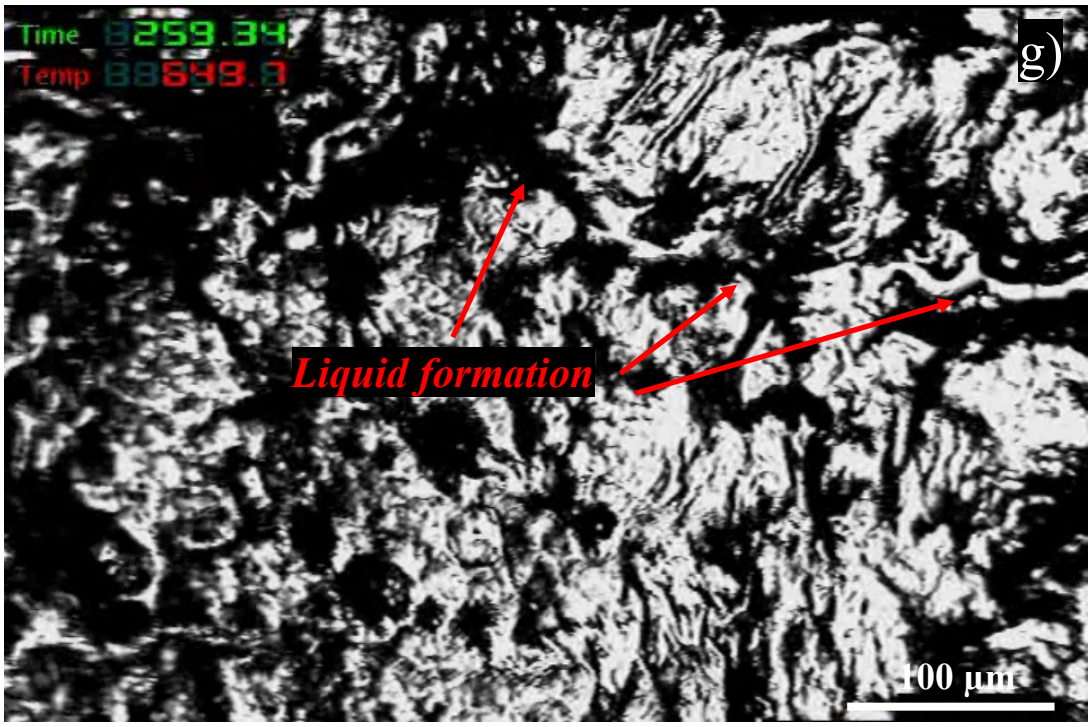

Figure 5-2: Laser confocal microscope images (extracted from video), with a heating rate of 60 ˚C min^{-1} from 20 ˚C up to a maximum of 750 ˚C, a) Polished compact at 500 ˚C, b) Initial crack formation at 610 ˚C, c) Crack propagation stage through compact 612 ˚C, d) Crack growth and initiation 616 ˚C e) Crack growth 618 ˚C f) hydrogen loss period, no crack growth 631 ˚C g) liquid formation and structural movement 649 ˚C

From Figure 5-2b, crack formation is initiated at 610 ˚C and clearly visible, apparent at a significantly lower temperature (by 50 ˚C) than the melting point of pure aluminum (660 °C). Although the cracks appear at this temperature, it is to be noted that the focus of the microscope required adjustments at 550 ˚C as the sample appeared to be dilating. This dilation prior to cracking is likely the result of thermal expansion of the aluminum matrix.

Once initiated at 610 °C, crack spreading was very rapid, almost instantaneously up to a temperature of 620 ˚C (time of 10 s) and shown through Figure 5-2b, to Figure 5-2e. The rapid formation of these cracks occurs when the pressure produced by the blowing agent overcomes the constraints imposed by the pressed aluminum powder, relieving the internal stress of the structure. Rapid crack

formation was then followed by a period of decreased activity from 620 ˚C (slow crack propagation or no visible cracking at all) until the melting temperature of aluminum was reached (near 660 ˚C) shown in Figure 5-2f. During this period of decreased activity (620 °C – 660 °C), hydrogen was released freely from the fully formed network of fissures. Evidence of hydrogen out-gassing (and combustion) from an open crack network within the compact before expansion, is audible from the foaming furnace (expandometer) prior to reaching the foam melt temperature (and during melting) as hydrogen is being combusted. Figure 5-3 shows an etched compact highlighting the particle orientation explaining the favored orientation for crack formations being perpendicular to the compaction axis.

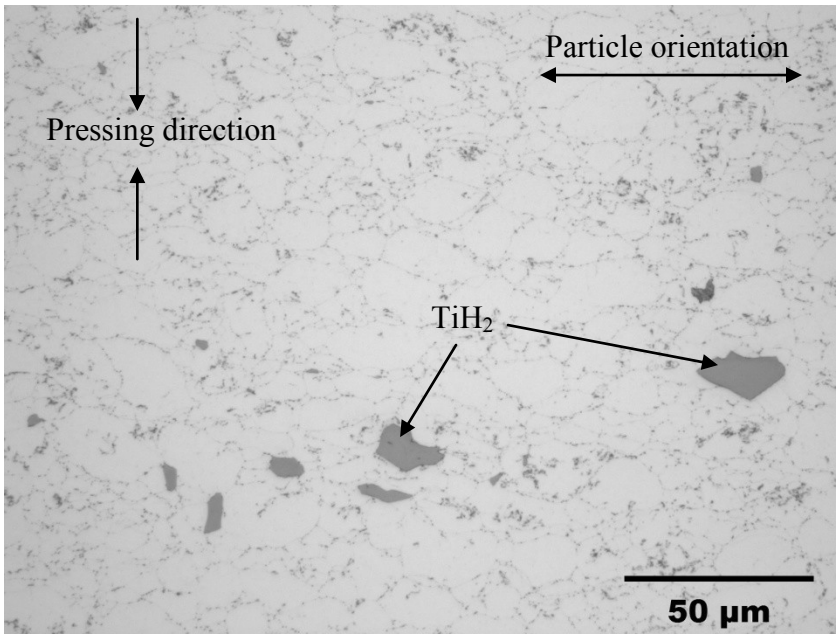

Figure 5-3: Pure aluminum compact etched for 15 s, 0.5 vol% hydrofluoric acid

From Figure 5-2g, as the compact reaches the melting temperature of the aluminum (660 ˚C), cracks are filled with liquid and large "blocks" of solid compact between the liquid filled cracks appear to shift quickly. These "blocks" which divide the structure, appear to consist of semi-solid or solid compact sections separated by a liquid interface which can be observed during the early

foaming stage. This is likely the result of the melting of the compact in conjunction with the oxide network keeping the structure together as it starts expanding. As expected, cracks form at temperatures significantly higher by 135 °C than the recorded dehydrogenation onset of loose powders through DSC as a result of the high heating rate and the tightly constrained TiH_2 particles within the highly dense compact. The foaming steps as observed through confocal microscopy are summarized in Table 5-2. This shows that the cracks are initiated before the melting temperature is reached.

Table 5-2: Foaming events observed through confocal microscopy, DSC and expansion curves

Temperature	*Confocal Microscope*	*DSC measured 10 °C min^{-1}*	*Foaming furnace (for Al foam produced at 750 °C*
475 °C		*Dehydrogenation onset*	
502 °C & 669 °C		*Bulk dehydrogenation peaks*	
550 °C	*Sample dilation*		*Slight expansion, dilation of the foam – crack formations*
610 °C	*Crack initiation*		
610 °C - 620 °C	*Crack spreading*		
620 °C - 660 °C	*Hydrogen loss period (no crack spreading)*		
660 °C	*Foaming onset (rapid foaming due to small sample size)*		Larger expansions/melting of compact (slow due to large mass) – hydrogen loss
> 660 °C	*Foaming*		Rapid expansion
715 °C			Maximum expansion
715 °C >			Rapid collapse

5.3 Foaming Curves and Heating Rates

The sample temperature of the foam in the expandometer was measured with the sample introduced into a cold crucible to observe the thermal events of the sample. Figure 5-4 depicts representative curves for a foam produced at 750 °C (more shown in following section) showing the furnace temperature and sample heating profile. Until the melting point of the compact is reached at 660 °C, a slight expansion of the foam (from 150 s (550 °C) to 370 s (660 °C)) is observed in Zone 1 which can be correlated with thermal expansion and the onset of crack formation. When the melting point of pure aluminum is reached at 660 °C, there is a step in expansion at 370 s, identified as Zone 2. It can be seen that this step

persists for the duration of the compact melting period until 546 s, represented by a constant sample temperature. Due to the high heat of fusion of aluminum 10.71 kJ mol^{-1} [147], a great deal of thermal energy is required for bulk melting of the sample once the onset melting temperature is reached. With the lack of semi-solid, there is potential for significant loss of hydrogen at this stage along with low levels of encapsulation as the compact is melting and is unable to fully contain the gas. Once the compact has completely melted, as seen from the sample temperature measurements in Figure 5-4, bulk expansion occurs very rapidly within 90 s and the maximum volume expansion is reached at 716 °C, well before the sample reaches the set point temperature of 750 °C. Unlike previous studies on Al-Si foams, there is no semi-solid region available to help the nucleation of round cells below 660 °C [10, 11, 20, 86, 142].

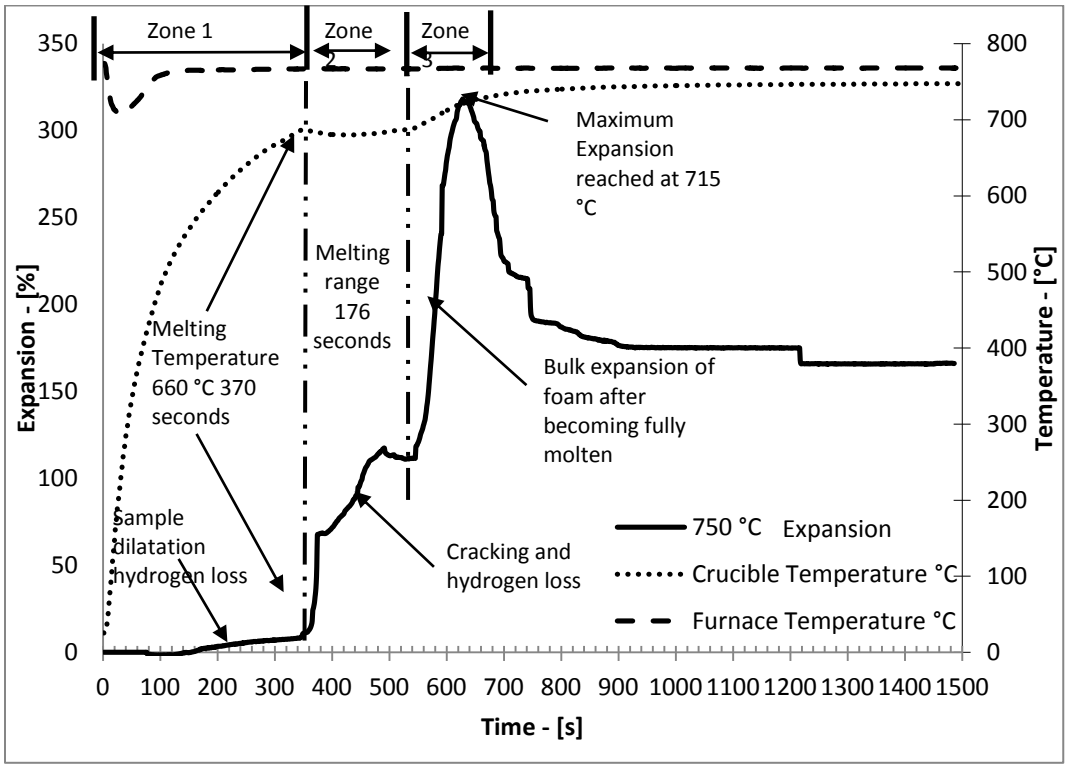

Figure 5-4: Pure aluminum foamed at 750 °C based on a 20 mm compact

Once the foam has reached maximum expansion, rapid collapse is observed as the temperature of the sample keeps increasing. The increased temperature can be

associated with higher fluidity which enhances foam collapse once the blowing gas has stopped releasing hydrogen [149]. The topic of viscosity and stability will be addressed in greater depth in Chapter 7 and Chapter 8.

5.4 Variation of Foaming Temperatures and Heating Rates

Foaming curves shown in Figure 5-5 were produced at 710 ˚C and 750 ˚C to observe the effects of the heating rate and furnace temperature on foaming. In both instances the same foaming steps are apparent at both temperatures and rapid bulk expansion is initiated once the compact is fully molten. Once the sample reaches maximum expansion, there is again a significant decrease in volume, highlighting the poor stability of the foam at both 710 °C and 750 °C. With the lower furnace set point, the foam takes longer to melt and expand. The maximum expansion is significantly reduced by the longer time it takes to melt and is proportional to the furnace set point. The longer time delay in reaching the melting point can be translated to a higher level of hydrogen loss.

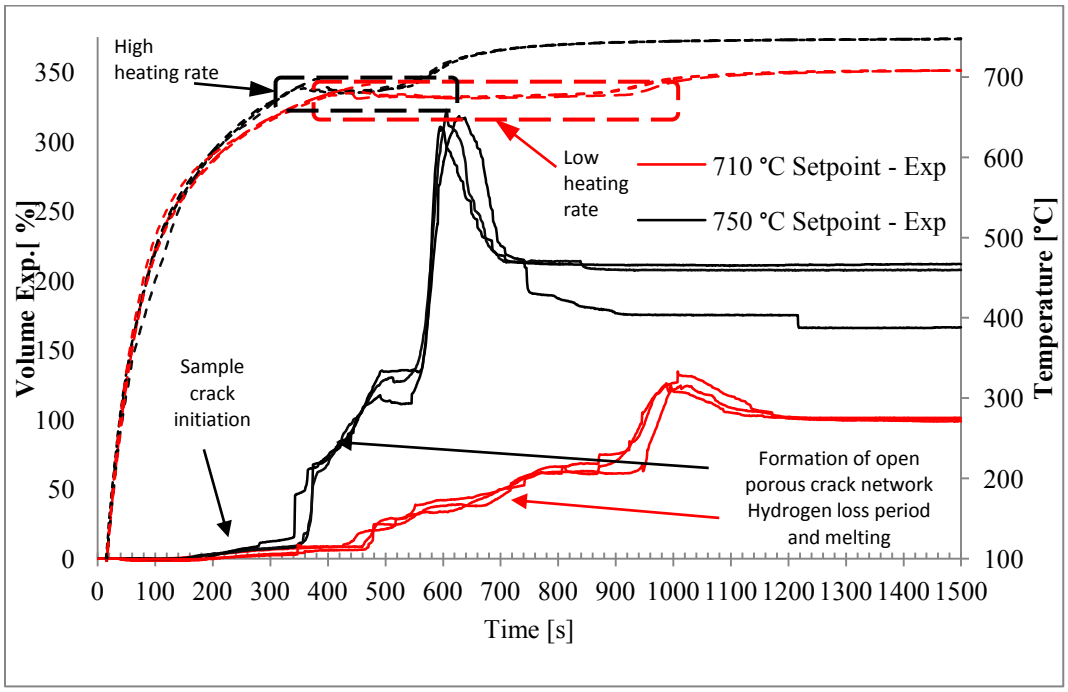

Figure 5-5: Foaming curves at 710 ˚C and 750 ˚C for pure aluminum

Heating profiles of the foams are shown more closely in Figure 5-6. Since a resistance furnace is used along with relatively large samples (8.55 g), the sample required significantly more time to melt than the sample in the confocal microscope with a set heating rate.

The average time for the samples produced at 750 °C to reach the melting temperature is 351.7±16.01 s while it is 462.7±16.2 s for the foam produced at 710 °C. However, the time required to melt the foam produced at 750 °C was on average 196.0±17.8 s being less than half of the time for the 710 °C samples at 431.3±15.3 s. This window leaves significant time for the foam to lose hydrogen. As a result, the bulk expansion of the foam produced at 710 °C is limited on average to 127.7 ± 1.5 vol% in contrast to the samples produced at 750 °C, which yielded and expansion of 311.0 ± 5.5 vol%. These values have been tabulated in Table 5-3. The heat flux input during melting will be discussed in Chapter 7 in comparison to Al-Zn based foams.

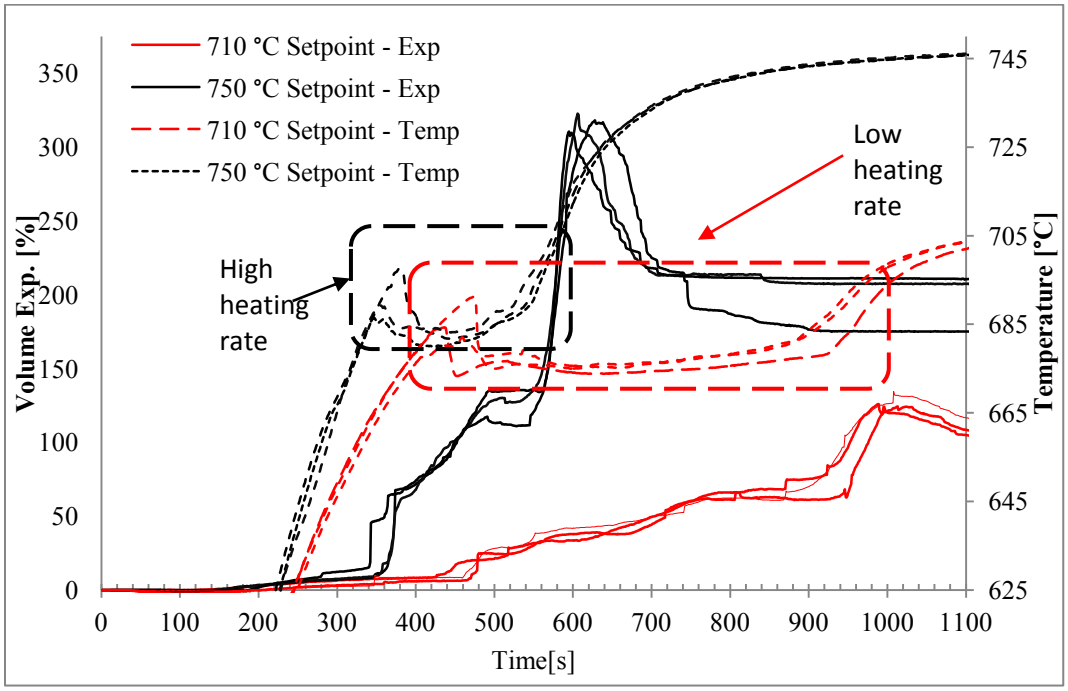

Figure 5-6: Foaming temperature for pure aluminum foam produced at 710 °C and 750 °C furnace set point

Table 5-3: Foaming conditions at different furnace setpoints

Foaming Temperature (°C)	*Melting Onset (s)*	*Melting time (s)*	*Bulk expansion onset (s)*	*Maximum Expansion (vol%)*	*Maximum Expansion temperature (°C)*
Pure Al - 710 °C	462.7 ± 16.2	431.3 ± 15.3	894 ± 5.0	127.7 ± 1.5	696.0 ± 1.5
Pure Al - 750 °C	351.7 ± 16.0	196.0 ± 17.8	547.7 ± 6.6	311.0 ± 5.5	716.3 ± 5.1

For a furnace setpoint of 750 °C, the maximum expansion is reached on average at 716.3 ± 5.1 °C in contrast to a set point of 710 °C, where the maximum expansion is reached at 696.0 ± 1.5 °C. These results indicate that pure aluminum foams can be formed at low levels of superheat if the heating rate is sufficiently high to suppress the hydrogen loss period by minimizing the melting time. A rapid linear heating rate is difficult to attain, but introducing a sample into a pre-heated furnace and crucible can supply a desirable high heating rates.

Figure 5-7 shows foam expansion curves for a wide range of furnace set points where the sample is introduced into a hot furnace and crucible. High temperature set points produce high heating rates while low set points generate low heating rates which translate to lower expansion. However, it is also likely that a higher level of hydrogen dissociation occurs at these higher temperatures.

The relationships between the furnace set point, expansion and time required for melting the compact are shown below in Figure 5-8. At 690 °C for instance foam expansion is marginal even though the furnace set point was above the aluminum melting point indicative of substantial hydrogen loss.

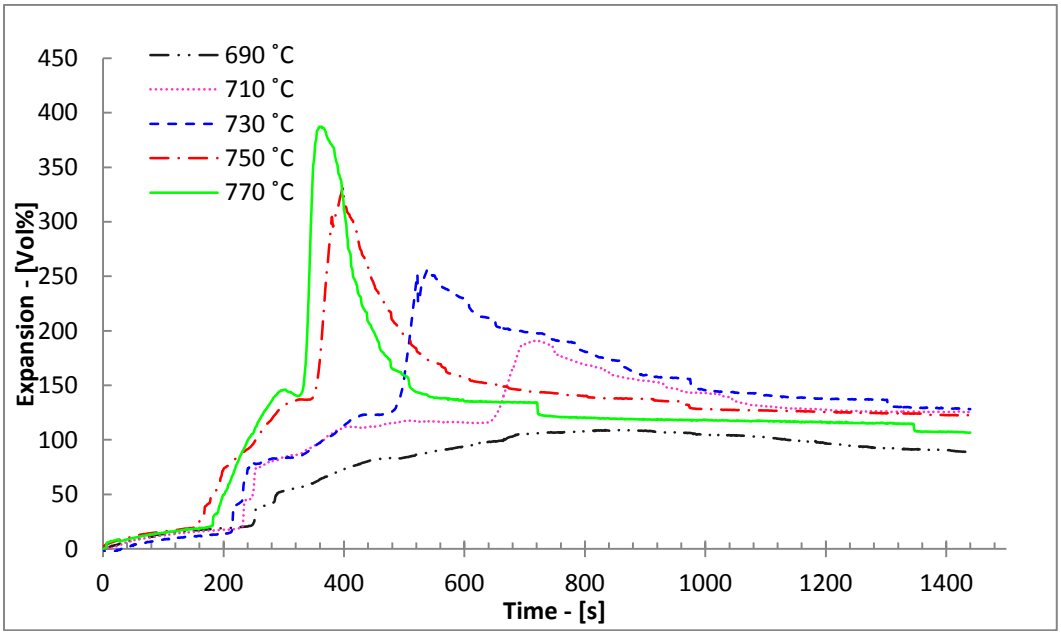

Figure 5-7: Foaming curves generated at a variety of set points from 690 °C to 770 °C

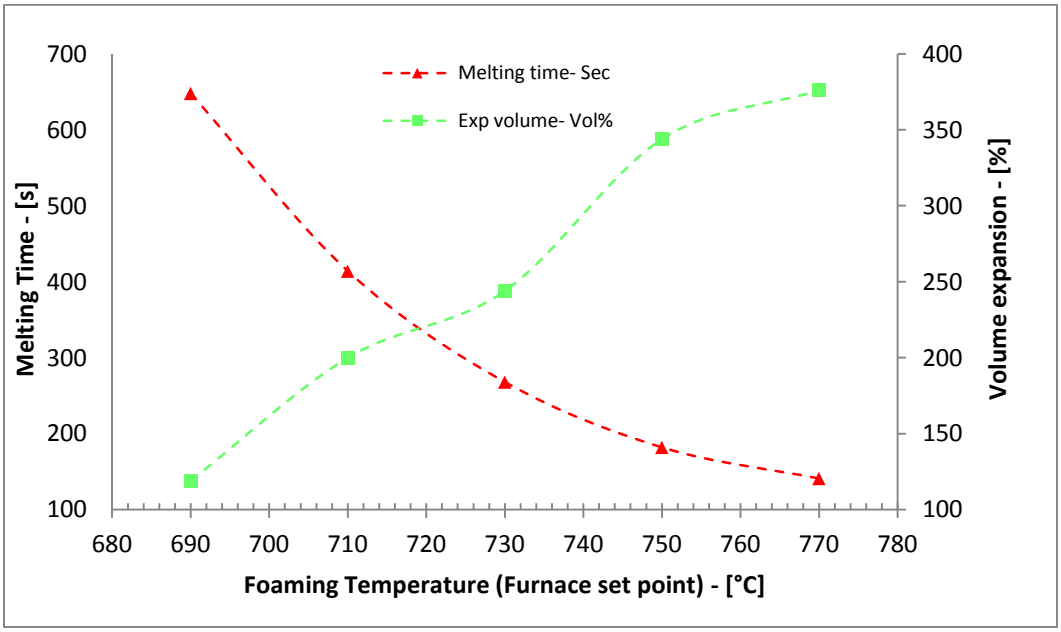

Figure 5-8: Time required for the sample to melt in relation to foaming temperature and the volume expansion with respect to foaming temperature.

In contrast, the foam produced at 770 ˚C in Figure 5-8, shows very high levels of expansion near 400 vol% due to the high heating rate but the obvious gains were offset by the increase in melt fluidity which favors drainage and collapse. In

summary, if an induction furnace was used, for instance, where high heating rates could be easily attained, improved expansion at lower temperatures could be achieved without a significant increase in fluidity, thus reducing drainage and collapse. This would enable the production of foam at very low temperatures.

5.5 Foam Structures

To observe crack formation in actual samples, air quenched foam samples were cut and polished. A foaming temperature of 710 °C (as shown in Figure 5-10) was chosen for ease of comparison with Al-10wt% zinc foams produced under the same conditions in Chapter 7. In Figure 5-9a, the sample is heated for 300 s, one can observe that cracks have not yet formed and hydrogen release is not apparent. From the micrograph it can be seen that TiH_2 particles are visible and imbedded in the aluminum.

At 500 and 550 s in Figure 5-9 and Figure 5-10, the pure aluminum samples have reached the melting temperature according to the expansion curves, where large horizontal cracks can be seen with the naked eye in the centre of the sample, corresponding to the release of hydrogen. A series of small microcracks are also visible through micrographs spread uniformly throughout the sample. This is consistent with the observations derived from confocal microscopy experiments shown in Figure 5-2. At this stage, it is evident that hydrogen is being outgassed to the atmosphere and cannot be contained within the compact highlighting the inefficiency of the foaming process. At this stage the bulk of the expansion is related to the space occupied by the crack network. Supplementary micrographs of the structures are available in Appendix B.

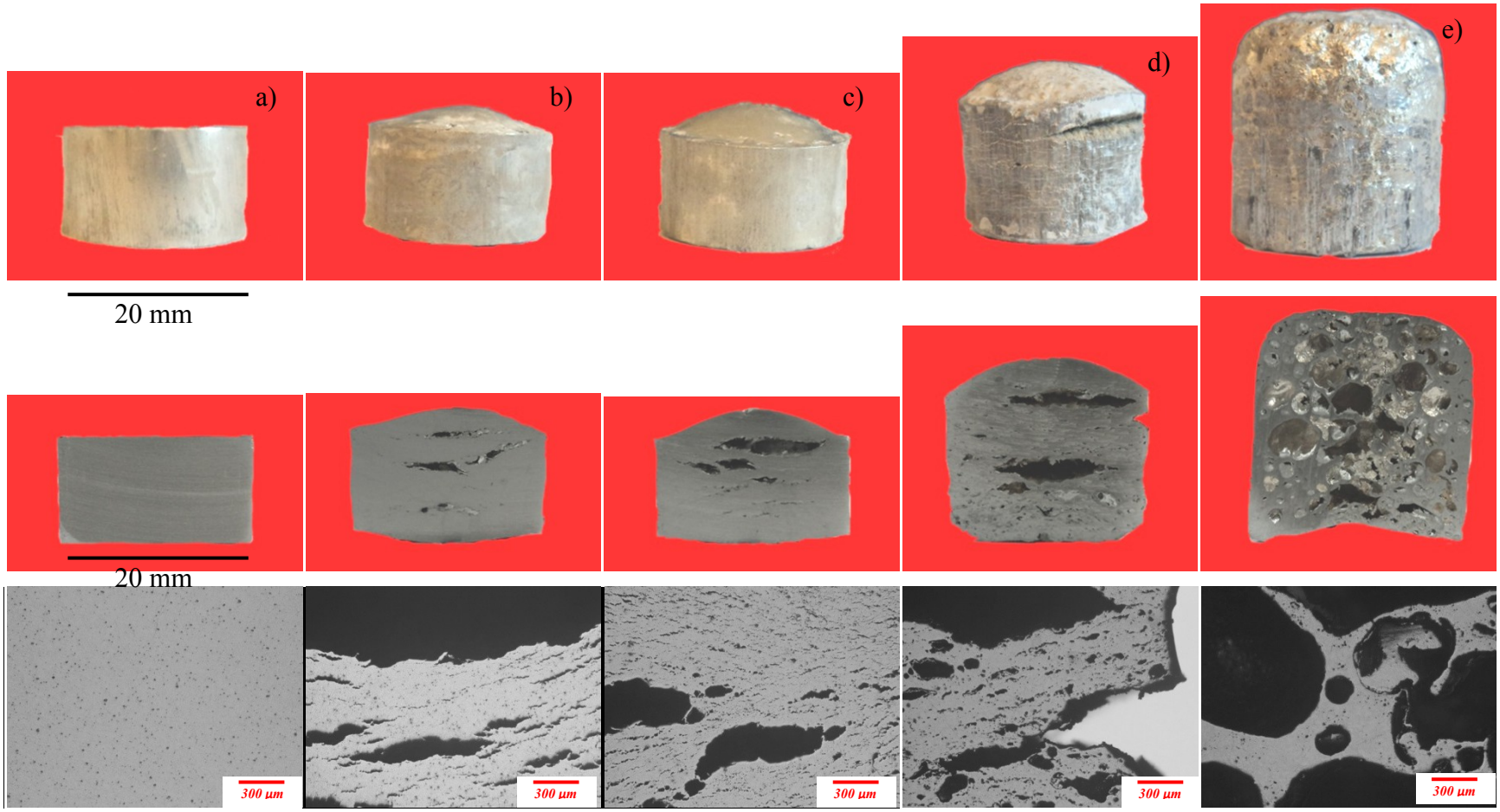

Figure 5-9: Pure aluminum foams produced at 710 °C at select time intervals showing the outer and inner structure, supported by micrographs, a) 300 s, b) 500 s, c) 550 s, d) 750 s and e) 950 s.

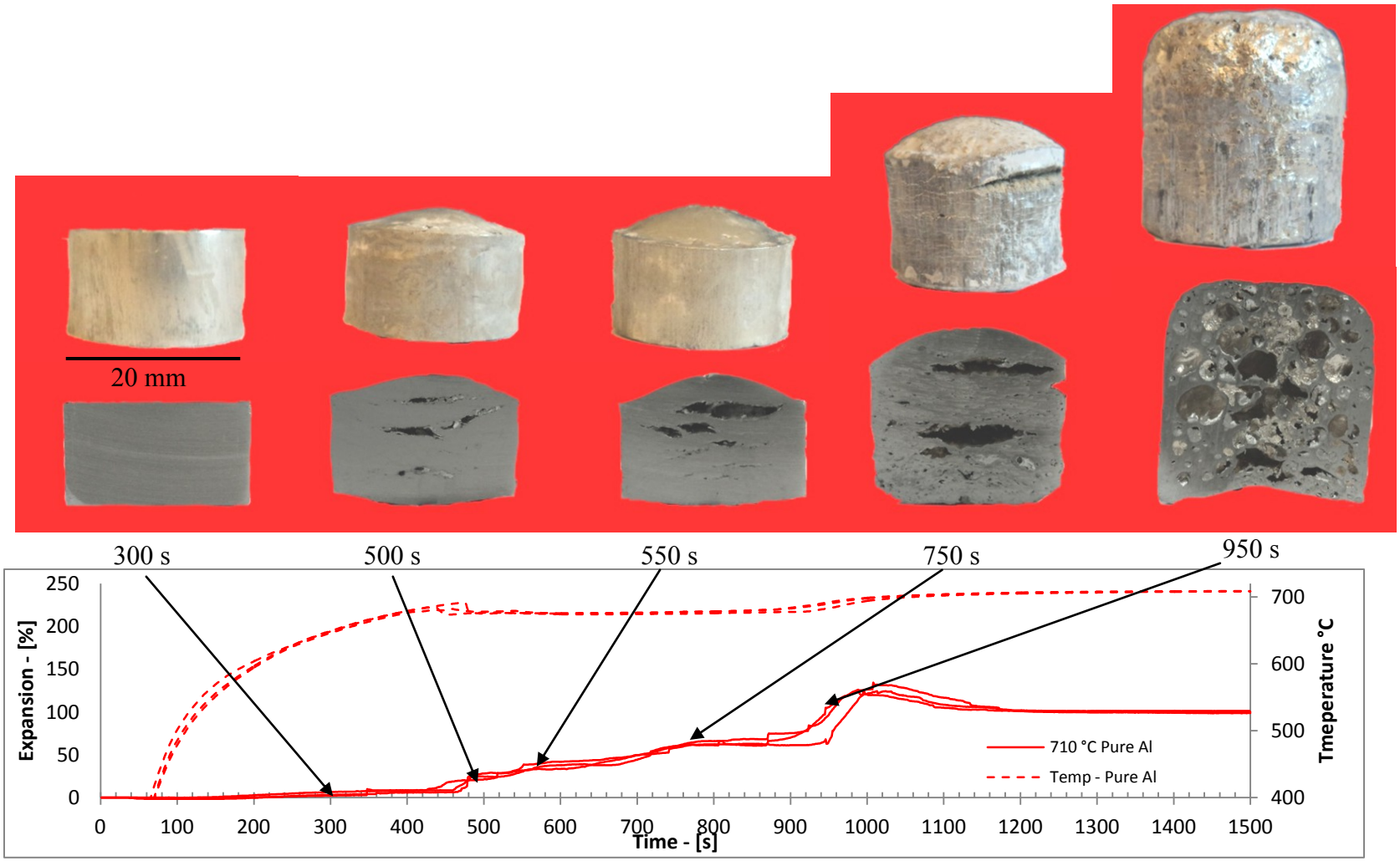

Figure 5-10: Pure aluminum foam produced at 710 °C, 300 s, 500 s, 550 s, 750 s, 950 s

At 750 s on the other hand, large cracks are also visible but some pores are becoming rounder with less horizontal cracks as the compact is nearly melted indicating a reduction in surface tension but hydrogen is still free to escape to the atmosphere. Once the sample is fully molten after 950 s, in Figure 5-9d, bubbles become rounder and large round cells are formed. The cracks are no longer visible at this temperature and the outside of the foam has a round structure and a fully developed foam is formed.

Based on the evolving structure of the pure aluminum foam presented in Figure 5-9 and Figure 5-10, the large crack formations are attributed to the cooling of the specimen as hydrogen is still being released from the blowing agent during cooling. This is supported by the fact that the large cracks formed span across the width of the sample while foams which completely melted display smaller cells distributed evenly throughout the sample. However, the fissure network of small cracks shown in Figure 5-9 is believed to be responsible for bulk hydrogen loss before the sample is completely molten. Once molten, bubbles are formed from the network of small cracks (as opposed to larger ones) yielding a fairly equiaxed cell structure rather than large pores spanning across the sample. An in-depth analysis comparing the pore nucleation in Al-Zn and Al-Si-Zn foams in comparison to pure aluminum will be presented in Chapter 7 and Chapter 8.

5.6 Pure aluminum foaming mechanism

Important time and temperature values are shown in Table 5-2 highlighting foaming events observed in the expansion furnace and during *in-situ* confocal microscopy as well as DSC. Correlated results obtained from confocal microscopy and sample temperature measurements indicate that although the cracking phenomenon occurs prior to reaching the aluminum melting temperature, the majority of the hydrogen loss occurs during the melting of the sample. A high heat of fusion at a given temperature is therefore not beneficial for foaming but rather a gradual formation of liquid would ensure the containment of the blowing

gas. An appropriate alloy with a semi-solid region would also reduce the dependence on heating rate as seen through Figure 5-5.

The observed phenomenon through confocal microscopy, DSC and the foaming curves is illustrated schematically in Figure 5-11. Zone 1 in the diagram indicates the initiation of cracks at 610 °C and hydrogen loss before melting. The initial onset temperature of crack formation is, however, expected to vary depending on TiH_2 powder size and distribution along with sample heating rate. Zone 2 on the other hand indicates the process whereby the compact is melting, and simultaneously losing hydrogen through an open fissure network. Finally, Zone 3 indicates the bulk foaming of the matrix once the entire structure becomes molten.

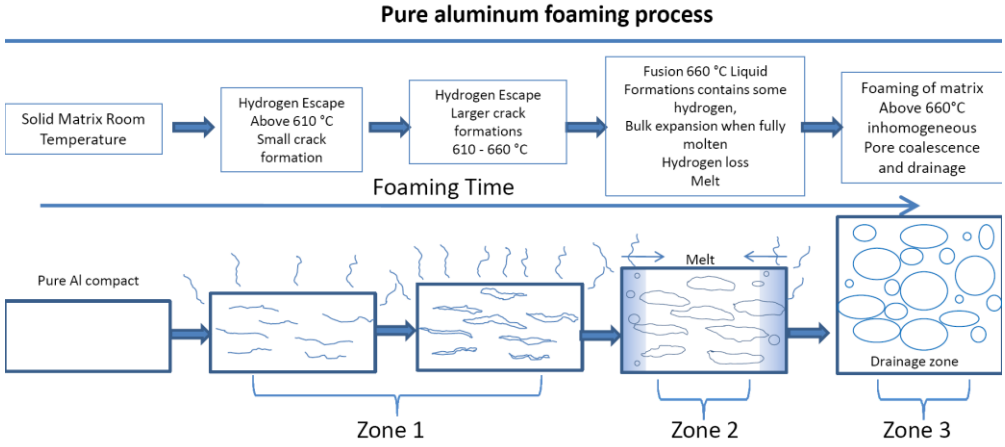

Figure 5-11: Pure aluminum foaming mechanism

This information provides the basis for choosing an appropriate alloying element. An element which creates a liquid phase below 610 °C (in this case) would be beneficial in generating uniform nucleation of the pores and reduce hydrogen loss. Based on Table 3-1 in the Objectives section, selecting zinc elemental powder which forms a eutectic at 381 °C, while exhibiting a large semi-solid region would be an ideal candidate for a variety of TiH_2 hydride conditions.

5.7 Conclusion

In conclusion, it is evident that an open porous crack network forms well below the melting temperature of pure aluminum. The crack network, observed through confocal microscopy, has been shown to form at 610 °C and persists until the compact is fully molten. Although cracks can form at low temperatures, the majority of the hydrogen loss can occur while the compact is melting if insufficient liquid is available. The use of high heating rates is favorable in reducing hydrogen loss which would otherwise escape through the open porous network. Alternatively, a specially designed alloy, can generate a uniform nucleation of pores, exhibit a reduced foaming temperature and suppress crack formations without having to increase the heating rate.

6 Solid State Diffusion in Compacts

Hot pressing conditions were optimized for pure aluminum as outlined in Chapter 4 in order to achieve a density above 94 % theoretical [4]. This high density, helps reduces hydrogen loss and the adverse effects of internal oxidation of the compact which can result in poor foamability. In order to keep the process consistent, the same pressing conditions were applied to the Al-Zn and Al-Si-Zn systems. Due to the high solid solubility of zinc in aluminum (82 wt% at 350 °C) as shown in the phase diagram in Figure 3-1, there was possibility of significant zinc dissolution in the aluminum matrix during pressing or sample heating. To a lesser extent, there was also the possibility of silicon diffusion which is used in the form of a pre-alloyed powder in the compact to form a eutectic at 577 °C. Therefore, a theoretical analysis coupled with empirical data will show the effects of diffusion.

It has been shown under certain conditions in literature by Lumley and Schaffer [120], that if parameters are not well controlled in liquid state sintering using an Al-Zn matrix (low heating rate and small particle size), dissolution of zinc in the aluminum can hinder the level of transient liquid phase formation and retard sintering as a result of significant diffusion [120]. In this particular foaming process, a hot pressing step at 350 °C is used to densify the compact prior to foaming. In the actual foaming process, the heating rate before the transient liquid phase forming temperatures is significantly higher and is driven by the furnace and sample temperature differential. As will be shown in Chapter 7 and 8, the heating rate of the foam with a furnace set point of 710 °C is fairly constants at approximately 317 °C min^{-1} up to the eutectic forming temperature of 381°C. As the temperature climbs further towards the setpoint it tapers off as the temperature gradient between the furnace and sample is reduced. The main concern is therefore in the pressing procedure when the powders are solid.

In order to estimate and to quantify the effect of zinc dissolution, an analysis using Fick's second law was utilized. The 3-D transient mass transfer equation, synonymous to the heat transfer equation is defined by [117]:

$$\frac{\partial}{\partial x}\left(D\frac{\partial C}{\partial x}\right)+\frac{\partial}{\partial y}\left(D\frac{\partial C}{\partial y}\right)+\frac{\partial}{\partial z}\left(D\frac{\partial C}{\partial z}\right)-\frac{\partial C}{\partial t}=0 \qquad \textbf{Equation 6-1}$$

Where C is be defined as the species concentration, x, y and z the distance, t the time and D the diffusivity of the system. This particular equation, in this state, is a non-linear second order partial differential equation which can be difficult to solve analytically due to the dependence of the diffusivity term D. Diffusion couples can be quite complex with respect to determining the diffusion function D. For instance, as diffusion is taking place, the diffusivity can change as a function of concentration and the diffusion interface can drift, which is known as the Kirkendall effect [117]. Furthermore, as one species diffuses in one direction the other can counter diffuse resulting in a complex function for diffusivity. Assuming a constant diffusivity over concentration, the equation can be re-written in the following form:

$$D\left(\frac{\partial^2 C}{\partial x^2}+\frac{\partial^2 C}{\partial y^2}+\frac{\partial^2 C}{\partial z^2}\right)-\frac{\partial C}{\partial t}=0 \qquad \textbf{Equation 6-2}$$

Diffusivity, in this case, is assumed to be constant and therefore the equation becomes a linear second order partial differential equation where analytical solutions are known for an array of simplistic geometries given initial and boundary conditions [161]. In the 1-dimensional form it can be re-written as:

$$D\frac{\partial^2 C}{\partial x^2}-\frac{\partial C}{\partial t}=0 \qquad \textbf{Equation 6-3}$$

Here a simple system is considered whereby zinc diffuses from a constant source through aluminum with the interval 0 <= x < ∞ as shown in Figure 6-1. An initial constant zinc or Al-12wt%Si concentration Cx is assumed to diffuse in the x direction into the aluminum as shown below:

$$0 \leq x \leq \infty$$

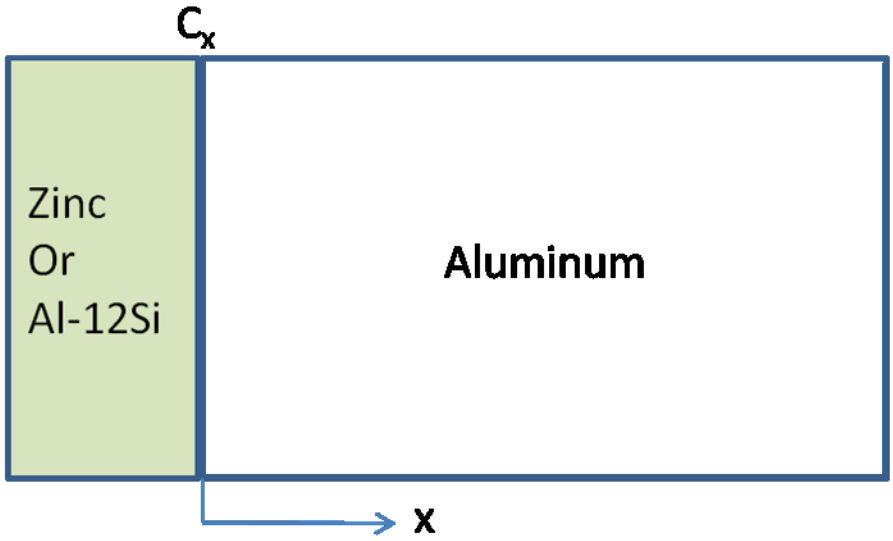

Figure 6-1: Diffusion diagram

The system initial and boundary conditions are summarized below:

Initial Conditions:

C (x,0) = Co= 0

C (0,t) = Cx

Boundary Conditions:

C(x,0)=Co=0

Certain assumptions have been made in relation to the problem and are outlined below:

1- Diffusivity is a constant over the concentration profile

2 - Zinc diffuses as solute with a constant source concentration since zinc has a high solid solubility (up to 82 wt%) in aluminum as opposed to aluminum which has very limited solubility in zinc (1.2 wt%).

3- Oxides on the pressed powder outer surfaces along with impurities are neglected

4- A constant diffusivity coefficient with no drift and mass flow in 1 direction

5-Assume bulk polycrystalline diffusion (Not the effect of grain boundary diffusion)

6- No application of pressure through hot pressing

7- Die warm up time not taken into account, but only steady state temperatures

8- No Kirkendall effect

With the initial and boundary conditions, the general analytical solution obtained from the separation of variable method gives [161, 162]:

$$\frac{C(x,t)-C_x}{C_o-C_x} = erf\left(\frac{x}{2\sqrt{Dt}}\right) \qquad \textbf{Equation 6-4}$$

The diffusion coefficients must now be computed in order to generate diffusion profiles. Since diffusion is a temperature activated process, it is dependent on an activation energy and is described through an Arrhenius type relationship as follows:

$$D = D_o e^{\left(\frac{-Q}{RT}\right)} \qquad \textbf{Equation 6-5}$$

Where R is the gas constant, 8.314 J $(mol\text{-}K)^{-1}$, Q is the activation energy, T (k) the temperature and D_o the diffusivity constant. These values are tabulated below for bulk polycrystalline diffusion for each system in Table 6-1:

Table 6-1: Diffusivity data for aluminum, silicon and zinc, self diffusivity and solute diffusivity

Self Diffusivity			
Species	***Do ($m^2 s^{-1}$)***	***Q ($J\,mol^{-1}k^{-1}$)***	***REF***
Zinc	3.10E-06	8.60E+04	[163]
Aluminum	1.71E-04	1.42E+05	[117]
Silicon	9.00E-05	4.95E+05	[117]
Solute diffusivity in aluminum			
Species	***Do ($m^2 s^{-1}$)***	***Q ($J\,mol^{-1}k^{-1}$)***	***REF***
Zinc	1.40E-04	1.29E+05	[117]
Silicon	9.00E-05	1.76E+05	[117]

With this data, the diffusivity coefficients for self diffusion and solute diffusion in aluminum can be computed and are shown in Figure 6-2.

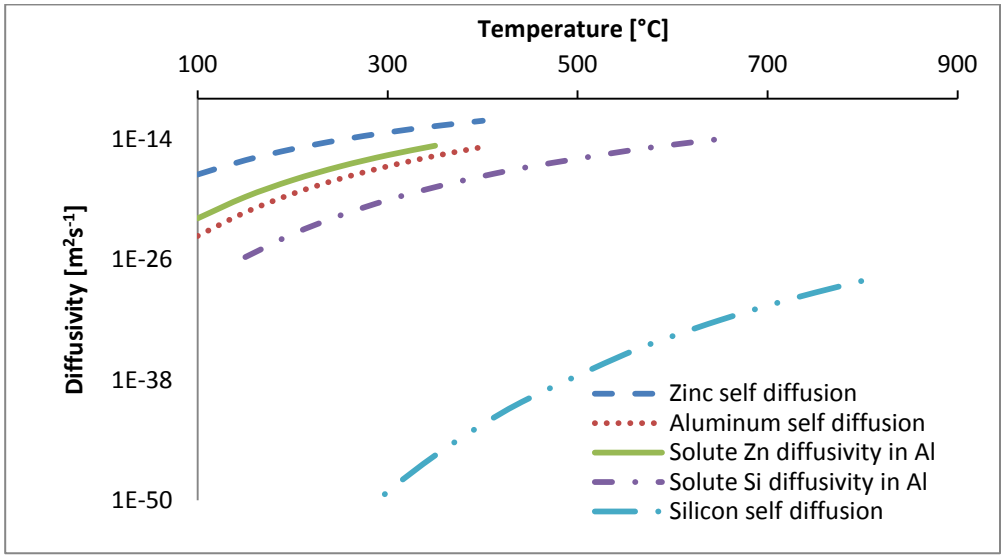

Figure 6-2: Self diffusivity of Al, Si and Zn and solute diffusivity of Zn and Si in aluminum with respect to temperature

It can be observed from Figure 6-2 that the diffusivity coefficient of zinc is the highest. This is expected since zinc has the lowest melting point and the temperatures (pressing and eutectic formation) are near its melting temperature. Moreover, the diffusivity of solute zinc in aluminum is quite high, especially at

350 °C. On the other hand, the self diffusivity of silicon along with its diffusivity in aluminum is several orders of magnitude lower than zinc. The diffusivities at 350 °C corresponding to the pressing temperature are tabulated in Table 6-2.

Table 6-2: Diffusivity coefficients at 350 °C

Species	*Diffusivity coefficients at 350 °C*
Zinc - Self	1.91×10^{-13}
Aluminum - Self	2.12×10^{-16}
Silicon - Self	2.82×10^{-46}
Zinc in Aluminum	2.14×10^{-15}
Silicon in Aluminum	1.57×10^{-19}

Now that the diffusivity coefficients have been computed, general solutions can be generated for Equation 6-3.

6.1 Zinc Diffusion

The computed diffusion profiles stemming from the zinc powders present in the aluminum compacts were computed. Figure 6-3 shows the effect of time on the diffusion of zinc through the aluminum at 350 °C.

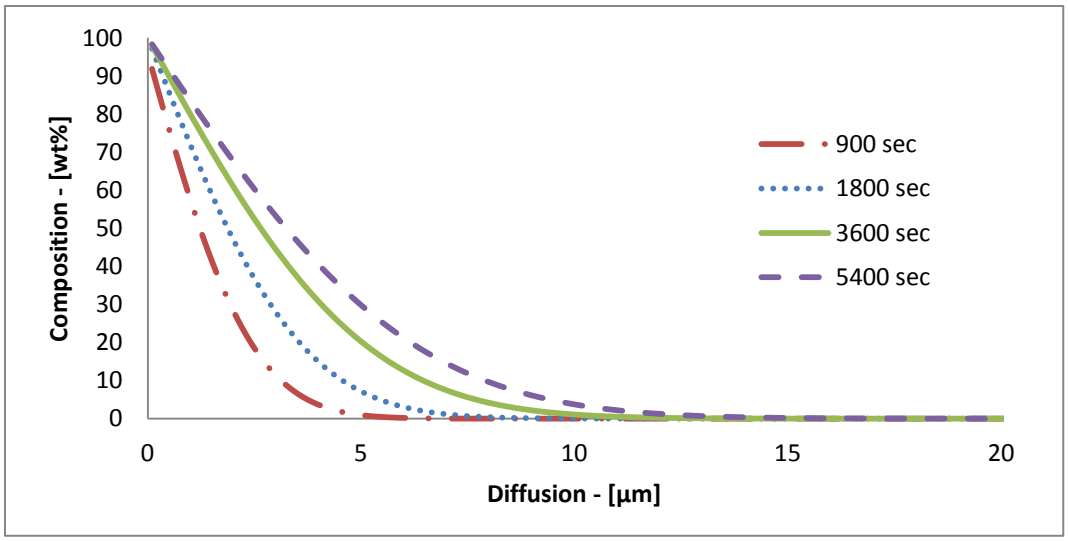

Figure 6-3: Zinc diffusion profile in aluminum as a function of time at a pressing temperature of 350 °C

It can be noted that diffusion increases with time. Pressing times used to produce compacts in this study vary between 1800 s (20 mm dies) and 3600 s (30 mm dies). A diffusion profile between the aluminum and the zinc of 6.5 µm can be generated in 1800 s and 10 µm at 3600 s, both pressed at 350 °C. It is to be noted that, the steel die warm up time is not included in these diffusion profiles and therefore, the actual time that the pressed powders are at 350 °C is significantly less. In this case, the zinc powder has a mesh size of -100 (-150 µm) and a mean particle size of 66.5 µm and as a consequence has the potential for an important level of diffusion in comparison to particle size. As a result, this could be an influential factor when smaller particles are used.

For instance, as outlined by Lumley and Schaffer [120], through liquid state sintering, if very small particles are used along with a slow heating rate, the transient liquid phase can be suppressed due to high levels of diffusion (<45 µm powders at 1 °C min^{-1}). With such a low heating rate it is expected that diffusion would be seen where it would take 19800 s to reach the pressing temperature alone compared to the 1800 – 3600 s pressing times in this case. On the other hand they showed that higher heating rates and larger powders (125-150 µm

powders at 40 °C min $^{-1}$) significantly enhanced the amount of liquid phase during the sintering process [120]. This is important because this particular foaming process relies on transient liquid phase formations. Although their process differs since their samples were not hot pressed, it is therefore imperative to assess the diffusion. In this case, the initial heating rate up to the eutectic liquid forming temperatures of 381 °C (approximately 317 °C min^{-1}), is much higher than what was reported in literature. This leaves little time for significant solid state diffusion to occur before bulk melting takes place, initiated through the melting of the transient liquid phase. Therefore, the process could be more dependent on the pressing.

In order to look at the effects of pressing temperature on the diffusion interface, profiles calculated with a constant pressing time of 1800 s were generated and have been plotted in Figure 6-4.

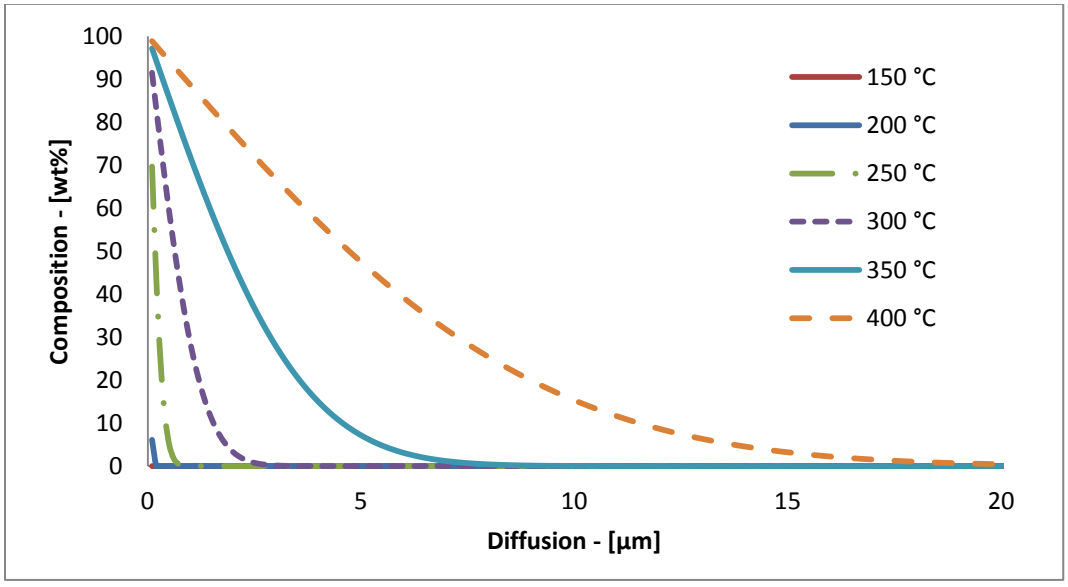

Figure 6-4: Diffusion of zinc in aluminum as a function of pressing temperature at a pressing time of 1800 s

It can be seen that as temperature is lowered from 350 °C, the diffusion interface is decreased tremendously from 6.5 µm at 350 °C to 2.5 µm at 300 °C and 1 µm at 250 °C. It is important to keep in mind that proper compact density is essential for foaming in order to produce adequate foams and therefore lower pressing temperature may result in open porosity in the compact. At 400 °C the diffusion profile is quite a bit larger than at 350 °C being over 15 µm. In this condition, since diffusion is enhanced, if fine powders are used they have the potential of dissolving entirely in the aluminum without forming a transient liquid phase (381 °C – Al-94wt%Zn, see phase diagram is Figure 3-1). Pressing above 350 °C in this case would not be feasible due to the larger particle size without forming the liquid phase.

Backscattered secondary electron images were taken along with Energy Dispersive Spectroscopy (EDS) in order to analyze pressed powder compacts. Three conditions were selected and compared, consisting of a cold pressed sample, a sample pressed at 350 °C for 1800 s and another pressed for 3600 s at 350 °C. Figure 6-5a shows a linescan analysis of a cold pressed compact. It appears there is possible diffusion but in reality it is relative to where the particle was sectioned and the penetration depth and control volume of the electron beam in the matrix. The EDS analysis shows a transition zone of a few µm to be on average 2.4 ± 0.4 µm. Since the powders were cold pressed in a cold die, there is no diffusion due to heat and pressing of the sample. The interface from the EDS analysis shows no aluminum present in the zinc particle and no zinc present in the aluminum. Significant diffusion will be shown in Chapter 7 as the transient liquid phase spreads through the matrix. The extracted diffusion data is summarized in Table 6-3.

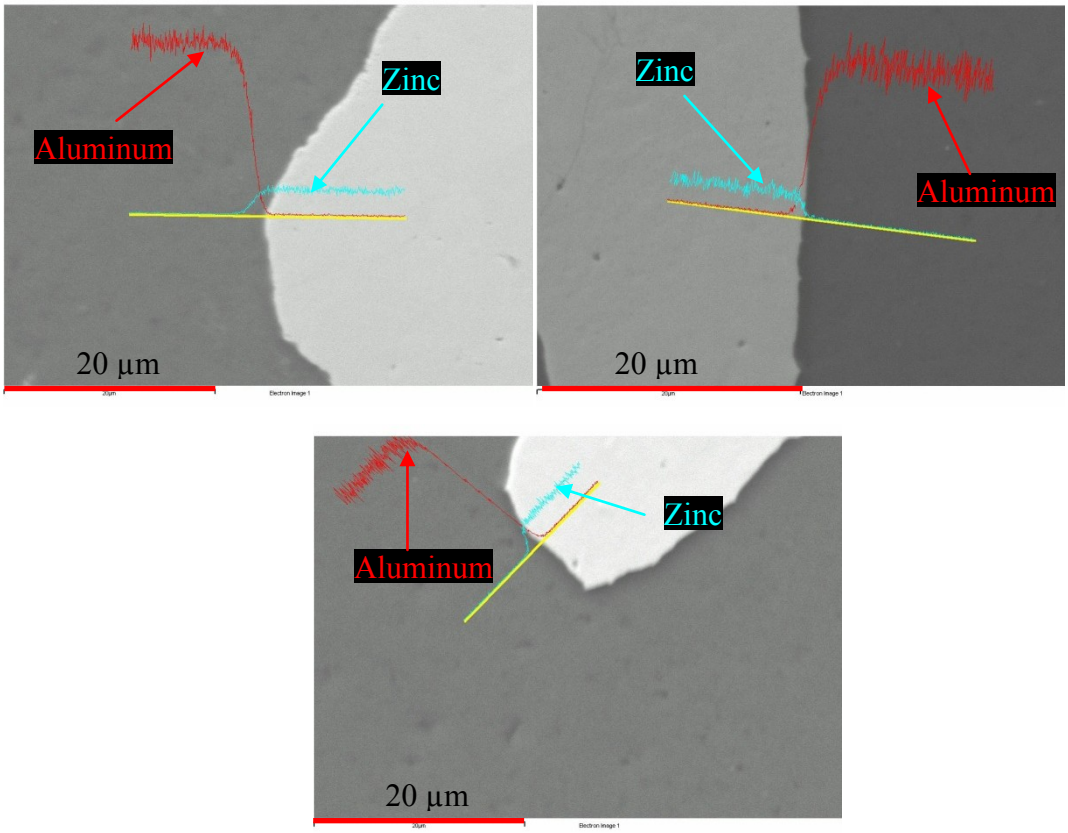

Figure 6-5: Backscattered electron images showing EDS analysis of diffusion for pressed compacts a) Cold compaction b) Compacted at 350 °C for 1800 s d) Compacted at 350 °C for 3600 s

A hot pressed sample at 350 °C for duration of 1800 seconds is shown in Figure 6-5b. There appears to be no significant diffusion observed through several interface measurements (more data shown in Appendix C). The interface between the zinc and aluminum was measured to be on average 2.2 ± 0.5 µm which is significantly smaller than what was predicted by the model to be near 6.5 µm. Moreover, this value is actually smaller than what was measured through the cold pressed powders so this could be due to simple variations depending how the particles were sectioned for polishing and again the penetration depth and control volume of the electron beam. From the EDS data, there was no significant zinc diffusion in the actual aluminum matrix beyond the few micron thick interface layer. The low diffusion in this case can be attributed to the oxides on the particles

and the slow warm up time of the dies hindering the diffusion process. Moreover, the theoretical analysis provides more of a worst case scenario based on the assumptions made.

Table 6-3: Al-Zn diffusion data for compacted powders

Diffusion Interface		
Cold Pressed	***Hot Pressed 1800 s - 350 °C***	***Hot Pressed 3600 s - 350 °C***
2.4 ± 0.4 µm	2.2 ± 0.5 µm	2.8 ± 0.4 µm

Powders were subsequently pressed at 350 °C for 3600 s in order to evaluate if diffusion was in fact a potential issue for longer pressing times. In Figure 6-5 c no significant diffusion is seen, comparable to Figure 6-4a and Figure 6-4b, and the average interface between the aluminum and the zinc was measured to be 2.8 ± 0.4 µm. The model predicted a diffusion of 10 µm which is much higher than what was actually measured. If significant diffusion was occurring, it would be evident through the EDS measurements where long tapered profiles would be seen as will be shown in Chapter 7 (Figure 7-17) where the liquid phase is spreading through the compact. A clear interface between the aluminum and the zinc can be seen from the micrographs. The slightly higher interface size compared to samples pressed for 1800 s, is likely the result of variations between individual particle interface measurements due to sample sectioning or slightly higher levels of diffusion. Comparing these results to DSC measurements in Figure 7-2 in Chapter 7, the phase formations reveals the formation of the transient liquid phase at 381 °C highlighting the low levels of solid state diffusion during compaction.

It can, therefore, be concluded that the diffusion of zinc in aluminum is not a significant factor during the pressing of compact powders. Moreover, pressing at higher temperatures would not be beneficial as the eutectic forms at 381 °C. The calculated diffusion profiles were shown to be larger than those measured. The calculated values did not take into account the inter diffusion between zinc and the aluminum and the presence of oxides. Calculating the interface values in this

manner ensures a worst case scenario analysis which was shown to be excessive. Additional EDS analysis data and micrographs are included in appendix.

6.2 Silicon Diffusion

Pre-alloyed silicon powders were also used in the production of compacts for foaming. In this case, the diffusion of silicon through zinc was not calculated since the majority of the matrix is comprised of pure aluminum and only 10 wt% of zinc was added in combination with silicon, resulting in only a small volume. Figure 6-6 shows the effect of time on the diffusion of silicon through aluminum at a pressing temperature of 350 °C.

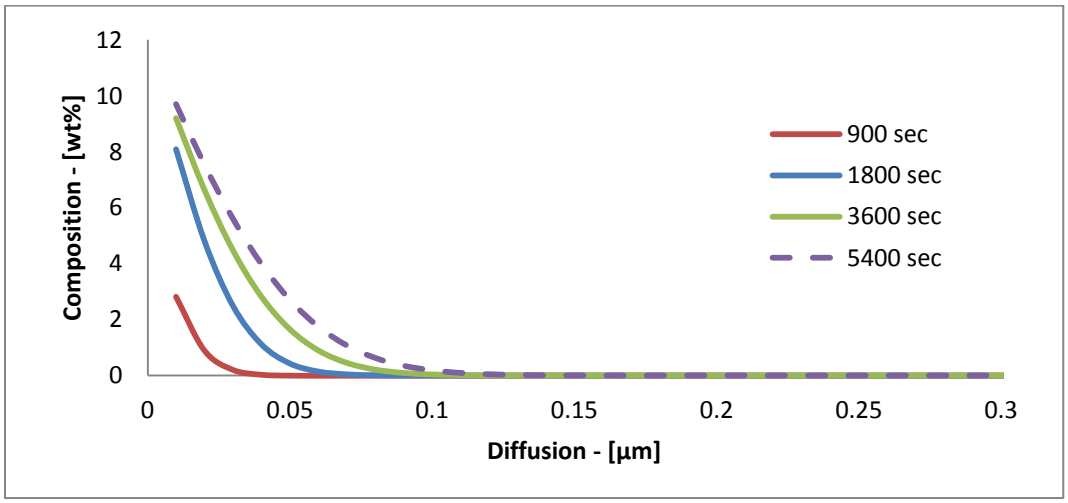

Figure 6-6: Silicon diffusion profile through aluminum pressed at a temperature of 350 °C

From Figure 6-6, it can be seen that, the diffusion of silicon is insignificant, being less than 0.1 µm at 5400 s. This is to be expected since silicon has a very low diffusivity in aluminum at these low temperatures. It is also to be noted that concentrations of silicon are already low in the pre-alloyed powders to start with.

The diffusion profiles were calculated for varied pressing temperatures at a time of 1800 s. These diffusion profiles can be seen in Figure 6-7. Similarly to Figure 6-6, the diffusion of silicon is minimal being approximately 0.2 µm at 400 °C.

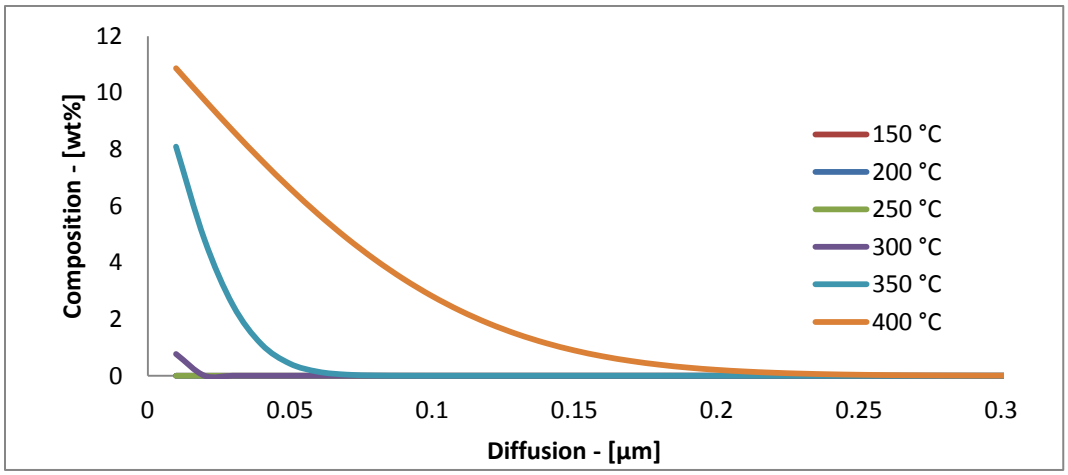

Figure 6-7: Diffusion profiles for silicon in aluminum at varying pressing temperature at a time of 1800 s

Unlike zinc, the atomic number of silicon is near to aluminum making it difficult to distinguish the pre-alloyed powders from the pure aluminum through electron microscopy. Furthermore, the low silicon content in the powders makes it more difficult to visualize. An EDS linescan is shown in Figure 6-8 displays a zinc and silicon particle embedded in the aluminum matrix. The linescan shows the silicon powder in the matrix and it can be clearly seen that is round.

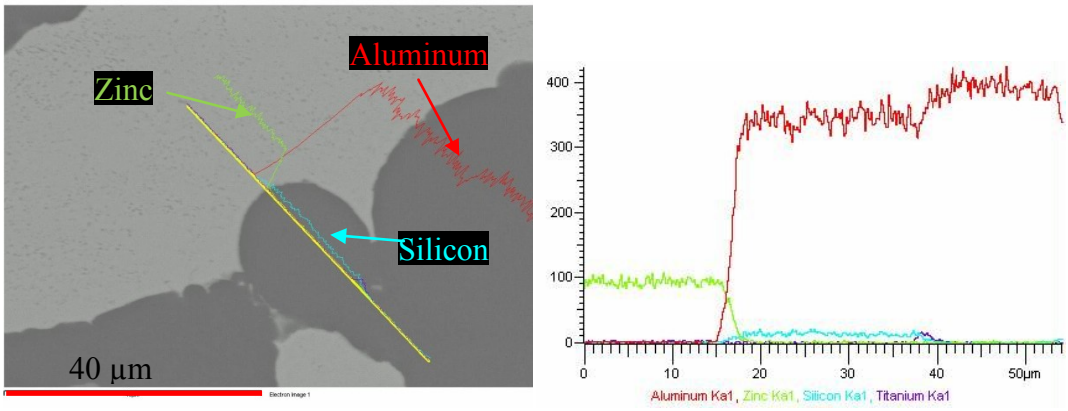

Figure 6-8: EDS linescan of an Al-3.59wt%Si-9.6wt%Zn compact pressed for 1800 s at 350 °C

An EDS map of an Al-3.59wt%Si-9.6wt%Zn compact is shown in Figure 6-9, highlighting the round Al-Si powder along with zinc and TiH_2 particles in the compact.

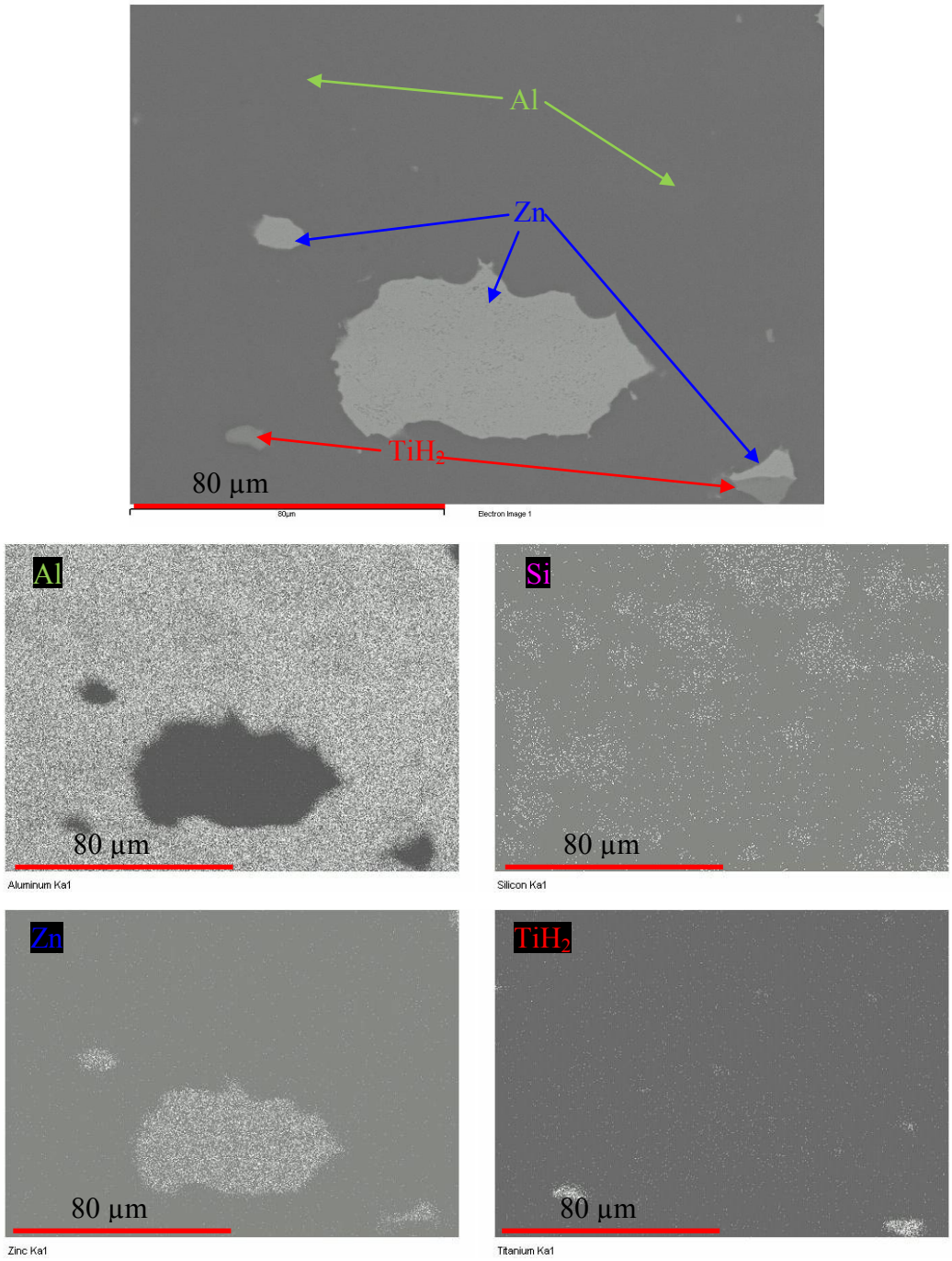

Figure 6-9: EDS map of Al-3.59Si-Zn sample pressed for 1800 s at a temperature of 350 °C

In this particular case the diffusion of silicon is not as crucial as zinc since it will form the eutectic liquid phase at 577 °C regardless of diffusion or not. Although it is desirable to obtain larger levels of liquid during the foaming process it is preferable if the pre-alloyed Al-12wt%Si eutectic powders melt. Based on the

calculated analysis and the evidence presented through electron microscopy, silicon is not believed to diffuse significantly.

6.3 Conclusions

Overall, based on the above analysis, given the particle size used, the effect of zinc dissolution is deemed insignificant during the hot pressing stage in this particular process. Furthermore, significant solid-state diffusion before the formation of the transient liquid phase during actual foaming is not believed to be an influential factor during the foaming process. Through this analysis, the diffusion of zinc in aluminum has been shown be less than 3 μm and therefore, the particle size and process in this case is acceptable.

The solid state diffusion of silicon from the pre-alloyed powders to the pure aluminum was determined to be unimportant and calculated as being below 1 μm at the temperatures of interest. Therefore, the use of silicon or pre-alloyed silicon powders is not believed to be a concern in term of diffusion and pressing temperature.

This page is intentionally left blank

7 Al-Zn Foams

Based on the analysis of pure aluminum in Chapter 5, elemental zinc was chosen as an alloying element for the foam. The reasons for choosing this alloy include; its low melting temperature (420 ˚C), its large semi-solid region, its potential to reduce surface tension, its formation of a low temperature eutectic and its high solid solubility in aluminum [58, 91, 144, 146, 149]. For these reasons, it was believed that zinc could help encapsulate more hydrogen by the formation of a transient liquid phase, while lowering the overall melting temperature of the alloy. This would then decrease the formation and spreading of the observed cracks, produced well below the melting point of pure aluminum (610 °C), ultimately resulting in a more uniform foam at lower temperatures.

The summarized concept is as follows; a transient liquid phase forms from the elemental powders as hydrogen starts to be released from the TiH_2. The liquid phase then slowly dissolves the aluminum, which increases fluid viscosity and results in a semi-solid containing primary α-aluminum grains or a viscous liquid. It is stipulated that the solid aluminum particles and/or the higher viscosity of the liquid could potentially create a strong resistance against drainage and coalescence of the foam. A lowered surface tension of the melt would also help enhance foam stability [58, 91]. Furthermore, the high zinc vapor pressure has the potential of supplying additional positive pressure within the foam cells. The described method has been termed reactive Stabilisation of the foam due to the formation of a liquid phase at early foaming stages.

In this chapter, in-situ confocal microscopy in conjunction with thermal analysis will be used to observe the transient liquid phase formation. This will be supported by foam expansion curves with sample temperature measurements throughout the foaming process. Secondly, the structural evolution of the foam (macrostructure and microstructure) will be discussed at specific time interval,

highlighting the pore formation of the foam. These results will then be assessed with respect to pure aluminum. Finally, the mechanisms pertaining to foam stability will be addressed.

7.1 Transient Liquid Phase Formation

Compacted powder precursors of Al-10wt%Zn, Al-33wt%Zn and Al-50wt%Zn were prepared for thermal analysis. A backscattered electron image of a representative compact (top view) is shown in Figure 7-1 which reveals the presence of zinc and TiH_2 powder embedded in an aluminum matrix. The zinc particles can be identified as the brighter particles; in the same figure TiH_2 can also be seen as smaller grey particles. From the micrograph, the TiH_2 appears to be fractured; this could result from either the compaction or the polishing stage. From the observation of several micrographs, the distribution of the different particles appears to be quite homogeneous in nature (no clumping or segregation) with no apparent diffusion of zinc as a result of hot compaction as discussed in Chapter 6. Additional micrographs sectioned perpendicular to the compaction axis showing the distributions of zinc and TiH_2 powders in the compacts for Al-10wt%Zn and Al-33wt%Zn are presented in Appendix D.

Differential scanning calorimetry (DSC) analysis shows the formation of a transient liquid phase, depicted by an endothermic reaction occurring at 381˚C in Figure 7-2 corresponding to the Al-94wt%Zn eutectic [144]. This phase corresponds to the lowest melting phase of the binary system, having the lowest Gibbs free energy. This is a typical eutectic formation which occurs in processes such as liquid state sintering as the compact is heated [118].

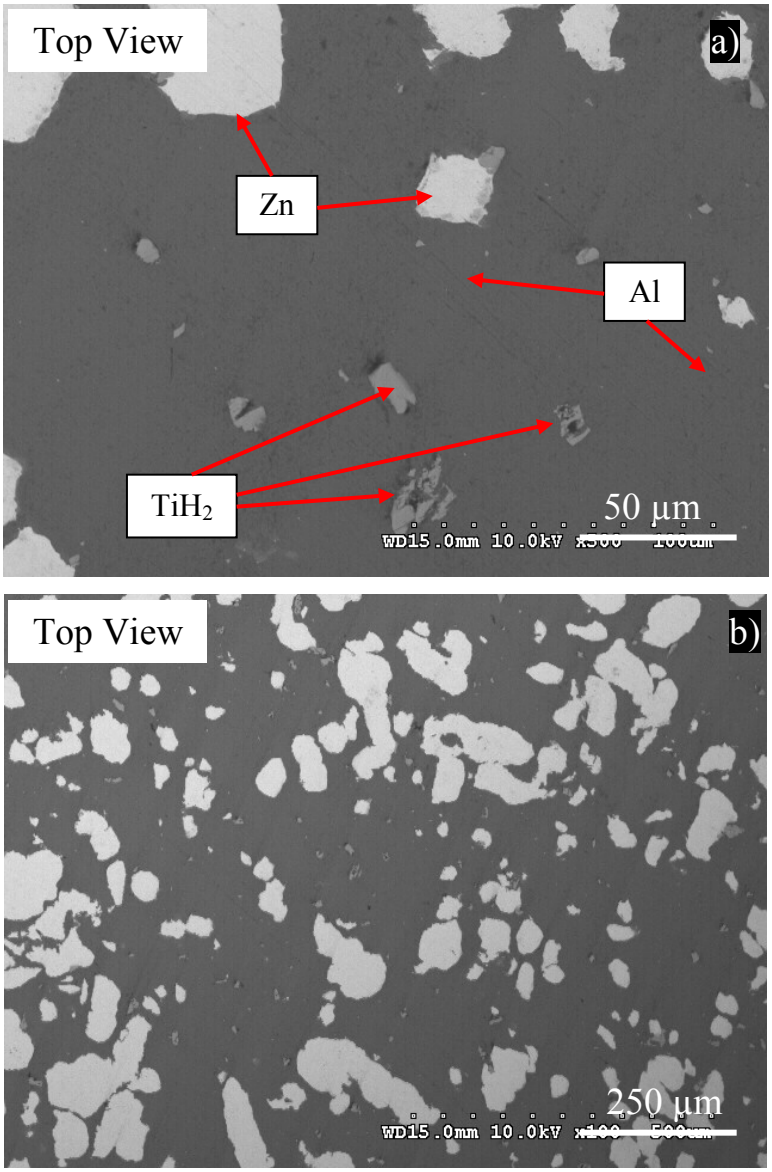

Figure 7-1: Sectioned Al-33wt%Zn compact showing particle distribution from the top view

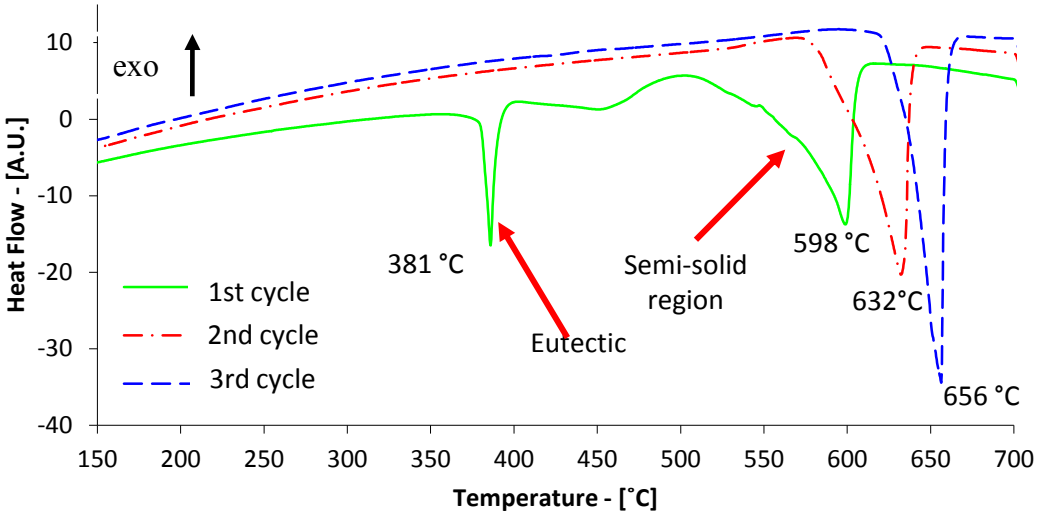

Figure 7-2: Al-33wt%Zn DSC curves showing the formation of eutectic at 381 °C

Under equilibrium conditions, this eutectic would not form if pre-alloyed powders were used. This transient phase formed due to the elemental powders reacting with the aluminum forming the liquid phase. On subsequent DSC heating cycles, the eutectic Al-94wt%Zn phase was not apparent in the analysis. This is the result of zinc completely dissolving in the matrix and/or being partly lost through vaporization as it has a very high partial pressure, which makes it especially volatile at higher temperatures [147]. The literature values for zinc vapor pressures along with the corresponding alloy compositions are outlined in Table 7-1 and Figure 7-3[146, 147]. DSC curves for the heating cycles reveal that the bulk alloy melting point increases from the first to the third heating cycle, with the first cycle the melting ranging between 541 - 598 ˚C (onset - peak), the second heating cycle melting between 599 – 632 ˚C (onset - peak), and the third cycle melting between 634 - 656 ˚C (onset - peak). Since 660 ˚C is the melting point of pure aluminum, this indicated that the majority or nearly all of the zinc had completely evaporated during or prior to the third heating cycle. This can also be confirmed by the fact that the peaks get progressively narrower with each heating cycle as the semi-solid region is suppressed. Zinc loss and vapor pressure will be discussed more thoroughly in the following, Section 7.7 (Zinc Evaporation).

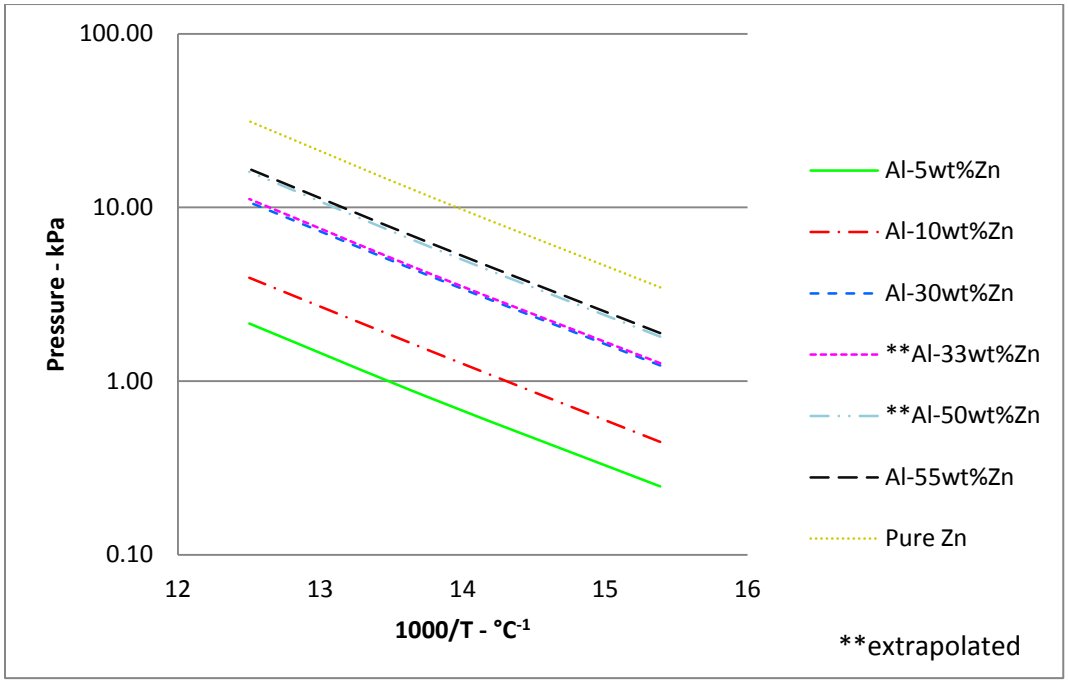

Figure 7-3: Zinc partial pressure values vs. composition [148]

Table 7-1: Al-Zn alloy vapor pressures [148]

Temp (°C)	*Composition (wt%)*	*Alloy Liquidus (°C)[144]*	*Alloy Vapor Pressure (Pa)[146]*	*Pure Zn Vapor pressure (Pa)[146]*	*Pure Zn Vapor pressure (Pa)[147]*
620	Al-33Zn	531-603	778	2118	1998
640	Al-33Zn	531-603	1085	2966	2824
690	Al-10Zn	622-645	847	6587	6409
710	Al-10Zn	622-645	1143	8918	8749

DSC measurements of TiH_2 loose powders show a gas release onset at 475 °C with dehydrogenation peaks at 502 °C and 569 °C. On the other hand using confocal microscopy reveals the initiation of crack forming temperatures at 610 °C in a pure aluminum compact. Comparing these gas release temperatures to the formation of the transient liquid formed at 381 °C, it is evident that the liquid phase has the potential to form at a much lower temperature than onset of hydrogen release. As indicated in Chapter 4, the release kinetics of the gas is affected by the compaction process and therefore, the introduction of a liquid

phase at such a low temperature could result in an earlier gas release onset in the foaming compact. Moreover, the formation of the Al-94wt%Zn eutectic at 381 °C corresponds well with the lowest recorded gas release temperatures for TiH_2 reported in literature of 380 °C [1, 6-8, 11, 20, 86, 142]. This would also account for variations in blowing agent gas release kinetics which has been shown to vary with powder size and distribution [1, 164].

DSC curves for the Al-50wt%Zn and Al-10wt%Zn were similar to those seen in Figure 7-2 with a larger eutectic peak and lower melting temperature for the Al-50wt%Zn and a smaller eutectic peak and higher melting point for the Al-10wt%Zn composition as shown in Appendix D.

In support of the thermal analysis, Figure 7-4a to Figure 7-4k shows the evolution of an Al-33wt%Zn compact under *in-situ* confocal microscopy (video image extraction) which was conducted to study the melt kinetics of the alloy. In this sample, no TiH_2 was added in order to unambiguously observe the melting kinetics between the elemental zinc and aluminum powders. Confocal microscopy illustrates in Figure 7-4d that the Al-94wt%Zn eutectic forms at the interface between the aluminum and the zinc powders at a temperature near 381˚C, corroborating the DSC results. The eutectic phase onset appears at a slightly lower temperature (369 ˚C) in the confocal microscope than measured in the DSC (374 ˚C) due to a slight thermocouple lag in the microscope as a result of a larger sample weight and higher heating rate.

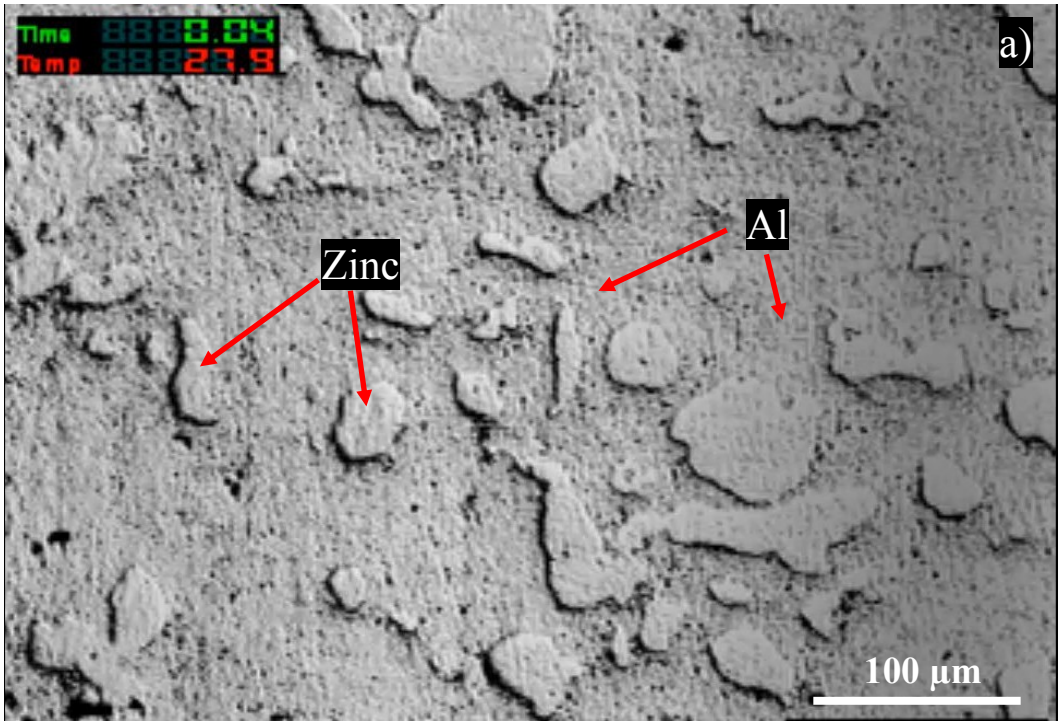
a)
Zinc
Al
100 µm

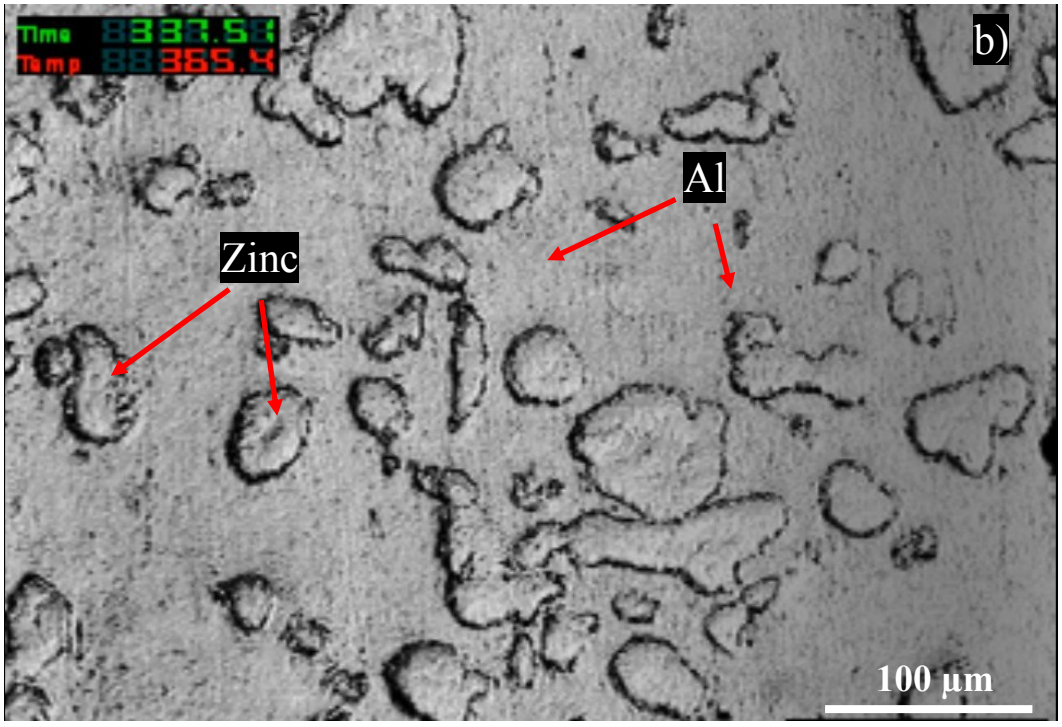
b)
Al
Zinc
100 µm

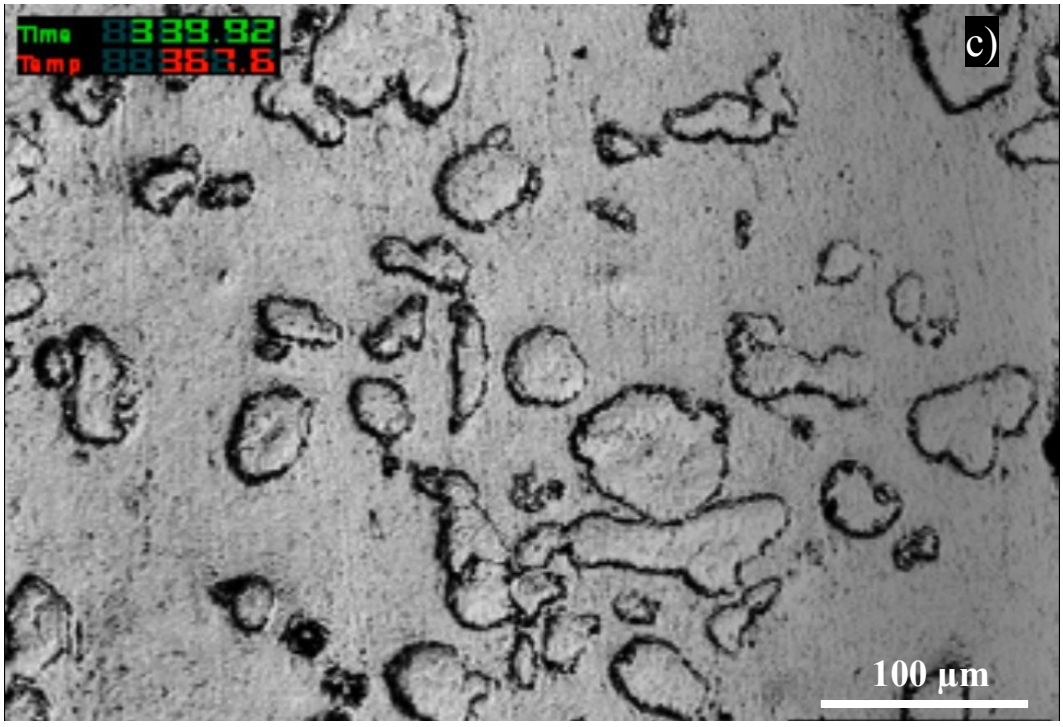
c)
100 µm

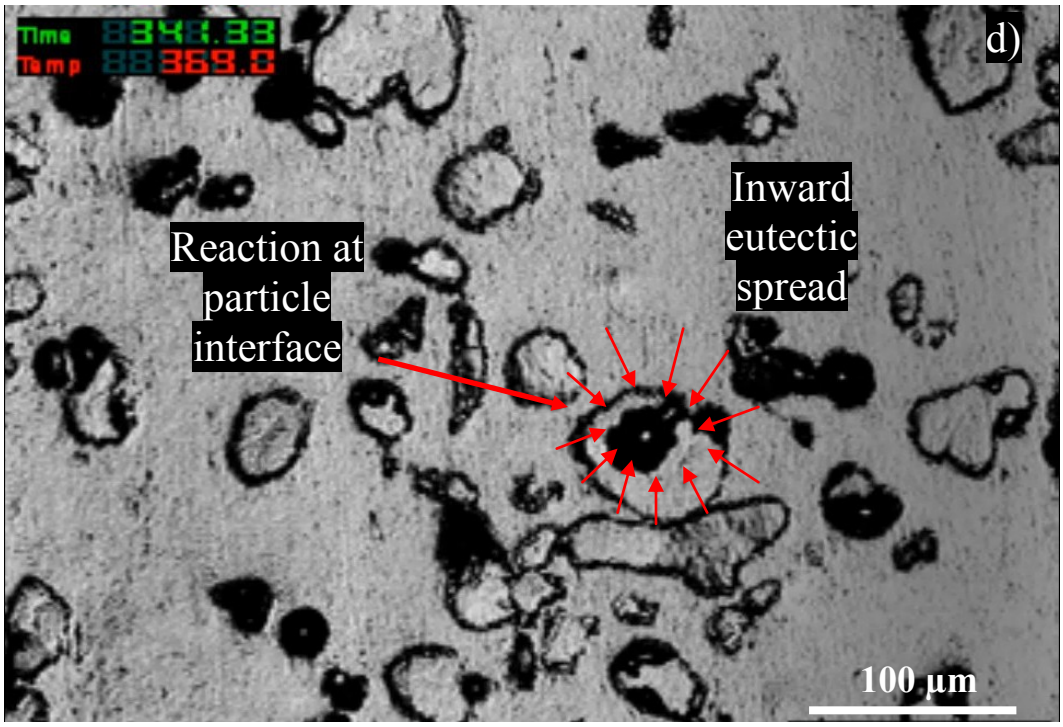
d)
Reaction at particle interface
Inward eutectic spread
100 µm

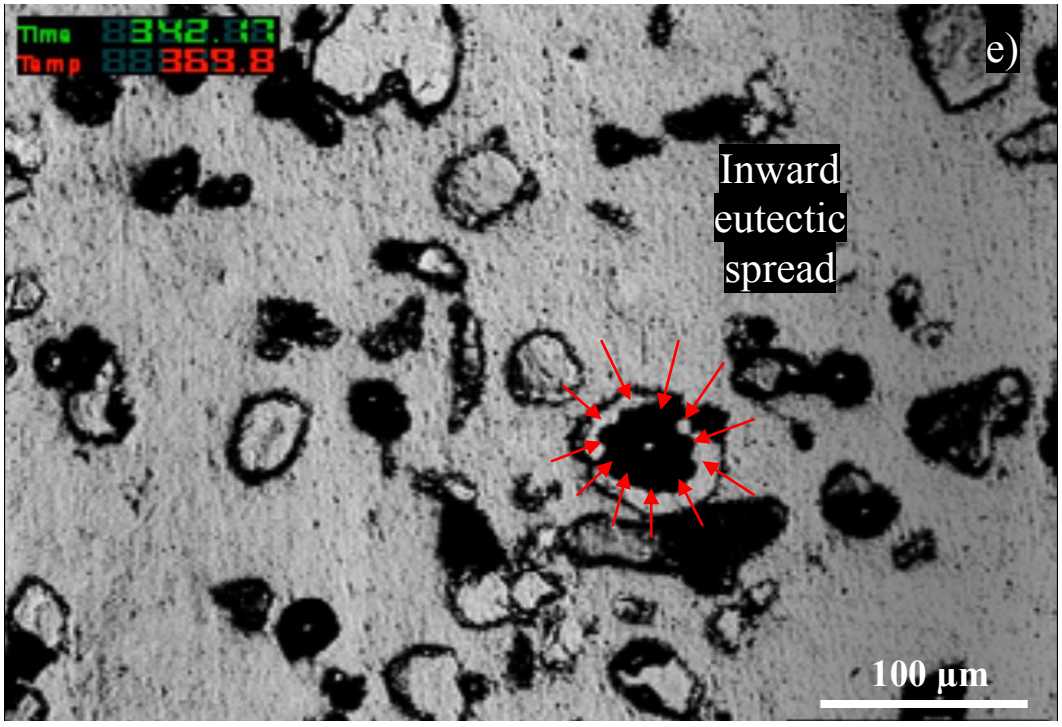
Time 8342.83
Temp 8369.8
e)
Inward
eutectic
spread
100 µm

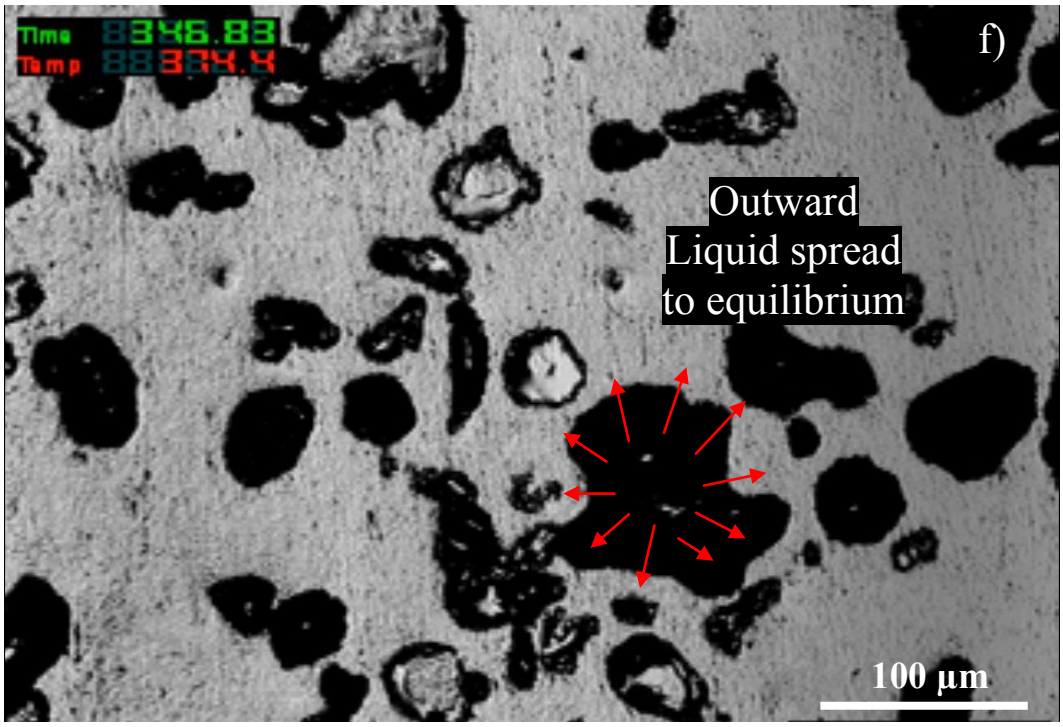
Time 8346.83
Temp 8374.4
f)
Outward
Liquid spread
to equilibrium
100 µm

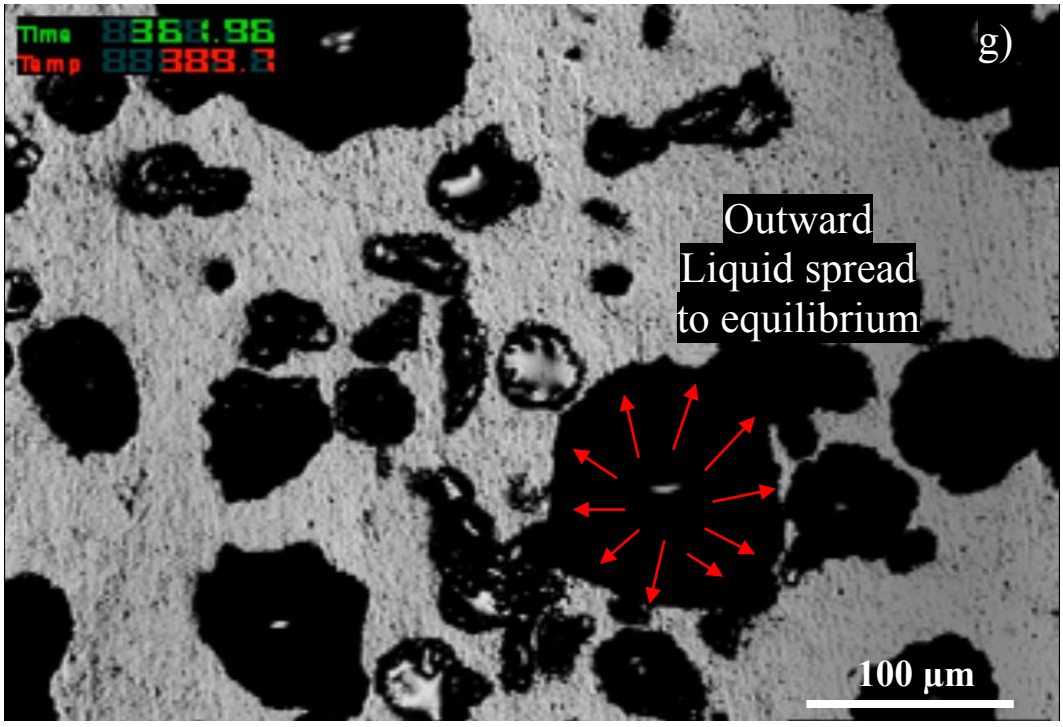
g)
Outward
Liquid spread
to equilibrium
100 µm

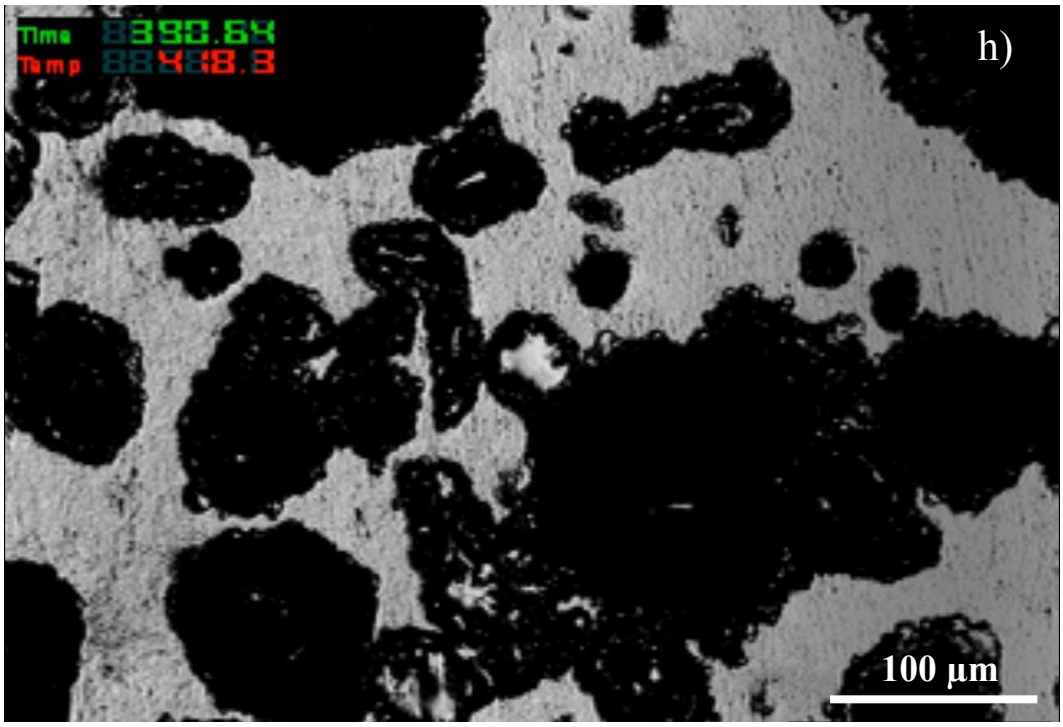
h)
100 µm

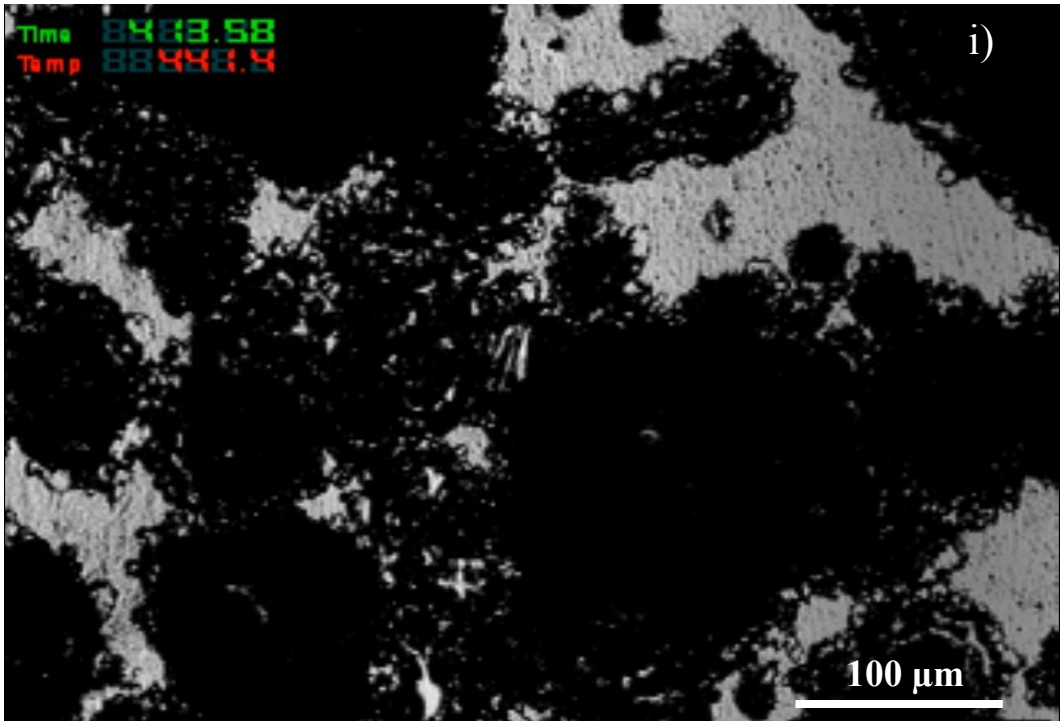
i)
100 µm

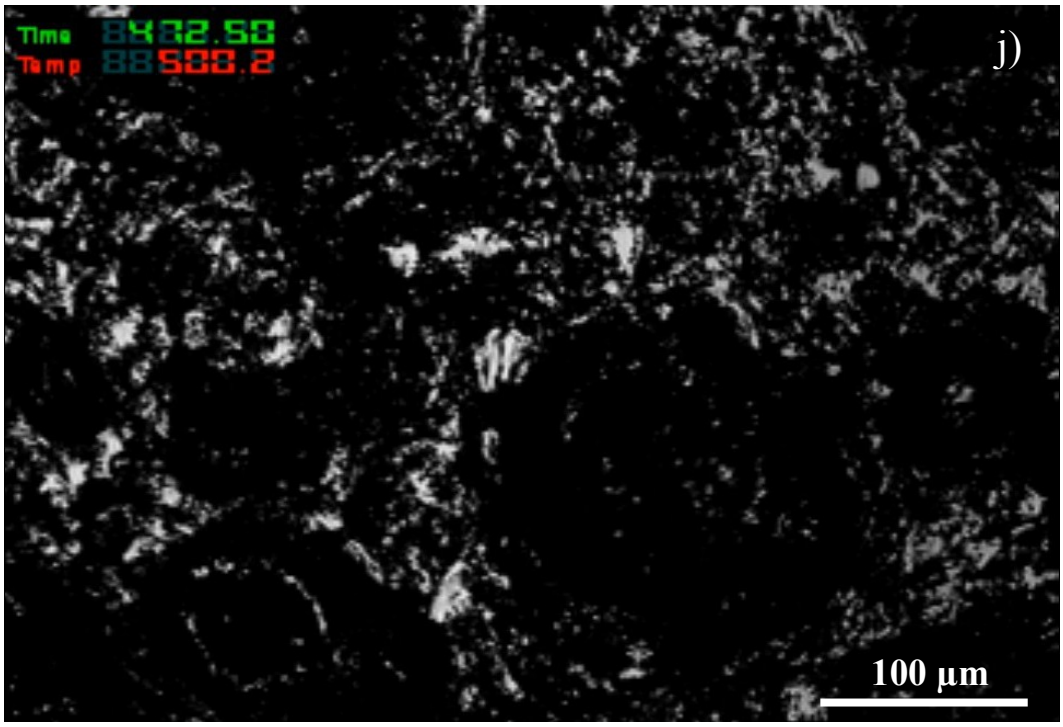
j)
100 µm

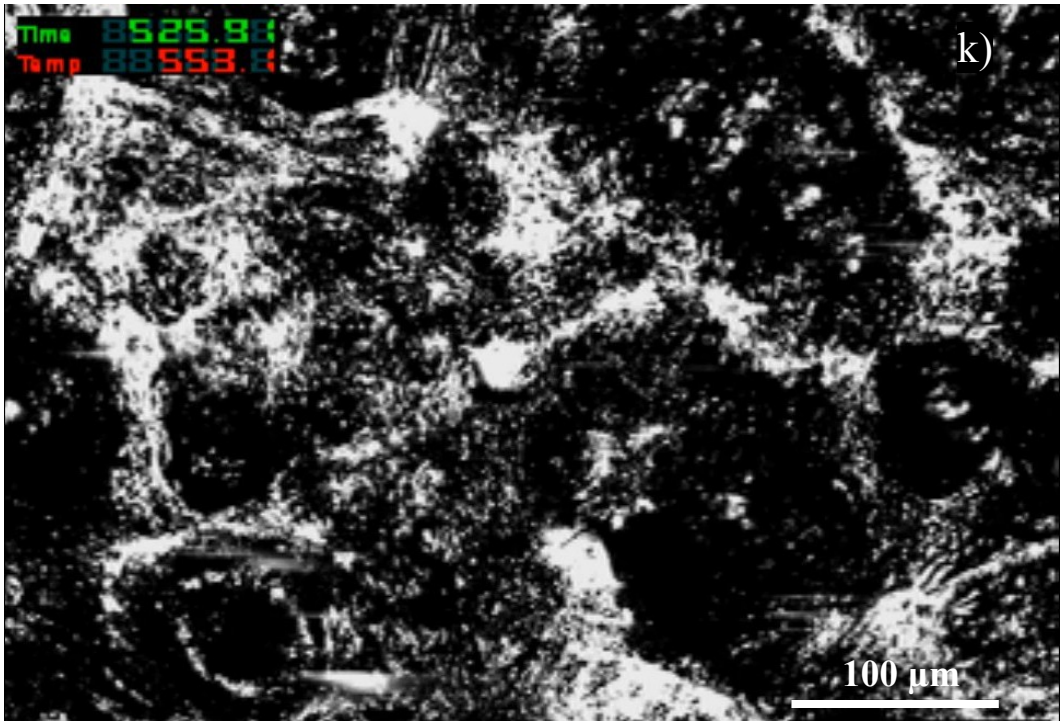

Figure 7-4: Al-33%Zn compact observed under confocal microscopy a) 27.9 ˚C, b) 365.4 ˚C, c) 367.6 ˚C, d) 369.0 ˚C, e) 369.9 ˚C, f) 374.4 ˚C, g) 389.7 ˚C, h) 418.3 ˚C, i) 441.4 ˚C, j) 500.2, k) 553.1 ˚C

Initially the eutectic phase forms at the Al/Zn powder interface and spreads quickly inward, consuming the zinc particles from 369 ˚C up to 380 ˚C (Figure 7-4d and Figure 7-4e). The reaction slows down rapidly once the zinc particles are consumed. Subsequently, there is a period of slow dissolution (Figure 6-4f and Figure 6-4i) of the solid matrix by the liquid phase spreading outwardly from 380 ˚C and persisting until 470 ˚C where the entire structure appears to become a viscous liquid. As the eutectic phase forms and the temperature increases, the concentration of aluminum in the liquid increases, hence the zinc-rich liquid is consuming the aluminum matrix towards an equilibrium concentration through reactive wetting. In Figure 7-4j, the outline of where the original zinc particles were can hardly be seen at 500 °C. Evidently, the heating rate affects melting kinetics, since the temperature spread of the eutectic phase ranges from 374 ˚C to 393 ˚C (peak 381 ˚C) in the DSC conducted at 10 ˚C min^{-1} while, under the higher heating rates of the confocal microscope (60 ˚C min^{-1}), the liquid phase appears at

369 ˚C and persists until 470 ˚C. It is expected that this phenomenon would be even more pronounced in the foaming furnace where the sample is exposed to higher initial heating rates. The high heating rates generated by the foaming process ensures that zinc is not prematurely dissolved in the structure prior to forming significant amounts of liquid. A comparison between the heating rates for the different characterization techniques are shown in Figure 7-5 (i.e.: DSC, foaming furnace and confocal microscope). It can be observed from Figure 7-5 that the initial heating rates during foaming are very high. Since the initial heating rates during foaming are much higher than in the confocal microscope, significant solid state diffusion is not regarded as an issue as indicated in Chapter 6. In liquid state diffusion of Al-Zn, low heating (1 °C min^{-1}) rates have been reported to significantly reduce the amount of transient liquid phase available [120]. In this case, again, the high heating rates ensure dissolution of the phase over a larger temperature range. The principal role of this eutectic transient liquid phase is to enhance the encapsulation of hydrogen before the sample reaches the semi-solid foaming temperatures. Once the semi-solid temperature is attained liquid is formed and foaming can occur.

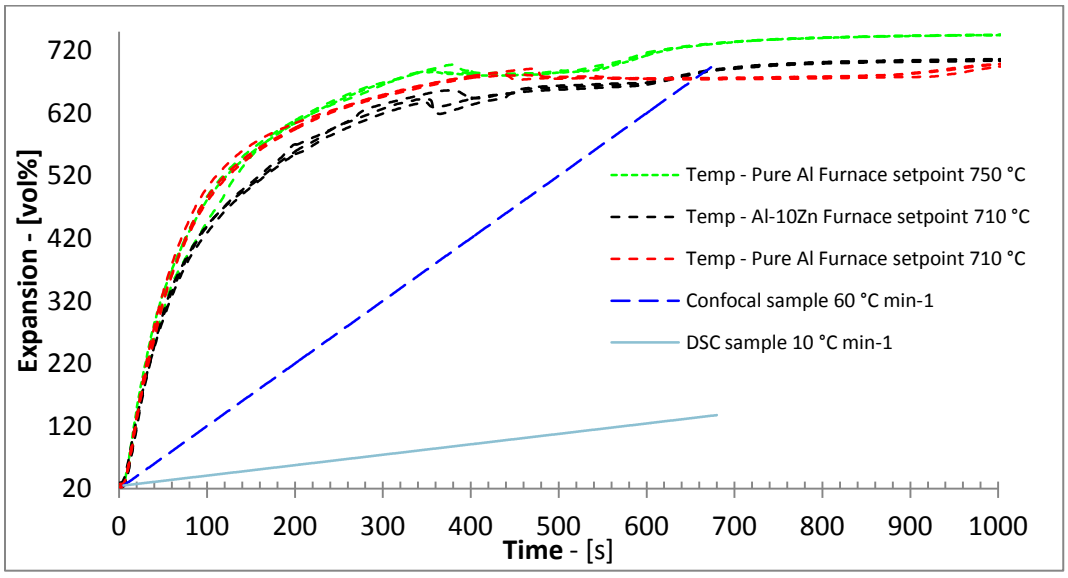

Figure 7-5: Heating rate comparison, Al-10wt%Zn – 710 °C, Pure aluminum – 710 °C, Pure aluminum – 750 °C, Confocal microscope 60 °C min-1, DSC 10 °C min-1

7.2 Foam Expansion and Sample Temperature

A comparison between the expansion curves of pure aluminum and Al-10%Zn produced at 710 °C is shown in Figure 7-6 with compact composition as the only variable. Sample temperature and expansion over time is shown. When looking at the pure aluminum curve, it is apparent that a large cracking/hydrogen loss period is initiated at an average time of 462.7 ± 16.2 s corresponding to the melting onset and persisting until 894.0 ± 5.0 s as observed in Chapter 5. In contrast, the Al-10wt%Zn composition only shows slight dilation prior to bulk expansion where the melting onset is measured on average to begin at 365.0 ±18.2 s. In the case of the Al-Zn system, a transient liquid phase and a semi-solid region ensures an adequate supply of liquid throughout the foaming process, rather than a large heat of fusion at a specific temperature as is the case for pure aluminum. As a result, the large dehydrogenation period is suppressed and is translated to higher levels of maximum expansion of the foam (293.7 ± 8.3 vol% for Al-10wt%Zn compared to 127.7 ± 1.5 vol % for pure aluminum). From the expansion profiles and data summarized in Table 7-3, the curves are reasonably reproducible.

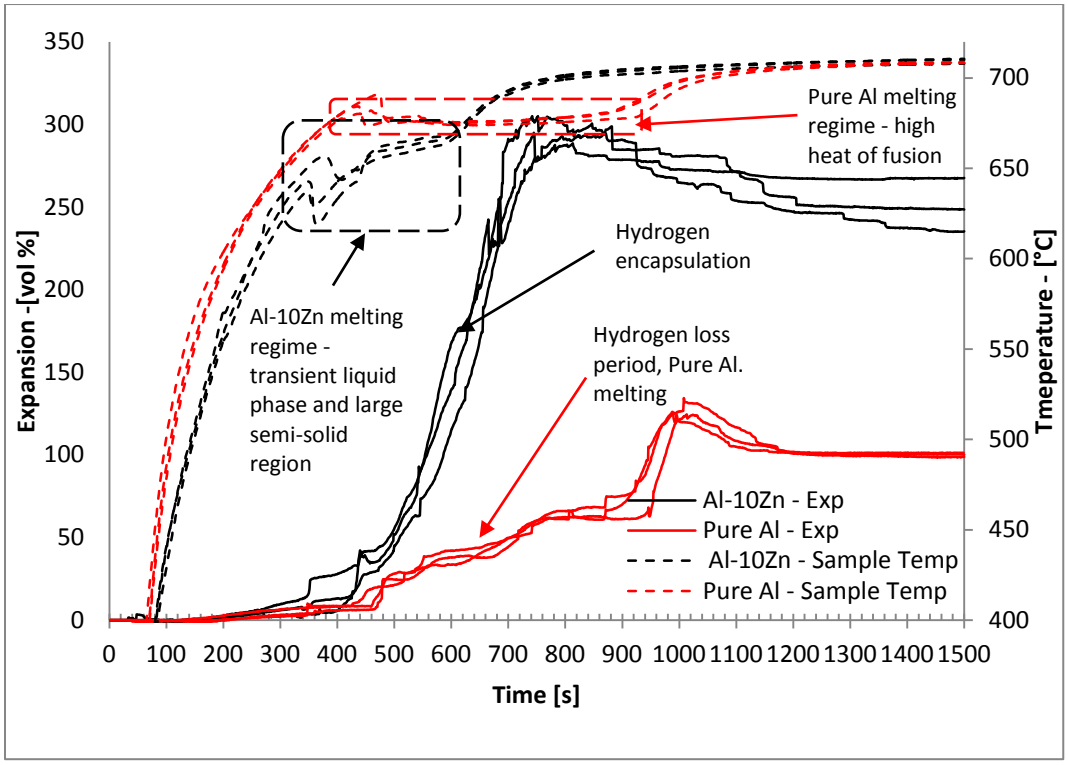

Figure 7-6: Al-10wt%Zn foams compared to pure aluminum foams produced at 710 °C with alloy composition at the only variable.

A focus on the heating curve profiles is shown in Figure 7-7. From the sample temperature measurements, the melting of the compact can be identified as the region where the temperature is more stable, where the heat in going towards melting the sample rather than heating it. From Figure 7-7, the melting time and temperature for the Al-10wt%Zn foam is significantly lower than pure aluminum. The time taken to melt the pure aluminum compact was 431.3 ± 15.3 s while the Al-10wt%Zn was 242.0 ± 17.6 s being almost half. As determined in Chapter 5, the majority of the hydrogen in the sample is lost during the melting regime of the pure aluminum. Therefore, the shorter time required to melt the sample along with an increase in liquid phase is beneficial in encapsulating the otherwise lost hydrogen. The slight variations between the temperature measurements shown in Figure 7-6 and Figure 7-7 are attributed to variations in the compact melting over the tip of the thermocouple which is located directly underneath the sample.

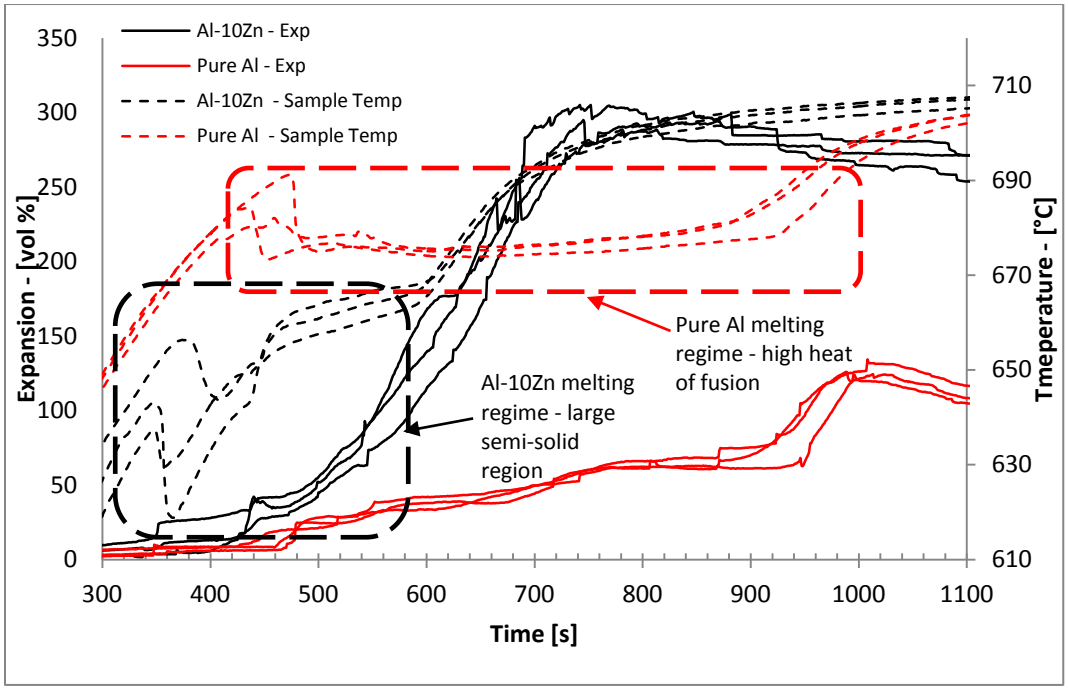

Figure 7-7: Pure aluminum and Al-10wt%Zn foam produced at 710 °C showing heating rates

Due to the high heat of fusion of aluminum 10.71 kJ mol^{-1} [147], a great deal of thermal energy is required for bulk melting of the sample at a given temperature once the onset melting is reached. In comparison, the energy required to melt the Al-10wt%Zn sample according to FactSage is 11.57 kJ mol^{-1} (over a temperature range of 32 °C) being slightly higher than pure aluminum. Although the energy required for melting the pure aluminum and Al-10wt%Zn alloy is similar, the gain in foaming efficiency in this case is related to the formation of the semi-solid region and the lower melting onset. Due to the lower melting onset, the rate of energy input from the furnace into the sample which melts at a lower temperature will be greater due to the larger temperature differential between the furnace and the sample. In other word, the Al-10wt% sample will require less time to melt than pure aluminum due to a lower melting point for an equivalent furnace setpoint. Therefore, the lower time required for melting and the gradual formation of liquid will result in the encapsulation of higher levels of hydrogen which can be translated to higher levels of expansion. This concept is evidenced from Figure

7-6 and Figure 7-7 as well as with Figure 5-6 in Chapter 5 comparing pure aluminum produced at 750 °C and 710 °C. It is also to be noted, the recorded sample temperature up to the matrix melting onset is consistently lower for the Al-10wt%Zn than pure aluminum in Figure 7-6 and Figure 7-7. This is due to the formation and spreading of the transient liquid phase shown in Figure 7-4. Due to the low levels of transient liquid phase and its low melting point, it is hard to identify the thermal event through sample temperature measurements from the bulk sample.

The calculated energy flux required to melt the samples with respect to time is calculated as follows:

$$\frac{\partial E}{\partial t} = \frac{\textbf{Heat of fusion}}{\textbf{Melting time}} \qquad \textbf{Equation 7-1}$$

The energy required to melt the pure aluminum sample is 3394 J compared to the Al-10wt%Zn alloy which is 3650 J for a 20 mm foam as shown in Table 7-2. The heat flux input from the hot air in the furnace into the pure aluminum sample during melting is 7.87 W, nearly half the energy flux going into the Al-10wt%Zn foam (15.08 W) at a furnace setpoint of 710 °C. The higher energy input shows the advantage of reducing the melting point and having a semi-solid resulting in a shorter melting time.

The same observations are made in Chapter 5 for pure aluminum, when the furnace temperature is increased to 750 °C from 710 °C, the temperature differential between the furnace and the sample is also increased. As a result the input energy flux into the sample is increased from 7.87 W to 17.32 W, resulting in a shorter melting time. Increasing the furnace temperature, therefore, has the same effect as reducing the melting temperature through alloying. Although alloying may be favorable in certain instances, however, a sample temperature increase passed maximum expansion also has to be considered due to the possible

reduction in bulk viscosity. The resulting reduction in bulk viscosity could result in increased foam degradation.

Table 7-2: Calculated sample heat flux input during melting for 20 mm diameter samples, heat of fusion calculated through FactSage

Furnace Temp (°C)	*Composition*	*Heat of Fusion (kJ mol^{-1})*	*Energy for melting (J)*	*Melting time (s)*	*Heat Flux (W)*
750	Pure Al	10.7	3394.0	196.0	17.3
710	Pure Al	10.7	3394.0	431.3	7.9
710	Al-10wt%Zn	11.6	3650.3	242.0	15.1
640	Al-33wt%Zn	12.2	3910.1	840.0	4.7

The recorded sample temperature at maximum expansion for the Al-10wt%Zn foam in Figure 7-6 is on average 699.3 ± 2.1 °C displaying a 293.7 ± 8.3 vol% expansion occurring at a time of approximately 782 s. On the contrary, pure aluminum maximum expansion is only 127.7 ± 1.5 vol% equivalent to a time of approximately 1000 s and a temperature of 696.0 ± 1.5 °C which reflects the large time window of hydrogen loss during the melting period occurring between 431.2 ± 15.3 s and 894.0 ± 5.0 s. When comparing both samples, maximum expansion in both instances occurs near 700 °C, only 11-14 °C below the furnace setpoint. In the case of pure aluminum processed at 750 °C, maximum expansion was reached at temperatures 34 °C lower than the furnace setpoint. It can then be concluded that, an increase in heat flux with the use of an alloying element can be beneficial in reducing foaming temperatures as long as the melting temperature is not significantly reduced with respect to the furnace setpoint.

Once, fully expanded, the pure aluminum shows severe degradation while the Al-10wt%Zn displays an increase in stability while maintaining expansion levels comparable to pure aluminum produced at 750 °C near 300 vol% expansion. The stability of the foam past maximum expansion will be addressed in Sections 7.6 in relation to stability mechanisms. Table 7-3 summarizes the above results comparing pure aluminum and Al-Zn foams.

Table 7-3 : Temperature, time and expansion measurements of Al-10wt%Zn and pure aluminum processed at 710 °C and pure aluminum processed at 750 °C

Foaming Temperature (°C)	*Melting Onset (s)*	*Melting time (s)*	*Bulk expansion onset (s)*	*Maximum Expansion (vol%)*	*Maximum Expansion temperature (°C)*
Pure Al 710 °C	462.7 ± 16.2	431.3 ± 15.3	894.0 ± 5.0	127.7 ± 1.5	696.0 ± 1.5
Al-10wt%Zn 710 °C	365.0 ± 18.2	242.0 ± 17.6	439 ± 2.6	293.7 ± 8.3	699.3 ± 2.1
Pure Al 750 °C	351.7 ± 16.0	196.0 ± 17.8	547.7 ± 6.6	311.0 ± 5.5	716.3 ± 5.1
Al-33wt%Zn 640 °C	332.0 ± 14.4	----	----	349.3 ± 17.1	638.3 ± 3.1

Al-33wt%Zn curves were also generated while measuring the sample temperature. Figure 7-8 shows Al-33wt%Zn foams produced at 640 °C over a time period of 2400 s. In this case, the foam expands very slowly. With the lower foaming temperature, the TiH_2 gas release dissociation is likely reduced since the volume expansion rate of the sample is not very high once it is fully molten in contrast to Figure 7-6 for the Al-10wt%Zn. Similarly to the Al-10wt%Zn foam, melting occurs over a range of temperature during which the sample is passing through the semi-solid region. The bulk melting onset, occurs after 332 ± 14.4 s where the expansion of the foam is shown to take off in Figure 7-8. Unlike pure aluminum and Al-10wt%Zn, the exact end of the melting period is hard to pin point through bulk sample measurement in Figure 7-8. With the other systems, a clear increase in sample temperature defines the melting regime from bulk sample heating. In this case it is apparent that near 618 °C, there is a slightly sharper increase in sample temperature corresponding to an approximate time of 840 s. This could signify the upper limit of the semi-solid region but it is not clearly defined. Moreover, the foam keeps expanding once the furnace setpoint is reached indicating a slow dissociation of the hydrogen.

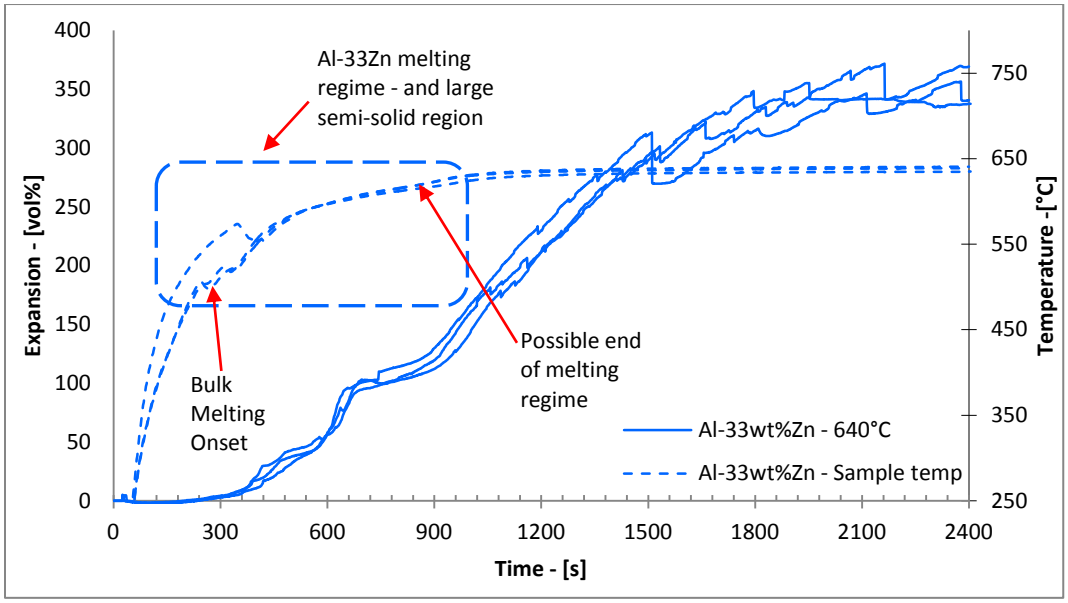

Figure 7-8: Expansion curve of an Al-33wt%Zn foam produced at 640 °C

The peak expansion of the foam is recorded at 349.3 ± 17.1 vol% and is reached at 2000 s, being well after the sample has attained the furnace setpoint of 640 °C. This is an excessively long time for foaming. Although the foaming takes place over a long period of time, the foam appears to suffer from lower levels of degradation than its Al-10wt%Zn counterpart. Sudden drops in the expansion curves can be observed over the foaming time which corresponds to the collapse (bursting) of foam bubbles. The heat of fusion of this alloy according to FactSage is 12.22 kJ mol^{-1} spanning over a temperature range of 74.7 °C. The energy required to heat the sample is only slightly higher than Al-10wt%Zn at 3910.1 J but the semi-solid region expands over a wider temperature range. The calculated average heat flux during melting in this case is very low, at a value of 4.7 W compared to the Al-10wt%Zn foam at 15.1 W. This would help explain the slow melting and expansion of the foam. The temperature measurement of one of the three samples differs slightly as a result of the sample position with respect to the thermocouple but once melted, the sample temperature is in line with the other measurements. Slow dehydrogenation is believed to be responsible for the low rate of expansion of the foam. For such a small sample size of 9.5 g, in this case,

this rate of expansion is unfeasible for any type practical (industrial) application or mass production (at least starting from a cold crucible or furnace).

Figure 7-9 shows a comparison between foams processed at 710 °C (pure aluminum and Al-10wt%Zn) and the Al-33wt%Zn foam processed at 640 °C. It is evident the foaming rate is significantly lower as well as the heating rate but the overall expansion is larger over a wider period of time.

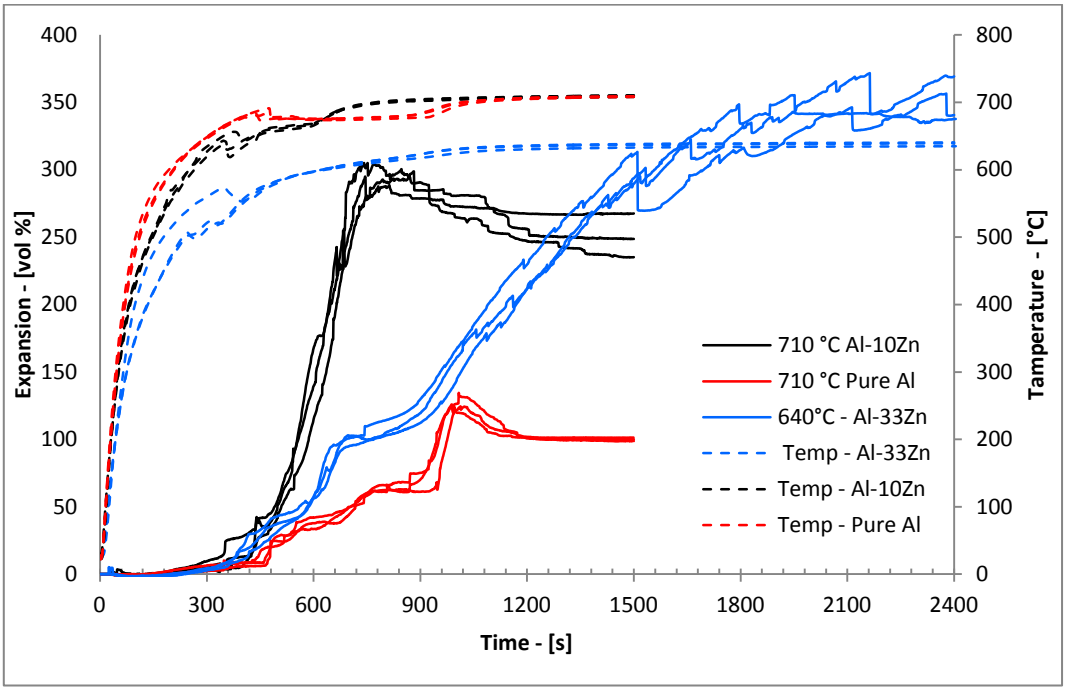

Figure 7-9: Al-10wt%Zn foam produced at 710 °C, Pure Al foam produced at 710 °C, Al-33wt%Zn foam produced at 640 °C

In summary, this analysis reveals that by adding as low as 10 wt% zinc to the compact, the foaming temperature can be drastically lowered, the sample melting heat flux increased, and expansion more than doubled. However, when zinc concentrations were increased further to 33 wt% and the foaming temperature was reduced to 640 °C, higher expansions were obtained at the expense of a longer foaming time.

7.3 Foam structure over time

Air quenched foam samples were cut and polished at specific time intervals in relation to foaming curves to reconstruct the macrostructural and microstuructural evolution of the foam. Aluminum and Al-10wt%Zn foams were produced at 710 °C based on expansion curves shown in Figure 7-6. The structures of the pure aluminum in comparison to Al-10wt%Zn foams produced at 710 C° are shown in Figure 7-10 and the evolution of the Al-10wt%Zn foam with respect to expansion in Figure 7-11. This comparison draws attention to cracks and how they can be suppressed by introducing a low melting point elemental powder to the compact without relying on conventional wrought or cast alloys compositions.

In Figure 7-10a, after the samples have been heated for 300 s, cracks have not yet formed in the pure aluminum sample but in the Al-10%wtZn composition, one can see the individual zinc particles. The diffusing zinc particles are seen as the brighter phase in the matrix. A closer look at the pore nucleation in the foam under the microscope reveals the formation of the pores at the centre of the diffusing zinc particles. The elemental zinc particles can be seen more closely spreading inside the compact and diffusing through the matrix as the pores are beginning to nucleate in a uniform manner in Figure 7-14. This will be explained in greater detail in Section 7.4.

At 500 and 550 s (Figure 7-10b and Figure 7-10c), the pure aluminum samples have reached the melting temperature according to the expansion curves, where large horizontal cracks can be seen with the naked eye in the centre of the sample, corresponding to the release of hydrogen. A series of other small microcrack are also visible through micrographs uniformly distributed throughout the sample at both times forming a network of porosity. At this stage, it is evident that hydrogen is being outgassed to the atmosphere through the network of crack and cannot be contained within the compact highlighting the inefficiency of the pure aluminum

system. On the contrary, the Al-Zn samples produced under this condition displays a large number of growing round pores which are uniformly distributed throughout the structure. At these times, no microcracks similar to pure aluminum are apparent in the sample. Although round pore are forming, some larger cracks can be seen. It is stipulated that these crack are produced during solidification due to the continued release of hydrogen below the alloy solidification point and shrinkage causing linear cracking through the small bubbles. At 600 s in Figure 7-11, the Al-10wt%Zn is beginning to expand into actual foam where a larger number of round cell are observed. At this point the large cracks are not seen in the sample supporting the previous statement.

At 750 s in Figure 7-10d, large cracks are still visible in pure aluminum with low levels of expansion. This shows evidence that hydrogen is still free to escape to the atmosphere but some pores are becoming closed off and rounder with less horizontal cracks as the compact is nearly melted. At this stage, the Al-10wt% composition has reached maximum expansion and a full foam with large cells is produced shown through Figure 7-10 and Figure 7-11. Finally, at 950 s, the pure aluminum compact is fully molten and has expanded to produce foam with larger round cells in Figure 7-10e rather than cracks. The pure aluminum foam at this stage is comparable to Al-10wt%Zn foam produced at 600 s. At 950 s in Figure 7-11, the Al-Zn mixture continues to demonstrate stability and appears to be coarsening over time in comparison to 750 s, showing low levels of foam degradation.

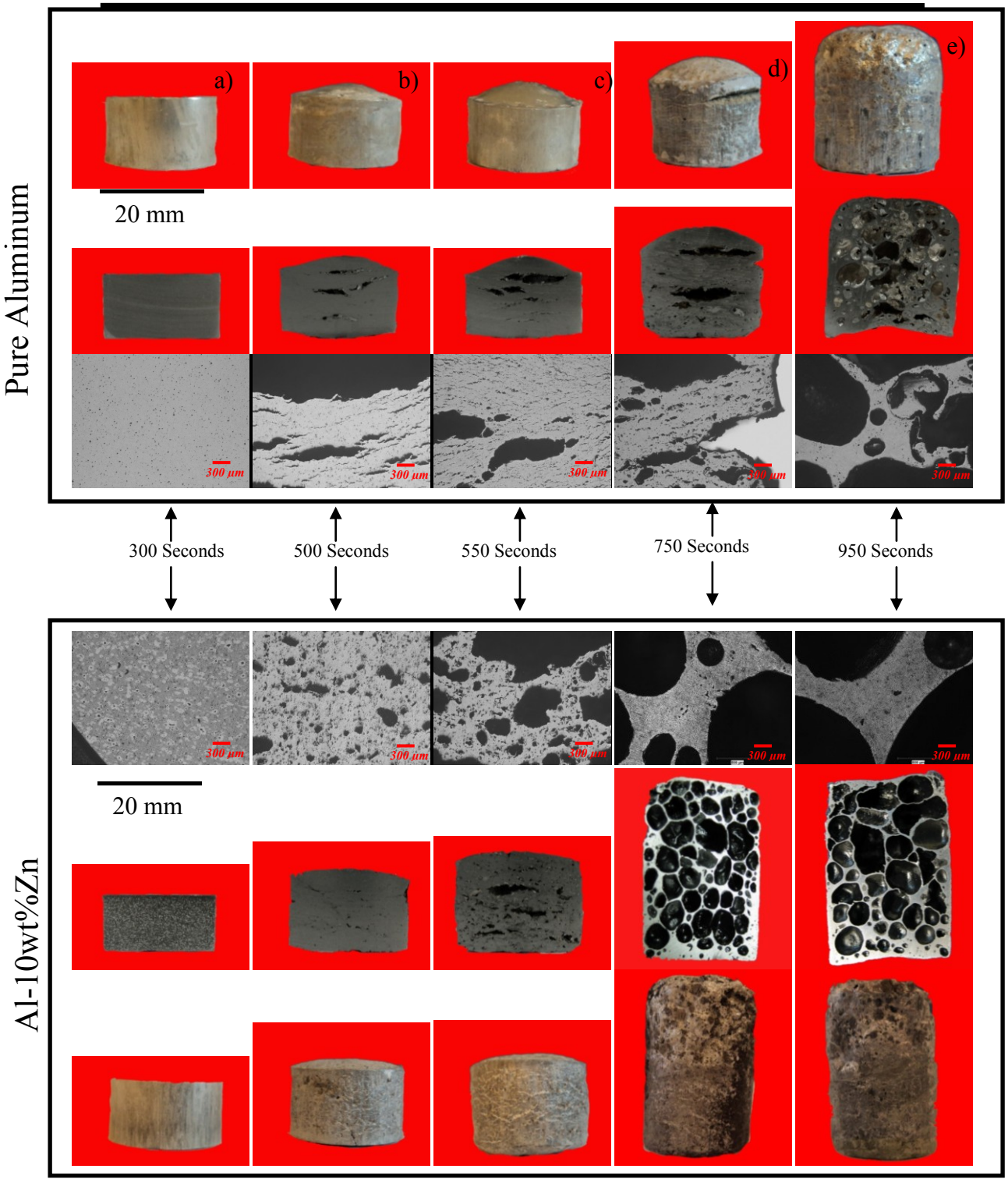

Figure 7-10: Pure aluminum foam structure compared to Al-10wt%Zn over time a) 300 s, b) 500 s, c) 550 s, d) 750 s, e) 950 s.

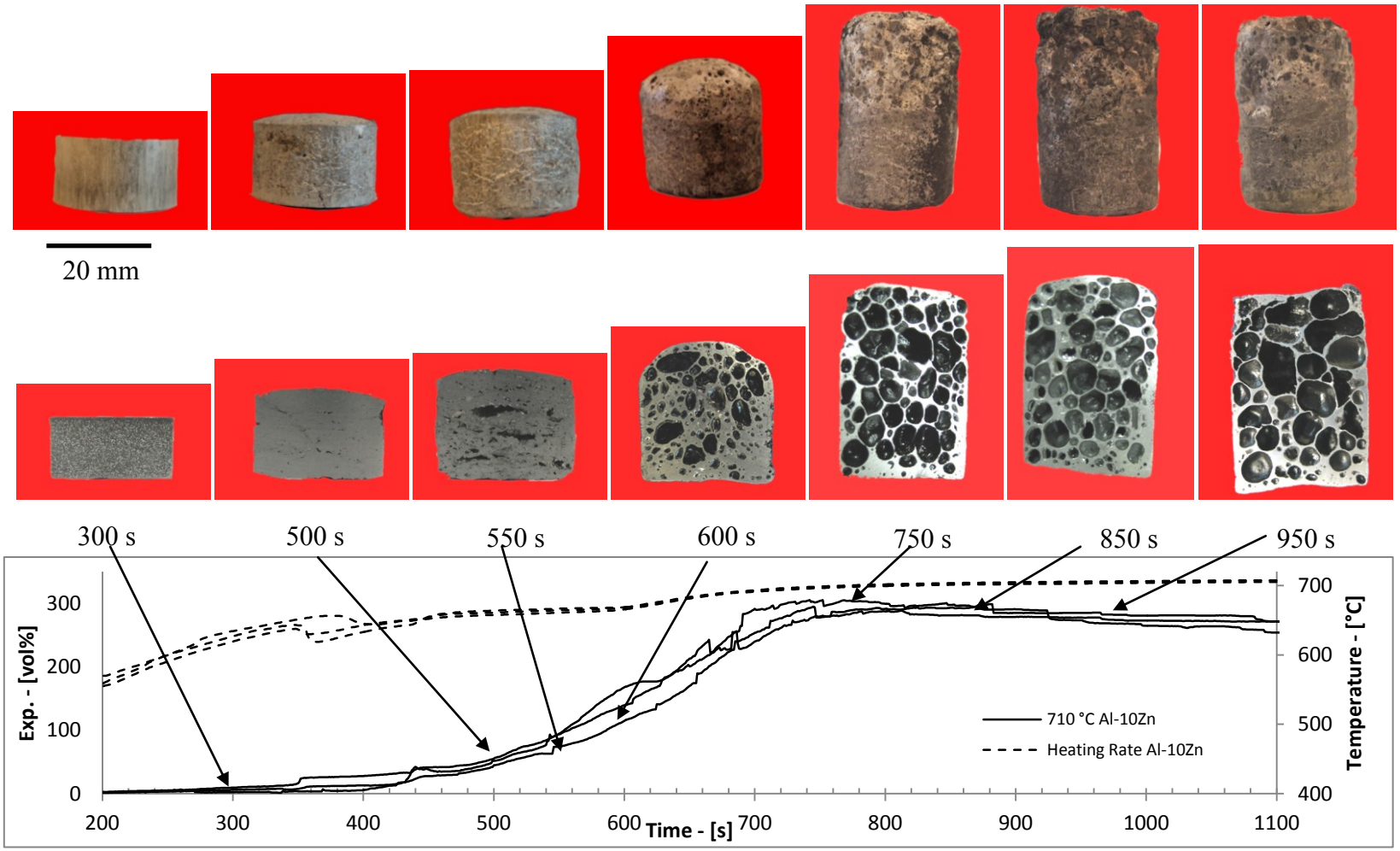

Figure 7-11: Al-10wt%Zn foam evolution over time foaming at 710 °C

Foam samples having an Al-33wt%Zn composition were also air quenched and sectioned at selected time intervals to observe the foam structure and evolution. At a foaming time of 300 s, it can be seen that no apparent bulk expansion is taking place. Like the Al-10wt%Zn composition, the pores at this stage are beginning to nucleate uniformly from the centre of the zinc particle (Figure 7-15 in the following subsection).

At 500 and 550 s, the foam is displaying low levels of expansion and the cross-sections reveal the formation of large cracks in the sample. Although these cracks form, they are believed to be associated with the solidification of the sample similarly to Al-10wt%Zn. This is evidenced by Figure 7-12 where the smaller cracks are shown to be progressing through what appears to be small pores, likely during solidification as a result of shrinking and continued gas release. This type of cracking can also be seen in welding defects through the formation of linear porosity and solidification. During this expansion time, the sample is melting and is in the semi-solid region according to the sample temperature measurements. From Figure 7-13, the porosity formation appears to be uniform in nature with pores having relatively similar sizes.

At foaming intervals of 750 s and 950 s, the cracks in the sample are no longer visible and the formation of larger round pores can be seen. The samples are melting at this point and the small pores formed in the matrix are beginning to coalesce, forming lager pores as higher levels of hydrogen are being released in the structure. In comparison, at 750 s the Al-10wt%Zn composition has reached maximum expansion and a full foam with large cells is produced shown through Figure 7-10 and Figure 7-11.The large amounts of liquid are favorable for bubble growth and gas encapsulation at this stage. From 1250 s through 1850 s in Figure 7-11, the foam is displaying typical foam expansion behavior where the foam is expanding and bubbles are slowly coarsening.

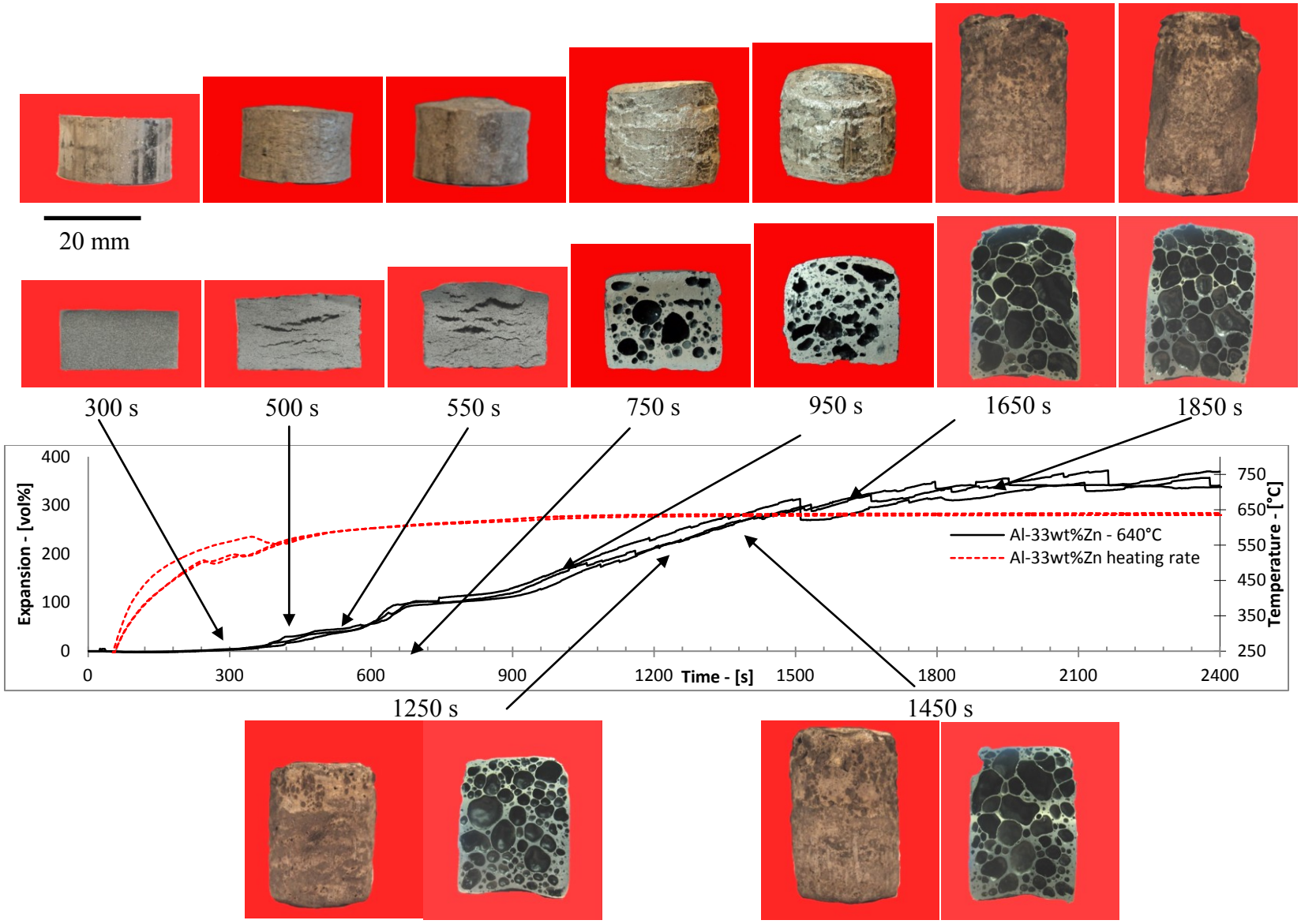

Figure 7-12: Al-33wt%Zn foam showing structure evolution, foaming curve and sample temperature

The expansion curves and structures of the foam reveal that, the zinc is capable of encapsulating some hydrogen at the early stage of foaming while displaying stability passed the maximum expansion.

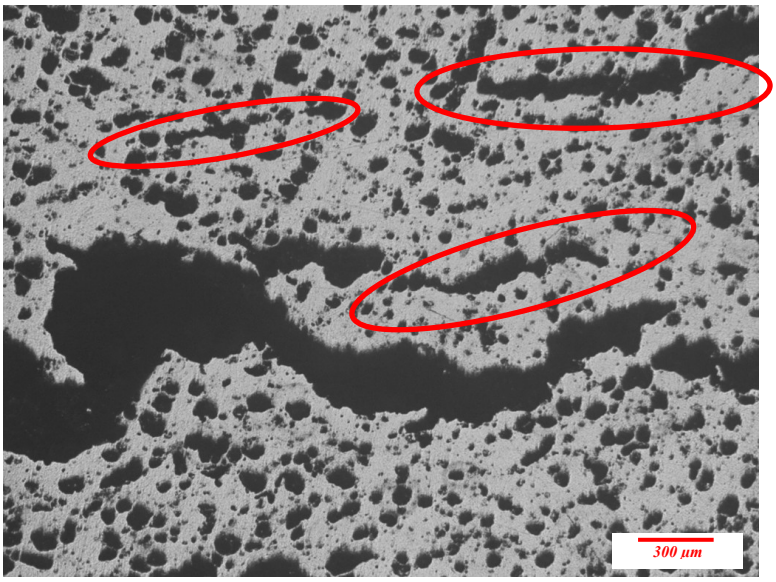

Figure 7-13: Crack formations in Al-33wt%Zn foams spreading during solidification

7.4 Pore Nucleation Microstructure

In support of the confocal microscopy analysis in Figure 7-2 where pore nucleation could not be visualized, air quenched samples of the evolving structures were produced to observe the nucleation of the pores. At a time interval of 300 s, the spreading of the zinc phase is displayed in the structure as the brighter phase in Figure 7-14 and Figure 7-15 for the Al-10wt%Zn and Al-33wt%Zn foams, respectively. In both instances, the pore nucleation onset is consistently centered within the dissolving Al-Zn phase. These observations are the result of the Al-94wt%Zn eutectic phase generated at the outer surface of the elemental zinc powder shown in Figure 7-2 which subsequently spreads through the matrix toward phase equilibrium. The intended purpose of the transient liquid phase is to enhance the level of liquid before the semi-solid temperatures are attained. Several micrographs in Appendix D show the nucleation of the pores as being uniform throughout the structure.

The average recorded temperature for the Al-10wt%Zn produced at 300 s is 626.6 ± 7.5 °C, just prior to the recorded temperatures for bulk melting onset of 365.0 ± 18.2. However, a thermal event can be observed in Figure 7-12 for the Al-33wt%Zn near 300 s corresponding to a temperature of 516.5 °C ± 6.4 °C being below semi-solid forming temperatures. The higher fraction level of transient liquid phase formation with Al-33wt%Zn composition, likely results in a lower heating rate measurement through the sample temperatures. Since the tip of the thermocouple is in contact with the surface underneath the sample, a more representative temperature is expected once the compact melts over the thermocouple due to better contact.

The formation of liquid is believed to release the pressure build-up in the matrix possibly allowing an earlier onset of gas release than in pure aluminum resulting in gas encapsulation even though the temperature recorded after 300 s is 626.6 °C. Results pertaining to the structure evolution of Al-7wt%Si foams shown in literature reveal that cracks are visible at early stages similarly to those observed in pure aluminum forming a fissure network. The network of cracks shown in literature are either formed prior or during the bulk melting of the foam but a certain level of liquid phase becomes available at 577 °C [10, 11, 20]. In contrast to this, the zinc phase melts at 381 °C, which accommodates an early onset of gas evolution at very low temperatures and would prevent pressure build-up in the structure suppressing the tendency of forming the crack network.

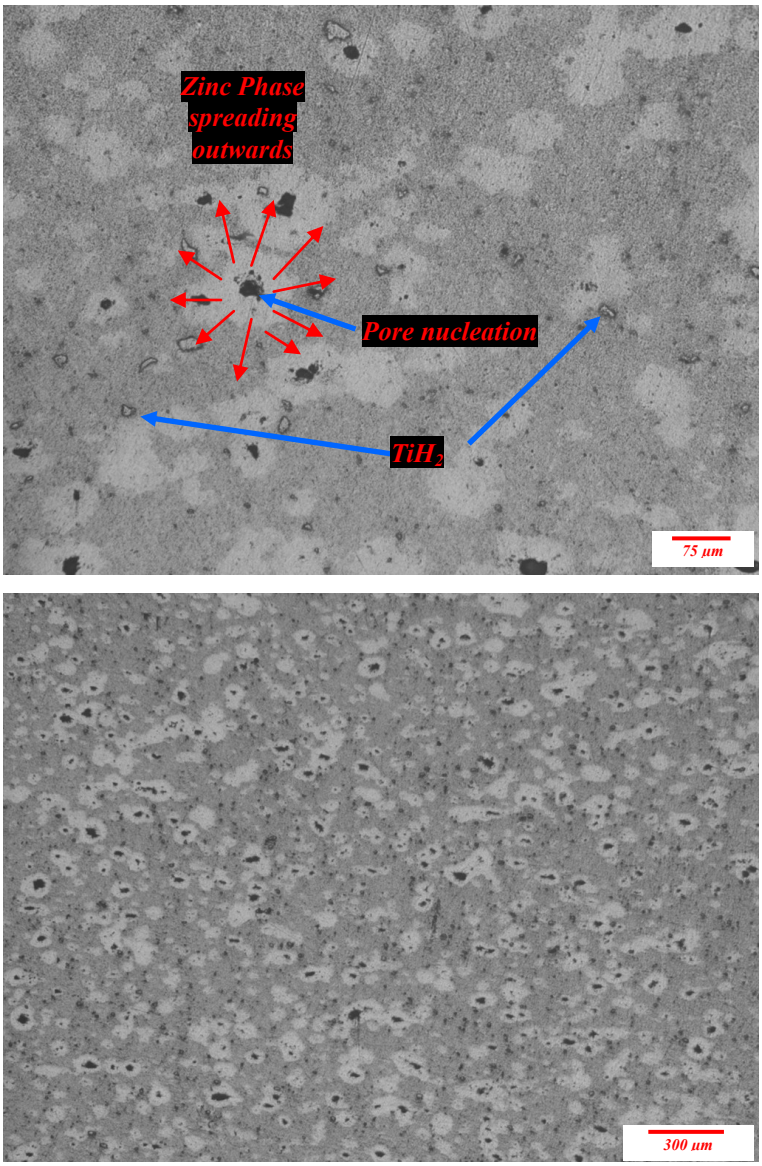

Figure 7-14: Uniform porosity nucleated throughout an Al-10wt%Zn sample produced at 710 °C for 300 s

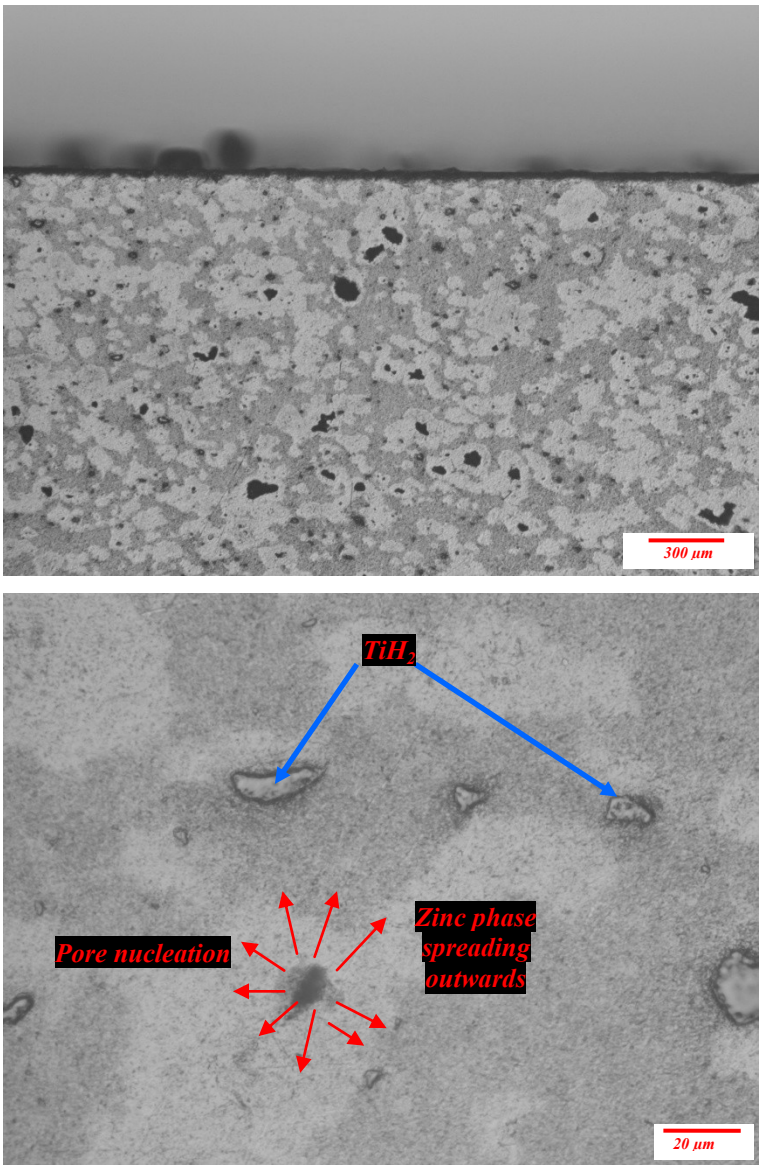

Figure 7-15: Al-33wt% Zn sample processed at 640 °C for 300 s

In pure zinc foams it has been stipulated that there exists two types of pores, type I pores forming at the blowing agent particles and the type II at grain boundary triple points through diffusion [77, 79]. In this particular case, the majority of the structure is comprised of pure aluminum powder and a uniformly distributed zinc phase which forms liquid at a lower temperature than pure zinc which also corresponds to the lowest recorded TiH_2 gas release temperature [1, 6-8]. It is believed that the nucleation of the pores occur strictly at the blowing agent

particles based on the observed nucleation of the pores. Moreover, it has been shown in literature that TiH_2 particles provide favorable nucleation sites for pores through heterogeneous nucleation [44]. It is also speculated that the evaporation of zinc could help in the nucleation of the pores due to high partial pressure. The continuous nucleation of porosity as a result of high zinc partial pressure as well as its evaporation has been highlighted in several processes such as liquid state sintering and transient liquid phase bonding [101, 115, 121, 123]. Figure 7-16 shows the original size of the zinc particles in a compact for the Al-33wt%Zn composition in comparison to a compact processed for 300 s. The spread of the zinc phase is evident through the observation of the larger zinc rich particulate.

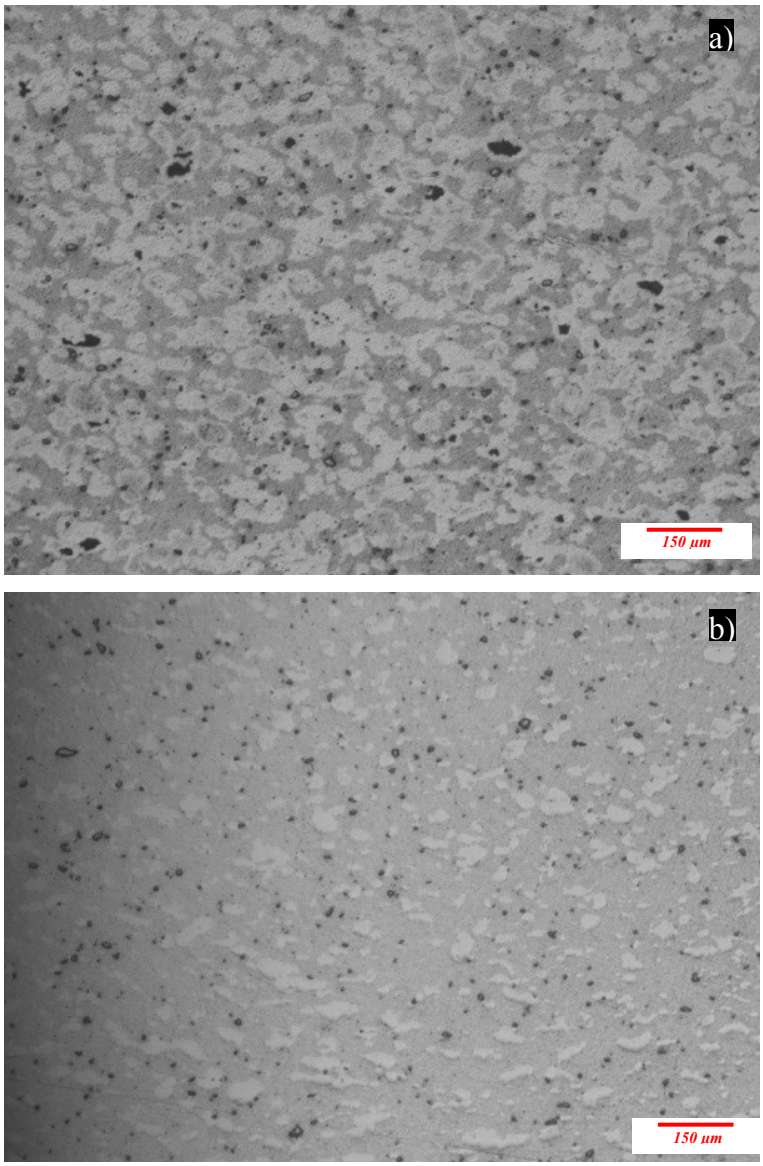

Figure 7-16: Comparison between a foam sample processed at 300 s (a) and a compact (b) of Al-33wt%Zn.

EDS analysis in Figure 7-17 demonstrates the diffusion of the zinc phase where a high concentration of zinc is apparent near the centre of the particle where the pore is forming, displaying a gradually lower concentration towards the aluminum. This is a clear indication that the Al-94wt%Zn phase generated by the elemental powder additions is consuming the matrix confirming the observations in Figure 7-2 from the confocal microscope.

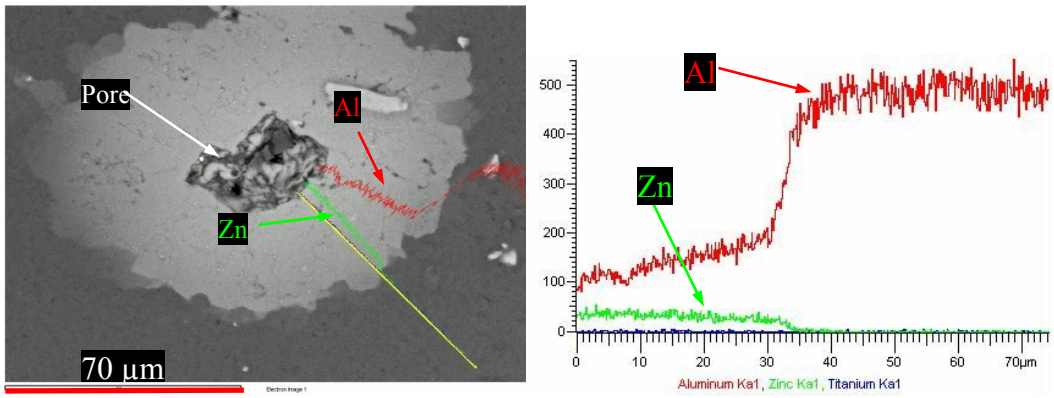

Figure 7-17: EDS analysis of an evolving pore from and Al-10wt%Zn sample processed at 710 °C for 300 s.

Through the sample evolution, the nucleation of round pores becomes more evident at 500 and 550 s. Micrographs of the evolving microstructure of Al-10wt%Zn are shown in Figure 7-18a and Figure 7-18b. At this point, in both cases, zinc particles are no longer visible and are completely dissolved in the aluminum. In Figure 7-18c and Figure 7-18d pure aluminum foams produced at 710 °C are shown to highlight the effect of the alloy on the suppression of the fissure.

The round pore formation highlights the lower surface tension as a result of greater liquid formation. This is supported by the extensive number of pores apparent in the structure which can only be generated by larger levels of liquid and hydrogen release. The samples which have a higher zinc concentration produce porosity which is more uniformly distributed and rounder than in Al-10wt%Zn. In the Al-10wt%Zn, a collection of small and large pores are apparent while in Al-33wt%Zn pores of similar size are apparent as displayed in Figure 7-13. In general, it has been shown that the addition of elemental zinc can be beneficial in the formation of uniformly distributed pores at the early stages of forming suppressing crack formation.

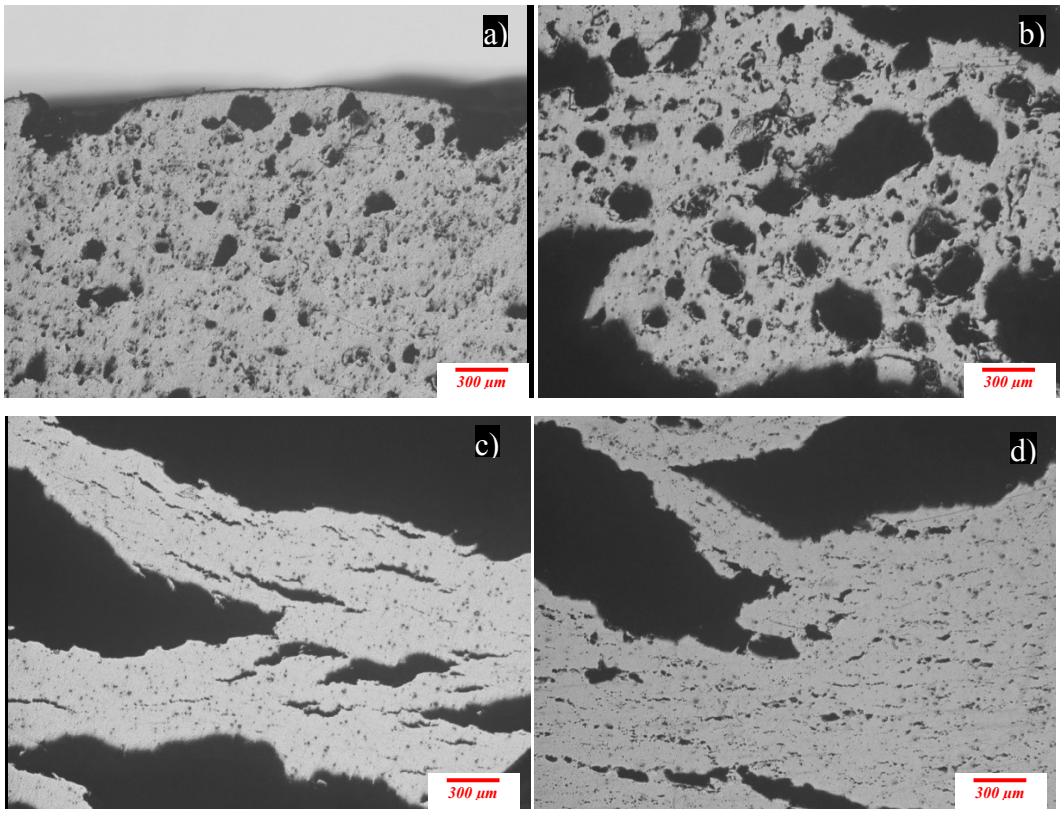

Figure 7-18: Foam produced at 710 °C a) Al-10wt%Zn for 500 s b) Al-10wt%Zn for 550 s c) pure aluminum 500 s d) pure aluminum 550 s

Based on the pore formation analysis, it is proposed that the Zn-Al phase generated through the eutectic formation suppressed the formation of the fissure network, helping the nucleation of uniformly distributed round pores. This encapsulation of blowing gas in return is translated to foam expansion and increased efficiency and lowered foaming temperatures.

7.5 Al-Zn foaming curves over time and temperature

Based on the *in-situ* microscopy and the DSC measurements, a series of expansion curves (using a preheated crucible) were generated starting at temperatures in the semi-solid region (Al-33wt%Zn - 580 °C and Al-50wt%Zn – 540 °C) and at the liquidus (Al-10wt%Zn - 650 °C). The semi-solid temperatures based on composition are outlined in Table 7-1. The temperatures were

subsequently increased by 20 ˚C until satisfactory expansion (near or above 300 vol%), and post maximum expansion stability were obtained. For each system 20 mm diameter and 30 mm diameter samples were produced. The internal pore structure between the samples of different sizes was comparable based on expansion level and structure. Al-33wt%Zn foaming curves are shown in Figure 7-19a and Figure 7-19b. The 30 mm samples took longer to foam as expected due to the higher mass and slower heating rate.

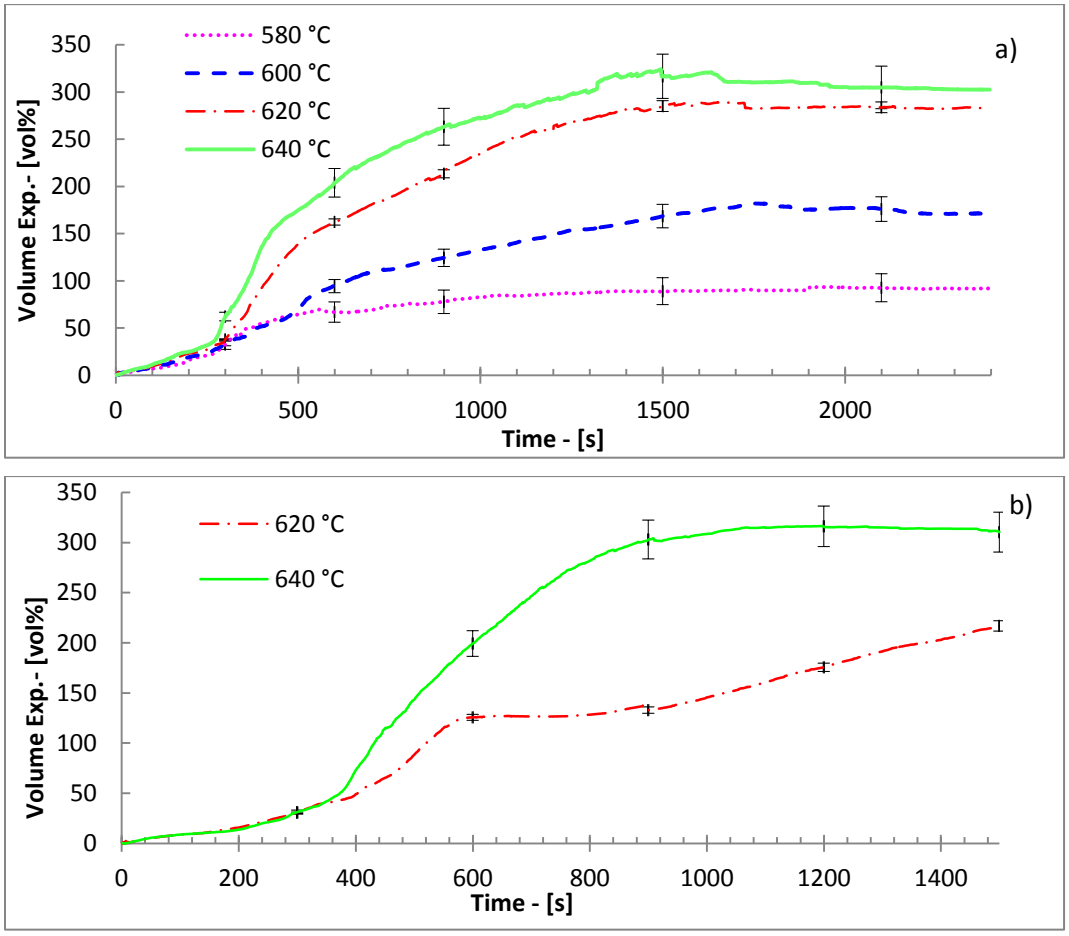

Figure 7-19: Al-33wt%Zn foam expansion curves a) 20 mm diameter samples, b) 30 mm diameter samples

It can be observed from the expansion in Figure 7-19 that the foam produced at semi-solid temperatures (580 °C and 600 °C) was not sufficiently porous with expansions below 175 vol%. This resulted in a very dense structure with thick cell

walls. Since zinc has a high solid-solubility in aluminum it is likely that liquid levels were not sufficient to foam as a result of diffusion of zinc into aluminum at slower heating rates. Only once the furnace setpoint was above the liquidus (620 to 640 ˚C approximately 20˚C above) did the foam expand to desirable levels. Individual curves for each sample are shown in Appendix D rather than curves with error bars.

Figure 7-20a and Figure 7-20b depicts the expansion curves of the Al-10wt%Zn system for 20 mm diameter foams and 30 mm diameter foams. It is apparent again in this case that a certain level of superheat in terms of furnace setpoint above the liquidus (690 °C and 710 °C or approximately 40 ˚C above liquidus) is required to produce foam with desirable expansion. Although there is stability, a slight decrease post maximum expansion is likely due to structure degradation through drainage and collapse. The data pertaining to the optimal conditions for the Al-10wt%Zn and Al-33wt% zinc are summarized in Table 7-4. Although foams could not be produced in the semi-solid region, a significant decrease in foaming temperature and increased stability post maximum expansion were attained. This is an obvious gain from the pure aluminum foam where high levels of superheat are required and high levels of collapse are observed.

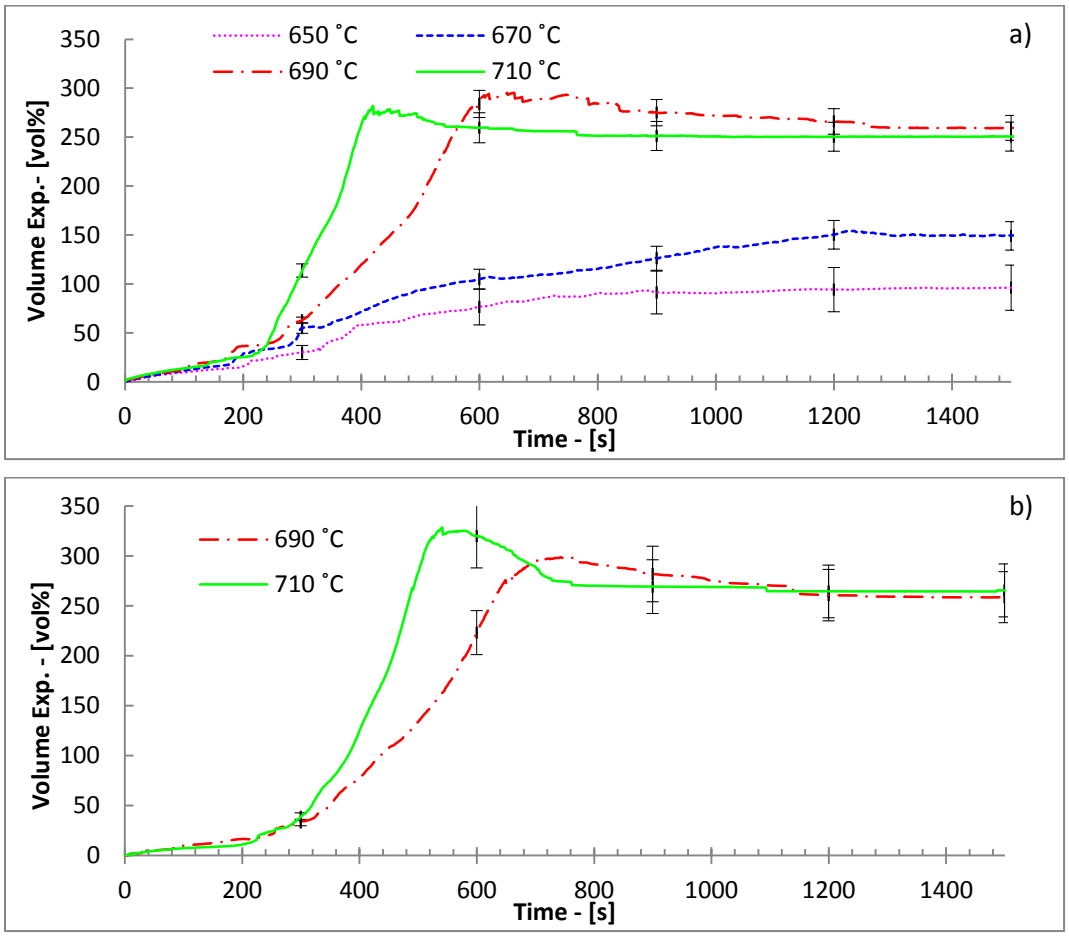

Figure 7-20: Al-10wt%Zn foam expansion curves a) 20 mm diameter samples, b) 30 mm diameter samples

The Al-50wt%Zn composition did not produce smooth curves or macrostructure; the expansion curves proved to be very unstable with low reproducibility, especially in the semi-solid region where a series of small localized collapses and expansion peaks could be observed. As a result, the foaming of Al-50wt%Zn appeared to generate several large localized bubbles rather than small, uniformly distributed bubbles of similar size. The Al-50wt%Zn curves are shown in Figure 7-21. The focus of the work was on the foams with a lower zinc concentration due to the lighter weight and expansion stability.

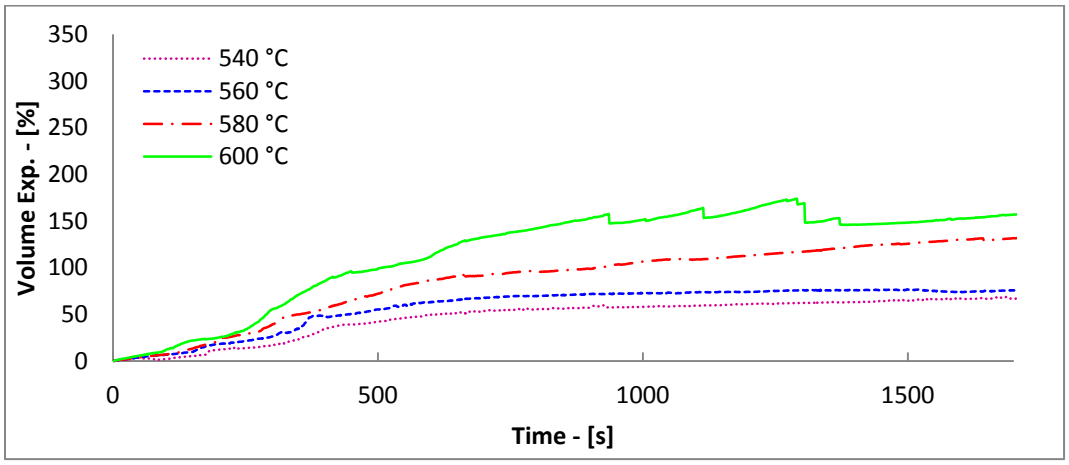

Figure 7-21: Al-50wt%Zn foam expansion curves

The summarized expansion levels based on composition and foaming temperature are displayed in Table 7-4 for both 20 mm and 30 mm samples.

Table 7-4: Al-Zn foaming conditions and expansions

Foaming temp (°C)	*Composition (wt%)*	*Alloy semi-solid region (°C)[13]*	*Max Expansion 20 mm diameter (Vol%)*	*Max Expansion 30 mm diameter (Vol%)*
620	Al-33Zn	531-603	298.4±11.8	216.8±11.2
640	Al-33Zn	531-603	329.4±18.4	321.3±12.5
690	Al-10Zn	622-645	285.1±12.4	304.4±13.8
710	Al-10Zn	622-645	291.7±16.3	334.6±7.2

7.6 Post Maximum Expansion Foam Stability

Post maximum expansion stability with the addition of zinc is important in comparison to pure aluminum. The post maximum expansion reductions have been tabulated in Table 7-5 (based on Figure 7-19a, Figure 7-20a and Figure 5-7) along with foaming temperatures after 1500 s for foams introduced in a hot crucible. By far, pure aluminum experiences the most reduction in expansion, most notably at 750 °C by as much as 36.7 %, likely due to the high surface tension and fluidity. By adding as low as 10 wt% Zn a significant increase in stability can be achieved with a maximum total % foam collapse between 11 and

12 % for foam produced at 710 °C. This corresponds to half the level of collapse relative to maximum expansion of the pure aluminum produced at 710 °C marking a substantial improvement. On the other hand, at concentrations of 33 wt%, the foam is significantly more stable and does not degrade extensively over a period of time of 2400 s (maximum of 8.2 %). Although the Al-Zn based foams can experience some level of collapse, an extended time window of stability is seen, especially for the Al-33wt% foam. This gain in stability is critical in the design of foam parts with more complex geometries where varied levels of heating rates can become important. The values of estimated stability times are shown below in Table 7-5 based on foam expansion curves.

Table 7-5: Collapse of 20 mm foam samples over time in a preheated crucible

Foaming temp (°C)	*Composition (wt%)*	*Max Expansion 20 mm diameter (Vol%)*	*Expansion after 2400 s - Vol%*	*Diff*	*% Collapse*	*Estimated Stability (s)*
620	Al-33Zn	298.4±11.8	274.0±6.2	24	8.2	>1000
640	Al-33Zn	329.4±18.4	303.3±14.6	26	7.9	>1000
Foaming temp (°C)	*Composition (wt%)*	*Max Expansion 20 mm diameter (Vol%)*	*Expansion after 1500 s - Vol%*	*Diff*	*% Collapse*	*Estimated Stability (s)*
690	Al-10Zn	285.1±12.4	250.7±14.28	34	12.1	>250
710	Al-10Zn	291.7±16.3	259.6±15.3	32	11.0	>120
710	Pure al	127.7 ± 1.5	100.0±1.2	27	21.7	<40
750	Pure Al	311.0 ± 5.5	197.5±27.5	114	36.7	≈10

The foam pore sizes for 30 mm diameter foams were measured based on the expansion curves in Figure 7-19 and Figure 7-20. The 30 mm foams were selected for pore size analysis due to the larger number of pores being more representative of a bulk sample. Moreover, the same expansion trends are observed going from 20 mm diameter foams to 30 mm diameter foams. Three foams samples for each condition (specific foaming times) were selected for comparison including; pure aluminum produced at 750 °C and foamed for 600 s, Al-10wt%Zn foam produced at 710 °C and foamed for 510 and 600 s respectively. Finally Al-33wt%Zn foams were produced at 640 °C for 1200 and 1500 s. The results reflect the optimal

range of stability based on alloy and composition. This data is summarized in Table 7-6 and Table 7-5. All foams for which measurements were taken are shown (pictures) in Appendix D along with supplementary data including the spherical diameter, roundness of the pores and individual pore size distributions.

In Figure 7-22a and Figure 7-23b, the macrostructure of a pure aluminum foam produced at 750 °C and time of 600 s is compared to a sample foamed for 1500 s. When comparing the two, is it obvious that the foam produced at 1500 s has significantly collapsed on itself reflecting expansion degradation seen in Figure 5-7 of Chapter 5. At the optimal foaming time of 600 s, the pure aluminum expanded by an average of 300 vol%, with an average pore count of 199 ± 22 and a cumulative pore area of 1061 ± 18 mm^2. In this instance, it is difficult to measure the optimal expansion range at different time intervals since the foam is very unstable and degrades very rapidly and therefore only the optimal expansion at 600 s is shown.

Table 7-6: Foam pore measurement data

Composition	*Foaming time (s)*	*# Pores*	*Expansion (Vol %)*	*Cumulative pore area (mm^2)*
Pure Al - 750 °C	600	199 ± 22	257±2	1061 ± 18
Al-10Zn - 710 °C	510	174 ± 27	301 ± 13	1021 ± 18
Al-10Zn - 710 °C	600	108 ± 27	303 ± 17	979 ± 45
Al-33Zn - 640 °C	1200	152 ± 22	314 ± 9	1110 ± 45
Al-33Zn - 640 °C	1500	153 ± 9	306 ± 18	1097 ± 5

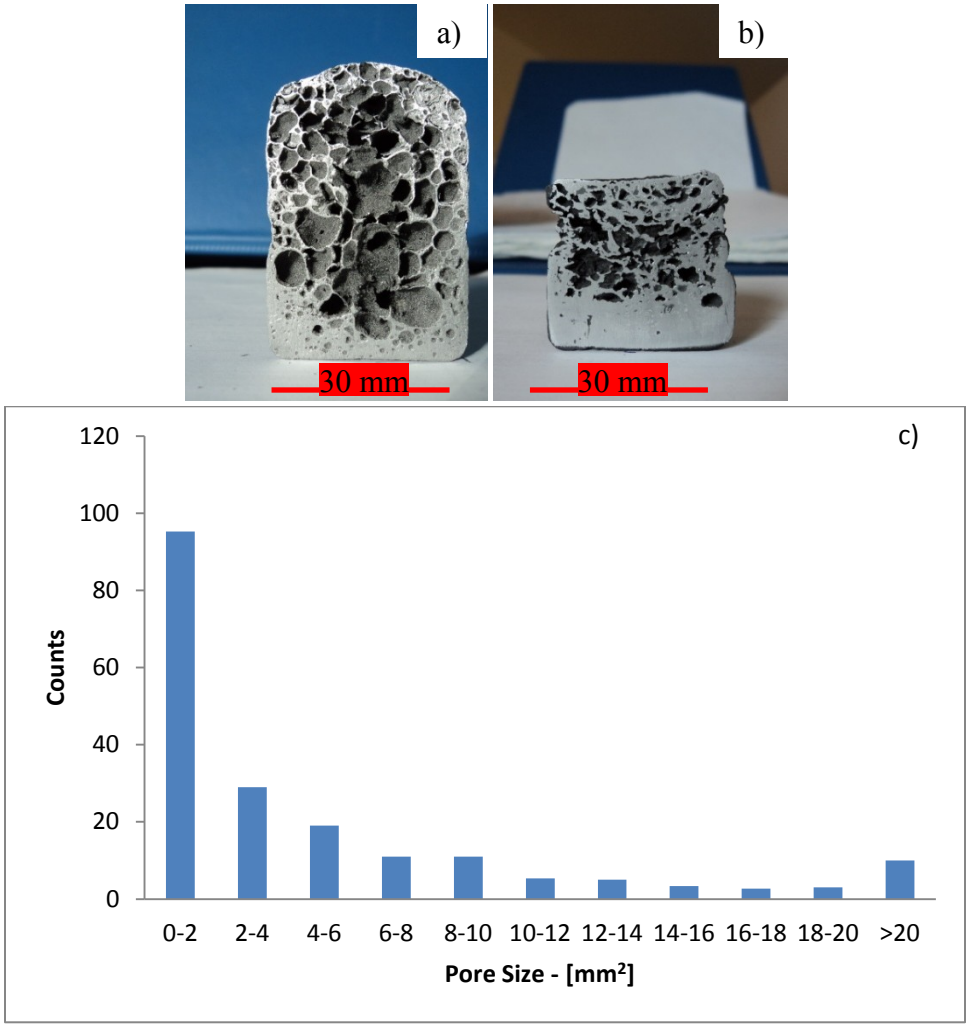

Figure 7-22: Pure aluminum foam produced at 750 °C a) 600 s b) 1500 s c) pore area distribution for foam produced at 600 s.

Al-10wt%Zn foam produced at 710 °C and time intervals of 510 and 600 s are shown in Figure 7-23. From a visual inspection it is apparent that the pore structure is fairly uniform and coarsens over the foaming period. This is evidenced through the measurement of pore area distribution of the foam shown in Figure 7-23d where at 510 s, the number of smaller pores is larger than at 600 s. A larger pore count above 20 mm^2 pores is observed over the 90 s foaming period from 8 to 16 pores. Although pores are coarsening in this instance, the overall expansion remains constant slightly above 300 vol% as shown in Table 7-6. The degradation (coalescence) of the foam is evidenced by the decreasing

number of pore during the foaming period from 174 ± 27 pores to 108 ± 27 pores. The cumulative pore area is also comparable between the two foaming conditions being 1021 ± 18 mm^2 and 979 ± 45 mm^2 for foams produced at 510 s and 600 s respectively. After 1500 s of foaming shown in Figure 7-23c, a thick drainage zone is seen through the accumulation of liquid at the bottom of the foam along with a slight decrease in maximum expansion. This foam evolution is considered to be a fairly standard degradation process but displaying an increased stability (reduced rate of decay) compared to pure aluminum.

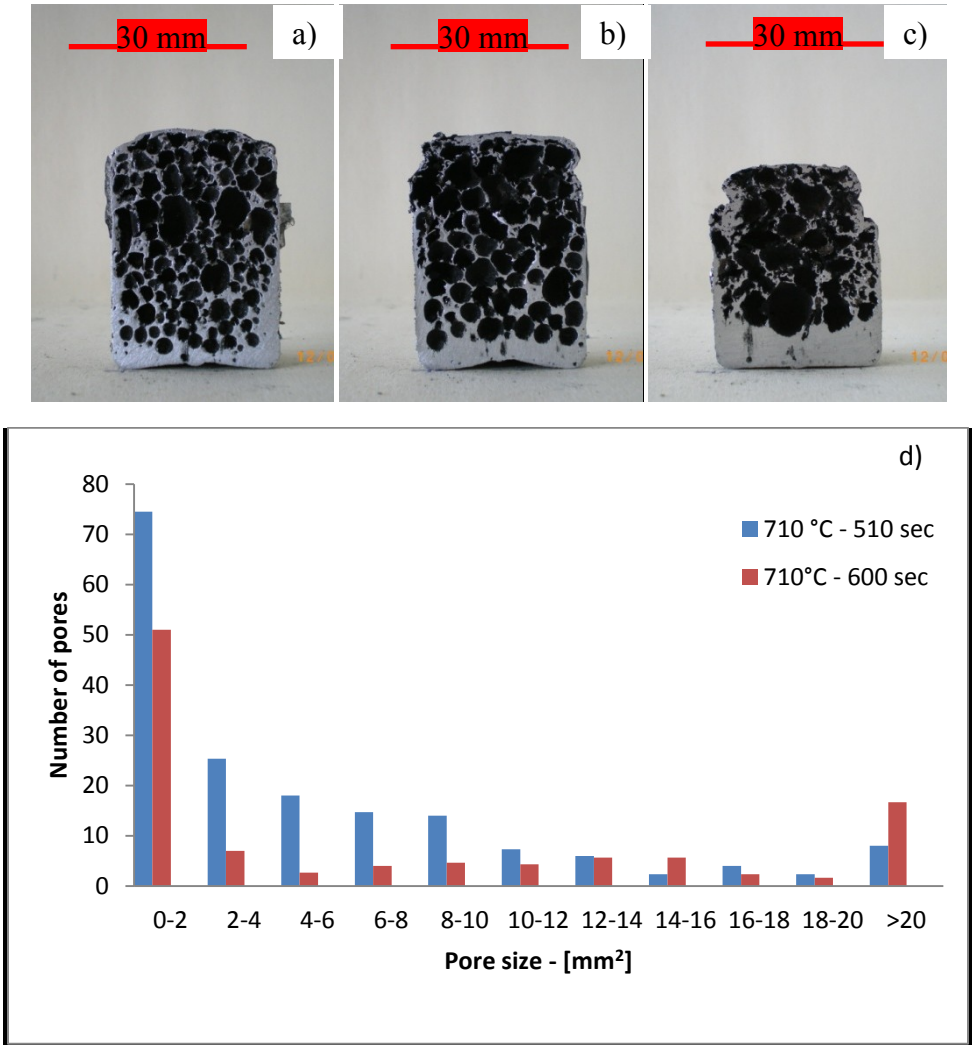

Figure 7-23: Al-10Zn foam produced at 710 °C a) 510 s, b) 600 s, b) 1500 s d) pore area distribution for foam produced at 510 and 600 s.

Al-33wt%Zn foam produced at 640 °C and foamed for 1200 s and 1500 s are shown in Figure 7-24. From visual inspection of the foams in Figure 7-24a and Figure 7-24b, the foam appears to have a larger variation in cell size than its Al-10wt%Zn counterparts. The foam expansions are consistent above 300 vol% expansion at both 1200 and 1500 s over a foaming period of 300 s.

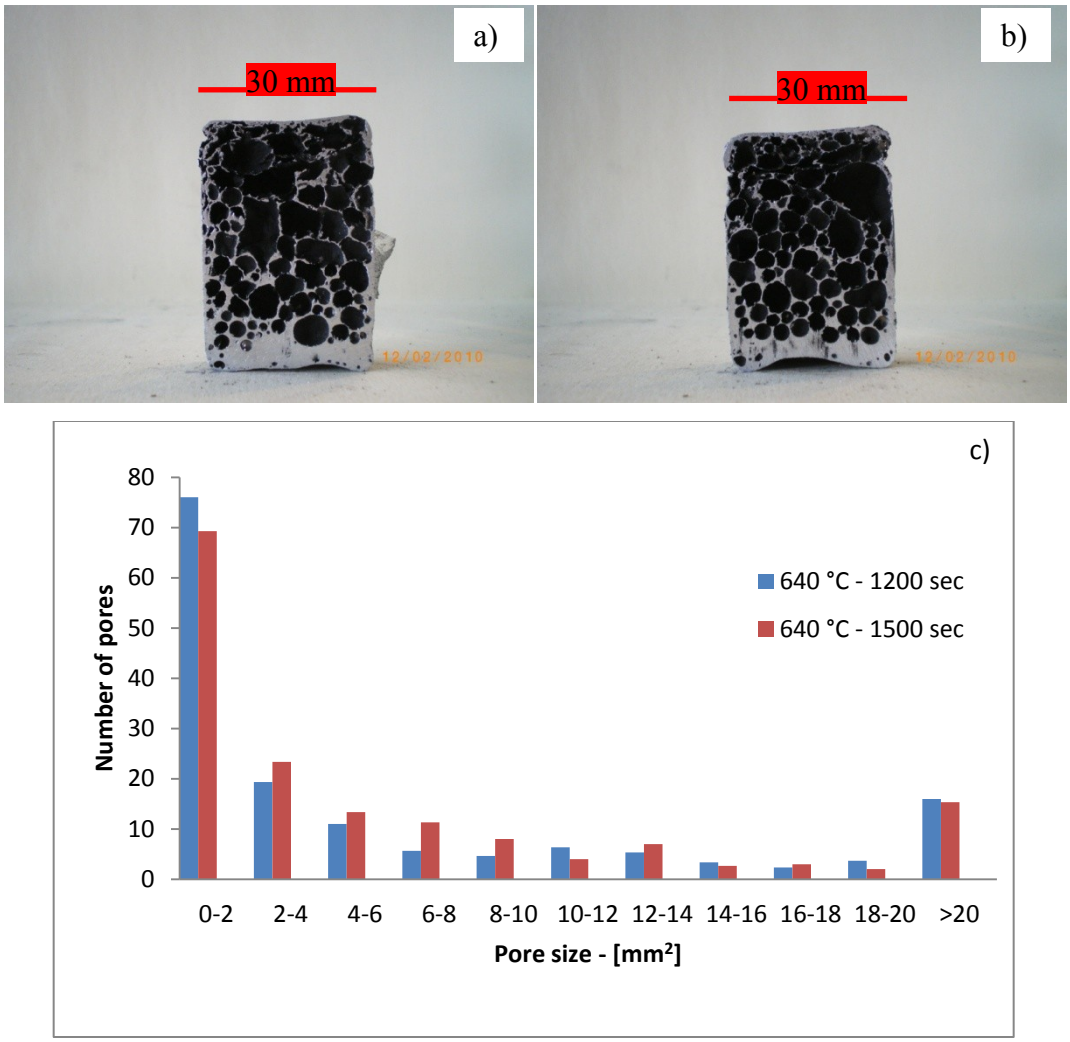

Figure 7-24: Al-33wt%Zn foam produced at 640 °C a) 1200 seconds b) 1500 seconds c) pore area distribution for foam produced at 1200 and 1500 seconds.

The average pore size shown in Figure 7-24c shows lesser coarsening of the pores in comparison to Al-10wt%Zn indicating a higher level of stability over the foaming period. This is also supported by an average pore number of 152 ± 22

and 153 ± 9 which indicates lower levels of coarsening. The average number of large pores above 20 mm^2 are consistent at 16 and 15 for the foams produced for 1200 s and 1500 s respectively. The average cumulative pore area between the foam produced at 1200 s and 1500 s is very close at 1110 ± 45 mm^2 and 1097 ± 5 mm^2. From these results, the coarsening rate (or degradation rate) of the foams is reduced, in return increasing the overall stability preventing large scale film rupture and drainage. The cumulative pore are in this case, is very similar to pure aluminum and Al-10wt%Zn at 1110 ± 45 mm^2 and 1097 ± 5 mm^2 for the foams produced at 1200 s and 1500 s.

From the data presented above, it is evident that the addition of zinc not only helps encapsulate hydrogen at the early stages but results in foams showing greater post maximum expansion stability. An increase in zinc content from 10 w% to 33 wt% is translated to an increase in foam stability from 120 s of stability to above 1000 s in 20 mm and 30 mm foams. As the amount of zinc is augmented, the foams can also be produced at lower temperatures for an equivalent foam expansion of 300 vol% with an increase in stability. The foam stability between the smaller and larger samples in terms of expansion is also in agreement. This is an important design criterion for foaming where enhanced stability is sought.

Based on foaming theory, it is understood that a certain level of solid constituent (particles) is requires to achieve stability in metal foams. These solid constituents create a disjoining pressure within the cell walls which stabilizes the foam [15, 44]. Physical properties such as viscosity and surface tensions also play an important role in foaming [13, 34, 36]. As outlined in Table 2-2 of the literature review, strong correlations show that in powder metallurgy foams, an optimal level of powder oxide is necessary to stabilize foam [21, 22, 69]. Korner *et al.*[53] suggest that the oxides present in the melt form a stabilizing network, forming a mechanical barrier against degradation. Unlike solid particle additions to the melt such as in the gas injection process, the oxides have been shown by several

researchers to form a complex network keeping the structure together forming a branched crumbled structure [36, 53, 69]. Microgravity experiments reveal that these oxides have a dominant effect on the reduction of coalescence of the pores independent of gravity [66-68].

In this particular case powder oxide contents fall within the experimentally determined range for stable foam of 1-6 wt% oxygen for aluminum as shown in Table 2-2 in the literature review. The zinc oxide content of the zinc powders was measured to be 0.079 wt% but the metal is nearly 2.5 time denser than aluminum. In order for the oxide levels of the Al-Zn alloys to be equivalent to aluminum, the values were converted to atomic %. These values are based on the assumption that the oxides formed for both aluminum and zinc are Al_2O_3 and ZnO, respectively.

From Table 7-7, it is apparent that the actual value of oxide content between the different foam compositions varies only slightly between 0.97 to 1.04 at%. These falling within the experimentally determined oxide range for foam stability. Another point to be made is that the aluminum would effectively have a tendency to reduce ZnO into Al_2O_3 under equilibrium conditions. From these results, it is determined that the oxide content cannot explicitly explain the extended stability incurred by the foam through the addition of zinc since there is a very small difference in the oxide content. One possibility is that the wetting of the aluminum oxide network is affected by the addition of zinc, increasing the foam stability. In the melt gas injection process, the use of solid particles is used to stabilize foam where favorable particle/melt wetting is required as indicated in Table 2-1. Asavavisithchai and Kennedy [64] has shown that by adding magnesium to aluminum foams containing alumina particulate, the improved wetting behavior of the alloy on the alumina resulted in better foam stability. Although this could be possible in this case, there is limited data available in literature correlating the effect of alloys on the oxide networks formed in powder

metallurgy foams. Other parameters such as fluidity (and viscosity) and surface tension have to be examined more attentively.

Table 7-7: Powder oxygen content used for foaming

Powder	***Density g cm^{-3} [147]***	***Molar mass [147]***	***O - wt%***	***O - at%***	
Al	2.71	26.96	0.37	1.04	Al_2O_3
Zn	7.14	65.39	0.079	0.64	ZnO
Al - Optimal range			0.1 to 0.6	0.28 to 1.69	Al_2O_3
Composition	***at% Zn***	***at % Al***	***Total O at%***		
Pure Al			1.04		
Al-10wt%Zn	4.23	95.77	1.02		
Al-33wt%Zn	16.79	83.21	0.97		

The multiple forces acting simultaneously on the foam include; gravity, gas pressure, surface tension and capillary forces [34, 36]. Since foams are a high energy system, they will always tend to reduce their state of energy by reducing their internal surface area due to the high interfacial free energy between the gas and liquid interface of the cell surfaces [34, 36]. The surface tension forces are responsible for suction of liquid into the Plateau borders from the cell wall, resulting in cell wall thinning and eventually collapse. Therefore, a low surface tension is desirable [13]. The surface tension will cause a tendency for cell wall thinning as a result of a capillary suction effect resulting in a pressure difference between the cell wall and the Plateau border as described below [12, 32, 44]:

$$P_G - P_{PB} = \Delta P = \frac{\sigma}{R} \qquad \textbf{Equation 7-1}$$

Where R is the Plateau border radius, σ the surface tension and ΔP the pressure difference between the Plateau border (P_{PB}) and cell wall (P_G – gas pressure). Ultimately, if the pressure difference is unbalanced, the foam cannot be stabilized and will degrade almost instantaneously. For a foam to be stable, the surface tension forces must be in equilibrium with the disjoining pressure through the

addition of surfactant or some type of particulate, as discussed above, and in Chapter 2. As noted, the network of oxide present in the melt are responsible for forming the disjoining pressure which balances the surface tension forces and the pressure differential generated by the melt. This can be described by equating the disjoining pressure to the pressure differential through [44]:

$$\frac{\sigma}{R} = \pi \qquad \textbf{Equation 7-2}$$

Where R is the radius Plateau border radius, σ the surface tension and π the disjoining pressure formed by the oxides. Therefore, if the surface tension of the melt is reduced, the disjoining pressure or the resistance for cell wall thinning and degradation will be reduced. This would then ultimately result in a lower pressure differential between the Plateau border and cell wall increasing the resistance to degradation.

When looking at a representation of foam cell wall thinning through a simple model based on two rigid disks, the cell wall thinning velocity can be interpreted as [32, 44]:

$$\dot{d} = \frac{2d^3\sigma}{3\eta R^2 R_{pl}} \qquad \textbf{Equation 7-3}$$

Where η is the viscosity of the liquid ($m^2\ s^{-1}$), σ is the surface tension ($N\ m^{-1}$), R the radius of the 2 discs (m), R_{pl} the radius of curvature of the Plateau border (m) and d the thickness of the cell wall (m).

From Equation 7-3, it is apparent that a decrease in surface tension would reduce the cell wall thinning velocity but at the same time, a reduction in viscosity would have the opposite effect and promote cell wall drainage. It was shown in Section

7.2 (Foam Expansion and Sample Temperature) that the foam reaches maximum expansion before it reaches the furnace setpoint. As a consequence, the viscosity of the foamed structure would decrease after maximum expansion as the temperature rises which would favor an increase in cell wall thinning resulting in increased coalescence of the pores and drainage as described through Equation 7-4. This is especially apparent at 750 °C for pure aluminum as shown in Table 7-3 where maximum expansion is reached at 716.3 ± 5.1 °C. The resulting post maximum expansion collapse as the sample is heated towards 750 °C is of 36.7 %. Although the foam would likely expand at temperatures much lower than 716 °C, much closer to melting point, the nature of this particular foaming process (through a resistance furnace) would produce very slow heating rates, in return yielding an increased hydrogen loss. In contrast to this, the pure aluminum foam produced at a furnace setpoint of 710 °C reached the maximum expansion at 696.0 ± 1.5 °C. The onset of bulk expansion in both instances was when the solid compact matrix was entirely melted at lower temperatures. It is known that the addition of zinc to aluminum can reduce the viscosity of the melt [165]. The viscosity of Al-Zn alloys reproduced from Jones and Bartlett [149] is shown in Figure 7-25.

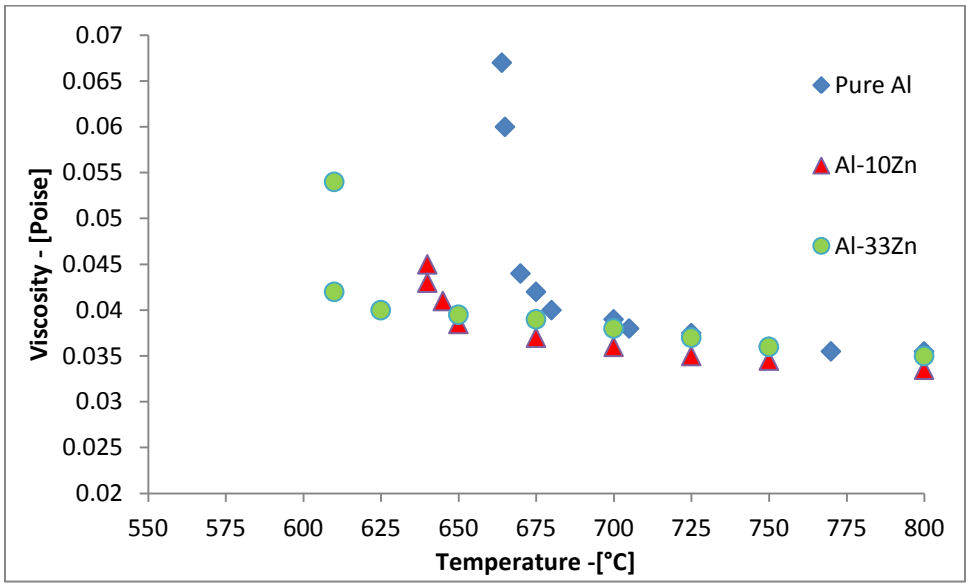

Figure 7-25: Al-Zn viscosity data

From Figure 7-25, it is evident that the decrease is viscosity is not significant above 700 °C but becomes important below 675 °C. With the addition of zinc to the foaming composition, the foaming temperature was reduced which is believed to have countered the reduction in viscosity of the alloy. As a result, the viscosity was similar between the alloys at the respective foaming temperatures as shown in Table 7-8 [149]. For the Al-10wt%Zn alloy with the lower zinc concentration, the viscosity is only slightly lower. On the other hand, the Al-33wt%Zn viscosity is comparable to pure aluminum foam produced at 710 °C at approximately 0.04 poise. From this information, it is determined that the addition of zinc does not increase nor decrease the viscosity significantly for the given foaming conditions. Although it is known that zinc effectively decreases the viscosity of aluminum [165], it is offset by the reduction in foaming temperature. In contrast elements such as, magnesium copper and nickel can increase the viscosity of the melt [149, 165]. Like the level of oxide content, viscosity alone cannot be a significant factor in dictating the increase in stability displayed for the zinc containing foams. However, the viscosities of the melt increase extremely rapidly near the melting point of the alloy which would hinder fluid mobility significantly [149]. This

could be the reason why zinc containing foams could not be produced at lower temperatures in the semi-solid region.

Table 7-8: Viscosity data for pure aluminum Al-10wt%Zn and Al-33wt%Zn

System	*Foaming Temperature*	*Viscosity (Poise) [149]*
Pure aluminum	710-750 ˚C	0.039-0.036
Al-10wt%Zn	690-710 ˚C	≈0.037
Al-33wt%Zn	620-640 ˚C	≈0.040

The other important property which influences foam stability is the surface tension of the melt. The addition of zinc to an aluminum melt has been shown to reduce the surface tension [46, 166]. Actual surface tension values for P/M foams can be difficult to determine due to the nature of the foam and the oxides contained in it. Nonetheless, surface tension under these conditions should be in correlation with the trends reported in literature for oxide free alloys. Surface tension values at 700 °C and 800 °C are shown in Figure 7-26 for Al-Zn alloys as well as the values for pure aluminum and pure zinc. The figure shows a reduction in surface tension as zinc is added to aluminum at the same time showing a reduction of surface tension with increased temperatures. Numerous authors have experimentally confirmed that a reduction in surface tension is beneficial in producing aluminum based foam [49-52, 58]. As a result, this would reduce the required disjoining pressure necessary to stabilize the foam as the pressure differential between the Plateau border and the cell wall is reduced as seen through Equation 7-2.

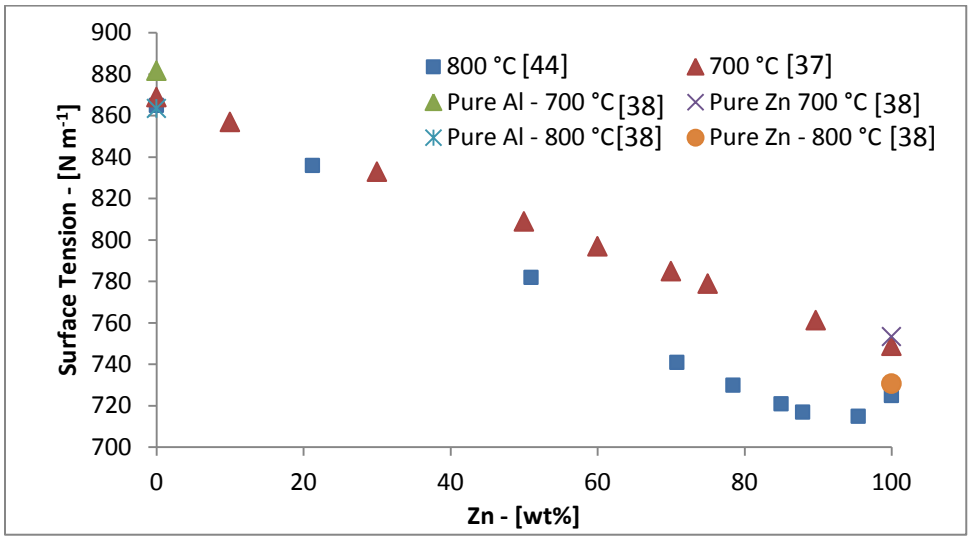

Figure 7-26: Surface tension values for Al-Zn alloys [68, 167-168]

By looking at the surface tension and comparing it to foam stability in Figure 7-19, Figure 7-20 and the data presented in Figure 7-23 and Figure 7-24, it is possible that in fact the reduction of surface tension is partly responsible for the enhanced stability observed in the foam. The greatest level of stability was observed for the Al-33wt%Zn foams produced at 620 °C and 640 °C which collapsed by 8.2 % and 7.9 % respectively showing an overall reduction of surface tension of 4.5 % at 700 °C compared to pure aluminum. As shown through Figure 7-24, the foam pore distribution was constant over a period of 500 s showing low levels of degradation. On the other hand the addition of 10wt%Zn resulted in an increase in stability (690 °C – 12.1 % collapse and 710 °C – 11.0 % collapse) but higher levels of post maximum expansion collapse could be observed in the foam where surface tension measurements would be closer to pure aluminum which were only reduced by 1.4 % at 700 °C. The reduction in the rate of cell wall coarsening could be supported by this hypothesis since the foams having a higher zinc concentration show lower foam coarsening and a reduced surface tension. Although surface tension reductions were small, it is possible that they helped reduced the required for increased stability. Moreover, the viscosity values are nearly constant for all the foaming conditions along with the oxygen

content of the foam. From these results, it is evident that there are several mechanisms operating simultaneously stabilizing the foam including viscosity, oxide contents and surface tension.

7.7 Zinc Evaporation

It has been well documented that zinc evaporation can be a nuisance in certain processes such as brazing and sintering [101, 115, 121, 123]. Since zinc has a high volatility, in this case as opposed to other processes, it can be beneficial in the sense that it is able to supply positive pressure within the pores as the foam is evolving in conjunction with the release of hydrogen from TiH_2. The indicated vapor pressure values are quite high especially at higher foaming temperatures and zinc concentrations as outlined in Table 7-1 and Figure 7-3. The high internal surface areas of the cells within the foam provides a favorable environment for high levels of evaporation especially through the thin cell walls. Moreover, since the pores are contained within the liquid metal foam, once the zinc equilibrium partial pressure is quickly reached, no subsequent zinc loss would be expected as the liquid movement inside the foam is restricted. Significant zinc loss is therefore limited to the surfaces exposed to the atmosphere while internal surfaces supply positive pressure without appreciable loss. The measured zinc loss inside the foam measured by inductively-coupled-plasma-mass-spectrometry (ICP-MS) is minimal. Internal zinc concentrations only diminished by 1 to 2 wt% for the Al-33wt%Zn composition after 25 minutes and remained within experimental error for the Al-10wt%Zn composition after 25 minutes of foaming as shown in Table 7-9 being below 1 %.

On the other hand in the DSC and in the confocal microscope, zinc evaporated and condensed on cooler surfaces of the apparatus away from the sample since equilibrium pressure was not reached and the specimen outer surfaces were favorable to evaporation. To illustrate the extent of zinc evaporation, recuperated Al-33wt%Zn samples (with no TiH_2) from the confocal microscope experiments

subjected to a heating cycle were observed under a scanning electron microscope. This shows evidence of a network of small openings and cracks which formed through the vaporization of zinc as seen in Figure 7-27, which subsequently condensed inside the microscope chamber.

Table 7-9: ICP foam compositional data for foam interior processed at various foaming temperatures

		Al-10wt%Zn			
Foaming Condition (°C)	***Foaming time (s)***	***Al (wt%)***	***Zn (wt%)***	***ratio***	***Diff %***
Compact - ICP	-	89.71	9.83	9.12	-
Compact - Theoretical	-	89.60	9.60	9.33	-0.11
690 °C	720	90.36	9.11	9.92	0.65
690 °C	1500	89.76	9.40	9.54	0.05
710 °C	510	90.16	9.36	9.63	0.45
710 °C	600	89.63	9.93	9.02	-0.08
710 °C	1500	89.21	9.70	9.19	-0.50
		Al-33wt%Zn			
Foaming Condition (°C)	***Foaming time (s)***	***Al (wt%)***	***Zn (wt%)***	***ratio***	***Diff %***
Compact - ICP	-	66.97	32.59	2.05	-
Compact - Theoretical	-	66.60	32.60	2.04	-0.37
620 °C	1500	68.32	31.22	2.19	1.34
640 °C	1200	66.51	32.88	2.02	-0.46
640 °C	1500	69.30	30.09	2.30	2.33

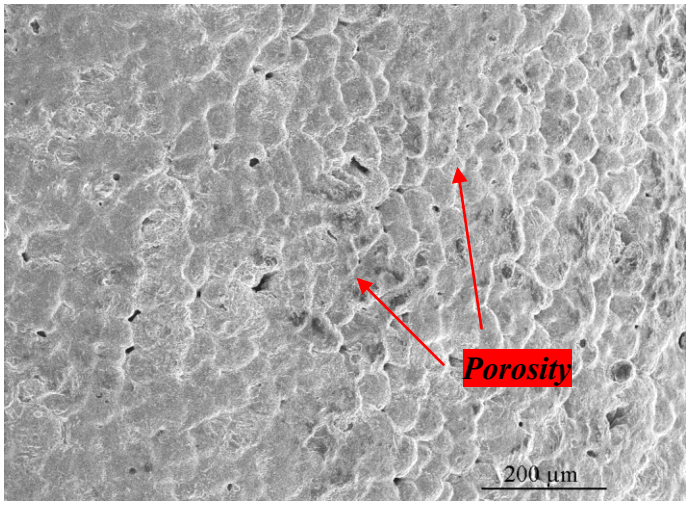

Figure 7-27: Compact process in the confocal microscopy highlighting porosity due to zinc evaporation

As a result it was then speculated that the outer surfaces could lose zinc through the foaming process. These surfaces would also be prone to oxidation in the actual foaming process which could result in a solid external shell, reducing the effects of external structure collapse.

Very thin slices were removed from the outer surfaces of the foam (approximately 0.5 mm) produced at selected conditions to look at the zinc content. ICP measurements from the outer surface of the foam samples are displayed in Table 7-10. Contrary to what was expected, the zinc concentrations at the outer surfaces of the foams were consistently higher by a few percent than those measured in the interior of the foam and in the compacts. The results also displayed considerable variability but again zinc levels were consistently higher by (approximately 1 wt% up to 7 wt%).

Table 7-10: ICP results of the outer shell for foams produced at various times and temperatures

Al-10wt%Zn					
Foaming Condition (°C)	***Foaming time (s)***	***Al (wt%)***	***Zn (wt%)***	***ratio***	***Diff %***
Compact - ICP	-	89.71	9.83	9.12	-
Compact - Theoretical	-	89.60	9.60	9.33	0.23
690 °C	300	87.87	11.61	7.57	1.78
690 °C	1500	84.72	13.83	6.13	4.00
710 °C	510	88.25	11.22	7.86	1.39
710 °C	600	86.31	13.03	6.62	3.20
710 °C	1500	86.55	12.17	7.11	2.33
Al-33wt%Zn					
Foaming Condition (°C)	***Foaming time (s)***	***Al (wt%)***	***Zn (wt%)***	***ratio***	***Diff %***
Compact - ICP	-	66.97	32.59	2.05	-
Compact - Theoretical	-	66.60	32.60	2.04	0.01
620 °C	1500	59.28	39.84	1.49	7.24
640 °C	1200	63.15	36.11	1.75	3.51
640 °C	1500	65.94	33.30	1.98	0.70

Based on these results and looking at the foaming process more closely, the foam walls are loosely constrained to the inner surfaces of the crucible and the piston of the expandometer. Although zinc has a high tendency to evaporate and the foam is produced in an oxygen saturated ambient atmosphere, the evaporating zinc would have a tendency to oxidize as it reaches the surface of the liquid foam. Therefore, rather than evaporating to the atmosphere could form an oxide network when in contact with oxygen at the surface of the foam resulting in a higher concentration of zinc-based oxides at the outer surface. The ICP cannot differentiate between zinc and zinc oxide and therefore, it is speculated that the increased zinc concentrations are a result of a thick network of zinc oxide formed at the outer surface.

Hanabe *et al.* [167] indicate that the high volatility of zinc promotes the formation of ZnO on melt surfaces in the DIMOX (Directed Melt Oxidation) process. They point out that as zinc makes its way to the surface of the melt through vaporization, breaking through the oxides present at the surface generating fresh oxide and initiating a cyclic oxide growth of Al_2O_3. In other words, as fresh ZnO forms at the external surface of the melt, the aluminum simultaneously reduces previously formed ZnO into Al_2O_3 [168]. The formation of Al_2O_3 is therefore stipulated to form through two possible reactions:

$$2Al + 4\,ZnO \rightarrow ZnAl_2O_4 + 3Zn \qquad \Delta G = -656.1\ kJ\ mol^{-1}\ @\ 710\ °C$$

$$2Al + 3ZnAl_2O_4 \rightarrow 4Al_2O_3 + 3Zn \qquad \Delta G = -492.2\ kJ\ mol^{-1}\ @\ 710\ °C$$

Or

$$2Al + 3ZnO \rightarrow Al_2O_3 + 3\,Zn \qquad \Delta G = -617.3\ kJ\ mol^{-1}\ @\ 710\ °C$$

The reaction takes place through either an intermediate spinel phase of $ZnAl_2O_4$ or by a direct reduction of ZnO to Al_2O_3. The associated thermodynamic values were obtained through FactSage. The reduction of surface formed ZnO into Al_2O_3 is thermodynamically favorable in this case. In another study, oxide has also been shown to form at the surface through the vapor phase, creating a whisker type structure favoring the diffusion of oxygen into the melt, forming higher levels of Al_2O_3[169]. Similar cyclic chains of events pertaining to the reduction of ZnO formation at the surface are described by Jayaram [170] where cyclic vapor phase oxidation is shown to promote the absorption of oxygen into the melt. This concept has been also shown to work with Al-Mg based alloys containing small amounts of Mg and often silicon containing melts. These DIMOX reactions all rely on the vaporization of a component in the melt such as magnesium, zinc or both [167, 170, 171].

In this particular instance, higher concentrations of zinc are measured on the outside of the foam surface as shown in Table 7-10. This likely indicates, a DIMOX type reaction occurring whereby a thick oxide network (rich in zinc) is formed on the outer surface of the foam of several microns thick. In response, this would create a solid oxide shell preventing the exterior collapse of the foam and supporting the higher zinc concentrations measured at the exterior of the foam. This solid oxide shell would then support the explained increase in post maximum expansion stability observed in Figure 7-19 and Figure 7-22 in contrast to pure aluminum which displays significant collapse in Figure 5-4 and also outlined in Table 7-5 The oxide layer created with pure aluminum would not be sufficiently strong to counteract the degradation of the foam in this case. Moreover, the external stability of the foam would also reduce the rate of internal collapse over time.

The hypothesis pertaining to the formation of a thick oxide would correspond well with the high levels of zinc loss seen in the DSC and confocal microscope. Those

samples were produced under an argon atmosphere where the zinc upon reaching the surface of the specimen would not oxidize but rather evaporate and condense as zinc on cooler surfaces of the apparatus. These concepts would therefore be important factors in explaining the enhanced past maximum expansion stability of Al-Zn in comparison to pure aluminum which rapidly collapses on itself. A solid external shell resistant to degradation would be formed.

7.8 Conclusions

It was shown that an Al-94wt%Zn eutectic transient liquid phase is formed at 381 °C through the addition of elemental zinc to the aluminum matrix corresponding to the lowest recorded dehydrogenation temperature in literature. The heating rate was sufficiently high not to prematurely dissolve the liquid phase (well above 60 °C s^{-1}). The formation of this transient liquid phase was shown to spread through the compact while simultaneously providing liquid for the uniform nucleation of pores. The formation of a small network of cracks as observed through pure aluminum could be suppressed, directly resulting in higher expansion levels nearing or above 300 vol%, at foaming temperatures lower than 40 °C below pure aluminum. As opposed to cracks, the early pore formation displayed a round morphology throughout the foaming process. The lowered melting temperature (semi-solid) through alloying was favorable in increasing the heating flux into the foam resulting in a reduced melting time.

A significant increase in post maximum expansion stability of the foam could be observed at zinc concentrations as low at 10 wt% in contrast to pure aluminum. The increased stability was attributed mainly to a combination of a lower surface tension of the alloys and to the evaporation of zinc creating a solid outer shell promoting overall stability and resistance to collapse. Although zinc lowers the viscosity of aluminum, the reduction in foaming temperature with the addition of zinc offset this reduction which would otherwise promote increased cell wall thinning and drainage. Zinc evaporation through the high surface area of the cell walls is thought to have also contributed to the overall post maximum expansion

stability supplying positive vapor pressure within the pores over the foaming period.

The proposed and improved foaming mechanism is shown in Figure 7-28 and compared to pure aluminum depicting the evolution through the foaming process.

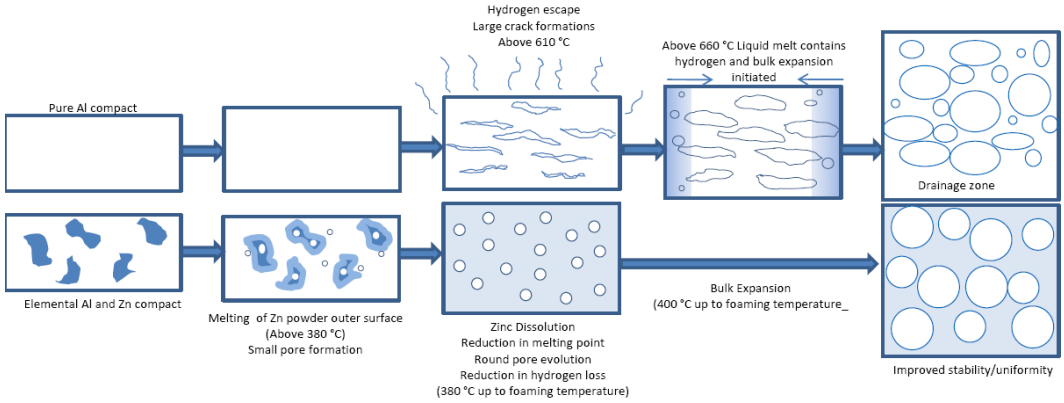

Figure 7-28: Al-Zn foaming process compared to pure aluminum

This page is intentionally left blank

8 Al-Si-Zn System

In the previous chapter, it was shown that hydrogen gas dissociated from TiH_2 could be effectively encapsulated with the introduction of elemental zinc powder in the aluminum matrix. The analysis showed that, with an increase in zinc content, foam could be produced at a lower foaming temperature with an enhanced stability while nucleating uniform pores rather than cracks. The transient liquid phase formed by zinc, suppressed crack formations which was directly translated to higher expansion. Furthermore, an increase in foam stability could be observed past maximum expansion which was attributed mainly to a lowered surface tension and to the formation of a thick outer oxide layer on the foam. Although zinc is highly effective in producing good foam, its major downside is its high density relative to aluminum which is approximately two and half times higher.

Based on these results, a ternary alloy was selected, enabling a reduction in foaming temperature, while reducing the surface tension of the alloy. After looking at various systems, as outlined in Table 3-1 in the Research Objectives Chapter, a silicon pre-alloyed eutectic powder was selected. The Al-12wt%Si powder consists of an aluminum rich eutectic which melts at 577 °C, unlike the transient liquid phase formed by the Al-Zn system (Al-94wt%Zn) at 381 °C. This powder appeared to have several advantageous characteristics based on an initial assessment including, a lower surface tension, lowered melting point, no apparent intermetallic formations and a low density of 2.33 g cm^{-1} compared to zinc (7.13 g cm^{-1}) [144]. Using this powder, in conjunction with a low level of zinc would result in hydrogen encapsulation by the zinc at early dehydrogenation stages shown in Chapter 7 with an overall reduction in foaming temperature and larger semi-solid attained with the use of Al-12wt%Si powder.

While Al-Si based foams have been studied in literature as pointed out in Chapter 2, their use in conjunction with elemental zinc has yet to be assessed. Available

literature on Al-Si based foams point to the formation of a fissure network similar to the one observed for pure aluminum and summarized in Table 5-1. Moreover, a certain degree of degradation past maximum expansion is noted in these studies (i.e.: reduced foaming efficiency) [1, 6-8, 87]. The addition of Mg and Cu to Al-Si based foams have also been studied by Garcia-Moreno displaying high levels of expansions [172].

8.1 Transient Liquid Phase Formation

Powder compacts were produced for the two selected compositions consisting of Al-2.4wt%Si-9.7wt%Zn and Al-3.59wt%Si-9.6wt%Zn. The compact compositions were selected as 20 wt% and 30 wt% Al-12wt%Si pre-alloyed powder keeping a zinc ratio of 10 % with respect to aluminum. These two powder concentrations were selected to study the effects of the eutectic powder content on foaming. The Al-12wt%Si powder is shown in the micrograph in Figure 8-1 where the small eutectic platelets can be seen in the round powder. The small platelet are also shown in Figure 8-14.

An SEM micrograph of an Al-3.59Si-9.6wt%Zn compact is shown in Figure 8-2 with the zinc phase as being light grey while the aluminum being dark grey and the TiH_2 a shade in between. It is difficult to differentiate the pure aluminum powder from the Al-12wt%Si powder in the SEM image due to the low concentration of silicon and the similar atomic number between aluminum and silicon. Consequently, an EDS analysis was performed on the compact showing the distribution of the Al-12wt%Si powders. From Figure 8-2, it is apparent that the Al-12wt%Si phase is spread uniformly. It is noted that, it was demonstrated in Chapter 6 that solid state diffusion was not a potential concern with the use of silicon in contrast to zinc. Additional micrographs of the Al-2.4wt%Si-9.7Zn and Al-3.59wt%Si-9.6wt%Zn compacts are presented in Appendix E where the silicon phase can be seen. No apparent segregation (clumping) of any powder was observed in any of the compacts.

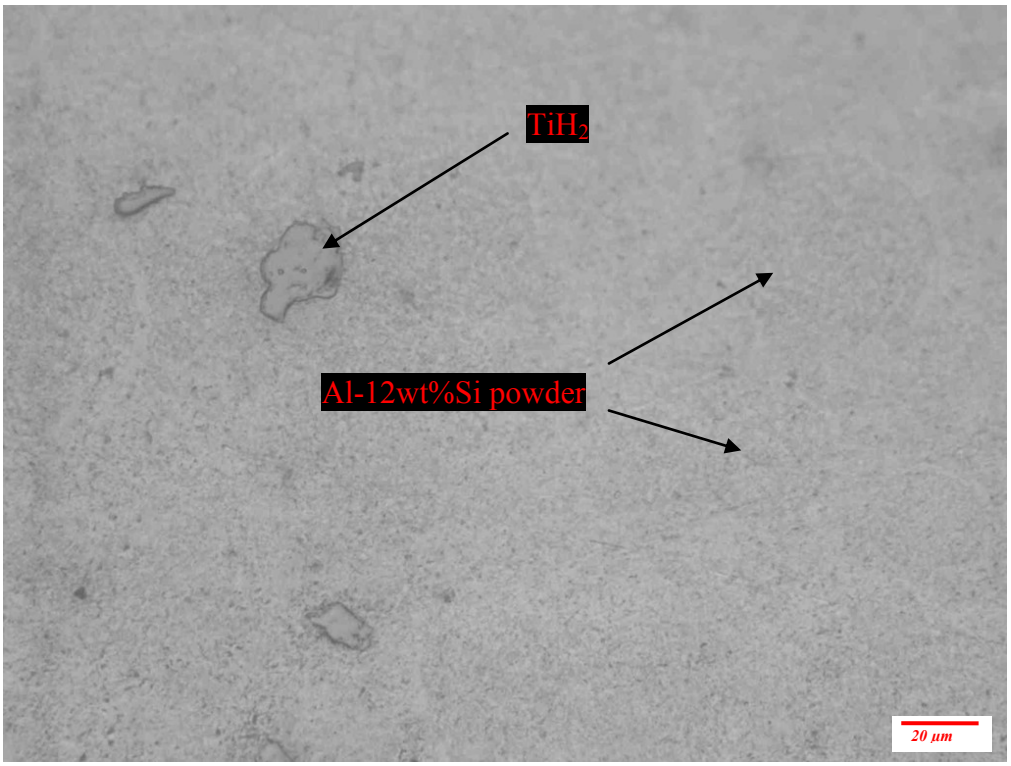

Figure 8-1: Al-3.59wt%Si-9.6wt%Zn compact

DSC analysis performed on an Al-3.59wt%Si-9.6wt%Zn compact is shown in Figure 8-3. It can be clearly seen from the first heating cycle that the Al-94wt%Zn eutectic forms at 381 ˚C similarly to what was observed in Figure 7-2 for the Al-Zn system. As the sample continues through the heating cycle, another peak is measured at 557-575 °C (onset – peak). This is then followed by another endothermic peak between 593-598 ˚C (onset peak) and finally the peak indicating the liquidus line at 606 – 630 °C.

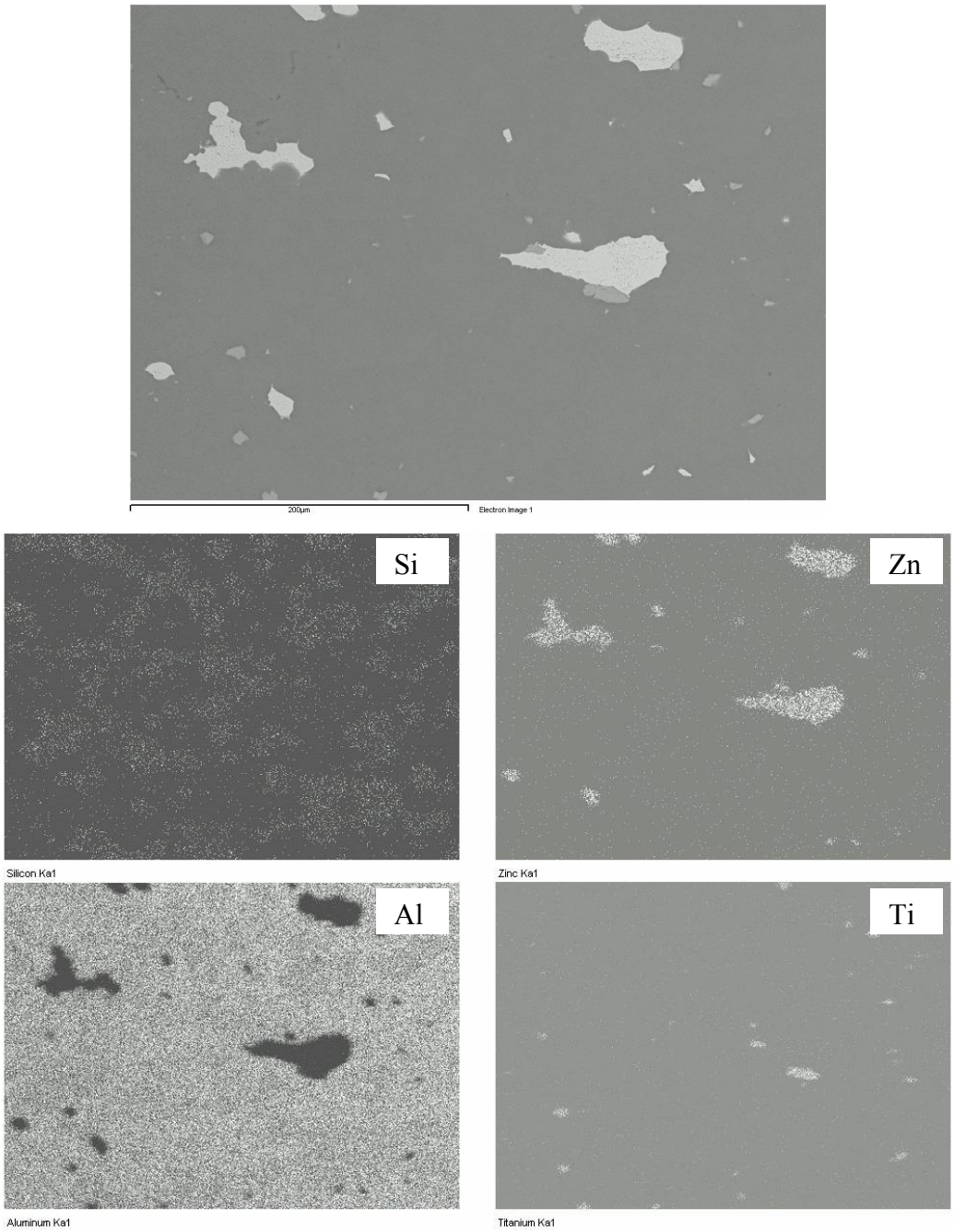

Figure 8-2: Secondary electron image supported by EDS analysis showing aluminum, zinc, silicon and titanium

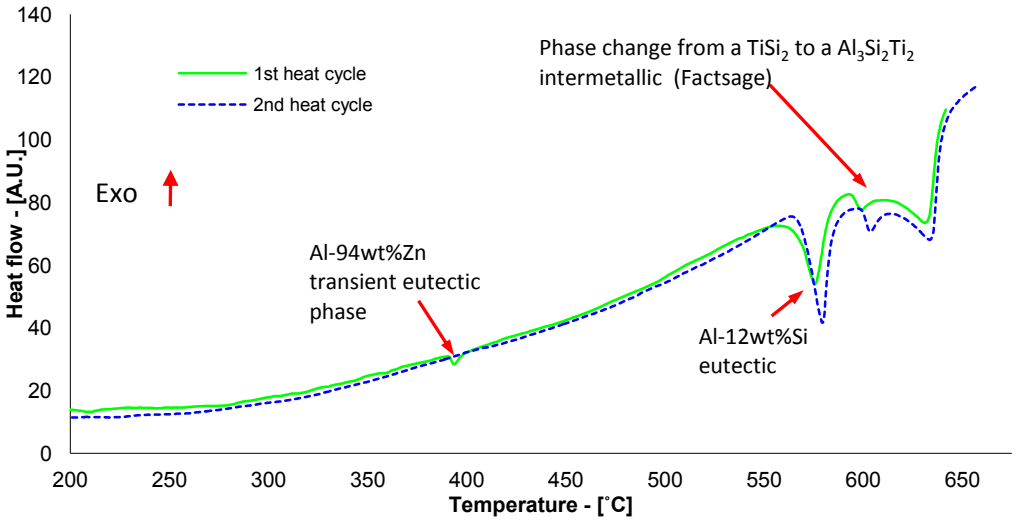

Figure 8-3: Al-3.59wt%Si-9.6wt%Zn foam DSC analysis

According to a FactSage analysis, there should be a liquid phase onset at 551 °C indicating the formation of ternary liquid. The measured onset of the liquidus phase is at 557 °C slightly above the predicted value. The large peak at 577 °C, likely corresponds to the bulk melting of the Al-Si eutectic. Since the alloy consists of pressed powders, the ternary formation phase is limited to the Al-12wt%Si powders in contact with the spreading Al-Zn liquid phase. The endothermic peak at 598 °C (according to FactSage), corresponds to a phase change from a $TiSi_2$ to a $Al_3Si_2Ti_2$ intermetallic which occurs in both heating and cooling. This would correspond to the reaction of the silicon and aluminum with the hydrogen dissociated titanium hydride. However, the two last peaks, are hard to discern since they appear to be convoluted making the onset difficult to determine. An isopleths generated by FactSage of the Al-Si-Zn system is shown in Figure 8-4 showing the equilibrium semi-solid region. The determined semi-solid regions from FactSage are tabulated in Table 7-1. Other isopleths are shown in Appendix E.

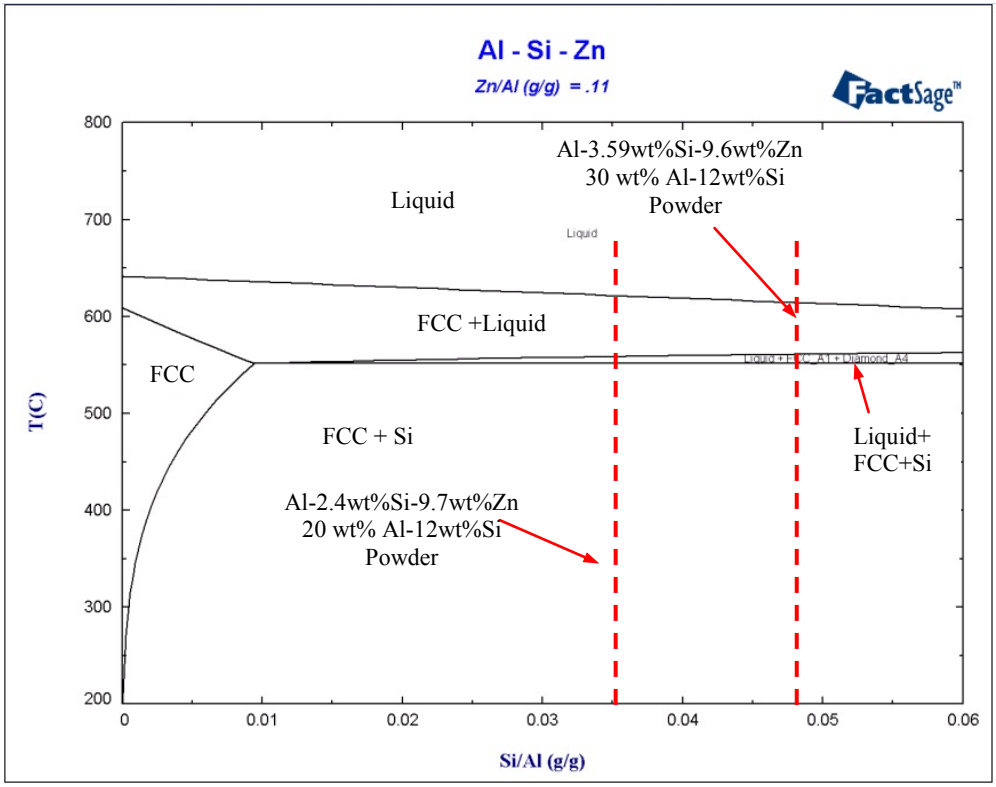

Figure 8-4: Isopleth of the Al-Si-Zn compositions

From the second heating cycle in the DSC, the zinc phase has dissolved in the matrix much like what was observed in Chapter 7 with an apparent Al-12wt%Si eutectic peak with a sharp onset unlike the first heating cycle. The endothermic peak at 698 °C corresponding to the intermetallic phase transformation of $TiSi_2$ to $Al_3Si_2Ti_2$ is still present along with the final endothermic peak delimiting the upper region of the semi-solid region. One observation is the onset of the Al-Si eutectic which occurs at a higher temperature after the first heating cycle (both compositions). This is likely due to the evaporation of zinc, suppressing the formation of a ternary liquid at 551 °C. Under higher heating rates on the other hand, and in actual foaming, zinc evaporation would be minimal as has been determined in the previous chapter.

Comparing the DSC results of the different compositions, the semi-solid onset associated the addition of the Al-Si phase occurs from approximately 557 °C

(onset) through the melting of the Al-Si eutectic extending up to 630 °C. In contrast, the Al-10wt%Zn foam shown in the previous chapter has a semi-solid region extending from 627 °C to 654 °C while the Al-33wt%Zn has a semi-solid extending from 553 °C to 598 °C. This represents a larger semi-solid region as well a reduction in melting point with the addition of 3.5 wt%Si to the matrix compared to the Al-10wt%Zn foam. Semi-solid temperatures according to FactSage and DSC have been tabulated in Table 8-1. Semi-solid regions calculated through FactSage appear to be in correlation with the DSC results with slight variations with the formation of an Al-Si-Zn liquid. Since this 3.59wt%Si is manifested through a 30 wt% (or 20 wt%) fraction Al-12wt%Si powder in the matrix, it is stipulated that, the pre-alloyed powders would generate significant liquid only at 577 °C and spread rapidly thought the matrix toward equilibrium similarly to the elemental zinc powders as shown through Figure 7-4.

Table 8-1: Alloys properties for Al-3.59Si-9.6Zn and Al-2.4wt%Si-9.7Zn compared to Al-Zn based systems

Composition	*Density (g cm $^{-1}$)*	*Semi-Solid - FactSage (°C)*	*Read from Phase Diagram [144]*	*DSC (°C)*	*Optimal Foaming Temp (° C)*
Al-10wt%Zn	2.88	607-641	622-645	627-654	710
Al-33wt%Zn	3.40	514-595	531-603	553-598	640
Al-3.59wt%Si-9.6wt%Zn	2.86	551-619	N/A	557-630	640-660
Al-2.4Wt%Si-9.7wt%Zn	2.87	551-624	N/A	549-635	660

Confocal microscope analysis of the pure aluminum foam in Chapter 5 reveals crack forming temperatures initiated at 610 °C. On the other hand, recorded dehydrogenation of the TiH_2 powder through DSC measurement is onset at 475 °C with the two main dehydrogenation peaks at 502 °C and 569 °C. Several authors have reported crack development in Al-Si based systems with liquid formations initiated at 577 °C. Although dehydrogenation has been known to vary with powder size and compaction [1, 164], the zinc based eutectic, again in this case, corresponds to the lowest recorded dehydrogenation temperatures of TiH_2 [1, 6-8, 11, 20, 86, 142]. Therefore, it is expected that the encapsulation of hydrogen will be initiated through the melting zinc phase in the same manner as

in Chapter 7. The lower onset of the semi-solid region through the addition of silicon can only be beneficial in reducing foaming temperature and increase the encapsulation of higher levels of hydrogen. Due to the high zinc vapour pressure, support for the DSC analysis through confocal microscopy could not be performed on these compositions but rather interrupted experiments at different foaming stages will be presented in a following section.

In whole, the use of an Al-12wt%Si phase increased the semi-solid region while decreasing the melting point without creating addition intermetallics other than those associated with the titanium phase. Therefore, larger expansion levels at reduced foaming temperatures are expected. Other stability related variables will be discussed in a following subsection. The DSC curves for the Al-2.4Si-9.7wt%Zn are similar to the Al-3.59wt%Si-9.6wt%Zn and are shown in Appendix E.

8.2 Foam Expansion and Temperature

Foaming curves for both Al-3.59wt%Si-9.6wt%Zn and Al-2.4wt%Si-9.7wt%Zn were generated while measuring the sample temperature. Figure 8-5 depicts the foaming curves for the Al-3.59wt%Si-9.6wt%Zn samples. Some sample dilation (or small expansion) is observed prior to bulk expansion similarly to the Al-Zn system. This can be attributed to the early encapsulation of hydrogen by the melting zinc rich eutectic as was the case in Chapter 7. From Figure 8-5, the bulk expansion initiation can be identified by the melting temperature of the Al-12wt%Si eutectic phase at 589.7 ± 1.5 (slightly above 577 °C) and a time of 340.0 ± 7.9 s. This slightly higher temperature (than the Al-Si eutectic) corresponds to the generation of liquid in the matrix enabling the encapsulation of higher levels of hydrogen. Moreover, between the melting of the eutectic and bulk expansion there is likely lag time for larger bubble formation and melting of the bulk sample over the thermocouple. The compact matrix contains 30 wt% Al-12wt%Zn phase which would become liquid at this temperature and diffuse

toward the equilibrium composition like the Al-Zn foam in Chapter 7. From the heating profile, it can be noticed that, due to the semi-solid phase, there is no large melting plateau displaying a stable temperature in contrast to pure aluminum presented in Figure 5-5.

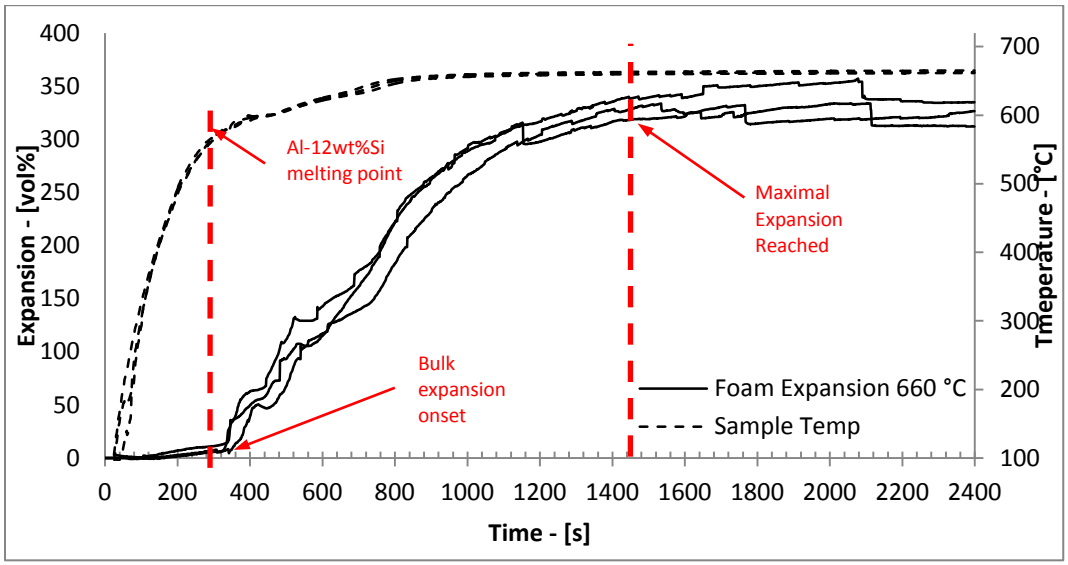

Figure 8-5: Al-3.59wt%Si-9.6wt%Zn foaming curve

Similarly to the Al-33wt%Zn system, the sample temperature measurements make it difficult to pinpoint melting events in correlation to expansion. From the foam expansion curve, the onset melting of the Al-12wt%Si phase delimits bulk expansion, but, it is unclear (from the temperature curves) when the sample is completely melted considering the furnace setpoint is only approximately 20-25 °C above the sample liquidus temperature. In the case of pure aluminum and Al-10wt%Zn, melting events could be directly correlated to sample temperature measurements because of the higher temperature differential between the furnace setpoint and melting temperature. In those instances significant increases in heating rate could be observed once the sample had completely melted as shown in Figure 5-5 and Figure 7-5. Another interesting observation is the ongoing expansion of the foam past the steady state temperature, similarly to Al-33wt%Zn

which reaches maximum expansion well after the sample is melted. Again, with lower foaming temperatures, the gas release kinetics of the TiH_2 are likely reduced and with a large semi-solid region, hydrogen encapsulation in increased. Figure 8-6 shows a close up of the sample temperature curves highlighting these observations. From Figure 8-6, only a small variation in the heating rate (slightly higher rate of temperature increase) is observed near 630 °C which would indicate the liquidus of the alloys corresponding to the temperature determined by DSC analysis.

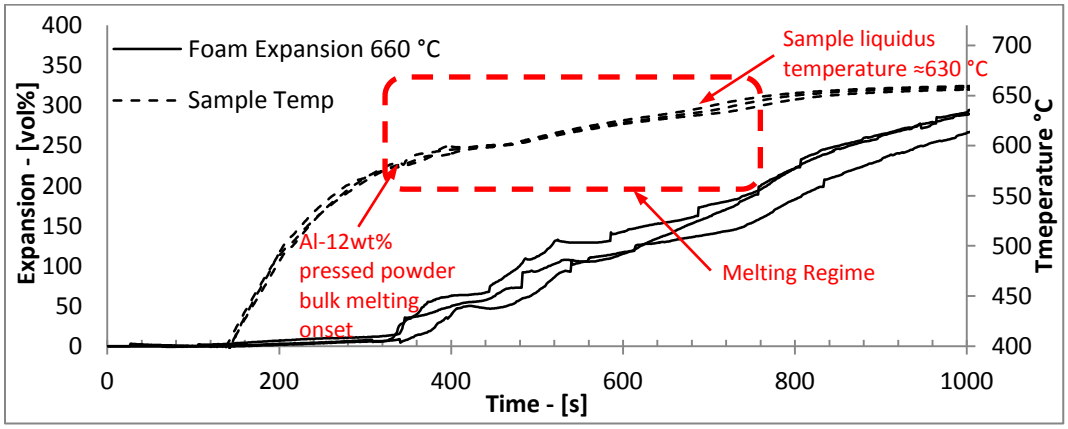

Figure 8-6: Al-3.59wt%Si-9.6wt%Zn foaming curve, highlighting the sample temperature

Comparing foaming curves for the Al-2.4wt%Si-9.7wt%Zn and Al-3.59wt%Si-9.6wt%Zn in Figure 8-7, it is apparent there is a similar behaviour with the Al-2.4wt%Si-9.7wt%Zn composition which displays a higher expansion. Although, it is apparent that the Al-2.4wt%Si-9.7wt%Zn composition has a slightly higher heating rate than its counterpart, the temperature curve is very similar. Based on phase formation data obtained from FactSage and DSC analysis, under equilibrium condition, the two alloys behave very similarly due to the small variation in silicon content. Therefore, from these results, varying the amount of pre-alloyed powder only has a marginal effect or none at all in terms of foaming. One explanation for the slight increase in expansion associated with the Al-2.4wt%Si-9.7wt%Zn composition is the higher level of oxide on the powders

yielding a higher disjoining pressure resisting drainage. Table 4-1 in the experimental procedures in Chapter 4 shows a very low oxide content of the eutectic powder of 0.152 wt%O in contrast to pure aluminum at 0.366-0.378 wt%O [21, 22, 69]. The impact of varying the amount of eutectic powder could also result in increased foam degradation (i.e.: drainage, cell coalescence). This will be discussed further in a following sub-section.

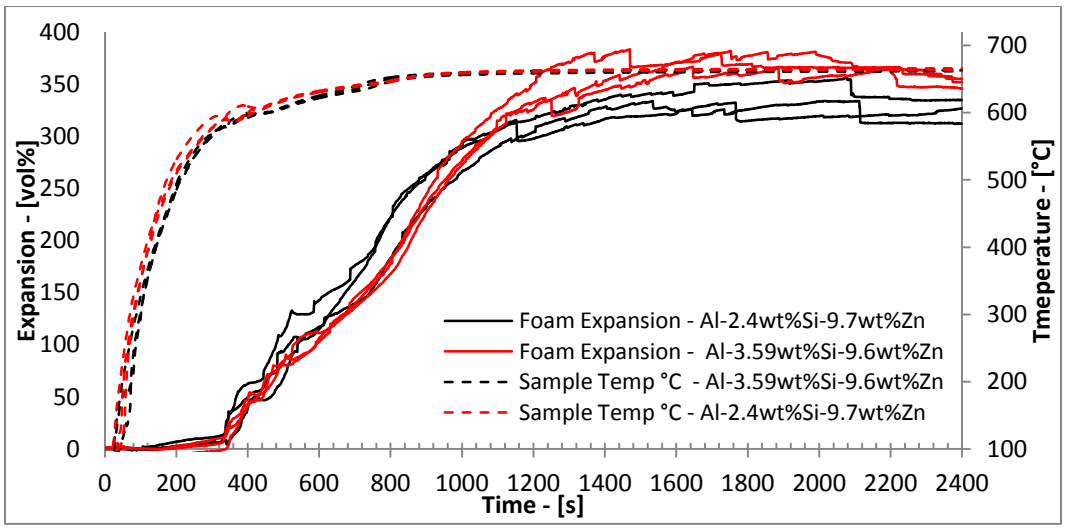

Figure 8-7: Al-2.4wt%Si-9.7wt%Zn and Al-3.59wt%Si-9.6wt%Zn foams produced at 660 °C

The maximum expansion of the Al-2.4wt%Si-9.7wt%Zn foam is recorded at 377.0 ± 8.7 vol% which is higher than any other foaming condition studied in this thesis with no appreciable post maximum expansion degradation after 2400 s as shown in Figure 8-7. On the other hand, a recorded maximum expansion value for the Al-3.59wt%Si-9.6wt%Zn is lower at a value of 341.3.0 ± 13.7. In comparison, the Al-33wt%Zn generated a maximum expansion of 349.3 ± 17.1 vol% at a furnace setpoint of 640 °C while the Al-10wt%Zn foam generated expansions of 293.7 ± 8.3 vol% at 710 °C while displaying a certain level of degradation. The expansion data has been summarized in Table 8-2.

Table 8-2: Expansion curve data for Al-2.4wt%Si-9.7wt%Zn and Al-3.59wt%Si-9.6wt%Zn compared to the other systems studied

Composition	*Foaming Temperature (°C)*	*Bulk Expansion Onset (s)*	*Bulk Expansion onset Temp (°C)*	*Max Expansion (Vol %)*	*Steady State Temp (°C)*
Al-2.4wt%Si-9.7wt%Zn	660	340.0 ± 7.9	589.7 ± 1.5	377.0 ± 8.7	664.7 ± 1.2
Al-3.59wt%Si-9.6wt%Zn	660	342.7 ± 0.6	581.3 ± 0.6	341.3 ± 13.7	664.0 ± 3.6
Composition	*Foaming Temperature (°C)*	*Bulk Expansion Onset (s)*	*Bulk Expansion Temp (°C)*	*Max Expansion (Vol %)*	*Max Expansion Temp (°C)*
Al-33wt%Zn	640	405 ± 15	--	349.3 ± 17.1	638.3 ± 3.1
Al-10wt%Zn	710	439 ± 2.6	--	293.7 ± 8.3	699.3 ± 2.1
Pure Al	710	894.0 ± 5.0	--	127.7 ± 1.5	696.0 ± 1.5
Pure Al - 750 °C	750	547.7 ± 6.6	--	311.0 ± 5.5	716.3 ± 5.1

The maximum expansion levels obtained for these foams are comparable to Al-33wt%Zn and even better than pure aluminum produced foam at 750 °C and Al-10wt%Zn foam produced at 710 °C. Figure 8-8 shows the Al-3.59wt%Si-9.6wt%Zn composition compared to Al-33wt%Zn foams produced at 640 °C. The comparison between the two alloys shows a faster expansion rate for the Al-3.59wt%Si-9.6wt%Zn which could be the result of higher sample heating rate due to the higher setpoint but the maximum expansion is comparable. It can be seen that the thermal events related to liquid formations has an earlier onset with the Al-33wt%Zn foam.

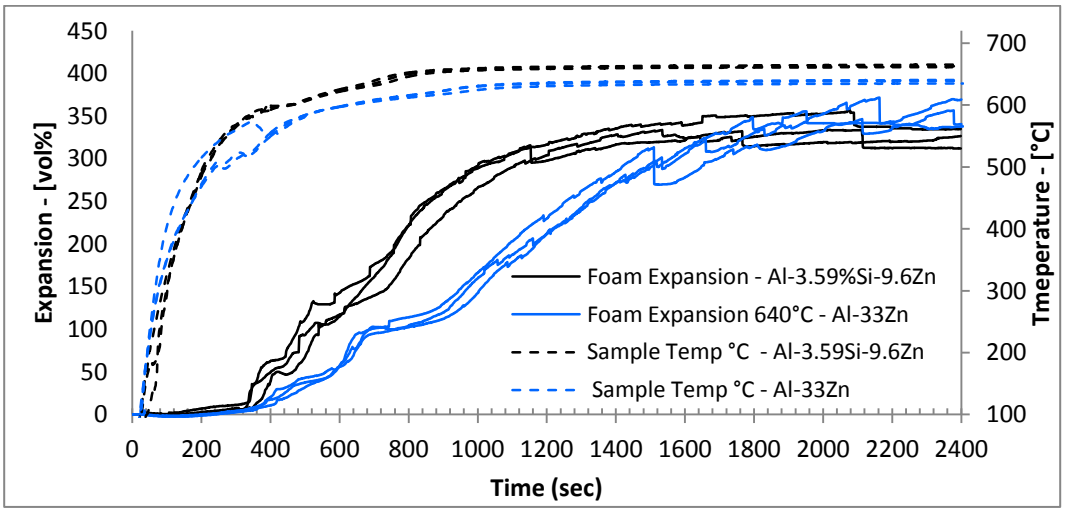

Figure 8-8: Al-33wt%Zn foams produced at 640 °C compared to Al-3.59wt%Si-9.6wt%Zn foams produced at 660 °C

The overall reduction in foaming temperature for equivalent or superior expansion with respect to the pure aluminum is approximately 90-100 °C. The main advantage here is high expansion and stability of the foam, having a low alloy density in contrast to Al-Zn based alloys. The various alloy densities have been outlined in Table 8-1. The density of the Al-2.4wt%Si-9.7wt%Zn and Al-3.59wt%Si-9.6wt%Zn are 2.87 g cm^{-1} and 2.86 g cm^{-1} respectively being slightly lighter than Al-10wt%Zn at 2.88 g cm^{-1} while being significantly lighter than Al-33wt%Zn alloys having a density of 3.40 g cm^{-1}.

8.3 Time Dependence on Foam Structure

Air quenched foam samples were produced, polished and sectioned at various time intervals to observe the evolution of the foam structure. A foaming curve for the Al-3.59wt%Si-9.6Zn foam is shown in Figure 8-9 depicting the evolution of the foam over 2400 s. From macrostructural observations, at 300 s, the formation of pores is barely visible along with what appears to be small crack like pores similar to those observed in Al-Zn foams (the microstructure is detailed in Section 8.4). However, at 500 s, pore formation is obvious. From preliminary observations, the pores appear to be oblate and oriented perpendicular to the foaming direction and more numerous than those observed in the Al-Zn system in Figure 7-11 and Figure 7-12. Helwig *et al.*[172] stipulate that in Al-Si based foams, coalescence of pores in the semi-solid region can occur through the rupture of solid bridges oriented preferentially in the direction perpendicular to pressing. Simultaneously, they note that coalescence can occur isotropically through the rupture of liquid films. However, in this case, in combination with this mechanism, it is also possible that cracks can spread through the foam during solidification as the blowing agent is still releasing bulk hydrogen at early foaming stages while the liquid phase is being suppressed. This is supported by the fact that, wide cracks are observed at the early foaming stages (solidified samples) which span between half and the whole width the sample in both Al-Si-

Zn and Al-Zn based foams. These cracks are longer than any pore observed in the fully expanded structure where bulk hydrogen release has taken place already. This is displayed in Figure 8-9 comparing the foam produced at 500 s which displays a large fissure across the structure while the foam produced at 750 s contains no crack at all but rather a collection of small pores. Moreover, solidification cracking can also occur through a series of pores which is known to form crack like porosity in welding. In whole, a combination of the two mechanisms is likely occurring in the foam.

At 550 s, the foam already appears to be forming larger pores and higher expansion. Although larger pores are beginning to form, some oblate pores are observed. From the sample temperature curve, it appears the sample at this temperature is in the semi-solid region at approximately 618 °C, being almost entirely melted. The foam then begins to display clear round cells at 750 s, where it is completely in the liquid region corresponding to a sample temperature of 637 °C being slightly above the alloy melting temperature of 630 °C according to DSC measurements.

The foam then displays an increased level of expansion after 950 s and reaching a maximum expansion of approximately 306.3 ± 9.7 vol% at 1200 s. At this stage, the pore morphology appears to be quite uniform in nature and does not show high levels of coalescence while attaining the furnace setpoint temperature of 660 °C. From 1200 s up to 2400 s, coarsening of the foam appears to be slowly taking place, which no structural degradation (reduction in volume expansion). The foam expansion remains constant for this period of time, which highlights the high level of stability in contrast to the pure aluminum system described in Chapter 5. The overall pore distribution of the foam appears more uniform than those observed for the Al-33wt%Zn foams in Figure 7-12.

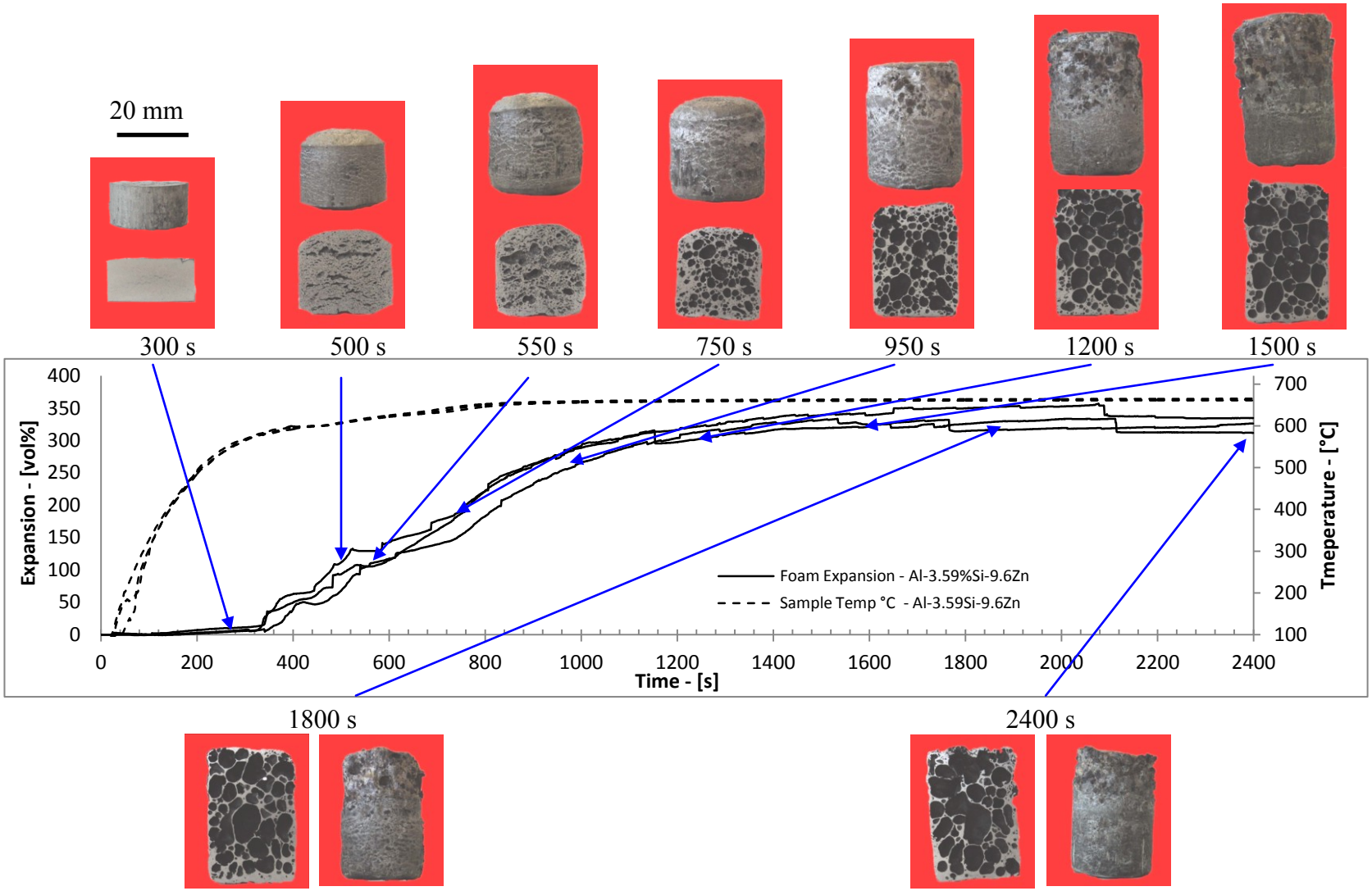

Figure 8-9: Al-3.59%Si-9.6wt%Zn foam evolution

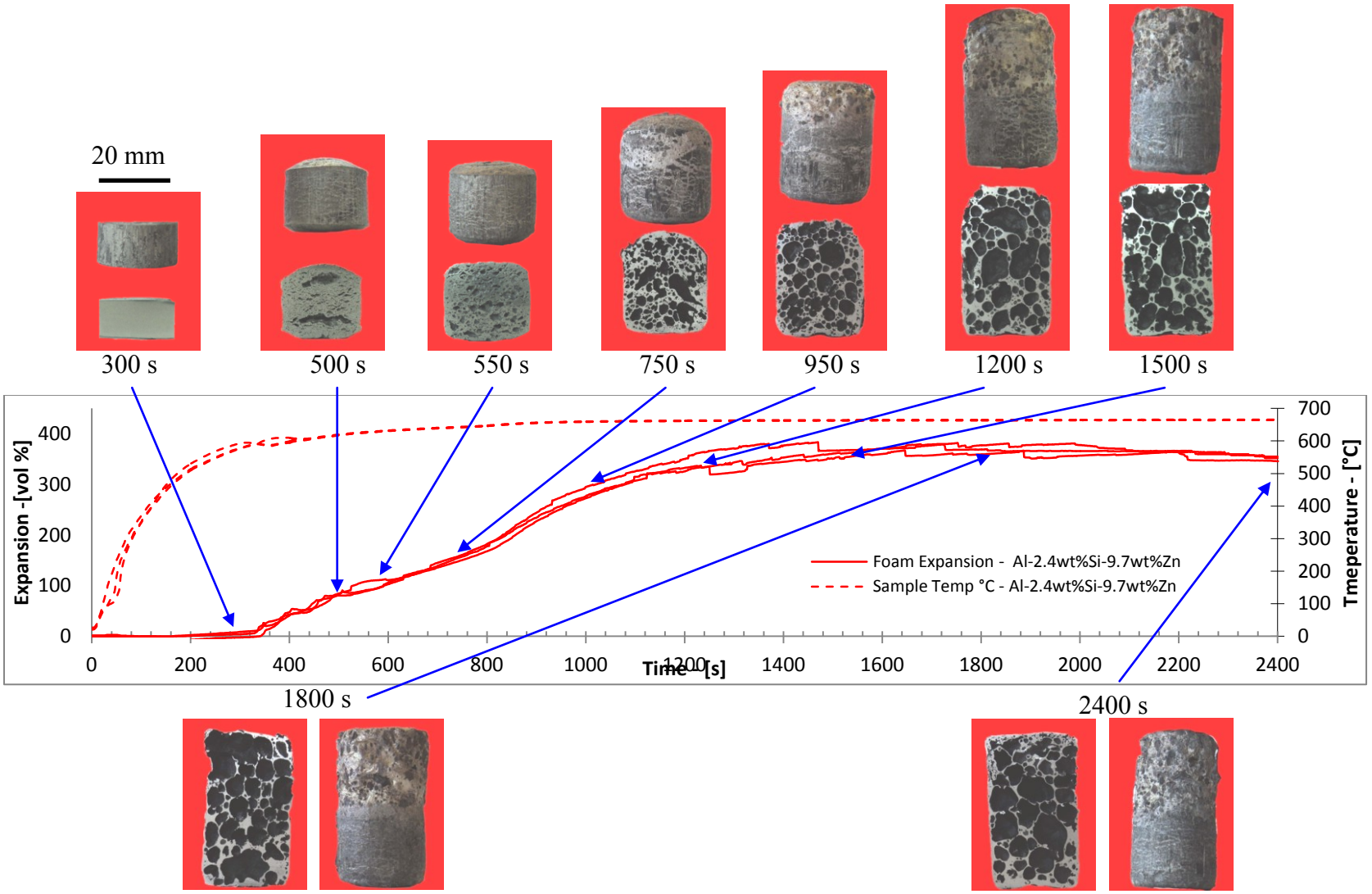

Figure 8-10: Al-2.4%Si-9.7wt%Zn foam evolution

Figure 8-10 depicts the Al-2.4wt%Si-9.7wt%Zn foams produced over a period of 2400 s at a foaming temperature of 660 °C. After 300 s of foaming, no cracking or pore formation is observed macrostructurally. Only after 500 s is pore formation observed. Similarly to the Al-3.59wt%Si-9.7wt%Zn foams, a collection of small pores is apparent along with large cracks spanning through the sample. After 550 s of foaming, the pores are becoming more defined and rounder as the alloy is melting through the semi-solid region.

The pores are becoming even more apparent at 750 s where the foam has reached the fully liquid state. One important observation is the few disproportionally large pores in the foams in contrast to the Al-3.59wt%Si-9.7wt%Zn composition. Between 750 s and 1200 s of foaming, the structure appears to expand and reach a maximum expansion of approximately 370 vol% which is higher than the Al-3.59wt%Si-9.6wt%Zn foams. Again through the evolution of the pores, there appears to be a consistent number of disproportionally larger pores in the structure. From 1200 s all the way to 2400 s of foams, the foam appears to be coarsening over this period of time as expected through the coalescence of pores. Pore size distribution with 30 mm foam samples will be discussed in a following subsection.

Although the two alloy composition are very similar, in terms of composition, the fact is that the Al-3.59wt%Si-9.6wt%Zn foam contains 10 wt% more eutectic powder than its counterpart which is believed to have a high impact on the initial foaming. From FactSage analysis, the difference in the semi-solid temperature range is only about 5 °C with the liquid phase onset occurring at the same temperature of 551 °C as shown in Table 8-1. As shown in Chapter 7, equilibrium alloy conditions (i.e.: semi-solid) are not necessarily representative of the actual system, for instance, the formation of the Al-94wt%Zn eutectic which form at 381 °C would not form if elemental powders were not used. In this case, the eutectic Al-12wt%Si powder would provide a larger liquid phase formation than a pre-

alloyed powder at the eutectic point. That said, the higher concentration of Al-12wt%Si is believed to help enhance the encapsulation of hydrogen gas.

8.4 Pore Nucleation Microstructure

In support of the DSC analysis, and the pore macrostructure shown in Figure 8-9 and Figure 8-10, the microstructure of the early foaming stages was studied. Samples were cut and polished to view the nucleation of the pores. Figure 8-11 displays the microstructure of an Al-3.59wt%Si-9.6wt%Zn sample foamed for 300 s. It is clear that, the nucleation is initiated at the centre of the zinc particles similarly to the Al-Zn based foams shown in Chapter 7 in Figure 7-14.

From this analysis, it can be deduced that an Al-94wt%Zn eutectic forms from the elemental zinc powders and spreads towards equilibrium while pores are being nucleated at their centre in a uniform manner through the foam. This being consistent with the Al-Zn based foams from Chapter 7 where the liquid forming temperatures correspond to the lowest recorded dehydrogenation temperatures of TiH_2 [1, 6-8]. The nucleation of the pores is therefore restricted to the TiH_2 particles serving as nucleating sites [44].

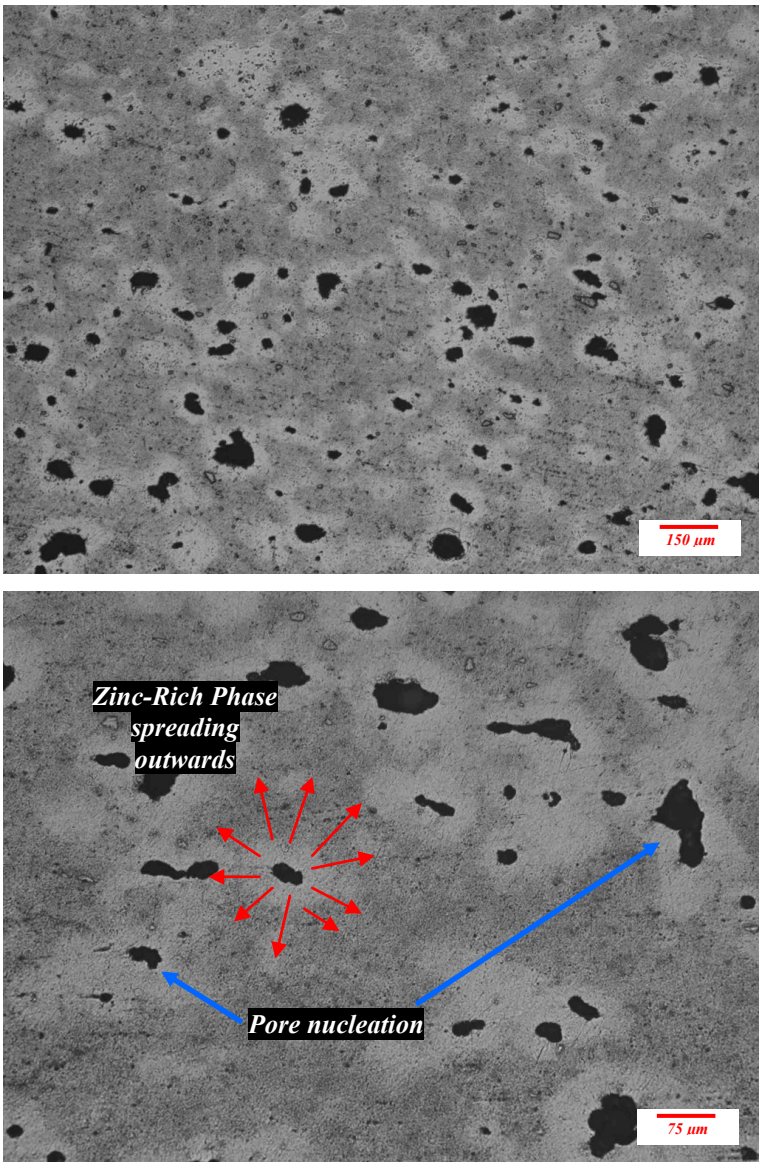

Figure 8-11: Al-3.59wt%Si-9.6wt%Zn foams produced at 660 °C for 300 s displaying a uniform nucleation of the pores

The Al-2.4wt%Si-9.7wt%Zn foam displays an identical behavior in terms of pore nucleation as observed in Figure 8-11. Although some formation of macro-cracks across the samples could be observed in the previous section, as with Al-Zn, the nucleation of the pores remained confined to the zinc particles. Some smaller cracks that did spread were surrounded by a zinc rich phase (i.e.: liquid) as evidenced through Figure 8-12. These again are believed to be apparitions

generated by the cooling of the sample as a result of pressure build up during solidification and the coalescence of adjacent zinc particles. These cracks only bridged across liquid interfaces preferably in the direction perpendicular to pressing. This is explained by the favored particle orientation due to the nature of the pressing itself. More micrographs are illustrated in Appendix E for both Al-3.59wt%Si-9.6wt%Zn and Al-2.4wt%Si-9.7wt%Zn foam compositions.

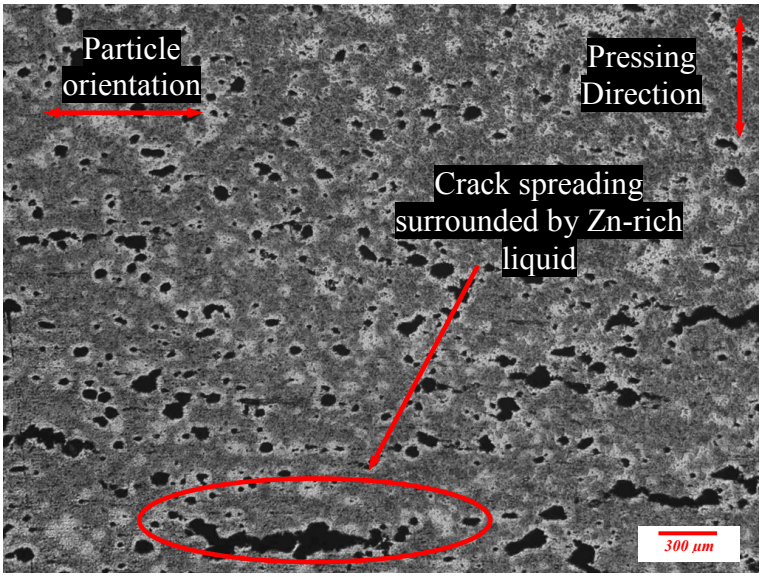

Figure 8-12: Al-3.59wt%Si-9.6wt%Zn foam produced for 300 s highlighting crack formations

In pure aluminum, on the other hand, large cracks spanning across the sample were observed in the cooled samples much like those observed here. The main difference is attributed to the network of fine cracks which formed in pure aluminum due to the lack of liquid as displayed through Figure 8-13 in comparison to Al-3.39wt%Si-9.7wt%Zn foams after 500 s of foaming. These microcracks resulted in the increased loss of hydrogen from the structure. In this case, the increased level of liquid results in the nucleation of uniform porosity confining the hydrogen.

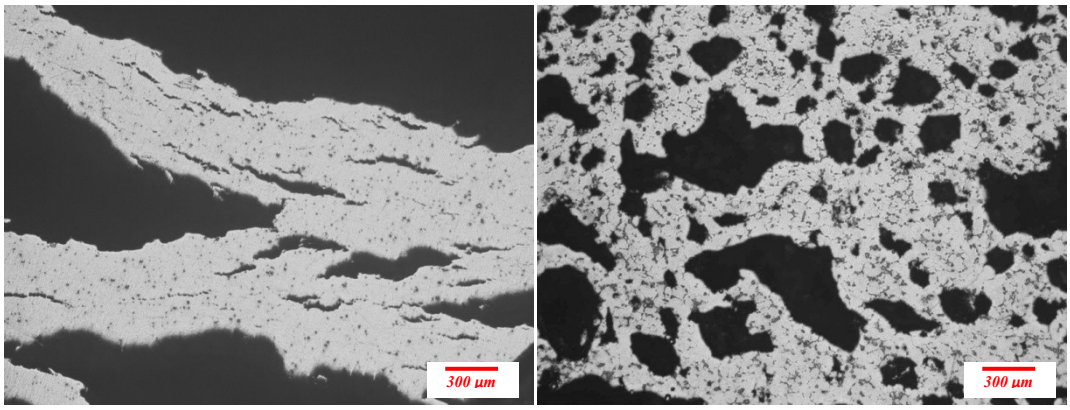

Figure 8-13: Pore evolution of: a) pure aluminum produced at 710 °C for 500 s and b) Al-3.39wt%Si-9.7wt%Zn foam produced at 660°C for 500 s

In contrast to available literature on Al-Si foams [10, 11, 20] where liquid formation is delimited by the eutectic temperature of 577 °C, the zinc in this case, not only ensures the formation of a ternary liquid at 551 °C, but also a transient liquid phase at 381 °C. It was highlighted by Yin *et al.* [86] that the morphology of the added silicon powder in the compacted PM foam structure was affected only once the foam was above its liquid forming temperature of 577 °C. In this case the Al-12wt%Si powders were dissolved in the zinc rich liquid to form a ternary eutectic at 551 °C generating supplementary liquid phase at a lower temperature. Yin *et al.* [86] also show that a network of cracks was apparent even at temperatures slightly above the eutectic temperature of 581 °C in an Al-7wt%Si foam [86]. The network of cracks formed was comparable to the pure aluminum in Chapter 5. However, no such network of cracks was observed in this work for both Al-Zn and Al-Si-Zn compositions. This low temperature eutectic allows for an earlier onset of gas evolution at low temperatures which prevents pressure build-up in the structure suppressing the tendency for crack formations otherwise observed in aluminum and Al-Si based foams [1, 6-8, 86].

The corresponding foaming temperature for the foam produced at 300 s was on average 567.0 ± 1.7 °C which corresponds to a temperature where the ternary liquid would have formed but the bulk Al-12wt%Si would still not have melted.

Figure 8-14 shows the formation of silicon platelets in the zinc rich region corresponding to the formation of the ternary liquid eutectic. In the same micrographs, due to the nature of the compact, Al-12wt%Si powder is observed where the majority remains undissolved at this stage. The formation of the ternary liquid is therefore restricted to the Al-12wt%Si particles in direct contact with the spreading Al-Zn liquid phase.

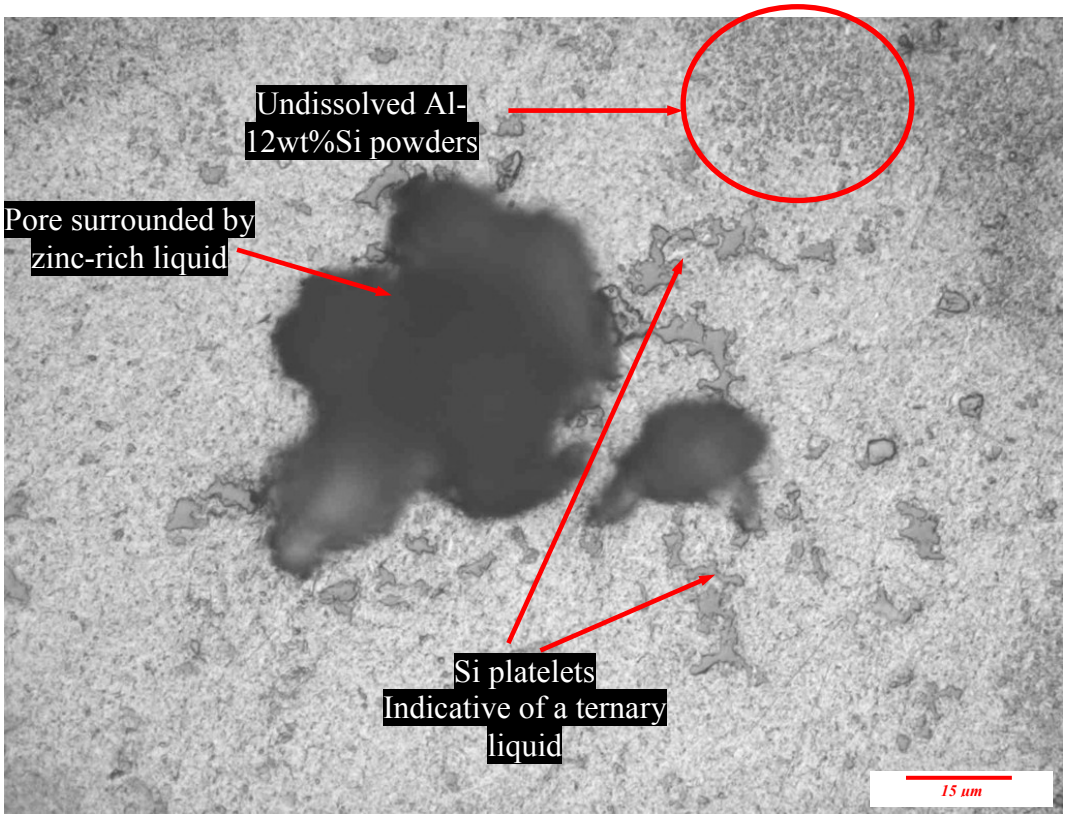

Figure 8-14: Al-3.59wt%Si-9.6wt%Zn foam produced for 300 s highlighting the different phases

The liquid fraction surrounding the pores which are formed at the centre of the zinc particles increase as the zinc-rich liquid diffuses in the matrix dissolving both pure aluminum powders and Al-12wt%Si forming a ternary eutectic. This is a reactive system unlike what is expected through equilibrium. FactSage analysis reveals that, under these conditions as shown through the isopleth in Figure 8-4, the alloy is completely in the semi-solid region where Al-12wt%Si powders

would not be present in powder form. If a pre-alloyed powder comprised of Al-3.59wt%Si-9.6wt%Zn was used, the nucleation of pores in the liquid phase could only be generated at temperatures above 551 °C as opposed to 381 °C in this instance. Figure 8-15 shows a line scan of the zinc rich region highlighting two undissoved round Al-12wt%Si particles in the melt. Away from the centre of the zinc rich phase, it can be seen that the concentration of aluminum gradually increases at the expense of the zinc concentration.

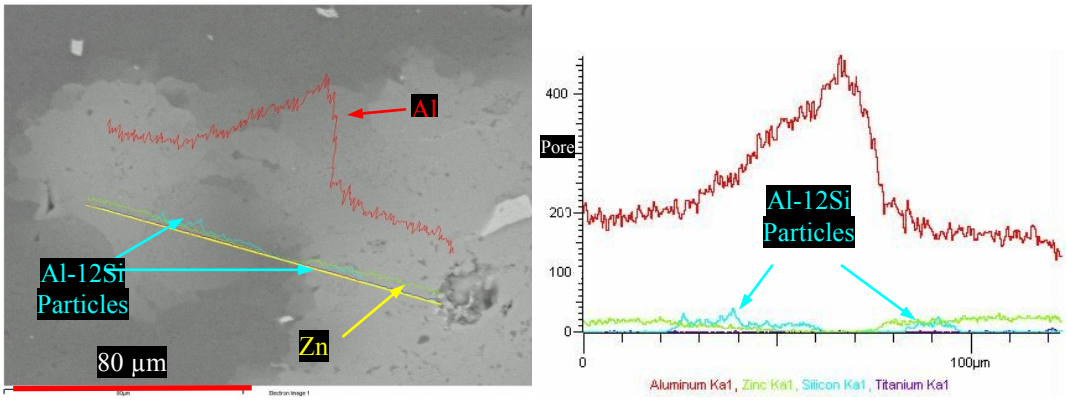

Figure 8-15: EDS Linescan of an Al-3.59Si-9.6wt%Zn foams produced at 660 °C for 300 s

An SEM image shows the distribution of the different phases in Figure 8-16 supported by and elemental EDS analysis. It can be seen that in fact, some round Al-12wt%Si powders are still intact while some silicon platelets can be seen in the zinc rich region (formerly liquid). As the zinc rich liquid spreads and the foaming temperature increases, it dissolved more aluminum and silicon into the liquid. After 500 s of foaming, the zinc rich phase has dissolved and numerous large pores appear in the structure, distributed uniformly. The foam structure is shown in Figure 8-17. The pore morphology comprises of a combination of large and small pores similar to the Al-10wt%Zn foams produced at a time interval of 500 s and furnace setpoint of 710 °C as shown in Figure 7-18. It is to be noted, in this case, that a similar morphology is attained 40 °C below the optimal foaming temperature for Al-10wt%Zn. This highlights the structures capacity to encapsulate the hydrogen gas as opposed to forming a network of cracks.

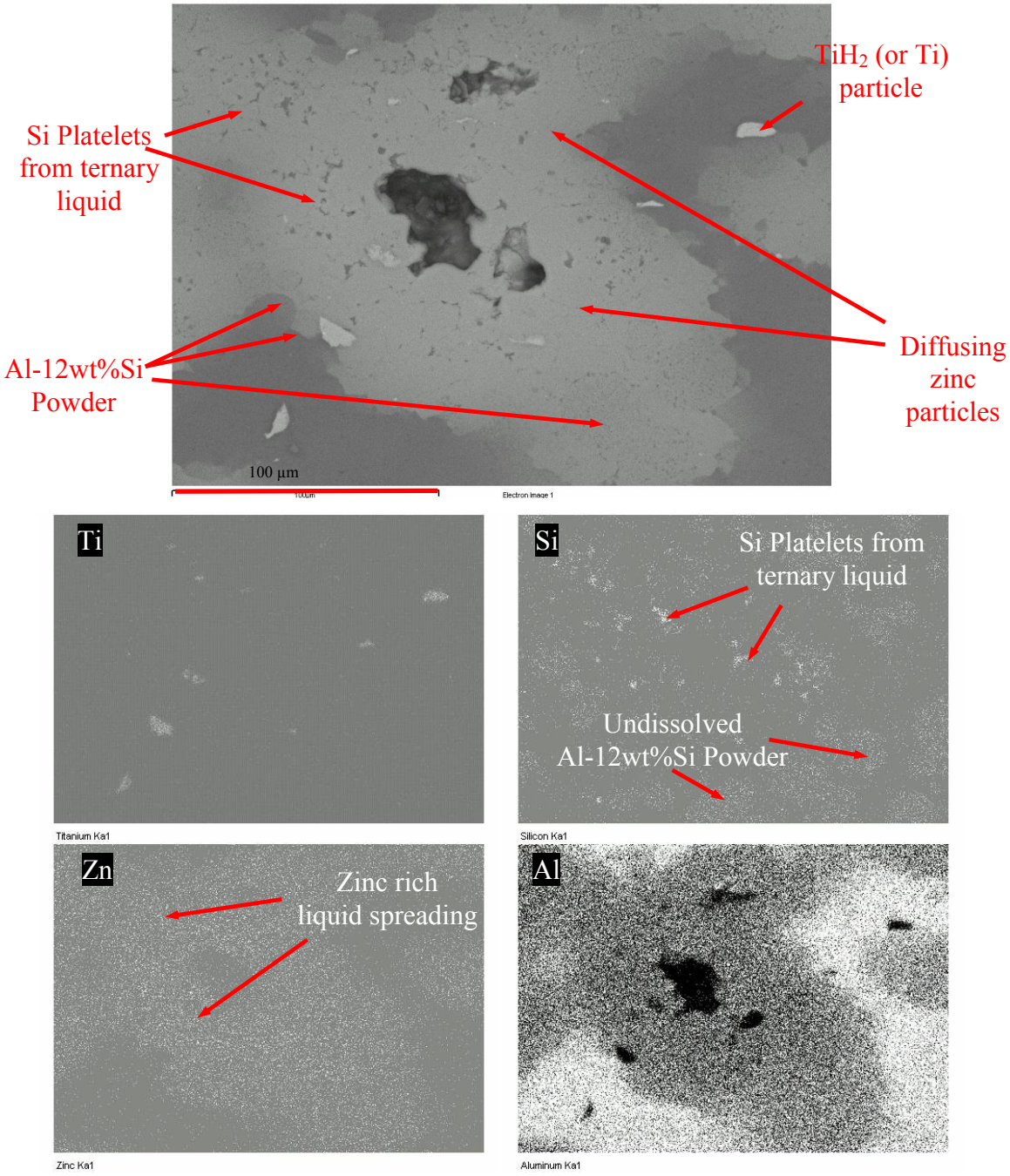

Figure 8-16: Backscattered secondary electron image with EDS of an Al-3.59wt%Si-9.6wt%Zn foams produced for 300 s displaying the spreading liquid zinc phase showing silicon platelets indicative of a ternary eutectic along with undissolved Al-12wt%Si powder

The microstructure appears to be that of typical Al-Si based foams whereby the zinc phase appears to have completely dissolved and platelets are forming around

the grain boundaries. The microstructure of both foam compositions of Al-3.59wt%Si-9.6wt%Zn and Al-2.4wt%Si-9.7wt%Zn under this condition appear very similar in nature since there is only a small variation in overall composition. Additional micrographs of each composition are shown in the Appendix E.

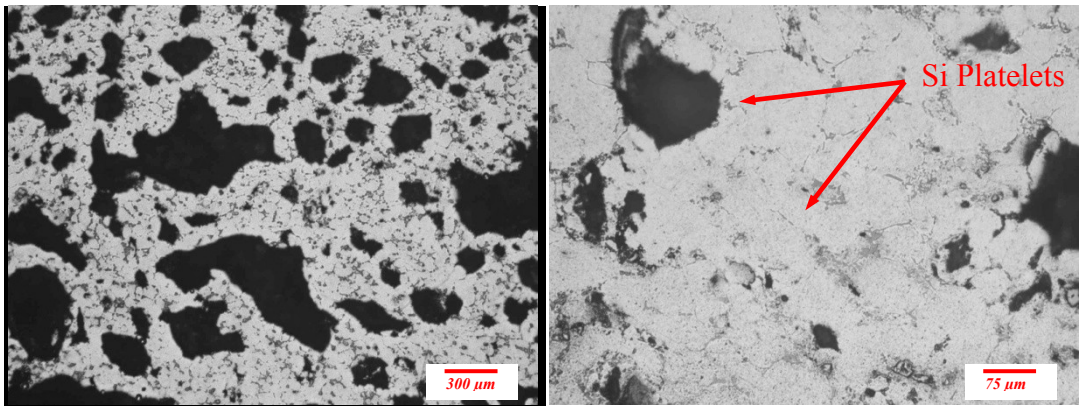

Figure 8-17: Al-3.59Si-9.6wt%Zn foams produced for 500 s at 660 °C

As the foaming progresses, after 550 s, the pores appear to be larger and more circular in shape in comparison to those produced at 500 s. This exemplifies the natural evolution of the foam as the hydrogen gas is being dissociated from TiH_2 and the pores become larger. The rounder pores also highlight the lowered surface tension of the alloy. Again, the microstructure appears to be typical of an Al-Si based alloy. According to the isopleth shown in Figure 8-4, the zinc is completely dissolved in the aluminum alloy with a silicon phase apparent in the alloy which is what is seen in Figure 8-17 and Figure 8-18. The corresponding foaming temperatures at 500 and 550 s are slightly below the liquidus (619 °C – FactSage) of the alloy itself at temperatures of 607.0 ± 1.0°C and 616.3 ± 1.5°C.

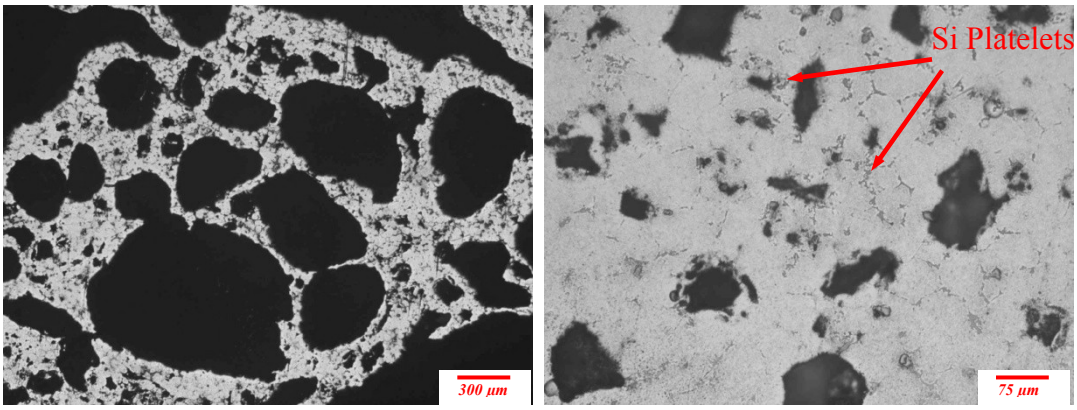

Figure 8-18: Al-3.59Si-9.6wt%Zn foams produced for 550 s at 660 °C

Based on the above analysis of the microstructure, it is apparent that the elemental zinc powders are beneficial for foaming as they act as pore nucleation sites similar to the Al-Zn compositions described in Chapter 7. The foaming temperature could be effectively reduced by the enhanced level of liquid formation as a result of the addition of silicon which produced a ternary eutectic. The formation of cracks was therefore suppressed in comparison to pure aluminum, resulting in high levels of expansion. The Al-12wt%Si powders become dissolved by the zinc rich eutectic as ternary eutectic temperatures are reached.

8.5 Foaming curves over time and temperature

Based on the data obtained from the DSC, macrostructural as well as microstructural analysis, a series of foaming curves were produced starting at 640 °C above the liquidus point of the alloy being 630 °C and 635 °C according to DSC analysis. Samples of both 20 mm diameter and 30 mm diameter were generated with the use of a pre-warmed crucible in which the compact was inserted.

Figure 8-19 shows the expansion curves for the Al-3.59wt%Si-9.6wt%Zn composition. It is apparent that the two set of curves for the 20 mm (Figure 8-19a)

and 30 mm (Figure 8-19b) diameter foams display similar trends and are reproducible although the larger samples took slightly longer to foam as expected. Both sets of foaming curves displayed a high levels of expansion (above 300 vol%) as well as post maximum expansion stability at low foaming temperatures. The maximum recorded expansion value for the Al-3.59wt%Si-9.6wt%Zn alloy was 418.6 ± 7.2 vol% produced at 660 °C with a sample size of 20 mm. With the 30 mm sample size, the maximum recorded expansion was slightly lower at 407.3 ± 7.0 vol%. Sectioned samples had comparable structures between 20 mm diameter compacts and 30 mm diameter compacts. The 30 mm diameter foam internal structures will be discussed in the next subsection. Supplementary data is presented in Appendix E, showing each foaming curve at different temperatures. The summarized expansion data is shown in Table 8-3.

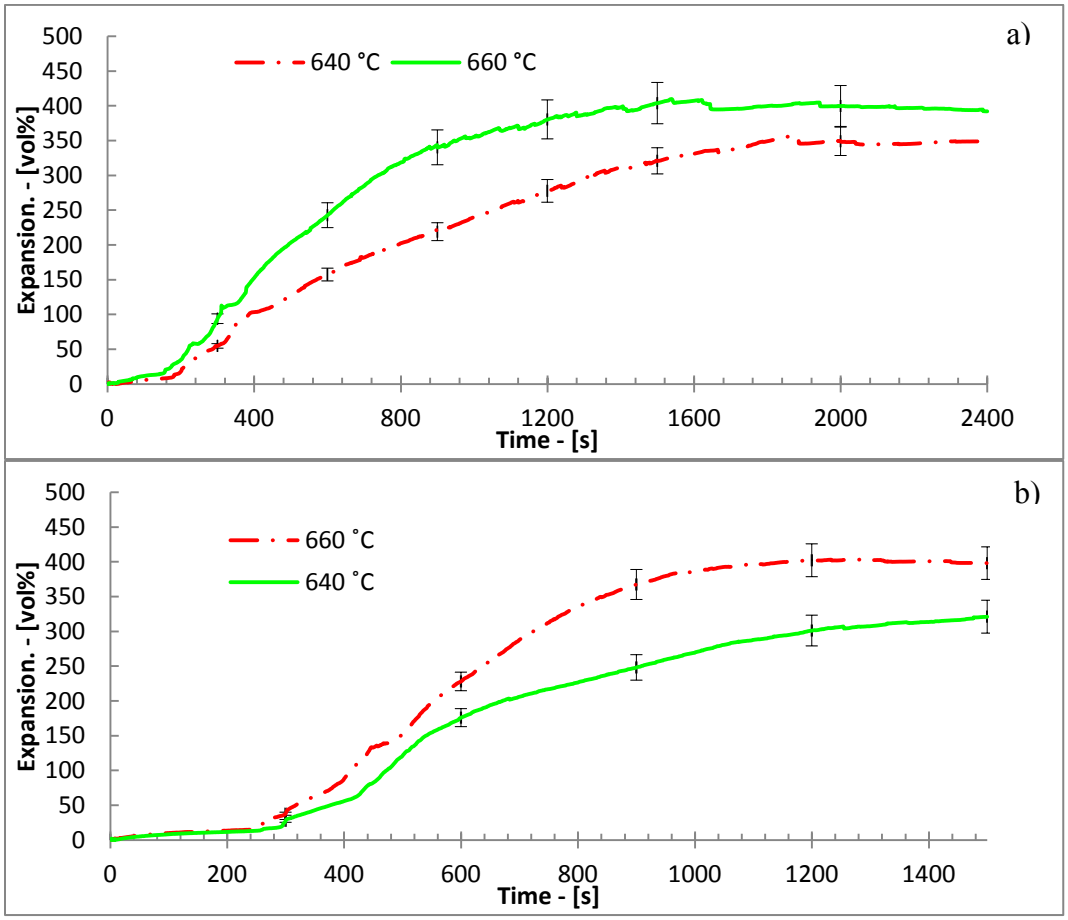

Figure 8-19: Foaming curves for the Al-3.59wt%Si-9.6wt%Zn a) 20 mm diameter samples, b) 30 mm samples

Figure 8-20 shows the Al-2.4wt%Si-9.7wt%Zn foaming curves produced at 640 °C and 660 °C. It can be seen that the results are similar to those obtained for the Al-3.59wt%Si-9.6wt%Zn with a larger maximum expansion of 441.7 ± 5.1 ˚C. This is consistent with the results obtain in the previous sub-section showing macrostructure where the Al-2.4wt%Si-9.7wt%Zn composition produced foams with slightly higher expansions at 660 ˚C. Maximum expansion for foams produced at 660 ˚C were 449.0±20.5 vol% and 441.7±5.1 vol% for 20mm and 30mm samples respectively The maximum expansion reached at 640 ˚C for the 30 mm diameter foam on the other hand was 281.3 ± 9.2 vol%, and it appeared the foam had not reached full expansion after 25 minutes of foaming. The 20 mm foam maximum expansion was 382.8 ± 24.1 vol%. From the 20 mm samples, it is evident that there was a higher level of degradation in comparison to the Al-3.59wt%Si-9.6wt%Zn foam.

Table 8-3: Expansion data for Al-Si-Zn based foams

Foaming temp (°C)	*Composition (wt%)*	*Alloy semi-solid region FactSage (°C)*	*Max Expansion 20 mm diameter (Vol%)*	*Max Expansion 30 mm diameter (Vol%)*
640	Al-3.59Si-9.6Zn	551-619	361.2±2.0	321.4±1.8
660	Al-3.59Si-9.6Zn	551-619	418.6±7.2	407.3±7.0
640	Al-2.4Si-9.7Zn	551-624	382.8±24.1	281.3±9.2
660	Al-2.4Si-9.7Zn	551-624	449.0±20.5	441.7±5.1
620	Al-33Zn	531-603	298.4±11.8	216.8±11.2
640	Al-33Zn	531-603	329.4±18.4	321.3±12.5
690	Al-10Zn	622-645	285.1±12.4	304.4±13.8
710	Al-10Zn	622-645	291.7±16.3	334.6±7.2

Both compositions demonstrated good foamability with high level of expansion at low temperatures and post maximum expansion stability with a variable sample size. The Al-3.59wt%Si-9.6wt%Zn appeared to have a favorable 20 °C range of foam stability where good past maximum expansion was shown. These compositions displayed foam expansion levels approximately 100 vol% higher than Al-Zn compositions. This can be attributed to either a larger release of hydrogen from the TiH_2 due to the higher foaming temperature or to an increased

hydrogen encapsulation as a result of a higher level of transient liquid phase and lowered alloy melting point.

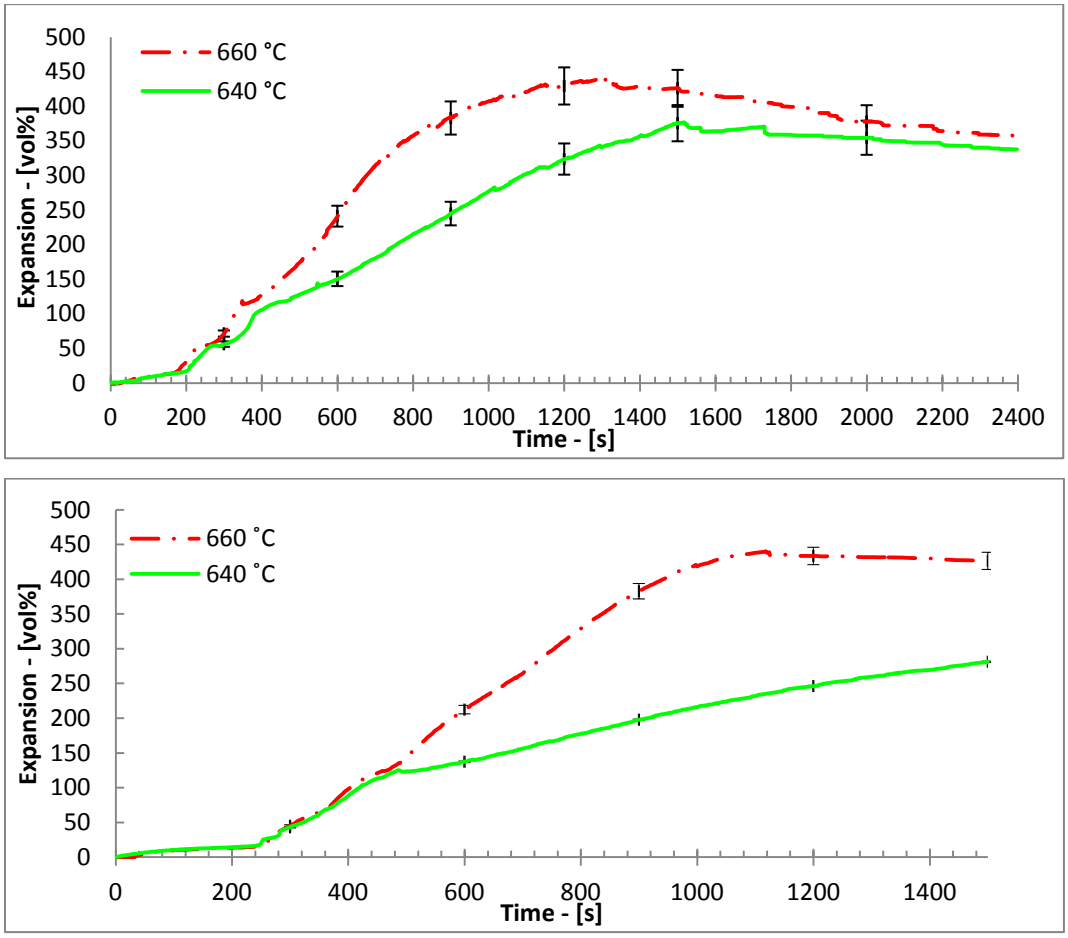

Figure 8-20: Al-2.4wt%Si-9.7Zn foaming curves 640 ˚C and 660 ˚C a) 20mm diameter sample, b) 30mm diameter sample

8.6 Post Maximum Expansion Foam Stability

It was shown that an increase in the transient liquid phase helped encapsulate the dissociated hydrogen gas from TiH_2 during the early stages of the foaming process. Much like Al-Zn based foams, enhanced post maximum expansion stability was also attained with Al-Si-Zn foams. The post maximum expansion reductions were tabulated in Table 7-5 for the Al-Si-Zn foams along with pure aluminum and Al-Zn foams for comparison. The maximum volume expansion

was compared to the volume after 2400 s of foaming (Al-Si-Zn and Al-33wt%Zn) or 1500 s (pure aluminum and Al-10wt%). The overall vol% collapse of the Al-3.59wt%Si-9.6wt%Zn foam produced at 660 °C is comparable to the Al-33wt%Zn composition produced at 640 °C at a value of 26 vol%. In term of % collapse relative to maximum expansion the Al-3.59wt%Si-9.6wt%Zn composition are far superior compared to Al-Zn based compositions. The % collapse of the foams are 3.3 % and 6.3 % for the foam produced at 640 °C and 660 °C compared to Al-33wt%Zn at approximately 8% for both foaming temperatures. The Al-2.4wt%Si-9.7wt%Zn composition on the other hand displays higher levels of degradation in comparison to the Al-3.59Si-9.6wt%Zn foams. These foams displayed collapse levels of 11.8 % and 20.2 % produced at 640 °C and 660 °C respectively. These levels of degradation are comparable to pure aluminum and Al-10wt%Zn foams although the degradation appears to be slower.

The estimated stability range for the Al-3.59wt%Si-9.6wt%Zn foams based on expansion curves in Figure 8-19 and Figure 8-20 at foaming temperatures of 640 °C and 660 °C were measured to be above 1000 s (600 s for Al-2.4wt%Si-9.7wt%Zn at 660 °C) respectively being comparable to Al-33wt%Zn foam stability. This stability time is exceptional for metal foams over the given period of time. Data pertaining to foam degradation is enumerated in Table 8-4.

Table 8-4: Collapse ratio of the different foams assessed

Foaming temp (°C)	*Composition (wt%)*	*Max Expansion 20 mm diameter (Vol%)*	*Expansion after 2400 s - Vol%*	*Diff*	*% Collapse*	*Estimated Stability (s)*
640	Al-3.59Si-9.6Zn	361.2±2.0	349.1±13.0	12.1	3.3	>1000
660	Al-3.59Si-9.6Zn	418.6±7.2	392.2±5.9	26.4	6.3	>1000
640	Al-2.4Si-9.7Zn	382.8±24.1	337.7±5.5	45.1	11.8	>1000
660	Al-2.4Si-9.7Zn	449.0±20.5	358.0±11.1	91	20.2	>600
620	Al-33Zn	298.4±11.8	274.0±6.2	24.4	8.2	>1000
640	Al-33Zn	329.4±18.4	303.3±14.6	26.1	7.9	>1000
Foaming temp (°C)	*Composition (wt%)*	*Max Expansion 20 mm diameter (Vol%)*	*Expansion after 1500 s - Vol%*	*Diff*	*% Collapse*	
690	Al-10Zn	285.1±12.4	250.7±14.28	34.4	12.1	>250
710	Al-10Zn	291.7±16.3	259.6±15.3	32.1	11.0	>120
710	Pure al	127.7 ± 1.5	100.0±1.2	27	21.7	<40
750	Pure Al	311.0 ± 5.5	197.5±27.5	114	36.7	≈10

Foam samples having a diameter of 30 mm were produced for pore analysis in support of the increased stability observed from the foaming curves. The 30 mm diameter samples were selected due to higher cell count which is believed to be more representative of an actual foaming process. For both Al-Si-Zn compositions, three foam samples were produced at each condition. Figure 8-21 displays Al-3.59wt%9.6wt%Zn foams produced at 710 s and 1500 s at 640 °C. A typical foam evolution can be seen from the structure at 710 s (Figure 8-21a) where a high count of small pores is seen whereas larger pores formed through growth and coalescence of smaller ones is shown in Figure 8-21b. This is highlighted by the measured pore size distribution in Figure 8-21c. The data pertaining to the Al-Si-Zn foams along with Al-Zn and pure aluminum are shown in Table 8-5. Additional pore analysis data is presented in Appendix E pertaining to roundness and cell spherical diameter.

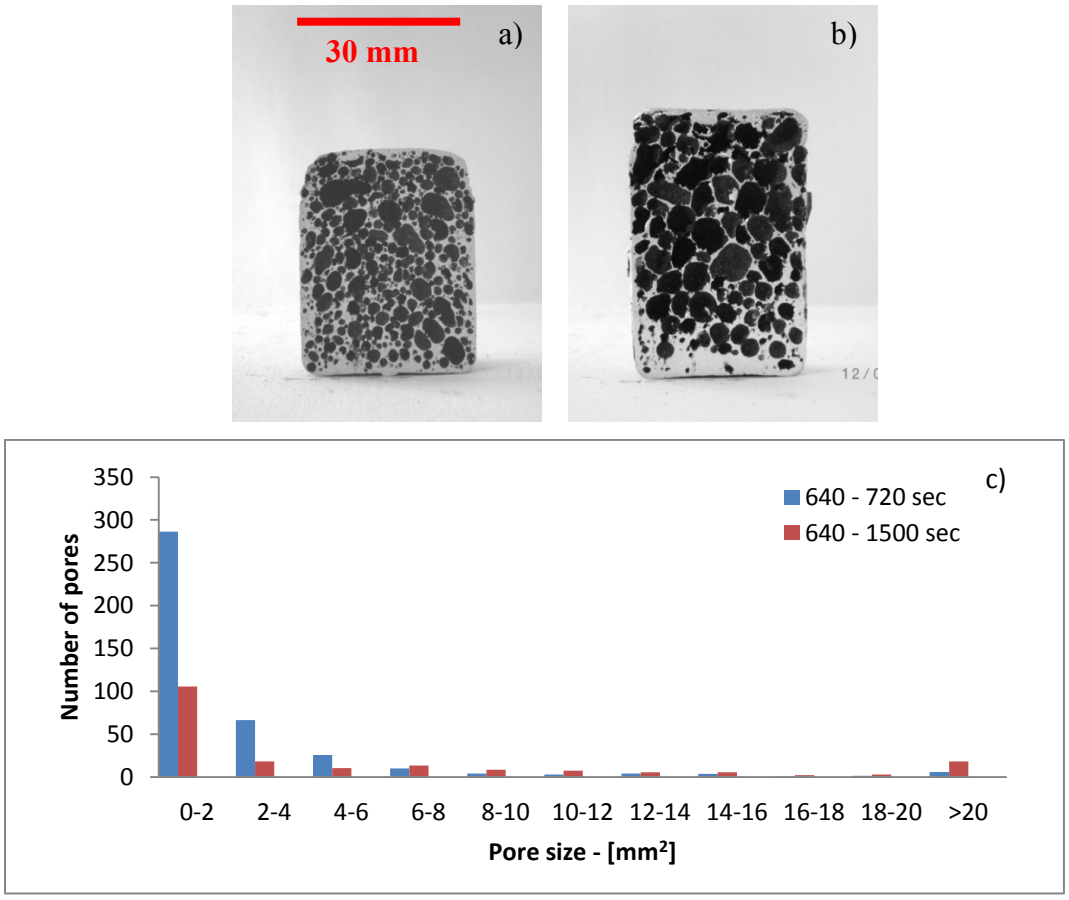

Figure 8-21: Representative Al-3.59wt%Si-9.6wt%Zn foams produced at 640 ˚C a) 720 s (12 min) b) 1500 s (25 min), c) pore area distribution for foam produced at 720 s and 1500 s

The foam evolution of the Al-3.39wt%Si-9.6wt%Zn composition in the optimal range spanning over 300 s from 1200 to 1500 s is shown in Figure 8-22 for foam produced at 660 °C corresponding to Figure 8-19. From the representative images shown in Figure 8-22a and Figure 8-22b, it can be seen that the pore morphology is similar. Looking more closely at the data, in Figure 8-22c, there appears to be a higher amount of larger pores on average after 25 minutes of foaming. This is confirmed by the growth in pore area as shown in Table 8-5 from 1093.3 mm^2 ± 46 to 1367 ± 34 mm^2 with a minimal difference in expansion. Although there is a trend, the variation is not large, highlighting the greater stability of the foam over the given period of time.

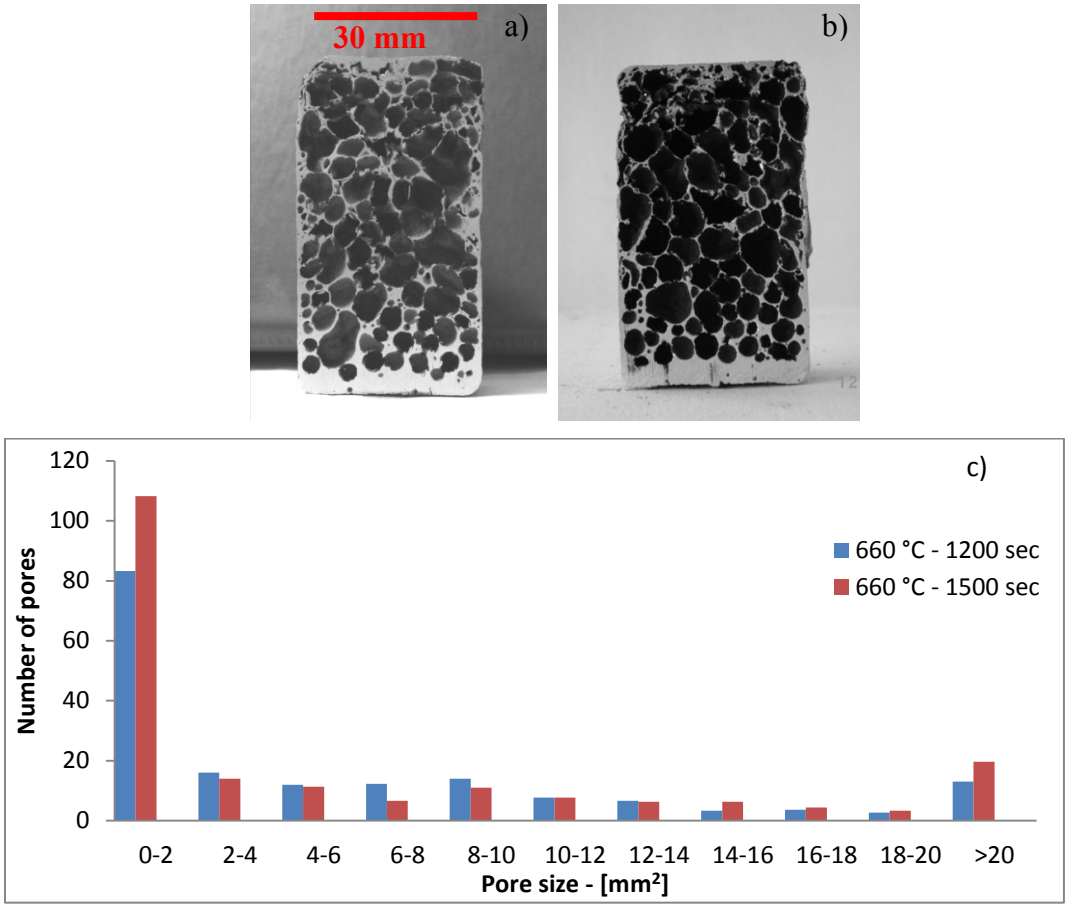

Figure 8-22: Representative Al-3.59wt%Si-9.6wt%Zn foam produced at a) 660 ˚C and 1200 s b) 660 ˚C 1500 s c) pore area distribution for foam produced at 1200 and 1500 s

Table 8-5: Aluminum foam pore size data

Composition	*Foaming time (s)*	*# Pores*	*Expansion (Vol %)*	*Cumulative pore area (mm^2)*
Pure Al - 750 °C	600	199 ± 22	257 ± 2	1061 ± 18
Al-10Zn - 710 °C	510	174 ± 27	301 ± 13	1021 ± 18
Al-10Zn - 710 °C	600	108 ± 27	303 ± 17	979 ± 45
Al-33Zn - 640 °C	1200	152 ± 22	314 ± 9	1110 ± 45
Al-33Zn - 640 °C	1500	153 ± 9	306 ± 18	1097 ± 5
Al-3.59Si-9.6Zn - 640 °C	720	480 ± 48	301 ± 13	957 ± 46
Al-3.59Si-9.6Zn - 640 °C	1500	208 ± 55	321 ± 2	1237 ± 29
Al-3.59Si-9.6Zn - 660 °C	1200	176 ± 18	402 ± 5	1093.3 ± 46
Al-3.59Si-9.6Zn - 660 °C	1500	208 ± 6	398 ± 9	1367 ± 34
Al-2.4Si-9.7Zn - 660 °C	1200	177 ± 15	434 ± 1	1121 ± 72
Al-2.4Si-9.7Zn - 660 °C	1500	192 ± 18	427 ± 7	1347 ± 54

Al-2.4wt%Si-9.7wt%Zn foams produced at 660 °C over a period of time of 300 s (1200 s and 1500 s) are shown in Figure 8-23 corresponding to Figure 8-20. From the representative foam images in Figure 8-23a and Figure 8-23b, it is evident that the foam does not coarsen significantly. Figure 8-23c reveals a similar pore size count for both foaming times indicating an increased stability. Table 8-5 shows that there is an increase in cumulative pore area from 1121 ± 72 mm^2 to 1347 ± 54 mm^2 indicative of slight pore coarsening. After 1500 s, there is a slightly higher count for larger pores as observed for the Al-3.59wt%Si-9.6wt%Zn.

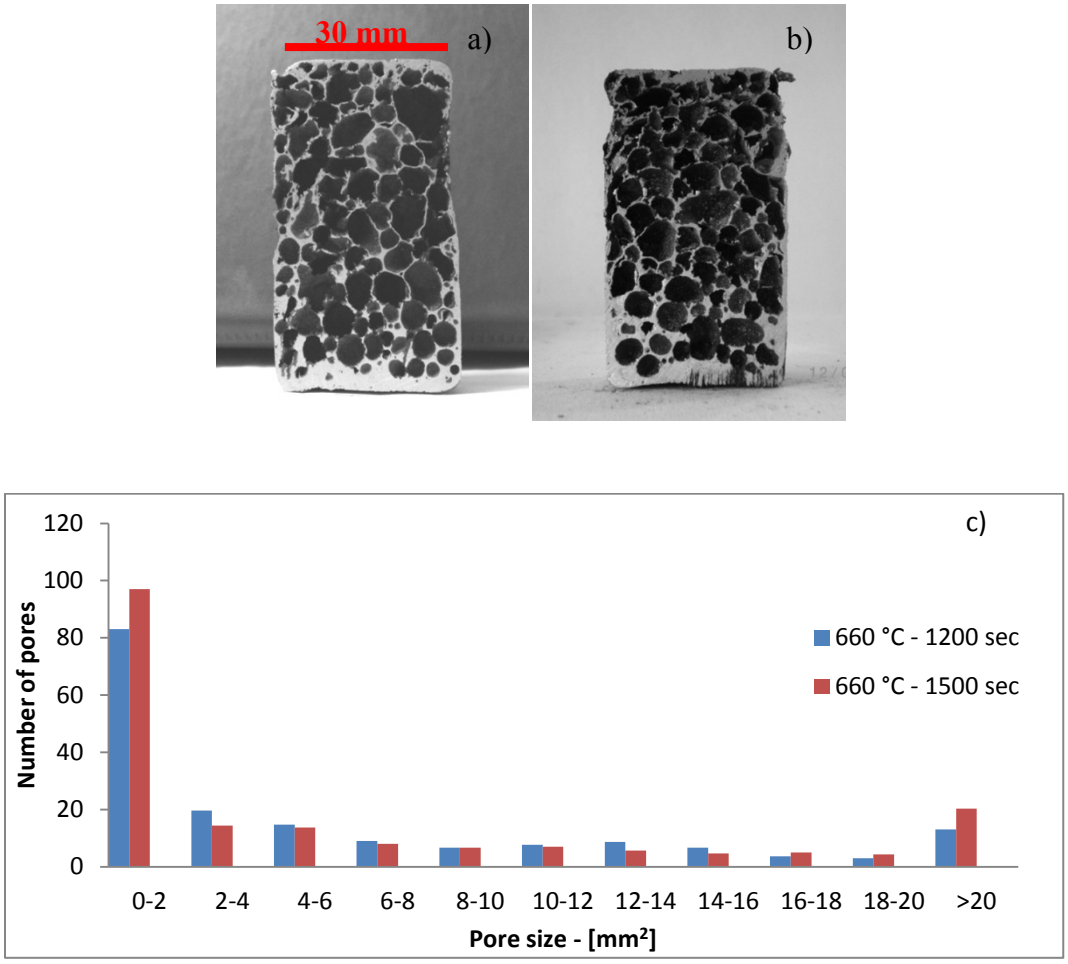

Figure 8-23: Al-2.4wt%Si-9.7wt%Zn foams produced at a) 660 ˚C and 1200 s b) 660 ˚C 1500 s c) pore area distribution for foam produced at 1200 and 1500 s

Post maximum expansion stability of Al-Si-Zn foam for both 20 mm and 30 mm diameter samples was shown to be superior to pure aluminum and Al-10wt%Zn foam over an extended period of time as confirmed by the pore analysis presented above. Overall, it is estimated that foam stability can extend over a duration time of 1000 s for Al-3.59wt%Si-9.6wt%Zn foams and 600 s for both Al-2.4Si-9.7wt%Zn while reducing the foaming temperature by 90 °C compared to pure aluminum.

Foaming theory indicates a complex interplay between several variables which are responsible for foam stability as outlined in Chapter 2 and Chapter 7. For powder metallurgy based foams these variables include, powder oxide content, alloy surface tension and bulk viscosity [13, 15, 34, 36, 44]. In order to stabilize powder metallurgy foams, it has been shown that it is essential to have a certain level of native powder oxide to create a disjoining pressure to counteract foam degradation [21, 22, 69]. These oxide particles have been shown previously to form a complex network in the foam helping keep the structure together [36, 53, 69]. Korner *et al.*[53] have suggested that the oxides present in the melt form a stabilizing network, forming a mechanical barrier against degradation. As a result these oxide networks help reduce the coalescence of the foams and increase overall stability [66-68]. It has also been shown through microgravity experiments that the oxide content has a dominant effect on cell coalescence [66-68]. In Section 7.6, it was determined that the Al-Zn based foams fell in the experimentally determined literature values for optimal oxygen content range for stable foams (0.28 to 1.69 at%O) ranging between 1.02 at%O and 0.97 at%O for Al-10wt%Zn and Al-33wt%Zn foams. The oxygen content of the Al-12wt%Zn powder used to produce the Al-Si-Zn foams was measured at 0.152 wt%O as shown in Chapter 3 which is more than half the value of the pure aluminum powder. The powder oxygen content data is summarized in Table 8-6.

Table 8-6: Foam oxygen content

Powder	*Density g cm^{-3}*	*Molar mass*	*O - Wt%*	*O – at%*	
Al	2.71	26.96	0.37	1.04	*Al_2O_3
Zn	7.14	65.39	0.079	0.64	*ZnO
Al-12wt%Zn	2.65	26.64	0.152	0.58	*Al_2O_3
Al - Optimal range			***0.1 to 0.6***	***0.28 to 1.69***	***Al_2O_3**

** Stable oxide composition*

Composition	*at % Zn*	*at % Al*	*at% Al-12Si*	*Total O at%*
Al-2.4wt%Si-9.6wt%Zn	4.26	74.14	21.59	0.92
Al-3.59wt%Si-9.6wt%Zn	4.21	63.54	32.24	0.87
Al-10wt%Zn	4.23	95.77	--	1.02
Al-33wt%Zn	16.79	83.21	--	0.97

The computed total at%O on for the Al-Si-Zn foams varied from 0.92-0.87 at% for the Al-2.4wt%Si-9.6wt%Zn and the Al-3.59wt%Si-9.6wt%Zn foams, respectively. These values are slightly lower than those calculated for the Al-Zn compositions by approximately 0.1 at%. Although the values are slightly lower, they fall within the experimentally determined optimal foam oxide composition range of 0.28 – 1.69 vol% oxygen content [21, 22, 36, 69]. If the oxygen levels were too low in this instance, poor foam stability would have been observed through high levels of drainage and coalescence which is not the case for the Al-Si-Zn foams. Again, there is a possibility that, the alloy itself could influence the wetting of the oxide by the melt, in return affecting the stability but limited literature is available on the effect of alloy on the oxide network. Since the foams displayed enhanced stability over a long period of time and low pore coalescence at maximum expansion with lower levels of oxides, it is believed other mechanisms in conjunction with an optimal oxygen content are responsible for the enhanced stability such as viscosity and surface tension of the alloys.

It was shown in Section 7.6 through Equation 7-2 and Equation 7-3 that the foam stability is affected by both surface tension and viscosity. The surface tension forces were determined to be responsible for the suction of liquid into the Plateau

borders from the cell walls resulting in thinning and finally collapse [12, 13, 32, 44]. On the other hand, the viscosity is described as the resistance to fluid motion and therefore an optimal viscosity is essential for good foam stability as discussed in Chapter 2 and Chapter 7. A reduction in viscosity would promote cell wall drainage increasing the foam degradation rate having the opposite effect of a reduction in surface tension. The reduction in surface tension on the other hand would reduce the required disjoining pressure necessary to stabilize the foam. Therefore it can be understood that a reduction in surface tension and simultaneous increase in viscosity would indeed help increase the stability life of the foam [10, 15, 41, 49-52].

Unlike pure aluminum foams, the Al-Si-Zn samples reached the furnace setpoint before maximum expansion as shown through Figure 8-7 and Table 8-4. As a result, there was no increase in foam temperature above the maximum expansion contributing to a supplementary decrease in viscosity which would promote the foam degradation process of drainage as observed in pure aluminum foam. This is similar to the Al-33wt%Zn composition shown in Chapter 7 where expansion took place after the sample reached the furnace setpoint. Specific data pertaining to viscosity of ternary alloy compositions in literature is scarce while data for binary alloy data is widely available [149, 165]. The addition of both zinc and silicon are known to decrease the viscosity of the aluminum independently from each other. Dinsdale and Quested [165] iterate the fact that ternary alloys typically follow similar patterns to binary alloys. On this basis, it is suggested that the addition of both zinc and silicon to aluminum decreases its viscosity. Given this information, the viscosity of the melt would likely be reduced by the simultaneous addition of silicon and zinc.

Binary aluminum alloy viscosity data reproduced from Jones and Bartlett [149] shows the viscosity of both Al-Zn and Al-Si in Figure 8-24. The lowest viscosity shown in Figure 8-24 is for the Al-12.4wt%Si alloy which is well below the

aluminum and Al-Zn alloys. From the curves, it can be seen that near the melting point of the alloy, there is a drastic increase in viscosity near solidification. With the addition of the alloying elements the melting point of the alloy is decreased along with the viscosity. The viscosity values for the silicon concentrations present in the foam at the respective foaming temperatures of 640 °C and 660 °C ranges between 0.040-0.039 Poise being consistent with the values of pure aluminum and Al-Zn foams produced at 710 °C as outlined in Table 7-8. Although the addition of both zinc and silicon reduce the viscosity of the alloy, this is offset by the reduced foaming temperature of the alloy which would, as a result, generate a higher viscosity likely consistent with the values for the optimum conditions of the Al-Zn alloys. In other words, there is a shift in the viscosity values as the melting temperature is decreased as shown in Figure 8-24. As has been discussed in Chapter 5 and Chapter 7, a high heating rate is required for foaming pure aluminum and certain alloys with higher melting points due to the early loss of hydrogen gas due to crack formations in the matrix. Therefore, an early encapsulation of hydrogen enables a reduction of the foaming temperature which is translated into a higher viscosity which would be beneficial for foaming, reducing the overall rate of cell wall thinning. In conclusion, the values of viscosity at the given foaming temperatures for the Al-3.59wt%Si-9.6wt%Zn and Al-2.4wt%Si-9.7wt%Zn foams are not believed to be significantly reduced due to the lowering of the foaming temperature, resulting in low levels of foam degradation. However, the composition having a lower concentration of Al-12wt%Si powder would have a slightly higher viscosity at 660 °C, possibly reducing overall drainage manifested through a slightly higher volume expansion.

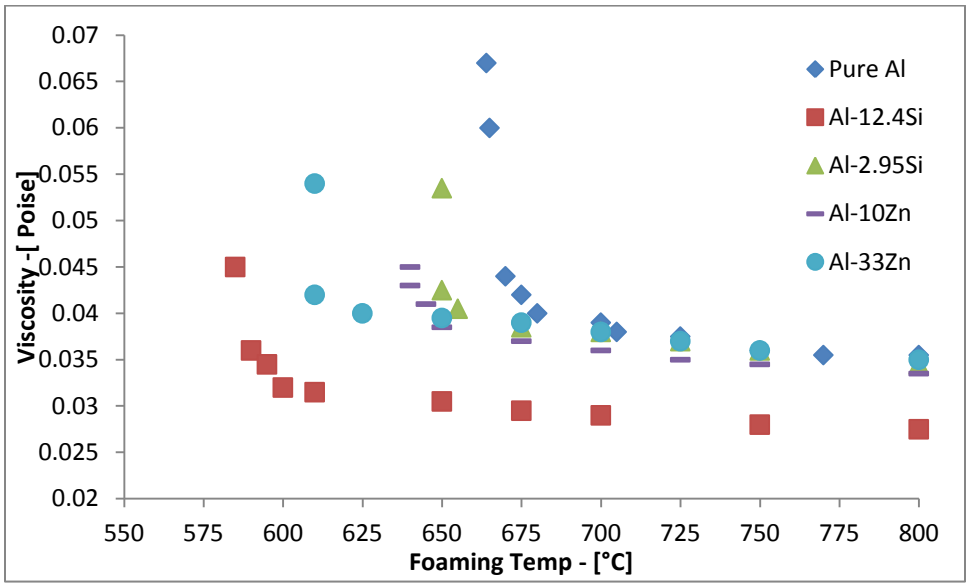

Figure 8-24: Viscosity data for pure aluminum, Al-Si and Al-Zn alloys [147]

Table 8-7: Viscosity data for pure aluminum Al-10wt%Zn and Al-33wt%Zn

System	*Foaming Temperature*	*Viscosity (Poise) [149]*
Pure aluminum	710-750 ˚C	0.039-0.036
Al-10wt%Zn	690-710 ˚C	≈0.037
Al-33wt%Zn	620-640 ˚C	≈0.040
Al-2.95wt%Si	640-660 ˚C	0.040-0.039

The other important property for foaming is the surface tension of the alloy. The independent addition of both zinc and silicon to an aluminum melt has been shown to reduce the surface tension of the melt [46, 166, 173]. In Chapter 7, it was shown that the surface tension of the melt could be reduced with the addition of zinc and that it was partially responsible for some level of increased stability. As with viscosity, the available surface tension data on aluminum ternary alloys is scarce [166]. From Figure 8-25, it can seen that both silicon and zinc reduce the surface tension of aluminum. The addition of 3 wt%Si is shown to reduce the surface tension of aluminum by 4 N m^{-1} and 10wt%Zn by 12 N m^{-1} from 769 N m^{-1} at 700 °C which is not a significant change. Although this is true, Keen [46] highlights the fact that there is variability in literature for both pure aluminum and

silicon surface tension values due to oxidation. Moreover, reported alloy surface tension values for silicon and zinc indicate they can also have a marginal effect on the lowering of the surface tension of aluminum [174]. As a result, it is possible in this case that surface tension only has a small effect on foaming. However, the ternary alloy surface tension may be lower.

Comparing the stability of the foam highlighted in Figure 8-22 and Figure 8-23, a reduction in melt surface tension would be consistent with increased foam stability. For instance, as pointed out and shown in Figure 8-10 with lower amounts of eutectic Al-12wt%Si powder in the Al-2.4wt%Si-9.7wt%Zn composition, the pore distribution is less uniform than the other composition. This could be the result of a slightly higher surface tension promoting higher levels of cell coarsening. However, this could be offset due to the total level of oxygen in the melt being slightly higher along with viscosity which would be beneficial for stability as shown in Table 8-6. Comparing the Al-Si-Zn foams to the Al-10wt%Zn composition, some level of degradation could be observed with 10 wt% zinc in the foam produced at 710 °C and 690 °C in Figure 7-20 reflecting optimal foaming temperatures. The addition of the silicon powder to this composition enabled a substantial melting point reduction along with increased expansion and stability of the foam. Generally, it is believed the addition of silicon and zinc both contribute to a low level of surface tension reduction which can increase foam stability over time, reducing the rate of cell degradation as described through Equations 7-2 and 7-3.

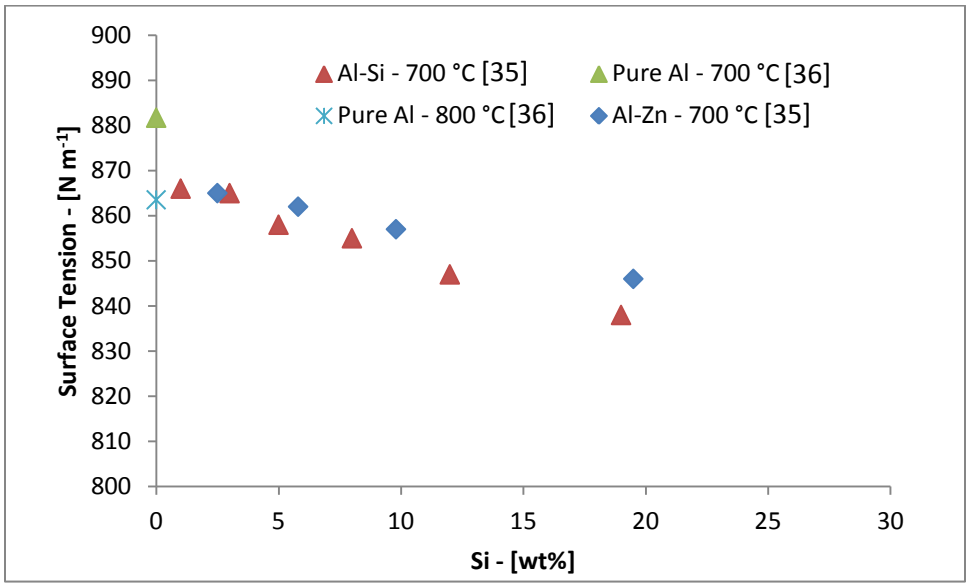

Figure 8-25: Surface tension data for pure aluminum, Al-Si and Al-Zn alloys [68, 167]

ICP analysis presented in Chapter 7 shows that there is no bulk evaporation of zinc from the samples as observed through DSC analysis and confocal microscopy. It was determined that a DIMOX (Directed Melt Oxidation) type process was responsible for restraining bulk zinc loss from the foaming structure and increasing the stability of the foam [167, 169-171]. The DIMOX process relies on the vaporization of an alloy component such as zinc or magnesium to break the aluminum oxide shell to onset the cyclic oxidation. Without the volatile component, only a thin aluminum oxide shell forms. Hanabe *et al.* [167] indicated that the high volatility of zinc promotes the formation of ZnO on melt/sample outer surfaces which is subsequently reduced to Al_2O_3, limiting the overall evaporation of zinc through the formation of a thick oxide shell. The addition of silicon to the melt however, has been attributed to an increase in melt wetting of the oxides favoring structural growth of oxide component of the DIMOX structure [171, 175]. It was stipulated in the previous chapter that a thick oxide shell was formed on the exterior faces of the foam, creating a solid shell enhancing stability. If in fact the silicon improves the process, which would mean a thicker shell would likely form on the outer surfaces of the foam in return enhancing stability to a greater extent. This would help explain the enhanced

stability of the foam observed in Figure 8-22 and Figure 8-23 in conjunction with the lowered surface tension. In the case of pure aluminum, the exterior oxide was not sufficiently solid to prevent a reduction in foam expansion. Although a DIMOX type reaction may occur on the outer surfaces of the foam, it would not prevent internal degradation and therefore several mechanisms are at play.

8.7 Conclusions

The overall foaming temperature could be lowered through the addition of Al-12wt%Si pre-alloyed powder in conjunction with low levels of elemental zinc by 50 °C in comparison to Al-10wt%Zn and by 90 °C compared to pure aluminum for an equivalent or higher expansion.

It is shown that the nucleation of pores is initiated at the centre of the elemental zinc particles which form a eutectic liquid at 381 °C. It was also revealed that the formation of a ternary liquid was formed at 551 °C which was initiated by the spreading zinc rich phase reducing the liquid onset of the semi-solid region.

The Al-Si-Zn alloys demonstrated high levels of expansion above 350 vol% and increased foam stability over an extended period of time of 600 s for the Al-2.4wt%Si-9.7wt%Zn and 1000 s for the Al-3.59wt%Si-9.6wt%Zn foam. Moreover, the density of the Al-Si-Zn alloys (Al-2.4wt%Si-9.7wt%Zn - 2.87 g $cm^{-1}$and Al-3.59wt%Si-9.6wt%Zn - 2.86 g cm^{-1}) was lower in contrast to the Al-33wt%Zn foam (3.40 g cm^{-1}) for an equivalent or higher expansion level.

Pore size analysis of the Al-Si-Zn foams reveal low levels of coarsening and stability over a period of time of 300 s being beneficial for larger complex geometries.

The overall enhanced post maximum expansion stability of the foam is attributed to a reduced surface tension through the addition of zinc and silicon. Although both zinc and silicon lower the viscosity aluminum for a given temperature, the reduced in foaming temperature yield a fairly constant viscosity. Moreover, a DIMOX reaction is believed to help enhance the foam stability via the formation of a thick outer oxide layer on the foam. The foaming mechanism is shown in Figure 8-26.

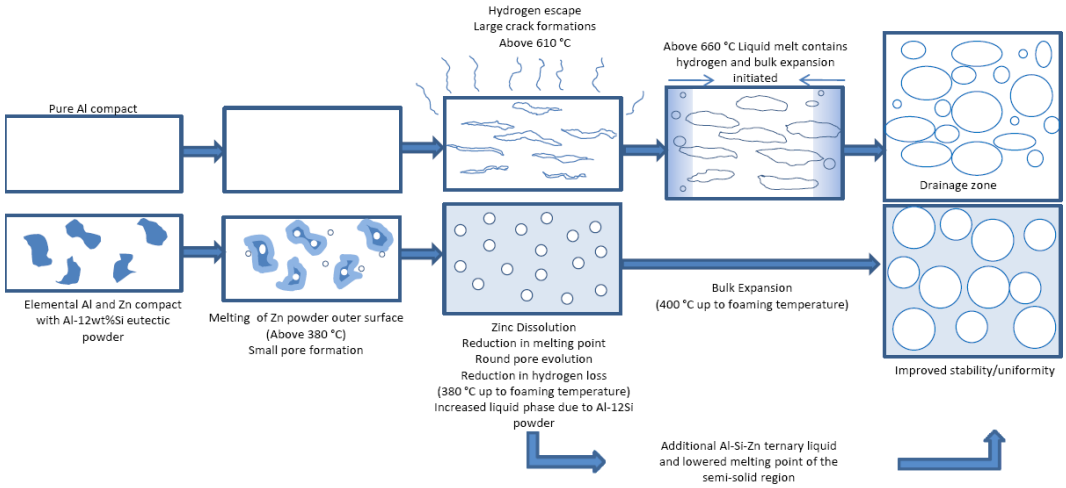

Figure 8-26: Al-Si-Zn foaming process compared to pure aluminum

This page is intentionally left blank

9 Mechanical Properties

Mechanical properties of the foam compositions discussed in Chapter 5, Chapter 7 and Chapter 8 were evaluated. This section will briefly cover uni-axial compression test data which was conducted on the foams produced, for comparison between alloys and to those available in literature. It is to be noted the actual focus of the thesis is on the development of alloys favorable for foaming rather than specific mechanical properties with respect to alloys.

Pure aluminum, Al-10wt%Zn, Al-33wt%Zn, Al-2.4wt%Si-9.7wt%Si and Al-3.59wt%Si-9.6wt%Zn foams were tested at optimal foaming conditions determined based on data from Chapter 5, Chapter 7 and Chapter 8.

9.1 Pure aluminum

Foam samples were cut to dimensions of 30 mm in diameter and height of 40 mm and were subjected to uniaxial compression. In conventional compression tests it is suggested that a specimen size ratio of d/h=0.5 (diameter/height) is to be used to have a balance between barreling and buckling effects in the compression specimen [133]. However, the minimum amounts of cells in the foam dictates the crushing behavior rather than size ratio itself, therefore it has been determined that a minimum of 4-6 cells is required as outlined in Table 2-4 [2, 16, 127-130].

Figure 9-1 depicts the three compression flow curves obtained for the pure aluminum foam samples produced at a furnace setpoint of 750 °C corresponding to a time of 660 s as shown Figure 8-22 (representative sample). As expected, the stress-strain profiles have the appearance of a typical ductile metallic foam which has a large smooth plateau stress over a large strain [2]. This can be compared to the stress-strain curve shown in Figure 2-12a of the literature review section. The three foams selected for the analysis had slightly different densities due to variations in the foaming process and machining operation as indicated on Figure

9-1. The foam with the largest density was the first to experience the onset densification point followed by the foam with the second largest density. Although the curves have slight differences in density they are very reproducible and give a curve profile of a typical ductile foamed material.

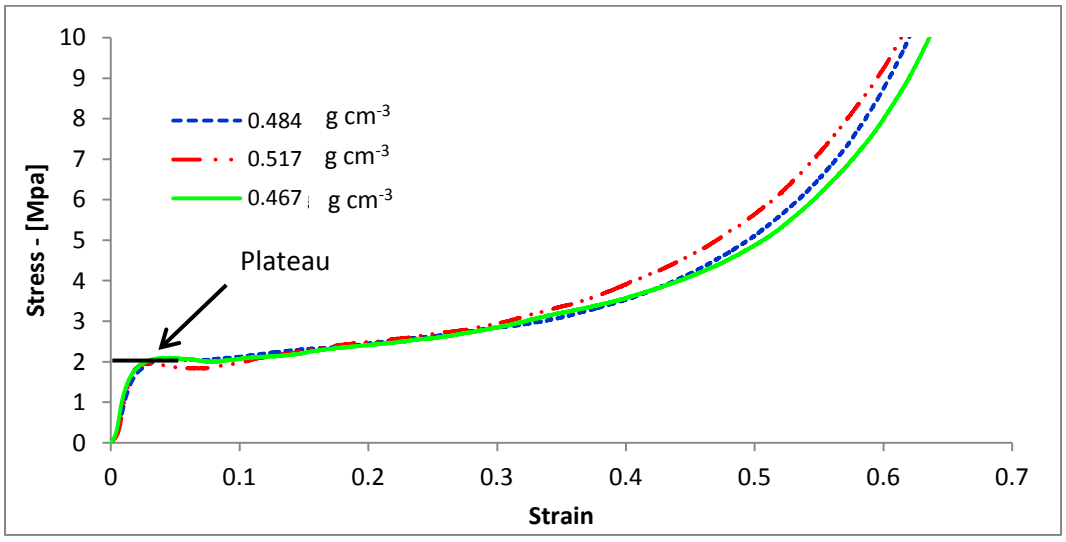

Figure 9-1: Pure aluminum stress-strain compression curve

From the stress-strain curve, the various properties were extracted. The corresponding plateau stress obtained from Figure 9-1 using the peak method is 2.05 ± 0.09 MPa with a max efficiency of 41.00 ± 2.65 %, an onset densification strain of 0.46 ± 0.02 and energy absorption capacity of 3.84 ± 0.31 kJ kg^{-1} up to the onset densification strain. The energy absorption capacity was calculated via Equation 3-3 while the onset densification strain with the use of Equation 3-4.

Table 9-1: Pure aluminum foam mechanical properties

Alloy	Density (g cm^{-3})	Relative density	Plateau stress (MPa) Tangent	Plateau stress (MPa) Peak	Max. Efficiency (%)	Onset densification strain	Energy absorption (kJ kg-1)
Pure Aluminum	0.49±0.03	0.18±0.01	1.68±.08	2.05±.09	41.00±2.65	0.46±0.02	3.84±0.31
Al-10Zn	0.45±0.02	0.19	2.73±0.23	3.25±0.22	40.00±2.00	0.52±0.03	9.58±1.14
Al-33Zn	0.64±0.01	0.16±0.01	0.82±0.26	1.13±0.55	31.33±4.13	0.51±0.09	4.75±2.43
Al-3.59Si-9.6Zn	0.36±0.01	0.13±0.01	2.03±0.21	2.85±0.31	47.75±5.12	0.61±0.06	10.58±1.59
Al-2.4Si-9.7Zn	0.38±0.03	0.11±0.01	1.23±0.12	1.50±0.17	45.67±4.62	0.68±0.03	12.21±1.99

The calculated values of plateau stress for the pure aluminum foams fall on the lower end of the values shown for Alulight type foam depicted in Table 9-2 and those described in Figure 2-13 which are manufactured through the powder metallurgy method. The calculated onset densification of 0.46±0.02 also corresponds to the lower range of the reported values. Values of compressive strength (plateau stress) for pure aluminum foam reported by Banhart *et al.* [3] for a relative density of 0.15 is of 3 MPa. In this case, for a slightly higher relative density of 0.18, the measured compressive strength is lower at 2.05±0.09 MPa. On the other hand, Kovacik and Simacik [75] report a compressive strength value of 3 MPa for a relative density of 0.22 indicating inter-study variability.

Table 9-2: Metal foam properties [21, 86, 177]

Property	*Cymat[16]*	*Alulight[16]*	*Alporas[16]*	*Al99.5-TiH_2[176]*	*Al99.6-TiH_2[75]*	*Al-12Si[75]*	*Zn[75]*
Relative Density - ρ/ρ_o	0.02-0.2	0.1-0.35	0.08-0.10	0.15	0.22	0.19	0.16
Structure	Closed Cell	Closed Cell	Closed Cell	Closed Cell	Closed Cell	Closed Cell	Closed Cell
Compressive Strength - σ_{pl}	0.04-7.0	1.9-14.0	1.3-1.7	3	3	8	7
Densification Strain - ε_D	0.6-0.9	0.4-0.8	0.7-0.82	--	--	--	--
Young's Modulus E - GPa	0.02-2.0	1.7-12	0.4-1.0	2.4	--	--	--
Energy Absorption 30% Strain MJ/m^3	--	--	--	0.72	--	--	--

In terms of energy absorption efficiency, the value is quite low at around 41 %. This low value level is due to the fact that the foam is quite wet (dense with thick Plateau borders) and has an inherent density gradient causing the onset densification strain to be quite low. The onset densification strain can be defined as the point where most of the cell pore space has been compressed and the cell walls come in contact with each other [13]. This density gradient can be observed in Figure 7-23 and Appendix D with large accumulations of liquid and thicker cell walls at the bottom portion of the foam as shown. This in turn will cause the weakest sections of the foam to crush (or collapse) under compression first, followed by those of higher density as seen in Figure 9-2 where the crushing of pure aluminum is taking place. It can be observed that the upper half of the foam, being less dense, crushes first. It is apparent that the density gradient affects the foam mechanical properties and effectively reduces the energy absorption efficiency of the foam displaying an increasing plateau stress [158, 177]. However, for homogeneous foams with a low density gradient, the foam typically crushed by the formation of randomly distributed bands [127, 131, 132].

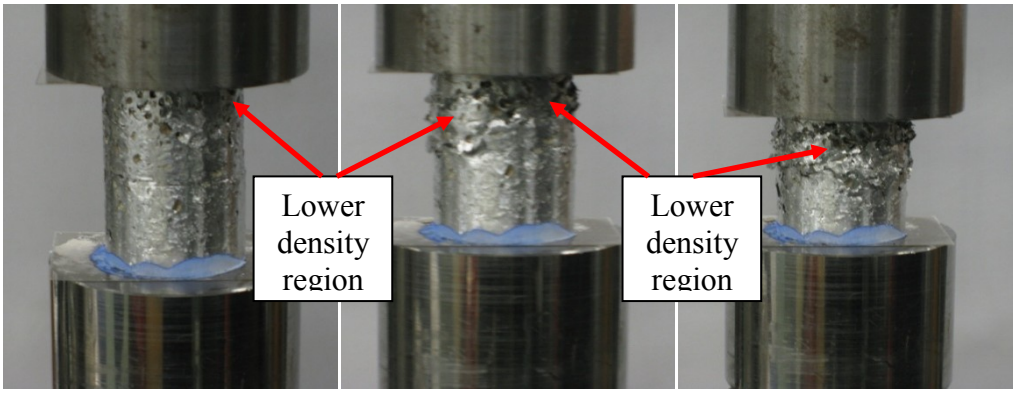

Figure 9-2: Crushing of pure aluminum foam at a strain rate of 10-3 s^{-1}

The energy absorption capacity of the pure aluminum foam composition on average is of 3.84 kJ kg^{-1} (1.87 MJ m^{-3}) which is comparable to those values in literature [2]. The compressive strength to density ratio of the foam is also calculated in terms of alloy strength with respect to density. In this case, for pure

aluminum the strength to density ratio is of 3.45 MPa (g cm^{-3})$^{-1}$. In general, pure aluminum mechanical properties fall within reported values in literature. In the following subsection they will be compared to the alloy compositions developed.

9.2 Al-Zn Foams

Samples were prepared for mechanical property assessment as described in Chapter 3. Typically zinc is only used in low concentrations in commercial wrought (1-8 wt%) and cast alloys for high strength [148]. In this instance, the alloys were explicitly designed with the transient liquid phase in mind rather than targeting a specific alloy and strength properties and therefore it is hard to compare strength values to those in literature.

Al-33wt%Zn foams were produced at a temperature of 640 ˚C with a foaming time of 1500 minutes which corresponds to the point of maximum expansion as shown in Figure 7-19. A representative sample of Al-33wt%Zn foam produced under these conditions is shown in Figure 7-24. The generated stress-strain curves can be seen in Figure 9-3.

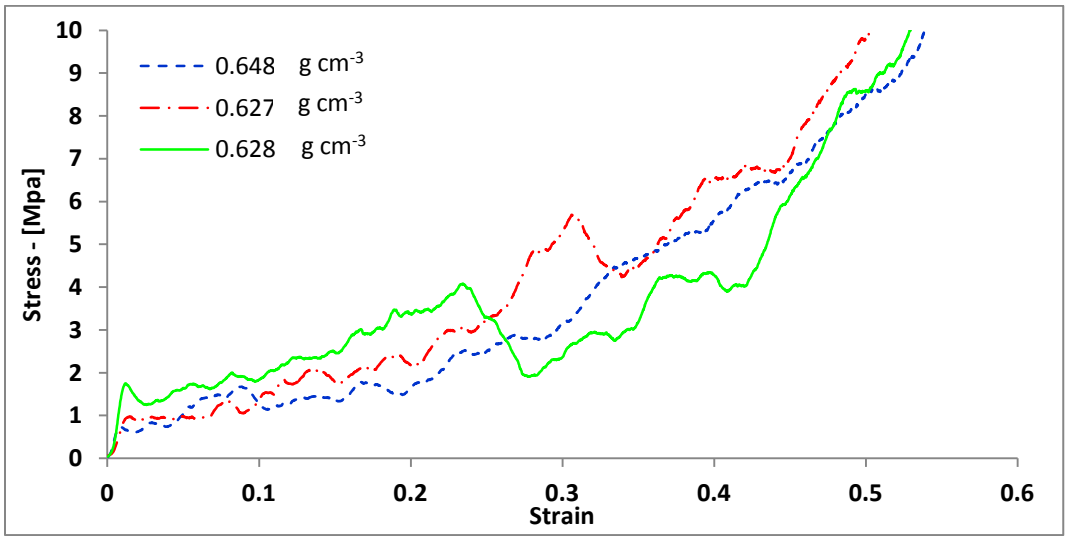

Figure 9-3: Stress-strain curves showing replicates for an Al-33wt%Zn foam produced at 640 °C and 1500 s, using a constant compression strain rate of 10-3 s-1

From a first observation, the curves have several peaks and valleys unlike those in Figure 9-1. This lack of smoothness is typically associated with more brittle foams as pointed out by Ashby *et al.* [2]. The apparent scatter between the replicate curves also highlights reproducibility issues with the system. The curve has a consistently increasing plateau stress rather than a flat behavior normally associated with homogeneous foams. This is a result of the density gradient as seen in Figure 7-24 caused by the drainage effects. From these results it is also evident the Al-33wt%Zn alloy is significantly more brittle than pure aluminum where cell wall collapse is likely to occur through fracturing rather than bending. By using a foamed 7075 alloy, Thornton and Magee [158] showed that the stress-strain curves were also highly irregular where cell wall fractures were apparent rather than bending as the alloy was more brittle than pure aluminum foam [158].

The plateau stress for the Al-33wt%Zn was 1.13 ± 0.55 MPa with significant variations between the three samples using the peak method which is significantly lower than 2.05 ± 0.09 MPa for the pure aluminum. These low values are not beneficial when looking at weight saving applications, especially if the foam structure is not completely uniform. The maximum energy absorption efficiency is also quite low in this case due to the rising plateau stress as a result of the large density gradient inherent in the foam. The onset densification in this case is slightly higher than the pure aluminum foams with a value of 0.51 ± 0.09. Figure 9-4 compares the mechanical properties of the Al-Zn system to that of pure aluminum. It can easily be seen that the Al-33wt%Zn composition is by far inferior in terms of plateau stress than the pure aluminum system for the same level of expansion. One thing to note about these stress-strain analyses is that the thick outer skin and the liquid drained areas were physically removed from foam samples, generating results less dependent on sample geometry. Although the skin and the drained areas were removed, a density gradient was still apparent.

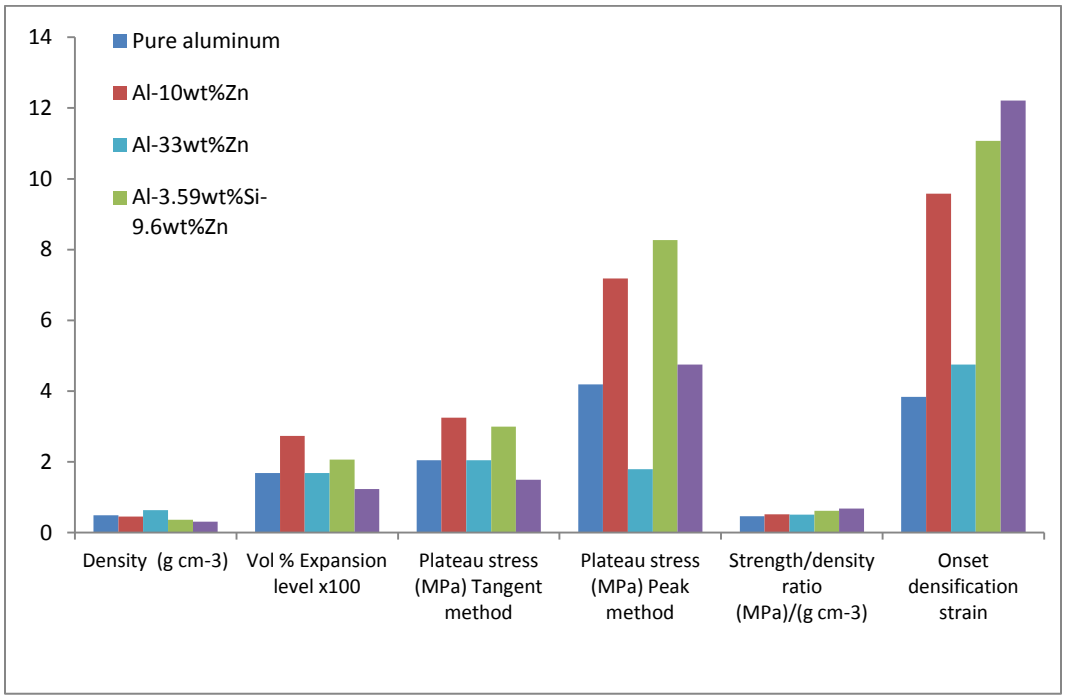

Figure 9-4: Pure aluminum, Al-10wt%Zn and Al-33wt%Zn mechanical property comparison

The energy absorption capability of the Al-33wt%Zn foam has a value of 4.75±2.42 kJ kg^{-1}, higher than pure aluminum at 3.84±1,14 kJ kg^{-1}. Although the value is higher, there is significant scatter in the results for the Al-33wt%Zn foams rendering it inferior due to its brittle nature. The calculated plateau stress, onset densification and efficiency are summarized in Table 9-1. Even if the Al-33wt%Zn foam display improved foam stability as shown in Table 7-5 and Figure 7-19 in comparison to pure aluminum, the stability is offset by poor mechanical properties.

Al-10wt%Zn foam stress-strain curves are shown in Figure 9-5 depicting smooth curves in contrast to the Al-33wt%Zn composition. Only a small variation between the samples in the curves is noticed. The curves can be characterized by a steady plateau strength increase up to the onset densification strain. The foams were produced at 710 ˚C at a foaming time of 510 s, corresponding to the point of maximum expansion as shown in Figure 7-20 and displayed in Figure 7-23

(representative sample). From the machining operation it was also noticed that unlike the Al-33wt%Zn composition, the alloy was fairly ductile although not as much as pure aluminum foam.

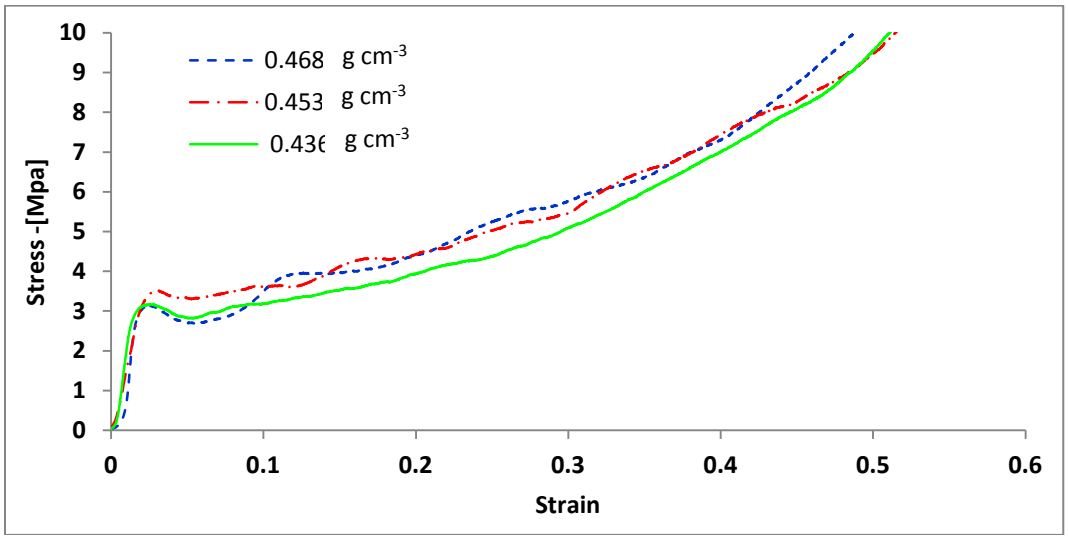

Figure 9-5: Stress-strain curves showing replicates for an Al-10wt%Zn foam produced at 710 °C and 8.5 minutes, using a constant compression strain rate of 10-3 s-1

A plateau stress of 3.25 ± 0.84 MPa was obtained using the peak method being superior to both pure aluminum at 2.05 ± 0.09 MPa and the Al-33wt%Zn alloy at 1.13 ± 0.55 MPa. Again, it could be observed during the compression tests that crushing took place from the top to the bottom of the foam indicative of a density gradient. The recorded plateau stress is related to the weakest section of the foam that starts to collapse first under compression. The efficiency is on average 40.00 ± 2.00%, which is comparable to that of pure aluminum. The onset of densification value of 0.52 ± 0.03 (based on the efficiency method) correlates with the Al-33wt%Zn and slightly higher than the pure aluminum foam. Mechanical property data for Al-10wt%Zn foam are summarized in Table 9-1. Figure 9-4 shows that the properties of the Al-10wt%Zn foam are far superior to both of pure aluminum and Al-33wt%Zn with only a small addition of zinc.

When looking at the energy absorption capability of the Al-10wt%Zn foam, it has a value of 9.58 ± 1.14 kJ kg^{-1} being almost three times that of pure aluminum (3.84 ± 0.31 kJ kg^{-1}) which is beneficial for energy absorption applications. This means this alloy is very strong, lightweight and at the same time having favorable pore characteristics.

The small gain in weight due to the addition of zinc is made up by the significant increase in mechanical properties. It is well known that 7xxx wrought and 7xx.x cast series aluminum alloys containing zinc are used for high strength applications. Typically, 7xxx series aluminum contain 1-8 wt% zinc with some low level of magnesium and therefore optimizing the foaming process using these low weight percent zinc values may be beneficial for production purposes [148].

9.3 Al-Si-Zn

Aluminum alloys containing silicon are generally used as wrought alloys for welding wire and brazing rods due to their low melting point, and for cast alloys due to their high fluidity [148]. In this case silicon was introduced in the alloy in the form of a pre-alloyed powder for stability related purposes. However, the addition of silicon in terms of mechanical properties has significant importance with regards to the foam.

Foams samples having a composition of Al-3.59wt%Si-9.6wt%Zn were prepared as described in the experimental procedure for mechanical testing. Samples were produced at 640 °C and 1500 s based on Figure 8-19 and shown in Figure 8-22 (representative sample). The compression stress-strain curves can be seen in Figure 9-6 and it is evident that there was a lower level of reproducibility between samples when compared to the pure aluminum in Figure 9-1 and Al-10wt%Zn system shown in Figure 9-5. Furthermore, it can be noted that there is a first maximum peak followed by a drop in the curves which tend to oscillate until

complete densification. This is the typical behavior of a brittle foam as outlined in literature [2, 13]. It could also be noticed during the machining operation that the Al-3.59wt%Si-9.6wt%Zn foams appeared to be quite brittle. However, although the foam stress-strain curves have a brittle behavior, they appear to have a higher densification strain than the pure aluminum and Al-Zn systems which confirms the fact that they have a more uniform cell structure. This is evident by looking at the definition of efficiency through Equation 3.3 [158, 177].

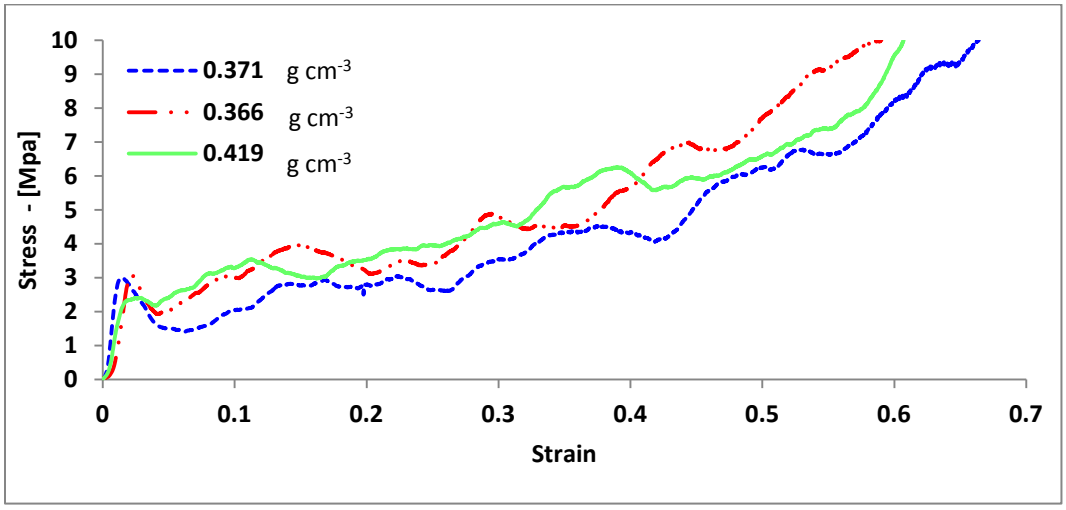

Figure 9-6: Al-3.59wt%Si-9.6wt%Zn stress-strain curves

The calculated values of density, plateau stress, efficiency, onset densification strain and energy absorption are summarized in Table 9-1. When comparing the densities of this particular foam, they are significantly lower than the other foams. In this case the average density of the foam is 0.36 g cm^{-3} compared to pure aluminum at 0.49 g cm^{-3} and the Al-10wt%Zn system at 0.45 g cm^{-3}. This is to be expected principally due to the higher foam expansion. Therefore, due to the difference in density it is harder to directly compare the mechanical properties strictly based on the particular foam. In order to have the densities correspond to each other, the amount of blowing agent and particle sizes would have to be altered. The foams produced in this thesis were therefore based on a fixed blowing agent ratio along with pressing parameters.

The plateau stress of the foams are at 2.03 ± 0.21 MPa and 2.85 ± 0.31 MPa for the tangent and peak method respectively in comparison to aluminum which is at 2.05 MPa and Al-10wt%Zn which is at 3.25 MPa for the peak method. By looking at these results it is noted that the Al-10wt%Zn is stronger, but at the same time denser. However, when the strength to density ratio is calculated, the Al-3.59wt%Si-9.6Zn is at 7.64 ± 1.28 (MPa)/(g cm^{-3}) while the Al-10wt%Zn stands at 7.19 ± 0.56 (MPa)/(g cm^{-3}). This means that on a weight basis the silicon alloy foam is stronger than the Al-10wt%Zn relative to density.

When looking at the onset densification strain, it is higher at an average of 0.61 ± 0.06 compared to the pure aluminum which is at 0.46 ± 0.02 and the Al-10wt%Zn at 0.52 ± 0.03. This again highlights the fact that the foam is more uniform in nature than the pure aluminum and Al-10wt%Zn, as the slope of the plateau stress is not as steep before reaching the densification strain. The summarized foam properties are shown in Figure 9-4.

Finally, comparing the energy absorption characteristics of the foams, the Al-3.59wt%Si-9.6wt%Zn value is at 10.58 ± 1.59 kJ kg^{-1} compared to pure aluminum at 3.84 ± 0.31 kJ kg^{-1} and Al-10wt%Zn at 9.58 ± 1.14 kJ kg^{-1}. The value obtained with the Al-3.59wt%Si-9.6wt%Zn system is close to the one obtained with the Al-10wt%Zn system but slightly higher. This would be beneficial in energy absorption applications as the foams are very light, strong and can absorb large quantities of energy.

The foam stress-strain curves for the Al-2.4wt%Si-9.7wt%Zn are depicted in Figure 9-7 and highlight the behavior of the foams. In this case foamed samples were produced at 660 ˚C and at a time of 1500 s as shown through Figure 8-20 and displayed in Figure 8-23 (representative sample). The stress-strain curves using this composition appear to be smoother than the Al-3.59wt%Si-9.6wt%Zn foams indicative of a more lightly alloyed composition with more ductility. It is

evident from the stress-strain curves and the density measurements that there is a large scatter in the data. It was also noticed during the machining and crushing operations that the foam was relatively ductile as opposed to the Al-33wt%Zn which was extremely brittle along with the Al-3.59wt%Si-9.6Wt%Zn foams.

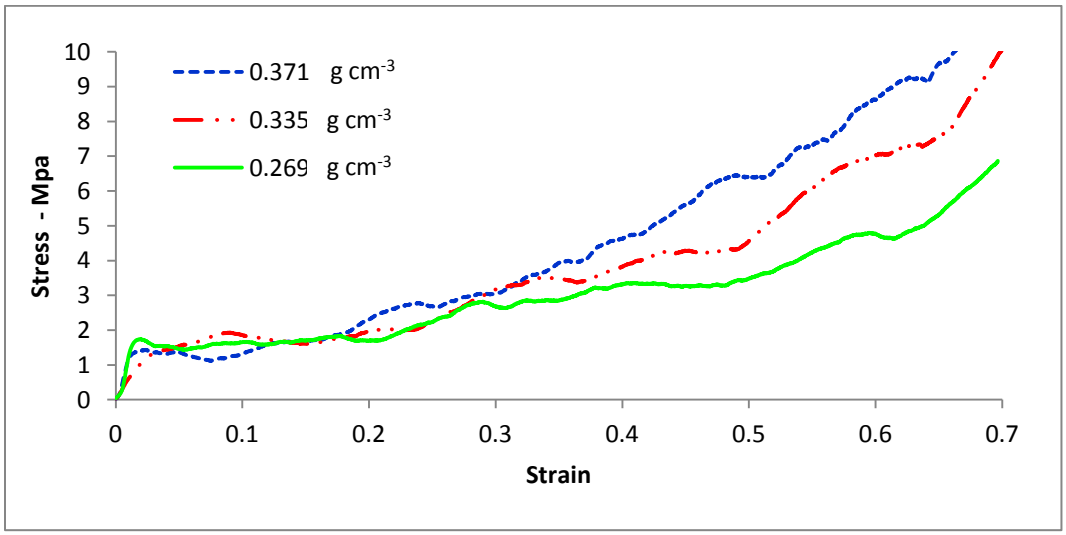

Figure 9-7: Al-2.4wt%Si-9.7wt%Zn stress-strain curves

The computed values for the mechanical properties are summarized in Table 9-1 for the Al-2.4wt%Si-9.7wt%Zn system. The density of the tested foams are slightly higher (0.38 ± 0.03 g cm^{-3}) than those having an Al-3.59wt%Si-9.6wt%Zn composition (0.36 ± 0.01 g cm^{-3}). On the other hand this value is significantly lower than the pure aluminum at 0.49±0.03 g cm^{-3} and the Al-10wt%Zn at 0.45 ± 0.02 g cm^{-3}. The lower density of the foamed alloy can be attributed to the slightly higher expansion in comparison to the Al-3.59wt%Si-9.6wt%Zn composition.

When looking at the plateau stresses of the foams, the tangent method results produced an average value of 1.23 ± 0.12 MPa compared to the peak method at 1.5 ± 0.17 MPa. These values are effectively lower than the pure aluminum at

2.05±0.09, the Al-10wt%Zn at 3.25±0.22 MPa and the Al-3.59wt%Si-9.6wt%Zn at 2.85±0.31 MPa using the peak method.

The onset densification strain in this particular case, is on average 0.68±0.03 being the highest of all foaming compositions which is very close to the value set on the compression machine of 0.7. The onset densification strain value of 0.68 ± 0.03 is significantly higher when compared to pure aluminum at 0.46 ± 0.02, Al-10wt%Zn at 0.52 ± 0.03 and the Al-3.59wt%Si-9.6wt%Zn at 0.61 ± 0.06. Lighter and more uniform foam will yield a higher densification strain. As the foams become lighter and the foam cell walls thinner, the thin cell walls also have more space to bend on each other which is another reason for the increased densification onset.

When comparing the energy absorption potential of the foam, the energy absorption potential of the Al-2.4wt%Si-9.7wt%Zn foam stands the highest at 12.21 ± 1.99 kJ kg^{-1}. This is comparable to the slightly lower values obtained for the Al-10wt%Zn system at 9.58 ± 1.14 kJ kg^{-1} and the Al-3.59wt%Si-9.6wt%Zn at 10.58 ± 1.59 kJ kg^{-1}. The lightweight, uniformity and high energy absorption potential of the foam would make it the most favorable in energy absorption applications.

9.4 Conclusions

Figure 8-2 shows that the Al-10wt%Zn, Al-2.4wt%Si-9.7wt%Zn and Al-3.59wt%Si-9.6wt%Zn foams all display favorable characteristic in terms of mechanical strength over pure aluminum and Al-33wt%Zn. However, the stability time for the Al-Si-Zn based foam is far superior to the Al-10wt%Zn foam and therefore this can be an important design consideration. Although Al-33wt%Zn foams showed favorable stability in terms of foam expansion, mechanical properties were very poor and indicative of brittle foam.

Compared to pure aluminum, an increase in plateau stress of 58 % was achieved with the Al-10wt%Zn alloy, a 39 % increase with the Al-3.59wt%Si-9.6wt%Zn composition and a 26% decrease with the Al-2.4wt%Si-9.7wt%Zn composition. When looking at the amount of energy absorption capacity of the alloys compared to pure aluminum, a gain of 148 % was made with the Al-10wt%Zn composition, a 175 % with the Al-3.59wt%Si-9.6wt%Zn alloy and a 218 % with the Al-2.4wt%Si-9.7wt%Zn composition.

10 Conclusions

The conclusions have been divided for each separate section of the results and discussion and are presented below.

10.1 Pure Aluminum

- In-situ observation of the pure aluminum foaming process revealed the formation of a porous crack network initiated at temperatures 50 ˚C below the melting point of pure aluminum. However, supporting expansion curves with sample temperature measurements reveal that the majority of the hydrogen is lost during the melting of the compact as a result of the high heat of fusion at 660 °C. Bulk expansion could only be initiated once the compact was fully melted.
- From this analysis it was concluded that, an alloy with a semi-solid region or the formation of a transient liquid phase would be beneficial in reducing hydrogen loss through the network of fissures. Alternatively, a higher heating rate would results in a reduced melting time enabling the encapsulation of more hydrogen.

10.2 Solid State Diffusion in Compacts

- The effect of zinc diffusion during hot pressing of the compacts was deemed insignificant. A measured diffusion interface of approximately 3 μm between aluminum and zinc is much less than the mean zinc powder size of 66 μm.
- It was determined that significant solid-state diffusion of zinc prior to the formation of the transient liquid phase formation at 381 °C during actual

foaming was not believed to be an influential factor during pressing at 350 °C.

- The analysis also showed that solid state diffusion of silicon in the aluminum matrix was negligible and much less important than zinc.

10.3 Al-Zn foams

- It was shown that an Al-94wt%Zn eutectic transient liquid phase is formed at 381°C corresponding to the lowest reported dehydrogenation temperature in literature and is initiated at the interface between the aluminum and zinc powder [20].

- The heating rate was sufficiently high not to prematurely dissolve the liquid phase (well above 60 °C s^{-1}). The formation of this transient liquid phase was shown to spread through the compact while simultaneously providing liquid for the uniform nucleation of pores.

- As opposed to cracks, the early pore formation displayed a round morphology throughout the foaming process. The lowered melting temperature (semi-solid) through alloying was favorable in increasing the heating flux into the foam resulting in a reduced melting time.

- The observed crack network formation in pure aluminum could be suppressed, directly resulting in higher expansion levels yielding a direct improvement of 229 % for Al-10wt%Zn foam produced at 710 °C. As opposed to cracks, the early pore formation displayed a spherical morphology throughout the foaming process. Moreover, the foaming temperature could be reduced by up to 60 °C, compared to pure aluminum for Al-33wt%Zn composition.

- A significant increase in post maximum expansion stability of the foam could be observed for zinc concentrations as low at 10 wt% in contrast to

pure aluminum. Expansion curves and pore analysis confirm the enhance stability, especially for the Al-33wt%Zn composition produced at 640 °C.

- It was shown that Al-33wt%Zn based foams have a post maximum expansion stability above 1000 s in contrast to pure aluminum foam produced at 750 °C is approximately 10 s. Al-10wt%Zn foams also display an extended stability of over 250 s when produced at 690 °C.

- The increased stability was attributed mainly to a combination of a lower surface tension of the alloys and to the evaporation of zinc creating a solid outer oxide shell through a DIMOX type reaction promoting overall stability and resistance to collapse.

- Zinc evaporation through the high surface area of the cell walls was also thought to have also contributed to the overall post maximum expansion stability supplying positive vapor pressure within the pores over the foaming period.

10.4 Al-Si-Zn Foams

- The foaming temperature could be lowered by 50 °C in comparison to Al-10wt%Zn and 90°C for pure aluminum through the addition of Al-12wt%Si pre-alloyed powder in conjunction with low levels of elemental zinc. Moreover, the density of the Al-Si-Zn alloys (Al-2.4wt%Si-9.7wt%Zn - 2.87 g $cm^{-1}$and Al-3.59wt%Si-9.6wt%Zn - 2.86 g cm^{-1}) could be lowered in contrast to the Al-33wt%Zn foam (3.40 g cm^{-1}) for an equivalent or higher expansion level.

- It is shown that the nucleation of pores was initiated at the centre of the elemental zinc particles similarly to the Al-Zn foams which formed a eutectic liquid at 381 °C. It was also revealed a ternary liquid was formed at 551 °C enabling an overall reduction in the semi-solid region onset temperature. As a result the fissure network formation was suppressed similarly to the Al-Zn system.

- The Al-Si-Zn alloys demonstrated high levels of expansion above 350 vol% and increased foam stability over an extended period of time of 600 s for the Al-2.4wt%Si-9.7wt%Zn and above 1000 s for the Al-3.59wt%Si-9.6wt%Zn foams. For a lower expansion level, the pure aluminum foam displayed a stability time of approximately 10 s.

- Pore size analysis of Al-Si-Zn based foams showed low levels of pore coarsening and degradation over a period of time of 300 s being beneficial for larger complex geometries.

- The overall enhanced post maximum expansion stability of the foam is attributed to a lowered surface tension through the addition of zinc and silicon. Although both zinc and silicon lower the viscosity of aluminum at a given temperature, the reduction in foaming temperature yield a fairly constant viscosity.

- A DIMOX reaction is believed to help enhance the foam stability via the formation of a thick outer oxide shell on the foam.

10.5 Mechanical Properties

- It was shown that the Al-10wt%Zn, Al-2.4wt%Si-9.7wt%Zn and Al-3.59wt%Si-9.6wt%Zn foam all display favorable characteristics in terms of mechanical strength over pure aluminum and Al-33wt%Zn.

- Although Al-33wt%Zn foams showed favorable stability in terms of foam expansion, mechanical properties were very poor and indicative of brittle foam.

- Compared to pure aluminum, an increase in plateau stress of 58 % was achieved with the Al-10wt%Zn alloy, a 39 % increase with the Al-3.59wt%Si-9.6wt%Zn composition and finally a 26 % decrease with the Al-2.4wt%Si-9.7wt%Zn composition.

- When looking at the amount of energy absorption capacity of the alloys, a gain of 148 % was made with the Al-10wt%Zn composition, a 175 % with the Al-3.59wt%Si-9.6wt%Zn alloy and a 218 % with the Al-2.4wt%Si-9.7 wt%Zn composition.

This page is intentionally left blank

11 Contributions to Original Knowledge

The contributions to original knowledge related to the foam compositions studied will be presented below. More specifically, these contributions pertain to the suppression of crack formation observed in pure aluminum foams with the use of a transient liquid phase as an effective melting point depressant and hence eliminating crack formation.

- The analysis of the pure aluminum foaming process revealed the formation of a porous crack network 50 ˚C below the melting point of pure aluminum through in-situ confocal microscopy. The foaming steps were correlated to expansion curves and microscopy clearly detailing the underlying mechanisms necessary for improvement. The analysis revealed that the bulk of hydrogen loss was during the melting of pure aluminum rather than to prior crack formation.

- The Al-Zn system was assessed for the first time starting from a low (10 wt%), medium (33 wt%) to high concentration (50 wt%) of zinc for its feasibility in forming an effective transient liquid phase. The results reveal the formation of a transient liquid eutectic phase at 381 ˚C observed under in-situ conditions. The formation of this transient liquid phase enabled the encapsulation of hydrogen at the early stages of foaming while suppressing the fissure network observed in pure aluminum.

- With the use of a transient liquid phase based on elemental zinc powders, uniform pore nucleation was demonstrated for the first time, initiated at the center of the zinc particles in contrast to a network of fissures formed in pure aluminum and other high melting temperature alloys.

- It was demonstrated that the addition of both zinc and silicon to aluminum have favorable physical properties such as surface tension and viscosity.

This resulted in superior stability compared to pure aluminum displayed through expansion characteristics and pore analysis showing reduced levels of foam degradation.

- It was shown that the use of pre-alloyed Al-12wt%Si powder along with elemental zinc produced an effective combination of a transient liquid and semi-solid phase. As a result a light alloy yielding high levels of expansion and good pore characteristics was obtained.

- The mechanical properties of the studied systems were characterized for the first time and compared to pure aluminum. The alloys presented mechanical properties and stability which are far superior to those of pure aluminum.

12 Future Work

The future work pertaining to the formation of a transient liquid phase for foam stability is presented below.

- The addition of pre-alloyed Al-33wt%Cu eutectic to pure aluminum in a compact should assessed as a potential candidate for an effective transient liquid phase possibly coupled with zinc.

- The developed systems should be coupled with treated TiH_2 blowing agent in order to minimize the temperature gap between the gas release and the alloy melt temperature. For example, Al-Si-Zn foams could be coupled with the nickel coated TiH_2 particles developed by Proa-Flores [1, 33].

- The DIMOX type reaction should be investigated more thoroughly and its effects on foaming and the formation of oxides.

- The use of different and more effective blowing agents other than TiH_2 should be explored such as carbonates or possibly combustible organic compounds for the creation of highly porous metallic media.

- The use of lubricants such as polyethylene glycol (PEG) in the powder compaction process should be explored as a possibility of omitting the hot compactions stage, saving manufacturing related costs.

This page is intentionally left blank

13 References

[1] P. M. Proa-Flores, "Aluminum foams fabricated be the PM route using nickel-coated titanium hydride powders of controlled particle sizes," Ph.D, Mining and Materials Engineering, McGill, 2010.

[2] M. F. Ashby, A. Evans, N. A. Fleck, L. J. Gibson, J. W. Hutchinson, and H. N. G. Wadley, *Metal Foams: A Design Guide*: Butterworth-Heinemann, 2000.

[3] J. Banhart, "Aluminium Foams for Lighter Vehicles," *International Journal of Vehicle Design,* vol. 37, p. 114, 2005.

[4] A. R. Kennedy, "Effect of compaction density on foamability of Al-TiH2 powder compacts," *Powder Metallurgy,* vol. 45, 2002.

[5] D. I. Baumgärtner F., Banhart J. , "Industrialization of Powder Compact Toaming Process," *Advanced Engineering Materials,* vol. 2, pp. 168-174, 2000.

[6] F. von_Zeppelin, M. Hirscher, H.Stanzick, and J. Banhart, "Desorption of hydrogen from blowing agents used for foaming metals," *Composites Science and Technology,* vol. 63, pp. 2293-2300, 2003.

[7] A. R. Kennedy, "The effect of TiH2 heat treatment on gas release and foaming in Al-TiH2 preforms," *Scripta Materialia,* vol. 47, pp. 763-767, 2002.

[8] B. Matijasevic and J. Banhart, "Improvement of aluminium foam technology by tailoring of blowing agent," *Scripta Materialia,* vol. 54, pp. 503-508, 2006.

[9] F. Baumgärtner, I. Duarte, and J. Banhart, "Industrialization of Powder Compact Foaming Process," *Advanced Engineering Materials,* vol. 2, pp. 168-174, 2000.

[10] J. Banhart, H. Stanzick, L. Helfen, and T. Baumbach, "Metal foam evolution studied by synchrotron radioscopy,," *Applied physics letters,* vol. 78, pp. 1152-1154 2001.

[11] L. Helfen, T. Baumbach, H. Stanzick, J. Banhart, A. Elmoutouakkil, and P. Cloetens, "Viewing the early stages of metal foam formation by computed tomography using synchrotron radiation," *Advanced Engineering Materials,* vol. 4, pp. 808-813, 2002.

[12] D. Weaire and S. Hutzler, *The Physics of Foams*. Oxford: Clarendon Press, 1999.

[13] L. J. Gibson and M. F. Ashby, *Cellular Solids*, 2 ed. Cambridge: Cambridge University Press, 1997.

[14] J. Banhart, "Manufacture, characterisation and application of cellular metals and metal foams," *Progress in Materials Science,* vol. 46, pp. 559-632, 2001.

[15] J. Banhart, "Metal Foams: Production and Stability," *Advanced Engineering Materials,* vol. 8, pp. 781-794, 2006.

[16] *Handbook of cellular metals*. Weinheim: WILEY-VCH, 2002.

[17] E. Maine and M. F. Ashby, "Cost Estimation and the Viability of Metal foams," *Advanced Engineering Materials,* vol. 2, pp. 205-209, 2000.

[18] A. Irretier and J. Banhart, "Lead and Lead Alloys," *Acta Materialia,* vol. 53, pp. 4903-4917, 2005.

[19] P. Schaffler and W. Rajner, "Process Stability in Serial Production of Aluminum Foam Panels and 3D Parts," *Advanced Engineering Materials,* vol. 6, pp. 452-452, 2004.

[20] I. Duarte and J. Banhart, "A study of aluminium foam formation--kinetics and microstructure," *Acta Materialia,* vol. 48, pp. 2349-2362, 2000.

[21] S. Asavavisithchai and A. Kennedy, "The Effect of Compaction Method on the Expansion and Stability of Aluminum foam," *Advanced Engineering Materials,* vol. 8, pp. 810-815, 2006.

[22] S. Asavavisithchai and A. R. Kennedy, "The Role of Oxidation During Compaction on the Expansion and Stability of Al Foams Made Via a PM Route (Adv. Eng. Mater. 6/2006)," *Advanced Engineering Materials,* vol. 8, 2006.

[23] A. Ibrahim, C. Körner, and R. F. Singer, "The Effect of TiH2 Particle Size on the Morphology of Al-Foam Produced by PM Process," *Advanced Engineering Materials,* vol. 10, pp. 845-848, 2008.

[24] T. Nakamura, S. VGnyloskurenko, K. Sakamoto, A. V. Byakova, and R. Ishikawa, "Developpement of new foaming agent for metal foam," *Materials Transations,* vol. 43, pp. 1191-1196, 2002.

[25] J. P. Sanders and P. K. Gallagher, "Kinetic analyses using simultaneous TG/DSC measurements," *Journal of Thermal Analysis and Calorimetry,* vol. 82, pp. 659-664, 2005.

[26] D. Lehmhus and G. Rausch, "Tailoring Titanium Hydride Decomposition Kinetics by Annealing in Various Atmospheres," *Advanced Engineering Materials,* vol. 6, pp. 313-330, 2004.

[27] D. Yang and B. Hur, "The relationship between thermal decomposition properties of titanium hydride and the Al alloy melt foaming process," *Materials Letters,* vol. 60, pp. 3635-3641, 2006.

[28] C.-J. Yu, H. H. Eifert, J. Banhart, and J. Baumeister, "Metal foaming by a powder metallurgy method: Production, properties and applications," presented at the Innovations in Materials Conference (IMC), Washington D.C., 1998.

[29] L.N. Padurets , Z. V. Dobrokhotova, and A. L. Shilov, "Transformations in titanium dihydride phase," *International Journal of Hydrogen Energy,* vol. 24, pp. 153-156, 1999.

[30] V. A. Lavrenko, V. Z. Shemet, S. K. Dolukhanyan, A. M. Kalinichenko, and I. N. Frantesevich, "Dokl Akad Nauk SSSR," vol. 262, pp. 136-139, 1982.

[31] H. Stanzick, M. Wichmann, J. Weise, L. Helfen, T. Baumbach, and J. Banhart, "Process Contron in Aluminum Foam Production Using Real-Time X-ray Radioscopy," *Advanced Engineering Materials,* vol. 4, pp. 814-823, 2002.

[32] V. Gergely and B. Clyne, "Drainage in standing liquid metal foams: modelling and experimental observations," *Acta Materialia,* vol. 52, pp. 3047-3058, 2004.

[33] P. M. Proa-Flores and R. A. L. Drew, "Production of Aluminum Foams with Ni-coated TiH2 Powder," *Advanced Engineering Materials,* vol. 10, pp. 830-834, 2008.

[34] A. J. Wilson, *Foams: Physics, Chemistry and Structure*. York: Springer-Verlag 1989.

[35] R. J. Pugh, "Foaming, foam films, antifoaming and defoaming," *Advances in Colloid and Interface Science,* vol. 64, pp. 67-142, 1996.

[36] J. Banhart, "Metal Foams: the Mystery of Stabilization," presented at the MetFoam 2005, Kyoto, Japan, 2005.

[37] E. Ozcivici and R. P. Singh, "Fabrication of Ceramic Foams Based on Silicon Carbide Matrix and Hollow Alumino Spheres," *Journal of the American Ceramic Society,* vol. 88, pp. 3338-3345, 2005.

[38] G. Gottstein, *Physical foundations of materials science*. Berlin: Springer-Verlag, 2004.

[39] D. Exerowa and P. M. Kruglyakov, *Foam and Foam Films* vol. 5. Amsterdam: Elsevier Science, 1998.

[40] A. Haibel, A. Rack, and J. Banhart, "Why are metal foams stable," *Applied physics letters,* vol. 89, 2006.

[41] C. Körner and R. F. Singer, "Processing of Metal Foams - Challenges and Opportunities," *Advanced Engineering Materials,* vol. 2, pp. 159-165, 2000.

[42] D. R. Lide, *Handbook of solubility parameters and other cohesion parameters* 77th ed.: CRC, 1996.

[43] T. Iida and R. I. L. Guthrie, *The physical properties of liquid metals*. Oxford: Oxford University Press, 1988.

[44] C. Koerner, *Integral Foam Molding of Light Metal*. Berlin: Springer-Verlag, 2008.

[45] "In situ optical measurement of liquid drop surface tension in gas metal arc welding," *J. Phys. D: Appl. Phys.,* vol. 31, pp. 1963-1967, 1998.

[46] b. J. Keene, "Review of data for the surface tension of pure metals," *International Materials Review,* vol. 38, pp. 157-192, 1993.

[47] D. M. Jacobson and G. Humpston, *Principles of Brazing*. Materials Park, Ohio: ASM International, 2005.

[48] M. M. Schwartz, *Brazing*, 2003.

[49] C. C. Yang and H. Nakae, "The effects of viscosity and cooling conditions on the foamability of aluminum alloy," *Journal of Materials Processing Technology,* vol. 141, pp. 202-206, 2003.

[50] H. J. Luo, X. M. Zhang, and Y. H. Liu, "Study on method of increasing viscosity in fabricating aluminum foam," in *Light metals 2005*, 2005.

[51] Z. L. Song, L. Q. Ma, Z. J. Wu, and D. P. He, "Effects of viscosity on cellular structure of foamed aluminum in foam process," *Journal of Materials Science,* vol. 35, pp. 15-20, 2000.

[52] B. Y. Hur, S. H. Park, and A. Hiroshi, "Viscosity and surface tension of Al and effects of additional elements," *Material Science Forum,* vol. 2006, pp. 51-56, 2003.

[53] C. Korner, M. Arnold, and R. F. Singer, "Metal foam stabilization by oxide network particles," *Materials Science and Engineering A,* vol. 396, pp. 28-40, 2005.

[54] B. P. Binks, "Particles as surfactants--similarities and differences," *Current Opinion in Colloid & Interface Science,* vol. 7, pp. 21-41, 2002.

[55] S. W. Ip, Y. Wang, and J. M. Toguri, "Aluminum Foam Stabilization by Solid Particles," *Canadian Metallurgical Quarterly,* vol. 38, pp. 81-92, 1997.

[56] G. Kaptay, "Interfacial criteria for stabilization of liquid foams by solid particles," *Colloids and Surfaces A: Physicochemical and Engineering Aspects,* vol. 230, pp. 67-80, 2003.

[57] G. Kaptay, "On the equation of the maximum capillary pressure induced by solid particles to stabilize emulsions and foams and on the emulsion stability diagram," *Colloids and Surfaces A: Physiochem. Eng. Aspects,* vol. 282-283, pp. 387-401, 2006.

[58] S. H. Park, Y.-S. Um, C. H. Kum, and B. Y. Hur, "Thermophysical properties of Al and Mg alloys for metal foam fabrication," *Colloids and Surfaces A: Physicochem. Eng. Aspects,* vol. 263, pp. 280-283, 2005.

[59] A. R. Kennedy and S. Asavavisitchai, "Effects of TiB2 particle addition on the expansion, structure and mechanical properties of PM Al foams," *Scripta Materialia,* vol. 50, pp. 115-119, 2004.

[60] G. Johansson and R. J. Pugh, "The influence of particle size and hydrophobicity on the stability of mineralized froths," *International Journal of Mineral Processing,* vol. 34, pp. 1-21, 1992.

[61] Y. Q. Sun and T. Gao, "The optimum wetting angle for the stabilization of liquid-metal foams by ceramic particles: experimental simulation," *Metallurgical and Materials Transactions A* vol. 33 A, pp. 3285-3292, 2002.

[62] S. Esmaeelzadeh, A. Simchi, and D. Lhemus, "Effects of ceramic particle addition on the foaming behaviour, cell structure and mechanical properties of P/M AlSi7 foam," *Materials Science and Engineering A,* vol. 424, pp. 290-299, 2006.

[63] A. R. Kennedy and S. Asavavisithchai, "Effect of ceramic particle additions on foam expansion and stability in compacted Al-TiH2 powder precursor," *Advanced Engineering Materials,* vol. 6, pp. 400-402, 2004.

[64] S. Asavavisithchai and A. R. Kennedy, "The effect of Mg addition on the stability of Al-Al2O3 foams made by a powder metallurgy route," *Scripta Materialier,* vol. 54, pp. 1331-1334, 2006.

[65] N. Babcsan, D. Leitlmeier, and J. Banhart, "Metal foams-high temperature colloids Part I. Ex situ analysis of metal foams," *Colloids and Surfaces A: Physicochemical and Engineering Aspects,* vol. 261, pp. 123-130, 2005.

[66] T. Wubben and S. Odenbach, "Stabilisation of liquid metallic foams by solid particles," *Colloids and Surfaces A: Physiochem. Eng. Aspects,* vol. 266, pp. 207-213, 2005.

[67] T. Wubben, H. Stanzick, J. Banhart, and S. Odenbach, "Stability of metallic foams studied under microgravity," *Journal of Physics: Condensed Matter,* vol. 14, pp. S-427-S433, 2003.

[68] F. Garcia-Moreno, P. Holm, and J. Banhart, "Metallic foam experiments under microgravity," *European Space Agency,* vol. 647SP, pp. 389-392, 2007.

[69] S. Asavavisithchai and A. R. Kennedy, "Effect of powder oxide content on the expansion and stability of PM-route Al foams," *Journal of Colloid and Interface Science,* vol. 297, pp. 715-723, 2006.

[70] A. Dudka, F. Garcia-Moreno, N. Wanderka, and J. Banhart, "Structure and distribution of oxides in aluminum foam," *Acta Materialia,* vol. 56, pp. 3990-4001, 2008.

[71] F. García-Moreno, A. Rack, L. Helfen, T. Baumbach, S. Zabler, N. Babcsán, J. Banhart, T. Martin, C. Ponchut, and M. D. Michiel, "Fast processes in liquid metal foams investigated by high-speed synchrotron x-ray microradioscopy," *Applied physics letters,* vol. 92, p. 134104, 2008.

[72] C. Korner, "Foam formation mechanisms in particle suspensions applied to metal foams," *Materials Science and Engineering A,* vol. 495, pp. 227-235, 2008.

[73] C. Körner, F. Berger, M. Arnold, C. Stadelmann, and R. F. Singer, "Influence of processing conditions on morphology of metal foams produced from metal powder " *Materials Science and Technology,* vol. 16, pp. 781-784, 2000.

[74] G. J. Davies and S. Zhen, "Metallic foams: their production, properties and applications," *Journal of Materials Science,* vol. 18, pp. 1899-1911, 1983.

[75] J. Kovcik and F. Simancik, "Comparison of zinc and aluminum foam behavior," *Kovove Materialy,* vol. 42, pp. 79-90, 2004.

[76] J. Banhart and D. Weaire, "On the road again: Metal foams find favor,," *Physics Today,* pp. 37-42, 2002.

[77] J. Banhart, "Foam Metal: The Recipe," *Europhysics News,* vol. 30, 1999.

[78] P. H. Thornton and C. L. Magee, "Deformation characteristics of zinc foam," *Metallurgical Transactions A,* vol. 6A, pp. 1801-1807, 1975.

[79] J. Banhart, D. Bellmann, and H. Clemens, "Investigation of metal foam formation by microscopy and ultra small-angle neutron scaterring" *Acta Materialia,* vol. 49, pp. 3409-3420, 2001.

[80] M. Saadatfar, F. Garcia-Moreno, S. Hutzler, A. P. Sheppard, M. A. Knackstedt, J. Banhart, and D. Weare, "Imaging of metallic foams using X-ray micro-CT," *Colloids and Surfaces A: Physicochemical and Engineering Aspects,* vol. 344, pp. 107-112, 2009.

[81] J. Banhart and J. Baumeister, "Deformation characteristics of metal foams," *Journal of Materials Science,* vol. 33, pp. 1431-1440, 1998.

[82] K.-T. Park, W.-J. Kim, and D.-H. Shin, "Analysis of a superplastic Zn-22% Al eutectoid," *Materials Science and Engineering A,* vol. 322, pp. 159-166, 2002.

[83] R. I. Todd, "Grain Boundary Tension Induced Strain Recovery Following Superplastic Flow," *Acta Metallurgica et Materialia,* vol. 42, pp. 2921-2928, 1994.

[84] K. Kitazono and Y. Takiguchi, "Strain rate sensitivity and energy absoption of Zn-22Al foams," *Scripta Materialia,* vol. 55, pp. 501-504, 2006.

[85] J. Kováčik and F. Simančík, "Use of zinc foam for filling of hollow steel profiles," in *MetFoam 2001*, Bremen, Germany, 2001.

[86] M. Yin, A. Zavaliangos, and R. Doherty, "Evolution of foaming in Al-Si through the semi solid state," presented at the TMS 2000 St. Louis, MO; USA, 2000.

[87] B. Kriszt, P. Cekan, and K. Faure, "Foamability of the Al-Si system," presented at the Cellular metals and metal foaming technology, Bremen, Germany, 2001.

[88] F. Simancik, K. Behulova, and L. Bors, "Effect of ambient atmosphere on the foam expansion," in *Metfoam 2001*, 2001.

[89] C. Korner, M. Hirschmann, V. Brautigam, and R. F. Singer, "Endogenous particle stabilization during magnesium integral foam production," *Advanced Engineering Materials,* vol. 6, 2004.

[90] J. Goicoechea, C. Garcia-Cordovilla, E. Louis, and A. Pamies, "Surface tension of binary and ternary aluminium alloys of the systems Al-Si-Mg and AI-Zn-Mg" *Journal of Materials Science,* vol. 27, pp. 5247-5252, 1992.

[91] J. W. Taylor, "The surface tension of liquid-metal solutions," *Acta Metallurgical,* vol. 4, pp. 460-468, 1956.

[92] N. D. Karsu, S. Yuksel, and M. Guden, "Foaming behaviour of Ti6Al4V particle-added aluminum powder compacts," *Journal of Materials Science,* vol. 44, pp. 1494-1505, 2009.

[93] R. E. Raj and B. S. S. Daniel, "Manufacturing challenges in obtaining tailor-made closed-cell structures in metallic foams," *International Journal of Manufacturing Technology,* vol. 38, pp. 605-612, 2008.

[94] R. E. Raj and B. S. S. Daniel, "Structural and compressive property correlation of closed-cell aluminum foams," *Journal of Alloys and Compounds,* vol. 467, pp. 550-556, 2009.

[95] M. Kobashi and N. Kanetake, "Processing of intermetallic foam by combustion reaction," *Advanced Engineering Materials,* vol. 4, pp. 745-747, 2002.

[96] M. Kobashi, N. Kanetake, and K. Kudo, "Self-Sustainable Blowing Process of Al-Ni Intermetallic Foam by Combustion Reaction," presented at the Metfoam 2007, Montreal, 2007.

[97] N. Kanetake and M. Kobashi, "Innovative processing of porous and cellular materials by chemical reaction," *Scripta Materialia,* vol. 54, pp. 521-525, 2006.

[98] M. Kobashi and N. Kanetake, "Self-Blowing Process of Al Foam Assisted by Exothermic Reaction," *Material Science Forum,* vol. 519-521, pp. 1335-1340, 2006.

[99] M. H. Sloboda, "Design and Strength of Brazed Joint," *Welding and Metal Fabrication,* 1961.

[100] W. F. Gale and D. A. Butts, "Transient liquid phase bonding," *Science & Technology of Welding & Joining,* vol. 9, pp. 283-300, 08 2004.

[101] W. D. MacDonald and T. W. Eagar, "Transient liquid phase bonding," *Annual Review of Materials Science,* vol. 22, pp. 23-46, 1992.

[102] R. S. Timsit and B. J. Janeway, "A novel brazing technique for aluminum and other metals," *Journal of Materials Research,* vol. 8, pp. 2749-2753, 1993.

[103] L. C. Tsao, W. P. Weng, M. D. Cheng, C. W. Tsao, and T. H. Chuang, "Brazeability of a 3003 Aluminum Alloy With Al-Si-Cu-Based Filler Metals," *Journal of Materials Engineering and Performance,* vol. 11, pp. 360-364, 2002.

[104] N. Bredzs and W. Rostoker, "Method and Composition for Exothermic Fluxless Brazing of Aluminum and Aluminum Base Alloys," 1968.

[105] K. Suzuki, M. Kagayama, and Y. Takeuchi, "Eutectic Phase Equilibrium of Al-Si-Zn System and Its Applicability for Lower Temperature Brazing," *Journal of the institute of light metals,* vol. 43, 1993.

[106] Zaluzec, "Thin film brazing of aluminum shapes," United States Patent, 1995.

[107] H. Kudo, H. Saito, and K. Toma, "Composition for Brazing Aluminum or Aluminum Alloy and An Aluminum Alloy Produc," United States Patent, 1991.

[108] A. Bartoszak, "Brazing Aluminum Based Parts," United States Patent, 1966.

[109] R. S. Timsit and B. J. Janeway, "Aluminum Brazing Sheet," United States Patent, 1993.

[110] W. F. Gale and D. A. Butts, "Transient liquid phase bonding," *Science and Technology of Welding and Joining,* vol. 9, pp. 283-300, 2004.

[111] A. A. Shirzadi and E. R. Wallach, "Nevv approaches for transient liquid phase diffusion bonding of aluminiumbased metal matrix composites " *Material Science and Technology,* vol. 13, pp. 135-142, 1997.

[112] J. R. Askew, J. F. Wilde, and T. I. Khan, "Transient liquid phase bonding of 2124 aluminium metal matrix cOl11posite," *Material Science and Technology,* vol. 14, pp. 920-924, 1998.

[113] Z. Li, W. Fearis, and T. H. North, "Particulate segregation and mechanical properties in transient liquid phase bonded metal matrix composite material," *Material Science and Technology,* vol. 11, pp. 363-369, 1995.

[114] B. McGurran and M. G. Nicholas, "A study of aluminum brazes using hot-stage scanning electron microscopy," *Journal of materials science,* vol. 19, pp. 2713-2718, 1984.

[115] R. A. Ricks, P. J. Winkler, M. Jroclossa, and R. Grimes, "Bonding of Al-Li alloys has been performed using roll clad zinc as an interface layer in order to overcome the tenacious oxide layer," in *Proceedings of the Conference on Aluminium Lithium Alloys V*, 1989, p. 447.

[116] R. M. German, P. Suri, and S. J. Park, "Review: liquid phase sintering," *Journal of Materials Science,* vol. 44, pp. 1-39, 2009.

[117] D. S. Wilkinson, *Mass transport in solids and fluids*: Cambridge University Press, 2000.

[118] R. M. German, *Liquid Phase Sintering*. New York: Plenum Publishing Corporation, 1985.

[119] R. M. German, S. Farooq, and C. M. Kipphut, "Kinetics of liquid sintering," *Materials Science and Engineering: A,* vol. 105-106, pp. 215-224, 1988.

[120] R. N. Lumley and G. B. Schaffer, "The effect of solubility and particle size of liquid phase sintering," *Scripta Materialia,* vol. 35, pp. 589-595, 1996.

[121] G. B. Schaffer, T. B. Sercombe, and R. N. Lumley, "Liquid phase sintering of aluminium alloys," *Materials Chemistry and Physics,* vol. 67, pp. 85–91, 2001.

[122] G. N. Romanov, "LiquidPhase Sintering of AluminumBased Powder Alloys," *Russian Journal of Non-Ferrous Metals,* vol. 51, pp. 347-351, 2010.

[123] R. N. Lumley and G. B. Schaffe, "Anomalous Pore Morphologies in Liquid-Phase-Sintered Al-Zn alloys," *Metallurgical and Materials Transactions A,* vol. 30A, pp. 1682-1685, 1999.

[124] (2010). *Cymat website*. Available: http://www.cymat.com/

[125] R. Brezny and D. J. Green, "Characterization of edge effects in cellular materials," *Journal of Materials Science,* vol. 11, pp. 4571-4578, 1990.

[126] Y. Sugimura, J. Meyer, M. Y. He, H. Bart-Smith, J. Grenstedt, and A. G. Evans, "On the mechanical performance of closed cell Al foams," *Acta Metallurgica,* vol. 45, pp. 5245-5259, 1997.

[127] A.-F. Bastawros, "Experimental analysis of deformation mechanisms in a closed-cell aluminum alloy foam," *Journal of the Mechanics and Physics of Solids,* vol. 48, pp. 301-322, 2000.

[128] P. R. Onck, E. W. Andrews, and L. J. Gibson, "Size effects in ductile cellular solids. Part I: modeling," *International Journal of Mechanical Sciences,* vol. 43, pp. 681-699, 2001.

[129] Y. Chino, M. Mabuchi, Y. Yamada, S. Hagiwara, and H. Iwasaki, "An experimental investigation of effects of specimen size parameters on

compressive and tensile properties in a closed cell aluminum foam," *Materials Transations,* vol. 44, pp. 633-636, 2003.

[130] I. Jeon and T. Asashina, "The effect of structural defects on the compressive behavior of closed-cell Al foam," *Acta Materialia,* vol. 53, pp. 3415-3423, 2005.

[131] K. Y. G. McCullough, N. A. Fleck, and M. F. Ashby, "Uniaxial stress-strain behaviour of aluminium alloy foams," *Acta Materialia,* vol. 47, pp. 2323-2330, 1999.

[132] E. W. Andrews, G. Gioux, P. Onck, and L. J. Gibson, "Size effects in ductile cellular solids. Part II: experimental results," *International Journal of Mechanical Sciences,* vol. 43, pp. 701-713, 2001.

[133] G. E. Dieter, *Mechanical Metallurgy*, 2nd ed.: McGraw-Hill, 1976.

[134] V. S. Deshpande and N. A. Fleck, "High strain rate compressive behaviour of aluminum alloy foams," *International Journal of Impact Engineering,* vol. 24, pp. 277-298, 2000.

[135] P. J. Tan, J. J. Harrigan, and S. R. Reid, "Inertia effects in uniaxial dynamic compression of a closed cell aluminum foam," *Material Science and Technology,* vol. 18, pp. 480-488, 2002.

[136] A. Paul and U. Ramamurty, "Strain rate sensitivity of a closed-cell aluminum foam," *Material Science and engineering A,* vol. 281, pp. 1-7, 2000.

[137] T. Mukai, H. Kanahashi, M. Mabuchi, T. G. Nieh, and K. Higashi, "Experimental study of energy absorption in a closed-celled aluminum foam under dynamic loading," *Acta Metallurgica,* vol. 48, pp. 921-927, 1999.

[138] T. Hamada, H. Kanahashi, T. Miyoshi, and N. Kanetake, "Effects of the strain rate and alloying on the compression characteristics of closed cell aluminum foams," *Materials Transactions,* vol. 50, pp. 1418-1425, 2009.

[139] R. Montanini, "Measurement of strain rate sensitivity of aluminum foams for energy dissipation," *International Journal of Mechanical Sciences,* vol. 47, pp. 26-42, 2005.

[140] J. Gassan and W. Harwick, "Behavior of aluminum foams under quasi-static and crash loadings," *Journal of Materials Science Letters,* vol. 20, pp. 1047-1048, 2001.

[141] D. Lehmhus and M. Busse, "Potential New Matrix Alloys for Production of Pm Aluminum Foams," *Advanced Engineering Materials,* vol. 6, pp. 391-396, 2004.

[142] A. R. Kennedy, "Evolution of foam structure during the heating of extruded Al-Si-TiH2 powders," *Journal of Materials Science Letters,* vol. 21, pp. 1555-1557, 2002.

[143] N. Kanetake, M. Kobashi, and S. Tsuda, "Foaming behavior of Aluminum precursor produced from machined chip waste," *Advanced Engineering Materials,* vol. 10, pp. 840-844, 2008.

[144] W. F. Gale, T.C.Totemeier, and C. J. Smithells, *Smithells Metals Reference Book*, 8th Edition ed.: Elsevier, 2004.

[145] G. B. Schaffer, T. B. Sercombe, and R. N. Lumley, "Liquid phase sintering of aluminium alloys," *Materials Chemistry and Physics,* pp. 85-91, 2001.

[146] A. Schneider and E. K. Stoll, "The vapor pressures of zinc over Aluminum-Zinc alloys," *Ztschr. Elektrochem.,* vol. 47, pp. 527-535, 1941.

[147] D. R. Lide, *Handbook of Chemistry and Physics*, 77th ed.: CRC, 1996.

[148] *Metals Handbook Desk Edition*, 2 ed.: ASM International, 1998.

[149] W. R. D. Jones and W. L. Bartlett, "The viscosity of aluminum and binary aluminum alloys," *Journal of the Institute of Metals,* vol. 81, pp. 145-152, 1952-1953.

[150] W.F Gale, *Smithells Metals Reference Book*, 8th Edition ed.: Elsevier, 2004.

[151] P. R. Sharps, A. P. Tomsia, and J. A. Park, "Wetting and spreading in the Cu-Ag system," *Acta Metallurgica,* vol. 29, pp. 855-865, 1981.

[152] Spherical Aluminum Silicon Powder [Online].

[153] F. Jalilian, "Zn and Al-Zn foams (internal report)," McGill University, Montreal 2007.

[154] LECO. (2010). *Nitrogen/Oxygen Determination by Gas Fusion* Available: http://www.leco.com/products/inorganic/nitrogen_oxygen_hydrogen/tc_400/tc_400.htm

[155] Q. M. Li, I. Magkiriadis, and J. J. Harrigan, "Compressive strain at the onset densification of cellular solids," *Journal of Cellular Plastics,* vol. 42, pp. 371-392, 2006.

[156] M. Avalle, G. Belingardi, and R. Montanini, "Characterization of polymetric structural foams under compressive impact loading by means of energy absorption diagram," *International Journal of Impact Engineering,* vol. 25, pp. 455-472, 2001.

[157] K. C. Chan and L. S. Xie, "Dependency of densification properties on cell topology of metal foams," *Scripta Materialia,* vol. 48, pp. 1147-1152, 2003.

[158] P. H. Thornton and C. L. Magee, "The deformation of aluminum foam," *Metallurgical Transactions A,* vol. 6A, 1975.

[159] (2010, February 17, 2010). Available: http://www.factsage.com

[160] P. J. Haines, Ed., *Principles of thermal analysis and calorimetry* (RSD Paperbacks. Cambridge: The Royal Society of Chemistry, 2002, p.^pp. Pages.

[161] D. Zill and M. Cullen, *Advanced Engineering Mathematics*: Jones and Bertlett, 1999.

[162] F. Incropera, D. P. Dewitt, T. L. Bergman, and A. S. Lavine, *Fundamentals of Heat and Mass Transfer*: Wiley, 2006.

[163] A. L. Hines and R. N. Maddox, *Mass Transfer: Fundamentals and Application*: Prentice-Hall, 1985.

[164] V. Bholse, E. G. Baburaj, M. Miranova, and K. Salama, "Dehydrogenation of TiH2," *Materials Science and Engineering A,* vol. 356, pp. 190-199, 2003.

[165] A. T. Dinsdale and P. N. Quested, "The viscosity of aluminium and its alloys - A review of data and models," *Journal of materials science,* vol. 39, pp. 7221-7228, 2004.

[166] J. Goicoechea, C. Garcia-Cordovilla, E. Louis, and A. Pamies, "Surface tension of binary and ternary aluminium alloys of the systems Al-Si-IVlg and AI-Zn-Mg," *JOURNAL OF MATERIALS SCIENCE,* vol. 27, pp. 5247-5252, 1992.

[167] M. Hanabe, V. Jayaram, and T. A. Bhaskaran, "Growth of Al2O3/Al composites from Al-Zn alloys," *Acta Materialia,* vol. 44, pp. 819-829, 1996.

[168] J. Wojewoda-Budka, N. Sobczak, J. Morgiel, and R. Nowak, "Reactivity of aluminum with polycrystalline ZnO substrate," *Journal of Material Science,* vol. 45, 2010.

[169] S.-J. Lee and I. S. Kim, "Study of the role of Mg and Zn in the directive oxidation of Al alloys," *Journal of Materials Science Letters* vol. 17, pp. 1357-1362, 1998.

[170] V. Jayaram, "The role of volatile solute elements in directed melt oxidation of aluminum alloys," *Journal of materials science,* vol. 31, pp. 4591-4598, 1996.

[171] M. Sindel, N. A. Travitzky, and N. Claussen, "Influence of Magnesium-Aluminum Spinel on the Directed Oxidation of Molten Aluminum Alloys," *Journal of the american ceramic society,* vol. 73, pp. 2615-2618, 1990.

[172] H. M. Helwig, F. Garcia-Moreno, and J. Banhart, "A study of Mg and Cu additions on the foaming behaviour of Al-Si alloys," *Journal of Materials Science,* vol. 46, pp. 5227-5236, 2011.

[173] S.-H. Park, Y.-S. Um, C.-H. Kum, and B.-Y. Hur, "Thermophysical properties of Al and Mg alloys for metal foam fabrication," *Colloids and Surfaces A: Physicochemical and Engineering Aspects,* vol. 263, pp. 280-283, 2005.

[174] J. R. Davis, *Aluminum and aluminum alloys*: ASM International, 1993.

[175] V. S. R. Murthy and B. S. Rao, "Microstructural development in the directed melt-oxidized (DIMOX) Al-Mg-Si alloys," *Journal of Material Science,* vol. 30, pp. 3091-3097, 1995

[176] J. Banhart, J. Baumeister, and M. Weber, "Aluminium Foams for Transport Industry," *Materials and Design,* vol. 18, pp. 217-220, 1997.

[177] J. T. Beals and M. S. Thompson, "Density gradient effects on aluminum foam compression behavior," *Journal of Materials Science,* vol. 32, pp. 3595-3600, 1997.

[178] E. Oberg, F. D. Jones, H. L. Horton, and H. H. Ryffel, *Machinery's Handbook*, 26 ed. New York: Industrial Press, 2000.

[179] Omega, "Revised Thermocouple Reference Tables," z218-220.pdf, Ed., ed: Omega, 2010.

This page is intentionally left blank

Appendix A: **Experimental Procedures**

The particle size analysis data showing the powder size distribution for the pure aluminum, zinc, TiH_2 and Al-12Si powders is shown below.

1. Al-12Si

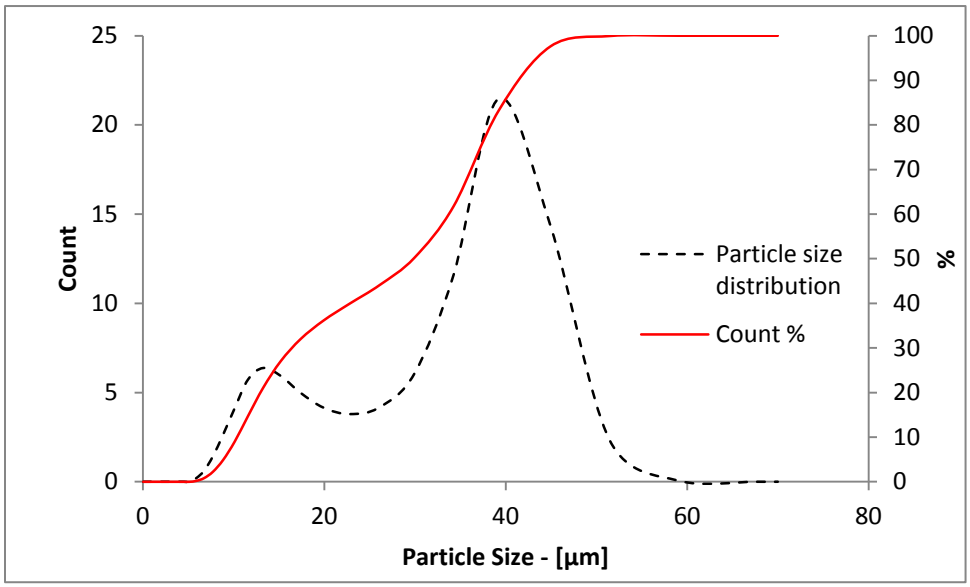

2. TiH_2

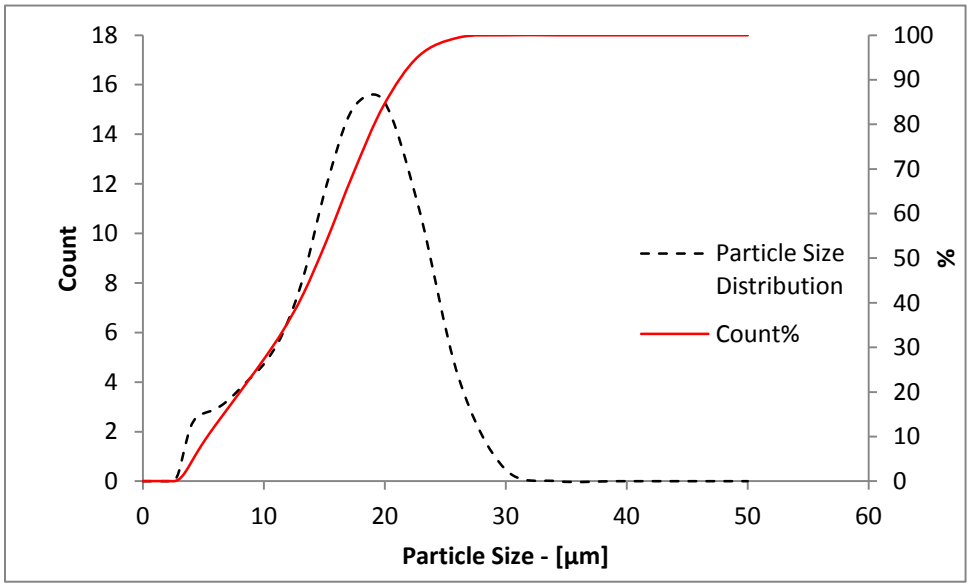

3. Zinc

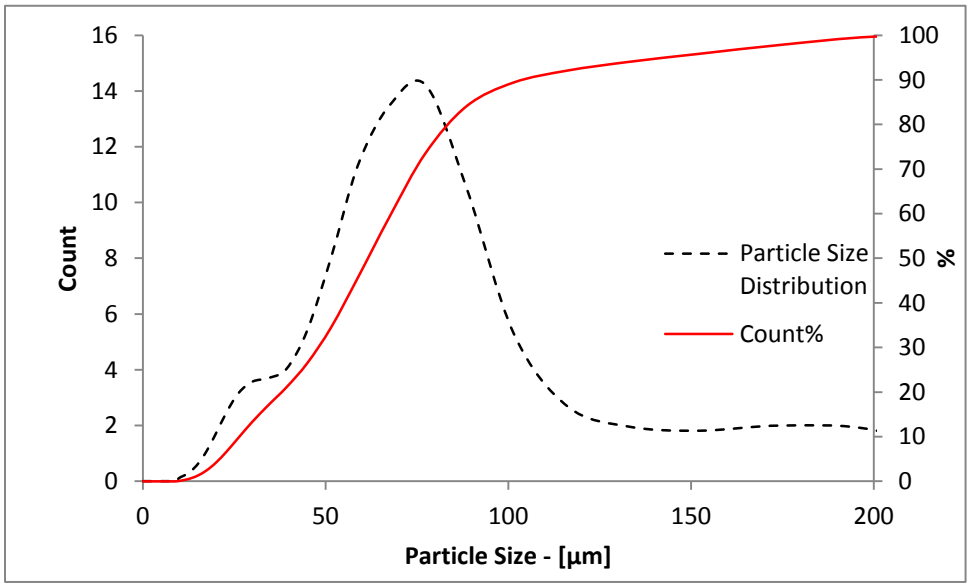

4. Pure Aluminum

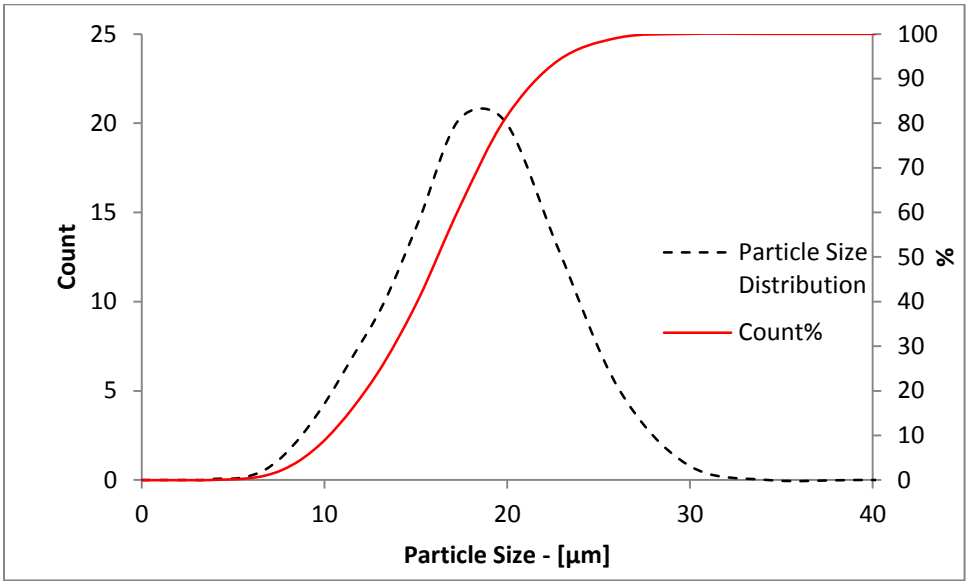

Expandometer design

The design of the expansion measuring device consisted of a counterbalanced long rod which would descend into the furnace crucible and touch the sample to translate the motion of the expanding foam from the hot zone to a cooler zone. The calibrated counterweight system and the plunger rod used for translating the motion are depicted in Figure A: 1 and can be seen on the Expandometer in Figure A:2. Once the plunger rod effectively translated the foam expansion motion away from the hot zone, the displacement was measured with a laser and recorded using a data acquisition system. The principal purpose behind the use of the plunger rod was to translate foam expansion motion because when the laser was aimed directly at the hot oxidized foam surface, a poor and noisy signal resolution was obtained. To validate (or calibrate) the counterbalancing of the plunger rod, tests were conducted in order to minimize the effects of the rod on the foam expansion and collapse. After several tests and curve analysis, it was determined that the effect of the plunger rod proved to be negligible once calibrated. The rod itself was initially to be fabricated with quartz which has a very low thermal expansion coefficient but due to time and financial constraints a 308 stainless steel rod was used instead. The motion of the rod was constrained in the vertical axis by two Teflon bearings counterbalanced by a circular ring outside an enclosure system. The plunger rod and the counterweight mechanism were fastened together with a thin flexible Nylon cord (0.4 mm). This system was built to be as compact as possible and to be easily operated by anyone. The plunger system was then attached to a hinged cross-member that could be easily moved to load and unload samples.

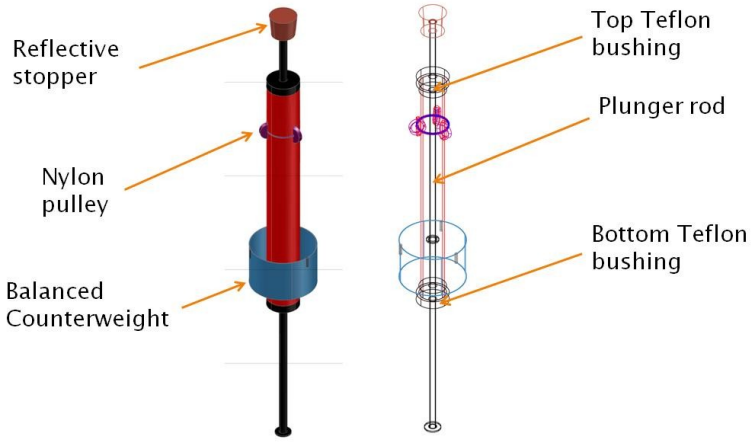

FigureA:1: Plunger rod and counterweight system

The tubular furnace along with the apparatus frame, were fastened to a concrete base in order for the structure to be rigid and to avoid vibration, whilst at the same time being cost effective. This can be seen from Figure A: where the entire furnace is depicted. The tubular furnace had to be well aligned with the plunger rod and was subsequently wrapped with insulation and an aluminum sheet; this was used to minimize the heat losses to the surroundings. A stainless steel crucible was inserted down the centre of the furnace very close to the furnace controller K-type thermocouple. A reference K-type thermocouple was also added to verify the furnace and sample temperature.

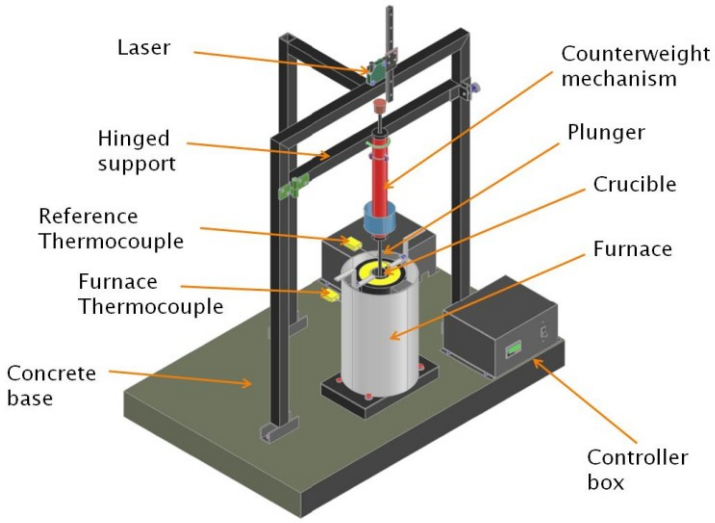

Figure A:2: Expandometer furnace

Tests conducted with the Expandometer furnace were compared to the curves using the box furnace. Although the heating rate varied between the two methods and that the foam was constrained to the crucible walls with the Expandometer unlike the box furnace, it was to be expected that the foaming time and expansion may vary slightly. It was shown that the expansion levels between the two methods appeared to be reproducible to an acceptable degree by comparing expansion curves. Expansion curves comparing both foaming methods are shown in Figure A:3 at temperatures of 600 ˚C and 620 ˚C. It can be seen in this case that the data is reproducible between the two methods. The four curves shown in Figure A:3 are averages of several (three to five) samples.

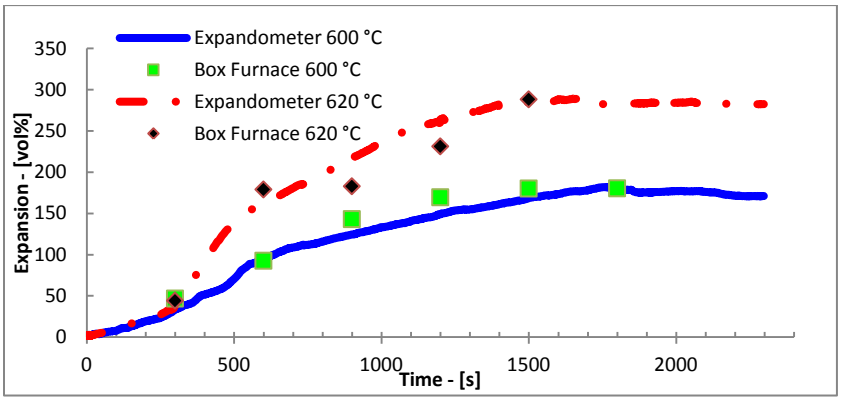

Figure A:3 : Expandometer foaming compared to box furnace foaming at 600 ˚C and 620 ˚C

System Accuracy and Sources of Error

Several factors in all equipment contribute to some level of inaccuracies which can be sources of error. They need to be well understood for calibration purposes and results analysis. The first aspect related to these inaccuracies in this case is the temperature profile present in the furnace. Like all other vertically oriented furnaces this specific one tends to be warmer at the bottom than the top as it is fastened in a vertical fashion. The measured temperature gradients within the crucible along with the equivalent expansion at different height are tabulated in Table A:1 and Table A:2. Since it is vertical, natural convection is inherently present in the furnace itself affecting the heating zones. Consequently, this results

in a hot lower section and a cooler top section where rising heat escapes to the surroundings by natural convection and radiation. Therefore, the larger the final foam size at maximum expansion, the more it will be affected by the temperature differences across its height. Based on the measurement made at various temperatures as seen in Table A:1 from within the crucible, a maximum temperature profile in the range of 10-20 ˚C across the foam sample is expected depending on foaming temperature. It is to be noted that foams typically do not exceed 2 inches (50.8 mm) in height during the foaming process, which translates to expansion levels of 577 vol% for the 20 mm diameter samples and 347 vol% for the 30 mm diameter samples. Based on this analysis, it was determined that an initial compact height of 10 mm (20 mm diameter compacts) and 15 mm (30 mm diameter compacts) were to be used in the foaming process, resulting in a compromise between foam size and temperature gradient effects. This temperature gradient can become especially important for the larger 30 mm diameter foams which are typically taller possibly resulting in an increase in drainage as a result of higher temperatures at the bottom of the foam. It is important to mention the temperature profile and difference effect because every industrial process possesses some variations which need to be understood. If these are properly understood than they can be accounted for in the process.

Table A:1: Expandometer furnace temperature profile, 30 mm diameter crucible

Furnace temperature profile				
30 mm diameter crucible				
Distance	***Equivalent foam expansion vol%***	***Furnace (inside crucible) Temp (˚C)***		
Bottom of crucible	N/A	660	706.8	746.4
1 " (25.4 mm)	123.9	656.2	701	739.3
2" (50.8 mm)	347.9	647.8	695.2	728.3
2.5" (76.2 mm)	571.8	637.2	676.3	717.4

Table A:2 : Expandometer furnace temperature profile, 20 mm diameter crucible

Furnace temperature profile				
20 mm diameter crucible				
Distance	***Equivalent foam expansion vol%***	***Furnace (inside crucible) Temp (˚C)***		
Bottom of crucible	N/A	660.4	708.4	746.6
1 " (25.4 mm)	238.8	656.5	703.3	739.2
2" (50.8 mm)	577.7	641.4	686.1	719.8
2.5" (76.2 mm)	916.5	624.8	671.2	708.1

The second source of error is related with the thermal expansion of the plunger rod which expands from room temperature up to the foaming temperature. The rod is manufactured from 308 stainless steel which has a thermal expansion coefficient $1.79x10^{-05}$ mm mm^{-1} $°C^{-1}$ [178]. When calculating the maximum expansion over the entirety of the rod from room temperature to 650 ˚C, an expansion of 0.6 mm (over 550 mm) will occur. Since it is highly improbable that the entire rod heats up to 650 ˚C this conservative approach is used to demonstrate the fact that rod expansion is not a significant factor. This 0.6 mm expansion is calculated to be equivalent to less than 6 vol% total volume expansion error. For example when foam expands to 300 vol%, the resulting error is calculated to be less than 2 vol%.

The K-type thermocouples used in the furnace have an accuracy of ± 2.2 ˚C [179]. The laser system used in measuring the vertical displacement has a resolution of <20 μm and a maximum working distance of 120 mm. It is believed that these two factors are not large sources of error.

This page is intentionally left blank

Appendix B: **Pure aluminum foams**

Structure evolution of pure aluminum foam produced at 710 °C.

a) 710 °C at 300 s

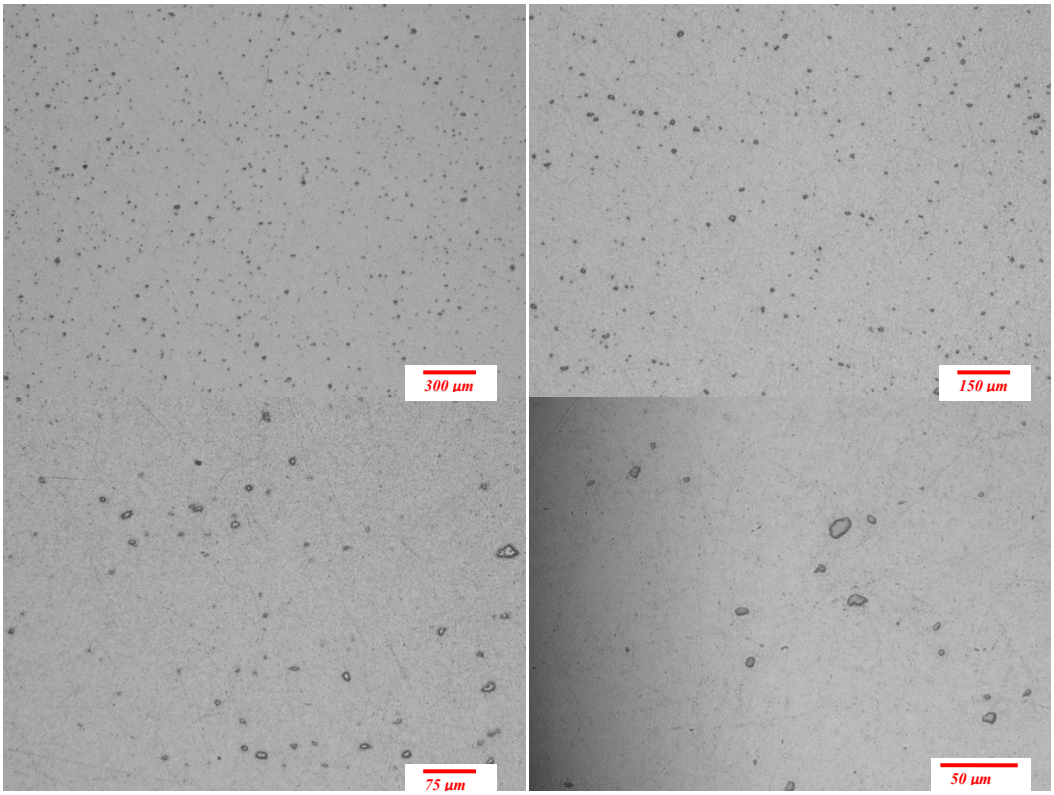

b) 710 °C at 500 s

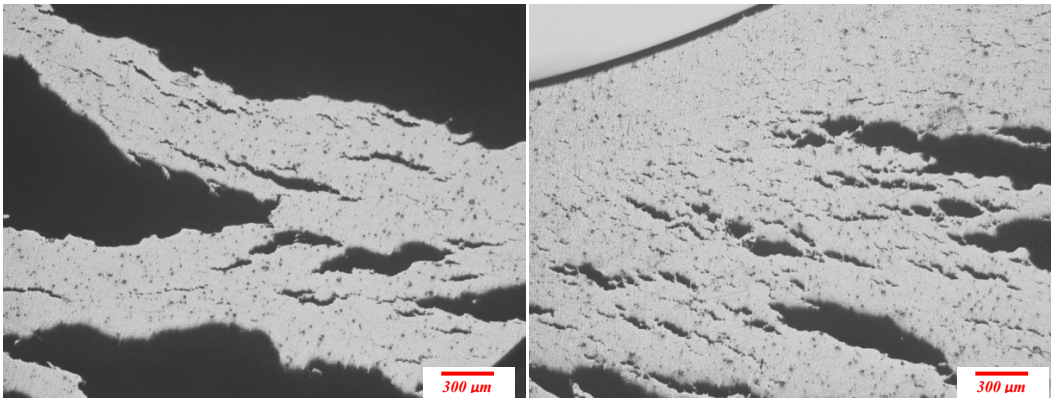

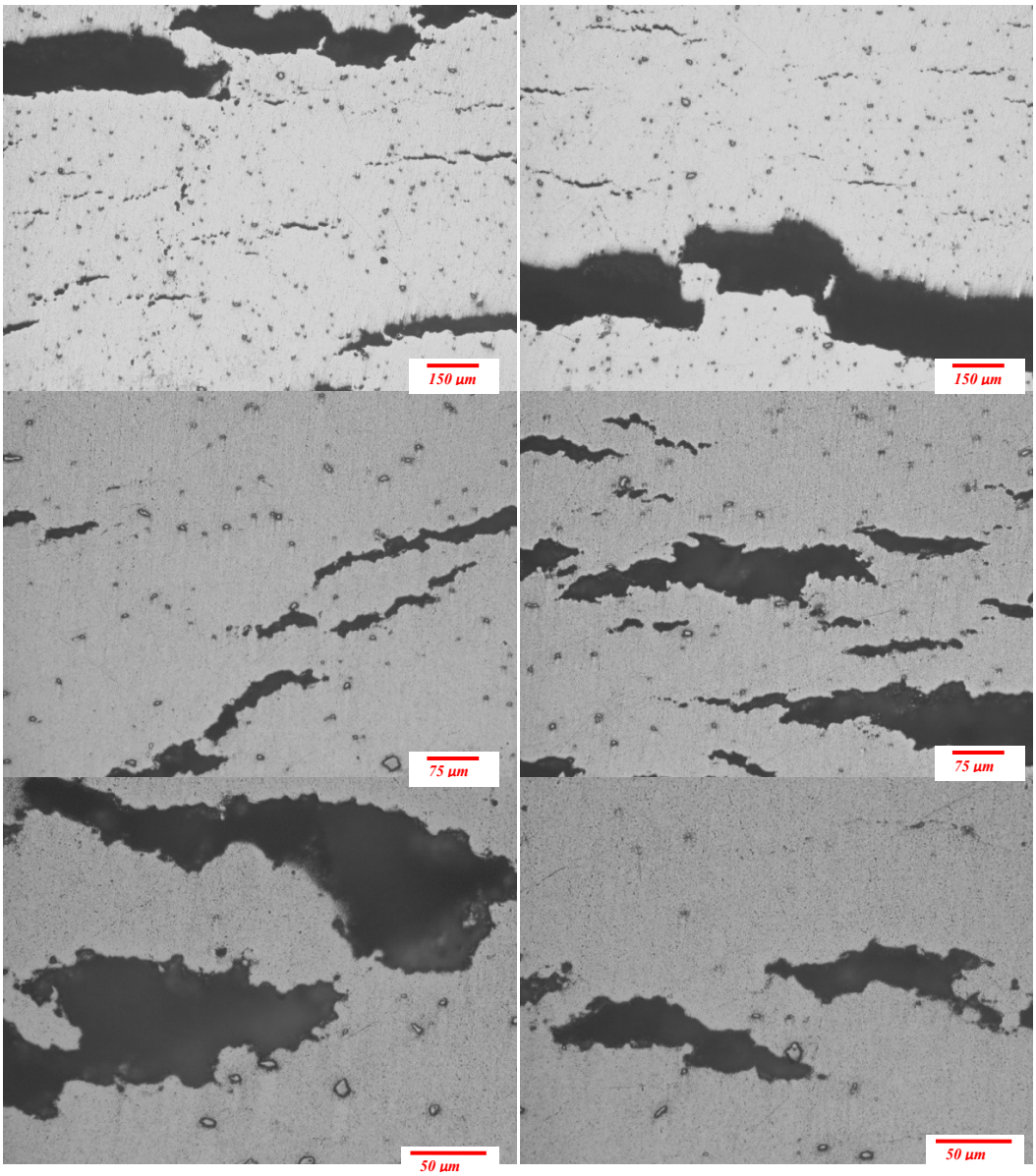
150 µm
150 µm
75 µm
75 µm
50 µm
50 µm

c) 710 °C at 550 s

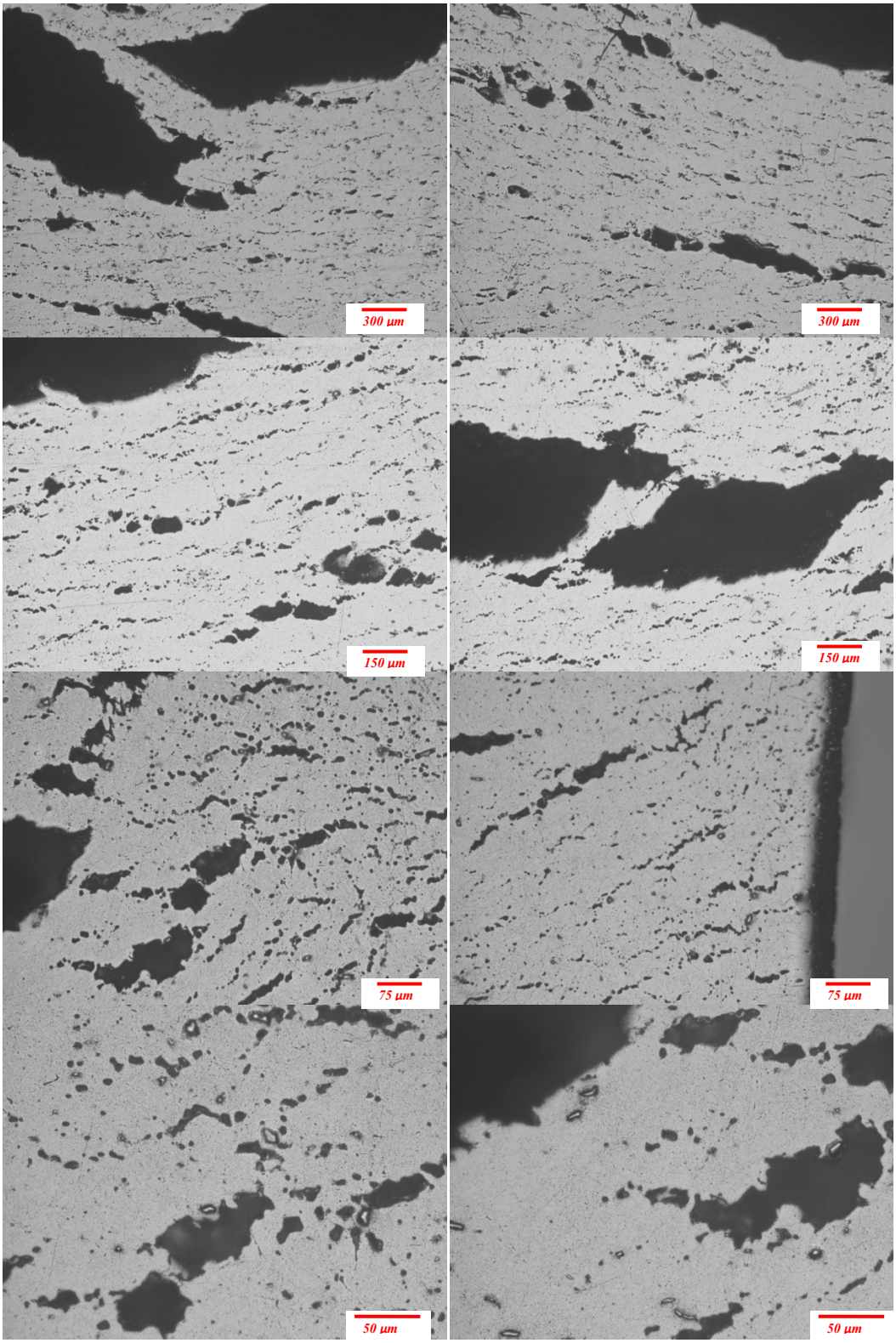

d) 710 °C at 750 s

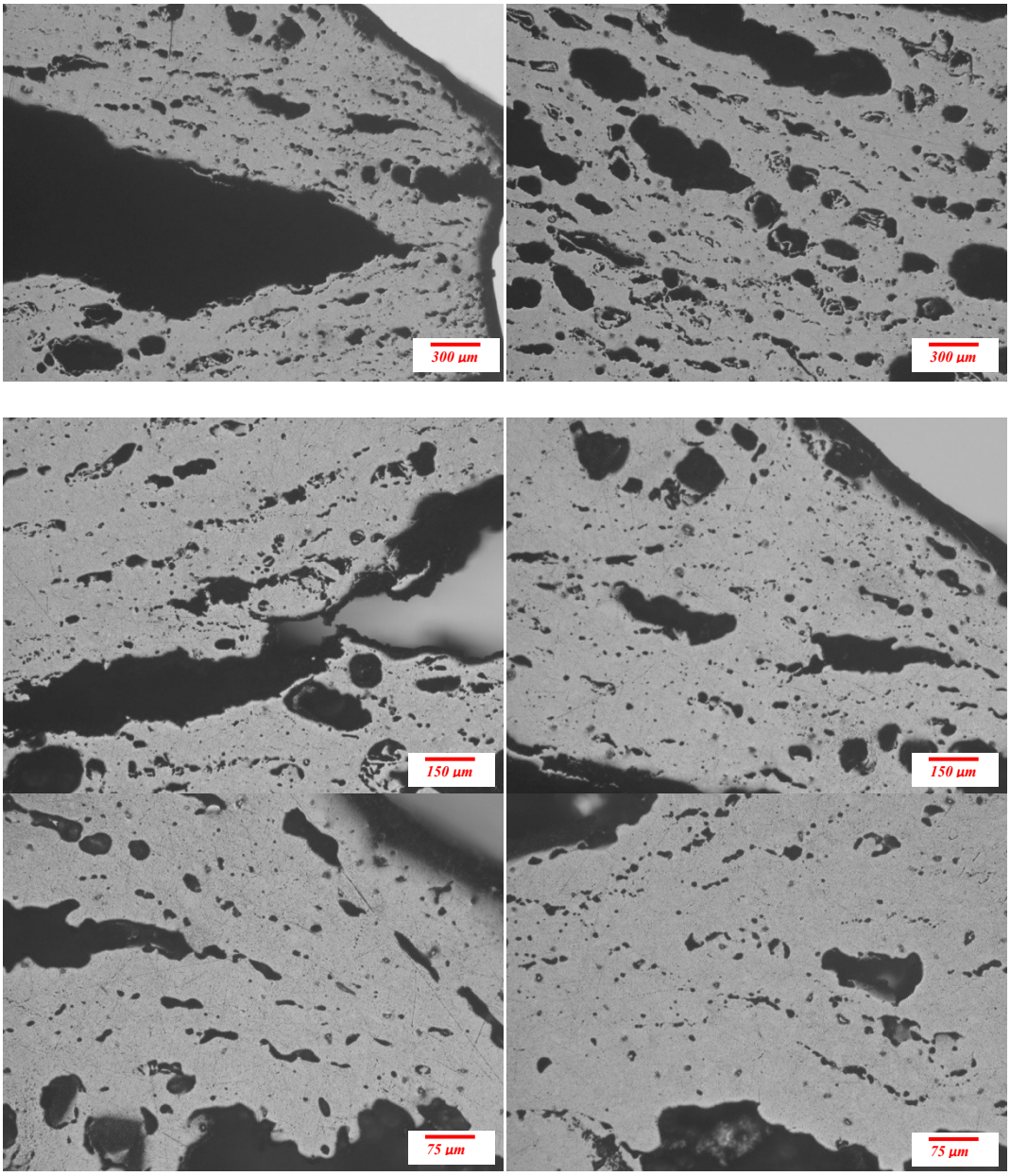

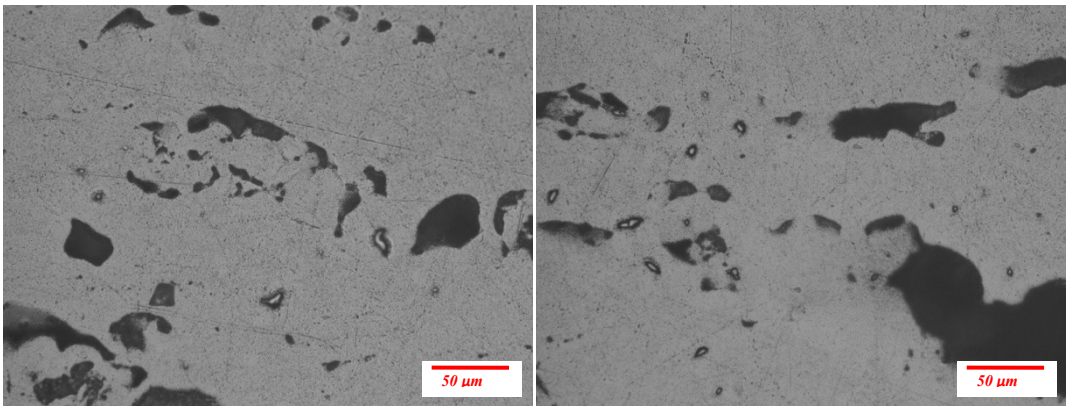

e) 710 °C at 950 s

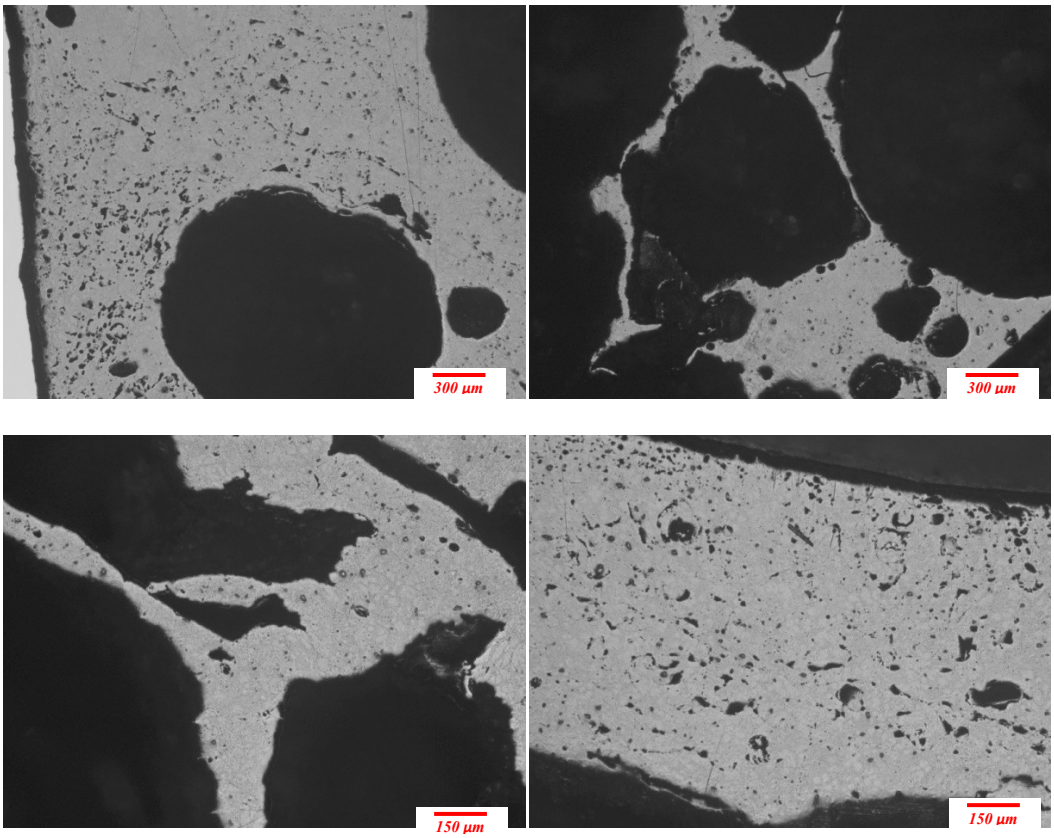

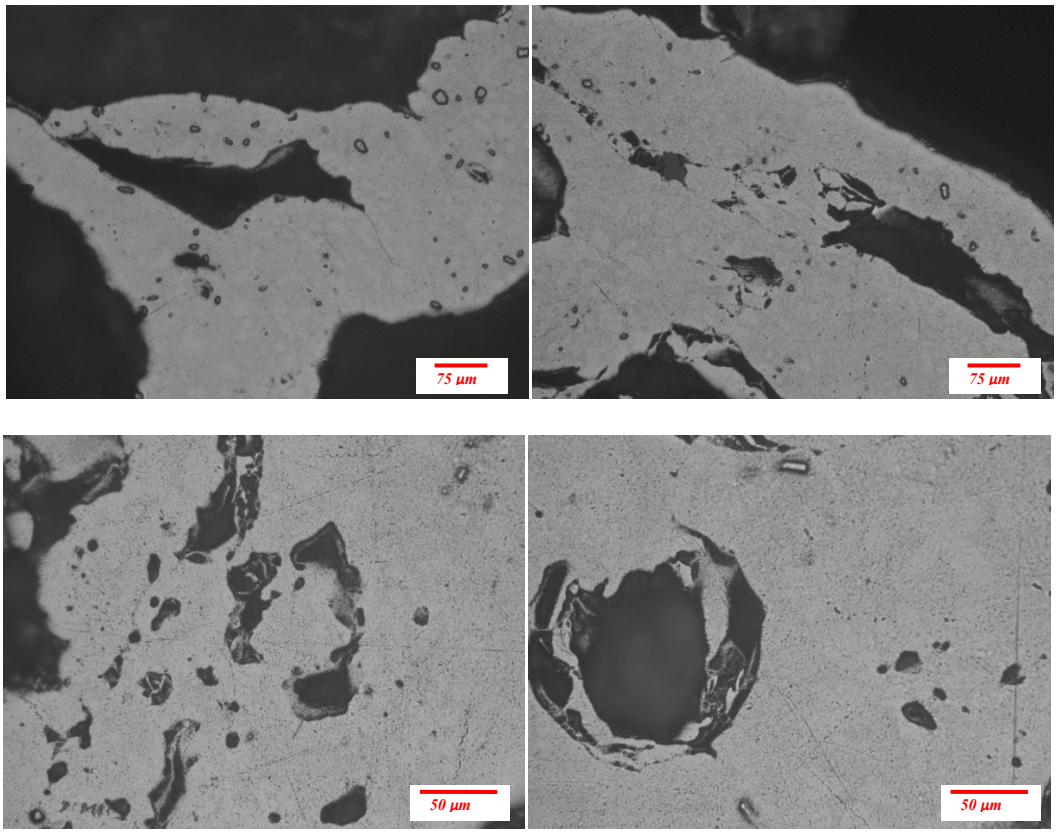
75 µm
75 µm
50 µm
50 µm

Appendix C: **Diffusion Data**

Cold Pressed powders

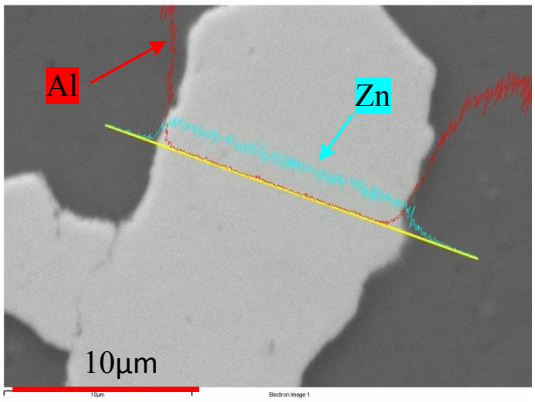

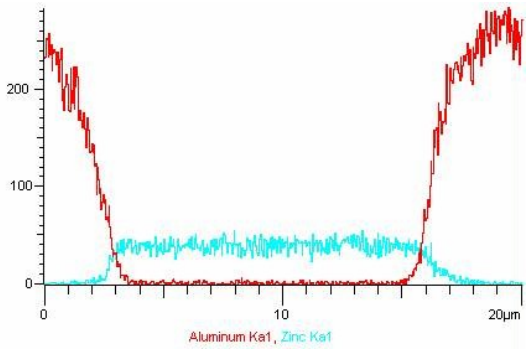

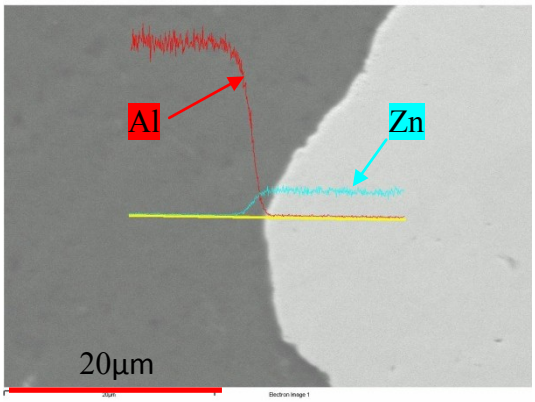

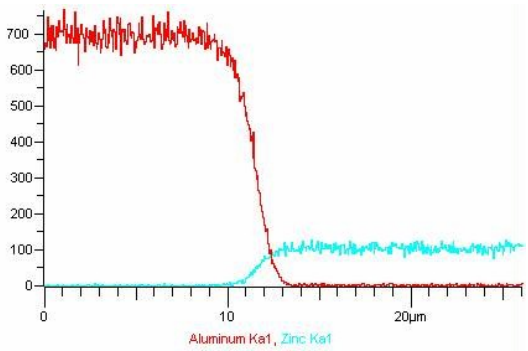

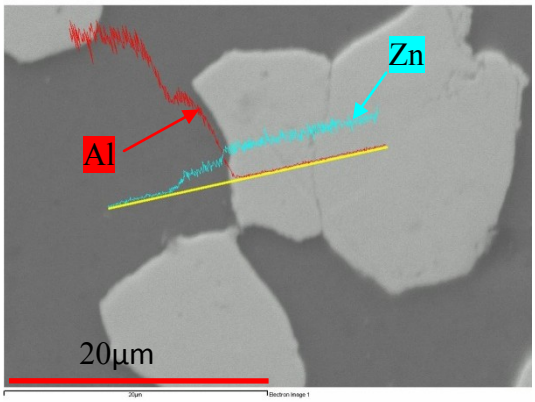

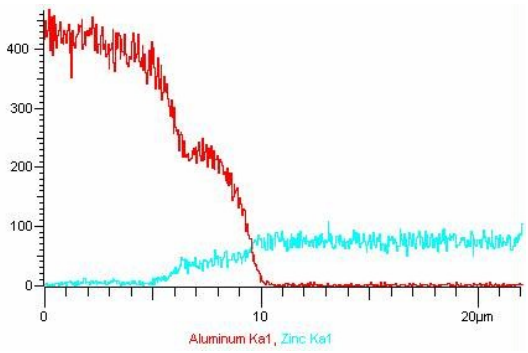

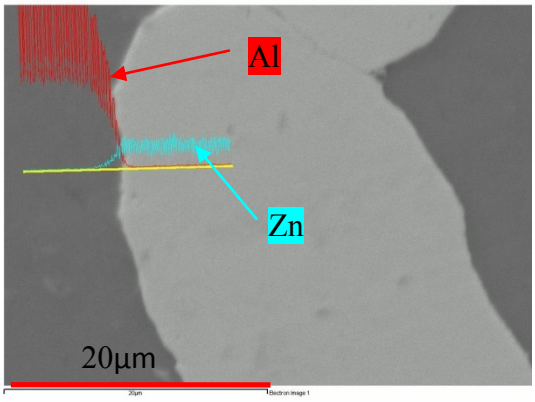

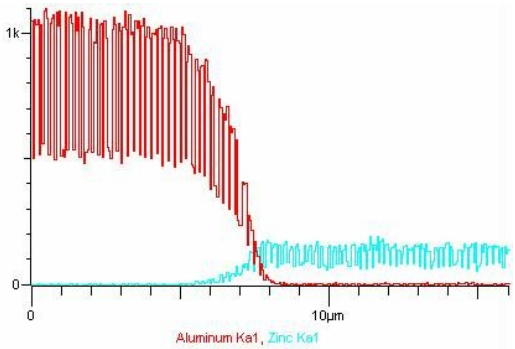

Hot Pressed powders at 350 °C for 1800 s

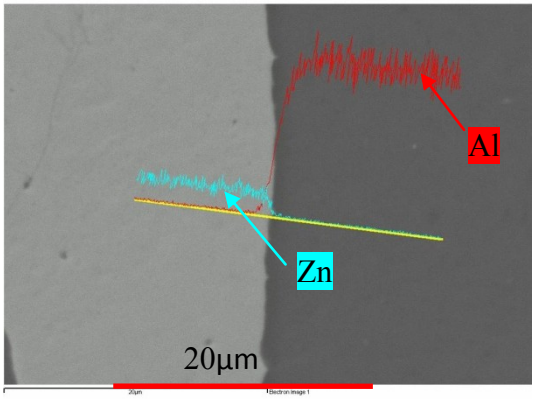

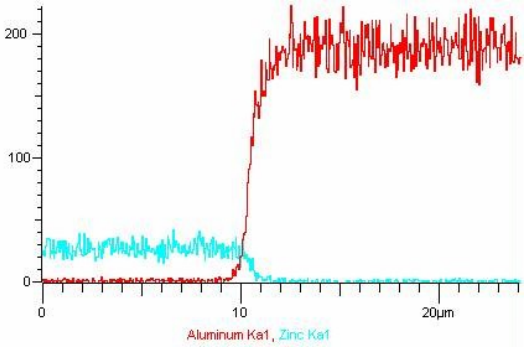

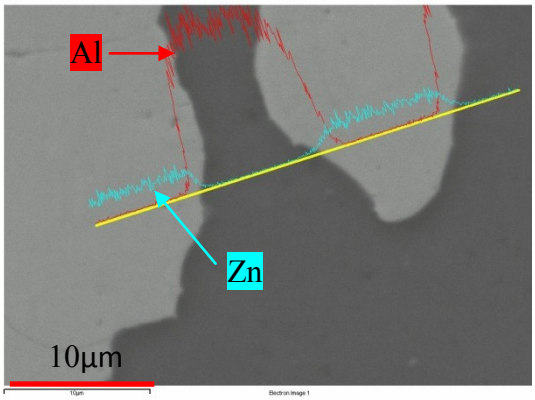

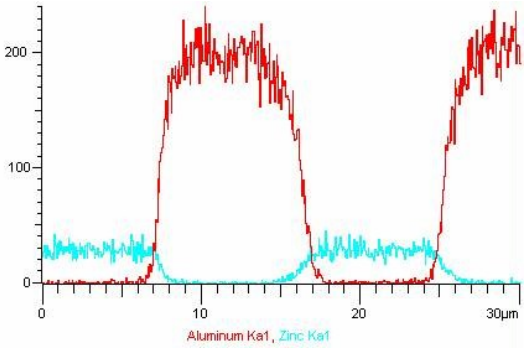

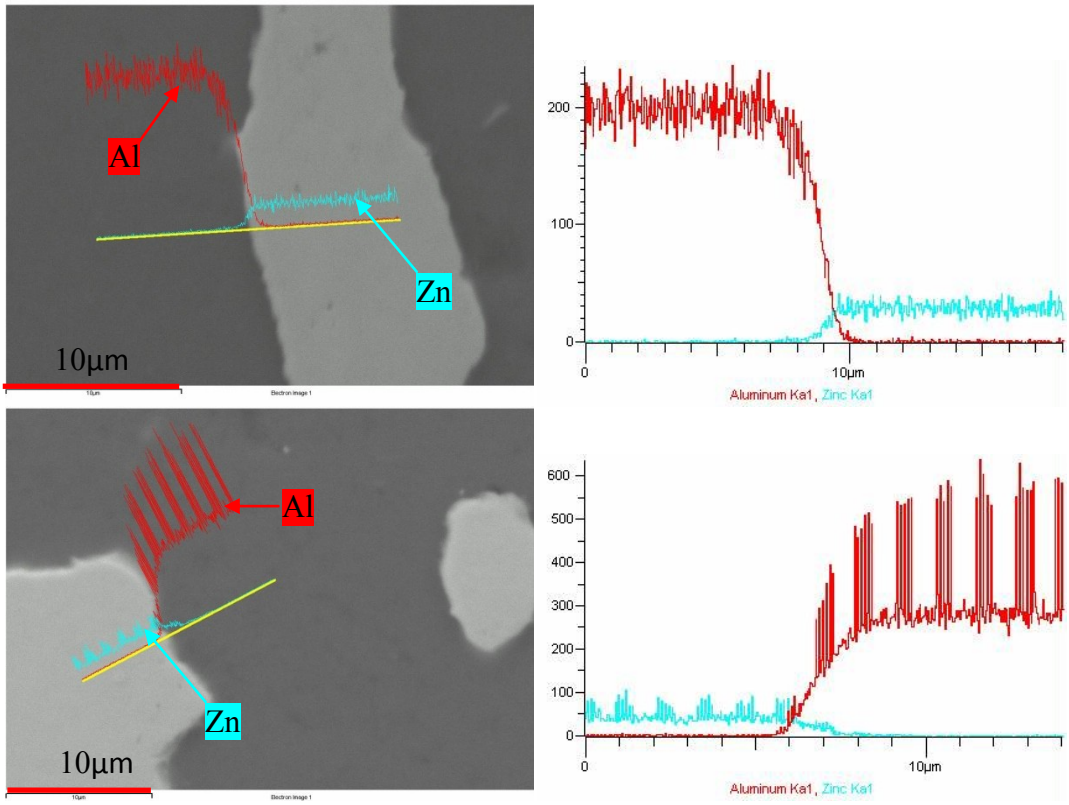

Hot Pressed powders at 350 °C for 3600 s

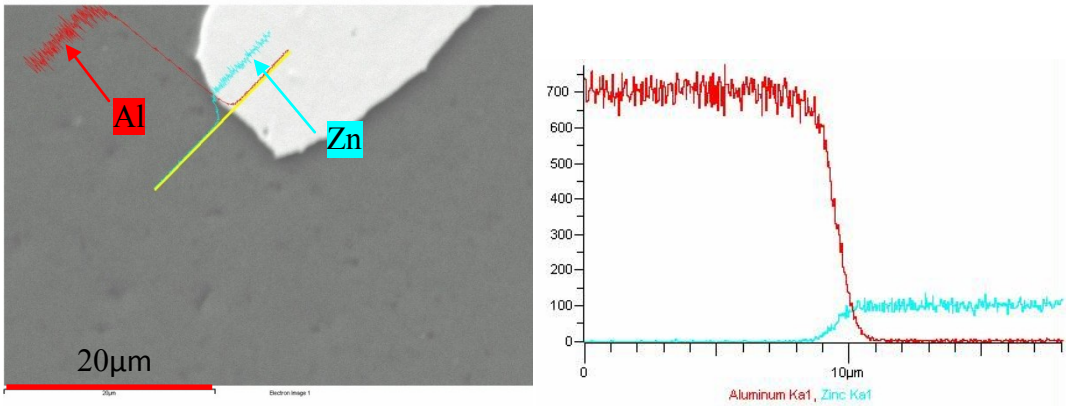

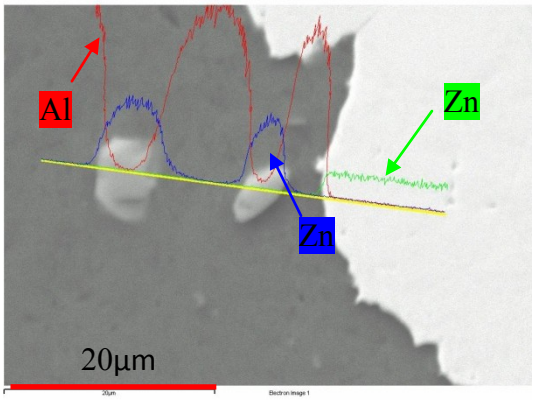
Al
Zn
Zn
20µm

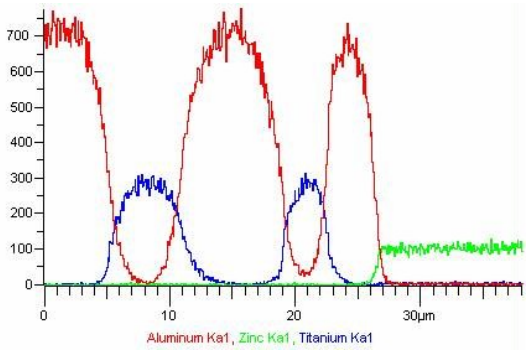
700
600
500
400
300
200
100
0
0
10
20
30µm
Aluminum Ka1, Zinc Ka1, Titanium Ka1

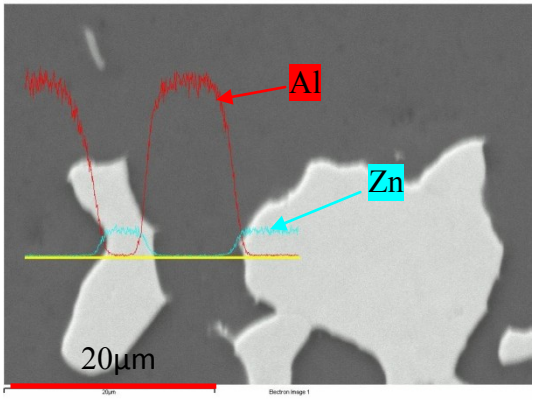
Al
Zn
20µm

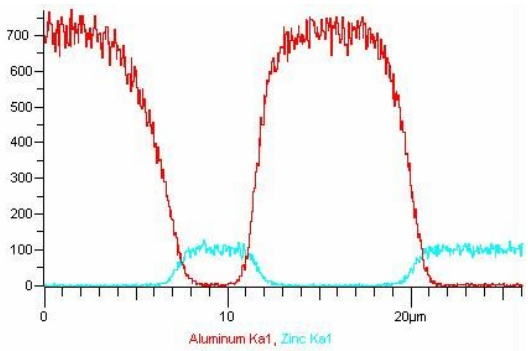
700
600
500
400
300
200
100
0
0
10
20µm
Aluminum Ka1, Zinc Ka1

2- Al-2.4wt%Si-9.7wt%Zn compacts pressed at 350 °C for 1800 s

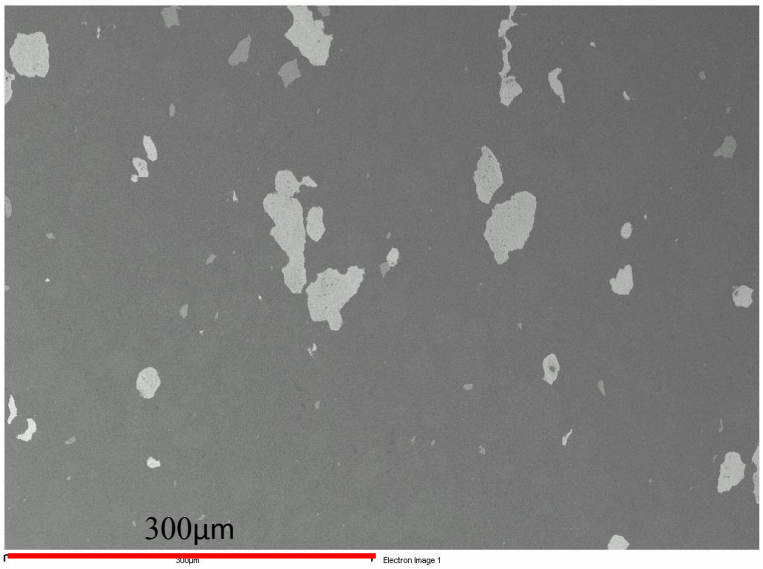

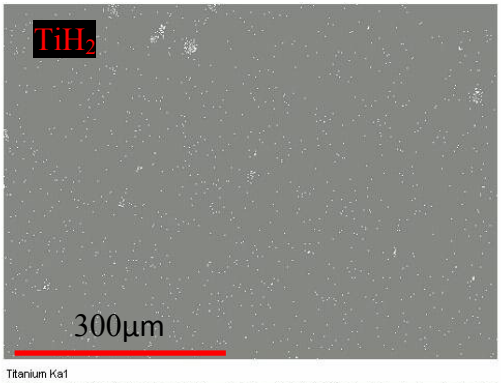

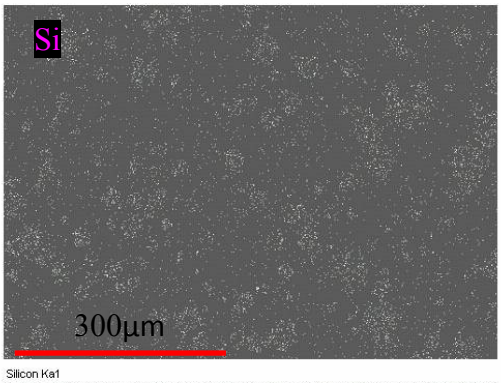

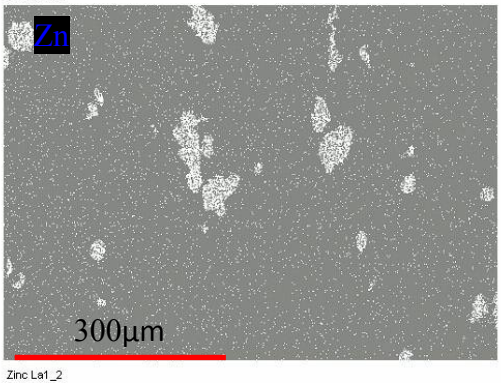

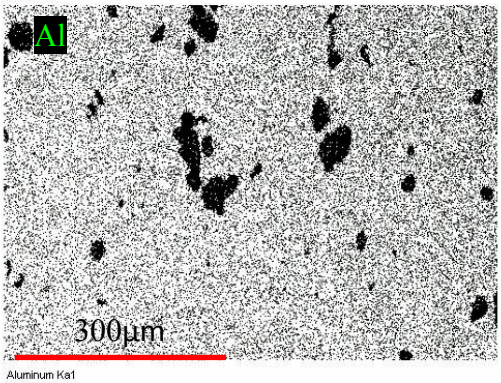

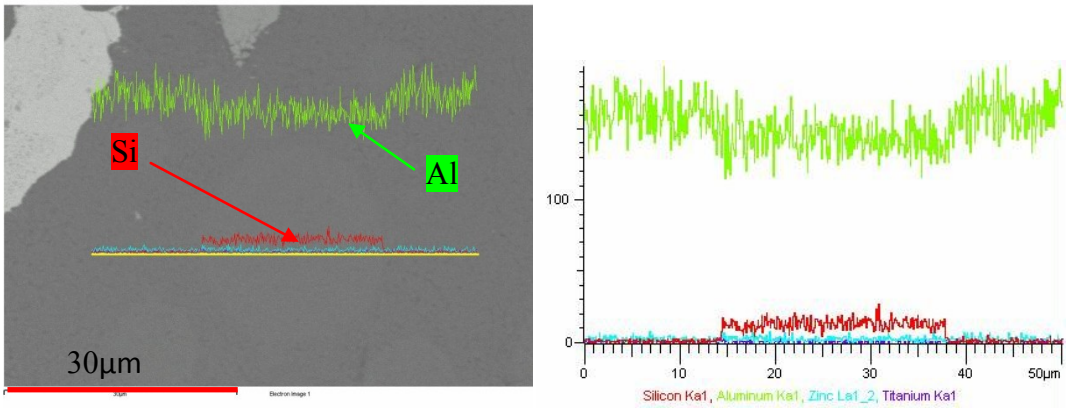
Si
Al
30µm
100
0
0
10
20
30
40
50µm
Silicon Ka1, Aluminum Ka1, Zinc La1_2, Titanium Ka1

Appendix D: **Al-Zn foams**

Micrographs showing the distribution of Zinc and TiH_2 within the aluminum compacted matrix.

Al-10wt%Zn-0.8TiH_2 - Compact

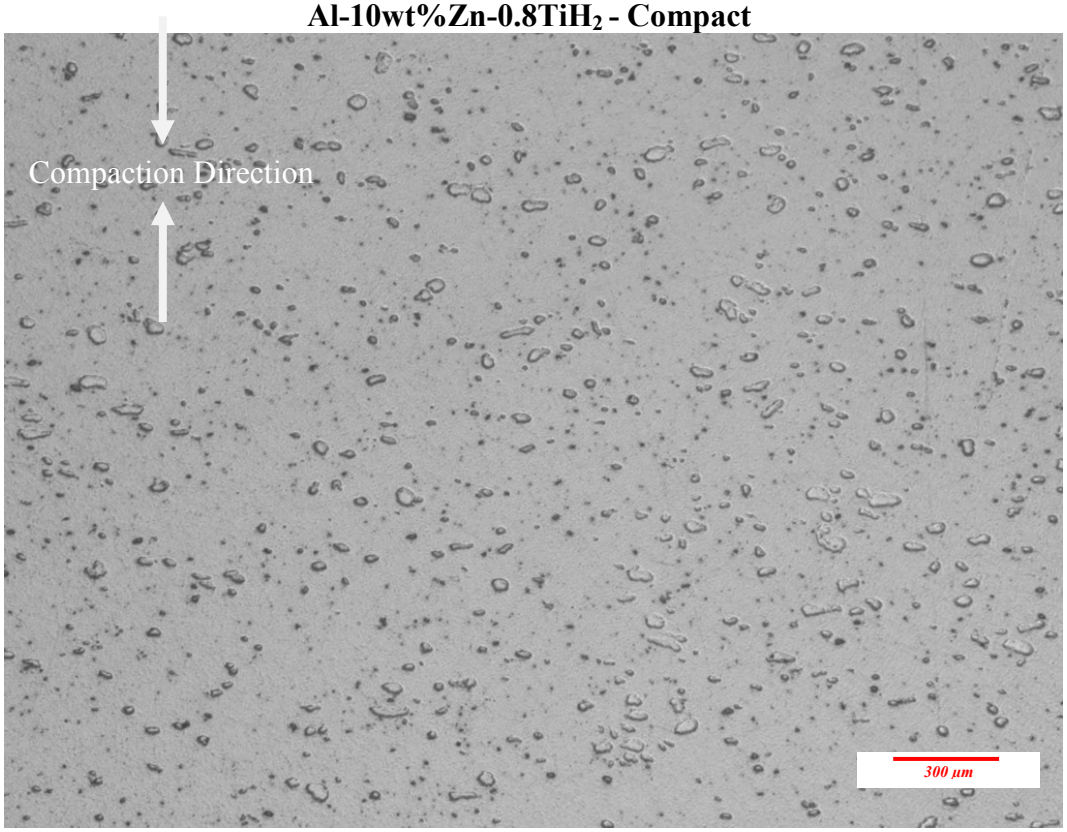

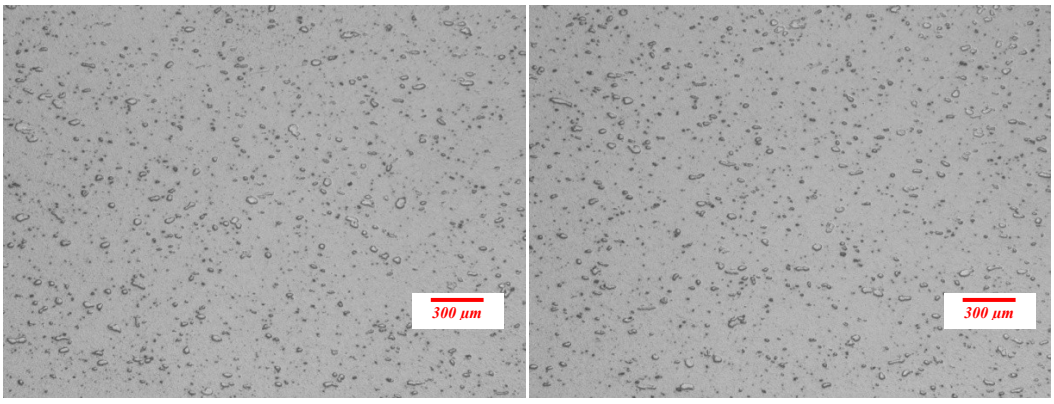

Al-10wt%Zn-0.8TiH_2 - Compact

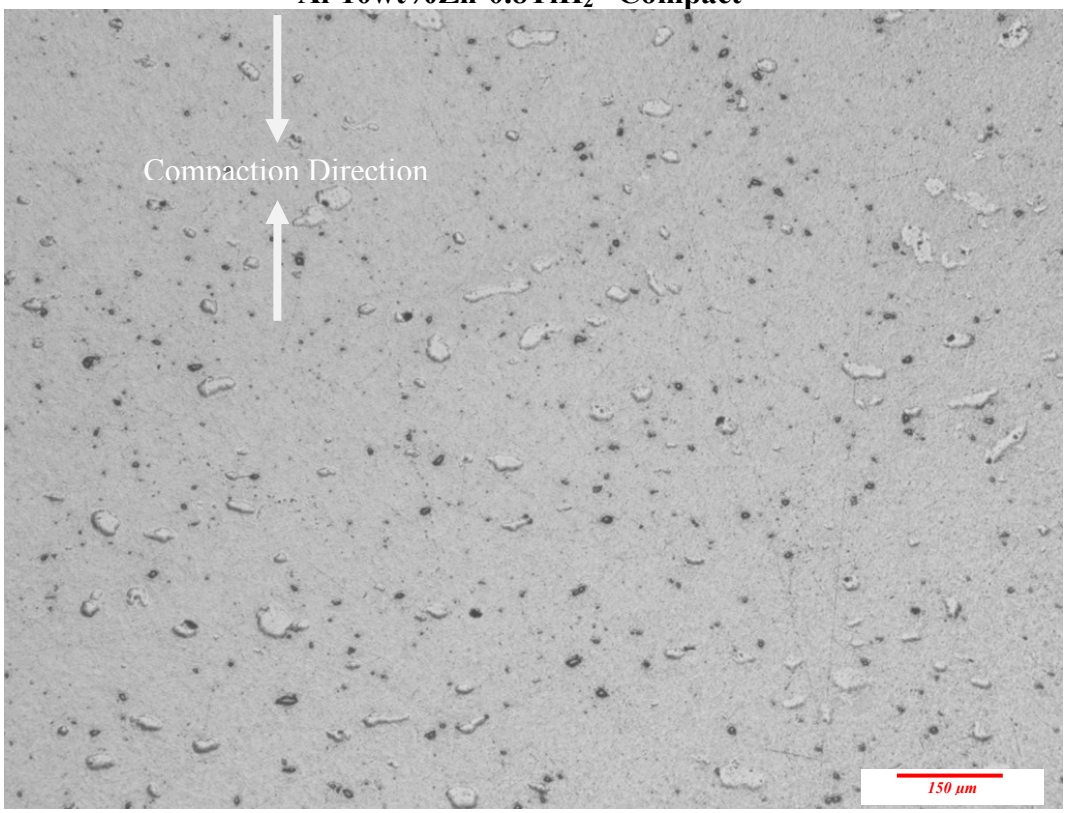

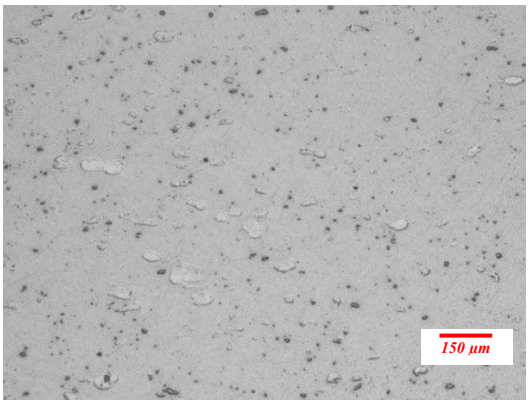

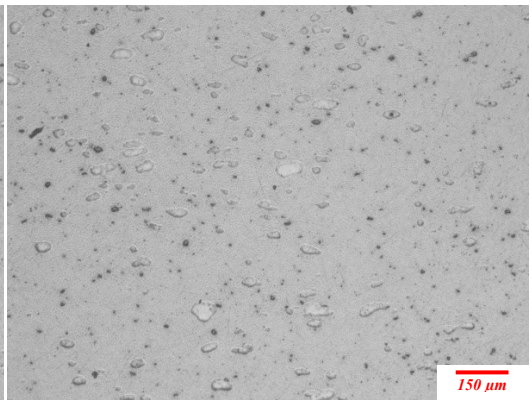

Al-10wt%Zn-0.8TiH_2 - Compact

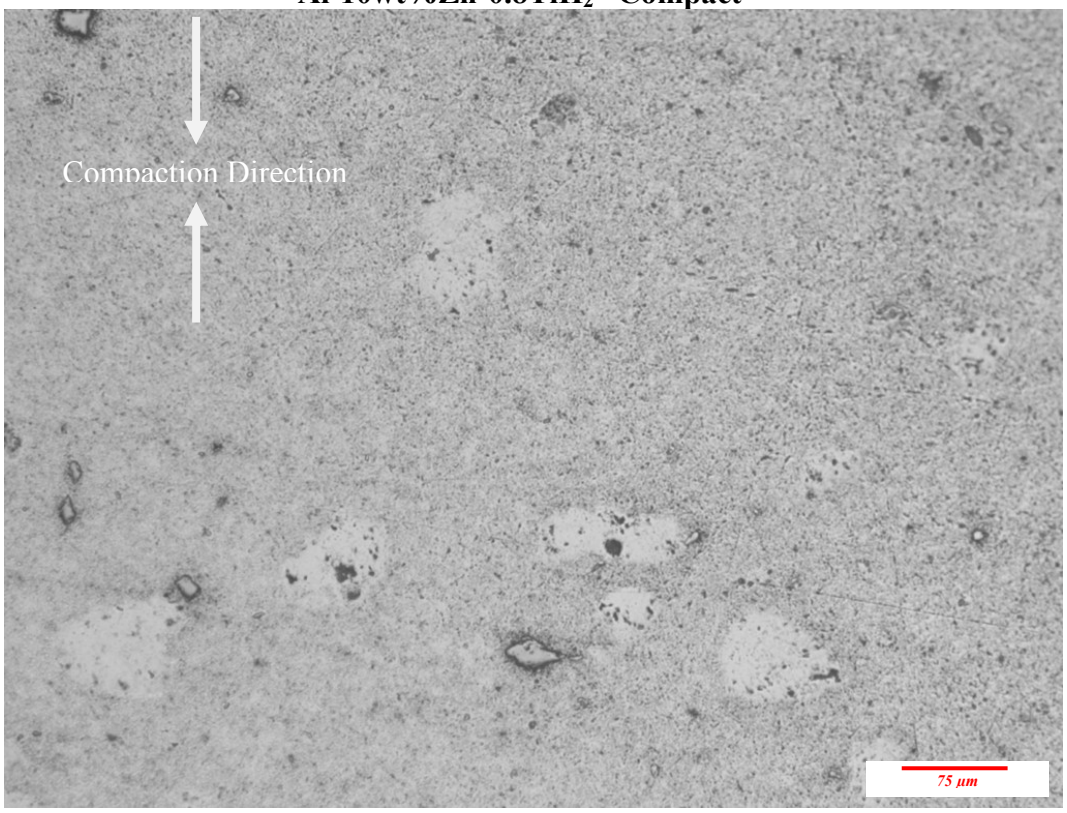

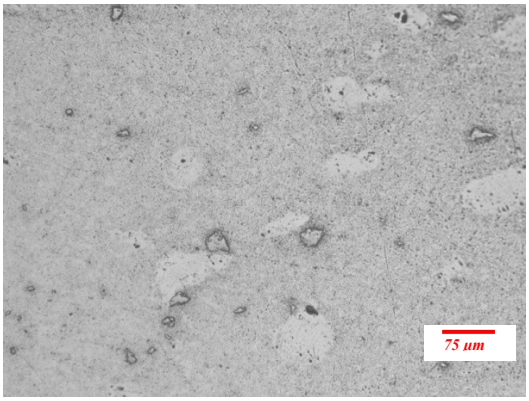

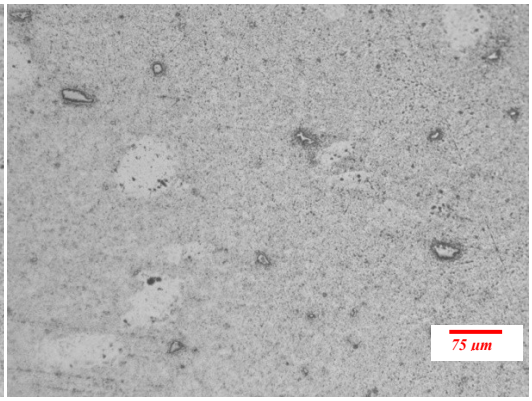

Al-10wt%Zn-0.8TiH$_2$ produced at 710 °C for 300 s

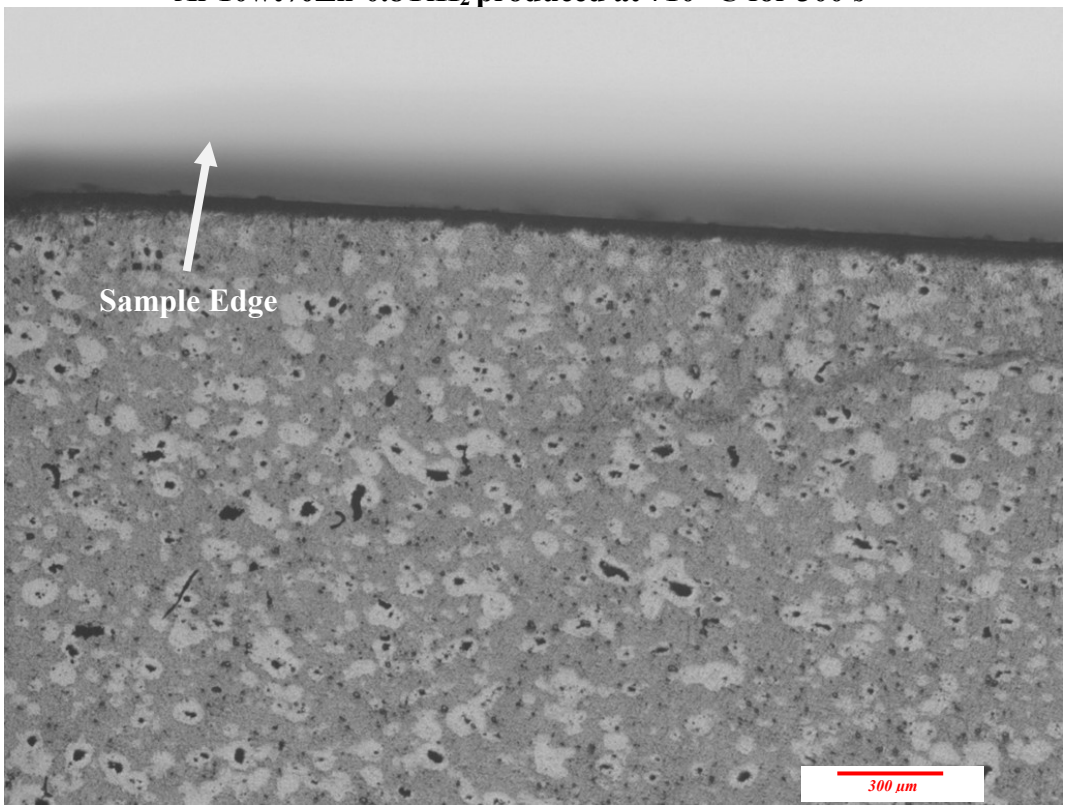

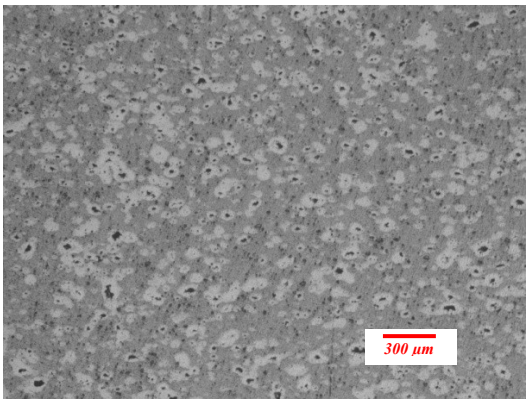

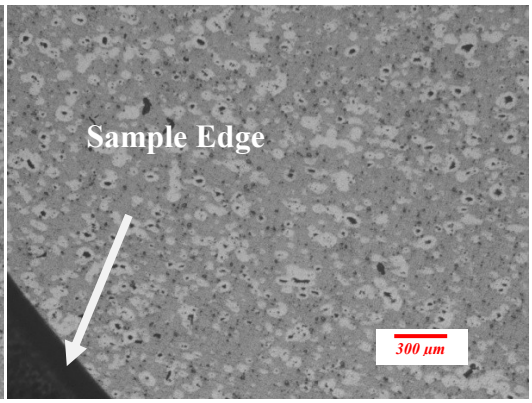

Al-10wt%Zn-0.8TiH_2 produced at 710 °C for 300 s

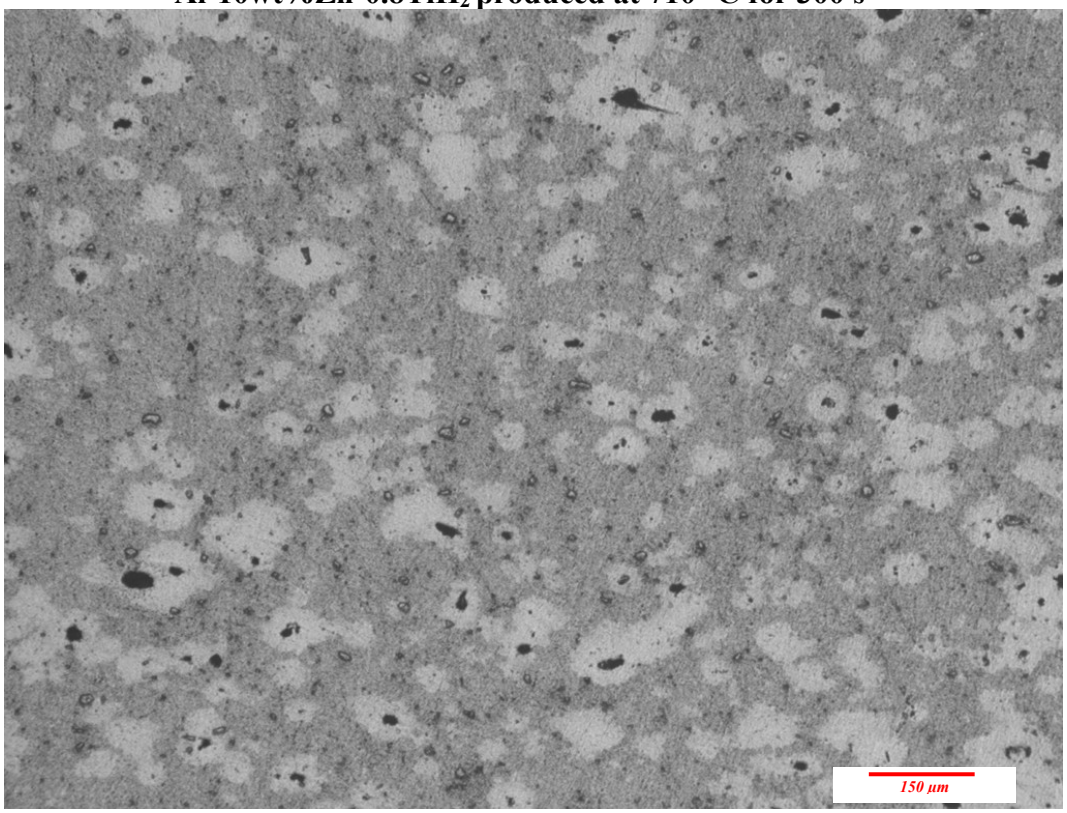

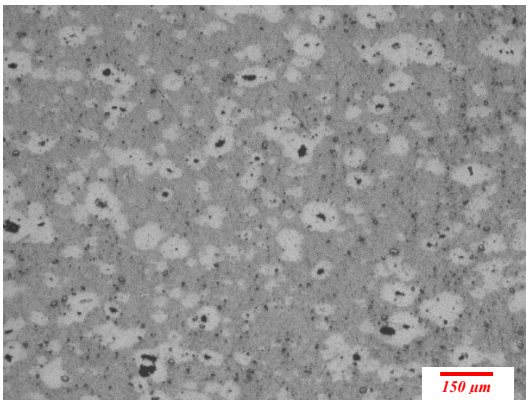

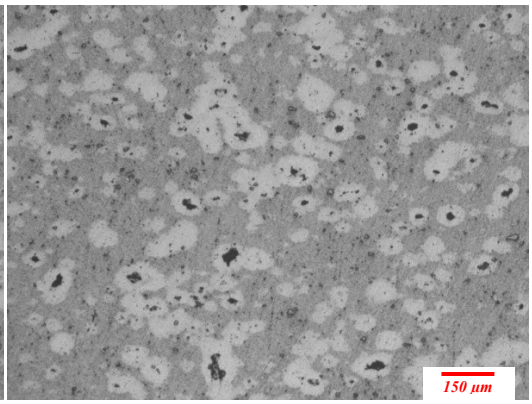

Al-10wt%Zn-0.8TiH$_2$ produced at 710 °C for 300 s

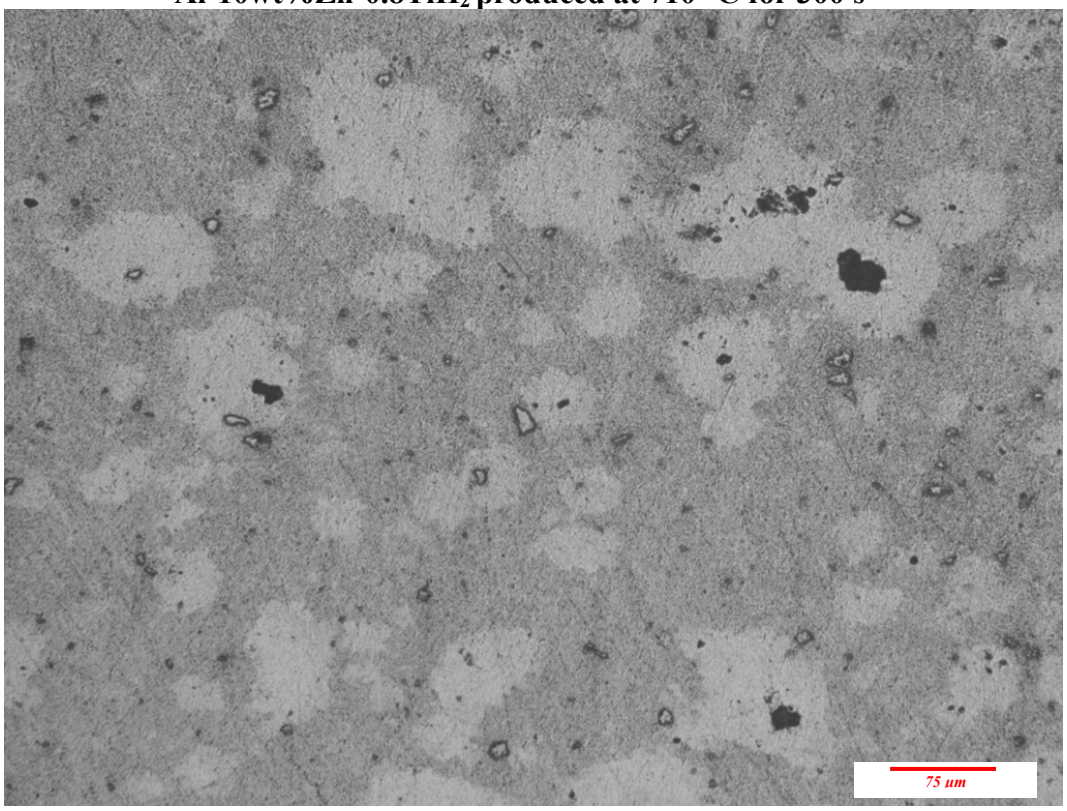

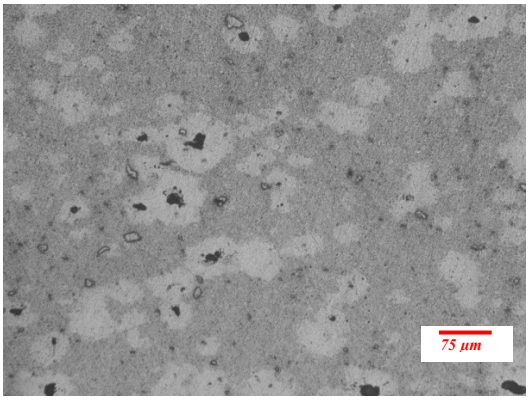

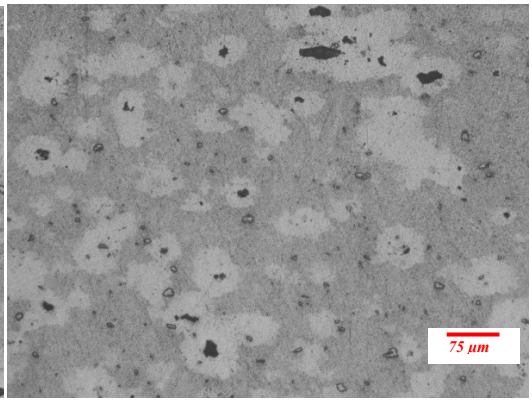

Al-10wt%Zn-0.8TiH_2 produced at 710 °C for 300 s

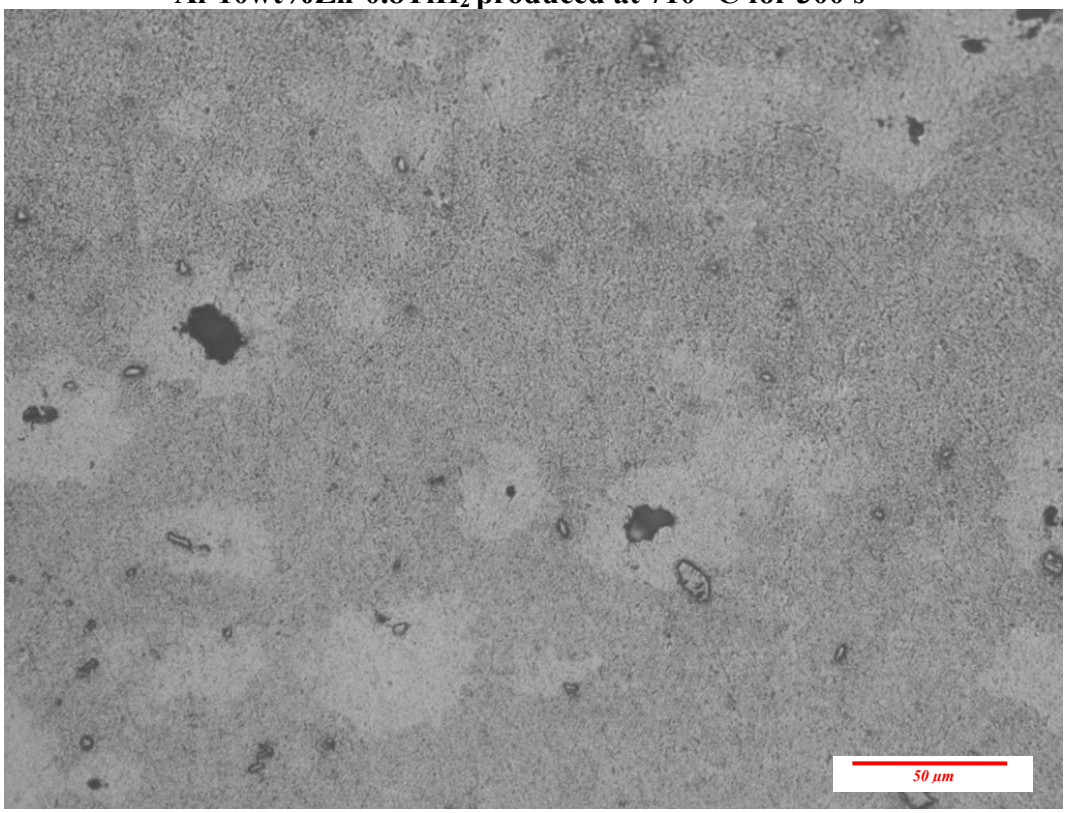

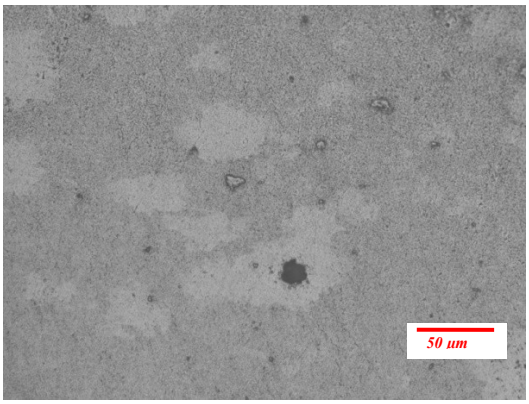

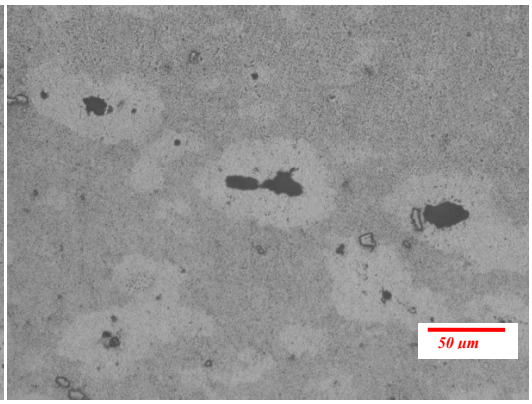

Al-10wt%Zn-0.8TiH_2 produced at 710 °C for 500 s

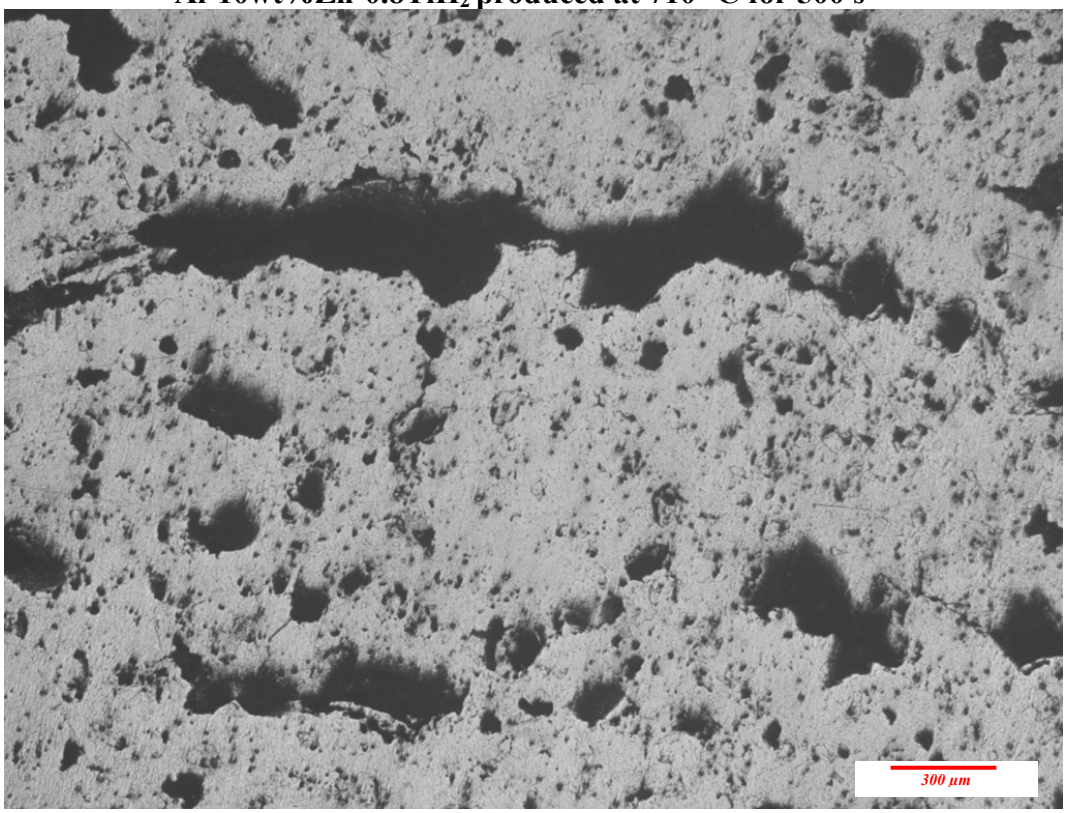

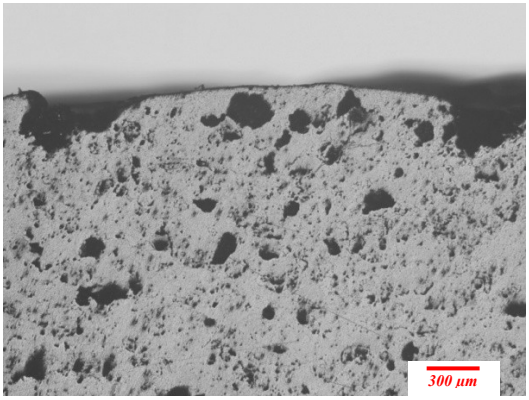

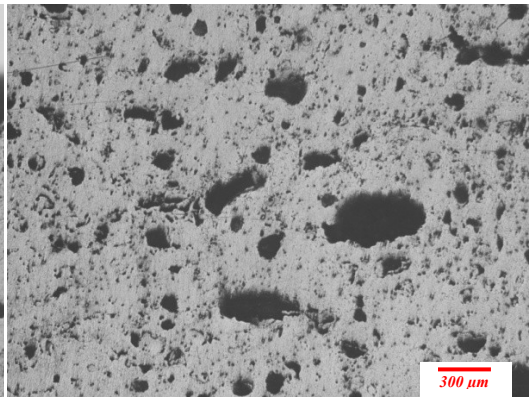

Al-10wt%Zn-0.8TiH_2 produced at 710 °C for 500 s

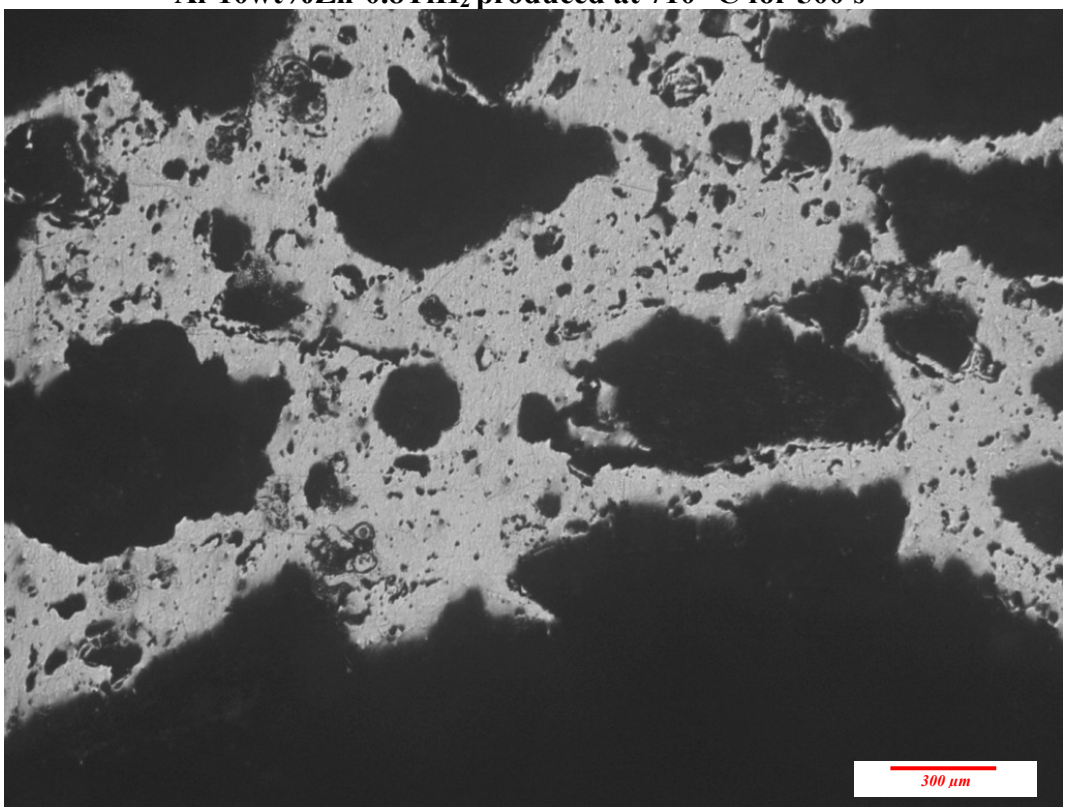

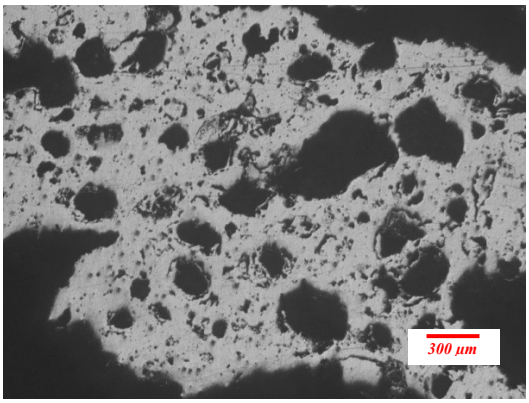

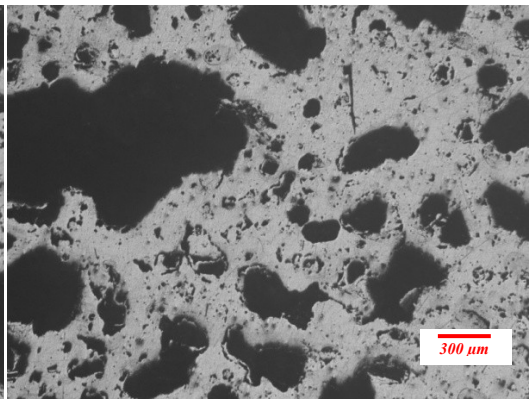

Al-33wt%Zn-0.8TiH_2 - Compact

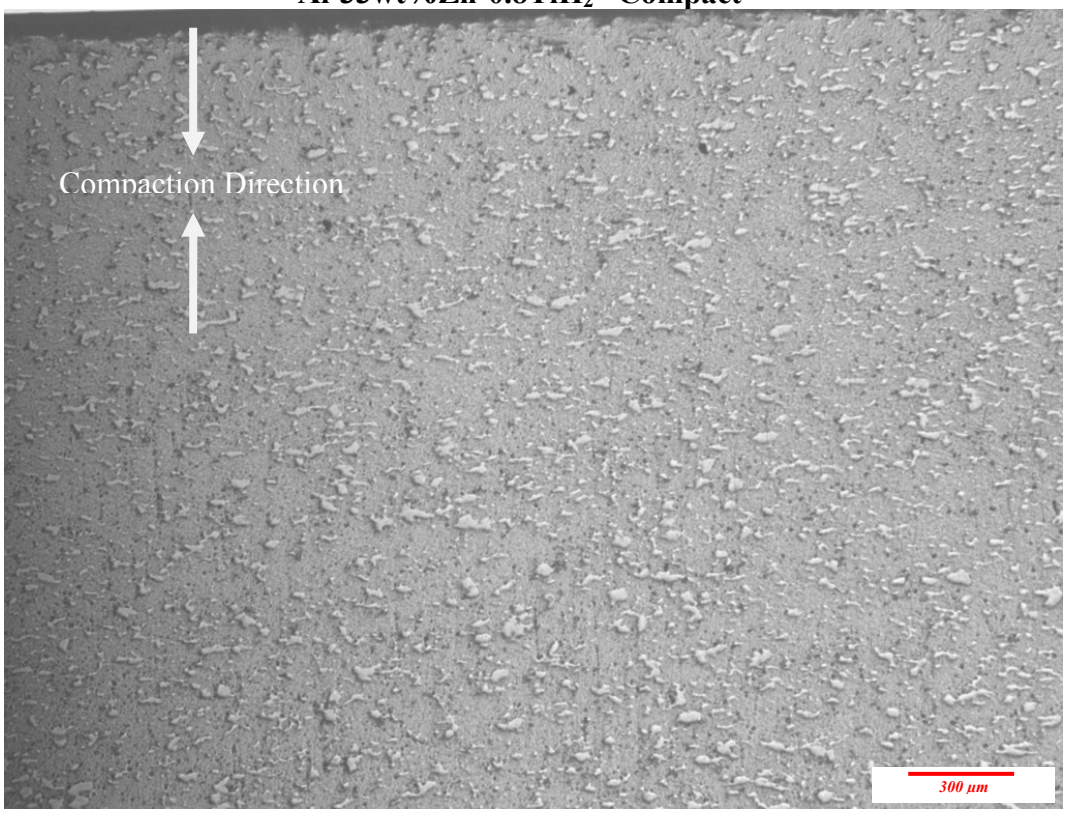

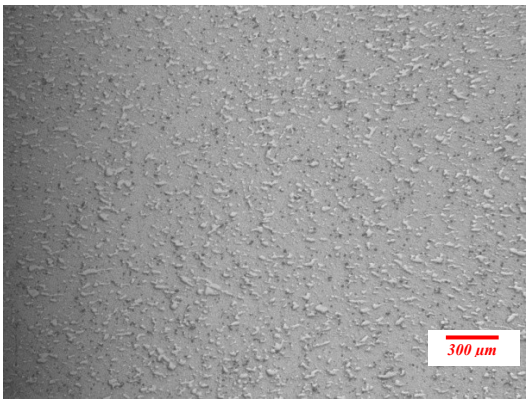

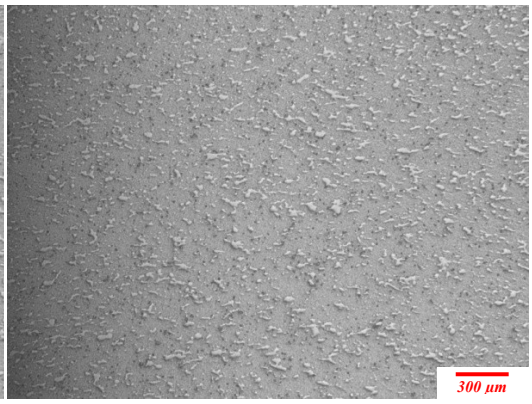

Al-33wt%Zn-0.8TiH_2 - Compact

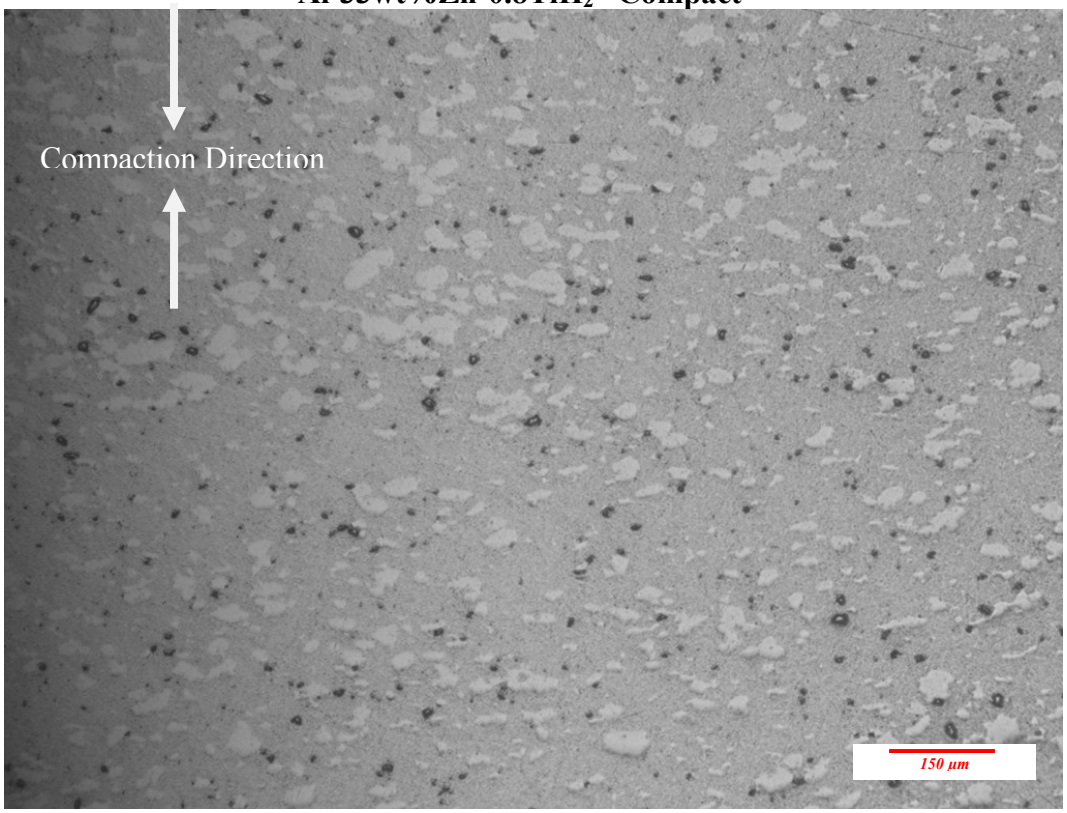

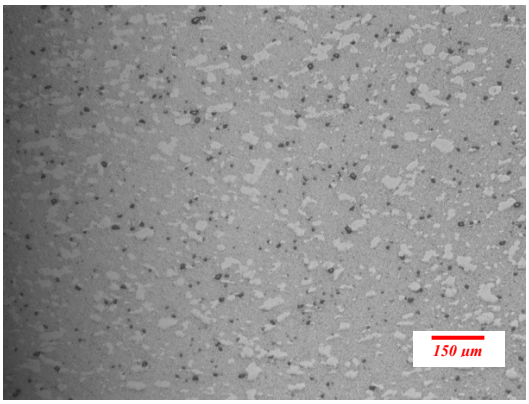

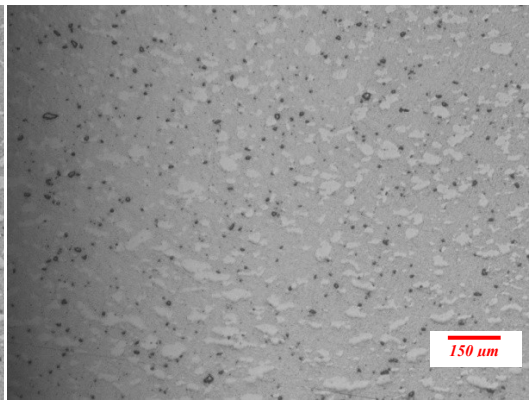

Al-33wt%Zn-0.8TiH_2 - Compact

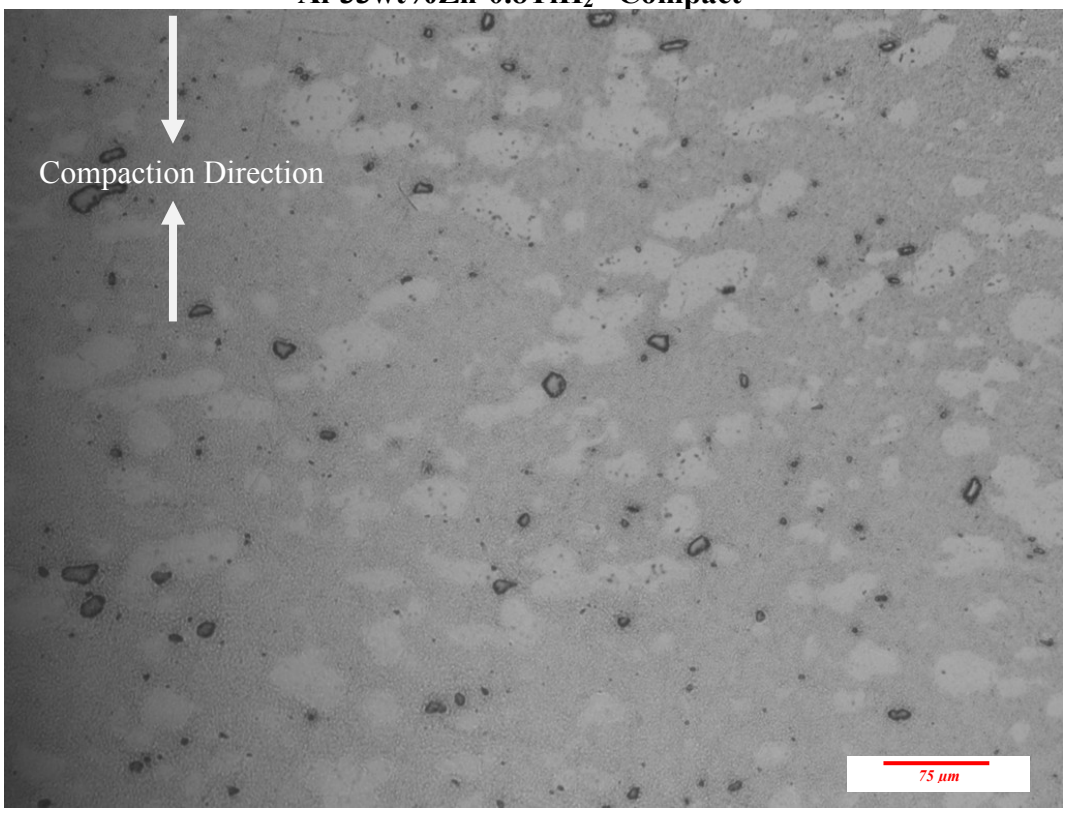

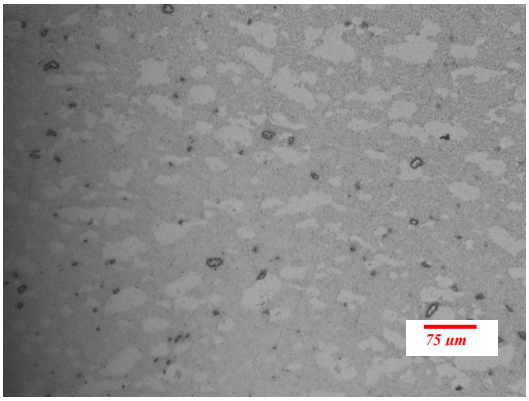

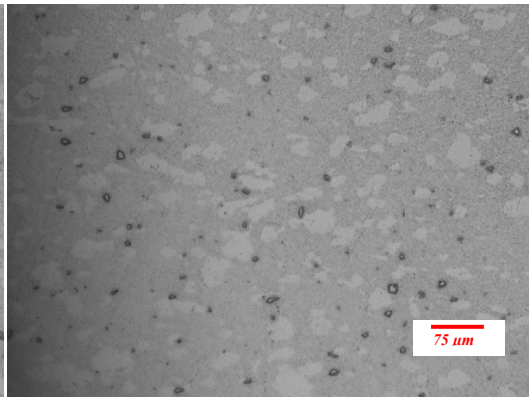

Al-33wt%Zn-0.8TiH_2 foamed at 640 °C for 300 s

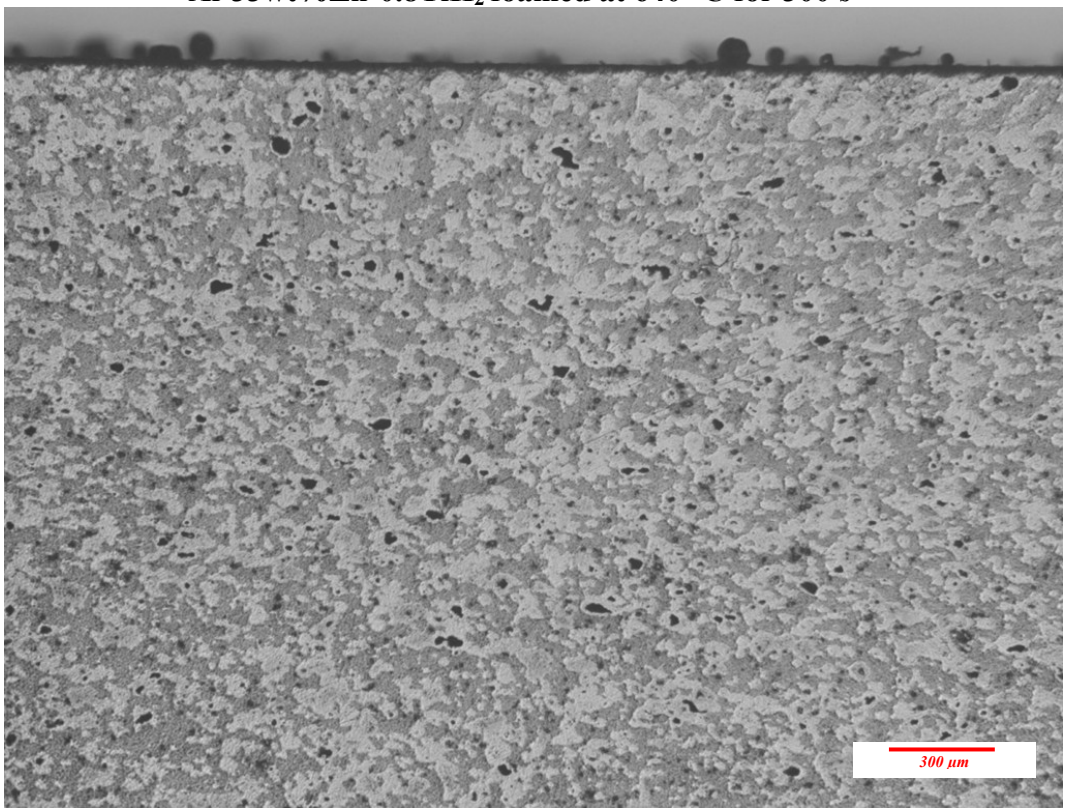

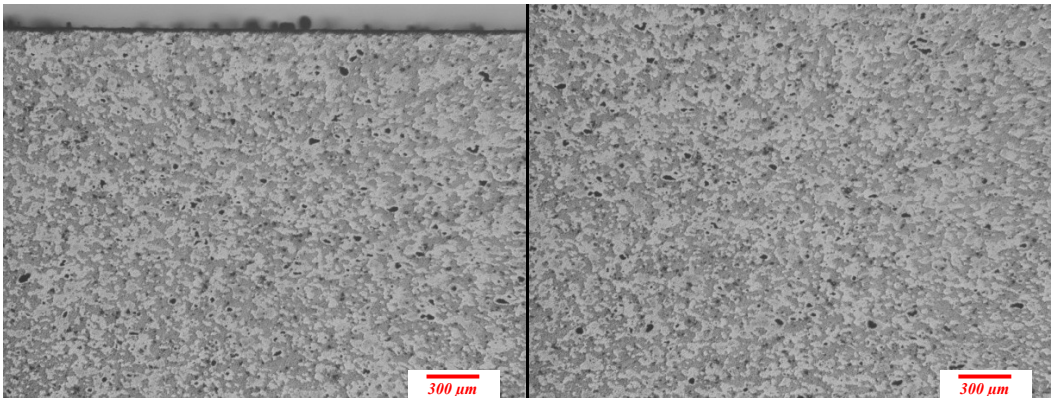

Al-33wt%Zn-0.8TiH_2 foamed at 640 °C for 300 s

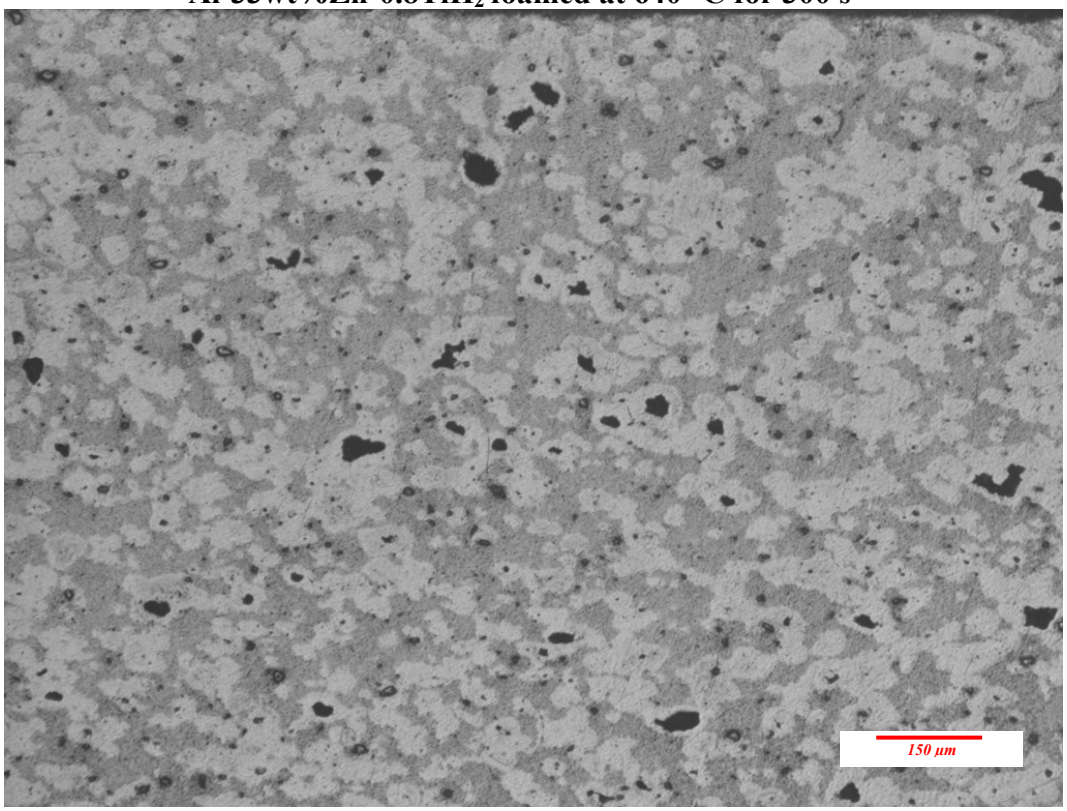

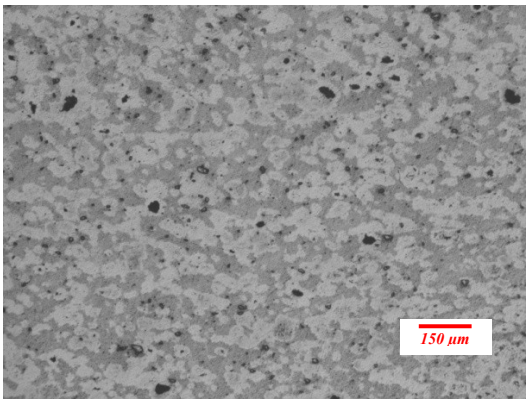

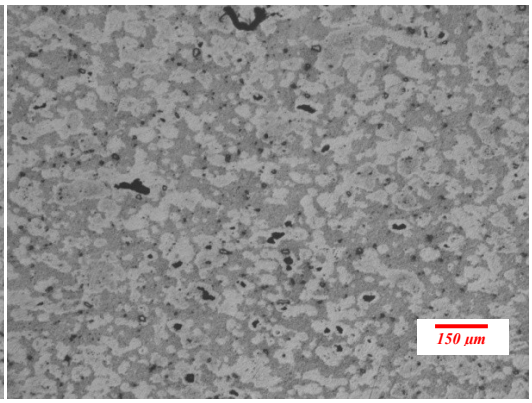

Al-33wt%Zn-0.8TiH_2 foamed at 640 °C for 300 s

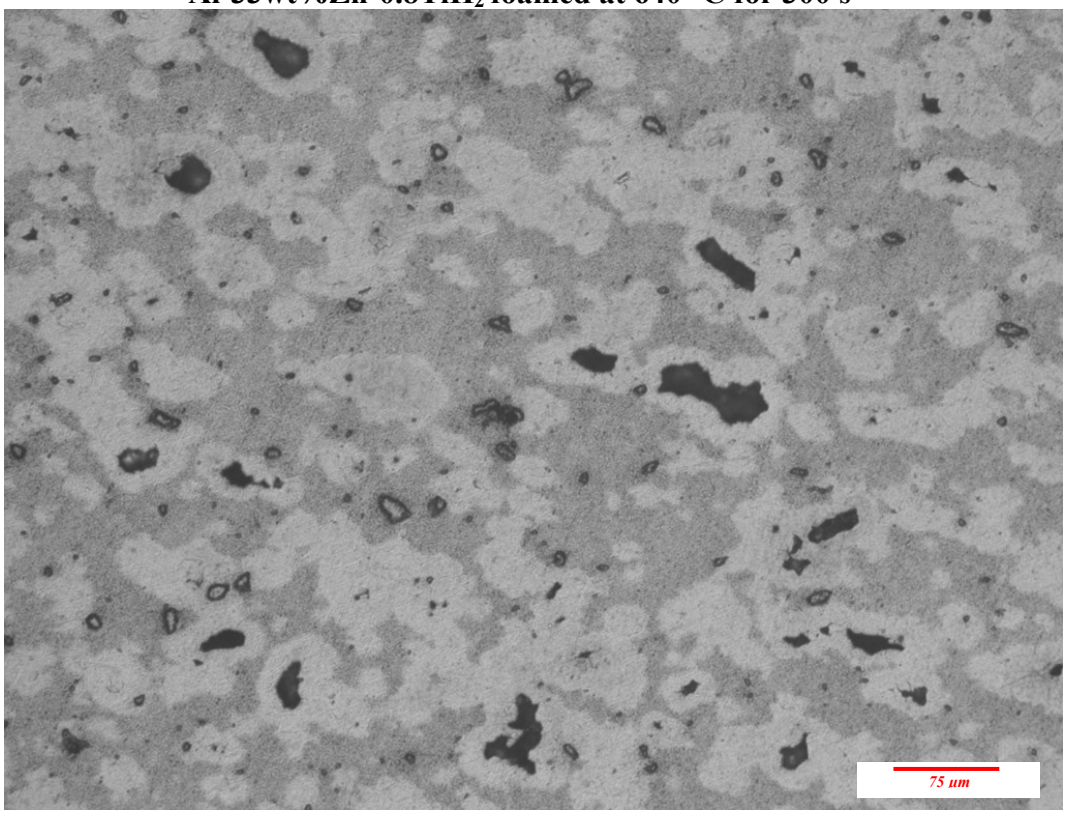

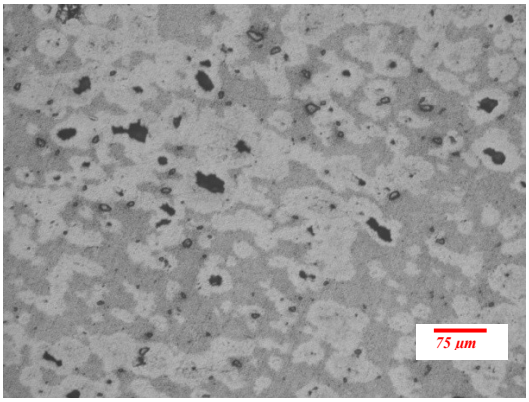

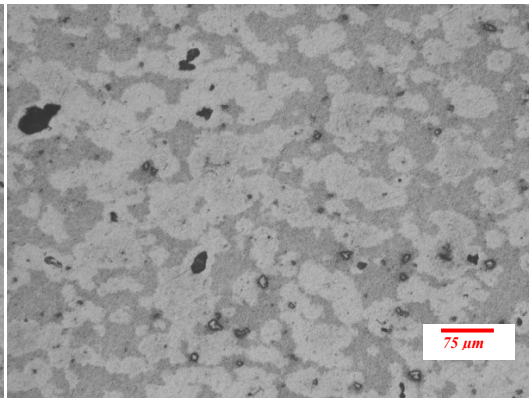

Al-33wt%Zn-0.8TiH_2 foamed at 640 °C for 300 s

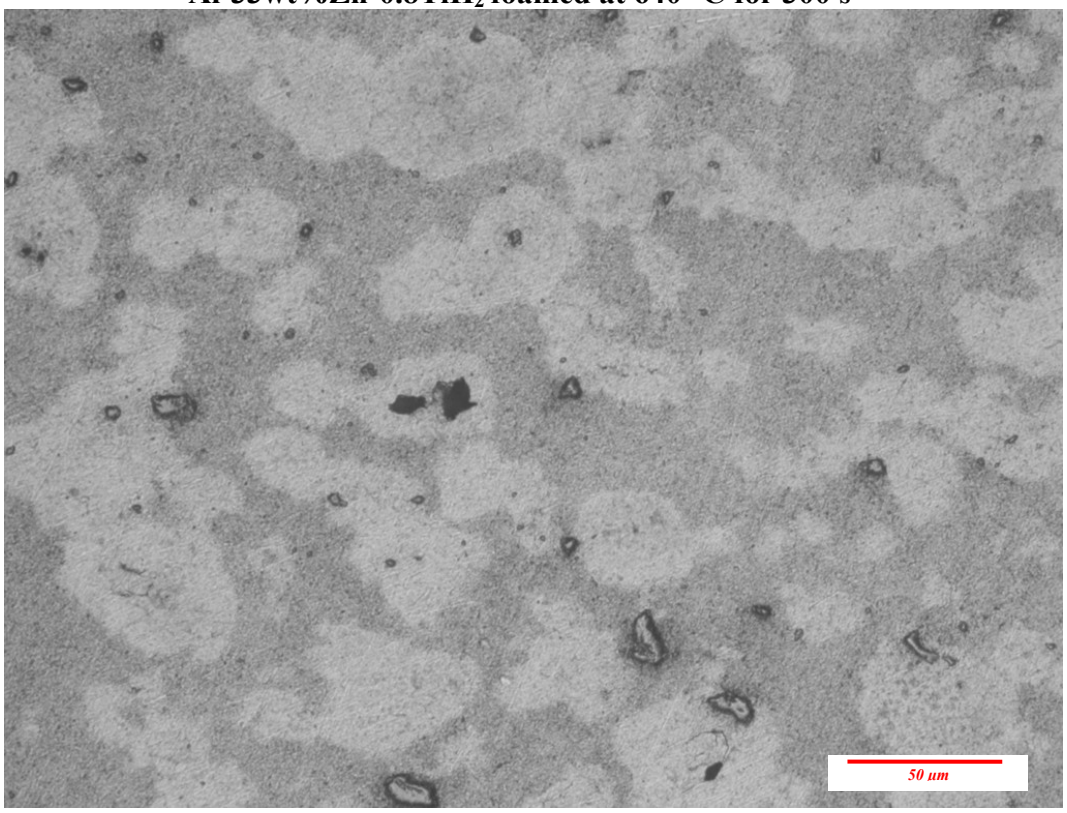

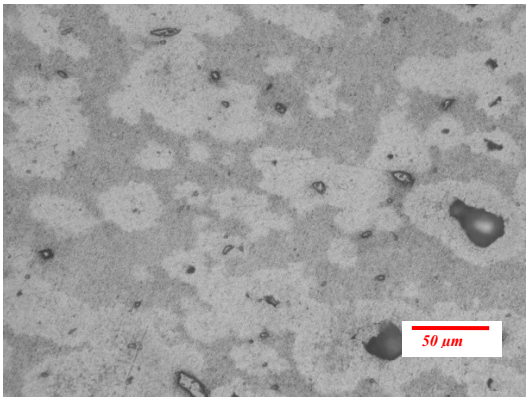

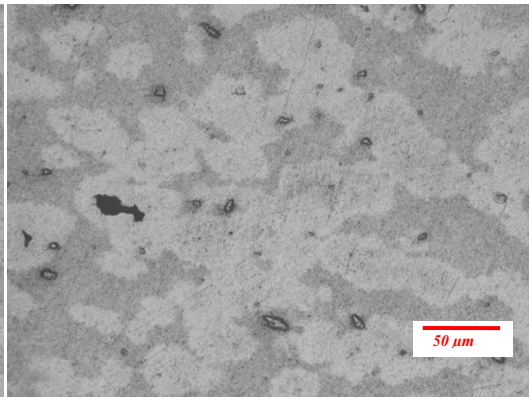

Al-33wt%Zn-0.8TiH_2 foamed at 640 °C for 500 s

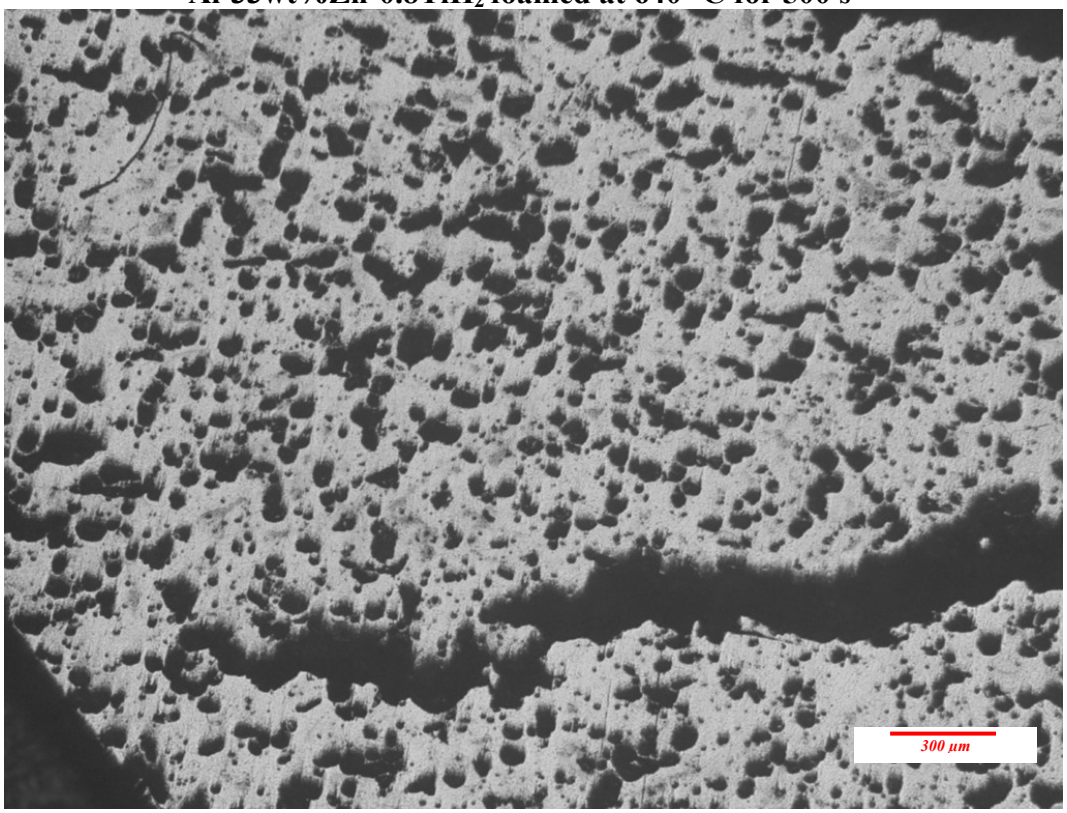

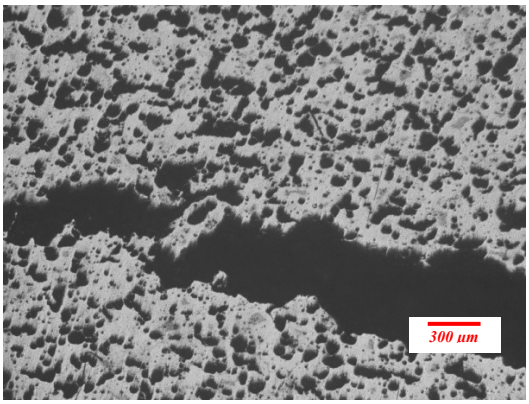

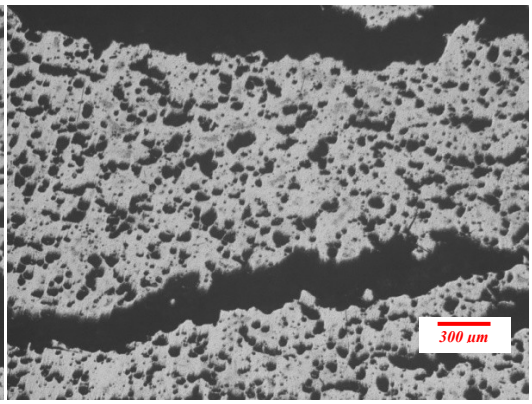

Al-33wt%Zn-0.8TiH_2 foamed at 640 °C for 500 s

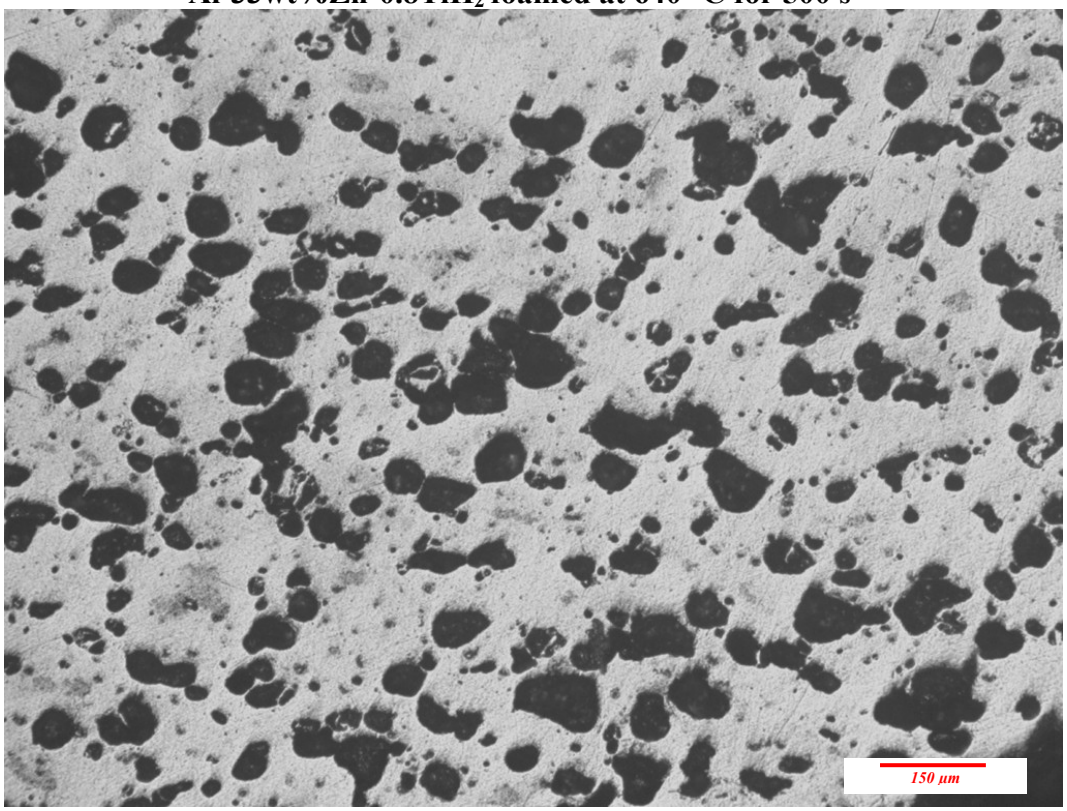

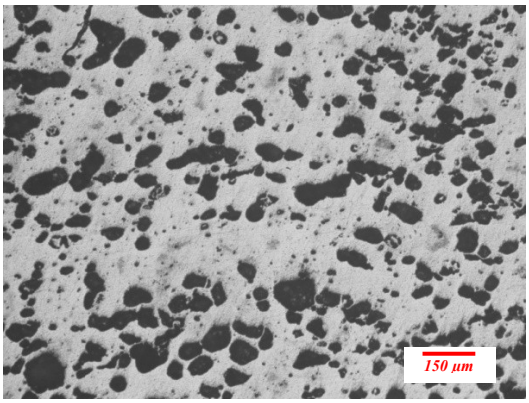

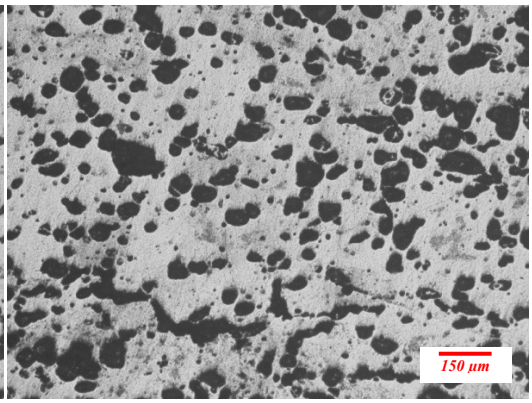

Al-33wt%Zn-0.8TiH_2 foamed at 640 °C for 500 s

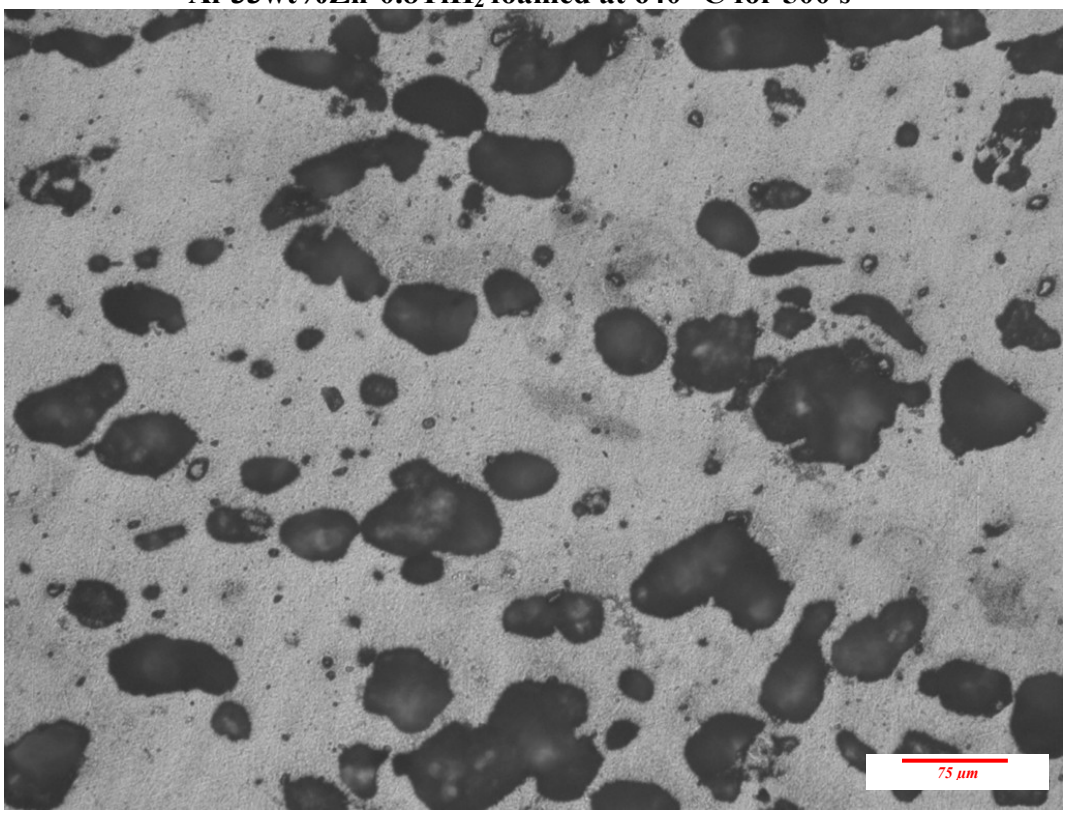

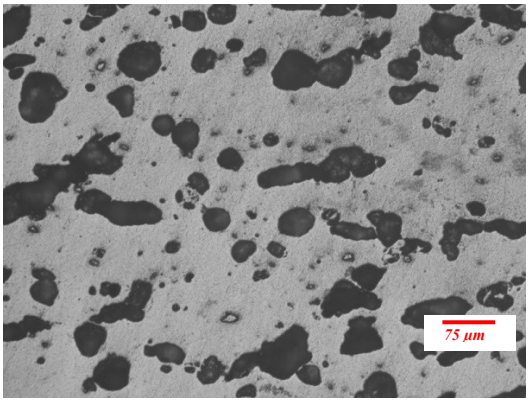

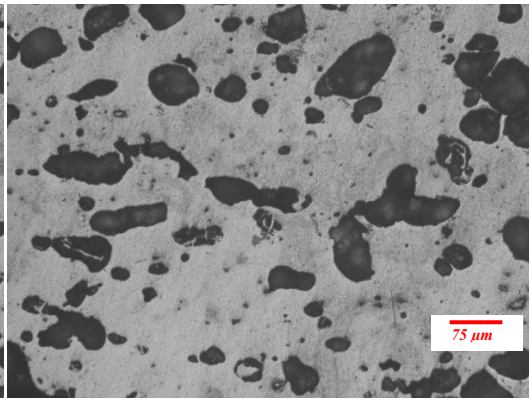

Al-33wt%Zn-0.8TiH_2 foamed at 640 °C for 500 s

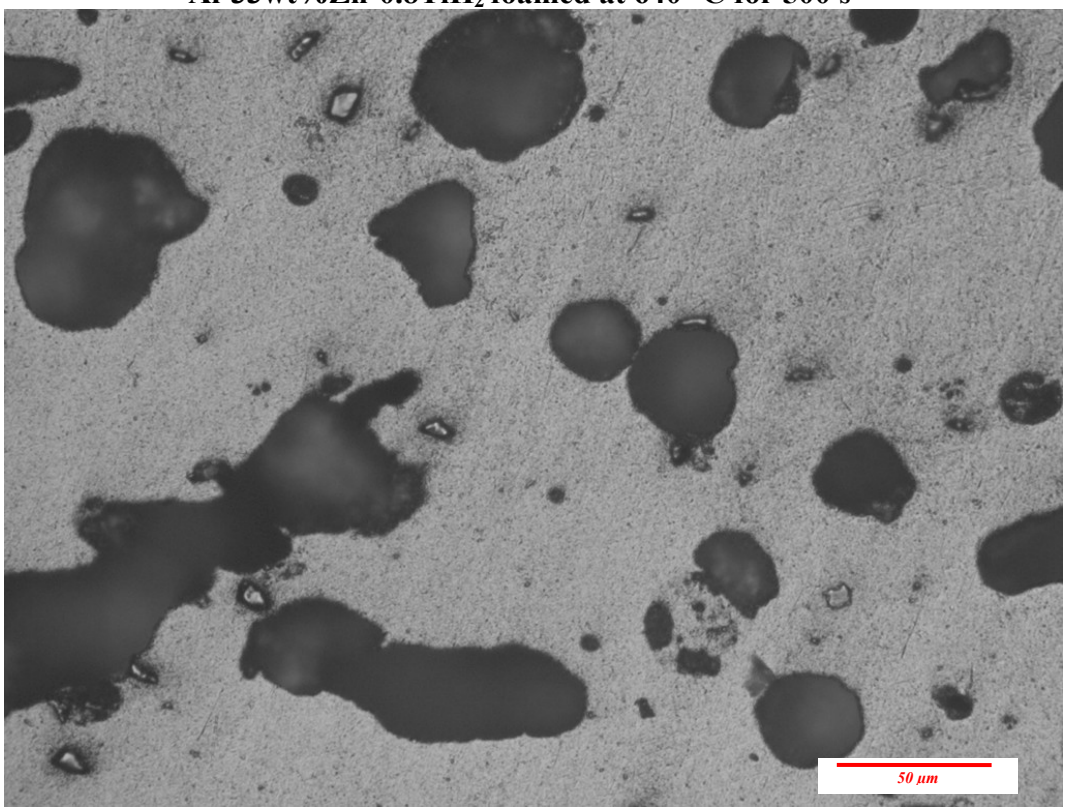

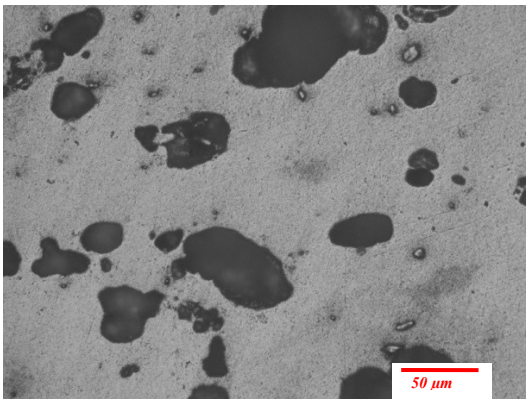

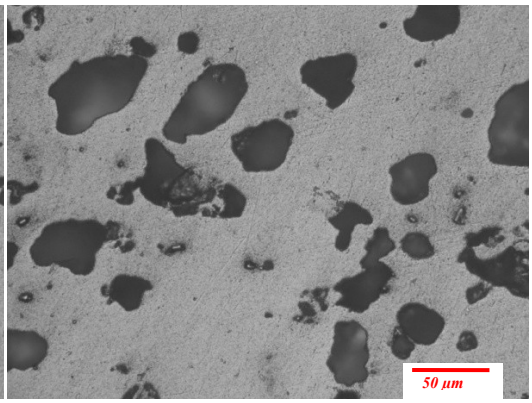

Al-33wt%Zn-0.8TiH_2 foamed at 640 °C for 550 s

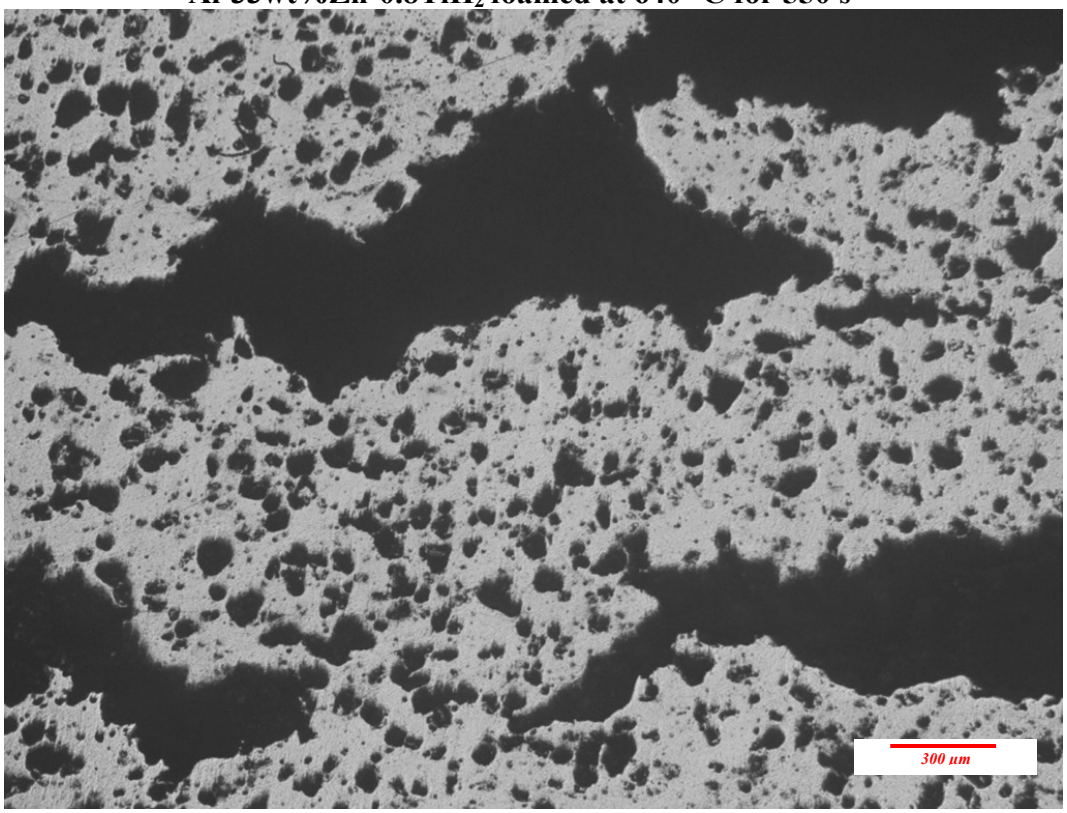

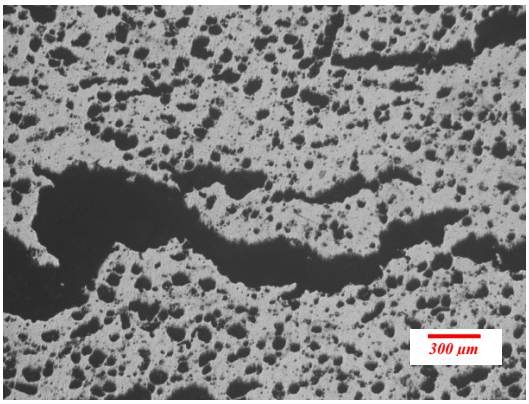

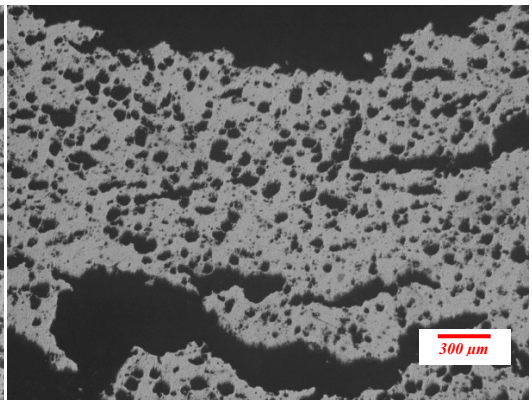

Al-33wt%Zn-0.8TiH_2 foamed at 640 °C for 550 s

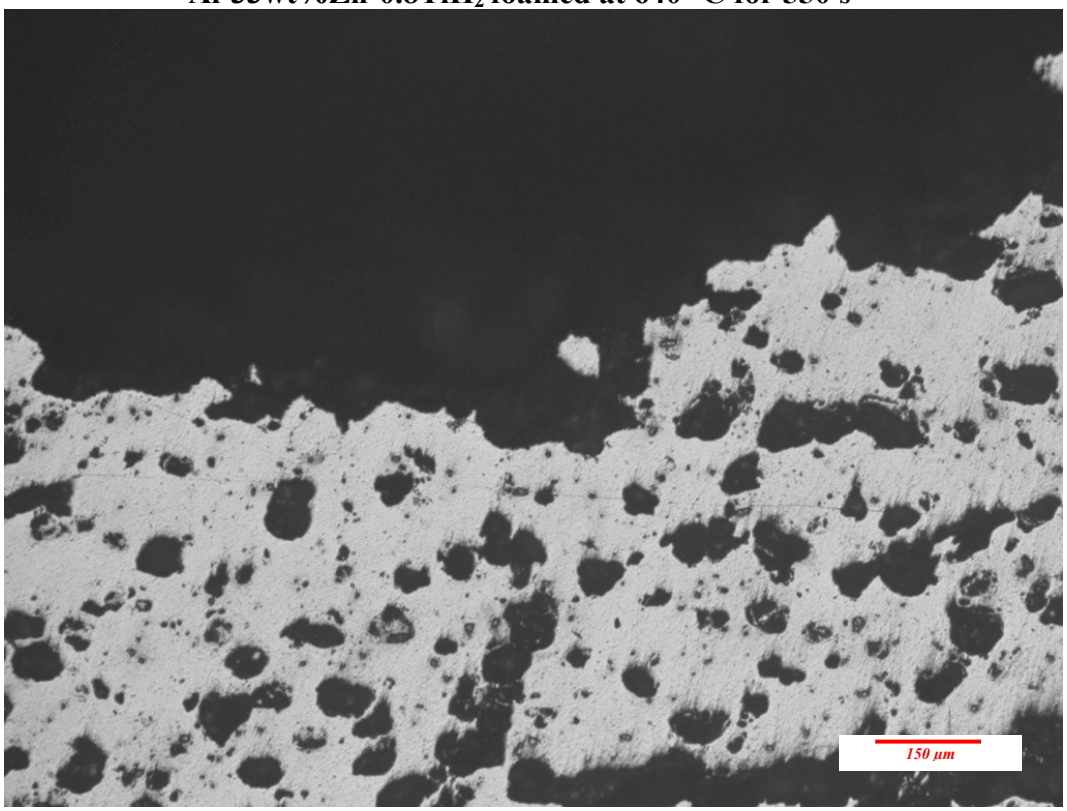

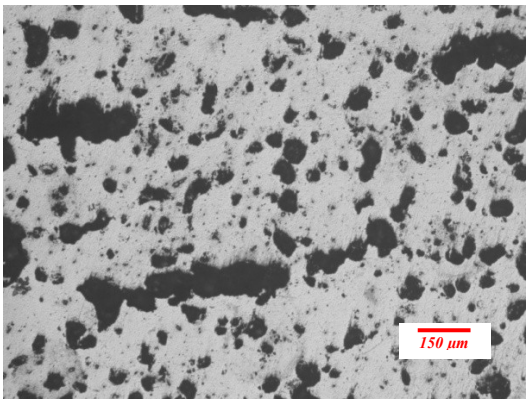

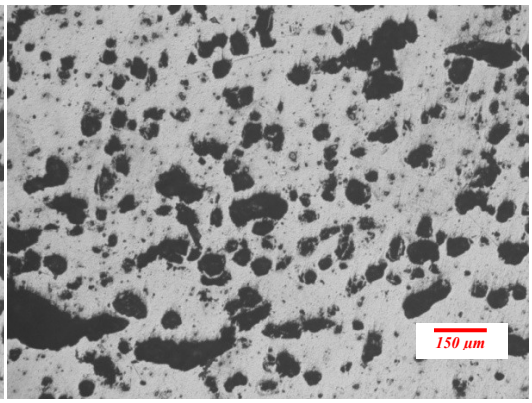

Al-33wt%Zn-0.8TiH_2 foamed at 640 °C for 550 s

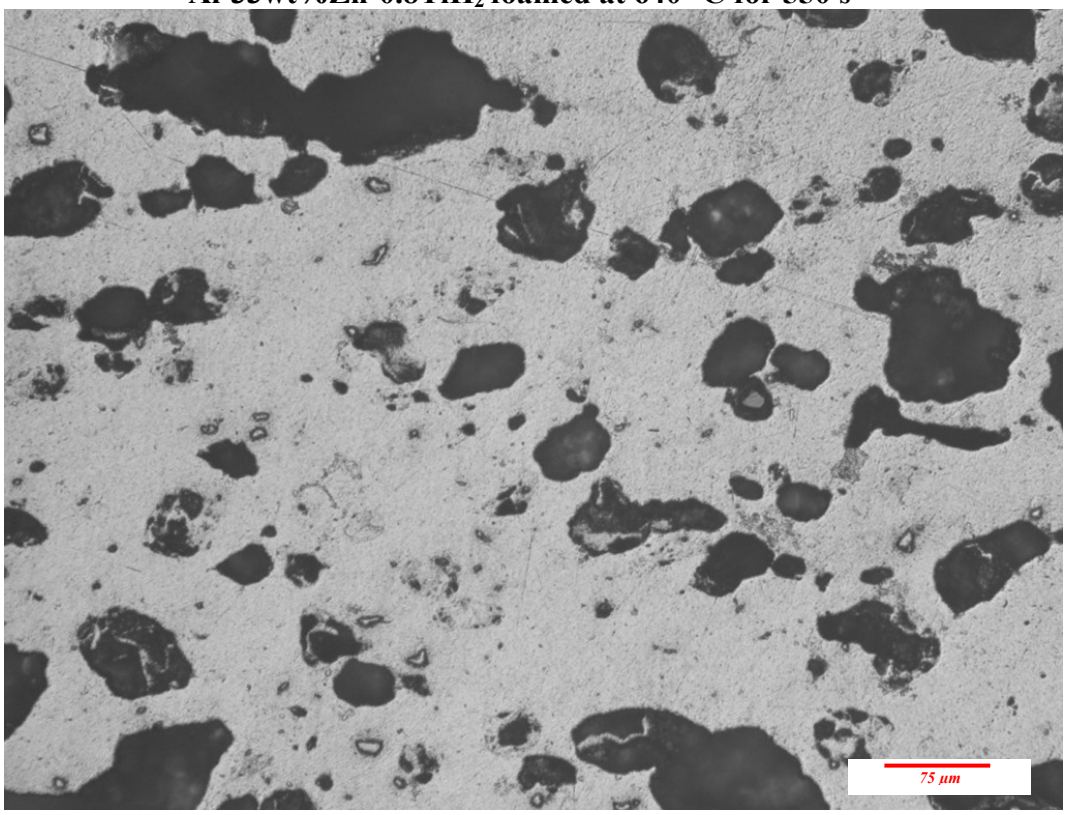

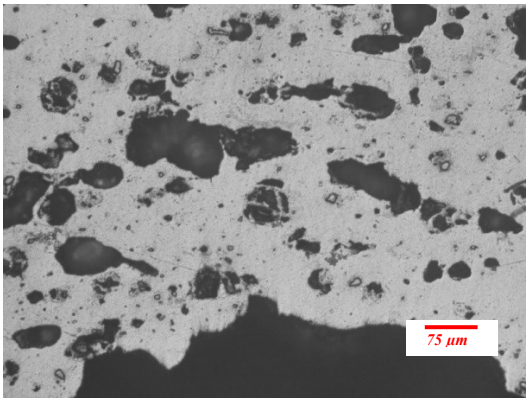

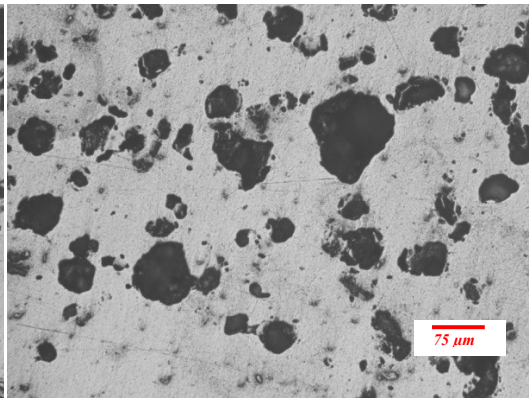

Al-33wt%Zn-0.8TiH_2 foamed at 640 °C for 550 s

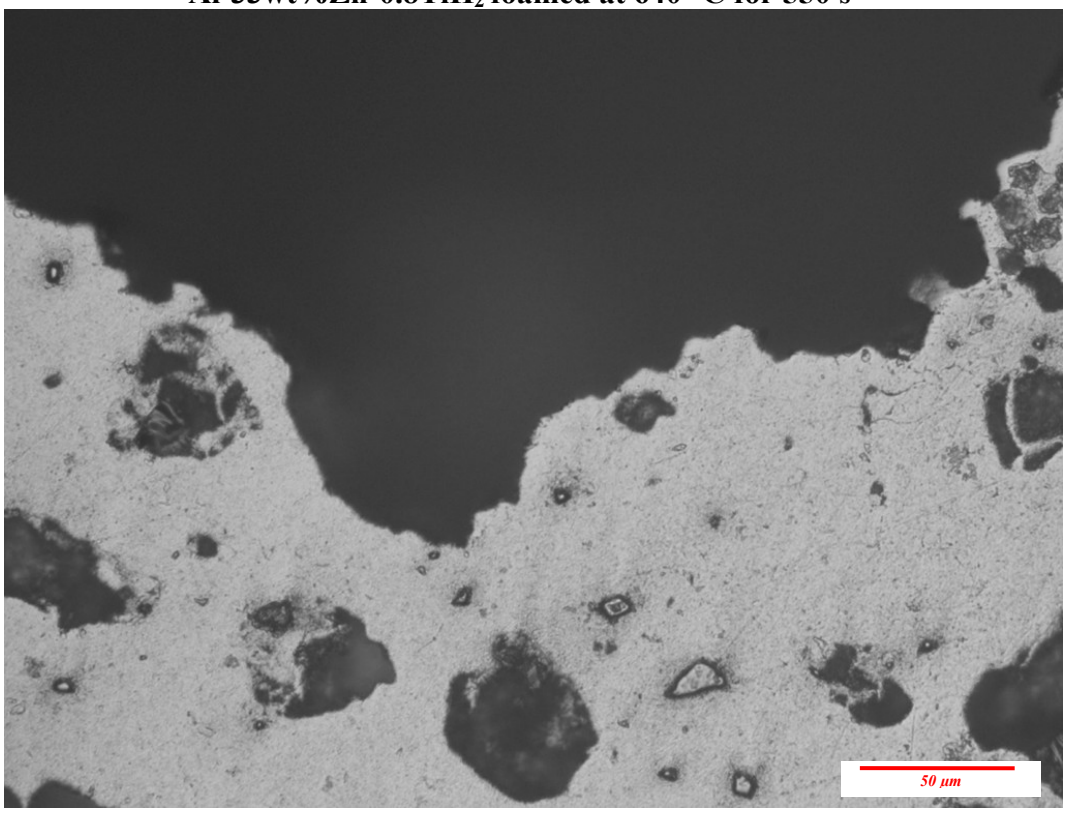

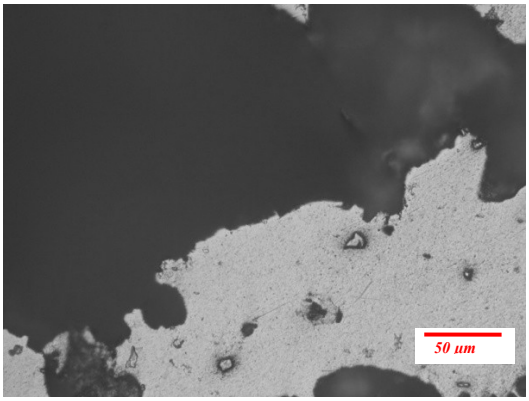

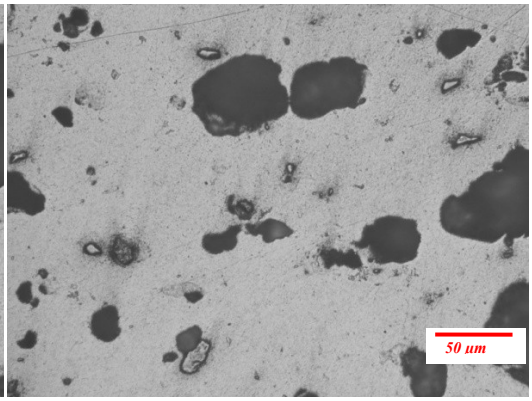

Al-10wt%Zn DSC curve

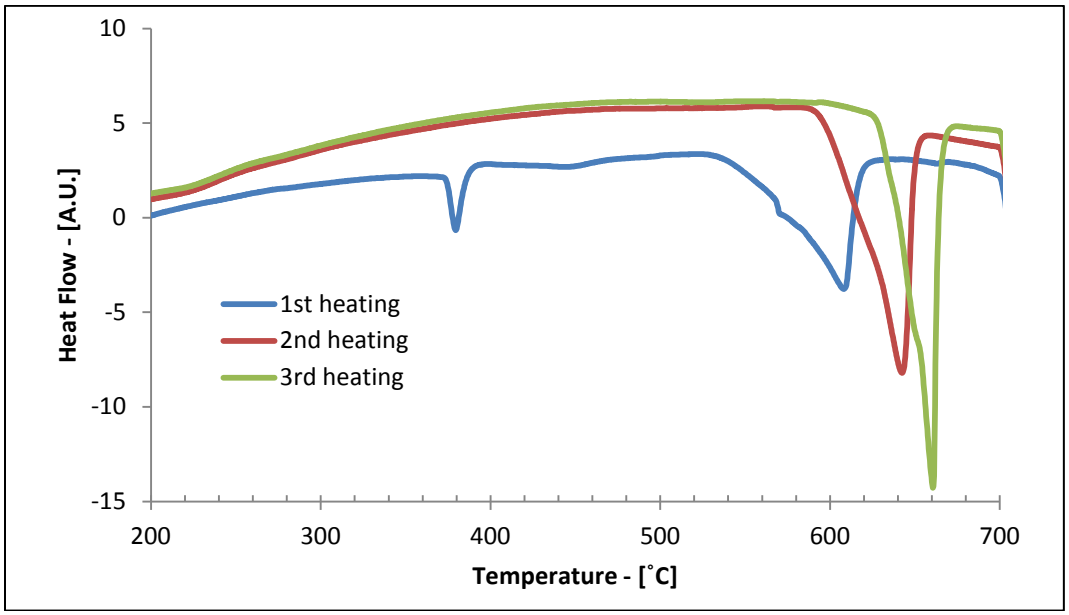

Al-50wt%Zn DSC curve

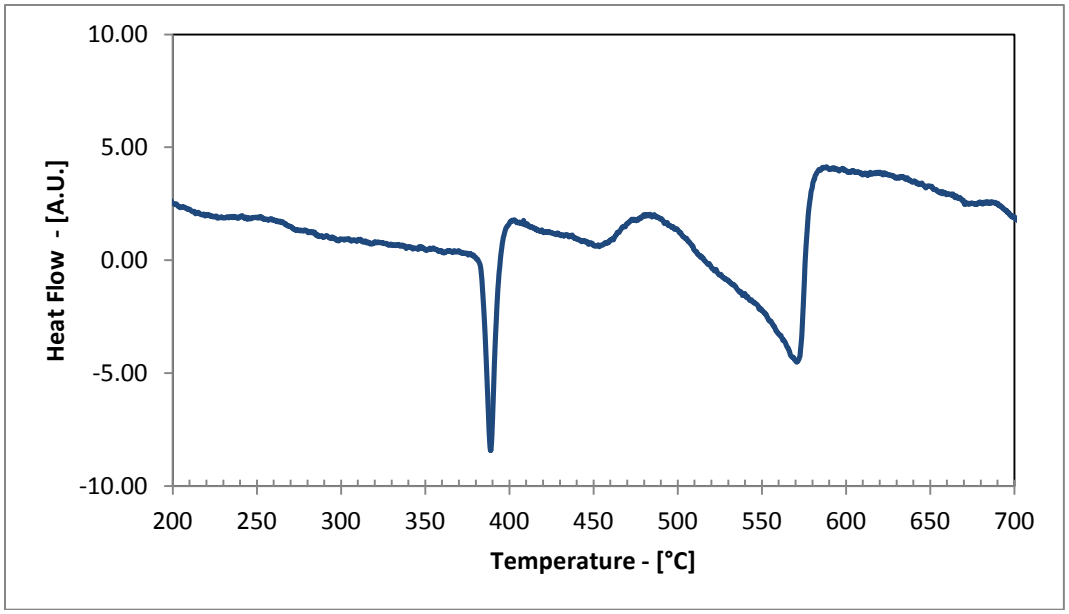

EDS analysis of Al-10wt%Zn foam produced at 710 °C for 300 s

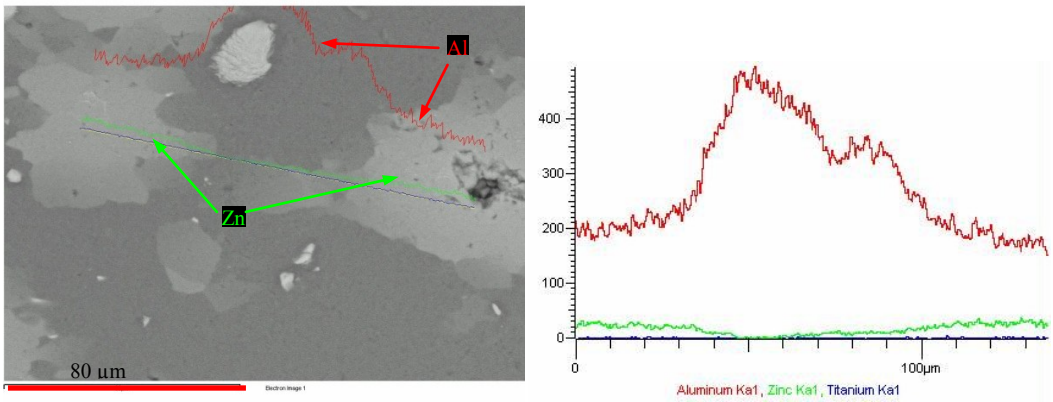

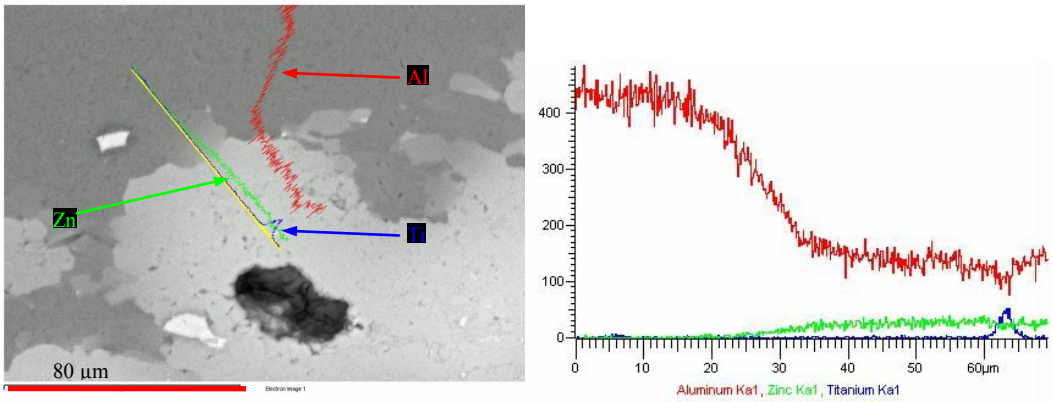

EDS analysis of Al-10wt%Zn foam produced at 710 °C for 300 s

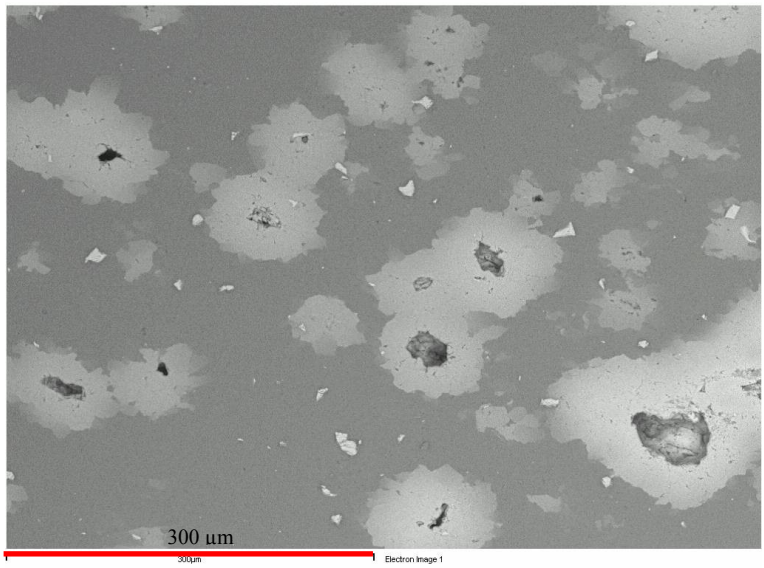

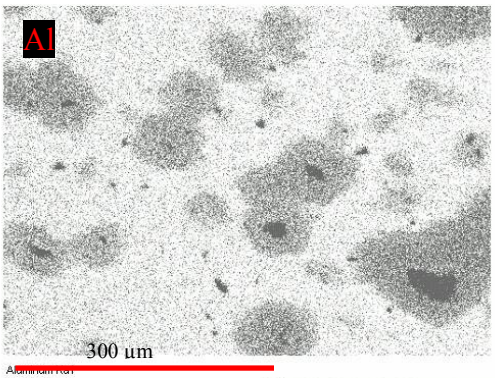

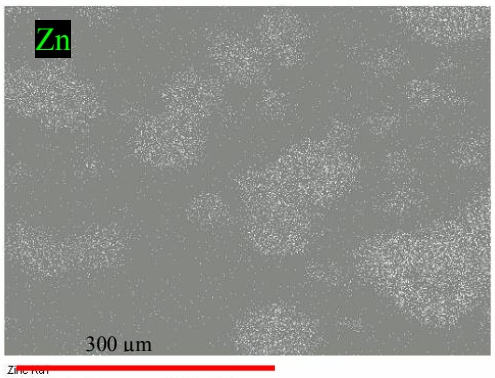

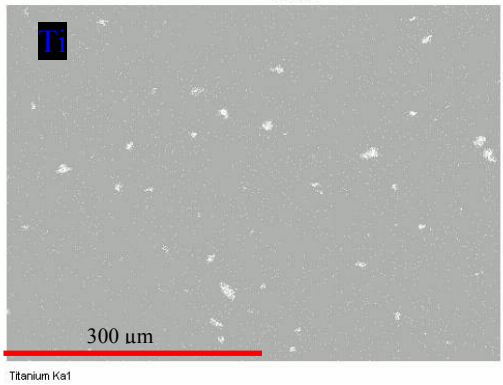

Foaming Curves

Al-10wt%Zn - 20mm

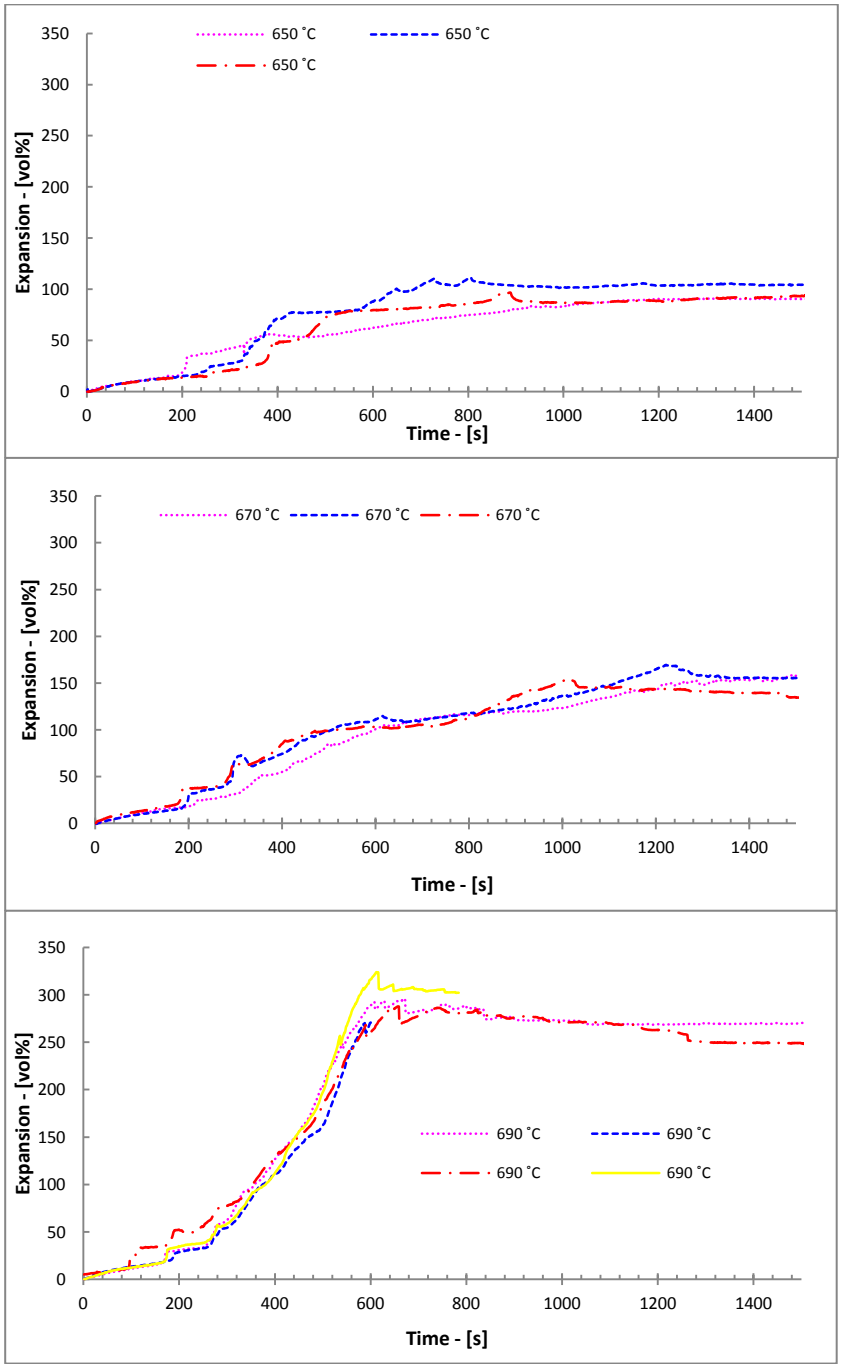

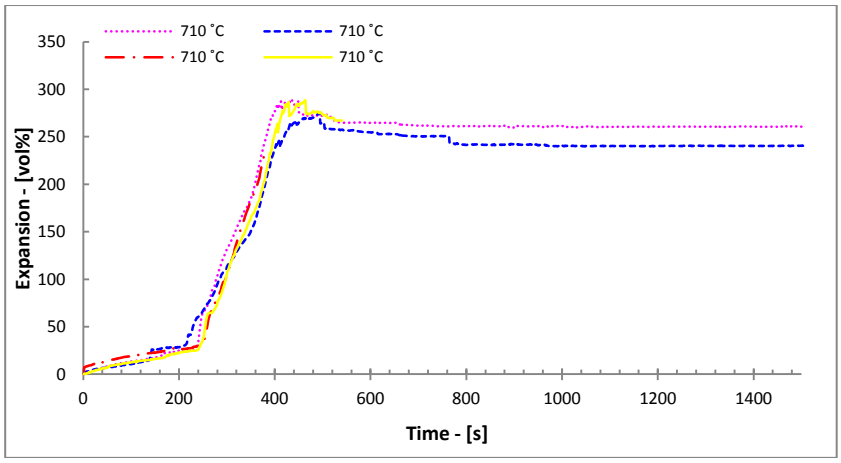

Al-33wt% Zn – 20mm

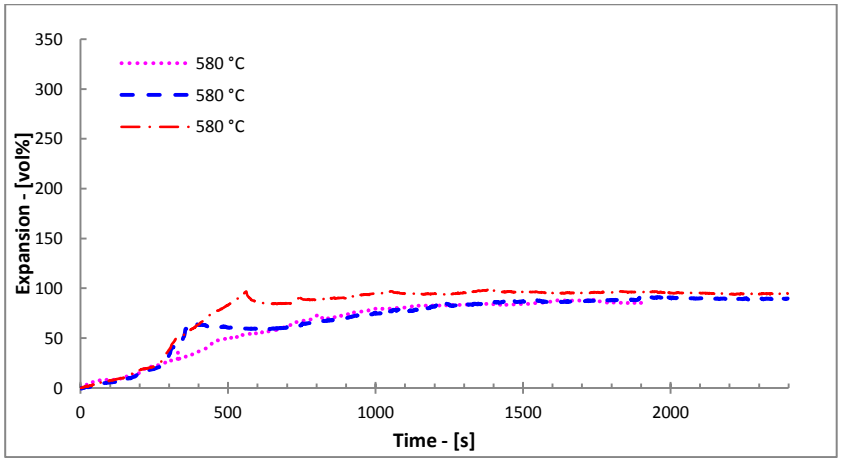

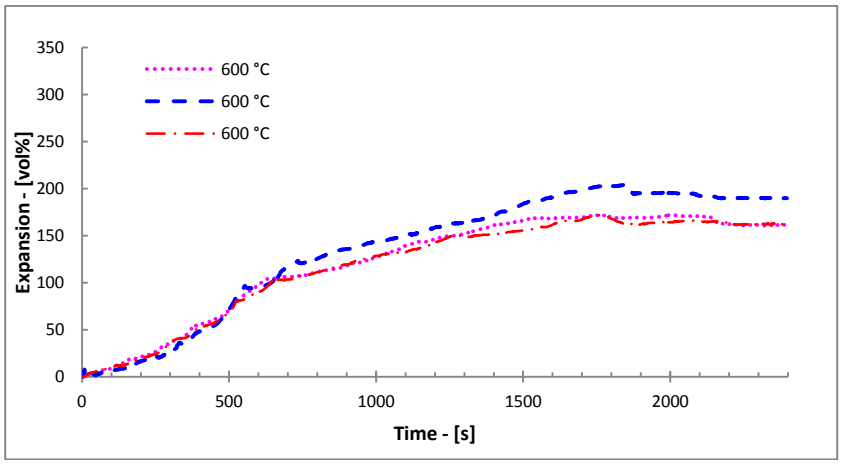

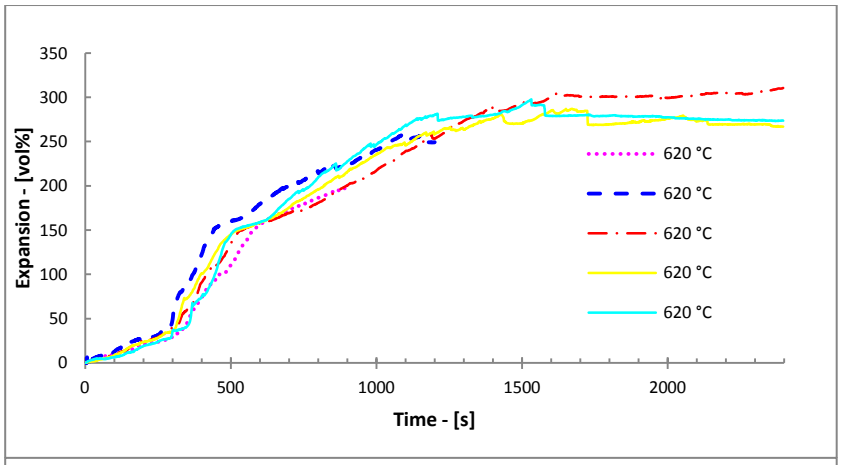
Expansion - [vol%]
Time - [s]
620 °C
620 °C
620 °C
620 °C
620 °C

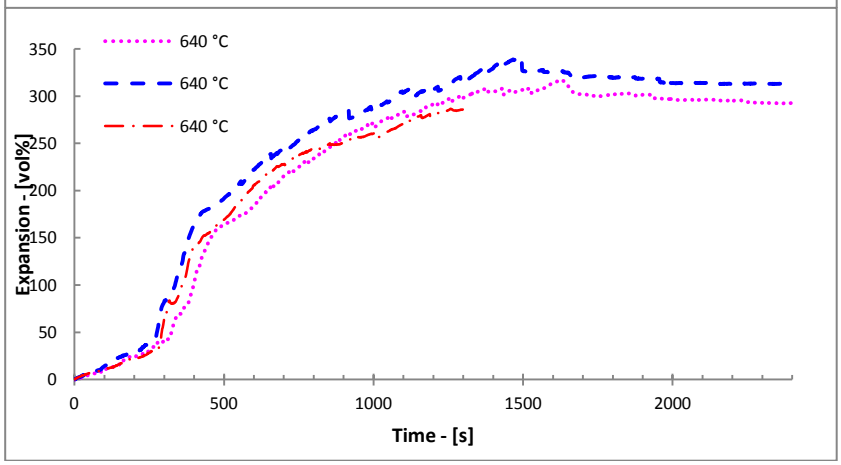
Expansion - [vol%]
Time - [s]
640 °C
640 °C
640 °C

Al-50wt% Zn

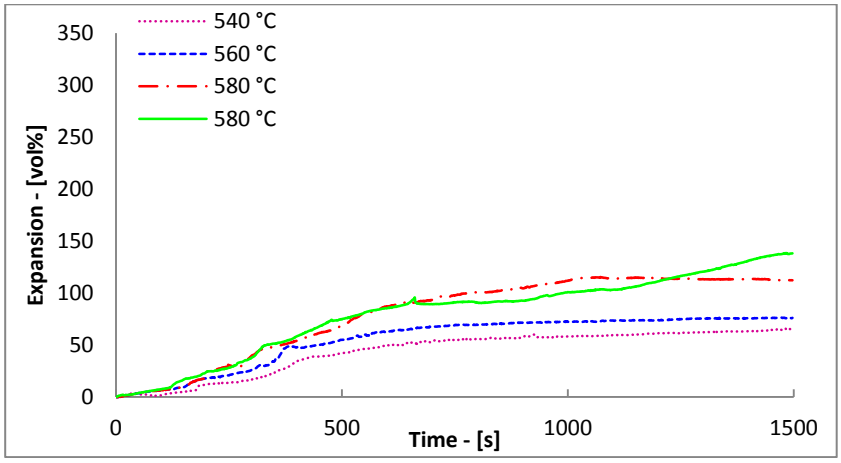
Expansion - [vol%]
Time - [s]
540 °C
560 °C
580 °C
580 °C

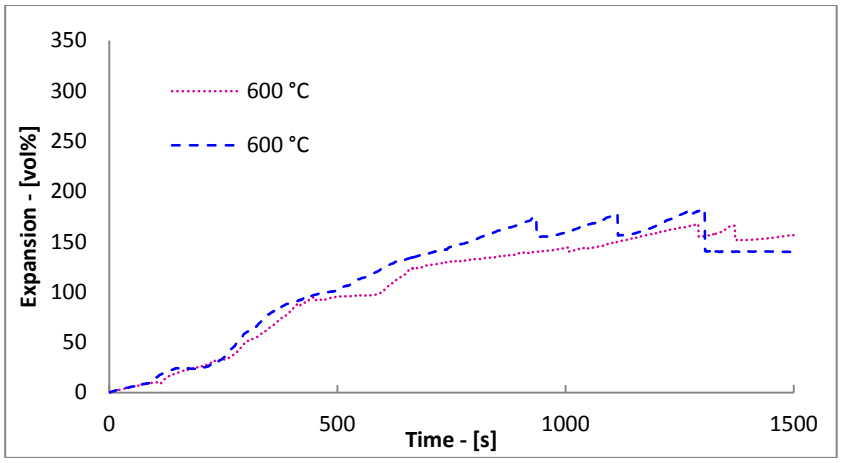
600 °C
600 °C
Expansion - [vol%]
Time - [s]
0
50
100
150
200
250
300
350
0
500
1000
1500

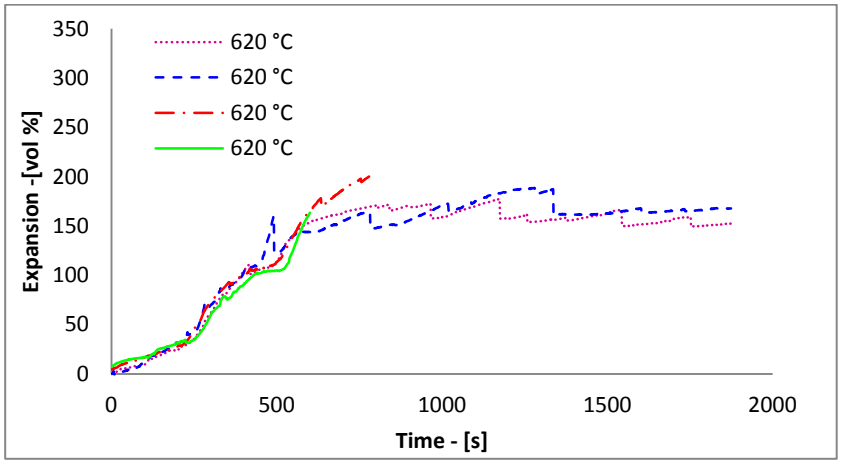
620 °C
620 °C
620 °C
620 °C
Expansion -[vol %]
Time - [s]
0
50
100
150
200
250
300
350
0
500
1000
1500
2000

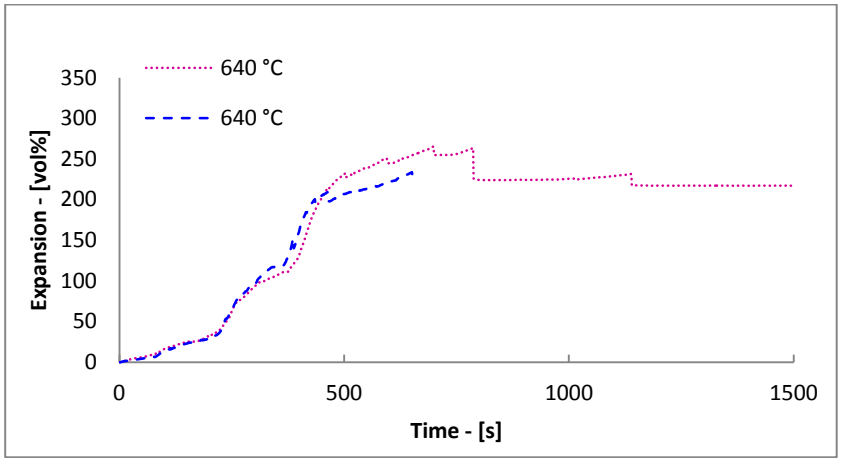
640 °C
640 °C
Expansion - [vol%]
Time - [s]
0
50
100
150
200
250
300
350
0
500
1000
1500

Al-10wt%Zn 30 mm samples

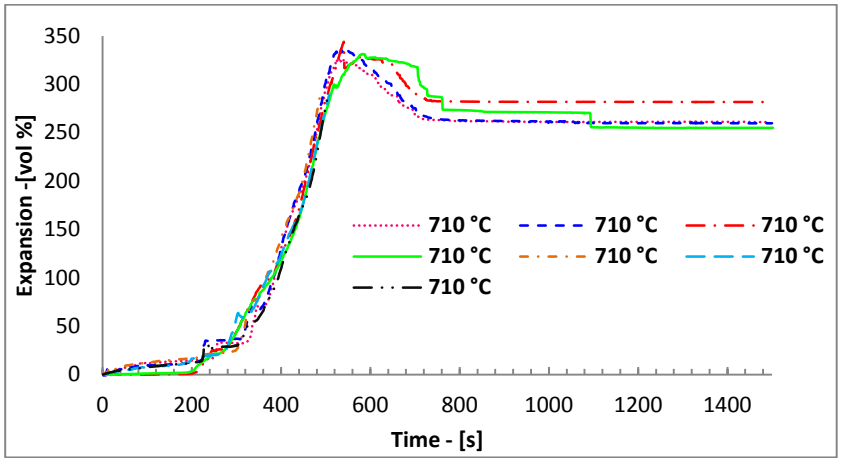

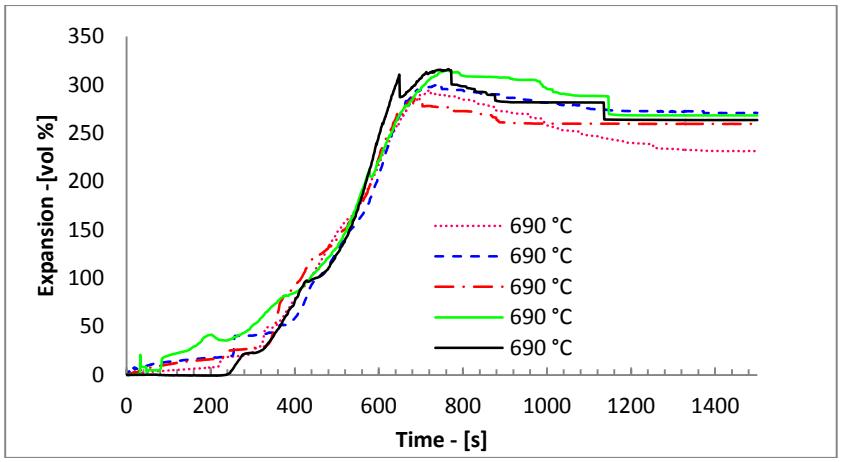

Al-33Zn 30 mm samples

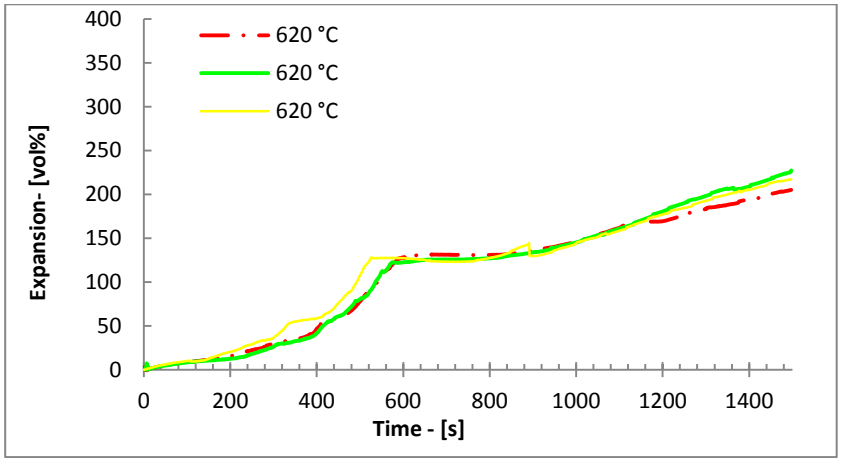

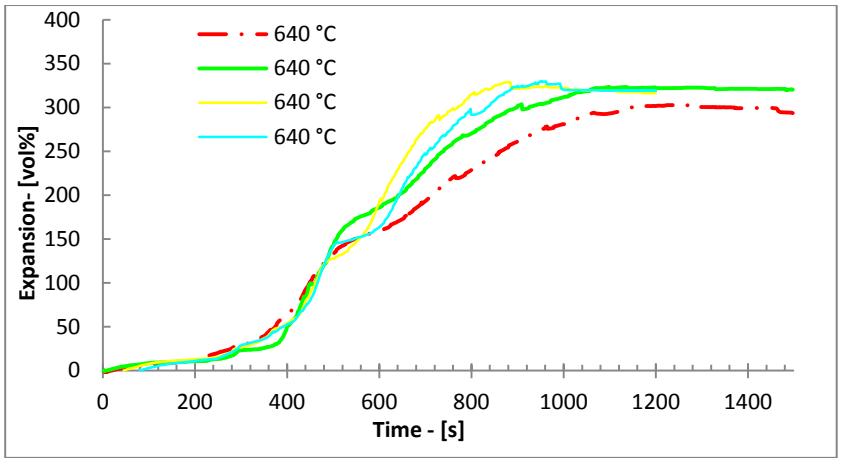
640 °C
640 °C
640 °C
640 °C
Expansion- [vol%]
Time - [s]
0
50
100
150
200
250
300
350
400
0
200
400
600
800
1000
1200
1400

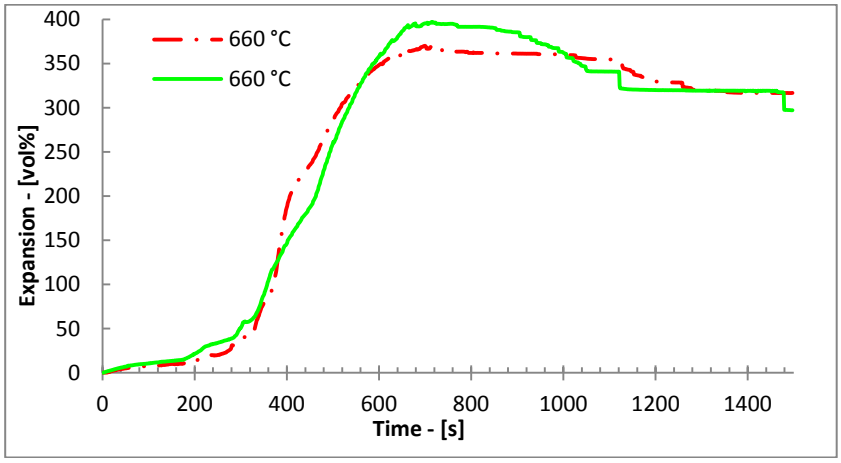
660 °C
660 °C
Expansion - [vol%]
Time - [s]
0
50
100
150
200
250
300
350
400
0
200
400
600
800
1000
1200
1400

Pore Size Analysis

Pure aluminum produced at 750 °C

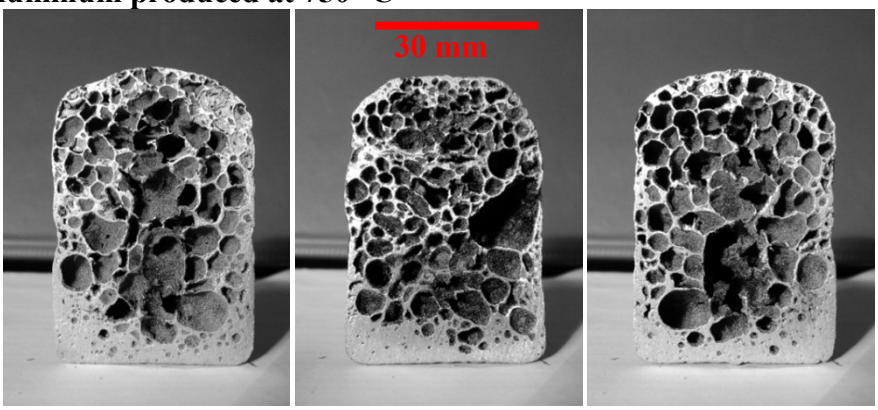

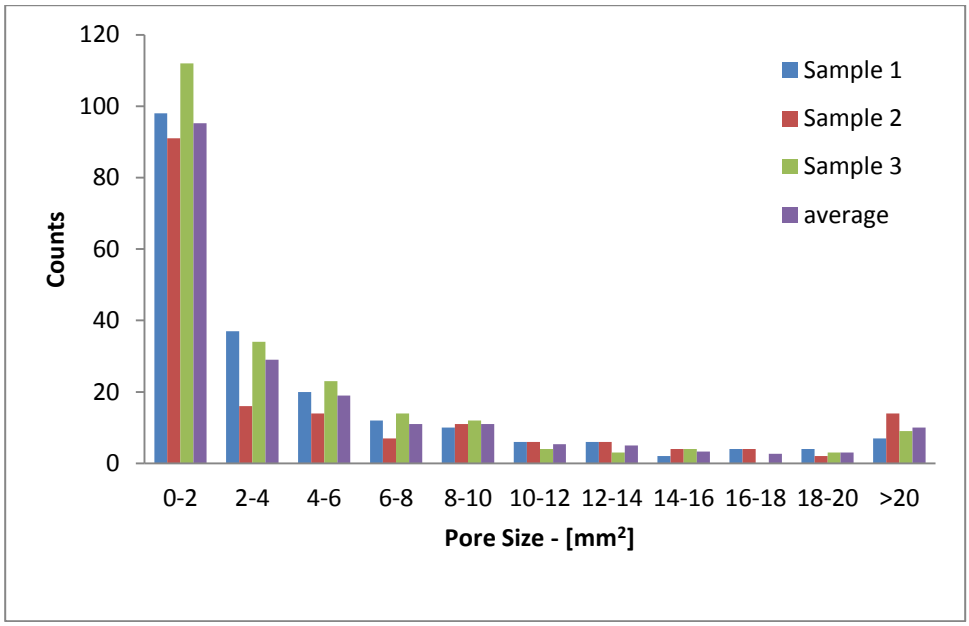

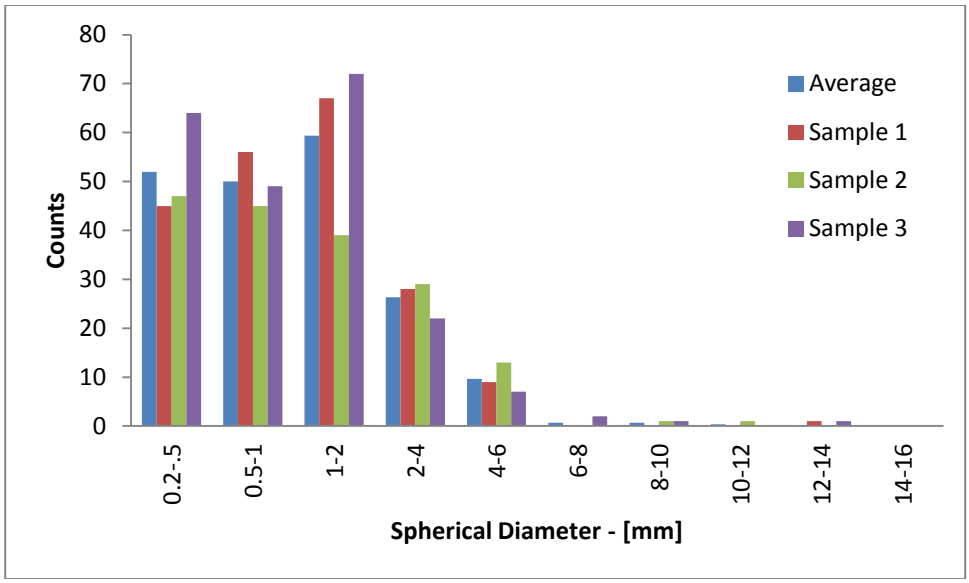
80
70
60
50
40
30
20
10
0
Counts
Average
Sample 1
Sample 2
Sample 3
0.2-.5
0.5-1
1-2
2-4
4-6
6-8
8-10
10-12
12-14
14-16
Spherical Diameter - [mm]

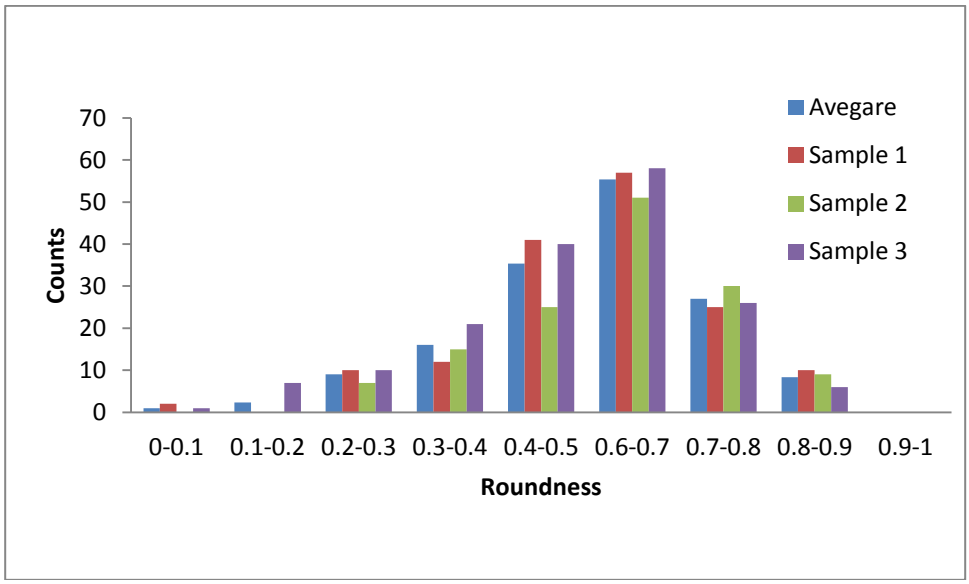
70
60
50
40
30
20
10
0
Counts
Avegare
Sample 1
Sample 2
Sample 3
0-0.1
0.1-0.2
0.2-0.3
0.3-0.4
0.4-0.5
0.6-0.7
0.7-0.8
0.8-0.9
0.9-1
Roundness

Al-10wt%Zn foam Produced at 710 °C for 510 s

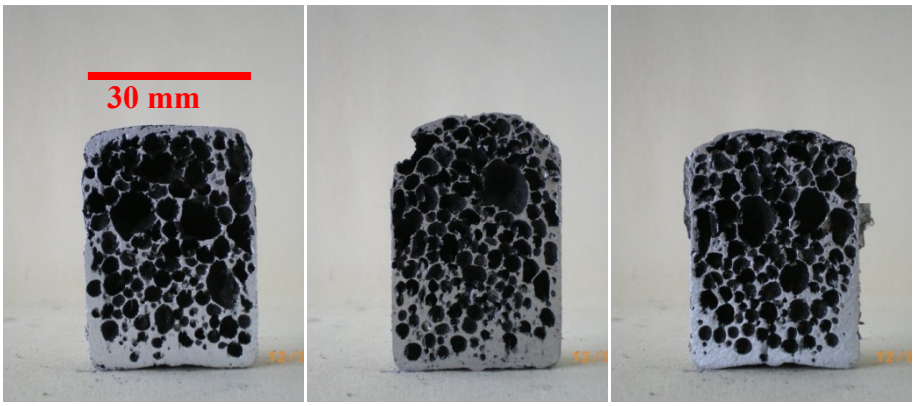

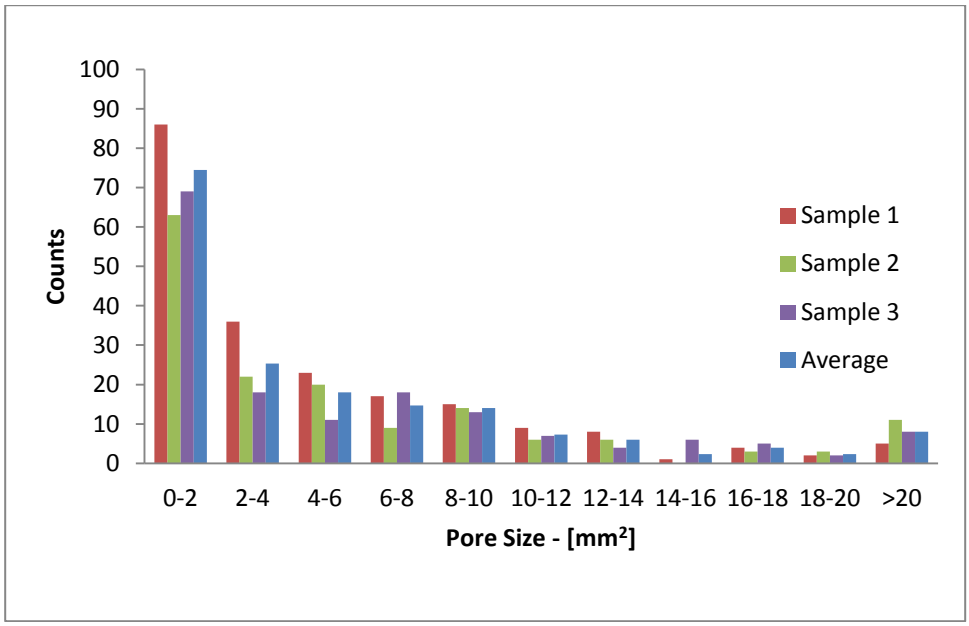

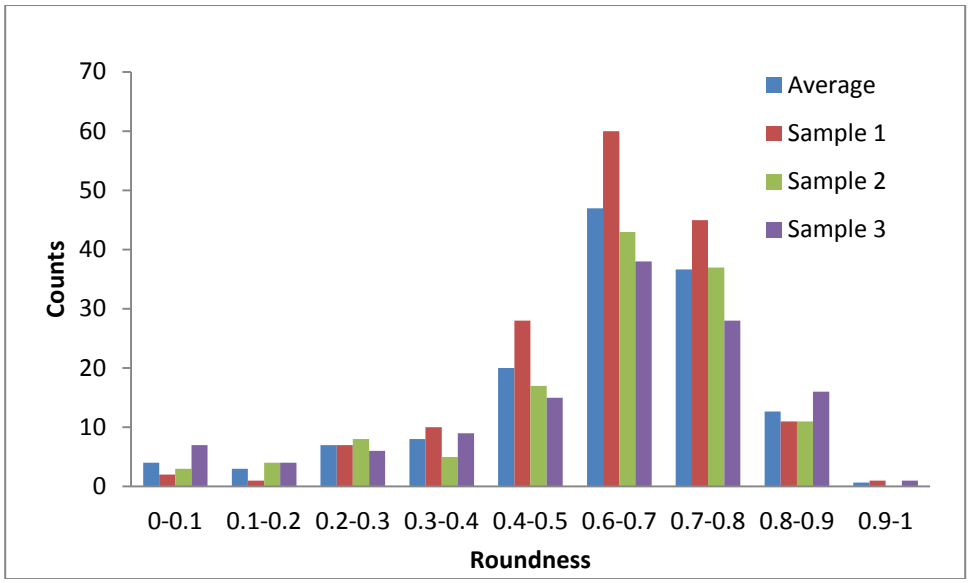

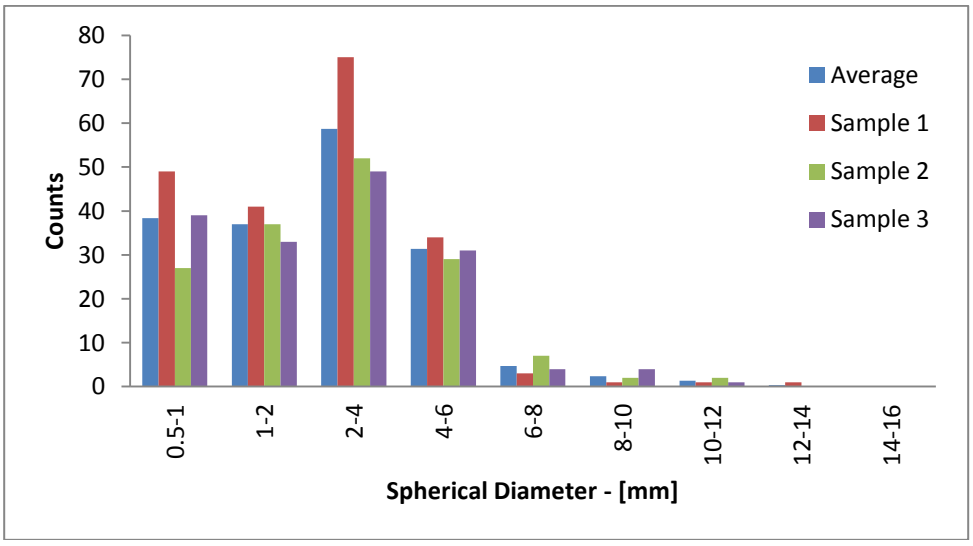

Al-10wt%Zn foam Produced at 710 °C for 600 s

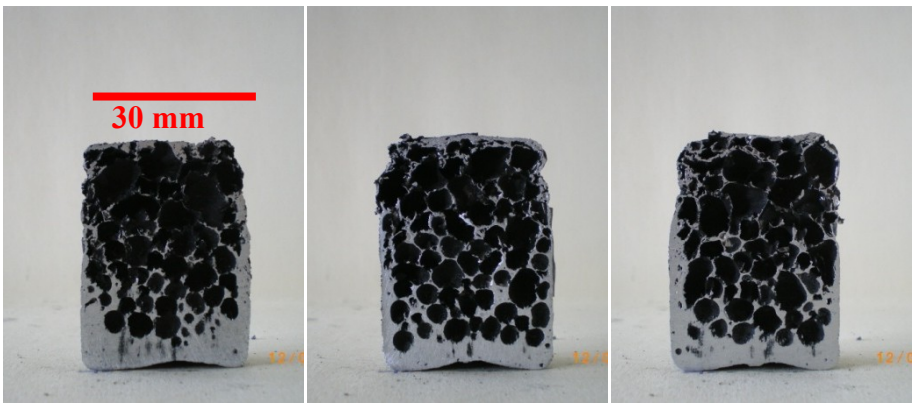

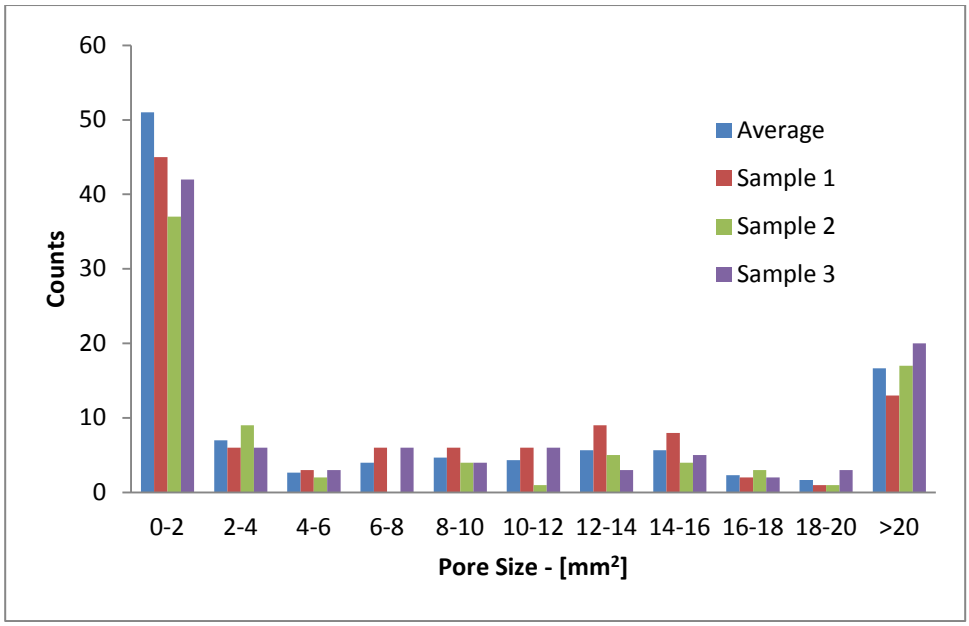
60
50
40
30
20
10
0
Counts
Average
Sample 1
Sample 2
Sample 3
0-2
2-4
4-6
6-8
8-10
10-12
12-14
14-16
16-18
18-20
>20
Pore Size - [mm²]

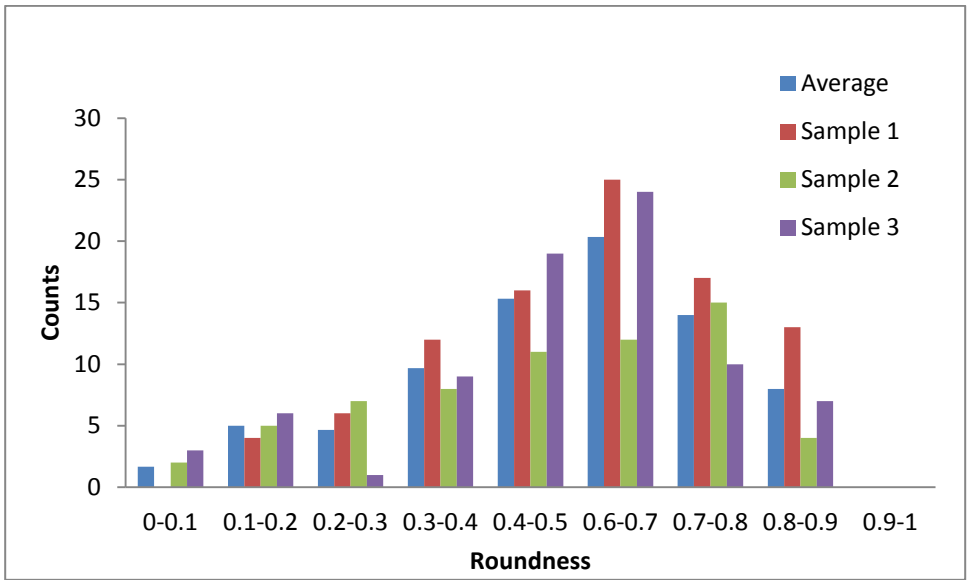
30
25
20
15
10
5
0
Counts
Average
Sample 1
Sample 2
Sample 3
0-0.1
0.1-0.2
0.2-0.3
0.3-0.4
0.4-0.5
0.6-0.7
0.7-0.8
0.8-0.9
0.9-1
Roundness

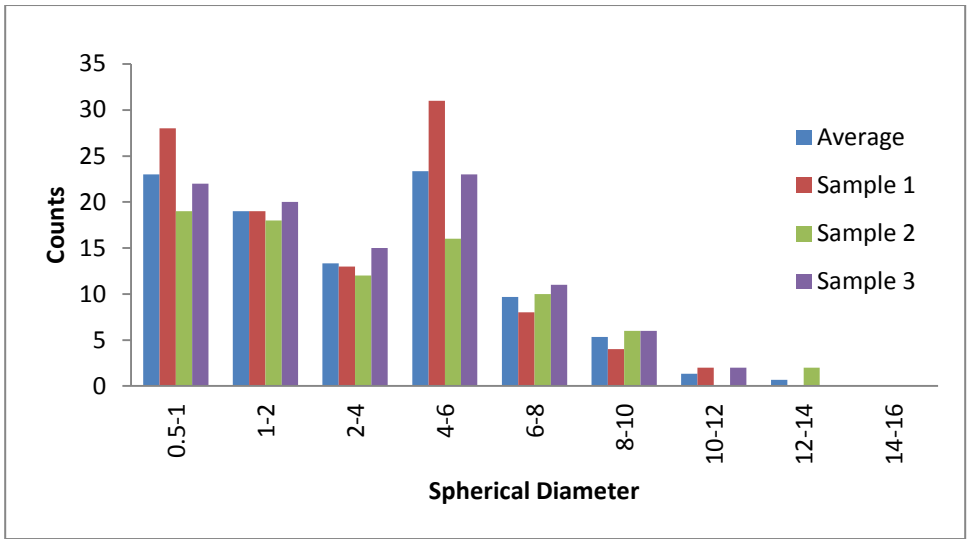

Al-10wt%Zn foam Produced at 710 °C for 1500 s

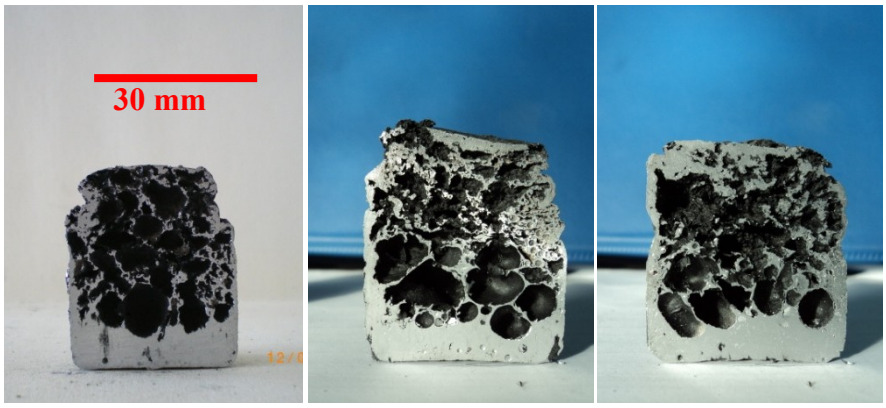

Al-33wt%Zn foam Produced at 640 °C for 1200 s

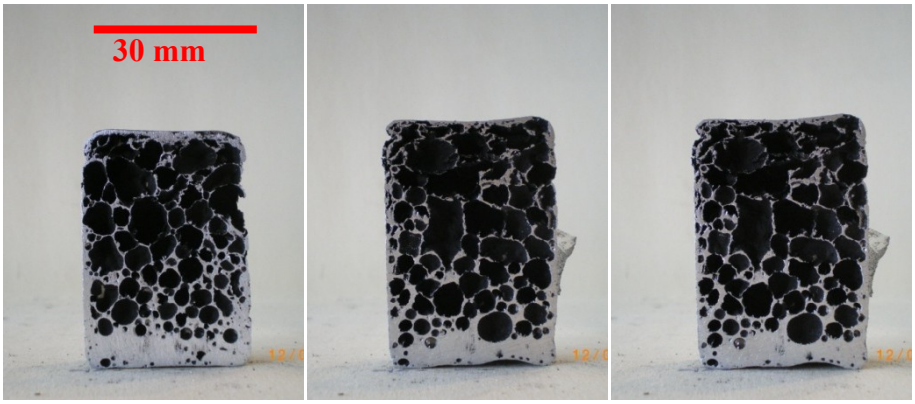

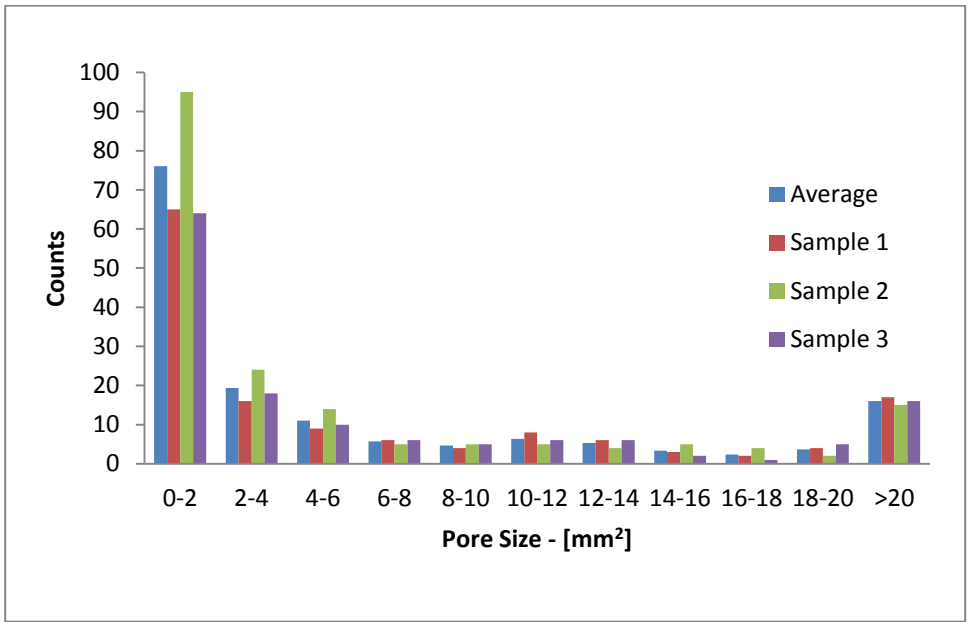

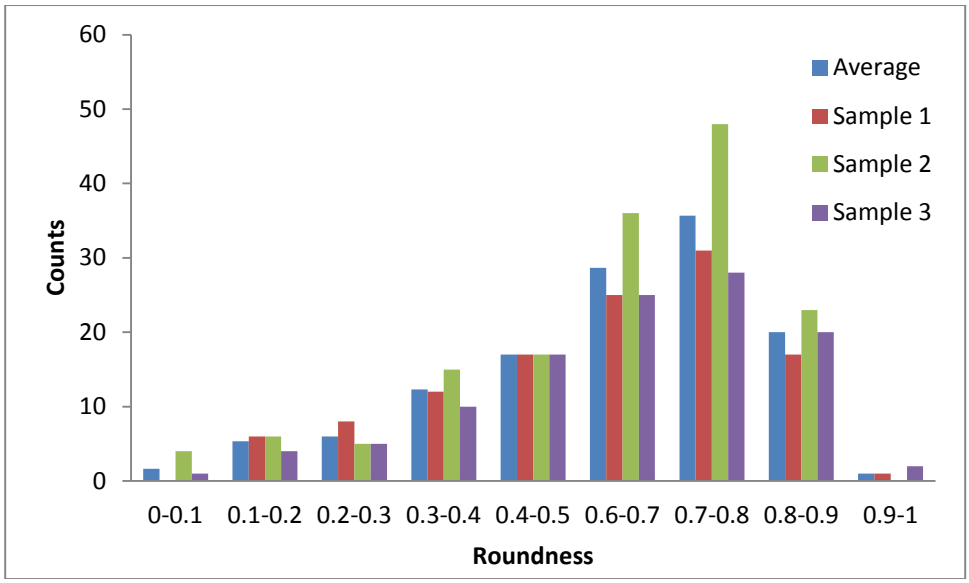

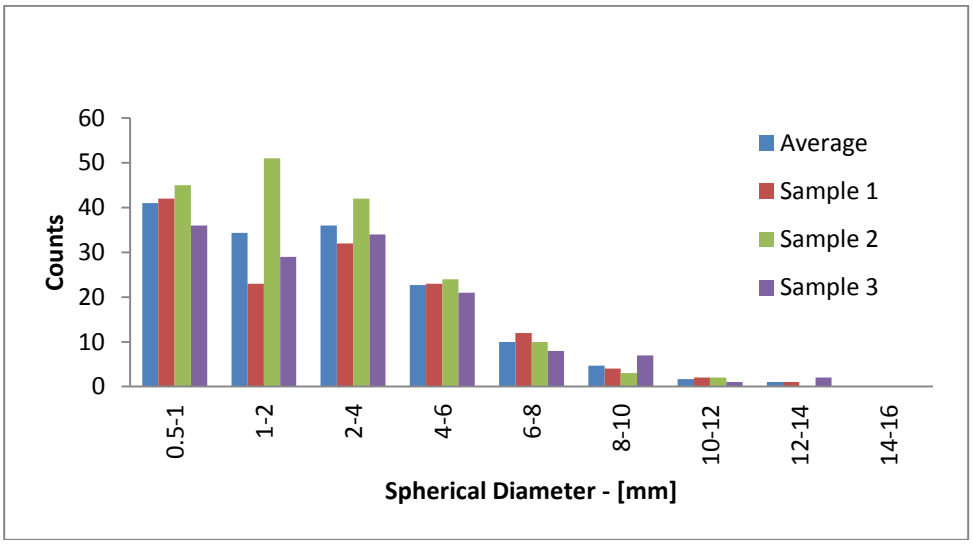

Al-33wt%Zn foam Produced at 640 °C for 1500 s

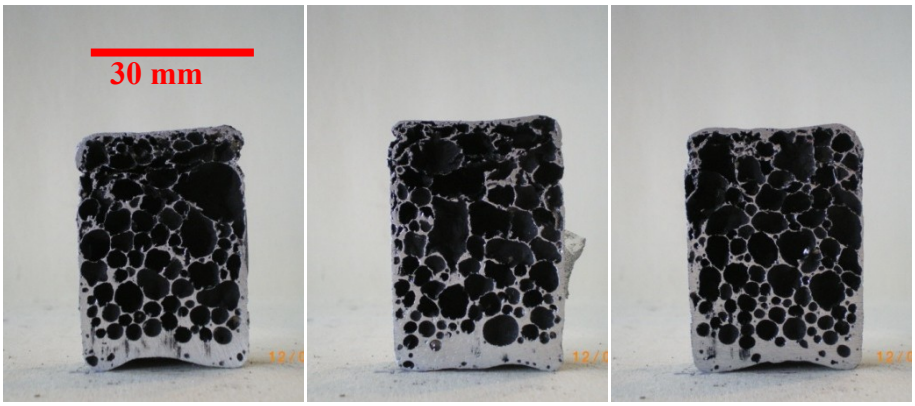

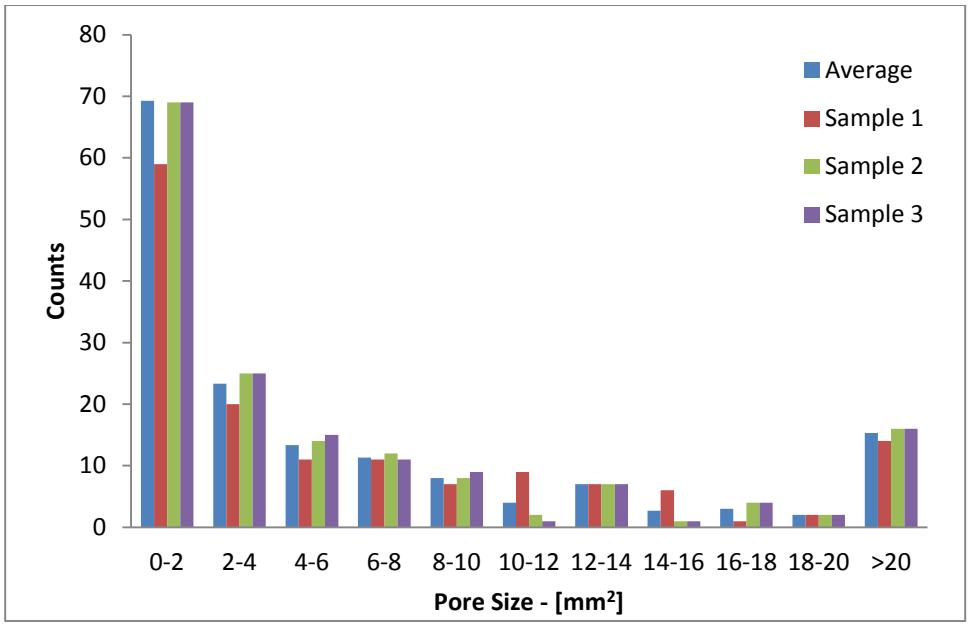
80
70
60
50
40
30
20
10
0
Counts
Average
Sample 1
Sample 2
Sample 3
0-2
2-4
4-6
6-8
8-10
10-12
12-14
14-16
16-18
18-20
>20
Pore Size - [mm²]

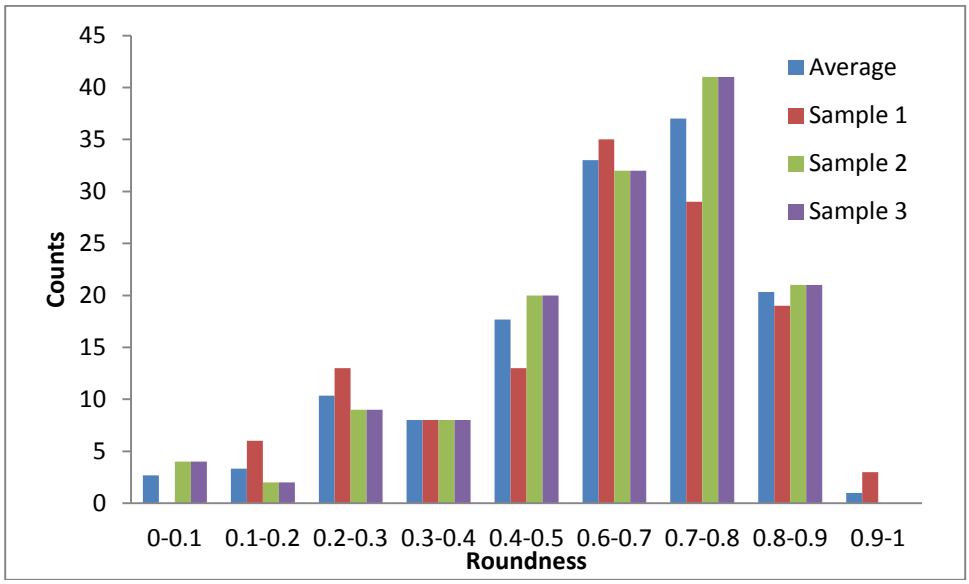
45
40
35
30
25
20
15
10
5
0
Counts
Average
Sample 1
Sample 2
Sample 3
0-0.1
0.1-0.2
0.2-0.3
0.3-0.4
0.4-0.5
0.6-0.7
0.7-0.8
0.8-0.9
0.9-1
Roundness

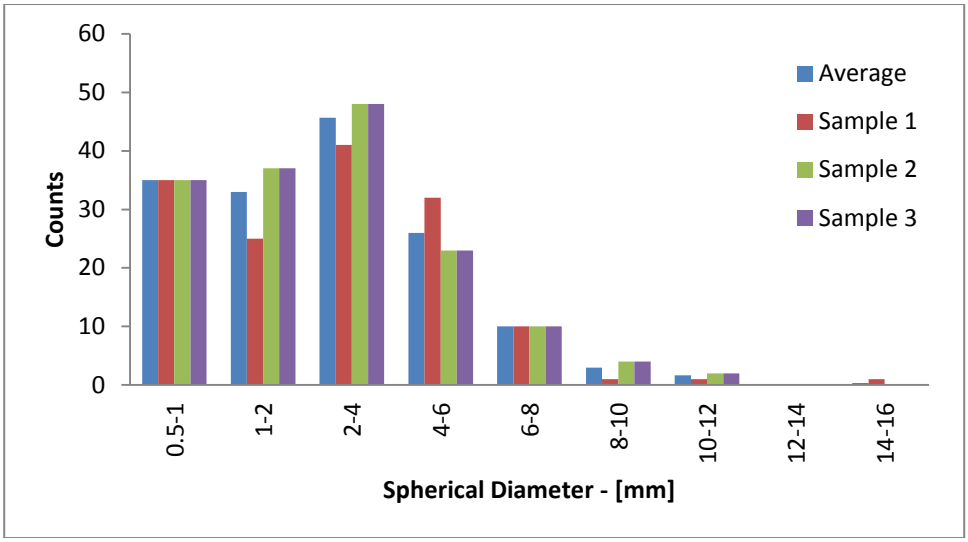
60
50
40
30
20
10
0
Counts
Average
Sample 1
Sample 2
Sample 3
0.5-1
1-2
2-4
4-6
6-8
8-10
10-12
12-14
14-16
Spherical Diameter - [mm]

This page is intentionally left blank

Appendix E: **Al-Si-Zn foams**

Al-2.4wt%Si-9.7wt%Zn DSC curves

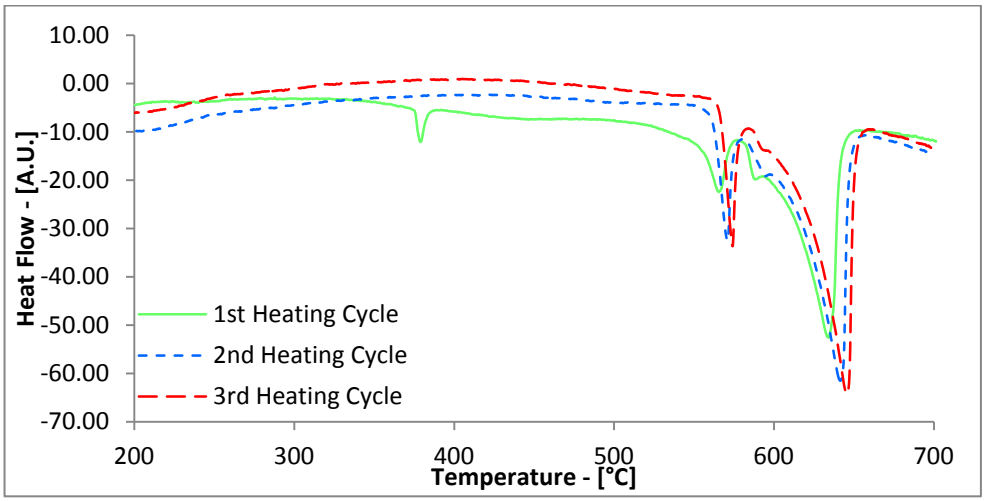

Al-Si-Zn isopleths generated through FactSage

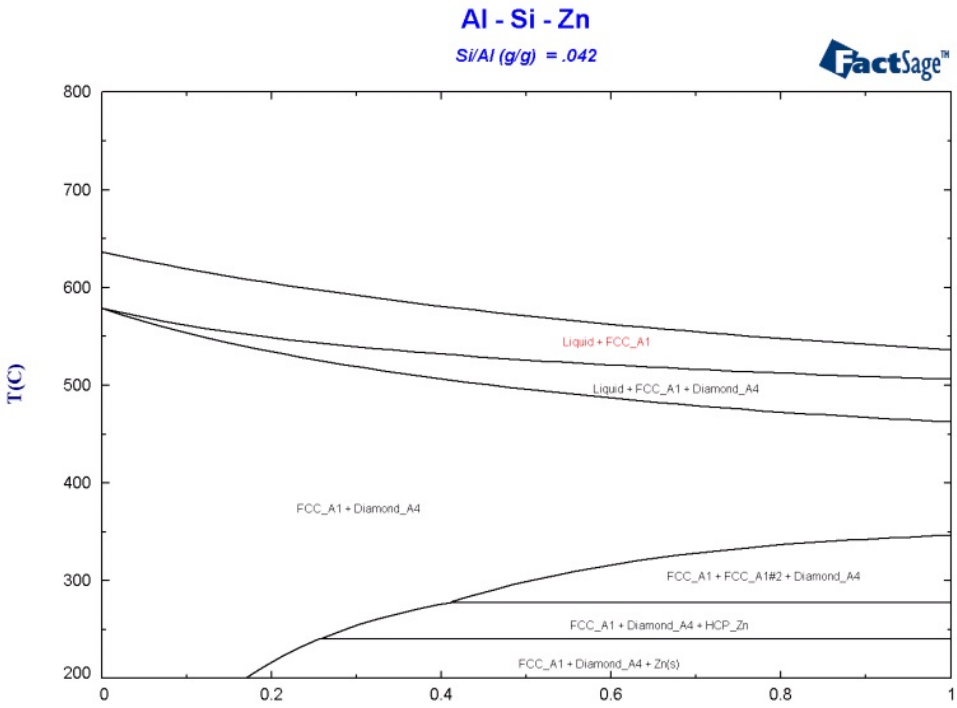

Zn/Al - g/g

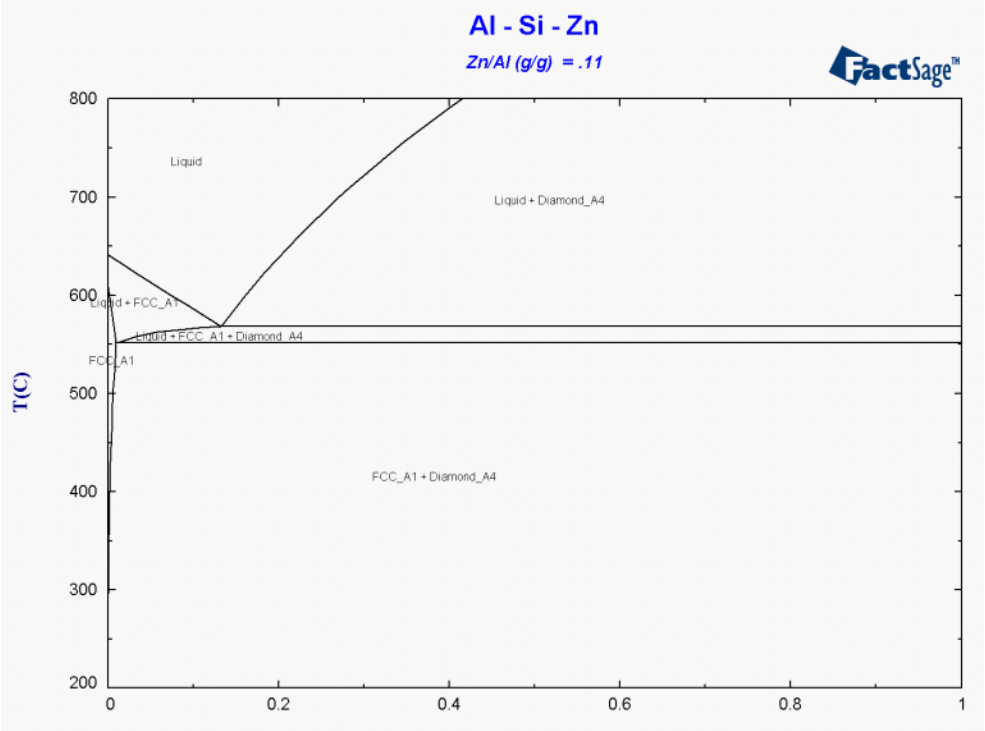

Si/Al - g/g

Electron image supported by EDS analysis of an Al-2.4wt%Si-9.7wt%Zn Compact showing the distribution of the various phases.

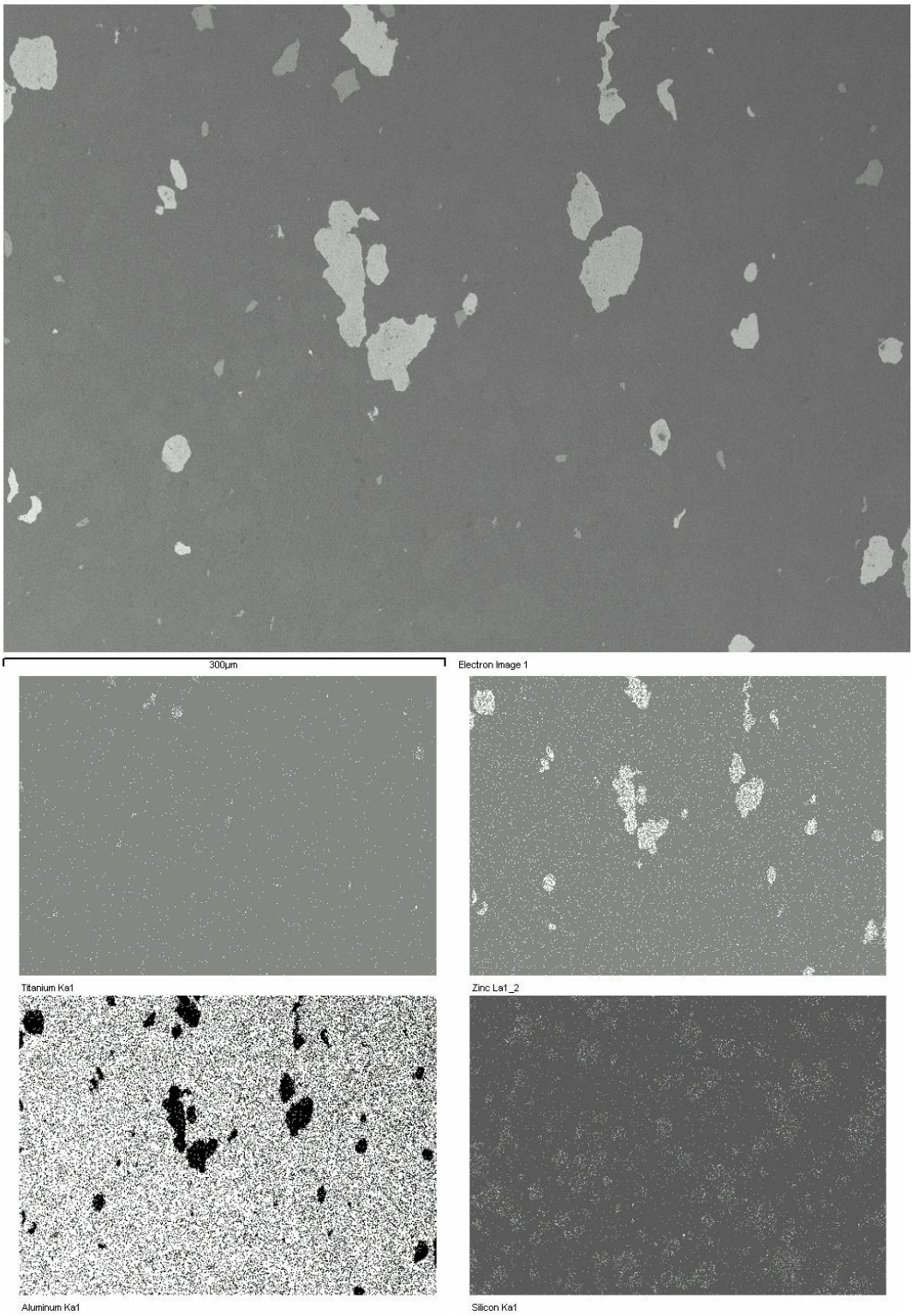

Al-2.4wt%-9.7wt%Zn compact

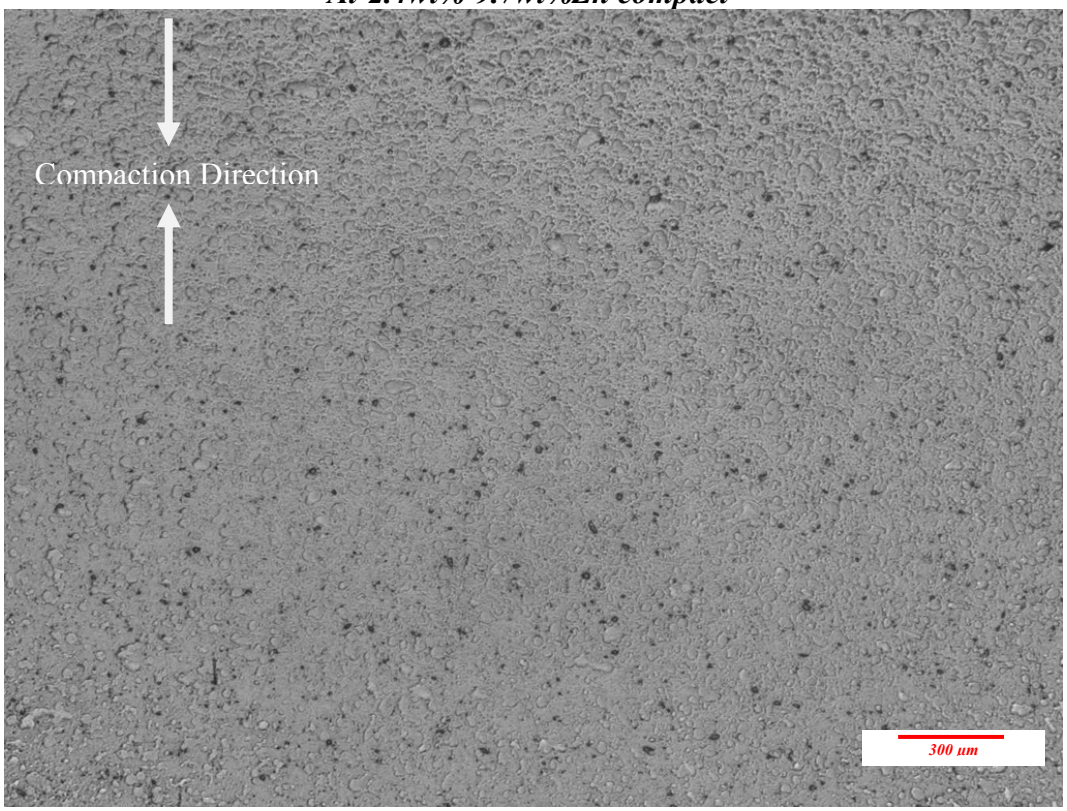

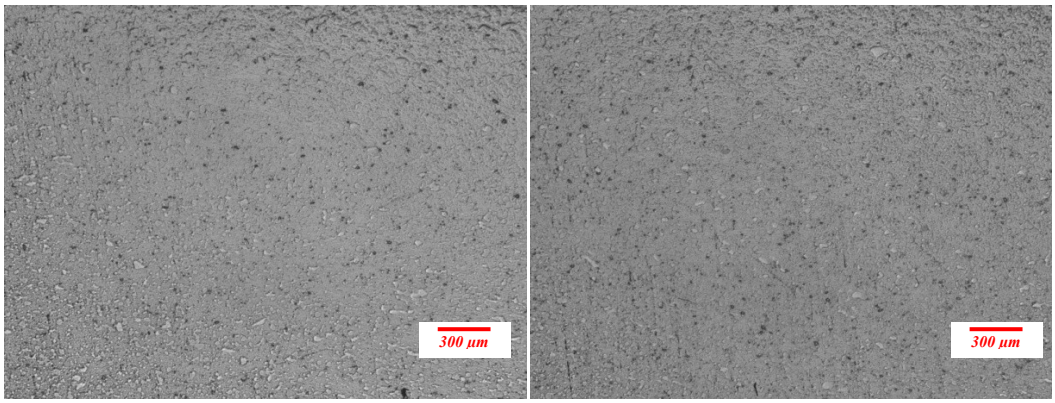

Al-2.4wt%-9.7wt%Zn compact

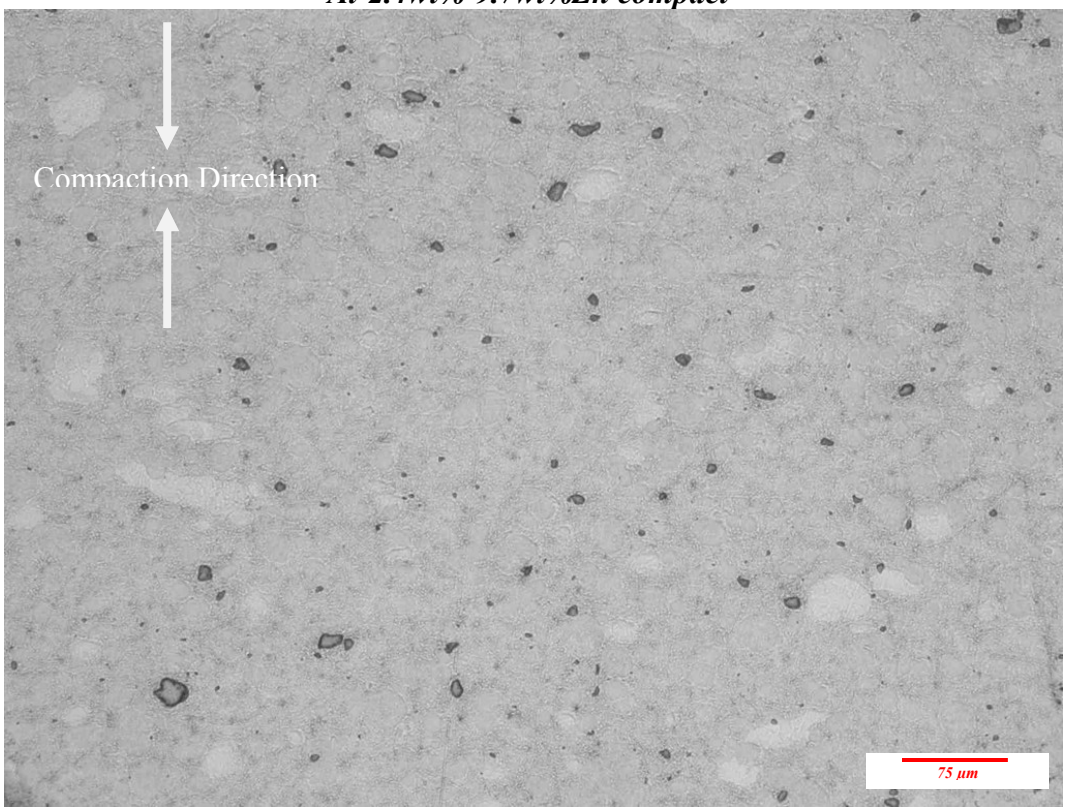

Al-2.4wt%-9.7wt%Zn 300 s

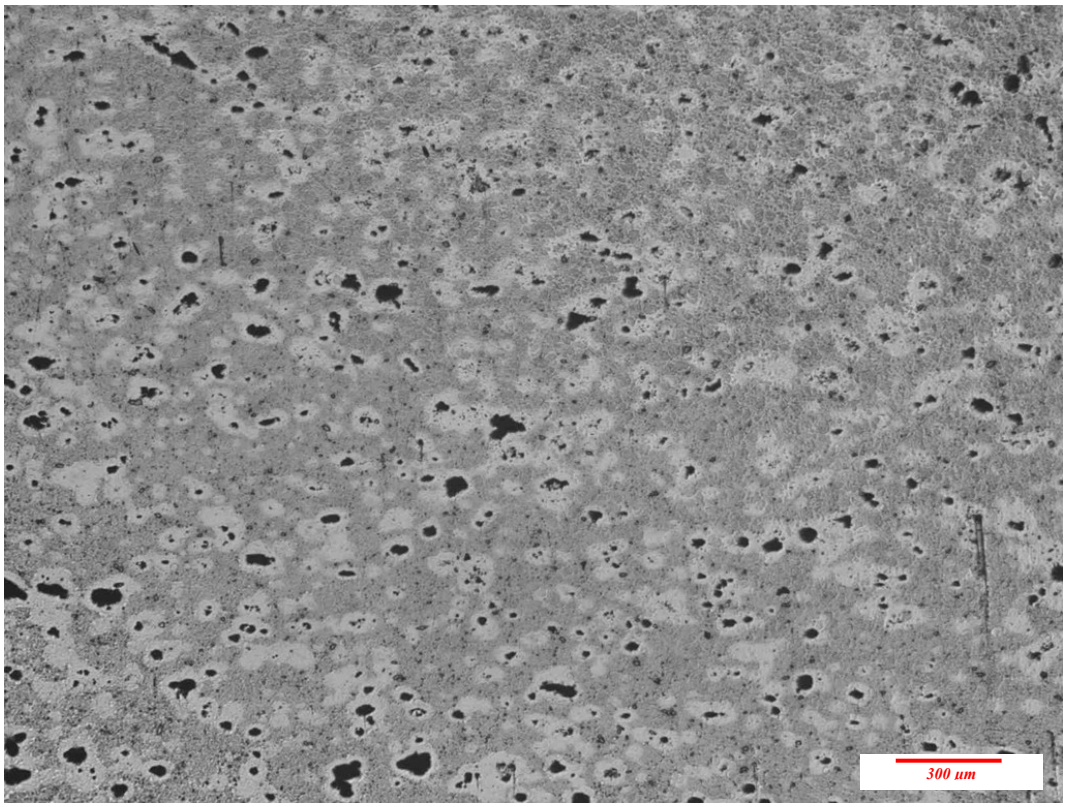

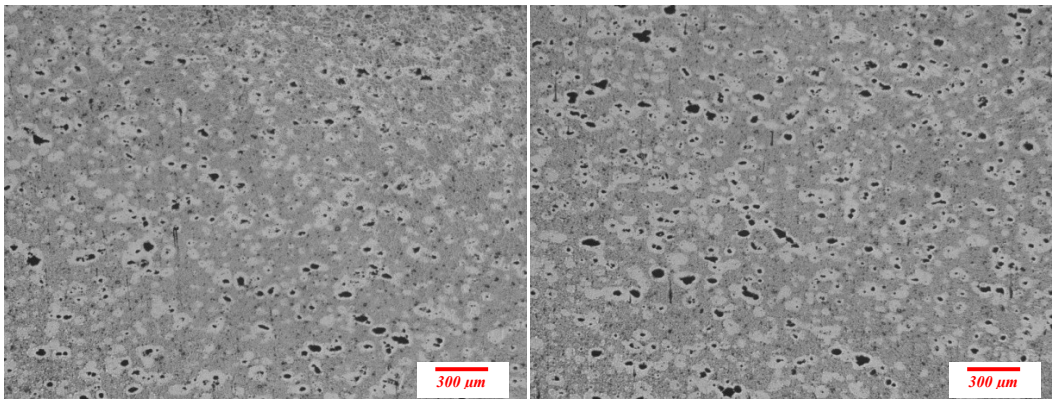

Al-2.4wt%-9.7wt%Zn 300 s

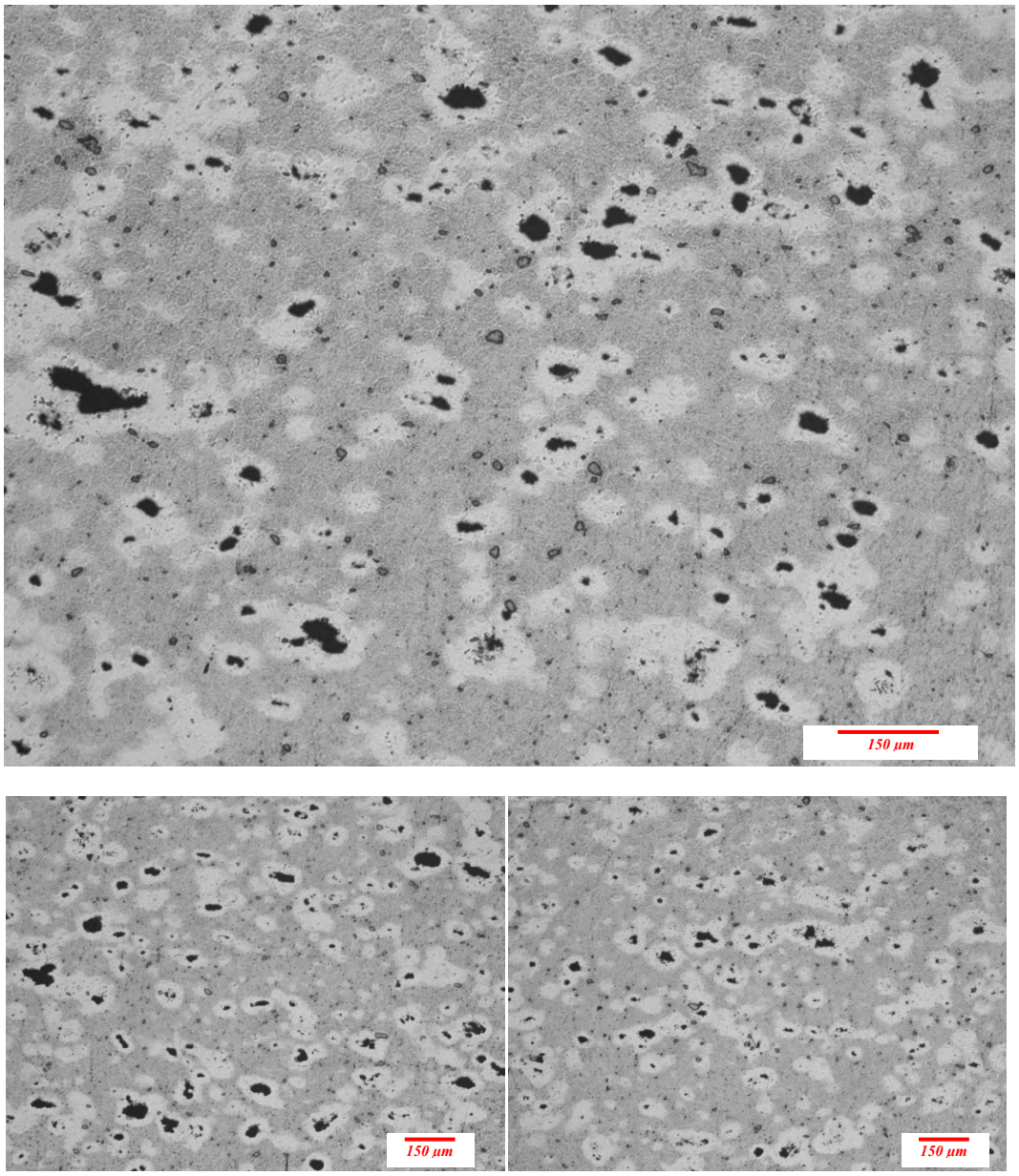

Al-2.4wt%-9.7wt%Zn 300 s

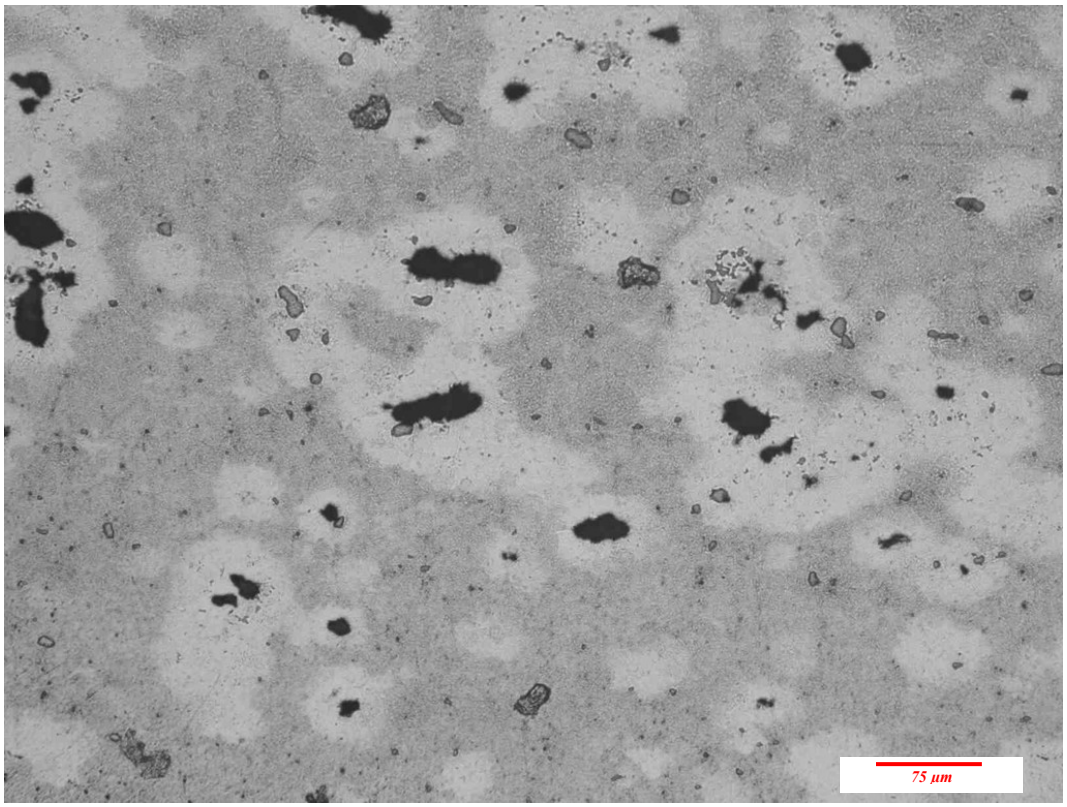

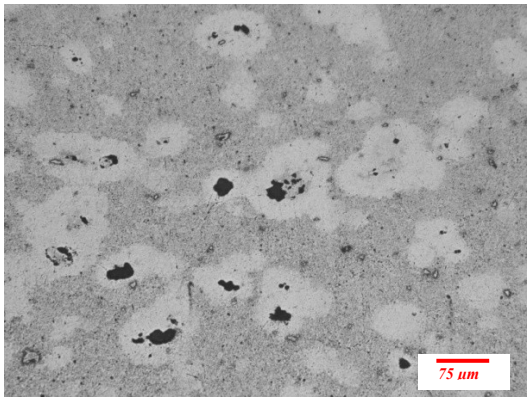

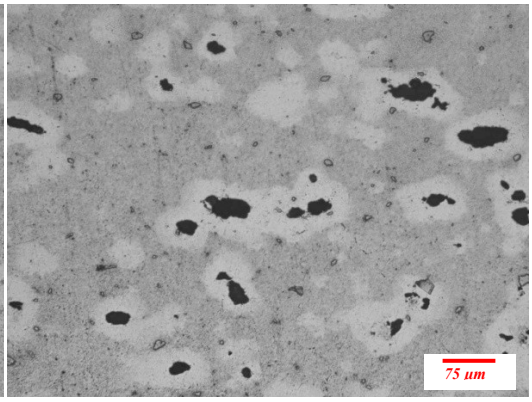

Al-2.4wt%-9.7wt%Zn 300 s

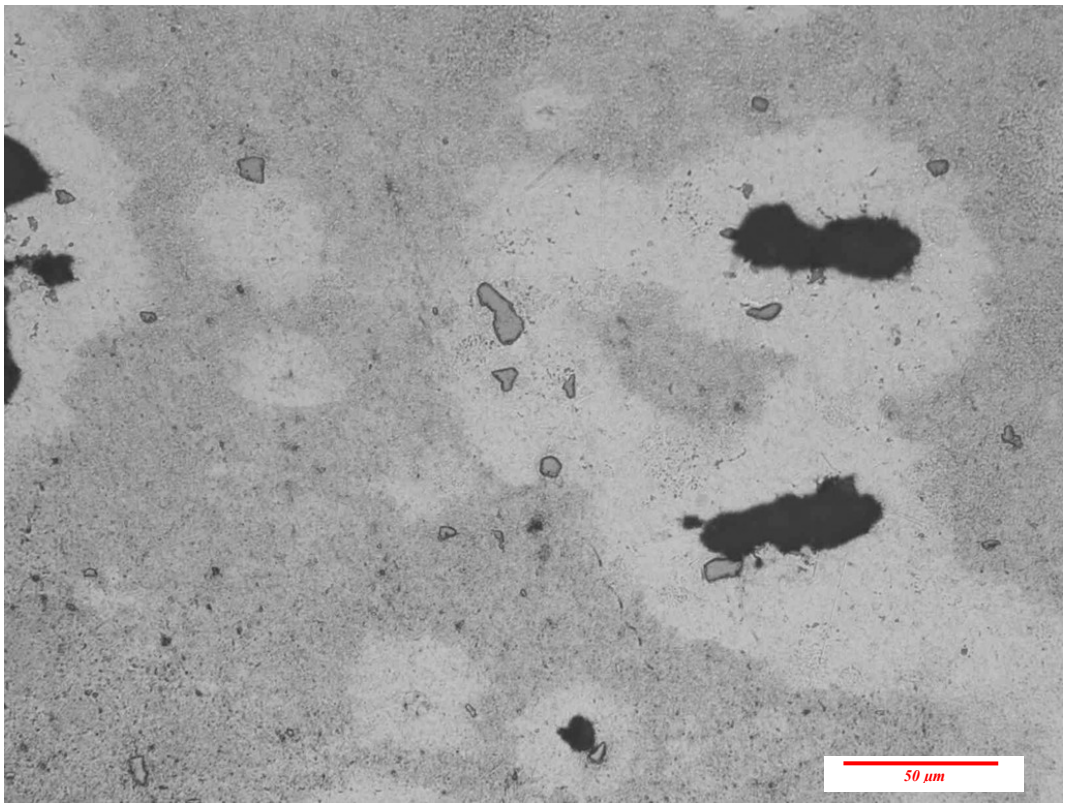

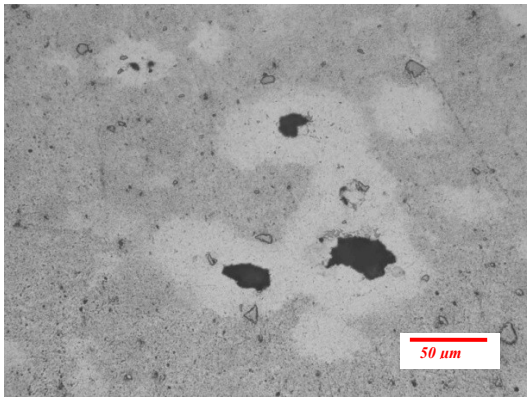

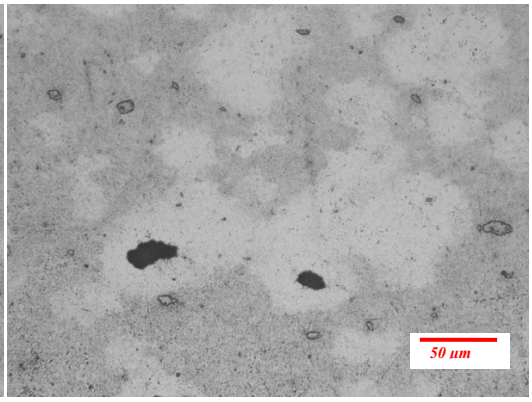

Al-2.4wt%-9.7wt%Zn 500 s

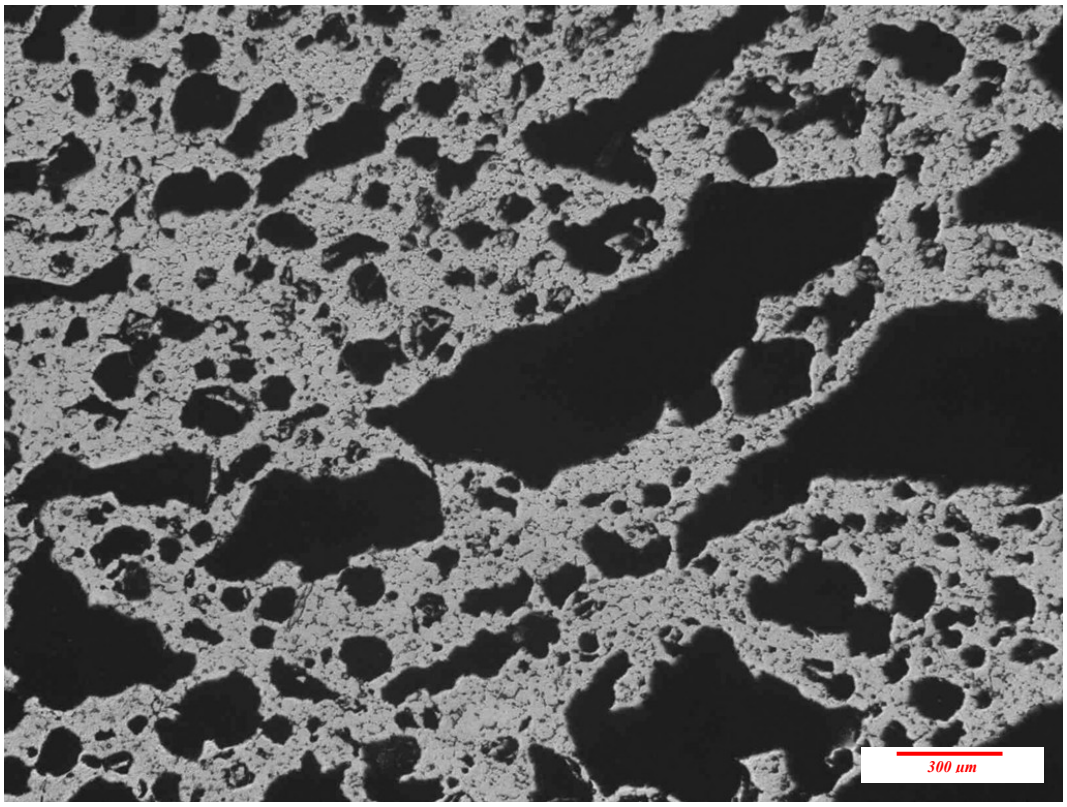
300 µm

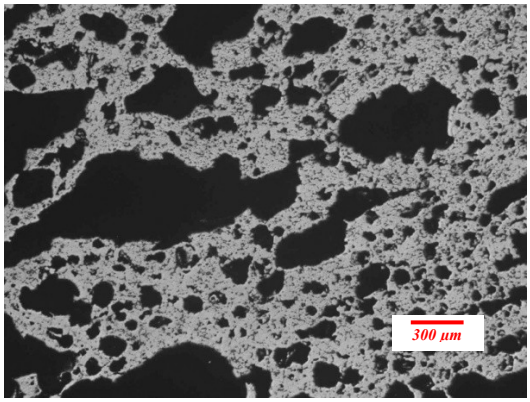
300 µm

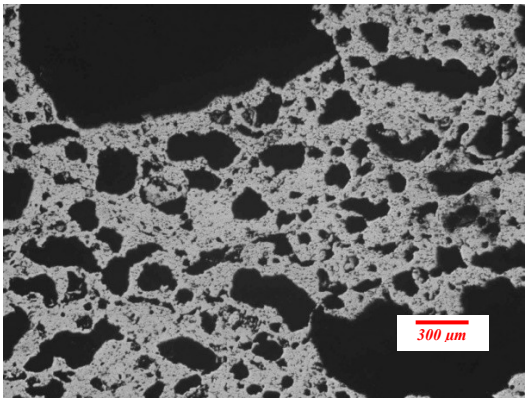
300 µm

Al-2.4wt%-9.7wt%Zn 500 s

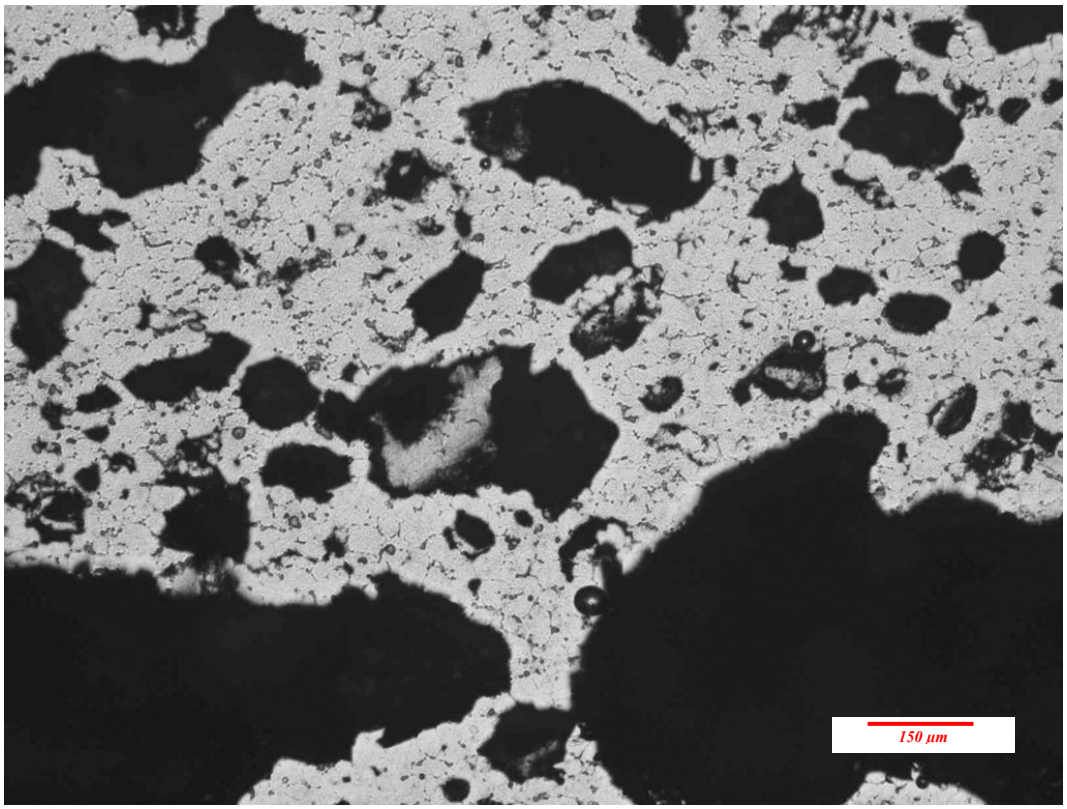

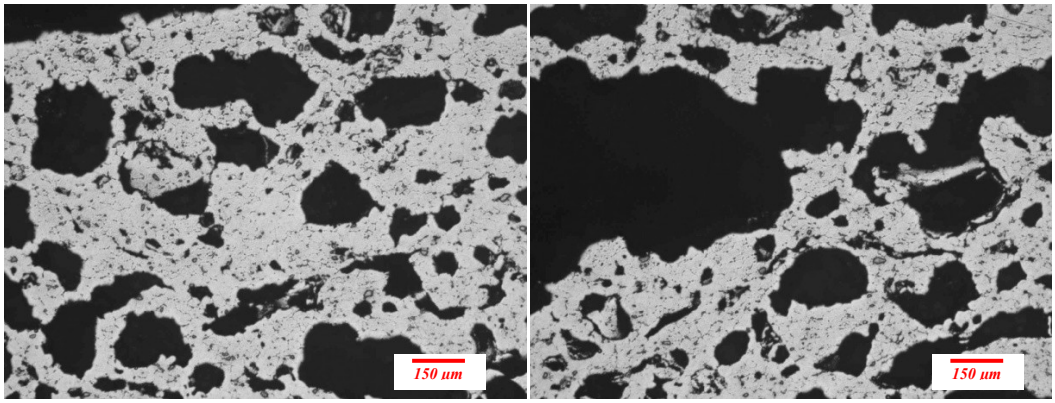

Al-2.4wt%-9.7wt%Zn 500 s

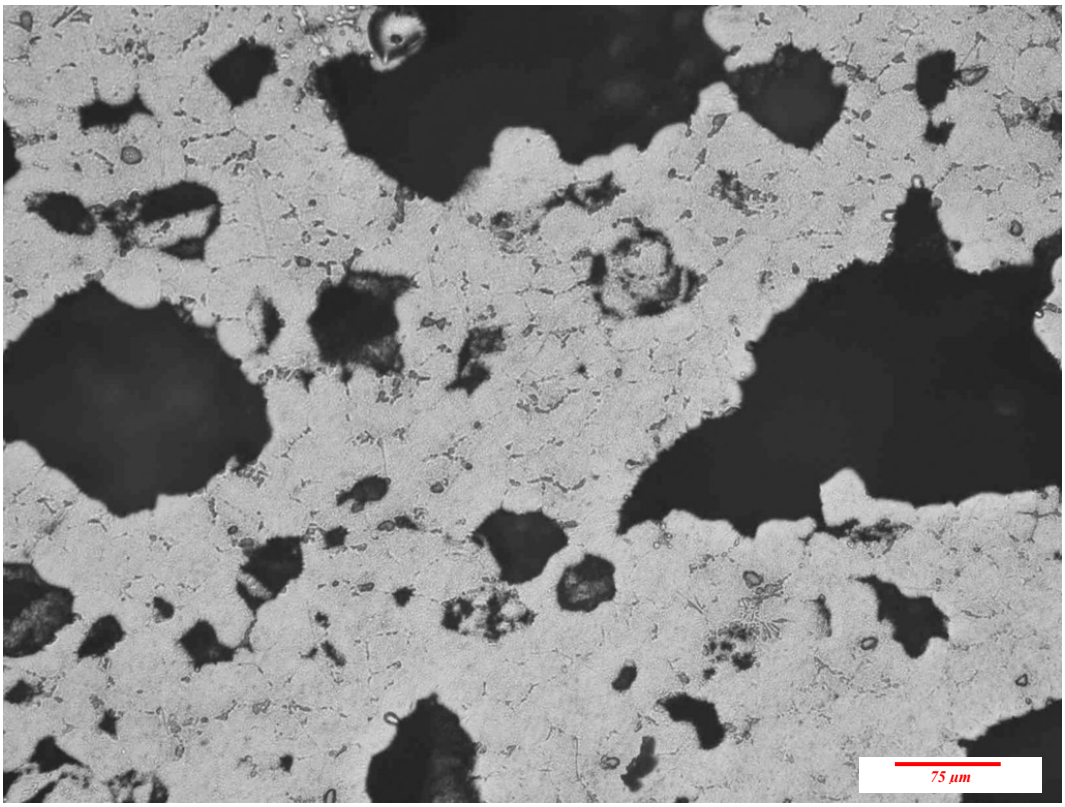

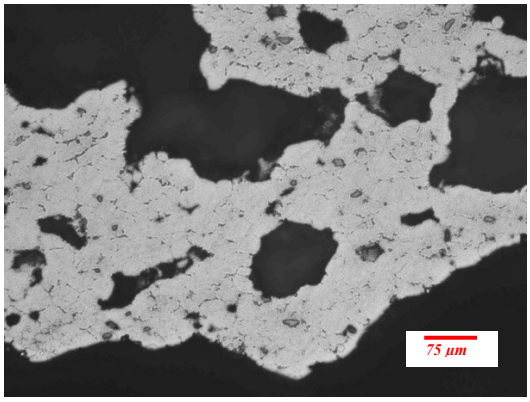

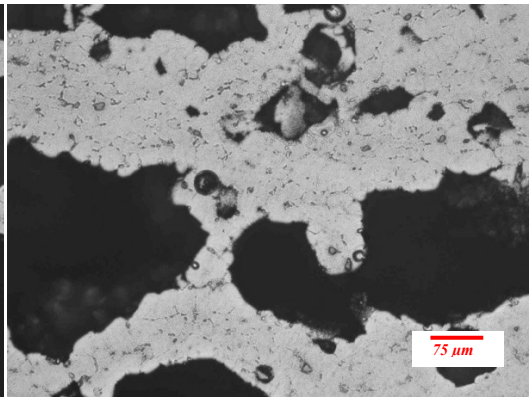

Al-2.4wt%-9.7wt%Zn 500 s

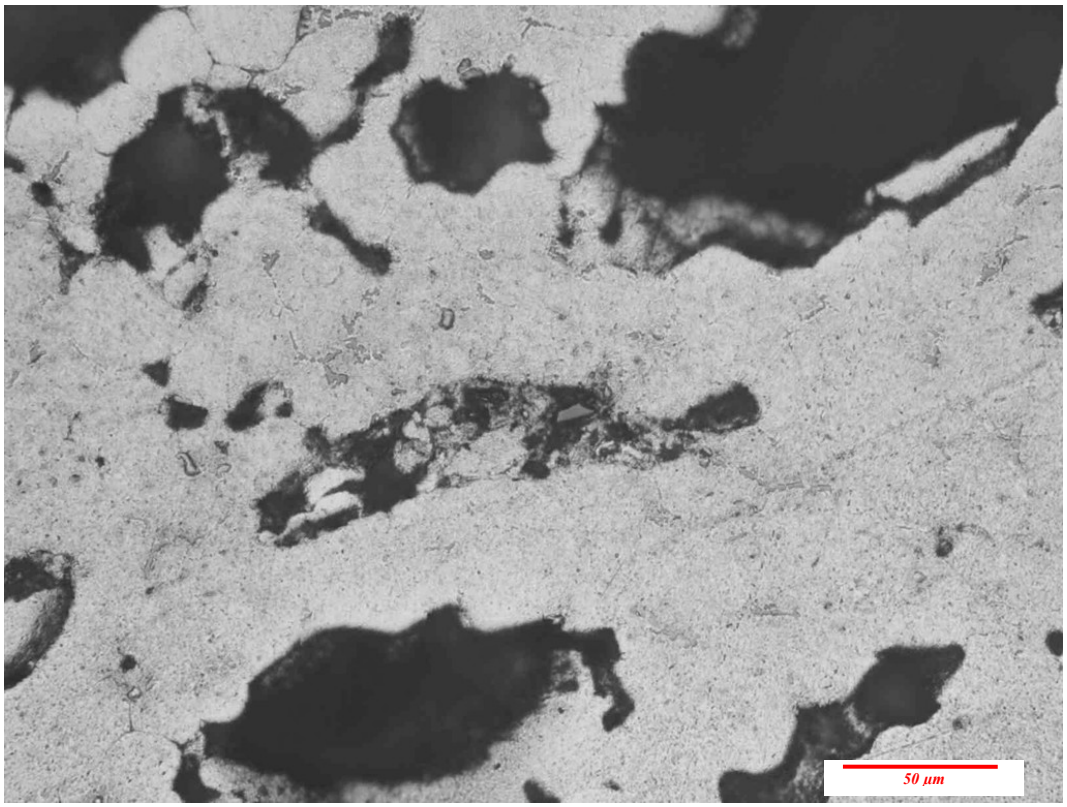
50 µm

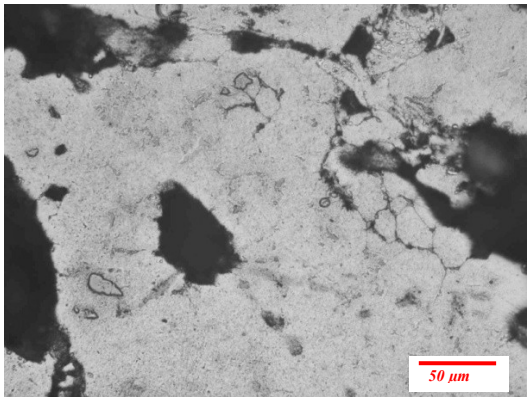
50 µm

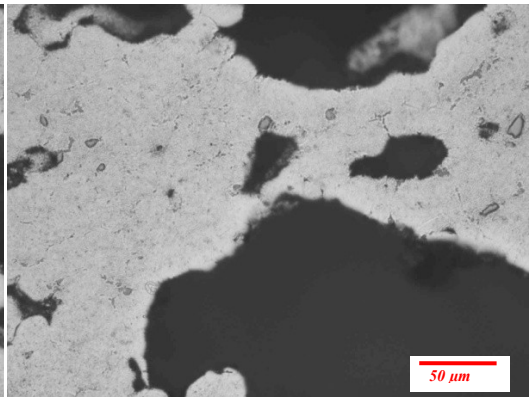
50 µm

Al-2.4wt%-9.7wt%Zn 550 s

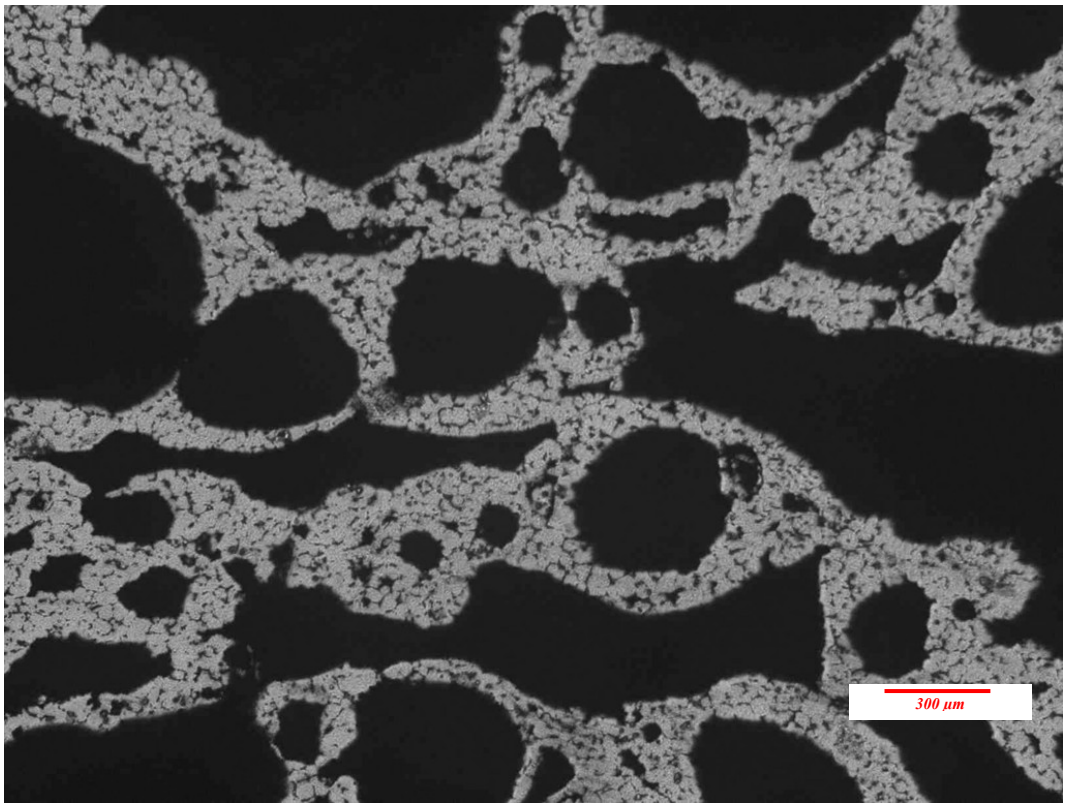

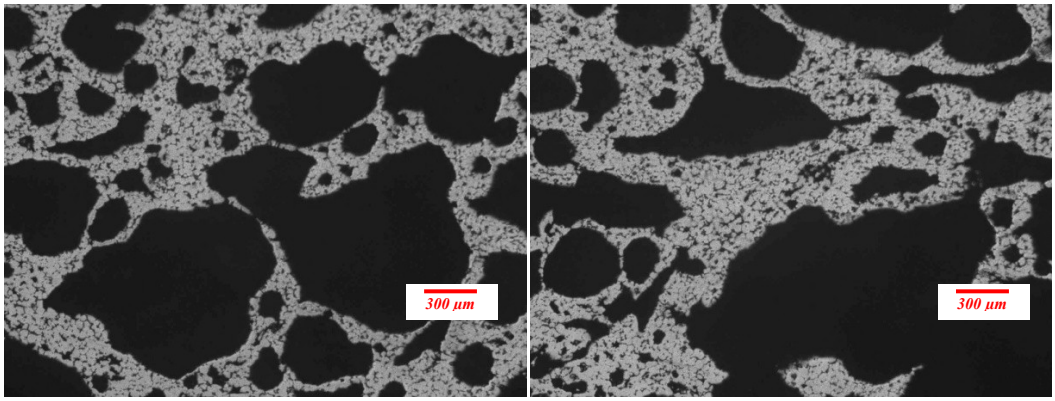

Al-2.4wt%-9.7wt%Zn 550 s

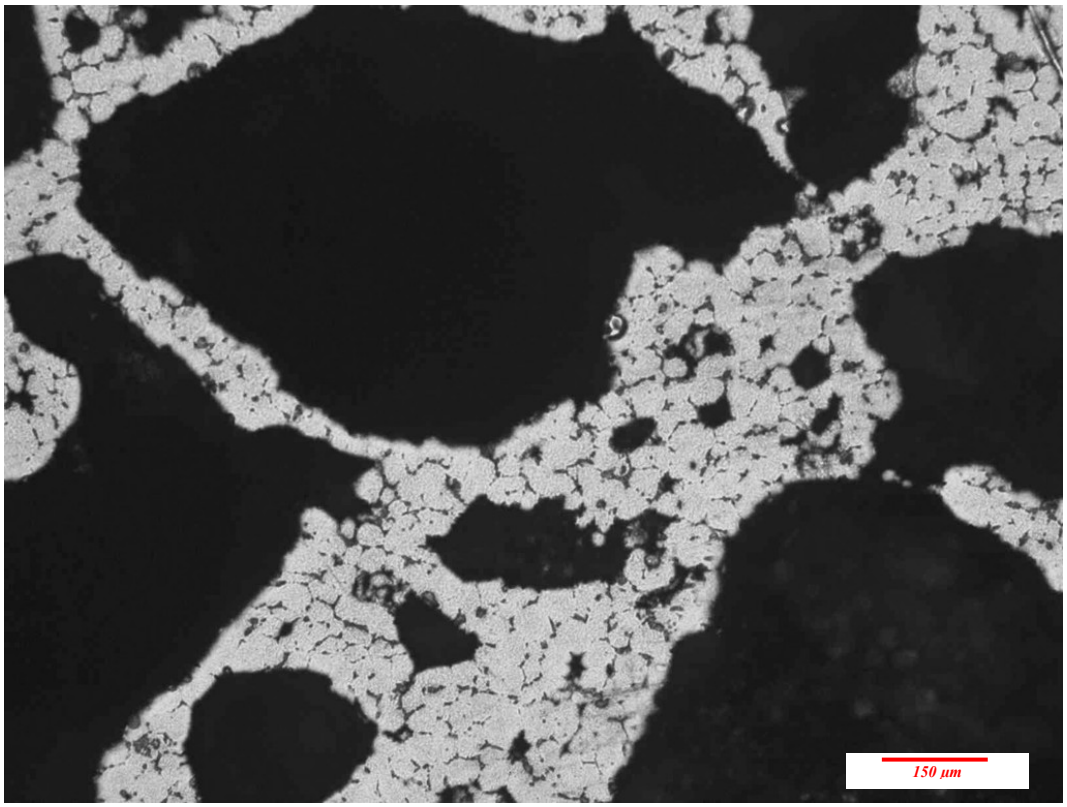
150 µm

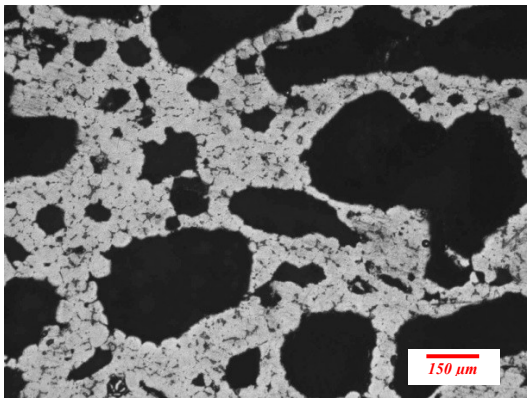
150 µm

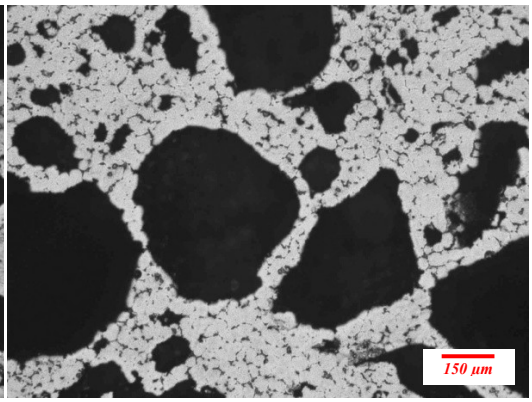
150 µm

Al-2.4wt%-9.7wt%Zn 550 s

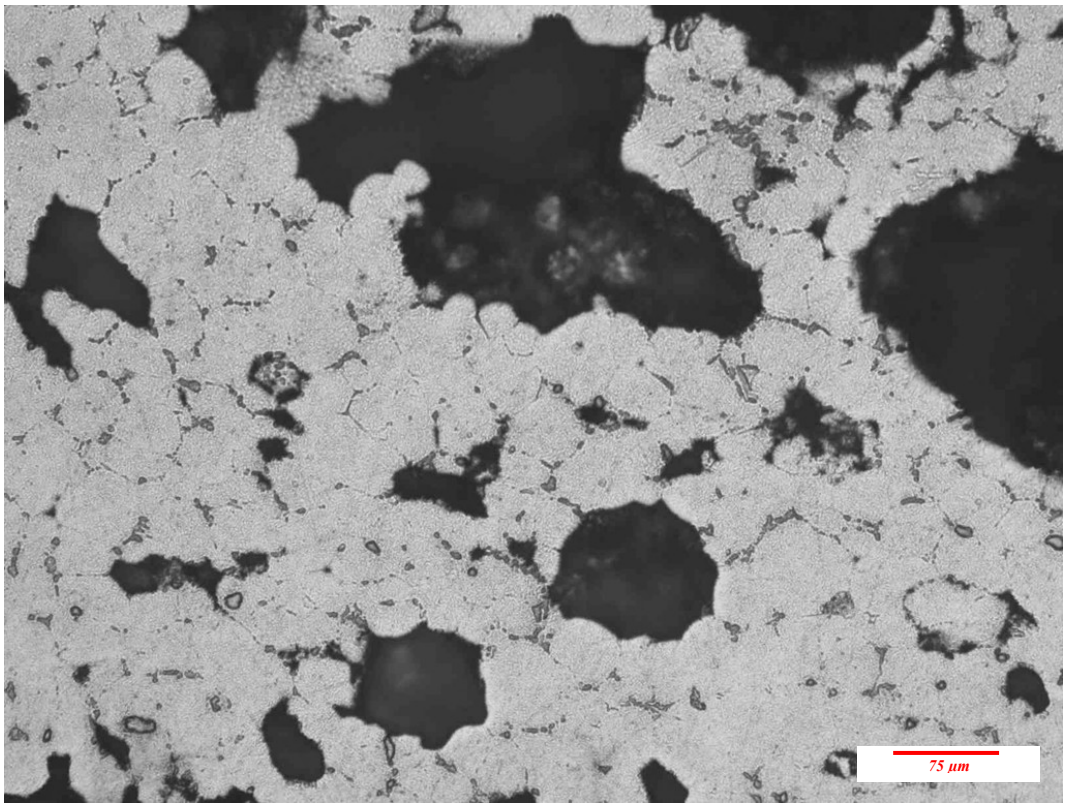

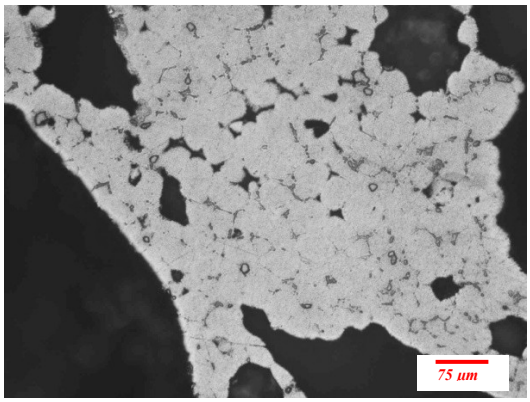

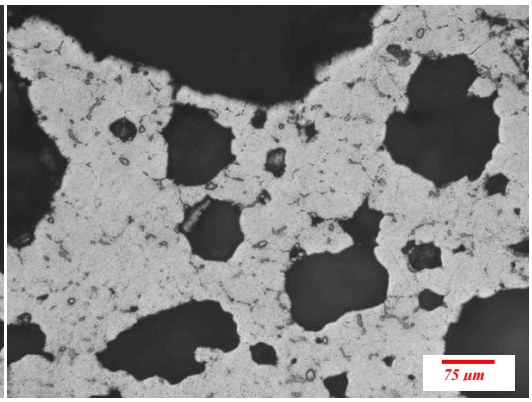

Al-2.4wt%-9.7wt%Zn 550 s

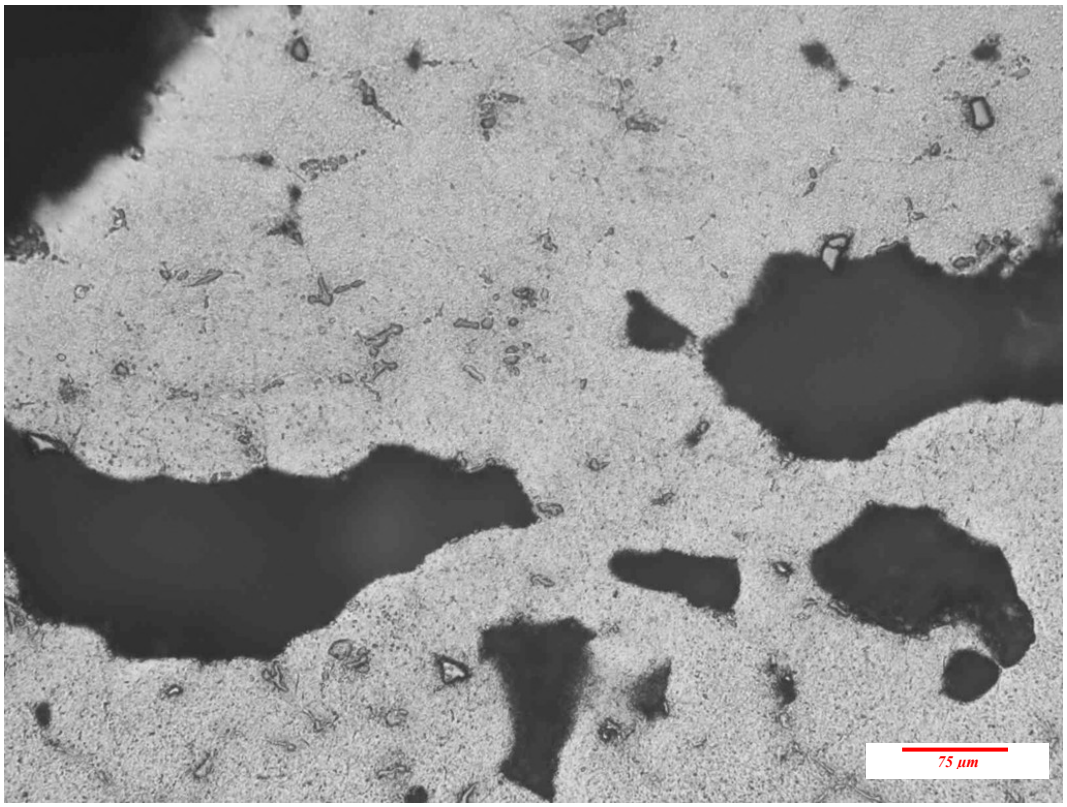

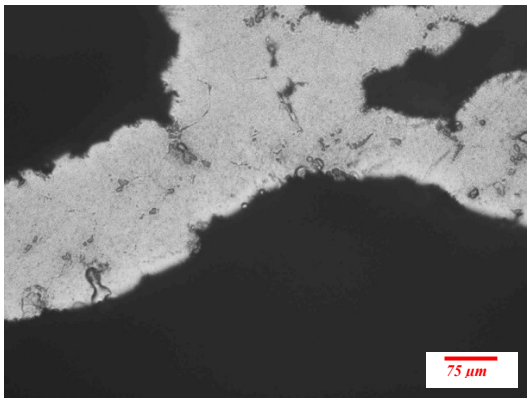

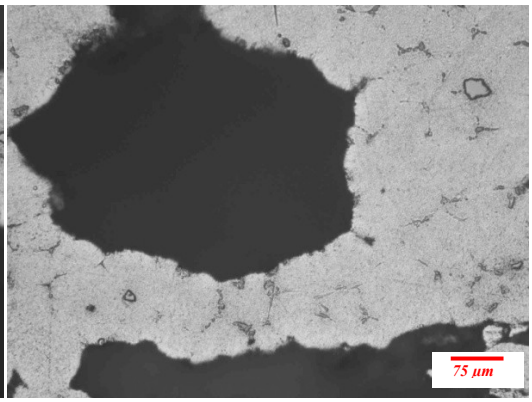

Al-3.59wt%Si-9.6wt%Zn Compacts

Al-3.59wt%Si-9.6wt%Zn Compact electron image supported by EDS analysis

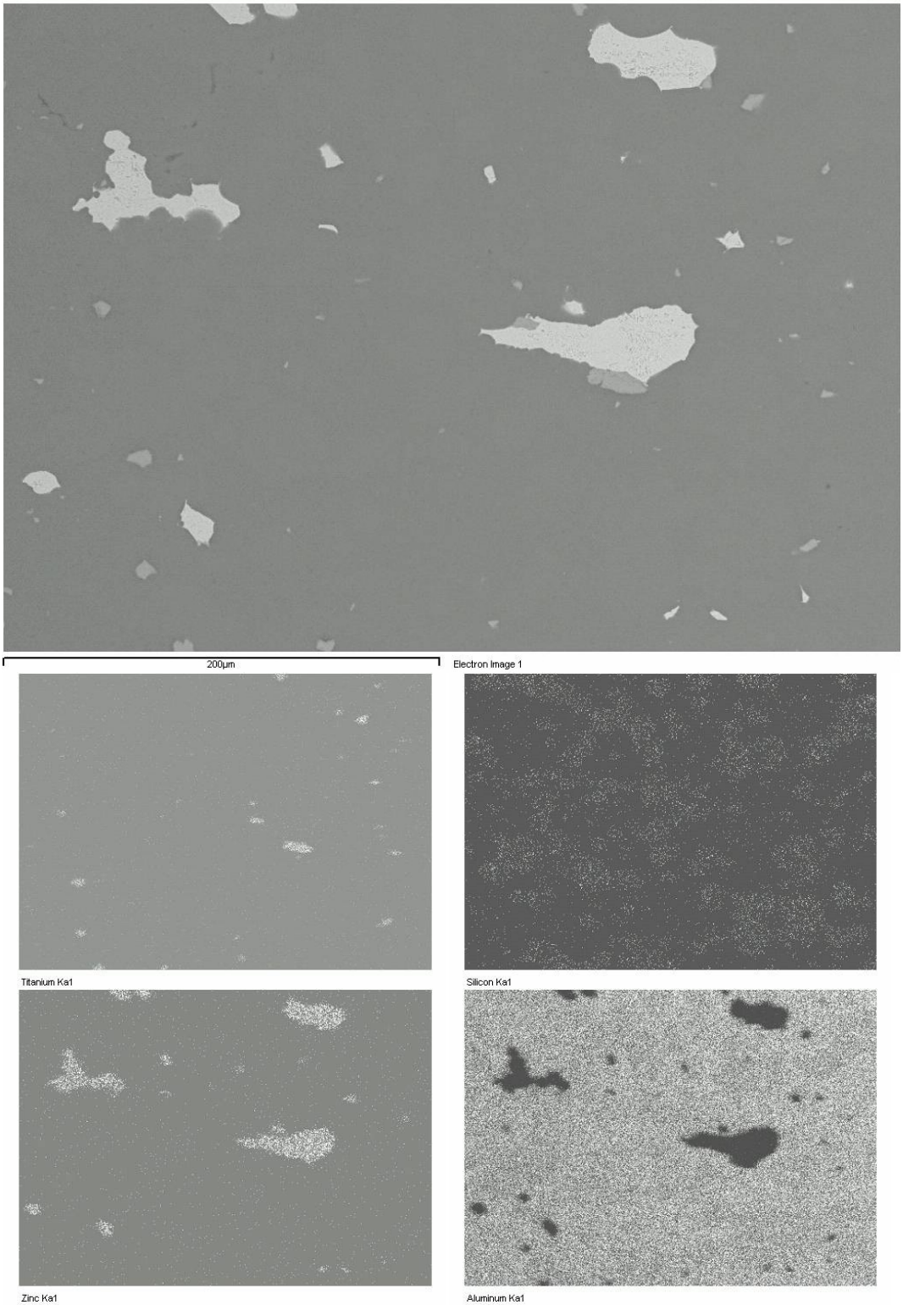

Al-3.59wt%Si-9.6wt%Zn Compacts

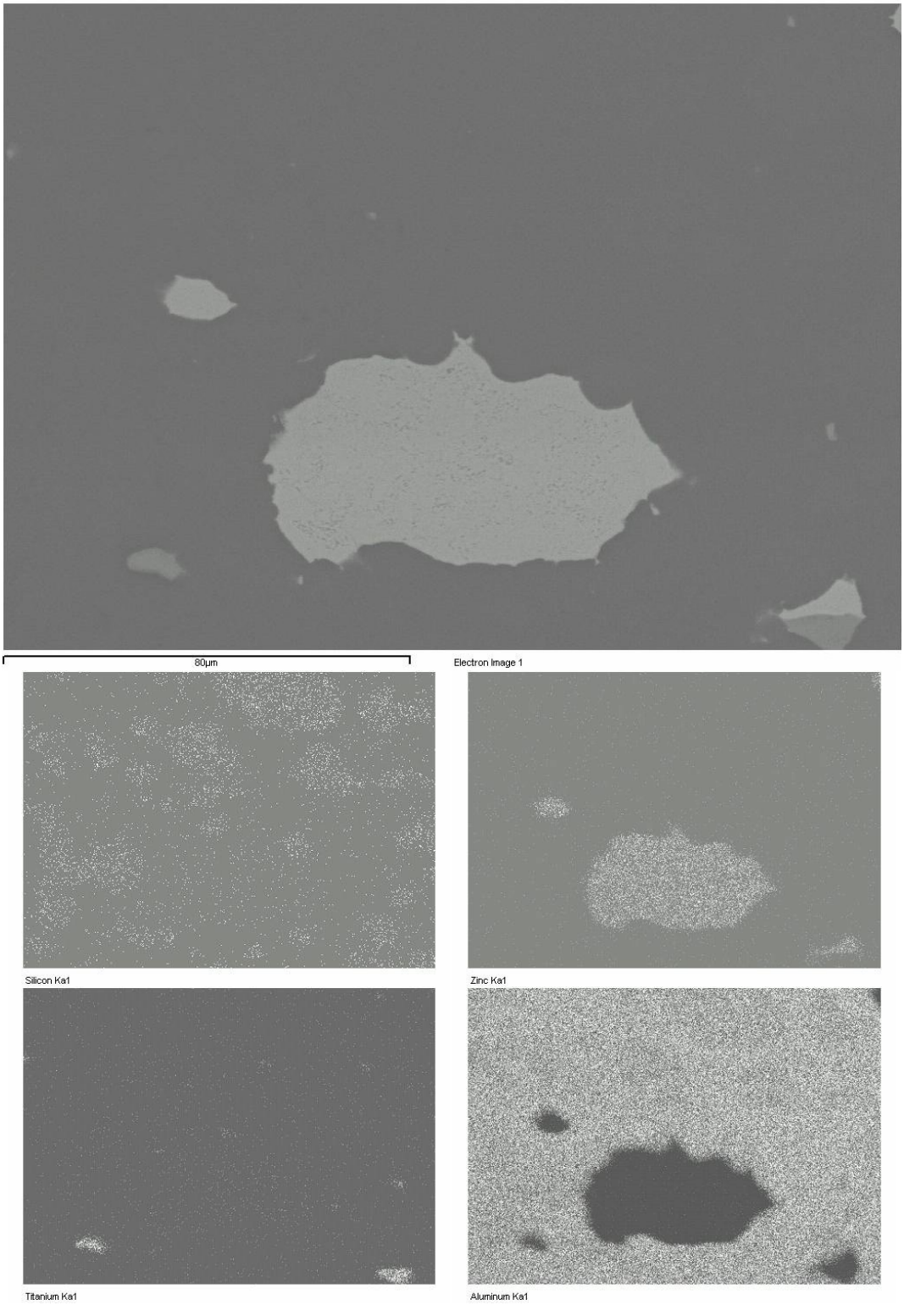

Al-3.59wt%Si-9.6wt%Zn Compacts

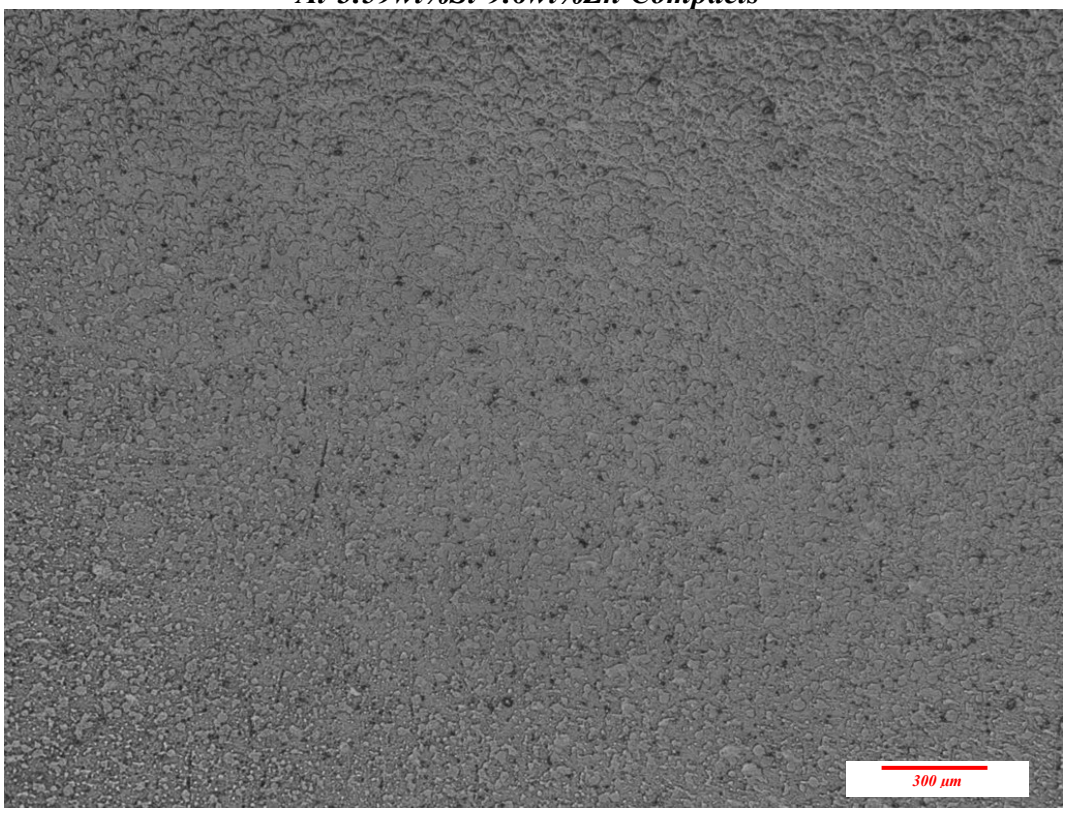

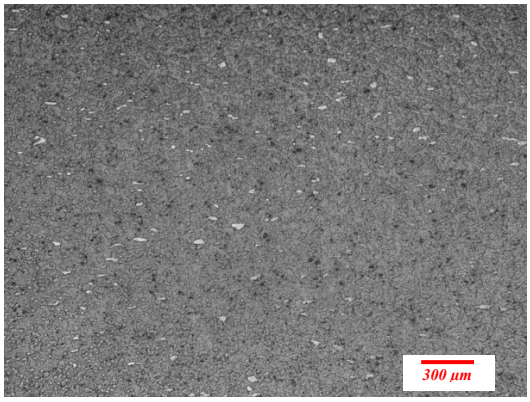

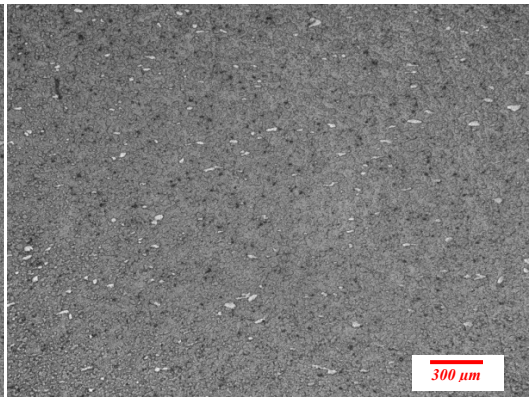

Al-3.59wt%Si-9.6wt%Zn Compacts

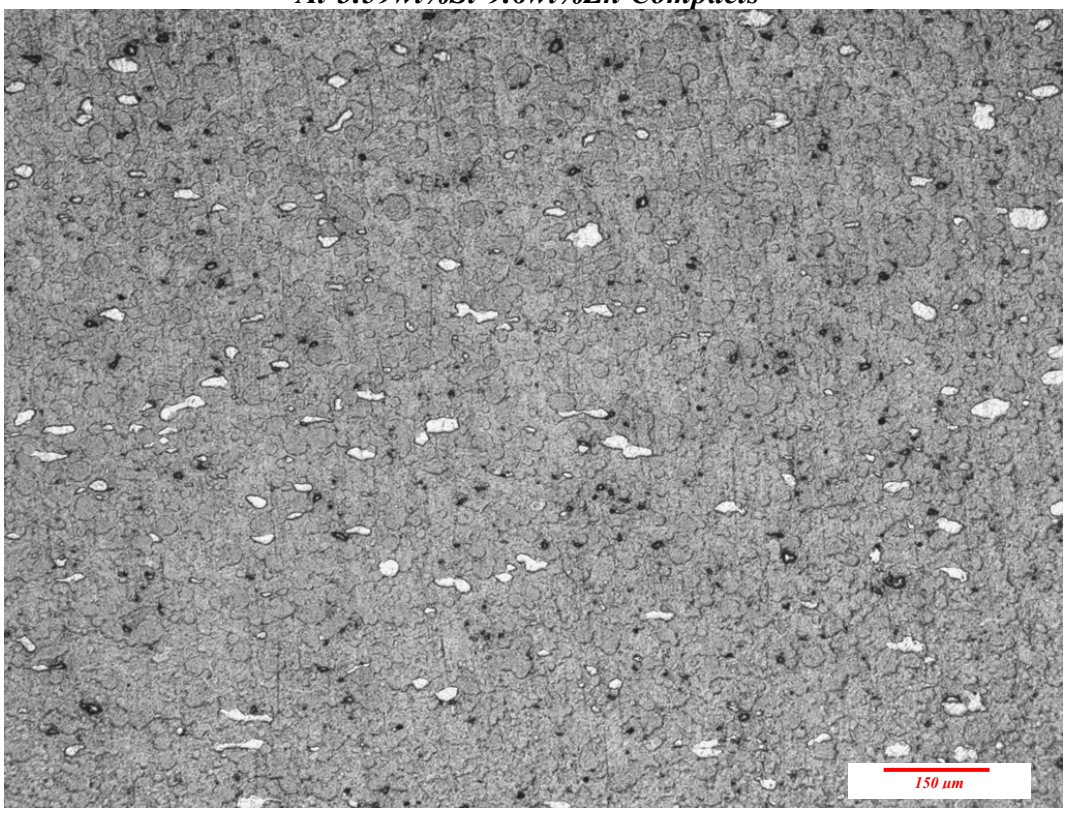

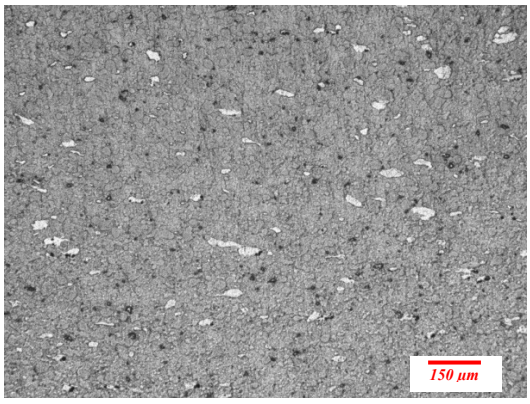

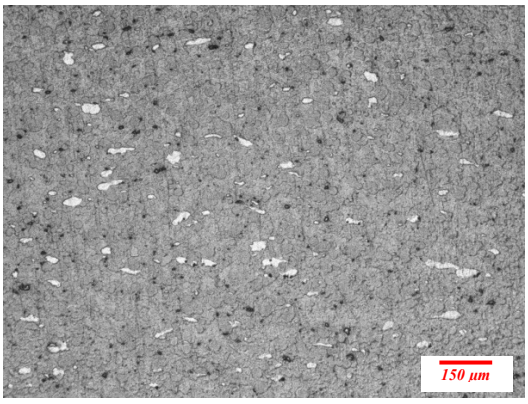

Al-3.59wt%Si-9.6wt%Zn Compacts

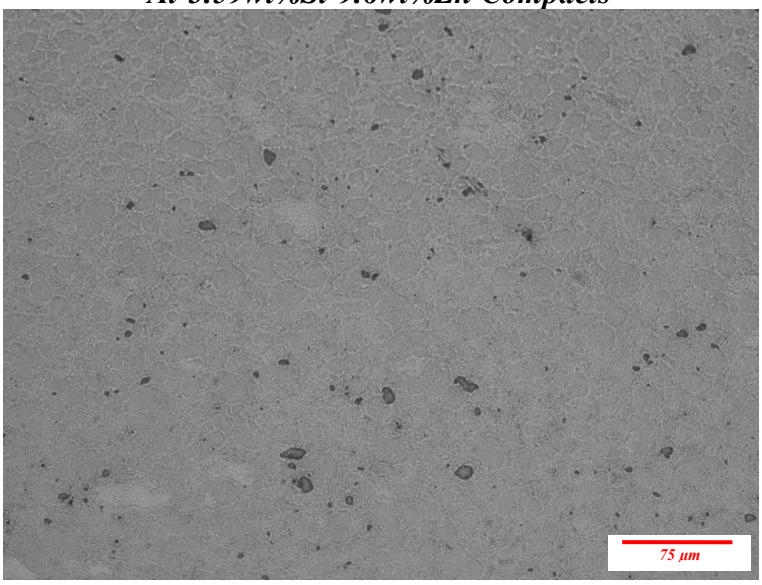

Al-3.59wt%Si-9.6wt%Zn Compacts

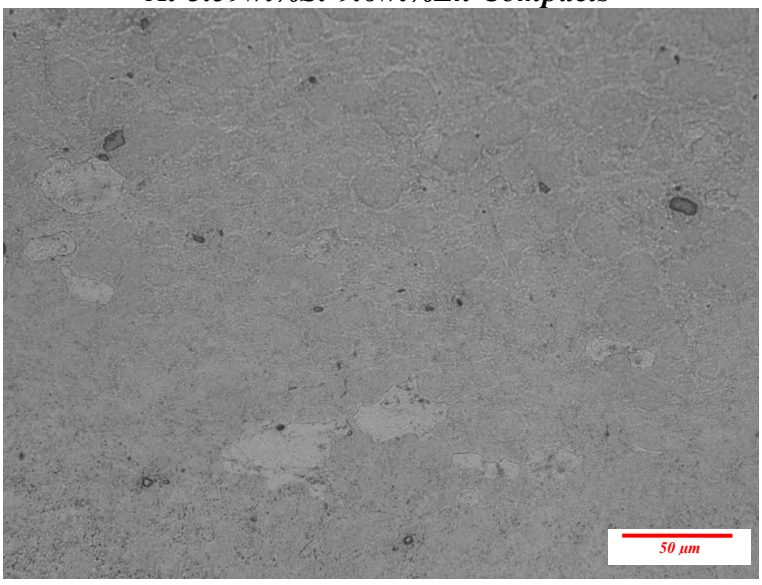

Al-3.59wt%Si-9.6wt%Zn 300 s

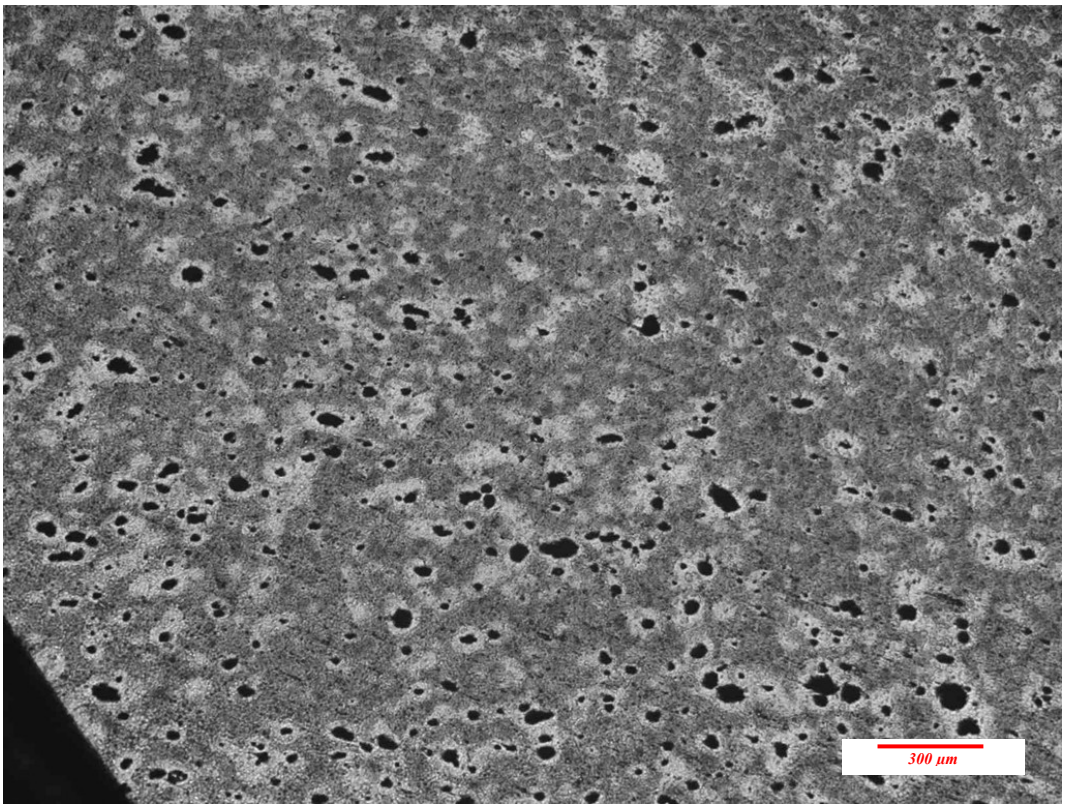

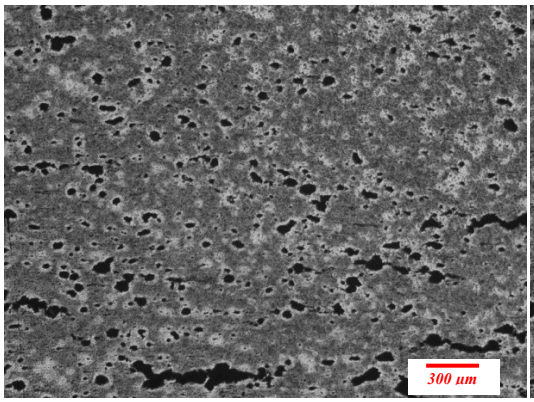

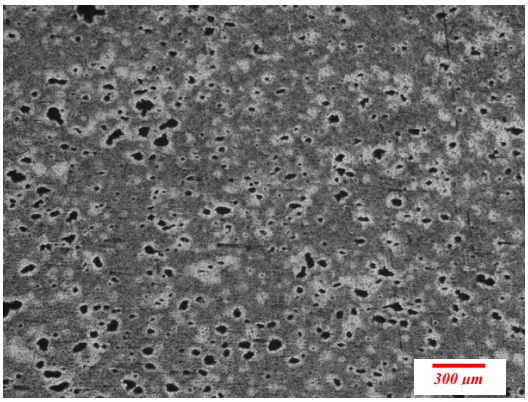

Al-3.59wt%Si-9.6wt%Zn 300 s

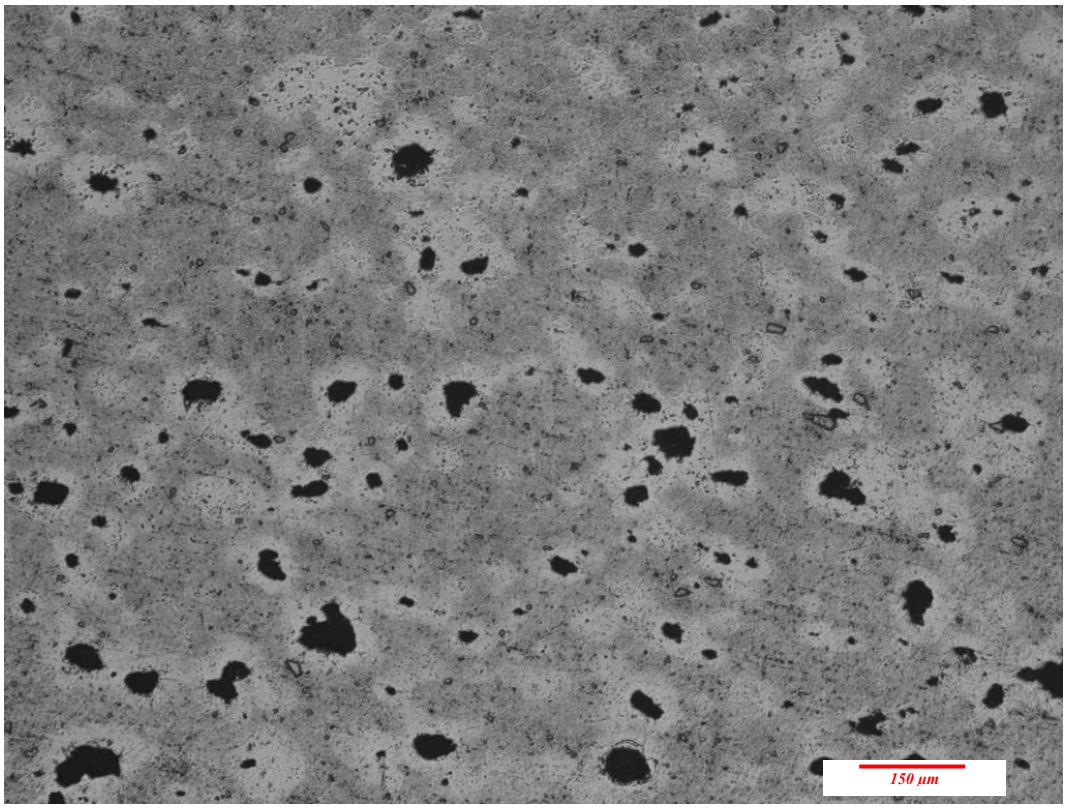

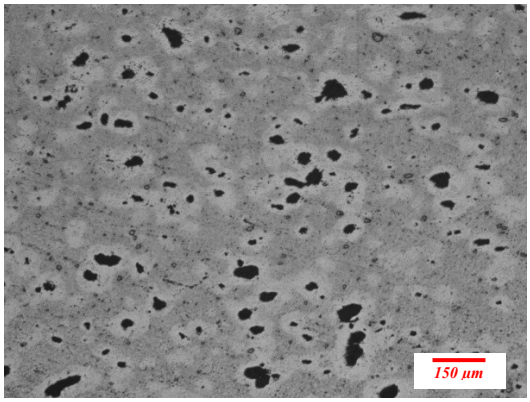

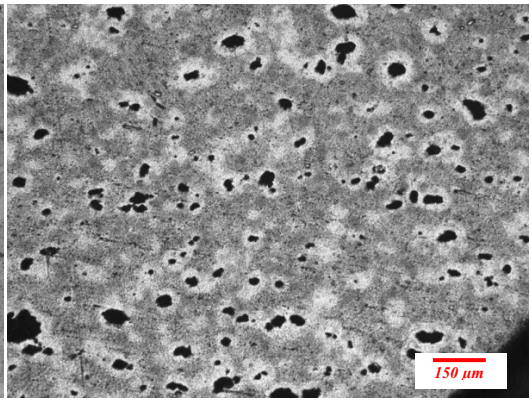

Al-3.59wt%Si-9.6wt%Zn 300 s

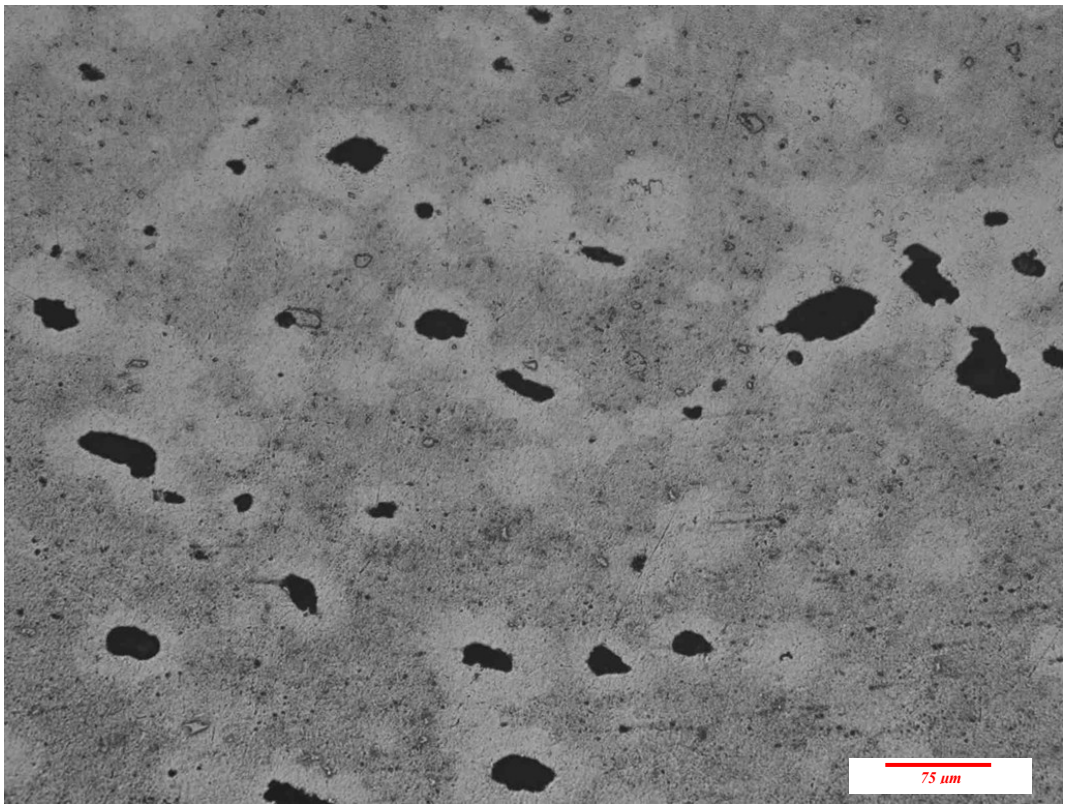

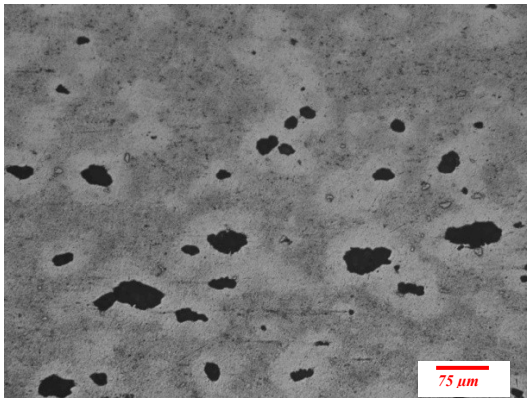

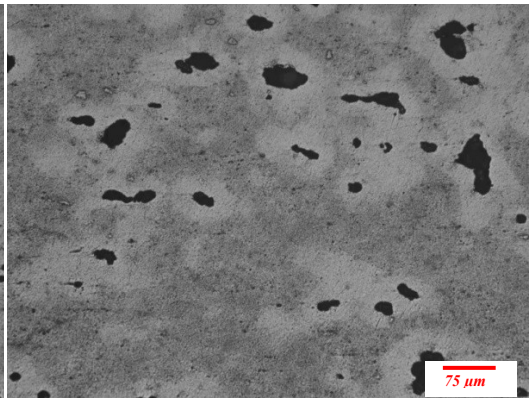

Al-3.59wt%Si-9.6wt%Zn 300 s

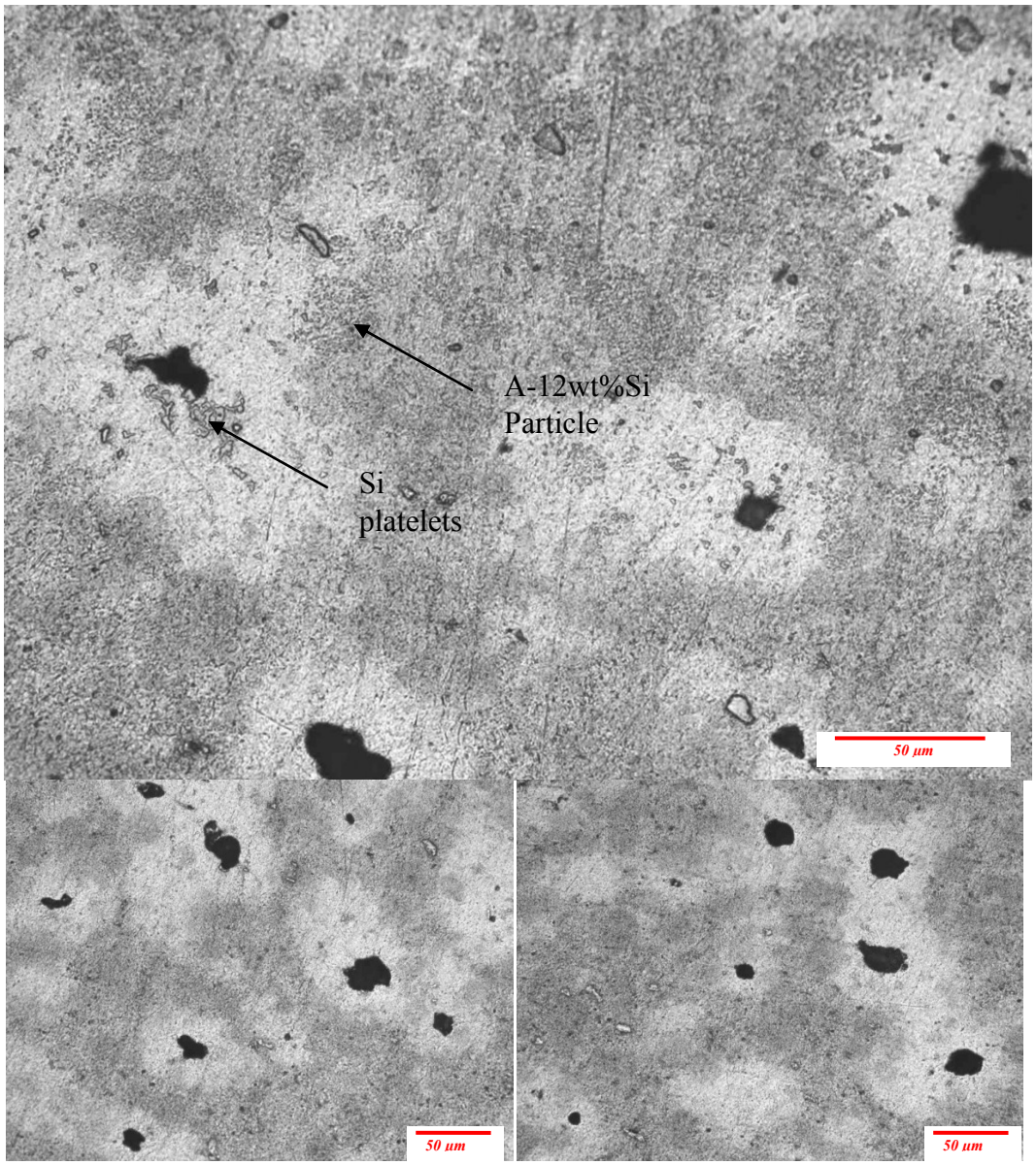

Al-3.59wt%Si-9.6wt%Zn 500 s

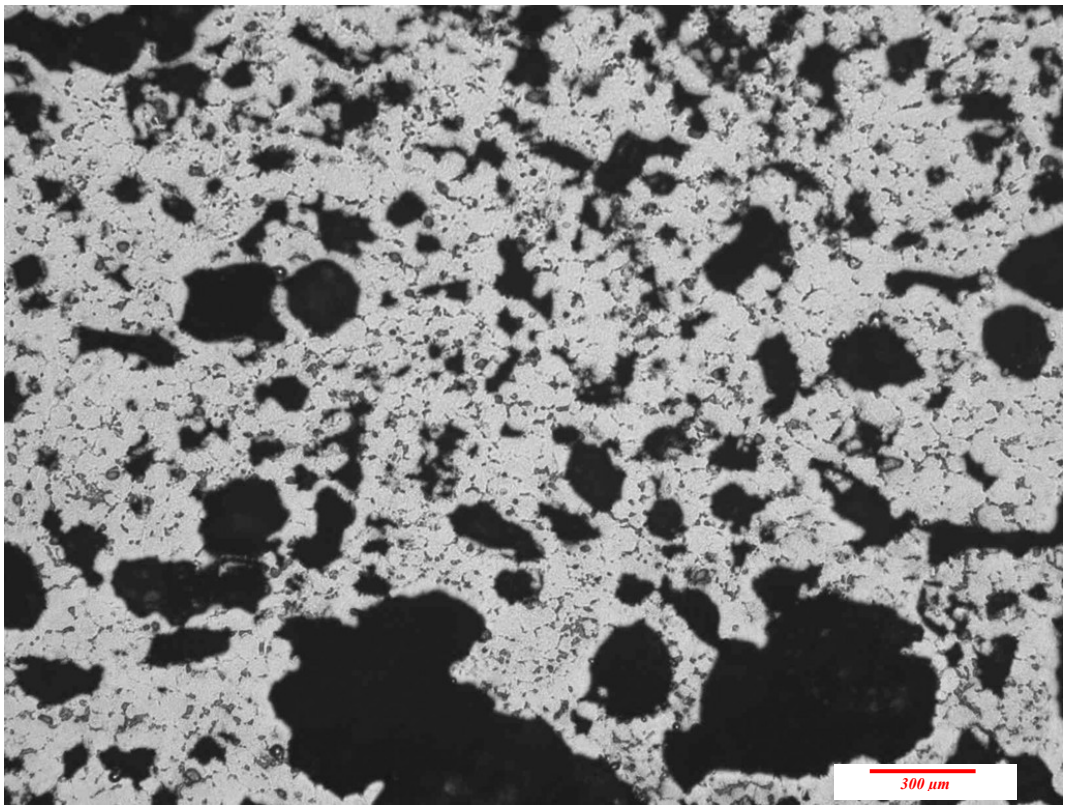

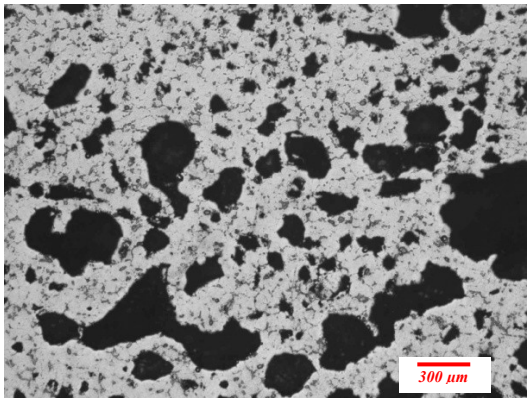

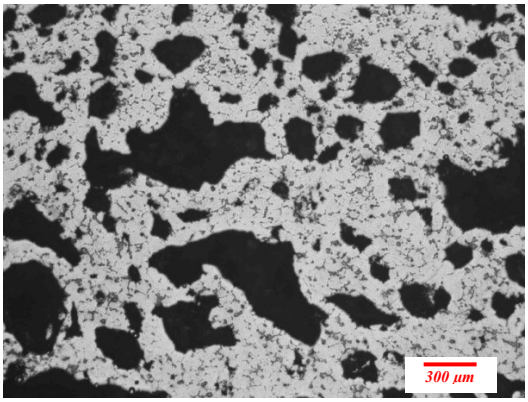

Al-3.59wt%Si-9.6wt%Zn 500 s

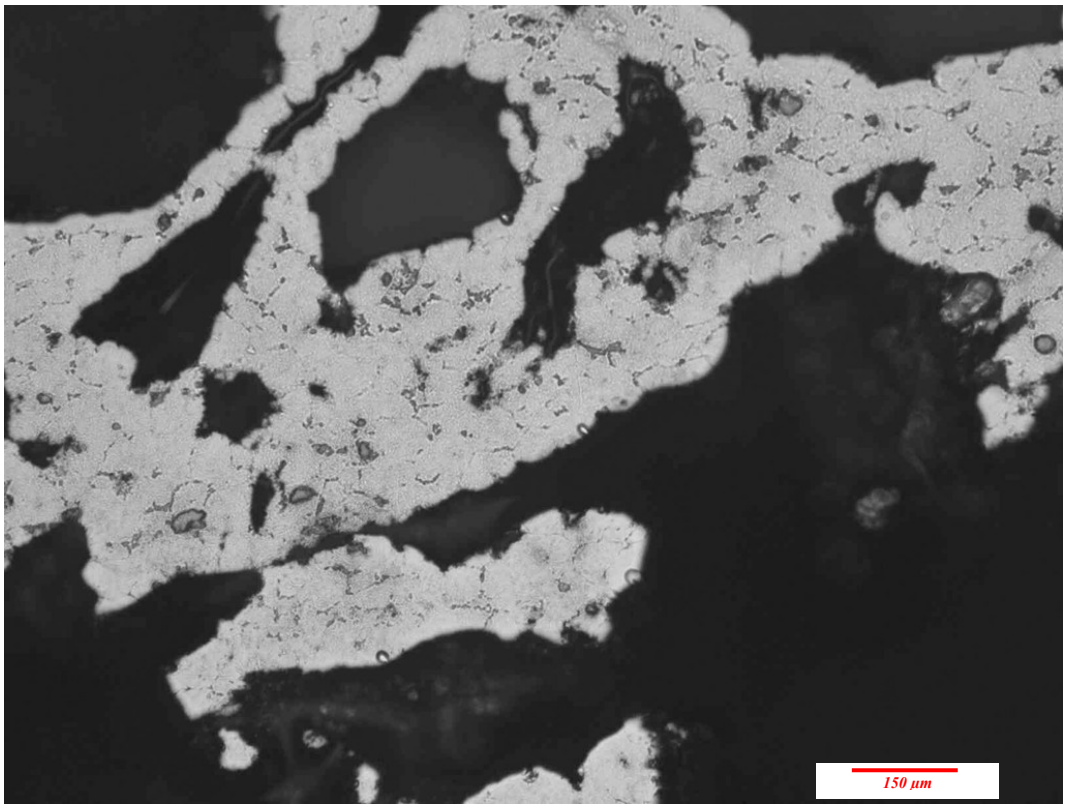

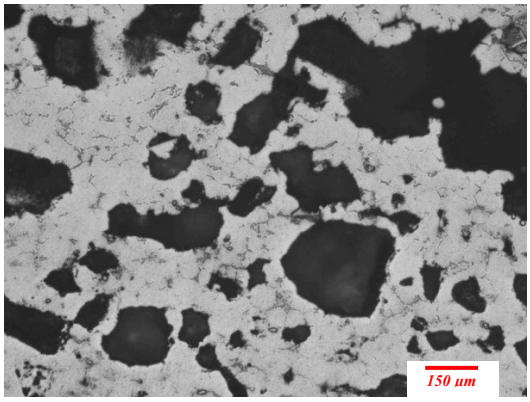

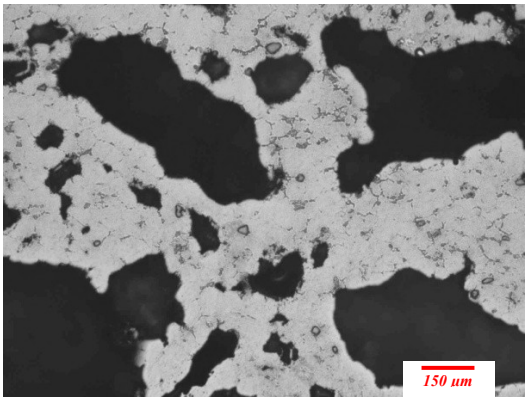

Al-3.59wt%Si-9.6wt%Zn 500 s

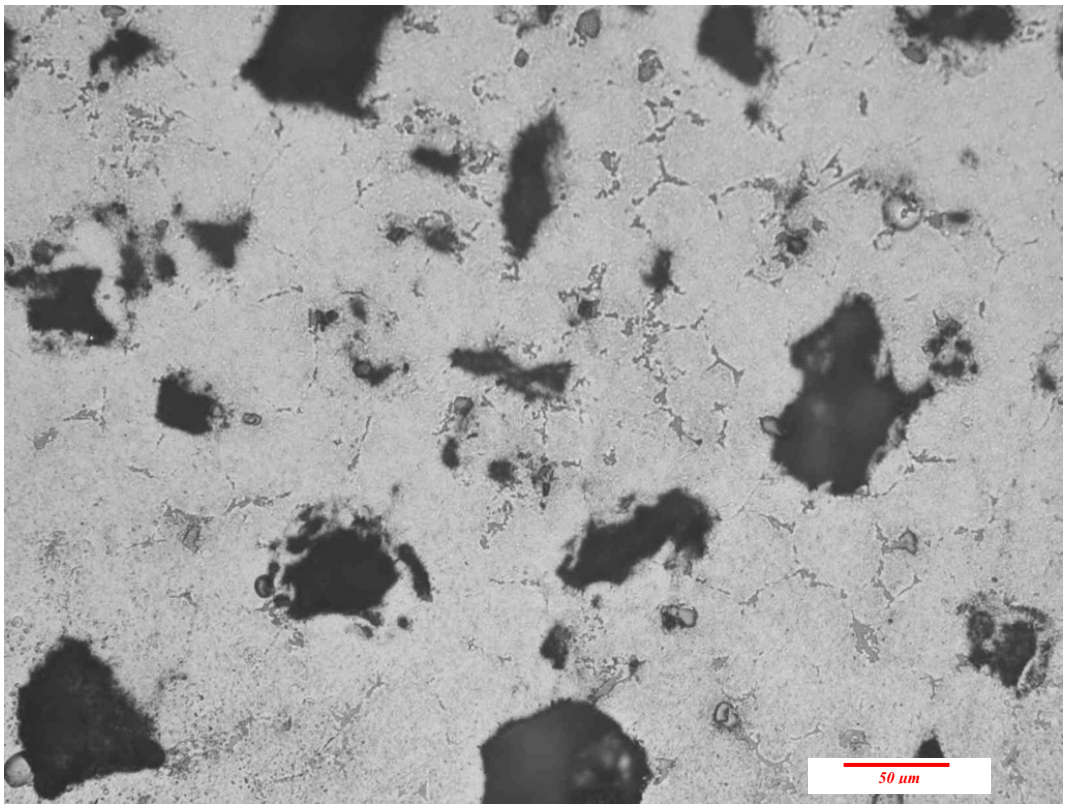

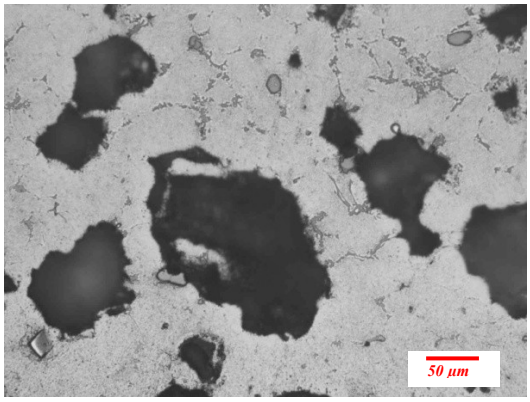

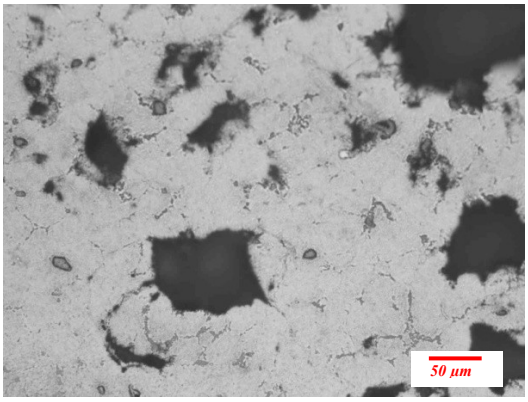

Al-3.59wt%Si-9.6wt%Zn 550 s

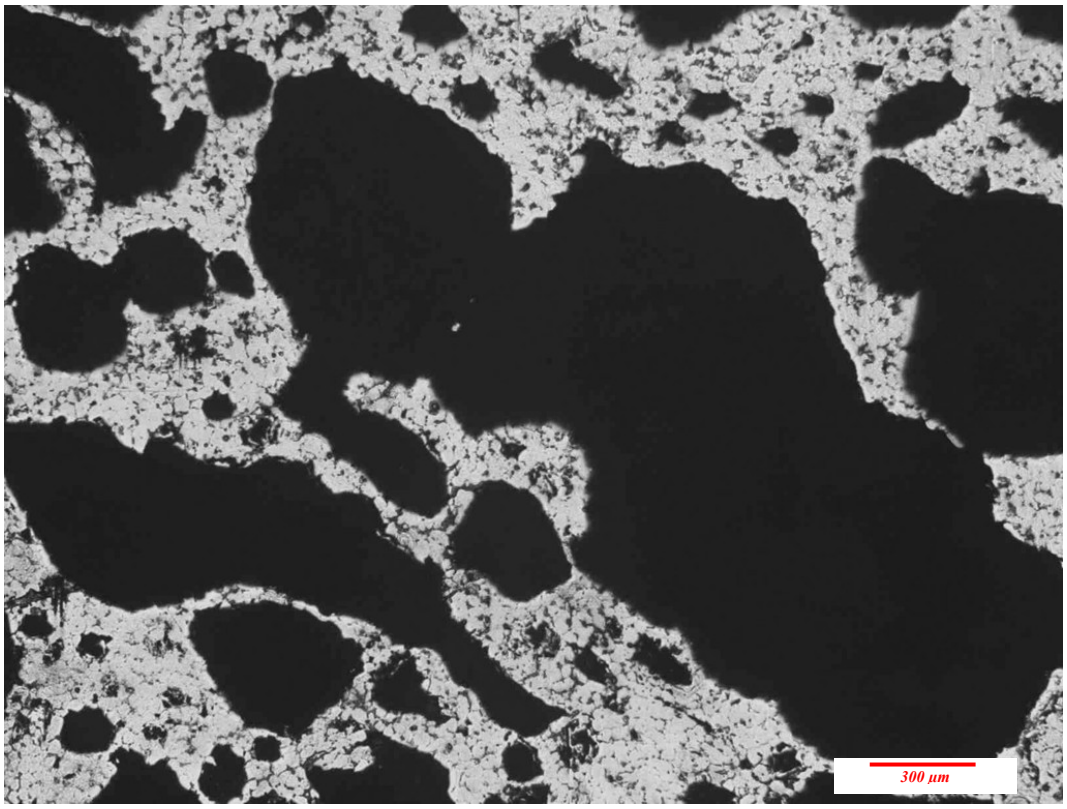

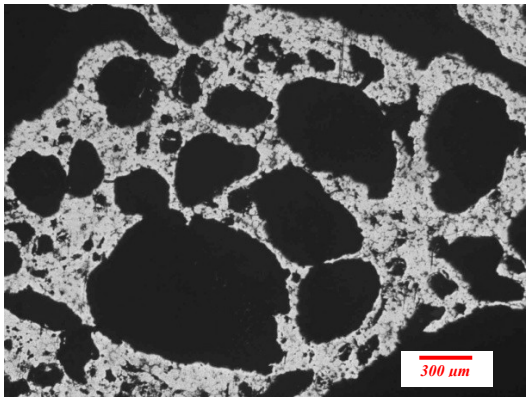

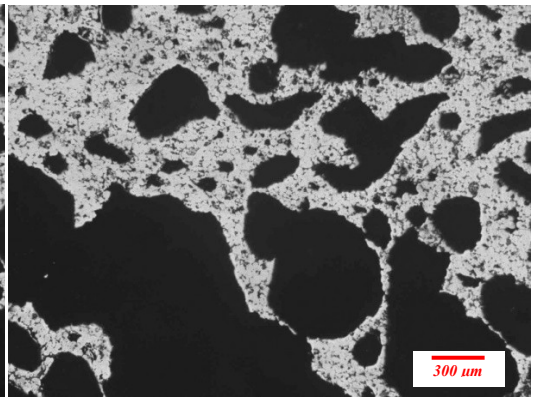

Al-3.59wt%Si-9.6wt%Zn 550 s

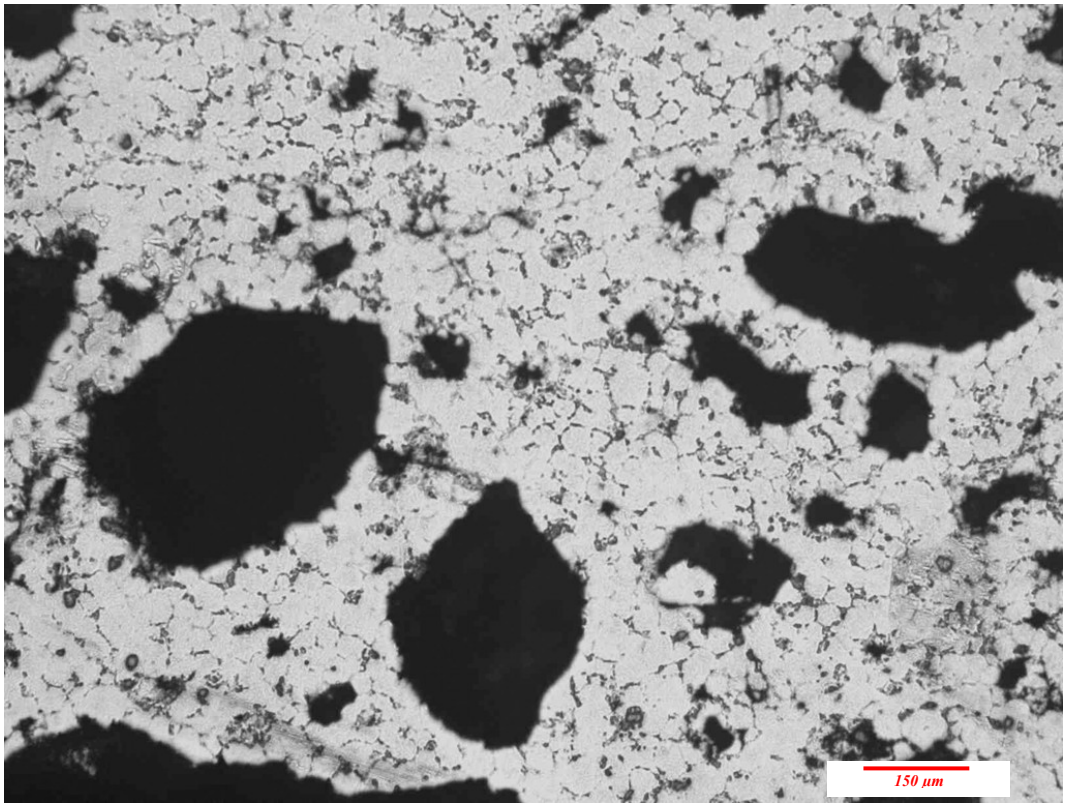

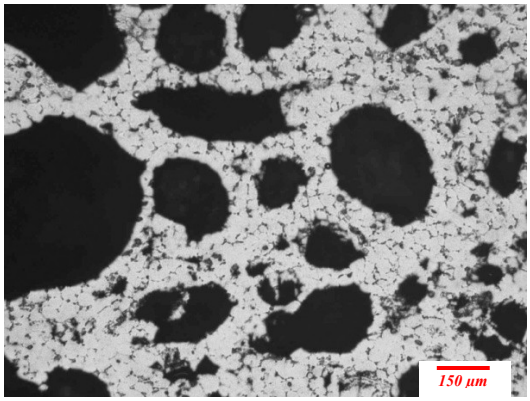

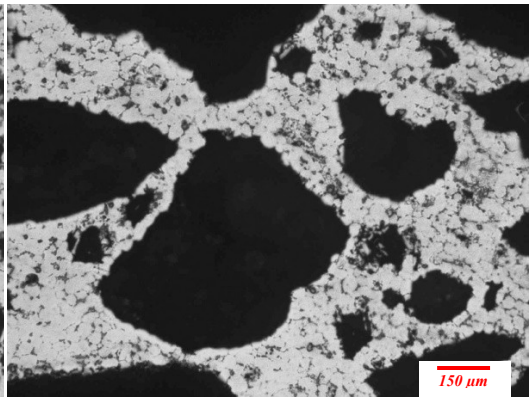

Al-3.59wt%Si-9.6wt%Zn 550 s

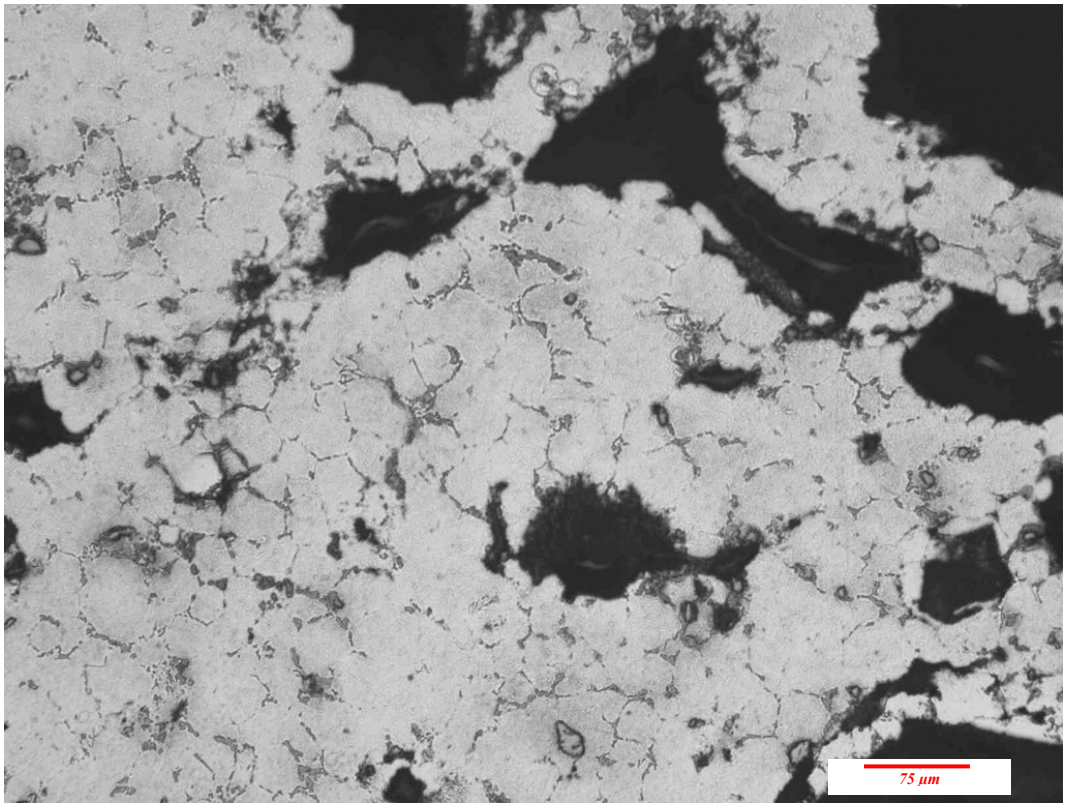

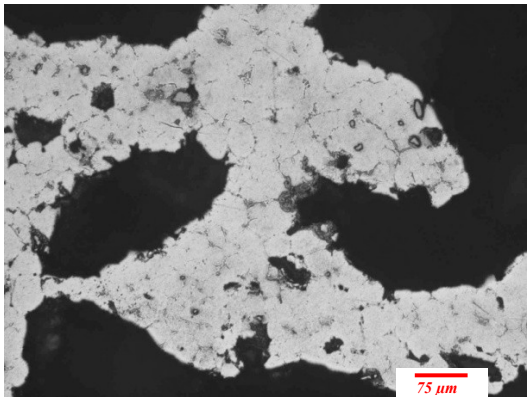

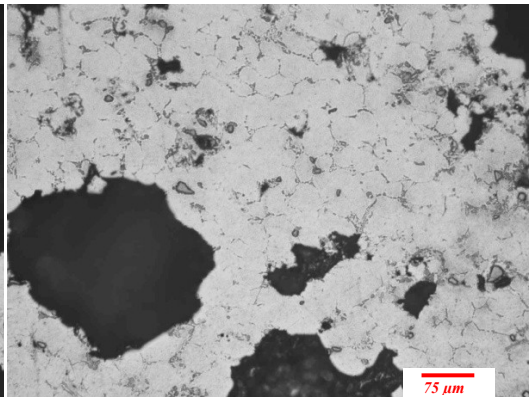

Al-3.59wt%Si-9.6wt%Zn 550 s

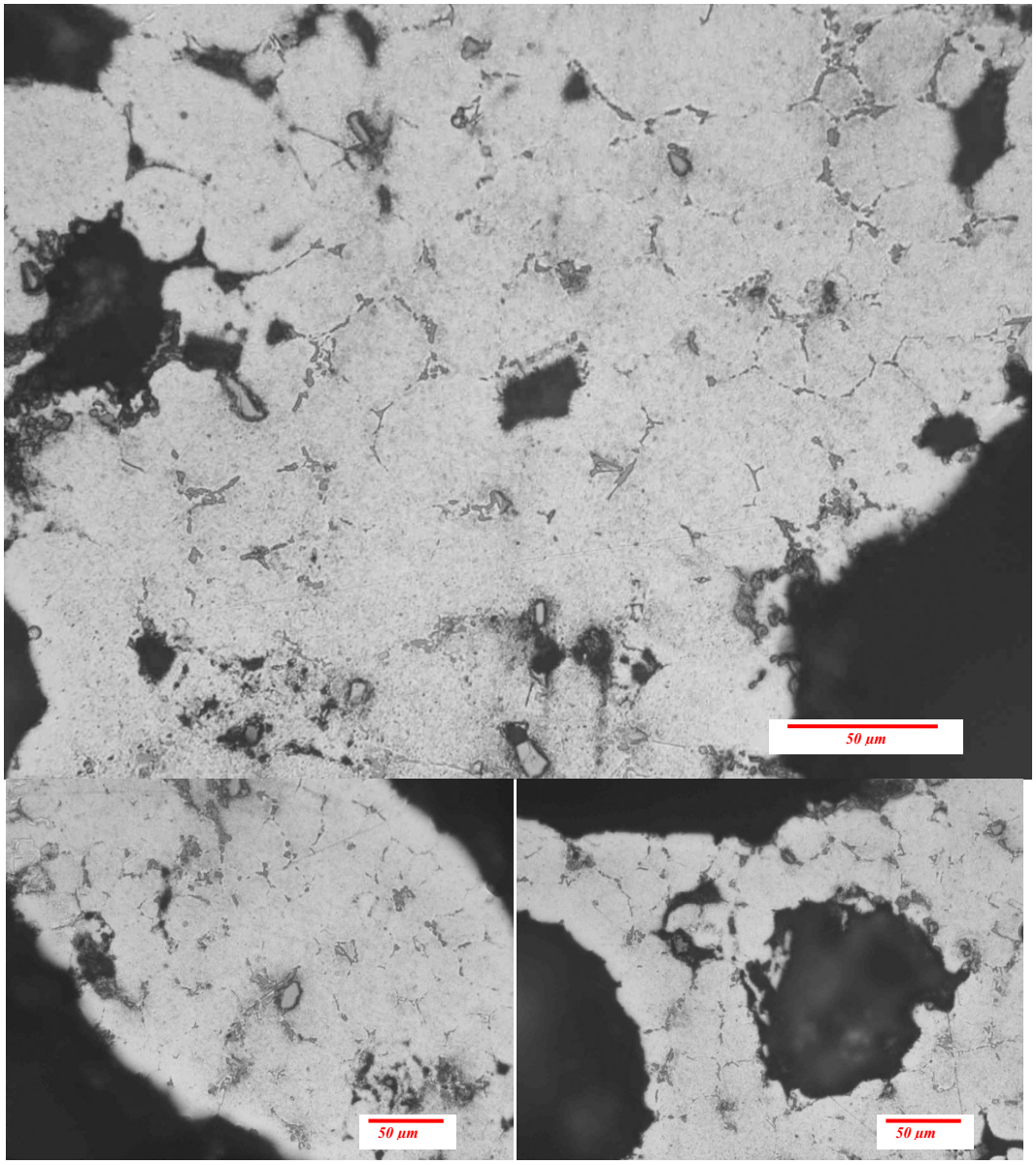

Al-3.59wt%Si-9.6wt%Zn 20 mm foaming curves

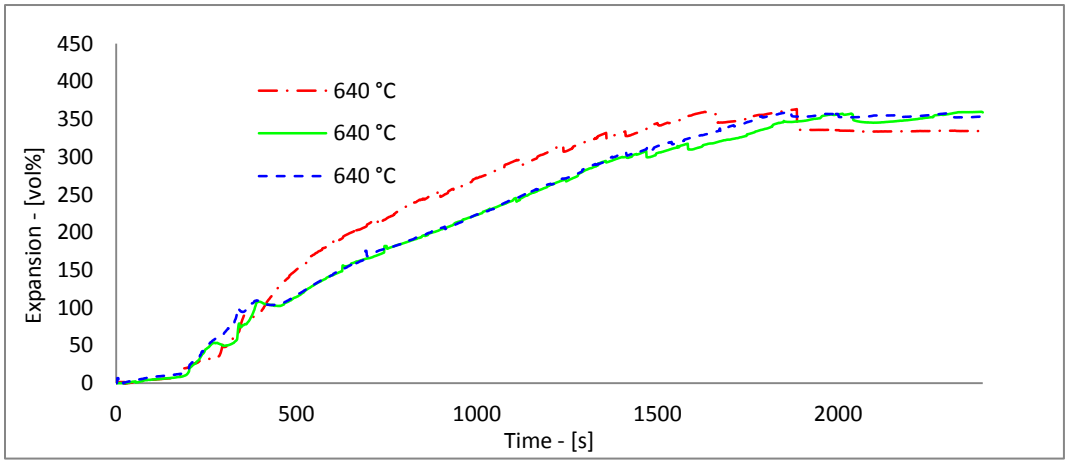

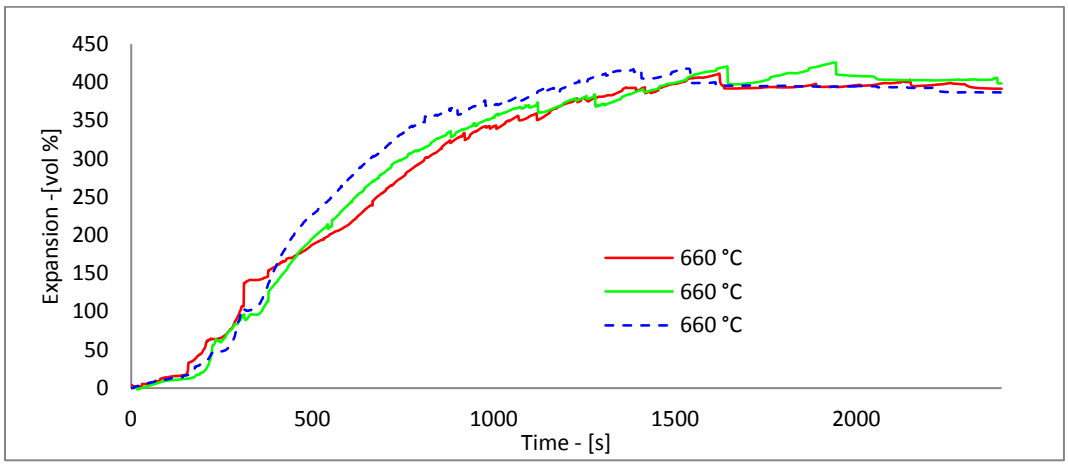

Al-3.59wt%Si-9.6wt%Zn 30 mm foaming curves

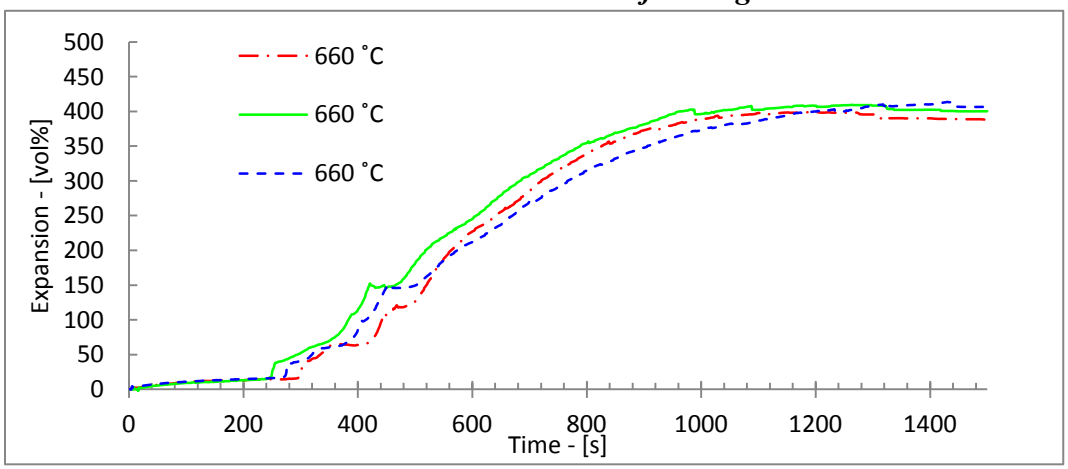

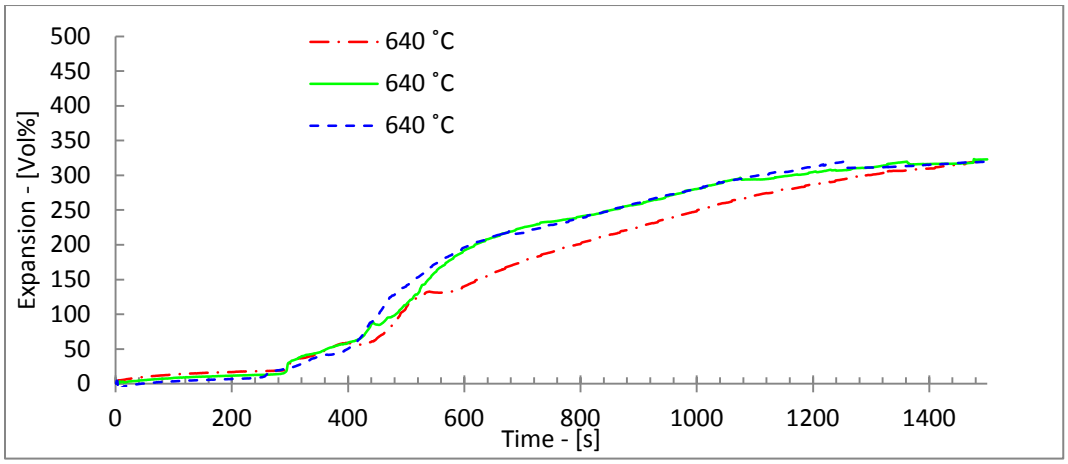

Al-2.4wt%Si-9.7wt%Zn 20 mm foaming curves

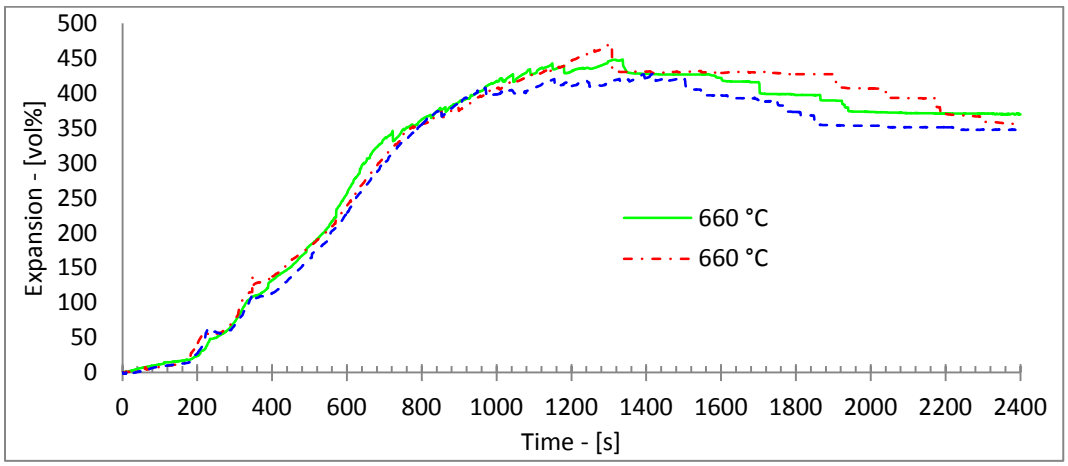

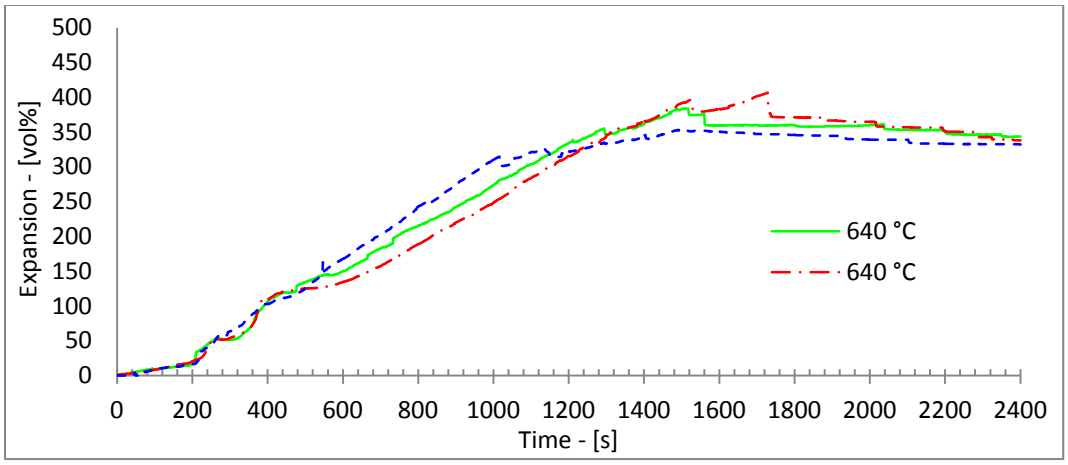

Al-2.4wt%Si-9.7wt%Zn 30 mm foaming curves

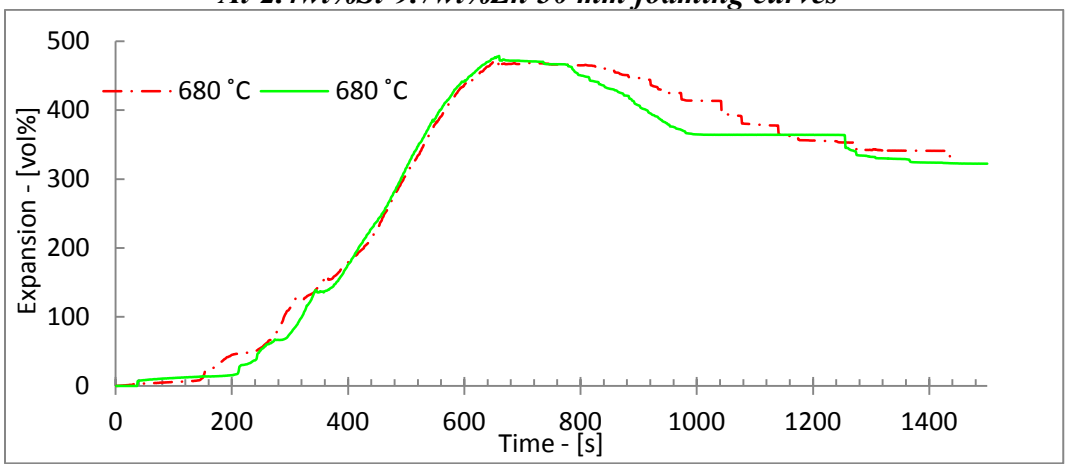

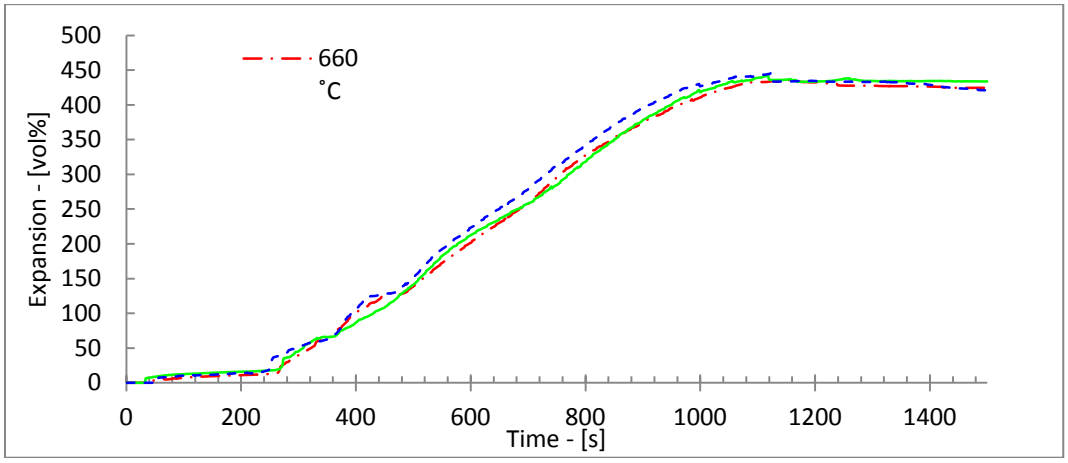

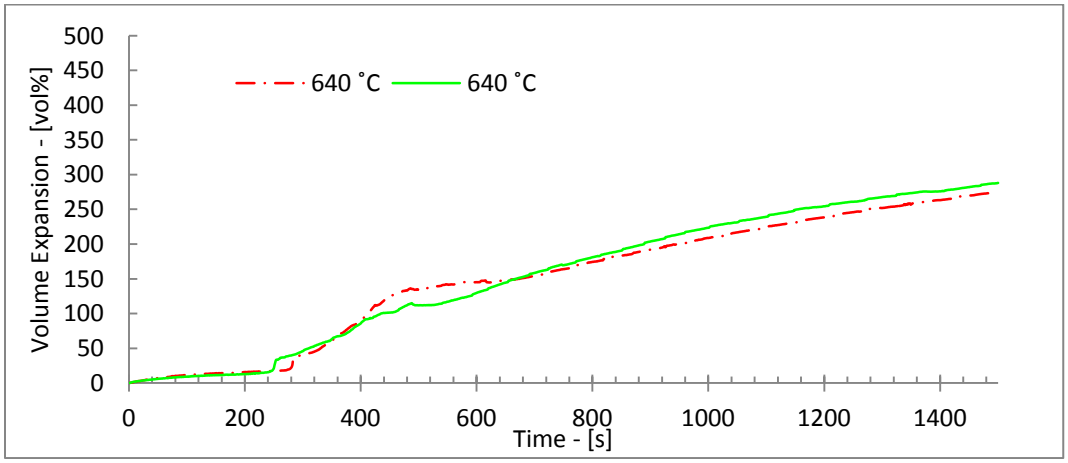

Al-3.5wt%Si-9.6wt%Zn foam Produced at 640 °C 720 s

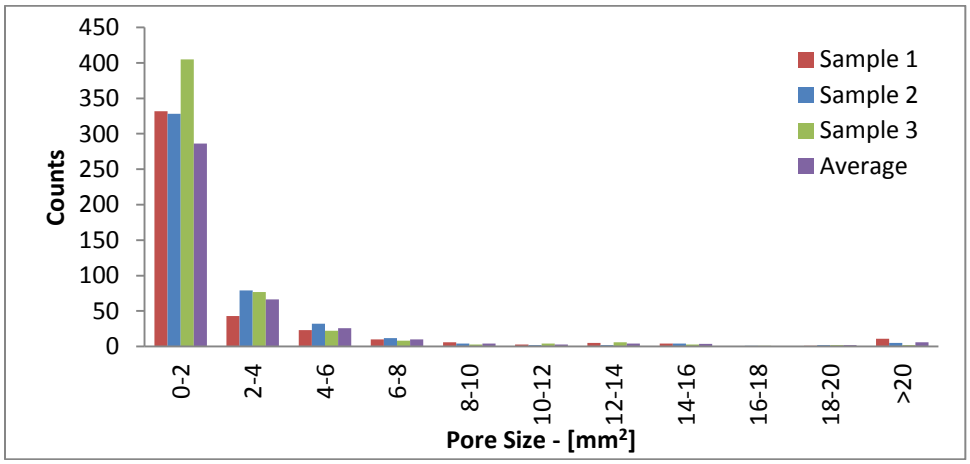

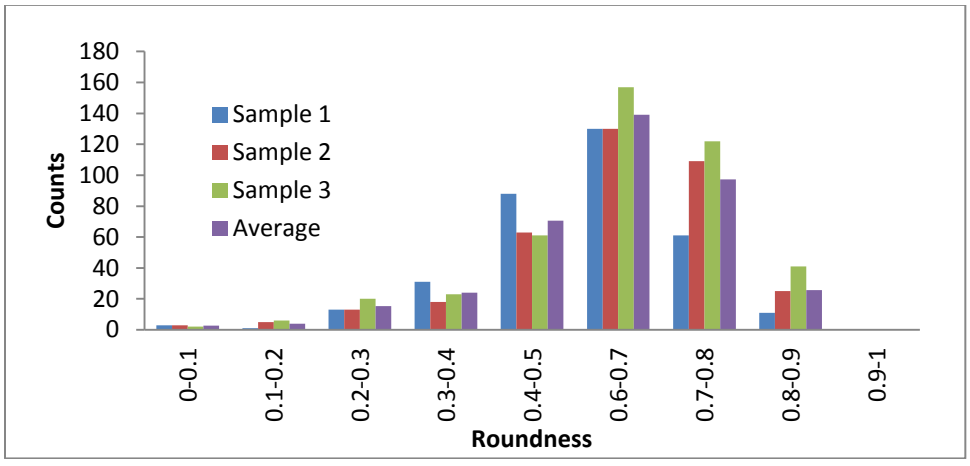

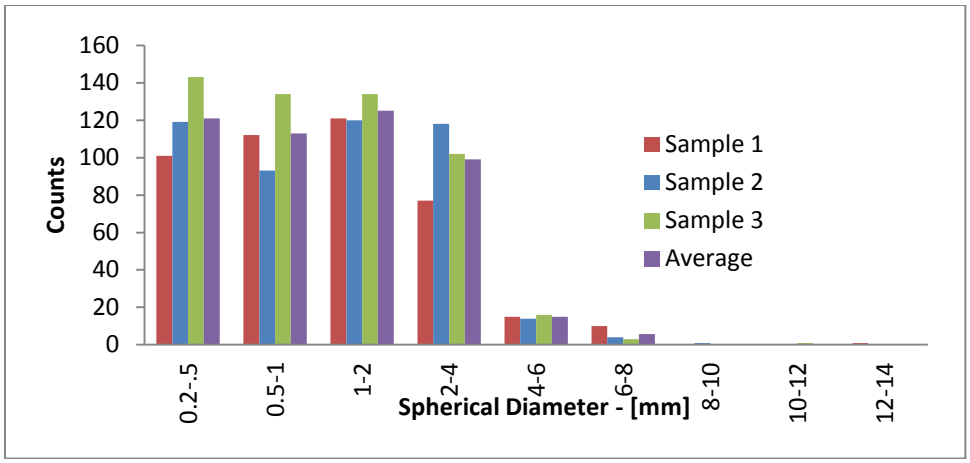

Al-3.5wt%Si-9.6wt%Zn foam Produced at 640 °C 1500 s

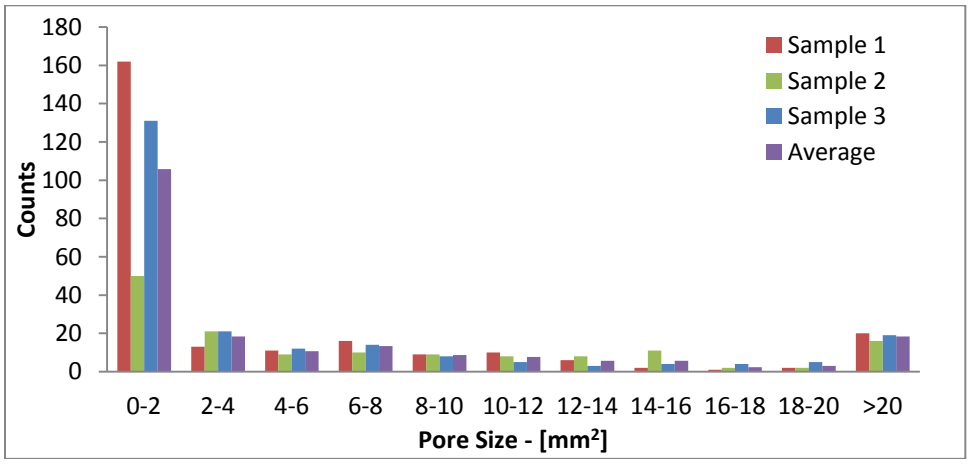

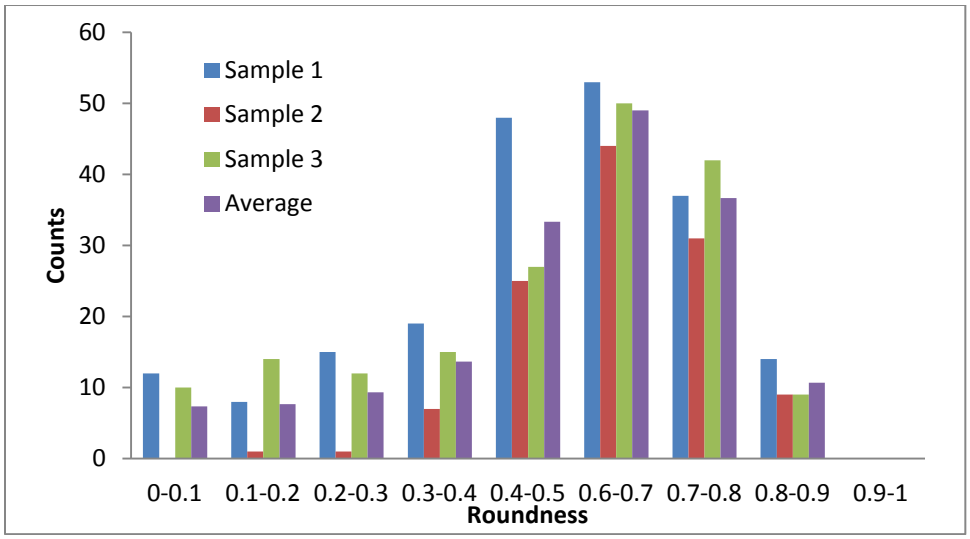
60
50
40
30
20
10
0
Counts
Sample 1
Sample 2
Sample 3
Average
0-0.1
0.1-0.2
0.2-0.3
0.3-0.4
0.4-0.5
0.6-0.7
0.7-0.8
0.8-0.9
0.9-1
Roundness

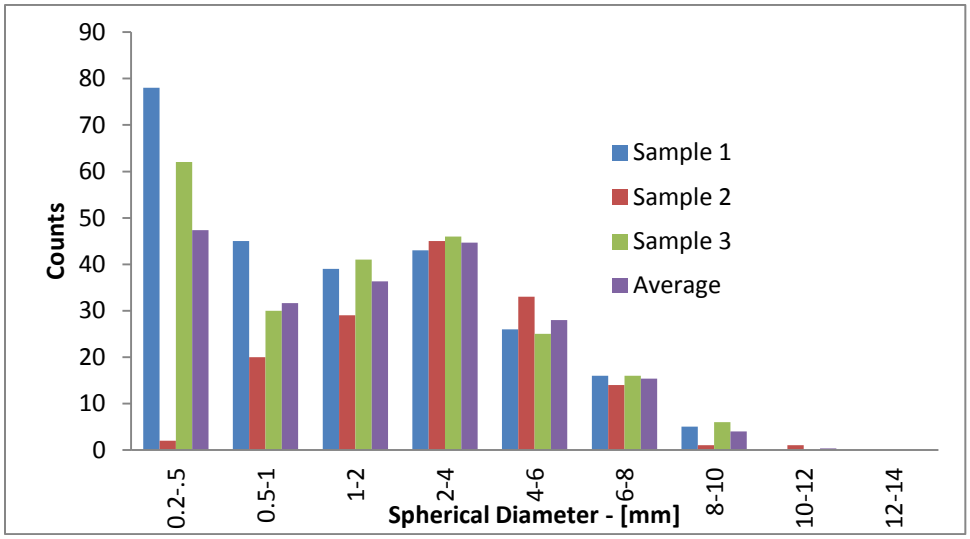
90
80
70
60
50
40
30
20
10
0
Counts
Sample 1
Sample 2
Sample 3
Average
0.2-.5
0.5-1
1-2
2-4
4-6
6-8
8-10
10-12
12-14
Spherical Diameter - [mm]

Al-3.5wt%Si-9.6wt%Zn foam Produced at 660 °C 1200 s

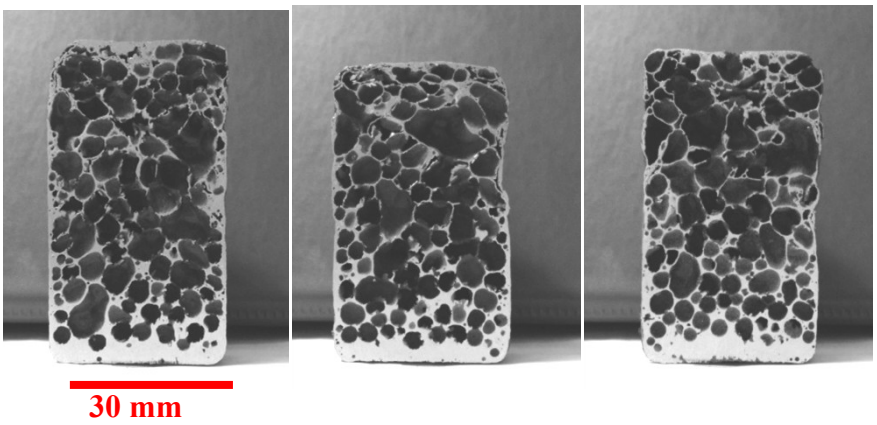

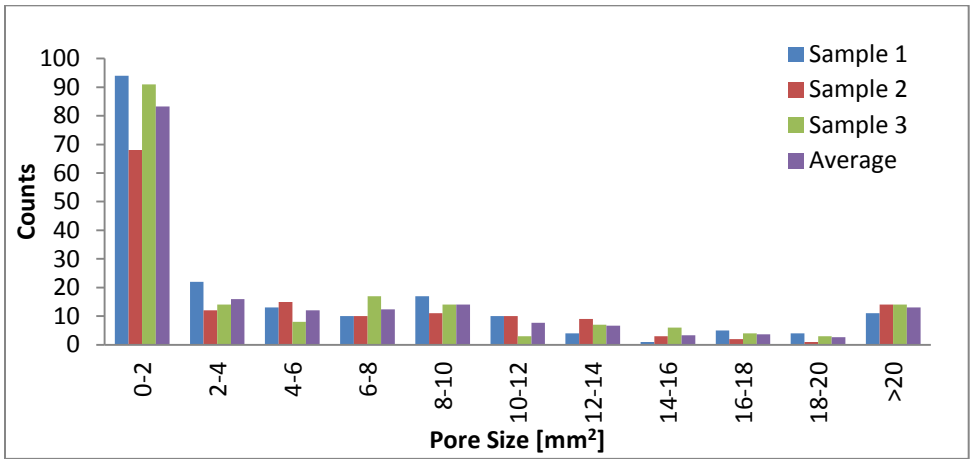

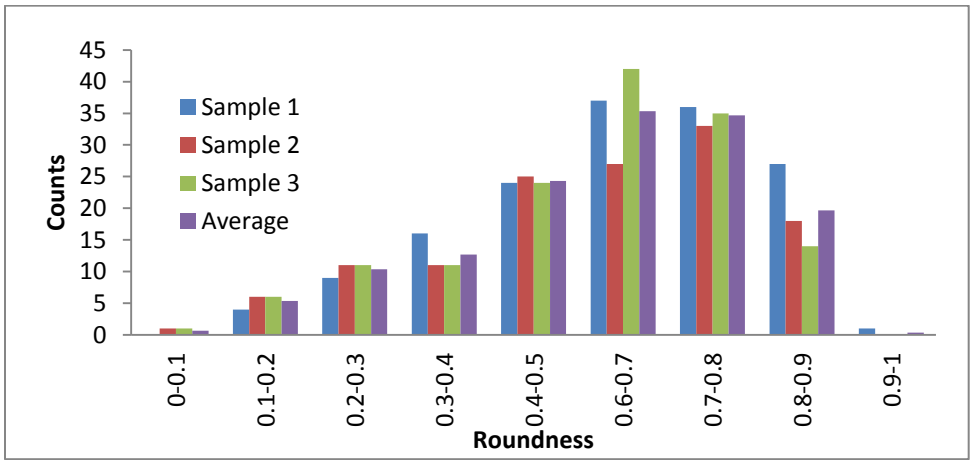

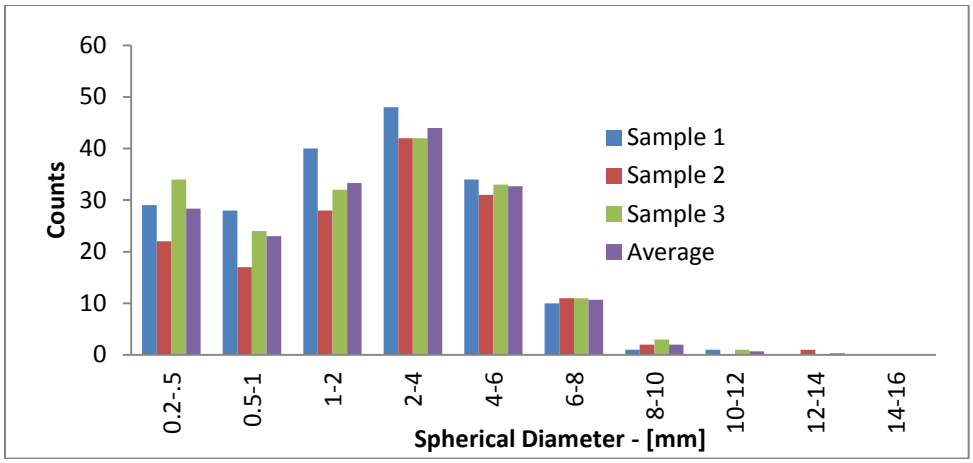

Al-3.5wt%Si-9.6wt%Zn foam Produced at 660 °C 1500 s

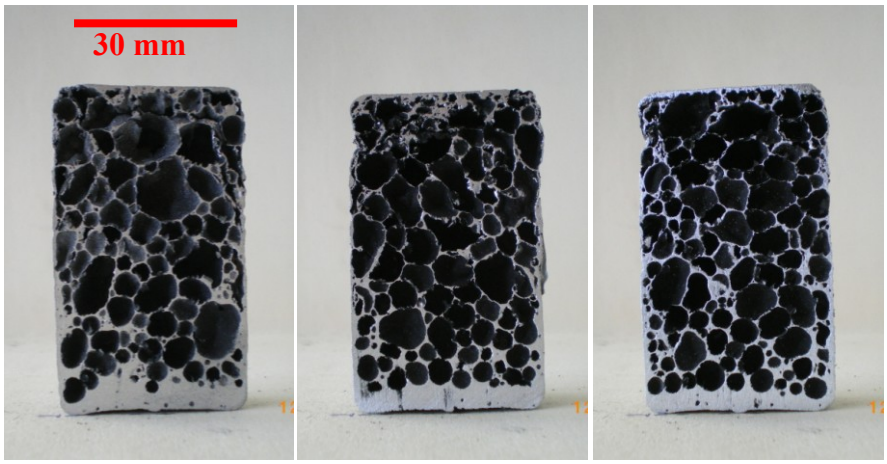

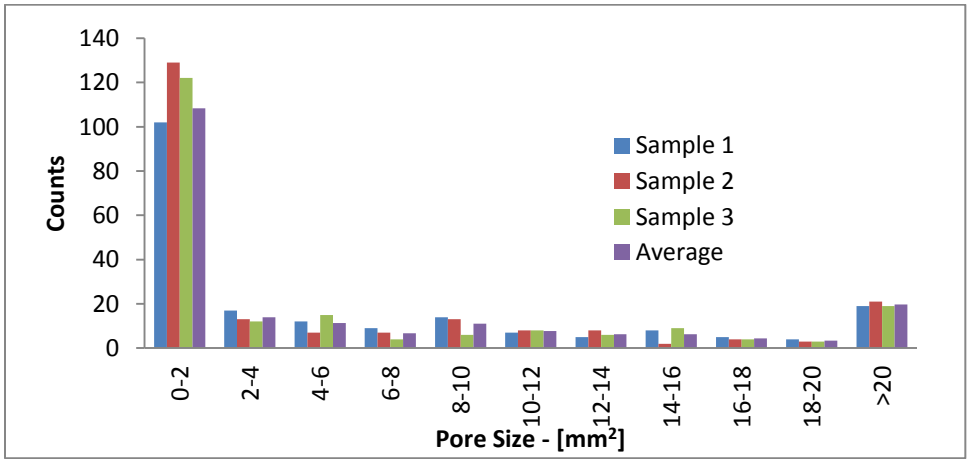

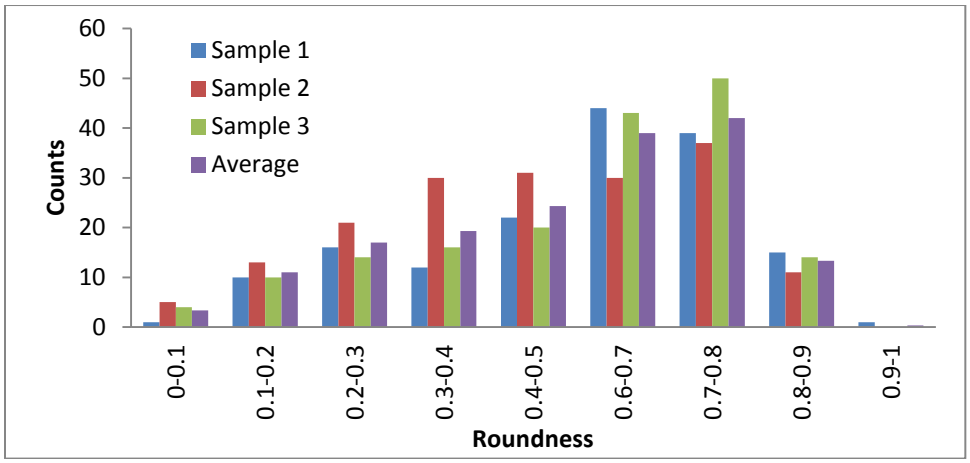

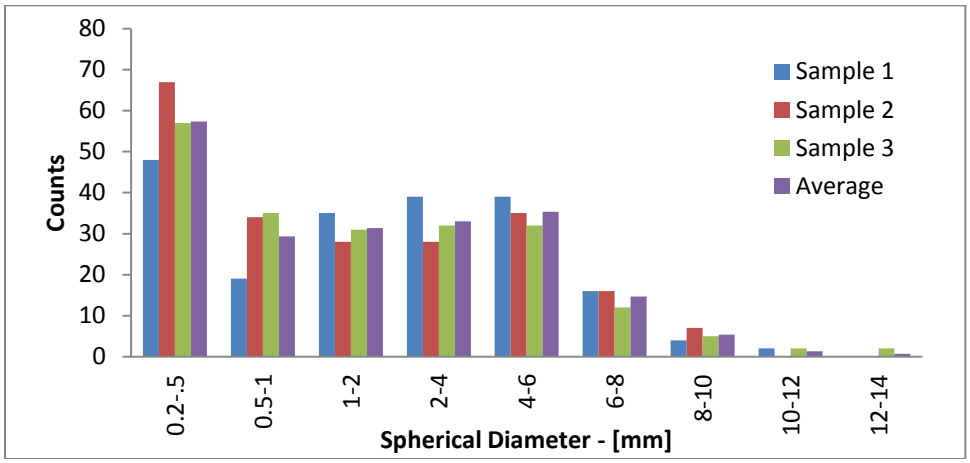

Al-2.4wt%Si-9.7wt%Zn foam Produced at 660 °C 1200 s

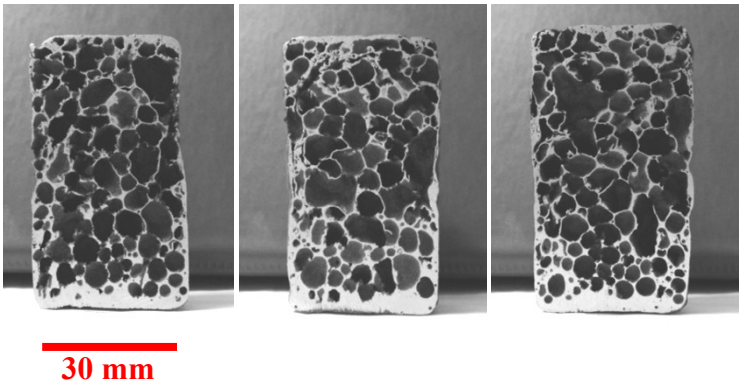

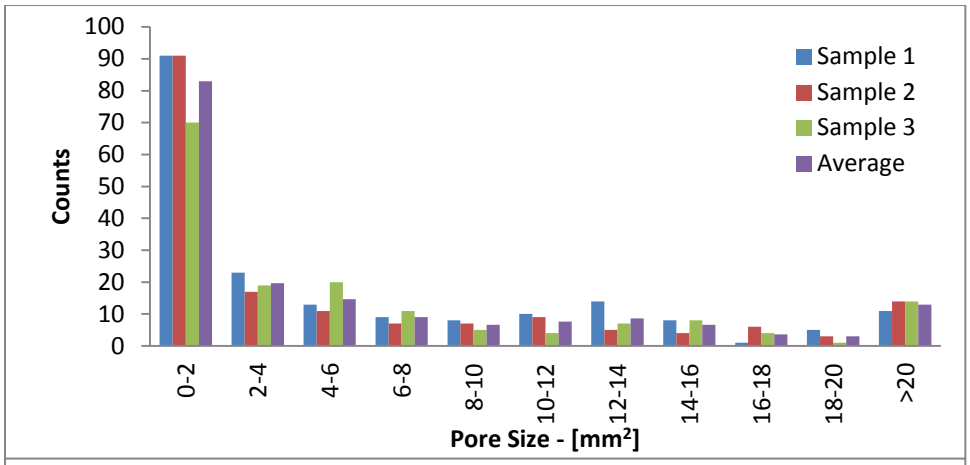
Counts
Sample 1
Sample 2
Sample 3
Average
0-2
2-4
4-6
6-8
8-10
10-12
12-14
14-16
16-18
18-20
>20
Pore Size - [mm²]

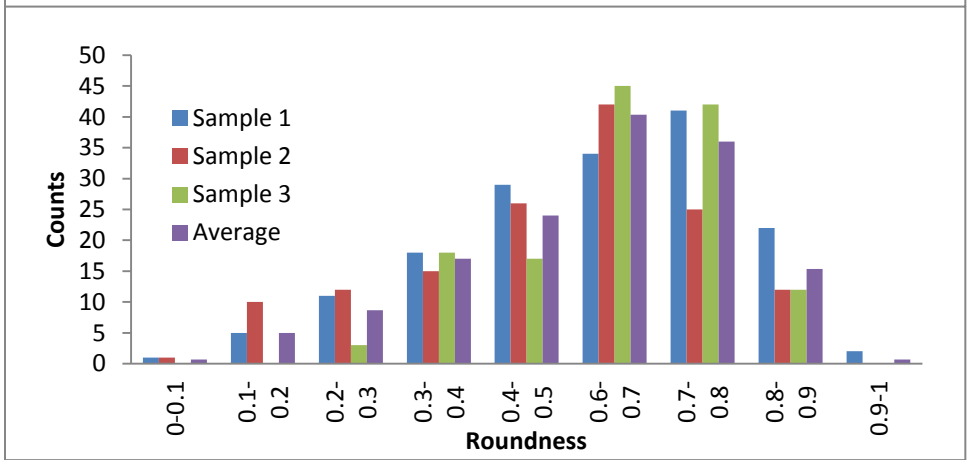
Counts
Sample 1
Sample 2
Sample 3
Average
0-0.1
0.1-0.2
0.2-0.3
0.3-0.4
0.4-0.5
0.6-0.7
0.7-0.8
0.8-0.9
0.9-1
Roundness

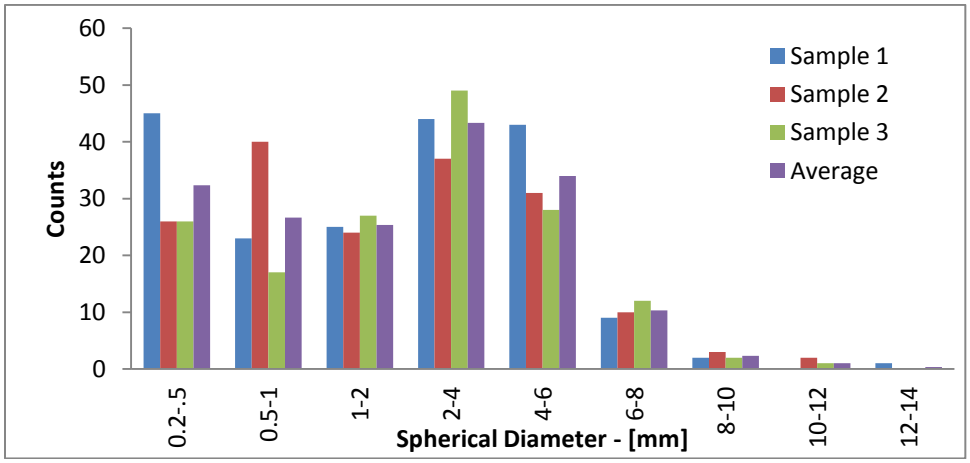
Counts
Sample 1
Sample 2
Sample 3
Average
0.2-.5
0.5-1
1-2
2-4
4-6
6-8
8-10
10-12
12-14
Spherical Diameter - [mm]

Al-2.4wt%Si-9.7wt%Zn foam Produced at 660 °C 1500 s

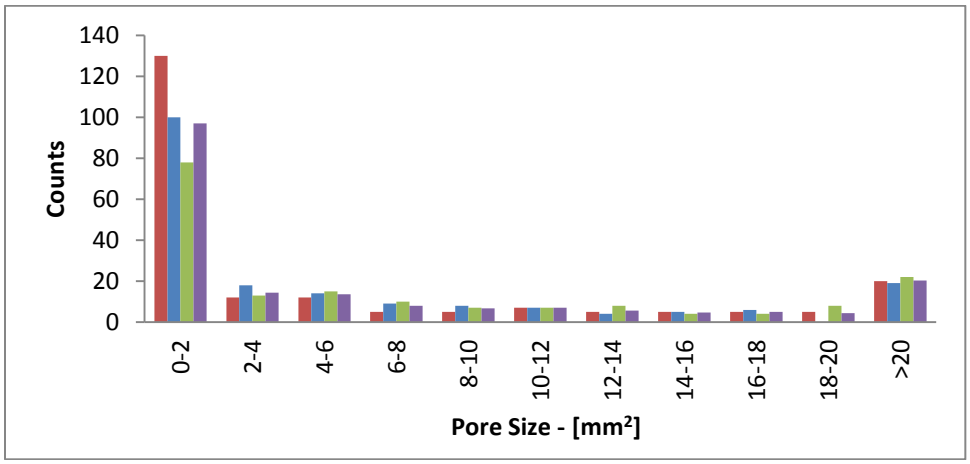

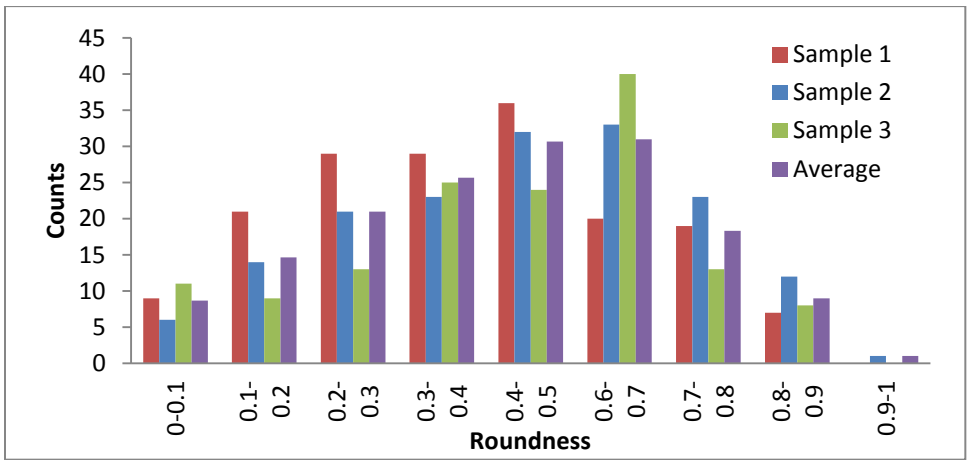

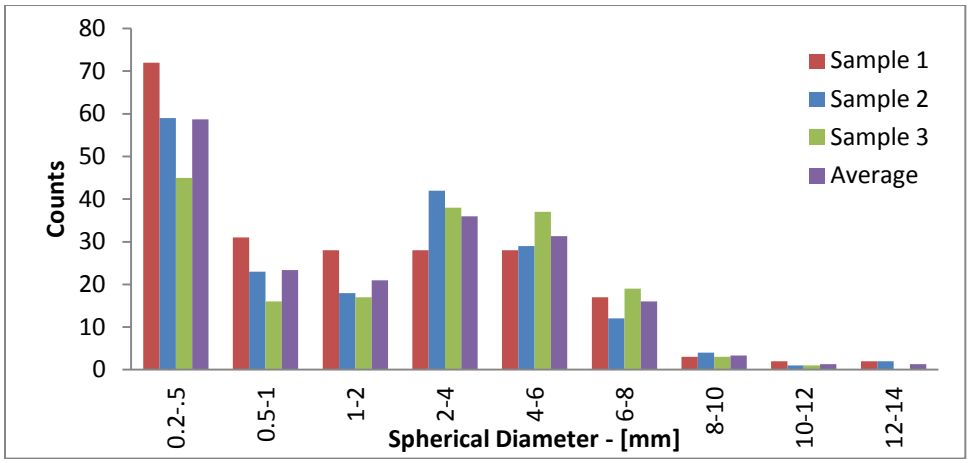
80
70
60
50
40
30
20
10
0
Counts
Sample 1
Sample 2
Sample 3
Average
0.2-.5
0.5-1
1-2
2-4
4-6
6-8
8-10
10-12
12-14
Spherical Diameter - [mm]